

REPORT DOCUMENTATION PAGE			2	Form Approved OMB NO. 0704-0188	
<p>The public reporting burden for this collection of information is estimated to average 1 hour per response, including the time for reviewing instructions, searching existing data sources, gathering and maintaining the data needed, and completing and reviewing the collection of information. Send comments regarding this burden estimate or any other aspect of this collection of information, including suggestions for reducing this burden, to Washington Headquarters Services, Directorate for Information Operations and Reports, 1215 Jefferson Davis Highway, Suite 1204, Arlington VA, 22202-4302. Respondents should be aware that notwithstanding any other provision of law, no person shall be subject to any penalty for failing to comply with a collection of information if it does not display a currently valid OMB control number.</p> <p>PLEASE DO NOT RETURN YOUR FORM TO THE ABOVE ADDRESS.</p>					
1. REPORT DATE (DD-MM-YYYY) 24-08-2014		2. REPORT TYPE Ph.D. Dissertation		3. DATES COVERED (From - To) -	
4. TITLE AND SUBTITLE Structural Characterisation of Proteins from the Peroxiredoxin Family			5a. CONTRACT NUMBER W911NF-12-1-0554		
			5b. GRANT NUMBER		
			5c. PROGRAM ELEMENT NUMBER 611102		
6. AUTHORS Amy Phillips			5d. PROJECT NUMBER		
			5e. TASK NUMBER		
			5f. WORK UNIT NUMBER		
7. PERFORMING ORGANIZATION NAMES AND ADDRESSES University of Canterbury 20 Kirkwood Ave Ilam			8. PERFORMING ORGANIZATION REPORT NUMBER		
9. SPONSORING/MONITORING AGENCY NAME(S) AND ADDRESS (ES) U.S. Army Research Office P.O. Box 12211 Research Triangle Park, NC 27709-2211			10. SPONSOR/MONITOR'S ACRONYM(S) ARO		
			11. SPONSOR/MONITOR'S REPORT NUMBER(S) 61663-CH.4		
12. DISTRIBUTION AVAILABILITY STATEMENT Approved for public release; distribution is unlimited.					
13. SUPPLEMENTARY NOTES The views, opinions and/or findings contained in this report are those of the author(s) and should not be construed as an official Department of the Army position, policy or decision, unless so designated by other documentation.					
14. ABSTRACT The oligomerisation of protein subunits is an area of much research interest, in particular the relationship to protein function. In the last decade, the potential to control the interactions involved in order to design constructs with tuneable oligomeric properties in vitro has been pursued. The subject of this thesis is the quaternary structure of members of the peroxiredoxin family, which have been seen to assume an intriguing array of organisations. Human Peroxiredoxin 3 (HsPrx3) and Mycobacterium tuberculosis alkyl hydroperoxide reductase (MtAhpE) catalyse the detoxification of reactive species, preferentially hydrogen peroxide and peroxynitrite respectively, and form an					
15. SUBJECT TERMS peroxiredoxin, tecton, supramolecular assembly, TEM					
16. SECURITY CLASSIFICATION OF:			17. LIMITATION OF ABSTRACT	15. NUMBER OF PAGES	19a. NAME OF RESPONSIBLE PERSON
a. REPORT	b. ABSTRACT	c. THIS PAGE			Juliet Gerrard
UU	UU	UU	UU		19b. TELEPHONE NUMBER +64-364-2987

Report Title

Structural Characterisation of Proteins from the Peroxiredoxin Family

ABSTRACT

The oligomerisation of protein subunits is an area of much research interest, in particular the relationship to protein function. In the last decade, the potential to control the interactions involved in order to design constructs with tuneable oligomeric properties in vitro has been pursued. The subject of this thesis is the quaternary structure of members of the peroxiredoxin family, which have been seen to assume an intriguing array of organisations. Human Peroxiredoxin 3 (HsPrx3) and Mycobacterium tuberculosis alkyl hydroperoxide reductase (MtAhpE) catalyse the detoxification of reactive species, preferentially hydrogen peroxide and peroxynitrite respectively, and form an essential part of the antioxidant defence system. As well as their biomedical interest, the ability of these proteins to form organised supramolecular assemblies makes them of interest in protein nanotechnology.

The work described focusses on the elucidation of the quaternary structure of both proteins, resolving previous debates about their oligomeric state. The factors influencing oligomerisation were examined through biophysical characterisation in different conditions, using solution techniques including chromatography, light and X-ray scattering, and electron microscopy. The insight gained, along with analysis of the protein-protein interfaces, was used to alter the quaternary structure through site-directed mutagenesis. This resulted in a level of control over the protein's oligomeric state to be achieved, and novel structures with potential applications in nanotechnology to be generated. The activity of the non-native structures was also assessed, to begin to unravel the relationship between peroxiredoxin quaternary structure to enzyme activity.

The formation and structure of very high molecular weight complexes of HsPrx3 were explored using electron microscopy. The first high resolution structural data for such a complex is presented, analysis of which allowed the theory of an assembly mechanism to be proposed.

Structural Characterisation of Proteins from the Peroxiredoxin Family



AMY PHILLIPS

A thesis submitted in partial fulfilment of the requirements for the degree of
Doctor of Philosophy in Biochemistry.

January 2014



ACKNOWLEDGEMENTS

Completing this thesis has certainly been an adventure! Through the thousands of earthquakes, good times and not so good times, there are many people without whom it would not have been possible, and even more without whom it would not have been as much fun! I would therefore like to express my thanks to the people who have supported me in the last three years.

First and foremost, my supervisor Juliet Gerrard - from my first visit to Canterbury your welcoming and inclusive attitude made the decision of where to study an easy choice. Since then your constant support and motivation have been truly appreciated, as has your dedication to your role, be it answering emails at every hour of the day or donating toothpaste! I couldn't have asked for a better supervisor, and working in your lab is an experience I'll always remember. I would also like to thank my co-supervisor Céline Valéry, you have been a great help. The advice, coffees and glasses of Reisling have always been there when I've needed them. Special thanks must go to the MacDiarmid Institute for their funding, but also many useful conferences, symposiums, and the opportunity to meet so many talented people.

The members of the Lott and Kingston labs in Auckland University helped me so much in the early part of my PhD. My co-supervisor Shaun Lott, after adopting me as an earthquake refugee and helping me find my feet in the lab, your support and generosity, (particularly at Christmas!) made my Auckland stay a lot more enjoyable. Jason Busby provided useful experimental advice and guidance, and I appreciate the patience! Siri McKelvie has been such a good friend; I have great memories of our chats, road trips and fun evenings. Kavestri Yegambaram is possibly the kindest person I know and has always made time for cheering me up when needed, however busy her life has been! The Chemistry crew have been amazing – Karima, Thomas, Mars, Romel and everyone else, thank you for your experimental advice, great friendship and not least the cheesecakes! Anna Matuszek has been such a close friend to me, my time in Auckland would not have been the same without knowing you.

The Prx team – it has been great. Thank you, Amy2, for your cheerfulness, useful discussions and lab favours....and to Jacob, for being one of the founding members of the team, setting up many protocols and bottomless pub quiz knowledge. Also the Winterbourn group at Otago University – in particular Mark Hampton and Alexamder Peskin for your help with setting up protocols, and many informative meetings. I am indebted to the rest of the Gerrard/Pearce/Dobson students, Kat, Akshita, Rachel, Eric, Mo; I have had so much fun working with you all. The much needed coffee breaks, afternoons of Frisbee, and many, many science puns. I could not have done without the SAXS team – Grant and Jeremy – for assistance with data analysis, beamtime playlist choices, and just knowing when Science requires chocolate. Luigi, from giving me a place to stay to presentation advice, and always being ready to offer help, I am very grateful. Madhu has always been on hand with wise words and friendship, and Susie – your help and guidance has always been spot on. Jackie – thank you for your help with TEM, and your constant hard work to keep the lab running smoothly.

Learning microscopy has been a huge highlight of this research, and for that I thank Adrian Turner for the maintenance of the microscope in Auckland, and to Alok Mitra and his group for accommodating us in the lab, their ongoing hard work and help with the TEM analysis, and many helpful discussions.

Finally, my family. Although we're often far apart, I am forever grateful to my parents. I am amazed and so thankful for your constant support of all my endeavours, whatever they be and wherever in the world I have chosen to do them! I would not be where I am without you, your encouragement has been unwavering. Maz. Your help with TEM processing has been invaluable. Many hours assistance with collecting data, and long days spent docking structures – you really went above and beyond to help, and have become my best friend. Dragging me on ocean adventures when all I wanted to do was hide away and study has made my life so much more exciting, and your passion for everything has been inspiring.

ABSTRACT

The oligomerisation of protein subunits is an area of much research interest, in particular the relationship to protein function. In the last decade, the potential to control the interactions involved in order to design constructs with tuneable oligomeric properties *in vitro* has been pursued. The subject of this thesis is the quaternary structure of members of the peroxiredoxin family, which have been seen to assume an intriguing array of organisations. Human Peroxiredoxin 3 (*HsPrx3*) and *Mycobacterium tuberculosis* alkyl hydroperoxide reductase (*MtAhpE*) catalyse the detoxification of reactive species, preferentially hydrogen peroxide and peroxynitrite respectively, and form an essential part of the antioxidant defence system. As well as their biomedical interest, the ability of these proteins to form organised supramolecular assemblies makes them of interest in protein nanotechnology.

The work described focusses on the elucidation of the quaternary structure of both proteins, resolving previous debates about their oligomeric state. The factors influencing oligomerisation were examined through biophysical characterisation in different conditions, using solution techniques including chromatography, light and X-ray scattering, and electron microscopy. The insight gained, along with analysis of the protein-protein interfaces, was used to alter the quaternary structure through site-directed mutagenesis. This resulted in a level of control over the protein's oligomeric state to be achieved, and novel structures with potential applications in nanotechnology to be generated. The activity of the non-native structures was also assessed, to begin to unravel the relationship between peroxiredoxin quaternary structure to enzyme activity.

The formation and structure of very high molecular weight complexes of *HsPrx3* were explored using electron microscopy. The first high resolution structural data for such a complex is presented, analysis of which allowed the theory of an assembly mechanism to be proposed.

CONTENTS

ABSTRACT	i
CONTENTS	ii
LIST OF FIGURES	vii
LIST OF TABLES.....	xi
ABBREVIATIONS	xiii
 CHAPTER 1 INTRODUCTION.....	 1
1.1 Oxidative stress	1
1.1.1 Reactive oxygen species are inevitable in aerobic life	1
1.1.2 Numerous systems exist to counteract ROS damage.....	2
1.2 The ubiquitous Prx family	5
1.2.1 Prxs are classified on cysteine content.....	5
1.2.2 Prxs follow a common, three step catalytic cycle	6
1.2.3 The Prx tertiary structure is highly conserved.....	8
1.2.4 Prxs exist in a number of oligomeric states.....	11
1.2.5 Hydroxidation of Prxs suggests roles beyond detoxification	20
1.3 Human Prxs	29
1.3.1 Prx knockouts show oxidative sensitivity	29
1.3.2 Human Prx3	30
1.4 Prxs of <i>Mycobacterium tuberculosis</i>	32
1.4.1 Components of the <i>Mycobacterium tuberculosis</i> antioxidant systems	32
1.4.2 Characterisation of MtAhpE	34
1.5 Self-assembling proteins in nanotechnology.....	39
1.6 Summary and significance of this research	41
1.7 References	44
 CHAPTER 2 MATERIALS AND METHODS.....	 57
2.1 Materials	57
2.1.1 Chemicals	57
2.1.2 Enzymes.....	57
2.1.3 Bacterial strains	58

2.1.4	Plasmids.....	59
2.1.5	Media	59
2.1.6	Antibiotics and other media additives	60
2.1.7	Oligodeoxyribonucleotides.....	61
2.1.8	Sodium dodecyl sulfate polyacrylamide gel electrophoresis (SDS-PAGE)	61
2.1.9	Buffers and solutions.....	63
2.2	Molecular biology.....	67
2.2.1	Competent cells.....	67
2.2.2	Bacterial culture	69
2.2.3	Polymerase chain reaction (PCR).....	70
2.2.4	DNA manipulations.....	72
2.3	Recombinant protein production.....	75
2.3.1	Protein expression.....	75
2.3.2	Protein purification by chromatography	78
2.3.3	His-tag removal	80
2.3.4	Protein concentration	82
2.3.5	Buffer exchange.....	82
2.4	Protein characterisation	83
2.4.1	Peptide sequencing	83
2.4.2	Determination of protein concentration.....	84
2.4.3	SDS-PAGE analysis	85
2.4.4	Mass Spectrometry	86
2.5	Biophysical techniques	87
2.5.1	Circular dichroism.....	87
2.5.2	Analytical size-exclusion chromatography (SEC)	87
2.5.3	Size-exclusion chromatography with in-line light scattering (SEC/SLS).....	90
2.5.4	Electron microscopy	91
2.5.5	Small angle X-ray scattering	92
2.5.6	Protein crystallisation.....	94
2.6	Peroxidase activity assay.....	95
2.6.1	Data collection.....	95
2.6.2	Data analysis.....	97
2.7	References.....	99
CHAPTER 3	<i>MYCOBACTERIUM TUBERCULOSIS</i> AHPE.....	102
3.1	Introduction.....	102
3.2	Design and generation of <i>MtAhpE</i> interface mutations	103

3.2.1	Dimer interface analysis	103
3.3	Purification of wildtype <i>MtAhpE</i>	106
3.3.1	Expression in an <i>E. coli</i> host	106
3.3.2	IMAC purification	107
3.3.3	Gel filtration chromatography.....	108
3.3.4	His-tag removal by rTEV protease	110
3.4	Characterisation of wildtype <i>MtAhpE</i>	111
3.4.1	Quaternary structure.....	111
3.5	The effect of N-terminal modifications	120
3.5.1	Analytical size-exclusion chromatography	121
3.5.2	Small angle X-ray scattering	122
3.6	Generation of interface mutations.....	125
3.6.1	Mutagenesis	125
3.6.2	Expression and purification of non-native proteins	127
3.6.3	Expression of the Q83A mutein.....	132
3.7	Characterisation of muteins.....	138
3.7.1	Analytical size-exclusion chromatography	138
3.7.2	SDS-PAGE analysis	139
3.8	Discussion	142
3.8.1	Quaternary structure of untagged <i>MtAhpE</i>	143
3.8.2	Quaternary structure of his-tagged <i>MtAhpE</i>	147
3.8.3	HMW forms of <i>MtAhpE</i>	148
3.8.4	Quaternary structure of <i>MtAhpE</i> muteins	149
3.8.5	Summary and outlook	150
3.9	References	152
CHAPTER 4	HUMAN PRX3	158
4.1	Introduction	158
4.2	Purification of wildtype <i>HsPrx3</i>	159
4.2.1	Expression in an <i>E. coli</i> host	159
4.2.2	Purification by chromatography.....	160
4.2.3	His-tag removal by rTEV protease	163
4.3	Characterisation of wildtype <i>HsPrx3</i>	164
4.3.1	Quaternary structure of <i>HsPrx3</i>	164
4.3.2	Peroxidase activity of <i>HsPrx3</i>	188
4.3.3	Crystallisation	190

4.4 Discussion	192
4.4.1 <i>HsPrx3</i> quaternary structure	193
4.4.2 His-tag stabilisation occurs through the coordination of metal ions	194
4.4.3 <i>HsPrx3</i> dodecamer assembly is controlled by a number of factors	195
4.5 References	199
 CHAPTER 5 INFLUENCING <i>HSPRX3</i> QUATERNARY STRUCTURE.....	204
5.1 Introduction.....	204
5.2 Design and generation of <i>HsPrx3</i> modifications.....	204
5.2.1 A-type interface analysis	205
5.2.2 Selection of mutations to alter assembly	209
5.3 Preparation of mutated <i>HsPrx3</i> constructs	212
5.3.1 Expression of non-native proteins in an <i>E. coli</i> host.....	212
5.3.2 Purification by chromatography.....	213
5.4 Characterisation of single residue mutations of <i>HsPrx3</i>	218
5.4.1 Quaternary structure of <i>HsPrx3</i> muteins	219
5.4.2 A combination of mutations generated a stable species	232
5.4.3 Peroxidase activity of <i>HsPrx3</i> muteins	237
5.5 Discussion	240
5.5.1 A-type interface stabilisation may rely on hydrophobic forces.....	241
5.5.2 Toroid formation relies on the folded C _p loop.....	242
5.5.3 Interface mutations may alter toroid geometry	243
5.5.4 HMW formation relies on the unwinding of the α 2 helix	244
5.5.5 Muteins give insight into HMW structure formation	246
5.5.6 Summary and outlook	246
5.6 References	249
 CHAPTER 6 ENGINEERING HMW STRUCTURES OF <i>HSPRX3</i>.....	253
6.1 Introduction.....	253
6.2 Toroid stacking occurs in response to a number of factors	253
6.2.1 Analysis of the literature	253
6.2.2 The R-type interface	255
6.2.3 His-tagged <i>HsPrx3</i> forms stacks of toroids	257
6.3.2 3D TEM reconstruction of the double toroid stacks	259
6.4 Generating nanotubes of controllable length	262

6.4.1	Acid pH leads to toroid association	263
6.4.2	Controlling nanotube length	266
6.4.3	3D cryo-electron microscopy structure of the nanotubes	268
6.5	Discussion	273
6.5.1	His-tag mediated assembly	273
6.5.2	Low pH induced assembly	274
6.5.3	Control of the length of the nanotubes.....	275
6.5.4	Conclusion	276
6.6	References	278
CHAPTER 7	SUMMARY AND CONCLUSIONS.....	280
7.1	Introduction.....	280
7.2	Quaternary structure of the proteins studied	281
7.2.1	<i>MtAhpE</i>	281
7.2.2	<i>HsPrx3</i> forms a dodecamer in response to reduction and neutral pH.....	282
7.2.3	<i>HsPrx3</i> active site architecture is key in toroid formation	283
7.2.4	HMW species of <i>HsPrx3</i>	285
7.4	Summary and future work	286
7.5	References	290
Appendix 1	Biophysical techniques	A
Appendix 2	In house crystallisation screens	Z
Appendix 3	<i>MtAhpE</i> information	KK
Appendix 4	<i>HsPrx3</i> information	RR
Appendix 5	Peptide sequencing results.....	WW
Appendix 6	<i>HsPrx3</i> mutein purification traces and gels.....	YY
Appendix 7	<i>HsPrx3</i> mutein SAXS values	DDD

LIST OF FIGURES

Figure 1.1: Peroxiredoxin mechanism relies on redox cycling.....	6
Figure 1.2: The Prx tertiary structure is based around a Trx fold.....	9
Figure 1.3: The active site structure stabilises and activates C_P^-	10
Figure 1.4: The dimer interface is stabilised by non-covalent interactions	12
Figure 1.5: Prxs can form different multimers.....	14
Figure 1.6: The oligomer interface is stabilised by loop and helix interactions	15
Figure 1.7: Important elements involved in the A-type interface are conserved.....	16
Figure 1.8: Individual residue movements contribute to interface dissociation	18
Figure 1.9: Prxs sensitive to hyperoxidation contain an additional helix	21
Figure 1.10: Prxs form a wide range of HMW structures.....	25
Figure 1.11: The R-type interface is stabilised by electrostatic interactions	28
Figure 1.12: Each monomer interacts with two others in the stack, causing a pitch	28
Figure 1.13: The <i>MtAhpE</i> monomer shows a compact structure	33
Figure 1.14: The <i>MtAhpE</i> A-type interface is stabilised by hydrophobic interactions	36
Figure 1.15: Sequences of Prxs show homologous interface regions.....	36
Figure 1.16: The B-type interface of <i>MtAhpE</i> is less extensive than the A-type interface ..	37
Figure 1.17: Significant changes occur in the active site with redox state	38
Figure 2.1: Typical elution profile of protein standards	89
Figure 2.2: A typical size-exclusion chromatography calibration curve	89
Figure 2.3: Calculation of HRP inhibition.....	98
Figure 3.1: The A-type interfaces from <i>MtAhpE</i> and a typical Prx overlay well.....	103
Figure 3.2: Interactions at the <i>MtAhpE</i> interfaces	105
Figure 3.3: Expression trials indicated 20°C was the optimal growth temperature for expression of <i>MtAhpE</i>	107
Figure 3.4: IMAC purification of wildtype <i>MtAhpE</i>	108
Figure 3.5: Gel filtration resulted in homogeneous samples of <i>MtAhpE</i>	109
Figure 3.6: rTEV cleavage of <i>MtAhpE</i> was successful in number of conditions.....	110

Figure 3.7: SDS-PAGE analysis of (1) hyperoxidised, (2) reduced and (3) non-reduced <i>MtAhpE</i> showed the presence of dimers	112
Figure 3.8: SDS-PAGE analysis of cross-linked wildtype <i>MtAhpE</i> suggests the presence of oligomers in solution.....	114
Figure 3.9: Analytical SEC indicated the redox sensitivity of wildtype <i>MtAhpE</i>	116
Figure 3.10: X-ray scattering data of <i>MtAhpE</i> in non-reducing conditions suggest a spherical particle	118
Figure 3.11: Comparison to theoretical scattering patterns suggested a dimeric species ...	118
Figure 3.12: A typical TEM micrograph show toroidal oligomers and HMW clusters of <i>MtAhpE</i>	120
Figure 3.13: The octamer building interface is composed of loop interactions.....	121
Figure 3.14: His-tagged <i>MtAhpE</i> is insensitive to redox conditions	122
Figure 3.15: Comparison to theoretical scattering suggests the presence of a B-type dimer in non-reducing conditions	124
Figure 3.16: Representative chromatograms obtained from IMAC purification.....	128
Figure 3.17: Representative SDS-PAGE gel of cell lysis and IMAC purification	129
Figure 3.18: Representative chromatograms obtained from gel filtration purification of <i>MtAhpE</i> muteins	130
Figure 3.19: Representative reducing SDS-PAGE gels of gel filtration purification.....	130
Figure 3.20: Two steps of chromatography resulted in highly pure mutein samples	131
Figure 3.21: SDS-PAGE analysis suggested successful expression of the Q83A mutein..	133
Figure 3.22: Q83A expression resulted in insoluble protein	134
Figure 3.23: Analytical SEC suggested <i>MtAhpE</i> muteins exist as a mixture of species....	139
Figure 3.24: Non-reducing SDS-PAGE revealed the ability of muteins to form dimers ...	141
Figure 3.25: Reducing SDS-PAGE revealed that the oligomers seen previously were mostly due to disulfide bond formation.....	142
Figure 3.26: Loop movements may lead to B-type interface formation.....	144
Figure 3.27: Possible mechanisms for reduced and hyperoxidised toroid formation of typical 2-Cys Prxs	146
Figure 4.1: Sonication resulted in incomplete lysis	160

Figure 4.2: Representative purification chromatograms.....	161
Figure 4.3: SDS-PAGE gel of <i>HsPrx3</i> purification.....	162
Figure 4.4: SDS-PAGE of his-tag cleavage trials.....	164
Figure 4.5: SEC/SLS of <i>HsPrx3</i> in reducing conditions.....	166
Figure 4.6: X-ray scattering data suggested a toroidal particle	168
Figure 4.7: Experimental scattering data and theoretical scattering profiles.....	168
Figure 4.8: Electron micrographs of <i>HsPrx3</i> revealed hexagonal toroids	170
Figure 4.9: Class averages confirm the hexameric oligomer.....	171
Figure 4.10: 3D reconstructions from <i>HsPrx3</i> TEM data show a dodecameric toroid.....	172
Figure 4.11: Cryo-EM supported the hypothesis of open and closed toroids.....	173
Figure 4.12: Redox conditions significantly affect the oligomeric state of <i>HsPrx3</i>	175
Figure 4.13: X-ray scattering profiles indicate different structures in response to redox changes.....	175
Figure 4.14: An N-terminal his-tag stabilises the dodecameric oligomer of <i>HsPrx3</i>	178
Figure 4.15: Scattering data for his-tagged <i>HsPrx3</i> appears unchanged by redox conditions	180
Figure 4.16: EDTA caused the dissociation of his-tagged toroids	182
Figure 4.17: pH changes significantly affect <i>HsPrx3</i> oligomerisation	184
Figure 4.18: Oligomeric state of non-reduced <i>HsPrx3</i> shows concentration dependence .	187
Figure 4.19: Tagged <i>HsPrx3</i> showed lower activity than the untagged construct.....	189
Figure 4.20: Needle-like crystals of <i>HsPrx3</i> were seen in initial screens.....	191
Figure 4.21: Structural comparison of a decameric and dodecameric Prx	192
Figure 4.22: Formation of the Prx toroid is dependent on a number of factors and may involve an oligomerisation intermediate.....	196
Figure 5.1: Hydrophobic packing stabilises the <i>BtPrx3</i> and <i>HsPrx3</i> A-type interface.....	207
Figure 5.2: Interface regions of <i>BtPrx3</i>	208
Figure 5.3: Bonding residues of the <i>BtPrx3</i> and <i>MtAhpE</i> A-type interfaces show some differences.....	210
Figure 5.4: Mutated proteins elute at different imidazole concentrations to wildtype <i>HsPrx3</i>	215

Figure 5.5: Gel filtration profiles of mutated <i>HsPrx3</i> proteins differed from wildtype	216
Figure 5.6: Representative mutein purification gels exemplified by S78A.....	217
Figure 5.7: All muteins were successfully prepared to high levels of purity	218
Figure 5.8: In non-reducing conditions, muteins showed altered quaternary structures	220
Figure 5.9: In reducing conditions muteins showed a variety of oligomeric states.....	223
Figure 5.10: Untagged S78A forms dodecameric rings and clusters.....	230
Figure 5.11: Electron micrograph of T104W revealed a heterogeneous population of toroidal species.....	231
Figure 5.12: The C47SS78A mutein prevents dodecamer dissociation	233
Figure 5.13: The C47SS78A mutein shows no environmental sensitivity	235
Figure 5.14: EM analysis of the C47SS78A mutein revealed stacks and interlocked toroids	237
Figure 5.15: Activity data suggests all muteins affect protein function	239
Figure 6.1: His-tagged <i>HsPrx3</i> forms stacks of toroids.....	258
Figure 6.2: Histogram representing the relative proportions of structures in wildtype constructs	259
Figure 6.3: The 3D reconstruction of <i>HsPrx3</i> stacks suggests a conserved mechanism	261
Figure 6.4: Toroid association occurs in response to pH.....	265
Figure 6.5: The presence of sulfate ions influences nanotube length	268
Figure 6.6: Cryo-EM revealed straight nanotubes exist in solution	269
Figure 6.7: 3D reconstructions indicate differences in assembly mechanisms between tagged and untagged <i>HsPrx3</i> toroids	270
Figure 6.8: Docking the 3D reconstruction with crystal structures gave insight into the assembly mechanism	272
Figure 7.1: Modifications of <i>HsPrx3</i> produced a variety of supramolecular structures	286

LIST OF TABLES

Table 1.1: Human Prx isoforms undertake essential roles within the cell.....	30
Table 2.1: Antibiotic concentrations.....	61
Table 2.2: Primers used for PCR reactions.....	62
Table 2.3: SDS-PAGE gel recipes.....	63
Table 2.4: Methylation of template DNA.....	70
Table 2.5: Standard PCR reaction.....	71
Table 2.6: Standard thermocycler programme.....	71
Table 2.7: Protein expression trials.....	76
Table 2.8: rTEV cleavage trials.....	81
Table 2.9: Protein standard concentrations.....	88
Table 2.10: Composition of well solutions for activity assay.....	97
Table 3.1: Particle dimensions suggest that <i>MtAhpE</i> exists primarily as a dimer.....	117
Table 3.2: Particle dimensions suggest that his-tagged <i>MtAhpE</i> exists primarily as a dimer	123
Table 3.3: A number of factors were varied in attempts to optimise SDM.....	126
Table 3.4: <i>MtAhpE</i> and muteins expressed at low levels.....	131
Table 3.5: A number of variations to the lysis buffer were considered to optimise solubility	135
Table 3.6: Lysis buffer compositions.....	136
Table 4.1: Cell press extraction provided a more efficient lysis technique.....	159
Table 4.2: Molecular weights from SAXS studies of <i>HsPrx3</i>	167
Table 4.3: The oligomeric state of non-reduced <i>HsPrx3</i> is sensitive to concentration.....	176
Table 4.4: Molecular weights and dimensions from SAXS show tagged <i>HsPrx3</i> is a constitutive dodecamer.....	181
Table 4.5: Relative proportions of oligomeric species in non-reducing conditions at various concentrations.....	187
Table 4.6: Positive crystallisation conditions.....	191
Table 5.1: Summary of rationale behind mutational design.....	211

Table 5.2: Good expressions of the <i>HsPrx3</i> muteins were seen in conditions optimised in chapter three.....	213
Table 5.3: SAXS data supported SEC/SLS results.....	226
Table 5.4: SAXS analysis indicated that the HMW species are redox sensitive.....	228
Table 5.5: The C47SS78A mutation stabilises the dodecamer.....	234
Table 5.6: Muteins showed altered activity rates.....	238
Table 5.7: Summary of mutein quaternary structures and activities	241
Table 6.1: Published structures of HMW are obtained from modified constructs	255
Table 7.1: Muteins mimicked different states of <i>HsPrx3</i>	284
Table 7.2: Suggestions for future mutational studies.....	288

ABBREVIATIONS

2D	2-dimensional
3D	3-dimensional
AhpC	alkyl hydroperoxide reductase C
AhpE	alkyl hydroperoxide reductase E
Amp	ampicillin
APS	ammonium persulfate
ATP	adenosine triphosphate
AUC	analytical ultracentrifugation
BCP	bacterioferritin comigratory protein
BME	β -mercaptoethanol
BSA	bovine serum albumin
BtPrx3	bovine peroxiredoxin 3
Cam	chloramphenicol
CD	circular dichroism
Cfu	colony forming units
C_P	peroxidatic cysteine
C_R	resolving cysteine
Cryo-EM	cryo-electron microscopy
Cv	column volume
Da/kDa	Dalton/kiloDalton
D_{max}	maximum particle dimensions
DMSO	dimethyl sulfoxide
DNA	deoxyribonucleic acid
DTPA	diethylene triamine pentaacetic acid
DTT	dithiothreitol

<i>E. coli</i>	<i>Eschericia coli</i>
EDTA	ethylenediaminetetraacetic acid
FF	fully folded
FPLC	fast protein liquid chromatography
FRET	fluorescence resonance energy transfer
GPC/SEC	gel permeation chromatography/size-exclusion chromatography
Gpx	glutathione peroxidase
GR	glutathione reductase
Grx	glutaredoxin
GSH	glutathione
H₂O₂	hydrogen peroxide
HEPES	2-[4-(2-hydroxyethyl)piperazin-1-yl]ethanesulfonic acid
HMW	high molecular weight
HRP	horse radish peroxidase
<i>HsPrx3</i>	human peroxiredoxin 3
IMAC	immobilised metal affinity chromatography
IPTG	isopropyl galactosidase
Kan	kanamycin
kV/V	kiloVolt/Volt
LB	lysogeny broth
LC-MS/MS	liquid chromatography tandem mass spectrometry
LU	locally unfolded
MALDI-TOF MS	matrix assisted laser desorption/ionisation time of flight mass spectrometry
MBP	maltose binding protein
MES	2-ethanesulfonic acid
MOPS	3-(N-morpholino)propanesulfonic acid
MS	mass spectrometry
<i>MtAhpE</i>	<i>Mycobacterium tuberculosis</i> alkyl hydroperoxide reductase E

MWCO	molecular weight cut off
nL/μL/mL/L	nanolitre/microlitre/millilitre/litre
NEB	New England Biolabs
OD	optical density
PCR	polymerase chain reaction
PDB	protein data bank
PDBePISA	protein data bank in Europe: proteins, interfaces, structures and assemblies
PDGF	platelet derived growth factor
PEG	polyethylene glycol
pI	isoelectric point
Prx	peroxiredoxin
R_G	radius of gyration
R_h	radius of hydration
RI	refractive index
RNA	ribonucleic acid
ROS	reactive oxygen species
Rpm	revolutions per minute
rTEV	recombinant tobacco etch virus protease
TEMED	tetramethylethylenediamine
Tet	tetracycline
Trx	thioredoxin
RALS	right angle light scattering
RI	refractive index
SAXS	small angle X-ray scattering
SDM	site directed mutagenesis
SDS-PAGE	sodium dodecyl sulfate polyacrylamide gel electrophoresis
SEC	size-exclusion chromatography
SEC/SLS	size-exclusion chromatography/static light scattering

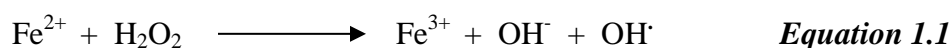
SOB	super optimal broth
SOC	super optimal broth with catabolite suppression
SOD	superoxide dismutase
Srx	sulfiredoxin
TAE	tris-acetate EDTA
TB	tuberculosis
TCEP	tris(2-carboxyethyl)phosphine
TE	tris-EDTA
TEM	transmission electron microscopy
TEMED	Tetramethylethylenediamine
Tet	tetracyclin
TFA	trifluoroacetic acid
TryP	tryparedoxin peroxidase
TSA	thiol specific antioxidant
UV	ultraviolet
WHO	world health organisation
X-Gal	5-bromo-4-chloro-3-indolyl- β -D-galactopyranoside

Chapter 1 Introduction

1.1 Oxidative stress

1.1.1 Reactive oxygen species are inevitable in aerobic life

Living in an aerobic environment enables higher amounts of adenosine triphosphate (ATP) to be generated than is possible in anaerobic conditions, but with this increase in efficiency comes a potentially damaging by-product – reactive oxygen species (ROS). Molecular oxygen can be completely reduced to water, but electron leakage from protein complexes within the respiratory chain can incompletely reduce oxygen, leading to the production of superoxide radical anions, hydrogen peroxide and other ROS (reviewed in Sies, 1993). These molecules are short-lived as they are rapidly converted to hydrogen peroxide (H_2O_2) by further spontaneous reduction or by enzymes such as superoxide dismutases (SOD). Under normal physiological conditions H_2O_2 production accounts for ~ 2% of oxygen uptake (reviewed in Inoue *et al.*, 2003). When this molecule comes into contact with transition metals such as Fe^{2+} or Cu^{2+} , hydroxyl radicals are generated through the Fenton reaction (Fenton 1894; reviewed in Halliwell and Gutteridge, 1984; equation 1.1). These are highly reactive species and react quickly with all biological molecules including proteins, lipids and nucleic acids (Stadtman, 1992; Ames, 1989).



ROS can also arise from exogenous sources, such as ionising radiation, redox-cycling drugs, or other intracellular reactions such as the respiratory burst exerted by phagocytes during an immune response (reviewed in Forman and Torres, 2001). Efficient mechanisms to minimise the production and deleterious effects of ROS are

therefore essential. The inhibition of normal cellular functions resulting from ROS damage has been linked to pathologies including cancer, Alzheimer's disease and aspects of aging (Harman, 1956; Wallace 2005; Rego and Oliveira 2003), making this process a focus of therapeutic development.

1.1.2 Numerous systems exist to counteract ROS damage

The first line of defence to counteract the effects of ROS and repair oxidised biomolecules is the removal of the reactive molecules through reduction. This is achieved either using nonenzymatic ROS scavengers, such as vitamins C and E as sinks, or by using catalysts such as catalase and SOD (Gaté *et al.*, 1999).

1.1.2.1 Superoxide dismutases

Present in virtually all aerobic and aerotolerant anaerobic organisms (and in some very rare aerobes), SODs (EC 1.15.1.1) are metalloproteins that fall into three classes (reviewed in Bannister *et al.*, 1987) – those containing copper and zinc at the active site (CuZn-SODs, found mostly in eukaryotic cytosols); those containing manganese (Mn-SODs which make up most mitochondrial and many bacterial SODs); and finally iron containing (Fe-SODs, of prokaryotes). SODs catalyse the dismutation of free radicals (equation 1.2) through a reaction involving the reduction and subsequent oxidation of the metal at the catalytic centre (Fridovic, 1995; McCord and Fridovich, 1969).

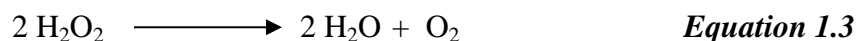


The H_2O_2 produced is able to diffuse through membranes to remote locations before reacting further. Its low reactivity allows it to function as a signalling molecule, specifically oxidising cysteine residues to influence enzyme function (Gough and Cotter, 2011). However, high cellular levels can be toxic, through the oxidation of non-

target proteins and biological molecules including nucleic acids and lipids (Imlay, 2003).

1.1.2.2 Catalases

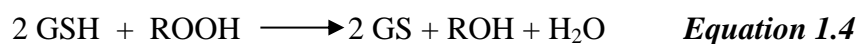
More accurately known as hydroperoxidases, catalases (EC 1.11.1.6) are peroxisomal, haem-containing enzymes that catalyse the reduction of H_2O_2 to oxygen and water (Wiesner, 1962; equation 1.3).



Theoretical K_m values calculated from studies of catalases show the reaction rates are maintained at $\sim 10^6 \text{ M}^{-1} \text{ s}^{-1}$, even at high concentrations of H_2O_2 . This, along with their resistance to saturation, has led to catalases often being referred to as catalytically perfect (Switala and Loewen, 2002; Alfonso-Prieto *et al.*, 2009).

1.1.2.3 Glutathione peroxidases

The glutathione peroxidase (GPx) family comprises a group of selenoproteins, which are well characterised in antioxidant defence (EC 1.11.1.9). Eight isoforms have been identified in humans (Placzek, 2013), all of which show a thioredoxin-fold structure and contain a catalytically active selenocysteine, except GPx7 and GPx8 which contain cysteine and have a much lower reactivity (reviewed in Flohé and Maiorino, 2013). GPxs catalyse the reduction of H_2O_2 , organic peroxides and lipid peroxides through electron transfer from glutathione (GSH) to the peroxide substrate (equation 1.4) via the catalytic selenocysteine and play an important role in H_2O_2 homeostasis (Prabhakar *et al.*, 2005).



The selenocysteine is oxidised to a transient selenenic acid form, which is rapidly reduced by GSH to glutathione disulfide (Epp *et al.*, 1983). Glutathione reductase (GR) recycles the enzyme back to its reduced form to continue the catalytic cycle (reviewed in Lu and Holmgren 2008).

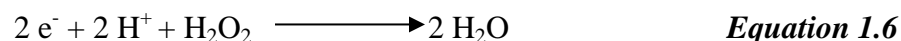
1.1.2.4 Peroxiredoxins

The first characterisation of a peroxiredoxin (Prx) began with the isolation of a small (25 kDa) protein which prevented degradation of other enzymes through oxidative damage (Kim *et al.*, 1985). This protein required a thiol-containing reductant and was therefore named thiol-specific antioxidant (TSA) (Kim *et al.*, 1988).

TSA-related proteins have since been found in all kingdoms and named the Prx family (Chae *et al.*, 1994a). Comprising up to 1% of the soluble protein content of cells (Kim *et al.*, 1989), Prxs are identified through their peroxidase activity via the oxidation of a thiol group on a conserved cysteine residue (Chae *et al.*, 1994b). Their abundance and the severity of knockout phenotype compared to that of catalase or GPx knockout phenotypes suggest that the Prxs are critical in antioxidant defence (Muller *et al.*, 2007). The Prx family of enzymes (EC 1.11.1.15) catalyse the reduction of H₂O₂, peroxynitrite and other organic hydroperoxides in the following reaction:



The net reaction with H₂O₂ therefore being:



1.2 The ubiquitous Prx family

1.2.1 Prxs are classified on cysteine content

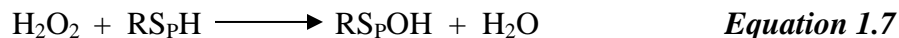
Prxs do not use redox active metal centres such as metal ions or haem, but instead contain a cysteine residue in the N-terminal domain which is essential for activity, and conserved in all species, except for the Prx of *Eubacterium acidamidophilum* which uses selenocysteine (Schröder, 2001). This residue – denoted the peroxidatic cysteine, C_P – is equivalent to an active metal centre and allows catalytic rates of $\sim 10^7 \text{ M}^{-1} \text{ s}^{-1}$ to be reached (Poole, in Flohé and Harris, 2007). Their high cellular concentration and upregulation in response to oxidative stress suggests that they play a key role in peroxide detoxification, and the discovery of functions beyond peroxidase activity has begun to uncover a complex range of activities related to cellular conditions (Rhee *et al.*, 2005).

Originally grouped according to the number of cysteine residues directly involved in catalysis, Prxs are generally classified as 2-Cys (found in animals, some plants and bacteria) or 1-Cys (present in archaeobacteria, animals and most plants; Chae *et al.*, 1994b). 2-Cys Prxs contain a resolving cysteine (C_R) in the C-terminal domain, additional to the conserved C_P , and are subdivided into typical or atypical, based on the catalytic mechanism. Typical 2-Cys Prxs represent the largest group of the Prx family; therefore, the mechanism described here considers the 2-Cys Prxs.

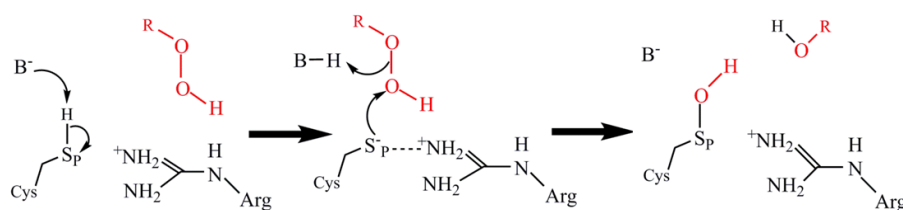
1.2.2 Prxs follow a common, three step catalytic cycle

1.2.2.1 Peroxidation

The thiol group of C_P (denoted S_P) is virtually unreactive with peroxides (Poole, in Flohé and Harris, 2007). The active site is organised so that > 90% of C_P thiol groups are deprotonated to thiolate at physiological pH (section 1.2.3.2; Wood *et al.*, 2003; Nelson *et al.*, 2008). The thiolate form (S_P[−]) is a stronger nucleophile, and can attack and reduce the peroxide substrate in a nucleophilic substitution reaction, releasing alcohol and water and becoming oxidised to the sulfenic acid form (S_POH; equation 1.7; Poole, in Flohé and Harris, 2007; figure 1.1A). It is not clear what deprotonates C_P or protonates the RO[−] leaving group of the substrate, but recent structural data suggest the substrate is well positioned for a water molecule to fulfil at least the latter role (Hall *et al.*, 2010).



A: Substrate reduction



B: Prx recycling

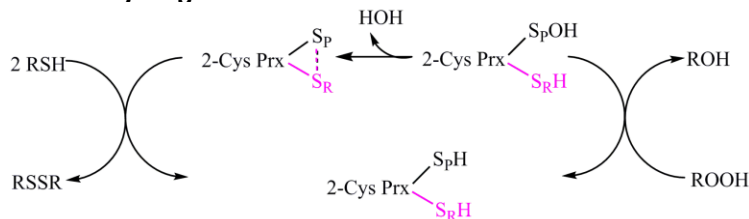


Figure 1.1: Peroxiredoxin mechanism relies on redox cycling

A: C_P is deprotonated by a base, after which it can attack the substrate, releasing water and the reduced substrate and becoming oxidised itself. The bases that deprotonate C_P and protonate the reduced substrate are denoted B but may not be the same. **B:** C_P from one subunit and C_R from the other condense to form an intersubunit disulfide bond. This is reduced by a thiol containing reductant (Wood *et al.*, 2003). Reaction shown represents a typical 2-Cys Prx.

1.2.2.2 Resolution

During this step, the sulfenic acid derivative S_POH is attacked by a free thiol group, releasing water and forming a disulfide bond between S_P and the attacking group. Prior to peroxidation, 2-Cys Prxs exist as non-covalent homodimers, stabilised mostly through hydrophobic interactions. C_P of one monomer is near to C_R of the other (see section 1.2.5.1 for further structural details), and so C_R of the apposing monomer can act as the attacking thiol group, forming an intermolecular disulfide bond (equation 1.8; Schröder, 2000; Ellis and Poole, 2007; figure 1.1B). It has been suggested that disulfide linkages can occur between corresponding cysteine residues (i.e., C_P-C_P , or C_R-C_R). Although only C_P is absolutely necessary for peroxidase activity, both are essential for proper maintenance of the 2-Cys Prx dimer structure after oxidation (Chae *et al.*, 1994c; Ellis and Poole, 2007).



1.2.2.3 Recycling

For catalysis to continue, the disulfide bond must be reduced to convert C_P back to the thiol form (S_PH ; equation 1.9), which requires a thiolate-bearing reductant. Although the identity of the reductant varies between Prxs, most appear to be redox proteins containing the motif $CxxC$, where x represents unconserved residues. Thioredoxin (Trx) or glutaredoxin (Grx) are effective with most 2-Cys Prxs (Verdougq *et al.*, 1999). The more N-terminal cysteine of the reductant attacks and reduces C_R , forming a mixed disulfide-bridged intermediate. The vicinal cysteine of the reductant then attacks the resulting half-cystine of C_P (Chae *et al.*, 1994a; figure 1.1B). C_R is essential for correct recycling of Prxs, with mutation allowing one round of catalysis but preventing recycling (Montemartini *et al.*, 1999). Recent research suggests that this is due to the steric inaccessibility of C_P after peroxidation, C_R thus providing an accessible residue for the reductant to attack (Cao *et al.*, 2011). Small reductants such as dithiothreitol

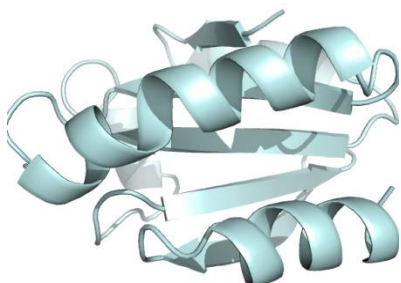
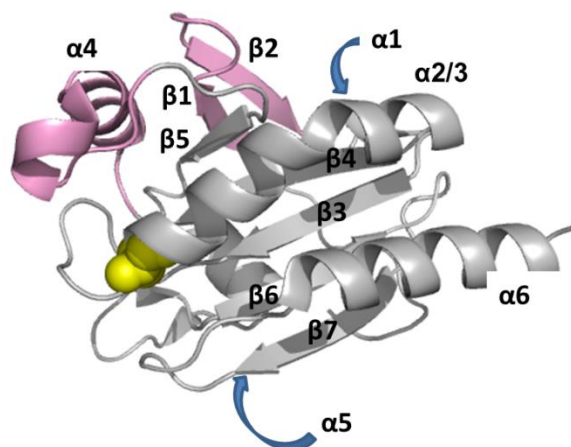
(DTT) are able to reduce Prxs with mutated C_R residues through direct attack of C_P, leading to the theory that the main role of C_R is in fact to protect Prxs from hyperoxidation (see section 1.2.4; Trujillo *et al.*, 2006). This is supported by studies which indicated that mutation of C_R increased the propensity of hyperoxidation (Jang *et al.*, 2004).



1.2.3 The Prx tertiary structure is highly conserved

1.2.3.1 Prx structure is centred around a Trx fold

The Trx fold consists of four β -sheets arranged as one parallel and one antiparallel pair, and sandwiched between two α -helices (Martin 1995; figure 1.2A). The Prxs contain C- and N-terminal extensions, along with some elements additional to the thioredoxin fold (figure 1.2B). In typical Prxs these form a 5-stranded β -sheet ($\beta 5$ - $\beta 4$ - $\beta 3$ - $\beta 6$ - $\beta 7$), on one side of which lie a $\beta 1$ - $\beta 2$ hairpin, $\alpha 5$ and $\alpha 1$ helices, and on the other side $\alpha 2/3$ and $\alpha 6$ helices. C_P is located in the first turn of the kinked helix $\alpha 2/3$ (figure 1.2B), which is composed of two adjoining helices and sometimes seen as two distinct helices (hence often referred to as helix 2/3). This basic structure is highly conserved, with differences between the Prx families seen mostly in the loop regions between these conserved secondary structure elements (reviewed in Hofmann, 2002).

A: The Trx fold**B: Typical 2-Cys Prx monomer****Figure 1.2: The Prx tertiary structure is based around a Trx fold**

A: The Trx fold comprises one pair of parallel and one pair of antiparallel β -sheets, sandwiched between two α -helices (as demonstrated by human thioredoxin, protein data bank (PDB) ID: 1ERT; Weichsel *et al.*, 1996). **B:** The tertiary structure of a typical 2-Cys Prx is an example of the well conserved monomer structure (bovine Prx3 [*BtPrx3*], PDB ID: 1ZYE; Cao *et al.*, 2005). The additional two helices and two β -sheets are highlighted in pink; C_P is shown as yellow spheres. Structural elements are labelled as suggested by Wood *et al.*, 2002. Arrows indicate helices behind the 5 β -sheets. Unless otherwise stated, all structural representations in this thesis were created using PyMol (DeLano, 2002).

1.2.3.2 The Prx active site shows a universal structure

Despite the high structural conservation, the Prx family shows low sequence conservation (typically 20 – 30% sequence identity). Some key residues are conserved, and the active site structure is universal across the subgroups of the Prx family. (Karplus and Hall, in Flohé and Harris, 2007). C_P is located in the first turn of helix $\alpha 2$ in a nearly universal PxxxTxxCP sequence. The proline, threonine and a sequentially distal arginine are all positioned in a conserved spatial arrangement within van der Waals contact with C_P (figure 1.3).

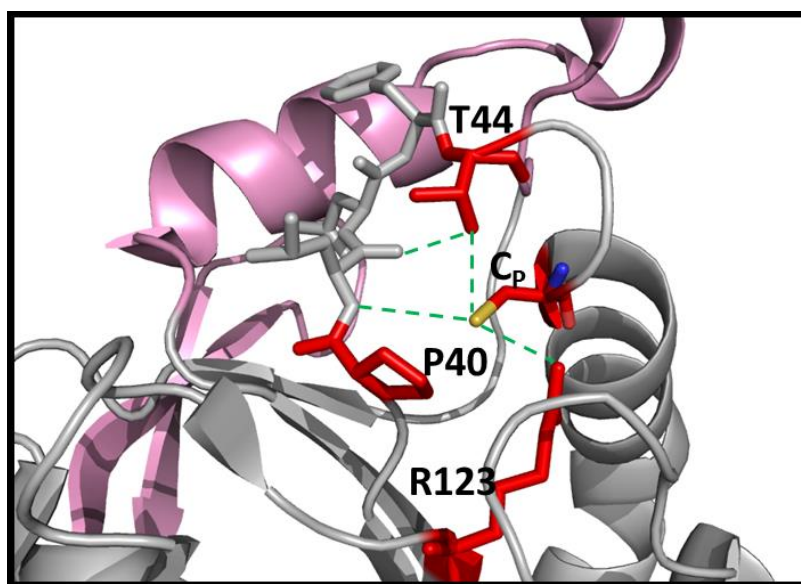


Figure 1.3: The active site structure stabilises and activates C_p^-

The spatially conserved arrangement of the catalytic triad (shown in red) Arg (R123), Thr (T44) and Pro (P40; numbering as for *BtPrx3* shown here; PDB ID: 1ZYE; Cao *et al.*, 2005) in the active site work to activate C_p in the reduced form of the enzyme. The primary role of P40 is thought to be shielding the active site from solvent molecules. The bonding network also includes the neighbouring residue to proline ($C_p - 6$). Pink regions are as in figure 1.2 for orientation.

The catalytic triad is made up of C_p , T44 and R123 (numbering for *BtPrx3* will be used; Cao *et al.*, 2005), which form a hydrogen bonding (H-bonding) network to activate and stabilise the C_p^- thiolate ion of the reduced enzyme ready for nucleophilic attack (figure 1.3). The positively charged R123 lowers the pK_a of the thiol by promoting ionisation and stabilising the thiolate form through electrostatic influence (Wood *et al.*, 2003). Mutation of this residue produces inactive and unstable enzymes, demonstrating its importance to catalysis (Montemartini *et al.*, 1999; Nagy *et al.*, 2011). The hydrophobic P40 repels solvent molecules, keeping the active site available (Poole, in Flohé and Harris, 2007). P40 also interacts with the neighbouring residue ($C_p - 6$; leucine in the case of *BtPrx3*), positioning this residue to act as an H-bond donor to the C_p thiolate, and an acceptor to T44 (Wood *et al.*, 2003). This prepares the hydroxyl group of T44 to accept H-bonds from the substrate, positioning it in the active site for an S_N2 reaction (Nagy *et al.*, 2011; Flohé *et al.*, 2002). The substrate oxygen atom that reacts with C_p

(denoted O_A , the substrate oxygen distal to C_P therefore denoted O_B) accepts H-bonds from C_P , the preceding residue ($C_P - 1$) and R123, and acts as an H-bond donor to T44 (Nakamura *et al.*, 2009). Examination of multiple structures with bound substrates indicate there are a number of positions within the active site where favourable substrate interactions can occur, suggesting a “track” along which the substrate can slide, stabilising O_A and O_B whilst allowing the making and breaking of bonds during the reaction (Hall *et al.*, 2010). The interactions provide an explanation for the high reactivity of Prxs and may also present a possibility for inhibitor design through a substrate or transition state mimic that occupies an increased area of the “trough”.

1.2.4 Prxs exist in a number of oligomeric states

Although the active sites are made up of residues from one monomer and the enzymes should therefore be able to function as a monomer, only the 1-Cys Prxs yeast bacterioferritin co-migratory protein (BCP) and plant PrxQ are known to be functionally monomeric (Rouhier *et al.*, 2004; Jeong *et al.*, 2000). Furthermore, many of the typical domain-swapped non-covalent homodimers have the ability to oligomerise to form higher order structures. This oligomerisation is dynamic and occurs in response to environmental factors, with the protein reverting to the dimeric form when conditions change (Wood *et al.*, 2002).

The mechanisms involved in oligomerisation are not well understood, but the dimer form appears to be associated with high ionic strength, high pH and oxidation; the oligomer therefore forming at low ionic strength, low pH and upon reduction of C_P (reviewed in Wood *et al.*, 2003a). However, the influence of these factors is still under question, with some discrepancies in the literature – for example, ionic strength has been seen by some groups to encourage Prx oligomerisation (Chauhan and Mande, 2001), while others suggest it actually inhibits assembly (Papinutto *et al.*, 2005). The conservation and evolutionary persistence of this oligomeric switching strongly

suggests an important relationship to function, and the study of this feature of Prxs has become an area of research interest (Chauhan and Mande, 2001; Matsumara *et al.*, 2008; Schröder *et al.*, 1998 and Kristensen *et al.*, 1999).

1.2.4.1 The dimer interface relies on non-covalent interactions

The dimer interface forms through an anti-parallel association of the $\beta 7$ sheets of two monomers, stabilised by H-bonds, hydrophobic interactions and salt bridges, and is denoted the B-type interface (Wood *et al.*, 2002; Sarma *et al.*, 2005; figure 1.4).

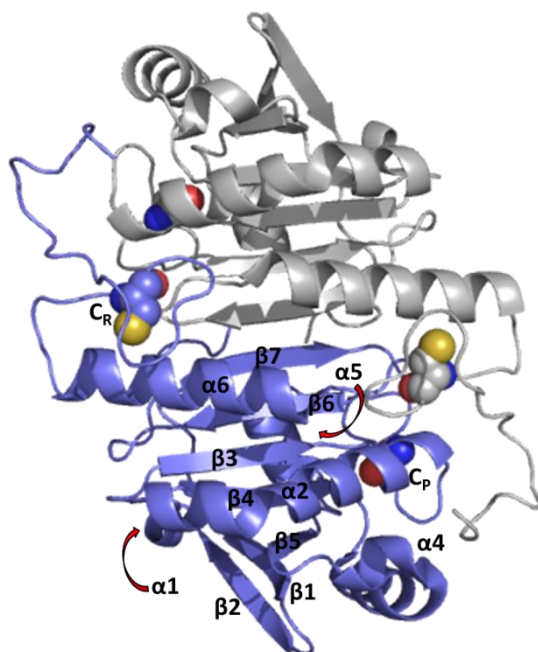


Figure 1.4: The dimer interface is stabilised by non-covalent interactions

Anti-parallel association of the $\beta 7$ sheets leads to dimerisation of monomers. The C-terminal arm of each monomer reaches across to contact the active site of the other; monomers are coloured blue and grey to highlight this. Labels are shown for the blue monomer only. The resolving and peroxidatic cysteine are shown as spheres (although the latter was mutated to serine for crystallisation in this case). PDB ID: 1N8J (Wood *et al.*, 2003).

When C_P becomes oxidised, a large conformational change occurs as the C-terminal arm reaches across the interface, allowing C_R to contact C_P of the other monomer. A disulfide bond can now form between the cysteines of the two monomers, covalently linking the subunits and forming a domain-swapped dimer. This typically buries ~1000 Å² and 30 residues per monomer, and represents the stable homodimeric functional unit of typical 2-Cys Prxs (Wood *et al.*, 2002; Alpey *et al.*, 2000).

1.2.4.2 The oligomer interface is an A-type interface

Prx dimers are able to associate further, into toroidal oligomers which can be composed of four, five or six dimers (Wood *et al.*, 2002; Li *et al.*, 2005; Schröder *et al.*, 2001; Cao *et al.*, 2005; figure 1.5). A second interface is involved in this association of Prx dimers, and appears to be less stable, forming and dissociating in response to a number of factors – most notably, redox state. It forms perpendicular to the β sheets through contacts between the loop and helix regions of the monomer (figure 1.6). This interface – denoted A-type (Sarma *et al.*, 2005) – is more highly conserved and widespread than the B-type interface, being recorded throughout all Prx subfamilies and comprising the dimer interface of some atypical Prxs such as human PrxV (Declercq *et al.*, 2001). These Prxs undergo a redox sensitive monomer-dimer transition, reminiscent of the dimer-oligomer behaviour of 2-Cys Prxs (Noguera-Mazon, 2006; section 1.2.5.6), and implicating the role of the A-type interface in the redox switch of Prxs. Together, these have led to the speculation that the A-type interface preceded the B-type interface in Prx evolution (Sarma *et al.*, 2005).

Typical A-type interfaces are stabilised through hydrophobic interactions between residues that are mostly located in four regions (referred to as I – IV, as suggested by Wood *et al.*, 2002). Region I is made up of the conserved loop-helix of the active site (using *BtPrx3* numbering for reference – residues 41-45; between the β3 sheet and α2 helix) and packs against region II (residues 73-85; helix α4). Region III (residues 103-

104; $\beta 5$ - $\alpha 5$ loop) contacts region IV (residues 116-120; $\beta 1'$ - $\beta 2'$ hairpin) making less extensive hydrophobic interactions (figure 1.6).

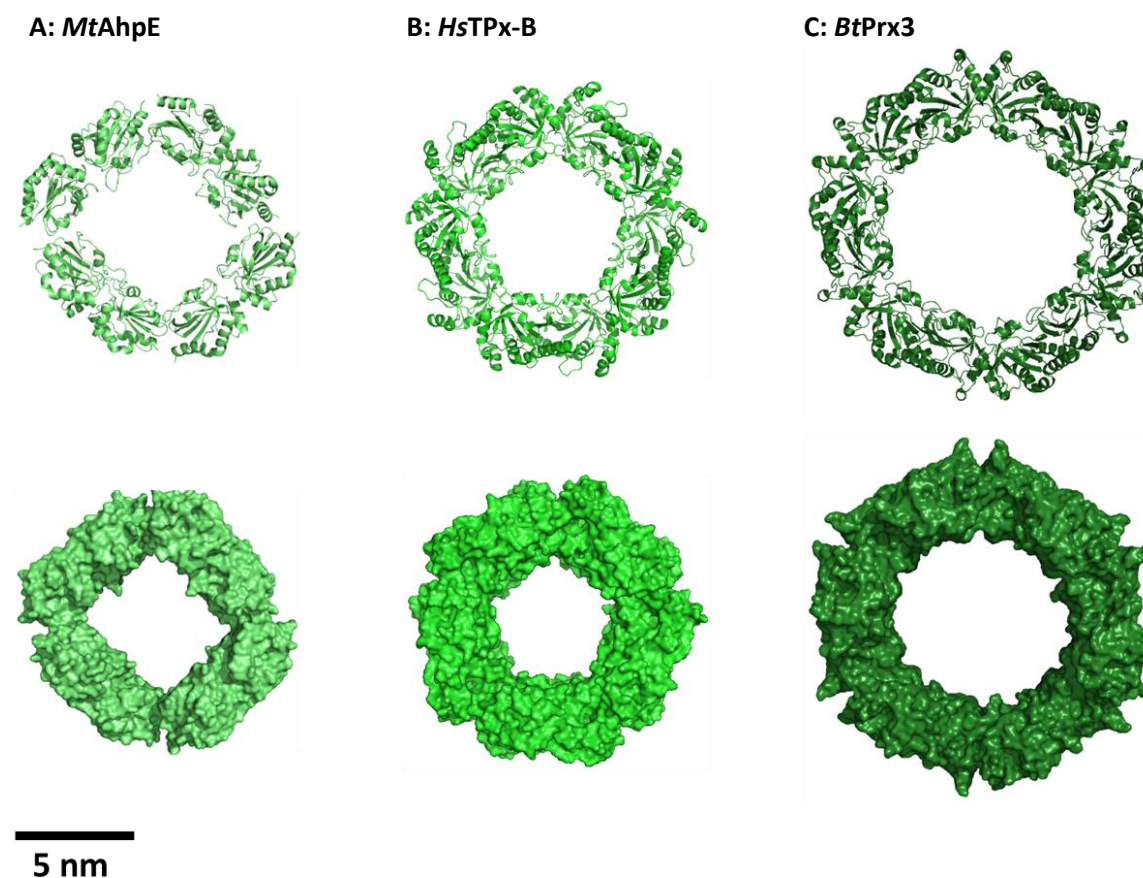


Figure 1.5: Prxs can form different multimers

Although most Prxs are able to associate into the typical, toroidal oligomer, the composition of this toroid can differ. The decamer (demonstrated here with human thioredoxin peroxidase B; PDB ID: 1QMV, Schröder *et al.*, 2000 [B]) is the most common; however, octamers (such as *Mycobacterium tuberculosis* AhpE; PDB ID: 1XXU, Li *et al.*, 2005 [A]), further discussed in section 1.4.2) and dodecamers (bovine peroxiredoxin 3; PDB ID: 1ZYE, Cao *et al.*, 2011 [C]) have been observed.

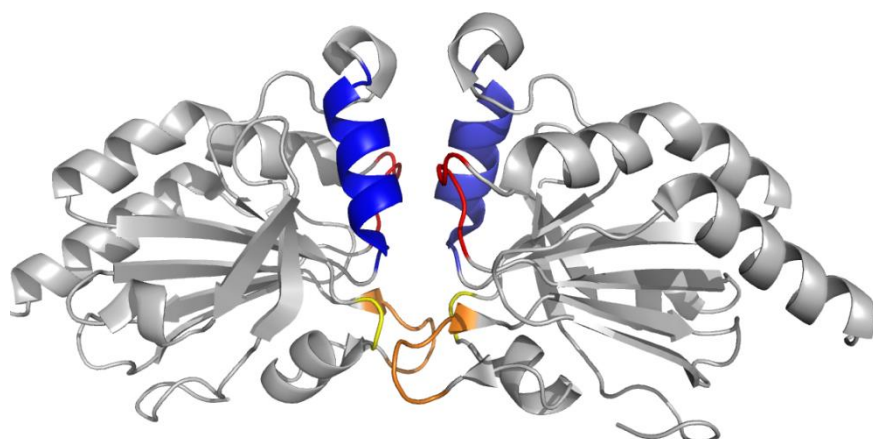


Figure 1.6: The oligomer interface is stabilised by loop and helix interactions

Region I (red) is composed of residues preceding C_P , and interacts with region II (blue), comprising residues from helix α_4 , burying a large hydrophobic area. The loops that make up regions III (yellow) and IV (orange) contact each other in a less extensive interaction. The A-type interface of *BtPrx3* is shown as a typical oligomer interface (PDB ID: 1ZYE; Cao *et al.*, 2005).

1.2.4.3 Catalysis involves conformation changes around the active site

A mechanism for the redox-sensitivity of the A-type interface has been suggested, based on comparison between crystal structures of different Prxs in varying oxidation states. This involves the C_P -loop, which forms above the active site and is comprised of the four residues preceding C_P (Wood *et al.*, 2002). The later publication of crystal structures of both the oxidised and reduced form of the 2-Cys PrxIV supported this theory (Cao *et al.*, 2011). However, PrxIV is unique in that it does not dissociate when oxidised, so while it can give some information about the changes that occur upon oxidation, it may not be representative. Eukaryotic 2-Cys Prxs contain two conserved elements – a loop between helix α_4 and the β_5 sheet containing the GGLG motif; and an additional helix at the C-terminal which contains the YF motif (figure 1.7A; Wood *et al.*, 2003b).

[illegible]

3D ribbon diagram of the B3 domain of the B3- α 2 loop. The diagram shows the protein structure with helices and loops. Key features labeled include $\alpha 6$, $\alpha 2$, C-terminal helix, B3- α 2 loop, C_R , and C_P .

A: PrxIV contains the GGLG motif (green), and the YF motif (cyan) contained in a C-terminal helix. **B:** In reducing conditions the C-terminus is folded into the helix, and C_P (shown as spheres) is buried in the folded helix $\alpha 2$. **C:** Upon oxidation, the N-terminal end of helix $\alpha 2$ unwinds into the disordered C_P loop, exposing C_P and allowing the disulfide bond to form, trapping the loop in this unfolded conformation. Image created using data deposited by Cao *et al.*, 2011; PDB ID: Reduced form (left) 3TJF; Oxidised form (right): 3TJG.

Prior to peroxidation, when C_P is reduced, the loop and helix containing the GGLG and YF motifs respectively pack together and bury helix α 2 (and, therefore, C_P), with C_R located 14 Å away (figure 1.7B). In order for the catalytic cycle to occur, the active site must undergo a conformational change to expose C_P and bring C_R within 2 Å for

disulfide bond formation. This involves at least local unfolding, whereby the first turn of helix $\alpha 2$ unwinds to form the disordered C_P loop, and expose C_P . This region exists in dynamic equilibrium between the pre-peroxidatic folded helix (the fully folded – FF – form), and locally unfolded (LU) loop, allowing the disulfide bond to form when the helix unwinds.

1.2.4.4 Active site unfolding promotes oligomer dissociation

When the $\alpha 2$ helix is fully folded, it pushes region I against region II (helix $\alpha 4$), stabilising the interactions which would otherwise be weak (refer to figure 1.6). As the helix unwinds, this effect is removed and the interface dissociates. The formation of the disulfide bond locks helix- $\alpha 2$ into the LU conformation (figure 1.7C), with the C_P loop also becoming more mobile and destabilising the A-type interface. This theory was based on a comparison of the oligomer of one Prx (AhpC) with the dimer of another (HBP23), and, with the lack of crystal structures of both conformations for one particular Prx, is therefore somewhat speculative (Wood *et al.*, 2002).

The crystal structure of tryparedoxin peroxidase (TryP) provides some support to this proposed mechanism – although the structure is of the reduced enzyme, three of the monomers show a locally unfolded active site, confirming that this region exists in dynamic equilibrium between FF and LU (discussed in section 1.2.5.3). These structures support the gross conformational changes suggested by Wood *et al.*; however, individual interactions differ. It was suggested that the LU state of AhpC leads to movement of F42 and exposure of W82, which in turn moves and leads to interface restructuring. However, the LU state of TryP did not result in movement of either of the equivalent residues (F48 and W87; figure 1.8). Phe50 of TryP (equivalent to Phe44 of AhpC), on the other hand, shifts by 5.5 Å, to a position that would project toward the other monomer, possibly causing a steric clash and interface dissociation when the LU is locked by disulfide bond formation.

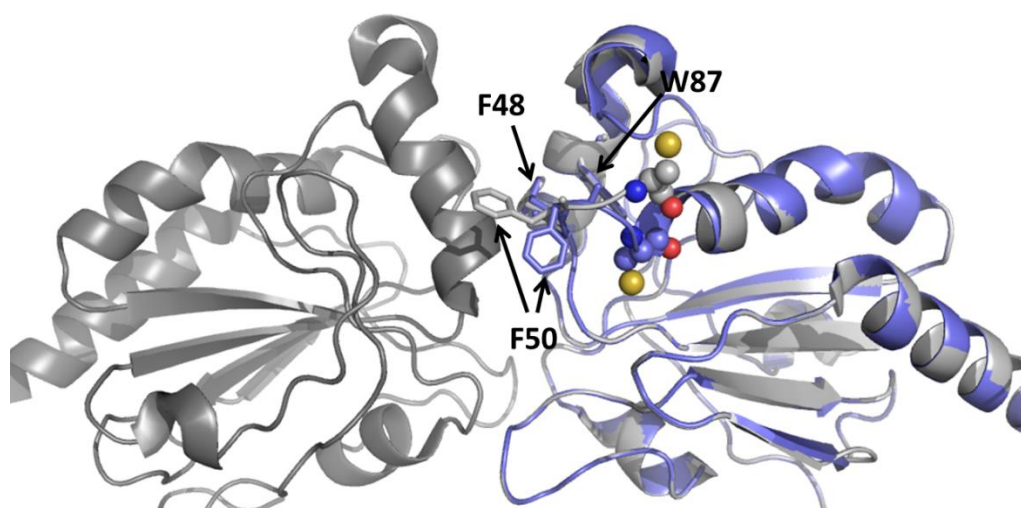


Figure 1.8: Individual residue movements contribute to interface dissociation

Overlaying a monomer with a folded active site (blue) with one that is in the locally unfolded conformation (light grey) reveals the increased mobility of the C_P loop (evident from the unwinding around C_P and its change in position). F48 and W87 (equivalent to F44 and W82 of HBP23 described by Wood *et al.*, 2002) show no significant movement. F50 adopts a different position, moving over 5 Å toward the next monomer in the toroid (dark grey), potentially introducing a steric clash. Image created using data deposited by Alphey *et al.*, 2000; PDB ID: 1E2Y.

Hydrophobicity is known to be important in stabilising interfaces, whereas individual interactions determine the specificity of association of transient interfaces (Clothin and Janin, 1975). The low stability, and inability of some Prxs to form the A-type interface despite high structural conservation, suggests that this interface is more reliant on specific interactions than hydrophobic packing. This specificity at the A-type interface presumably prevents incorrect assembly with other Prxs within the cell. It also means that analysis of the dissociation mechanism cannot necessarily be generalised between individual members of the Prx family. Until crystal structures of both oxidised, dimeric and reduced, oligomeric states of the same Prx are available, our understanding of the dissociation mechanism will be incomplete.

1.2.4.5 The implications of Prx oligomerisation are not fully understood

The active site is located near to the oligomer interface. This suggests that oligomer formation is key in maintaining the active site in a functional conformation. Interestingly, across the different multimers seen throughout the Prx family, it is the dimer interface that shifts arrangement, with the oligomer interfaces remaining equivalent (Gretes and Karplus, 2013). This further highlights the importance of this interface in Prx function.

It is not unusual to find the active site of enzymes located on subunit interfaces, with numerous examples of ring-like structures seen in enzymology. For example, cyanase exists as a functional decamer (Anderson *et al.*, 1994). However, whereas cyanase catalyses the hydrolysis of cyanate in a half-site binding reaction (i.e., stoichiometry of 2 monomers to 1 substrate molecule), the Prx active site is complete in the monomer. Therefore the oligomer must contribute to catalysis through a more subtle mechanism than simply bringing two halves of the active site together. There is evidence to suggest that the oligomer interface stabilises the FF active site, as mutations that stabilise the A-type interface enhance catalysis, presumably through impeding the loop movements that would usually cause destabilisation (Parsonage *et al.*, 2005). However, with prevention of dissociation leading to increased efficiency, this does not explain the necessity of the oligomeric switching. It may be that stabilisation of the toroid leads to an increased susceptibility to inactivation by hyperoxidation (discussed in section 1.2.4), and so the ability to switch quaternary structures is the result of a balance between catalytic efficiency and protection against hyperoxidation (Wood *et al.*, 2003b).

1.2.5 Hyperoxidation of Prxs suggests roles beyond detoxification

Early studies found that 2-Cys Prx engaged in the catalytic cycle became inactive with prolonged exposure to H_2O_2 (Chae *et al.*, 1994a). Crystallisation of Prxs extracted from erythrocytes that had been stored for long periods showed the presence of a sulfinic acid – $\text{S}_\text{P}\text{O}_2\text{H}$ – in the active site, suggesting a second oxidation had occurred before the disulfide bond formed. This prevented recycling back to the reduced form and thus rendered the enzyme inactive (Schröder *et al.*, 2000). Bacterial Prxs were noticed to be less susceptible to this “hyperoxidation” than those of plants, mammals or yeast, which have even been found further oxidised to sulfonic acid forms – $\text{S}_\text{P}\text{O}_3\text{H}$ (Rabilloud *et al.*, 2002).

1.2.5.1 Sensitivity to hyperoxidation suggests a role in cell signalling

Sequence alignment identified two features conserved in all Prxs that are prone to hyperoxidation –the GGLG motif, and YF motif-containing C-terminal helical extension (section 1.2.4.3). These motifs have been shown to be absent from all Prxs that cannot undergo hyperoxidation (exclusively prokaryotic; Wood *et al.*, 2003b). As the GGLG and YF regions pack against the $\alpha 2$ helix and C-terminus (figure 1.9), the unfolding associated with oxidation is impeded, slowing disulfide formation and leaving the sulfenic acid vulnerable to further oxidation by H_2O_2 (Wood *et al.*, 2003b). This is supported by mutational studies which show that deletion of the YF-motif containing C-terminal tail prevents inactivation by hyperoxidation (Koo *et al.*, 2002), and also explains the resistance of prokaryotic Prxs, as they lack this C-terminal region (Barranco-Medina *et al.*, 2009; Wood *et al.*, 2002).

Initially, the reduction of Prx hyperoxidation *in vitro* appeared to be impossible, as Trx and other reducing agents were ineffective. Conservation of this mechanism throughout Prx evolution therefore seemed surprising, as every catalytic cycle regenerates reduced

enzymes, susceptible to apparently irreversible inactivation. Later studies revealed that *in vivo* this reaction is in fact reversible, leading to the discovery of sulfiredoxin (Srx) (Woo *et al.*, 2003; Biteau *et al.*, 2003). Srx catalyses the regeneration of active Prx through an ATP and magnesium dependent mechanism, whereby C_P is first phosphorylated to allow formation of a thiosulfinate species with Srx. Prx can then be released in its sulfenic acid form to be reduced by the normal reductant, and Srx is recycled by a Trx (Roussel *et al.*, 2008; Roussel *et al.*, 2009).

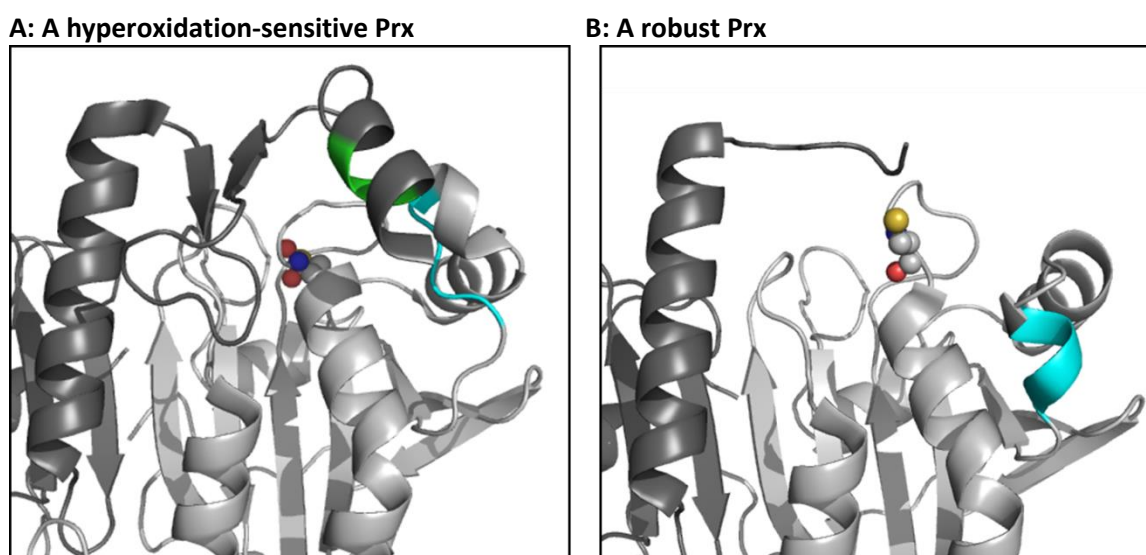


Figure 1.9: Prxs sensitive to hyperoxidation contain an additional helix

A: The active site of a hyperoxidation-sensitive Prx (human PrxII PDB ID: 1QMV, Schröder *et al.*, 2000) is enclosed by the helix containing the YF motif (green) and the loop containing the GGLG motif (cyan). **B:** Robust Prxs (*S. typhimurium* AhpC, PDB ID: 1YEP, Parsonage *et al.*, 2005) lack the C-terminal extension and helix, and without the GGLG motif the loop following helix α_4 folds into an additional helix (indicated in cyan).

Despite its toxicity, H₂O₂ is sometimes produced intentionally by cells – for example, production has been seen in response to wounding (Neithamme *et al.*, 2009). H₂O₂ is now well characterised as an intermediate in numerous signalling pathways (reviewed in Veal *et al.*, 2007; Stone and Yang 2006) – for example, platelet derived growth factor (PDGF) induces a transient increase in intracellular H₂O₂ levels, which controls the

activity of downstream enzymes through oxidation of active site cysteine residues (Chiarugi *et al.*, 2001). The realisation that Prx hyperoxidation was reversible, together with previous evidence of Prx's role in peroxide signalling cascades (Fujii and Ikeda, 2002) led to the suggestion that Prxs may be the regulators that determine whether H_2O_2 acts as a deleterious molecule or a signal (Wood *et al.*, 2003b). This is supported by *in vivo* studies showing that a number of 2-Cys Prxs were inactivated following the transient increase in peroxide associated with tumour necrosis factor (Rabbilloud *et al.*, 2002). Recently, GGLG and YF motifs have been discovered in prokaryotes allowing rapid inactivation and reactivation of Prxs, and presenting the possibility of a similar signalling role to the eukaryotic enzymes (Pascual *et al.*, 2010).

1.2.5.2 Quaternary structure may determine Prx activity

The number of Prx genes appears to increase with evolution, with higher organisms expressing considerably more isoforms than prokaryotes and archaea. This correlates with an increased number of subcellular locations, and also the emergence of multiple roles for these proteins within the cell. Prxs have been found to have other putative functions – for example, a human 1-Cys Prx has been found to have phospholipase A_2 activity, using a different active site, at low pH levels (Kim *et al.*, 1997; Chen *et al.*, 2000). As higher organisms generally express catalase and GPx, the role of Prxs in antioxidant defence appears less critical than in bacteria, which often lack other systems. Hyperoxidation has been seen to be coupled to the formation of high molecular weight (HMW) structures of up to 1000 kDa *in vivo*, whose formation can be induced by heat shock or H_2O_2 stress (Jang *et al.*, 2004). This led to the suggestion that these HMW structures may have discrete functions.

Chaperone proteins often exist as HMW structures, and the Trx fold has been found to play a role in some proteins' chaperone activity (Kern *et al.*, 2003). The resemblance of Prx structures to these chaperone proteins, and the appearance of HMW structures in times of cellular stress prompted investigation, and subsequent confirmation, of the *in*

vitro chaperone activity of several human and yeast Prxs. The HMW assemblies of a number of Prxs have been seen to effectively reduce protein aggregation of denatured proteins, with dissociation of the HMW forms preventing this activity (Moon *et al.*, 2005; Park *et al.*, 2011). Mutational studies showed C_P to be essential for HMW formation following H₂O₂ exposure, implicating hyperoxidation of this residue in driving assembly (Moon *et al.*, 2005). However, in some cases, mutation of C_P to serine has led to the fast formation of HMW complexes, even without H₂O₂ treatment. This suggests that there are two pathways of HMW complex formation: an H₂O₂-dependent pathway that relies on the hyperoxidation of C_P; and an H₂O₂-independent pathway. In some cases, hyperoxidation of C_P has been seen to lead to the formation of a stable, single toroid (Jönsson *et al.*, 2008). The formation of this toroid has been suggested to occur through a different mechanism to the reduced toroid (Muthuramalingam *et al.*, 2009), supporting the theory of H₂O₂-dependent and H₂O₂-independent assembly mechanisms. A clue to this mechanism was provided by the crystal structure of a Prx in complex with Srx (Jönsson *et al.*, 2008), which showed C_P to be flipped to the outside of the molecule, indicating that assembly of hyperoxidised toroids is very different from that of reduced toroids.

The reasons why the hyperoxidised toroids of some Prxs are able to associate further, whereas others appear to remain as single stable toroids, is not known. Of the few Prxs for which HMW structures have been recorded, a number are mitochondrial. This may suggest a link with localisation in regions of high oxidative stress (Gourlay *et al.*, 2003; Kato *et al.*, 1985). Prx chaperone activity has been seen to prevent α -synuclein aggregation *in vitro* (Jang *et al.*, 2004). These complexes could therefore exist as a protective mechanism, which would explain the overexpression of Prxs in diseases such as Alzheimer's and Parkinson's disease, which are associated with α -synuclein aggregation (Kim *et al.*, 2001). This theory is supported by a recent study which showed the protective effects of PrxI when it was overexpressed in an *in vitro* Alzheimer's model (Cimini *et al.*, 2013).

1.2.5.3 Organisation of HMW structures

The structure of HMW forms was one of the earliest recorded features of the Prxs, with “cylinder protein” observed in erythrocyte membrane and mitochondrial extracts (Harris, 1969; Kato *et al.*, 1985). Since then similar tubes have been reported, transpiring to be composed of laterally associated toroids (figure 1.10A). The similarity of this tubular assembly to a number of other chaperone proteins (for example, the GroEL complex, Xu *et al.*, 1997), supported a possible chaperone function.

Available literature indicates that the appearance of HMW species is widespread across the families, with a number of factors influencing their formation including hyperoxidation, phosphorylation and presence of metals ions (Jang *et al.*, 2004; Jang *et al.*, 2006; Kato *et al.*, 1985). Two examples that report both the structure and chaperone function of a HMW species in solution, formed after exposure to oxidative stress, saw spherical clusters (figure 1.10D; Jang *et al.*, 2004; An *et al.*, 2011). Although quite different to the stacked toroid assemblies, these are reminiscent of yet another Prx structure – a dodecahedral cage (Meissner *et al.*, 2007; figure 1.10C and D), which again show similarity to other chaperone proteins (for example, Malet *et al.*, 2012). The existence of HMW structures often identified through SEC analysis (for example, Moon *et al.*, 2005; Jang *et al.*, 2006), and few conclusive studies that directly linking the structure and activity, the question of whether the differing morphologies have different activities remains unanswered.

The tubular structures seen in early micrographs appear to be the most common arrangement when toroids associate, with a number of different groups reporting this structure from different Prxs (for example, Harris *et al.*, 2001; Gourlay *et al.*, 2003; Saccoccia *et al.*, 2012). The factors controlling this “stacking” of toroids are complex, with a number of conditions appearing to drive their formation. The active site has been identified as important to the activity and tertiary structure of Prxs (section 1.2.3.2), but also has a clear impact on the quaternary structure. Loss of active site architecture has

been attributed to the stacking of toroids (Saccoccia *et al.*, 2012), which is supported in the increased stacking seen in Prx samples where the active site has been disrupted through C_P mutation (Gourlay *et al.*, 2003).

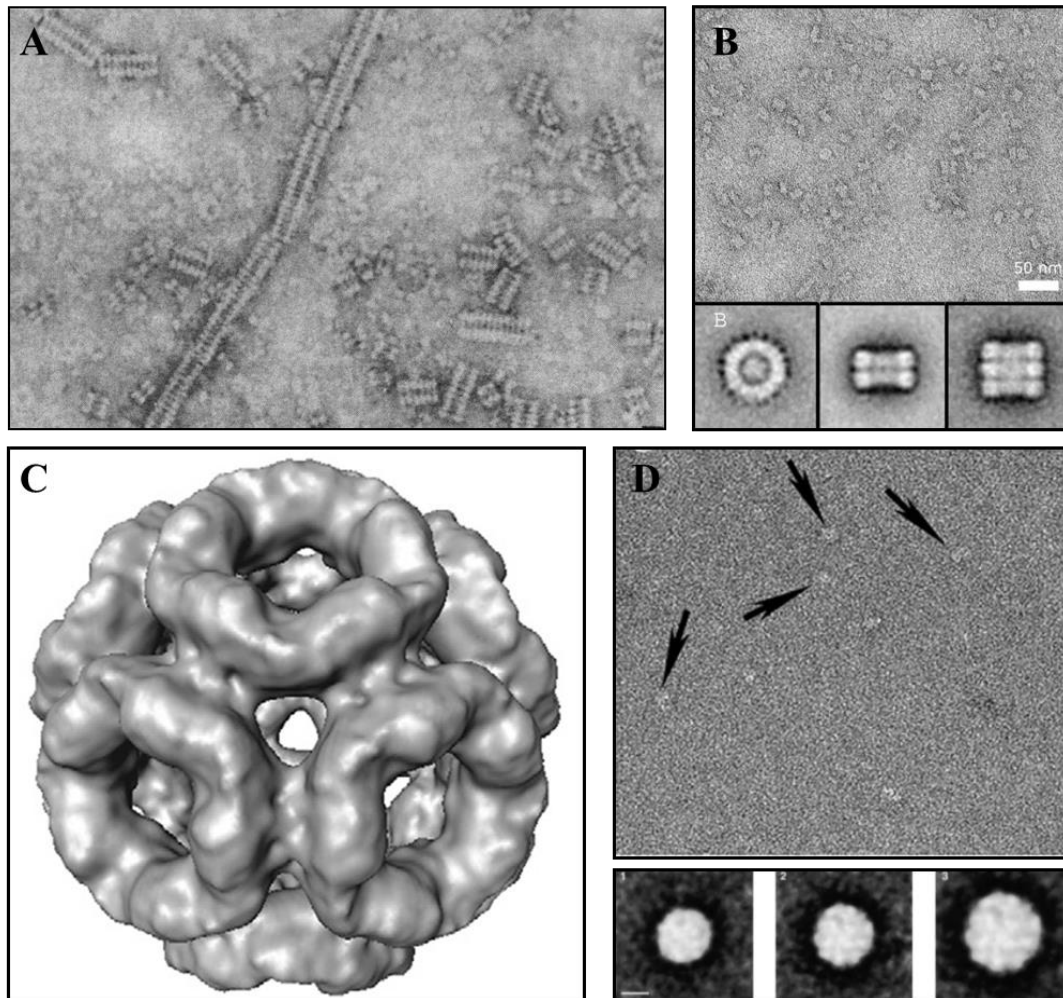


Figure 1.10: Prxs form a wide range of HMW structures

A: Early studies revealed tube-like structures in preparations of a mitochondrial Prx (Kato *et al.*, 1985). **B:** Small stacks of toroids are seen in preparations of *BtPrx3* (Gourlay *et al.*, 2003). **C:** The dodecahedral cage structure was solved by TEM reconstruction (Meissner *et al.*, 2007). **D:** Spherical structures have been seen to form after exposure to oxidative stress (Jang *et al.*, 2004; An *et al.*, 2011).

The first images of associated tubes were recorded by Harris (1969), as purified Prx1 from erythrocyte membranes was seen to form small stacks of toroids. Kato *et al.*, (1985) reported a similar result with murine Prx3, and went on to demonstrate that the formation of stacks and longer tubes required the presence of magnesium ions, with the addition of a chelating agent causing dissociation to toroids. *BtPrx3* has since been seen to behave similarly, with initial characterisation showing small stacks which could be encouraged to associate into longer tubes through the mutation of C_P (Gourlay *et al.*, 2003; figure 1.10B). Mutation of C_R of *BtPrx3* gave rise to the intriguing concatenated crystal structure that was later seen to exist in solution (Cao *et al.*, 2005; Cao *et al.*, 2007). However, in the case of both the mutant and wildtype *BtPrx3*, the stacks were recorded from samples in which the his-tags have not been removed, which has been seen in this thesis and by others to stabilise the oligomer and encourage HMW formation (Cao *et al.*, 2007; section 4.3.1.3).

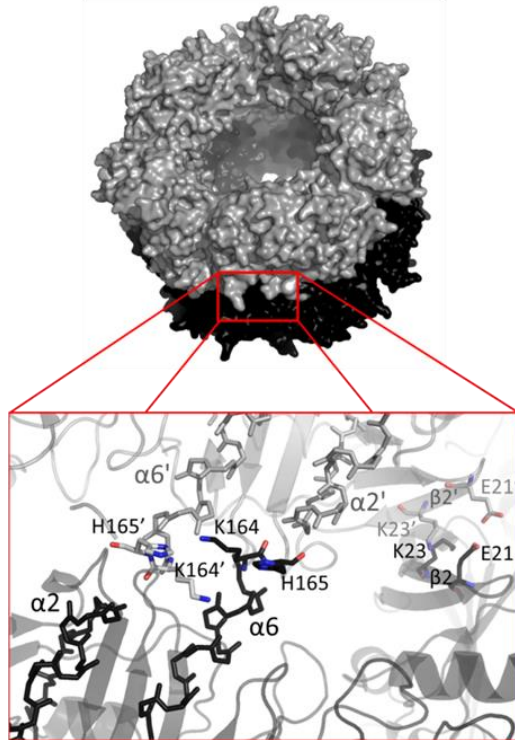
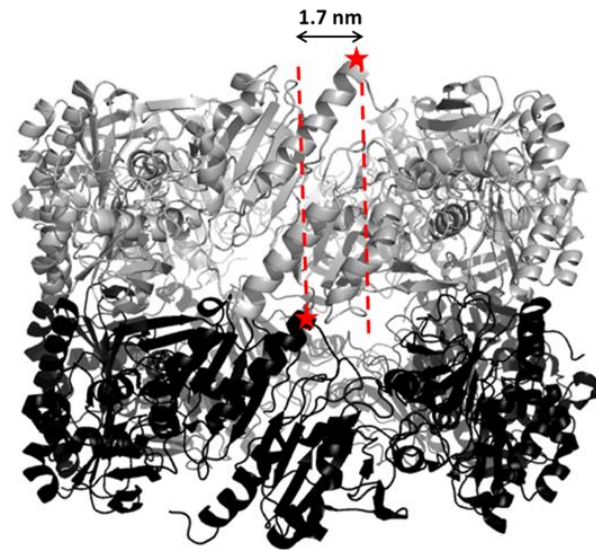
1.2.5.4 The “R-type” interface directs toroid stacking

The publication of a crystal structure of two stacked toroids during the course of this work gave some insight into the mechanism behind stacking, and potentially a physiological relevance of the stacks. Saccoccia *et al.*, (2012) demonstrated that lowering the pH encouraged stacking, suggested to be due to the disruption of the R123-C_P ionic bond which stabilises the active site (section 1.2.3.2). When C_P is hyperoxidised the S_PO₂H/S_PO₃H is unable to interact with arginine, and furthermore, its increased hydrophobicity and volume cause it to move out of the active site pocket, disrupting the active site architecture (Saccoccia *et al.*, 2012; Jönsson *et al.*, 2008).

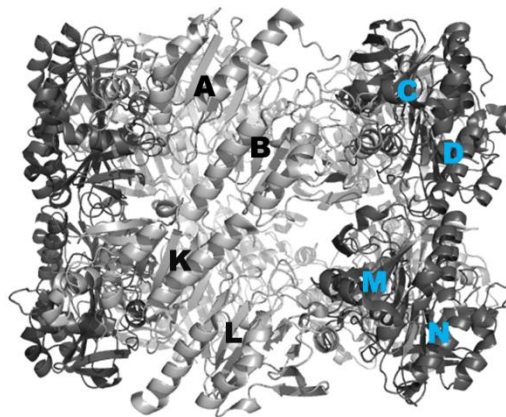
As C_P moves out of the active site, helix α_2 begins to unwind, preventing the C-terminus folding and packing against the active site (section 1.2.5.3). This results in a shift in the positioning of dimers within the toroid (compared to that of a reduced toroid), causing the α_6 helix to move into a position which allows the ends of the α_2 and α_6 helices to interact with equivalent helices of dimers in the toroid above or below

(figure 1.11). The carbonyl groups of these helices point toward the R-type interface, creating a negatively charged area which is stabilised by the positively charged lysine and histidine at the end of helix α_6 (figure 1.11A). Two polar contacts between the β_2 sheets of monomers further stabilises the interface. Whilst the helical interactions occur between dimers directly above and below each other in the stack, the β sheet interactions are with the next dimer, contributing to the rotation that is seen between the toroids (figure 1.11B and 1.12).

The elucidation of this interface led to a potential explanation for the chaperone activity of Prx HMW forms. It had been hypothesised that Prxs bind their unfolded substrates via disordered hydrophobic regions (Kumsta and Jakob, 2009). Saccoccia *et al.* (2012) proposed that the unfolded C-termini and active sites in the toroid stack could provide the unfolded hydrophobic region (Saccoccia *et al.*, 2012; Angelucci *et al.*, 2013). Substrate could therefore bind at the end of the stacks where these regions are exposed. This leads to the question of why the toroids associate into long tubes in some cases, which would occlude some binding sites; possibly hinting at another, as yet unknown, function for the very high weight structures of Prxs.

A: Interactions at the R-type interface**B: Cartoon representation of stacked toroids****Figure 1.11: The R-type interface is stabilised by electrostatic interactions**

A: Unwinding of the $\alpha 2$ helix allows contact between this and the $\alpha 6$ helix of the monomer below, in the region indicated by the red box. Electrostatic interactions stabilise the interface. **B:** Formation of the R-type interface interactions results in the toroids being rotated at 18° to each other. The C-terminal end of the $\alpha 6$ helices in two equivalent monomers in each toroid are indicated by stars, which exemplify the rotation, showing an approximate lateral shift of 1.7 nm relative to each other (as measured by PyMol analysis [DeLano, 2002]).

**Figure 1.12: Each monomer interacts with two others in the stack, causing a pitch**

Monomer B interacts with K from the toroid below, via the $\alpha 6$ and $\alpha 2$ helices. B also makes contact with monomer M, further along in the bottom toroid, through the $\beta 2$ sheets. The toroids, therefore, do not align directly on top of each other, but instead are rotated to each other. Dimers are coloured alternately light grey and dark grey around the toroid, with labels in black and cyan. PDB ID: 3ZVJ.

1.3 Human Prxs

Humans express six Prx isoforms: Prx1-4 are typical 2-Cys Prxs, Prx5 is an atypical 2-Cys Prxs, and Prx6 a 1-Cys Prx. Although the increased number of Prxs in higher organisms compared to bacteria would suggest an amount of redundancy within mammalian Prxs, this is largely not seen, with knockout mice displaying pathologies and shortened lifespan in some cases.

1.3.1 Prx knockouts show oxidative sensitivity

The first Prx to be discovered, torin, is now known to be human Prx2 (*HsPrx2*), and was identified through TEM analysis of a toroidal protein complex comprising 20 kDa subunits from human erythrocytes (Harris, 1968; Harris 1969). Since then the human Prxs have been found to occur a range of subcellular localisations, and carry activities beyond the reduction of peroxides. These are summarised in table 1.1. Their roles in ion transport and potential chaperone activity has led to the hypothesis that they have significant roles in apoptosis (Low *et al.*, 2008). The severity of knockout mice confirms their importance for normal cell function, supported by their promiscuous interactions with a number of regulatory and signalling proteins (Jin *et al.*, 1997; Hirotsu *et al.*, 1999). Many of the Prxs are upregulated in response to oxidised lipoproteins and other indicators of cellular stress, implicating them in the prevention of pathologies including atherosclerosis (Shau *et al.*, 1997). Although confirmed in some cases through knockout phenotype, (Low *et al.*, 2007; Park *et al.*, 2011b) this upregulation is, in many instances, unclear as to whether it is a cause or effect of the pathology. It is therefore unsurprising that the regulation of the Prxs has been suggested as a potential approach for therapeutics or their use as biomarkers (Cha *et al.*, 2009).

1.3.2 Human Prx3

Prx3 was discovered early in Prx research, with the identification of cylindrical structures from bovine mitochondria (Kato *et al.*, 1985). Being localised to the mitochondria, human Prx3 (*HsPrx3*) has a key role in the mitochondrial antioxidant defence system and homeostasis (Cox *et al.*, 2010). This in turn implicates *HsPrx3* in a variety of processes including cell differentiation and death, metabolic regulation, inflammation and diseases associated with ageing, and recent studies have highlighted *HsPrx3* as a key player in a number of cancers, notably cervical cancer (Safaeian *et al.*, 2012; Li *et al.*, 2013).

Table 1.1: Human Prx isoforms undertake essential roles within the cell

The six isoforms carry out a number of activities beyond their antioxidant function. The severity and shortened lifespan of knockout mice (of the murine equivalent Prx) highlights their importance, as detailed below.

Isoform	Cellular location	Additional roles	Knockout phenotype	Reference
Prx1	Erythrocyte cytosol	Cell proliferation, anti-apoptotic activity, possibly anti-viral	Haemolytic anaemia, inflammation and cancer, short lifespan	Jin <i>et al.</i> , 1997; Hirotsu <i>et al.</i> , 1999; Neumann <i>et al.</i> , 2003
Prx2	Erythrocyte cytosol	Haemoglobin stabilisation, membrane K ⁺ transport	Atherosclerosis, sensitivity to oxidative stress	Schröder <i>et al.</i> , 1998; Schröder <i>et al.</i> , 1999; Han <i>et al.</i> , 2012; Low <i>et al.</i> , 2007; Park <i>et al.</i> , 2011b
Prx4	Endoplasmic reticulum	Interact with and activate NF-κB	Not available	Chang <i>et al.</i> , 2011; Chen <i>et al.</i> , 2002; Schulte <i>et al.</i> , 2011
Prx5	Mitochondria, cytoplasm	Anti-apoptotic activity	Shortened lifespan through oxidative stress	Radyuk <i>et al.</i> , 2009
Prx6	Mitochondria	Role in reperfusion-ischemia oxidative stress, lipid metabolism	Reduced wound healing	Eismann <i>et al.</i> , 2009; Yang <i>et al.</i> , 2012; Kümin <i>et al.</i> , 2007

Although the crystal structure of *HsPrx3* has not yet been solved, there is a structure available for the bovine homologue (*BtPrx3*) – which shares 93% sequence identity with *HsPrx3*, and has therefore been taken to be representative of the structure of *HsPrx3*. *BtPrx3* shows some unusual structural features – whereas most of the 2-Cys Prxs have been seen form oligomers made up of five dimers, *BtPrx3* forms a dodecamer. The mechanism of Prx3 oligomerisation involves the two typical interfaces – the B-type dimer building interface, and the A-type dodecamer building interface (section 1.2.5.1 and 1.2.5.2). The crystal structure of *BtPrx3* shows a buried area of 1772 Å² at the B-type interface, with the oligomer building interface also comprising a large hydrophobic area of 1270 Å², principally involving the hydrophobic residues Leu41, Phe43, Phe45, Val73, Phe77, Leu103 and Leu120 (Cao *et al.*, 2005; section 5.2.1). This structure was only able to be solved with a CR mutation, and therefore a disulfide bonded structure of *BtPrx3* has not been seen.

Whilst the kinetics and roles of *HsPrx3* in a number of pathologies have been the subject of a considerable amount of research (for example, Peskin *et al.*, 2007; Peskin *et al.*, 2013; Li *et al.*, 2013; Simoni *et al.*, 2007), the structure and self-assembly have attracted surprisingly little interest. Generally considered to be a decamer (Winterbourn, personal communication), the crystal structure remains to be solved and in depth characterisations of the relationship of *HsPrx3* oligomerisation to environmental conditions is lacking. An understanding of the structural properties of the protein is essential if the self-assembly is to be controlled; and insight into the detailed mechanism could allow the design of small molecules to influence assembly. As well as the nanotechnological implications of controlling Prx assembly (section 1.5), altering the oligomerisation could have biomedical applications.

1.4 Prxs of *Mycobacterium tuberculosis*

1.4.1 Components of the *Mycobacterium tuberculosis* antioxidant systems

Mycobacterium tuberculosis (*M. tuberculosis*) lives in macrophages of the lungs and is a pathogenic bacterium responsible for nearly all forms of tuberculosis. The bacterium can survive inside the macrophage, despite low levels of nutrients and exposure to ROS produced by activated macrophages. Therefore, its antioxidant defence system must be extremely efficient. There are some unusual aspects of these antioxidant systems – unlike mammals, where the GPxs dominate, *M. tuberculosis* lacks a glutathione system and instead contains a system which includes mycothiol (the mycobacterial substitute for glutathione), KatG (a haem-containing enzyme with catalase, peroxidase and peroxynitrase activity), and at least five Prxs including AhpC, AhpE and TPx. This implicates the Prxs as having a major role in the antioxidant defence system of *M. tuberculosis* (Hugo *et al.*, 2009).

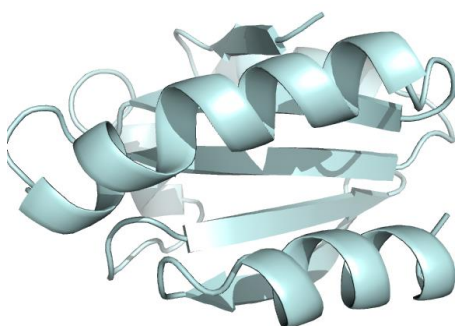
1.4.1.1 *M. tuberculosis* alkyl hydroperoxide reductase E

M. tuberculosis alkyl hydroperoxide reductase E (*MtAhpE*) is a 1-Cys Prx found in the proteome of *M. tuberculosis*, and is conserved among many *Mycobacteria*. Showing a relatively low rate of H₂O₂ reduction ($8.2 \times 10^4 \text{ M}^{-1}\text{s}^{-1}$ compared to that of TPx – $4 \times 10^7 \text{ M}^{-1}\text{s}^{-1}$; Hugo *et al.*, 2009), *MtAhpE* appears to be a highly selective peroxidase preferentially reducing peroxynitrites. Kinetic studies show the rate of *MtAhpE* peroxynitrite reduction to be equal to that of TPx, which had been thought to be the primary enzyme in *M. tuberculosis* antioxidant defence (rates of 1.9×10^7 and $1.5 \times 10^7 \text{ M}^{-1}\text{s}^{-1}$ respectively; Hugo *et al.*, 2009; Jaeger *et al.*, 2004; Hu and Coates, 2009) and ten times faster than that of catalase peroxidase. This suggests that *MtAhpE* is highly

significant in the pathology of this bacterium, and a possible drug target (Hugo *et al.*, 2009). Most Prxs and bacterial TPxs show specificity toward alkyl hydroperoxides (Choi *et al.*, 2003), so *MtAhpE* may be the primary defence against peroxynitrites. Compromising its function could therefore increase the bacterium's susceptibility to the host immune response.

Although it contains only one cysteine residue (C45 – concluded to be C_p by its sequence position PxxxTxxC), *MtAhpE* is structurally more similar to 2-Cys Prxs, with AhpC of *Salmonella typhimurium* (StAhpC) and TryP of *Crithidia fasciculata* being the closest structural homologues, matching with an root mean square difference of 1.4 – 1.5 Å at the C α position (Li *et al.*, 2005). The most notable structural differences are the lack of the C-terminal helical extension in *MtAhpE*, which contributes to dimerisation in many 2-Cys Prxs (figure 1.13). However, *MtAhpE* can form non-covalent dimers with A-type interfaces equivalent to the oligomer interface of 2-Cys Prxs (section 1.2.5.2). The enzyme has been suggested to exist as dimers and octameric rings in solution, supported by crystal packing data.

A: The Trx fold



B: The *MtAhpE* monomer

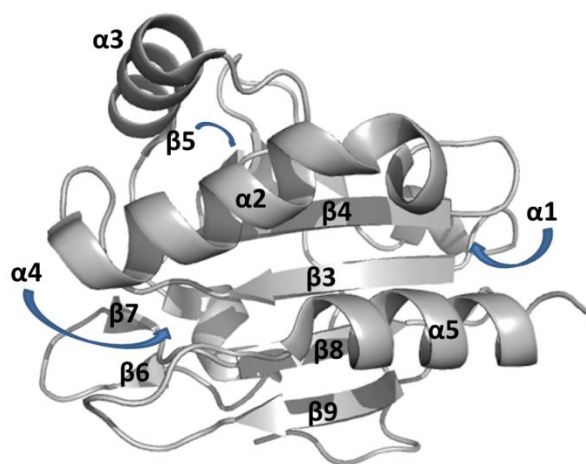


Figure 1.13: The *MtAhpE* monomer shows a compact structure

The crystal structure of *MtAhpE* shows few extensions to the basic Trx fold. A small N-terminal tail adjacent to the $\beta 9$ sheet, and the $\alpha 3$ helix (numbering as suggested by Li *et al.*, 2005) constitute the main extensions to the basic structure, which is considerably less decorated than that of a typical Prx (figure 1.2). Arrows refer to structural elements behind the central β sheets.

1.4.2 Characterisation of *MtAhpE*

1.4.2.1 *MtAhpE* is a 1-Cys Prx with unusual oligomeric properties

Whilst the existence of oligomeric rings is well documented for 2-Cys Prxs, biochemical characterisation of the 1-Cys Prxs remains scarce. Many of the 1-Cys family are monomeric (for example, Kang *et al.*, 1998), following a similar reaction mechanism to the 2-Cys Prxs, relying on the redox cycling of C_P. Despite the lack of disulfide bond, some of these Prxs have been seen to switch between monomeric and dimeric species associated with catalysis (Noguera-Mazon *et al.*, 2006); some further association to tetramers has been seen (Kim *et al.*, 2003; Brystrova *et al.*, 2007). The *in vivo* presence or significance of these structures is unknown (Brystrova *et al.*, 2007). The dimer interface is usually equivalent to the 2-Cys oligomer interface, and appears to be redox sensitive, governed by the local unwinding of helix $\alpha 2$, suggesting similar structural events to those of 2-Cys Prxs (Noguera-Mazon *et al.*, 2006, Wood *et al.*, 2002).

The crystal structure of the 1-Cys Prx *MtAhpE* has been solved, suggesting an octameric ring with an outer diameter of 115 Å and inner diameter 55 Å (Li *et al.*, 2005; figure 1.5). Oxidation causes conformational changes around the active site and attendant oligomeric changes, similar to typical 2-Cys Prxs (Li *et al.*, 2005). However, in contrast to all other known examples, reduced or hyperoxidised *MtAhpE* forms a dimer, with the oligomer forming in oxidising conditions and dissociation of the B-type interface governing disassembly. This presents an intriguing situation; a tight A-type interface that appears to be resistant to redox-induced dissociation (Li *et al.*, 2005).

There are a number of structural differences that could contribute to this phenomenon. Additional C-terminal domains (such as the “arm” that contributes to the domain swapped 2-Cys dimer, figure 1.4, or the C-terminal extension that mediates dimerisation of hORF6, a related 1-Cys Prx [Choi *et al.*, 1998]) are absent, possibly impeding the

rapid formation of a B-type interface and promoting the A-type as the dimer interface. C-terminal truncations in some Prxs have been shown to affect oligomeric state (Koo *et al.*, 2002) and so this could contribute to the unusual oligomerisation of *MtAhpE*. An N-terminal extension parallel to the $\beta 9$ sheet that appears to be unique to *MtAhpE* could also contribute to the increased stability of the B-type interface (section 1.3.2.3). A run of three proline residues is seen at the C-terminal end of helix $\alpha 3$. Although not an uncommon motif at a helical terminus, this motif is not conserved in other Prxs. The A-type interfaces are generally more flexible than the B-type so the structural rigidity conferred by proline residues may contribute to the increased stability of the *MtAhpE* interface.

1.4.2.2 The A-type dimer interface

The *MtAhpE* A-type interface is principally made up of residues 39-42 from the $\beta 3$ - $\alpha 2$ loops, 72-76, 79 and 83 from helix $\alpha 3$, 94-97 from the $\beta 3$ - $\alpha 4$ loop, 110-113 from the $\beta 6$ - $\beta 7$ hairpin loop. This creates an interface which is 70% hydrophobic, with important contributions from Leu39, Phe41, Pro75, Ile79, Phe94, Trp95 and His97 (figure 1.14). These reflect the regions I – IV of typical 2-Cys Prxs (section 1.2.5.2; figure 1.15).

Interestingly, this interface can be destabilised through the formation of a disulfide bond with a free thiol group (Hugo *et al.*, 2009). Although the dissociation of this interface is not seen in solution, this suggests that, like other Prxs, the quaternary structure of *MtAhpE* could be influenced by redox state, perhaps similar to another 1-Cys Prx that dimerises with an A-type interface – *Populus tremula* D-Prx. The dimer of this Prx is destabilised when C_P is reduced by GSH (Noguera-Mazon *et al.*, 2006).

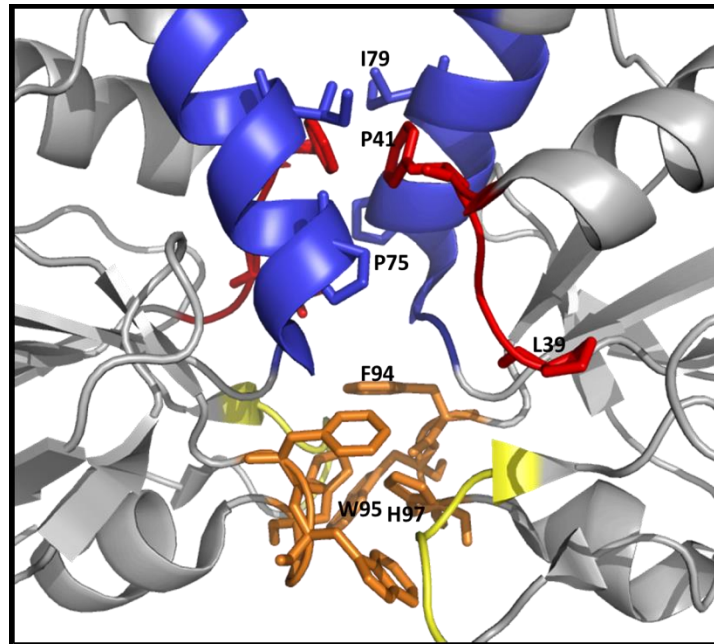


Figure 1.14: The *MtAhpE* A-type interface is stabilised by hydrophobic interactions

The interface is stabilised by interactions focused in the regions suggested by Wood *et al.*, (2002). Side chains of major hydrophobic contributors are shown as sticks, labels are shown for the right hand monomer only for clarity. Region I is shown in red, region II is blue, region III is yellow, region IV is orange. PDB ID: 1XXU (Li *et al.*, 2005).

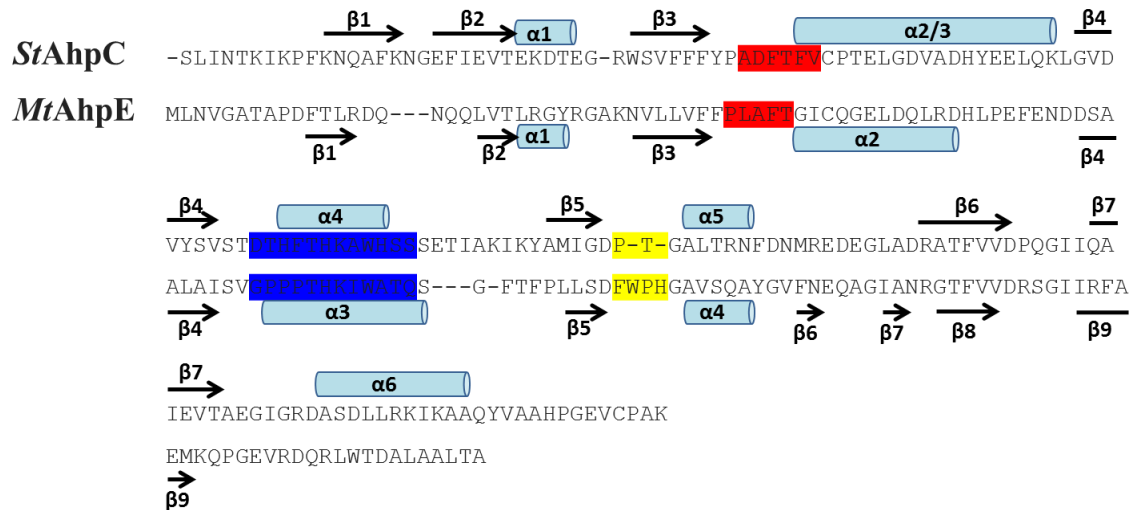


Figure 1.15: Sequences of Prxs show homologous interface regions

Regions I-IV (coloured as in figure 1.13) of the decamer interface of AhpC correspond to regions of the dimer interface *MtAhpE* (Wood *et al.*, 2002; Li *et al.*, 2005). The secondary structure elements of *MtAhpE* are shown below the sequence, that of AhpC above.

1.4.2.3 The B-type octamer interface

The octamer interface is less well studied than the dimer interface of *MtAhpE*, but has been considered to be analogous to that of other Prxs, as the protein can form similar toroids which can go on to form HMW structures (such as tubes of stacked rings, Li *et al.*, 2005). Interaction predictions using PDBePISA (Krissinel and Henrick, 2007) software suggested that this interface is discontinuous, comprised mostly of residues from the $\beta 9$ sheet (figure 1.16). The unique N-terminal tail interacts with $\beta 9$ of the other monomer (homologous to $\beta 7$ of 2-Cys Prxs), stabilising the B-type interface (Li *et al.*, 2005; figure 1.16).

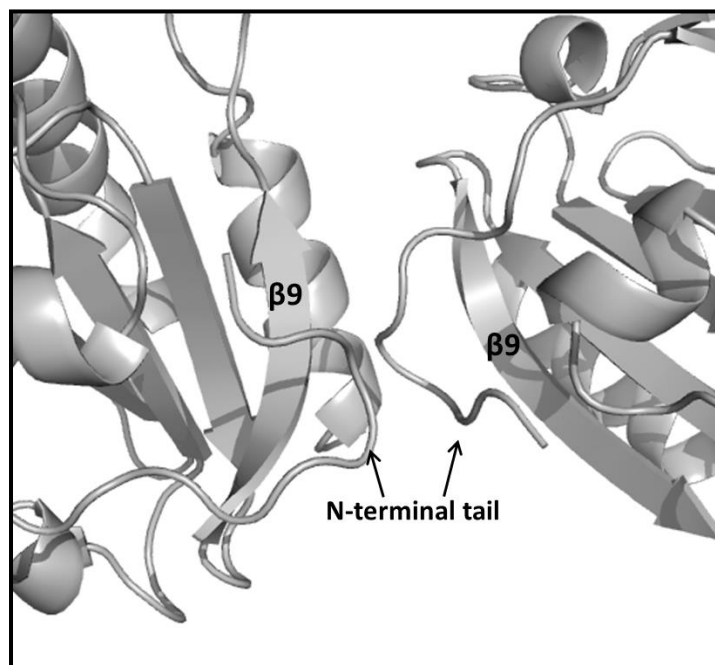


Figure 1.16: The B-type interface of *MtAhpE* is less extensive than the A-type interface

The N-terminal tails interact with the $\beta 9$ sheets of both their own monomer and the adjacent monomer, forming H-bonds. The relevance of this interface is questioned due to its small area and flexible regions involved. PDB ID: 1XXU (Li *et al.*, 2005).

1.4.2.4 The active site of *MtAhpE*

The reduced active site of *MtAhpE* shares the universal architecture, with C_P stabilised by Arg116, Thr42 making the typical H-bonds (section 1.2.3.2), and the conserved Pro38 repelling solvent molecules. The loop between β 9 and α 5 covers the active site (figure 1.17A). The typical network of stabilising interactions can therefore occur (section 1.2.3.2; Li *et al.*, 2005). The residues preceding C_P are involved in the A-type interface, as with typical Prxs.

When oxidised, with no C_R to bond with, C_P appears to rotate, R116 flips outward and the β 9- α 5 loop moves, forming a channel ~ 7 Å wide, allowing the reductant to enter and reach C_P (figure 1.17B; Li *et al.*, 2005). A shift is seen at the end of the C_P containing helix, but the helix unwinding seen in typical Prxs does not occur which could be key in the redox-insensitivity of the *MtAhpE* dimer interface.

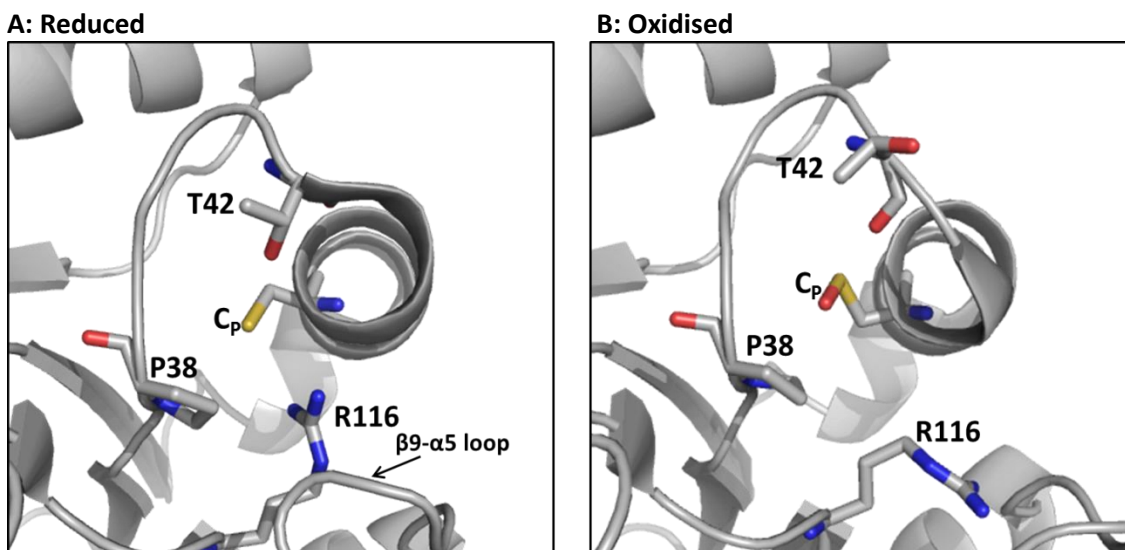


Figure 1.17: Significant changes occur in the active site with redox state

A: In the reduced state C_P and R116 point toward each other, forming an architecture similar to that of the 2-Cys Prxs (section 1.2.3.2). **B:** Once oxidised some helix unwinding is seen, but not to the extent of typical Prxs. R116 moves away from the active site, as does the β 9- α 5 loop, forming a channel through which reductant can access C_P. PDB ID: 1XXU (Li *et al.*, 2005)..

MtAhpE is therefore an interesting member of the 1-Cys family – structurally more similar to typical 2-Cys Prxs (see section 3.2), but with an A-type interface which is not sensitive to changes in redox conditions. Although these features have been suggested by previous studies (Li *et al.*, 2005), extensive biochemical characterisation had not been carried out.

1.5 Self-assembling proteins in nanotechnology

One of the first and most fundamental challenges of nanotechnology is the formation of desired shapes (Kim and Whitesides, 1995). While huge advances have been made in casting, moulding and other techniques, self-assembly is becoming recognised as a powerful approach to generating structures with a range of sizes and complexities, while at the same time minimising the manufacturing required (Kim and Whitesides, 1995).

With the concept of nanotoxicology becoming a growing concern (Thorley and Tetley, 2013), the exploitation of natural systems has obvious advantages over conventional materials used in nanotechnology. The intrinsic self-assembling nature of many biological molecules, coupled with the precision and functionality that these molecules can provide, at a low cost of production, makes them extremely attractive as building blocks for nanomaterials, and has become an important aspect of bottom-up manufacturing (Mendes *et al.*, 2012).

The self-assembly properties of nucleic acids have been manipulated to generate 2-dimensional (2D) arrays and 3-dimensional (3D) objects (Rothemund, 2006; Doll *et al.*, 2013), as well as dynamic structures that change shape in response to stimuli (Seeman, 2005). Although these advances are a promising step toward functional nanodevices, the use of nucleic acids is hindered by the limited architecture available and difficulty in functionalising the structures (Jaeger and Chworos, 2006). Lipids, saccharides and carbohydrates have all been explored as building blocks for supramolecular materials

(reviewed in Mendes *et al.*, 2012), with significant success seen in the use of peptides in this area (for example, Mendes *et al.*, 2012). Although synthesis of peptides is easy, the process is expensive; and whilst functionalising the subunits is more successful than other materials, the structures are quickly disrupted and tolerate only small modifications (Matsui *et al.*, 2001; Nuraje *et al.*, 2004). Proteins have long been recognised for their potential in nanotechnology, with the multiple interactions that drive their self-assembly offering the possibility of fine control over the assembly process, and a high degree of directionality. Considerable progress has been made in creating artificial protein constructs with predictable assembly properties, with a number of useful building blocks (or tectons) emerging (Miranda *et al.*, 2009; Ballister *et al.*, 2007; Medalsy *et al.*, 2008). The formation of protein nanotubes has been achieved, with some level of control over the length and reversibility of the structures (Miranda *et al.*, 2009; Ballister *et al.*, 2007; Medalsy *et al.*, 2008). However, an obstacle in the development of the field is the paucity of stable protein tectons with the ability to self-assemble into a variety of nanoarchitectures. The flexibility and functional diversity that comes from having 20 chemically different amino acid constituents does, of course, bring with it a new level of complexity, meaning that despite their promising nature, the use of proteins as tectons for nanostructures is not trivial.

In nanotechnology, tectons are molecules which aggregate into assemblies of controlled geometries (Su *et al.*, 1995). The repertoire of structures available to the Prx family provide an exciting possibility for their use as tectons in nanotechnology. A deeper understanding of the conditions that prompt the formation of discrete Prx structures could enable them to be used as switchable devices which form tubes, cages or rings upon exposure to an environmental trigger; with the potential to disassemble or associate into a different structure when conditions change.

The high molecular weight forms of Prxs adopt shapes that have been identified as particularly useful natural assemblies (section 1.2.5.3; Heddle, 2008), and similar protein structures have developed for nanotechnological applications. For example, cage

structures formed by ferritin-like protein (FLP) have been used to provide an isolated environment in their internal cavity, in which nanoparticles of iron oxide were grown (Allen *et al.*, 2002). The potential to use protein nanotubes as scaffolds to grow nanowires of electrodes has been highlighted (Valenzuela *et al.*, 2008), but to this date directed self-assembly with a variety of supramolecular structures from one protein has not been achieved.

1.6 Summary and significance of this research

Until the last decade, research into Prxs was scarce, and as a consequence the details of their structure-function relationship are not fully unravelled. Detailed structural studies on the Prxs are still scarce, further complicated as new data reveals aspects of experimental procedure previously thought to be unimportant to have potentially significant impacts on Prx structure (further discussed in chapter four).

Although a vaccine and multiple drugs are available, tuberculosis (TB) still kills around 1.3 million and infects over 8 million people a year (World Health Organisation report, 2013), with little improvement being made to these figures each year. Thus, drug development is a very active field of TB research, and the identification of new drug targets is essential. Cervical cancer kills over 270,000 women each year (American Cancer Society report, 2013), and more than five million people in America are currently living with Alzheimer's (Alzheimer's Association 2013). Further research into *MtAhpE* and *HsPrx3* therefore has clear importance from a biomedical perspective.

Homo-oligomeric structures remain somewhat mysterious, with their formation and poorly understood in many cases (Devenish and Gerrard, 2009). Understanding of the interactions that are involved often opens up new avenues for drug design (Higuerueol, *et al.*, 2009). Furthermore, with elucidation of the exact interactions involved, comes the potential to control the formation of these structures. The two systems studied in this

thesis present self-assembling toroids with different dimensions. A deeper understanding and comparison of the mechanisms which result in different quaternary arrangements from structurally similar subunit could highlight the use of Prxs as templates for designing molecules which self-assemble into toroids of tuneable size.

To be able to explore avenues to alter the oligomeric properties, the quaternary structure of the proteins must be known. The first aim of this project was therefore to elucidate the quaternary structure of *MtAhpE* in solution (chapter three), and identify the structural changes that were brought about by environmental factors. The factors in the unusual stability of the A-type interface were of interest, and the second part of chapter three sought identify key residues in this stability, through the introduction of mutations. This approach was also used to pursue the possibility to alter the quaternary structure of *MtAhpE*.

The second system that was investigated was the 2-Cys *HsPrx3*. The quaternary structure of *HsPrx3* was previously in question; therefore, answering this issue was the first goal of the *HsPrx3* work. A detailed characterisation of the oligomeric state of *HsPrx3* in a number of conditions was the next goal, in order to unravel the factors that influence assembly. Discrepancies in the literature have led to an unclear picture of Prx assembly, and so consideration of subtle elements of *in vitro* practices including purification techniques and the use of affinity tags was important. An increased knowledge of these factors allowed the prediction of mutations which would alter self-assembly in a controllable way; and these were subsequently introduced.

Finally, given the potential uses for tube or cage structures in nanotechnology, the formation of such structures and conditions that encouraged their assembly were investigated in the case of *HsPrx3*. Hypotheses regarding the mechanisms of HMW self-assembly were tested, with the aim to develop robust and reproducible methods of producing physically homogeneous preparations of HMW structures. Visualisation of these structures was important. Solving the structure of the HMW assemblies through

transmission electron microscopy (TEM), to a resolution that allowed identification of the interactions was the final goal of this project, in order to elucidate an assembly mechanism.

1.7 References

- Alfonso-Prieto, M., Biarnes, X., Vidossich, P. and Rovira, C. (2009) The molecular mechanism of the catalase reaction. *Journal of the American Chemical Society* **131**, 11751-11761.
- Allen, M., Willits, D., Mosolf J., Young, M. and Douglas, T. (2002) Protein cage constrained synthesis of ferromagnetic iron oxide nanoparticles. *Advanced Materials* **14**, 1562-1565.
- Alphey, M. S., Bond, C. S., Tetaud, E., Fairlamb, A. H. and Hunter, W. N. (2000) The structure of reduced Tryparedoxin Peroxidase reveals a decamer and insight into reactivity of 2-Cys Peroxiredoxins. *Journal of Molecular Biology* **300**, 903-916.
- Alzheimer's Association, (2013) Alzheimer's Disease Facts and Figures. *Alzheimer's and Dementia* **9**.
- American Cancer Society. (2013) Cancer Facts & Figures 2013. Atlanta: American Cancer Society.
- Ames, B. N. (1989) Endogenous oxidative DNA damage, aging, and cancer. *Free Radical Research Communications* **7**, 121-128.
- An, B. C., Lee, S. S., Lee, E. M., Lee, J. T., Wi, S. G., Jung, H. S., Park, W., Lee, S. Y. and Chung, B. Y. (2011) Functional switching of a novel prokaryotic 2-Cys peroxiredoxin (PpPrx) under oxidative stress. *Cell stress and chaperones* **16**, 317-328.
- Anderson, P. M., Korte, J. J., Holcomb, T. A., Cho, Y.-g., Son, C.-m. and Sung, Y.-c. (1994) Formation of intersubunit disulfide bonds and properties of the single histidine and cysteine residues in each subunit relative to the decameric structure of Cyanase. *Journal of Biological Chemistry* **269**, 15036-15045.
- Angelucci, F., Saccoccia, F., Ardini, M., Boumis, G., Brunori L., Di Leandro, R., Ippoliti, R., Miele, A.E., Natoli, G., Scotti, S. and Bellelli, A. (2013) Switching between the alternative structures and functions of a 2-Cys peroxiredoxin by site-directed mutagenesis. *Journal of Molecular Biology* **425**, 4556-4568.
- Ballister, E. R. Lai, A. H. and Zuckermann, R. N. (2008) *In vitro* self-assembly of tailorable nanotubes from a simple protein building block. *Proceedings of the National Academy of Science of the United States of America* **105**, 3733-3738.
- Bannister, J. V., Bannister, W. H. and Rotilio, G. (1987) Aspects of the structure, function and applications of superoxide dismutase. *Critical Reviews in Biochemistry* **22**, 111-180.
- Barranco-Medina, S., Lázaro, J.-J. and Dietz, K.-J. (2009) The oligomeric conformation of peroxiredoxins links redox state to function. *Federation of European Biochemical Societies Letters* **583**, 1809-1816.

- Berggren, M. I., Husbeck, B., Samulitis, B., Baker, A. F., Gallegos A. and Powis, G. (2001) Thioredoxin peroxidase-1 (peroxiredoxin-1) is increased in thioredoxin-1 transfected cells and results in enhanced protection against apoptosis caused by hydrogen peroxide but not by other agents including dexamethasone, etoposide, and doxorubicin. *Archives of Biochemistry and Biophysics* **392**, 103-109.
- Biteau, B., Labarre, J. and Toledano, M. B. (2003) ATP-dependent reduction of cysteine-sulfinic acid by *Saccharomyces cerevisiae* sulfiredoxin. *Nature* **425**, 980-984.
- Brystrova, M. F., Budanove, E. N., Novoselov, V. I. and Fesenko, E. E. (2007) Analysis of the oligomeric state of Rat 1-Cys peroxiredoxin. *Molecular Biophysics* **52**, 277-281.
- Cao, Z., Roszak, A. W., Gourlay, L. J., Lindsay, J. G. and Isaacs, N. W. (2005) Bovine mitochondrial Peroxiredoxin III forms a two-ring catenane. *Structure* **13**, 1661-1664.
- Cao, Z., Bhella, D. and Lindsay, J. G. (2007) Reconstitution of the mitochondrial PrxIII antioxidant defence pathway: General properties and factors affecting PrxIII activity and oligomeric state. *Journal of Molecular Biology* **372**, 1022-1033.
- Cao, Z., Tavender, T. J., Roszak, A. W., Cogdell, R. J. and Bulleid, N. J. (2011) Crystal structure of reduced and of oxidized peroxiredoxin IV enzyme reveals a stable oxidized decamer and a non-disulfide-bonded intermediate in the catalytic cycle. *Journal of Biological Chemistry* **286**, 42257-42266.
- Cha, M.-K., Suh, K.-H. and Kim, I.-H. (2009) Overexpression of peroxiredoxin I and thioredoxin I in human breast carcinoma. *Journal of Experimental and Clinical Cancer Research* **28**, 93.
- Chae, H. Z., Chung, S. J. and Rhee, S. G. (1994a) Thioredoxin-dependent peroxide reductase from yeast. *Journal of Biological Chemistry* **269**, 27670-27678.
- Chae, H. Z., Robinson, K., Poole, L. B., Church, G., Storz, G. and Rhee, S. G. (1994b) Cloning and sequencing of thiol-specific antioxidant from mammalian brain: Alkyl hydroperoxide reductase and thiol-specific antioxidant define a large family of antioxidant enzymes. *Proceedings of the National Academy of Sciences of the United States of America* **91**, 7017-7021.
- Chae, H. Z., Uhm, T. B. and Rhee, S. G. (1994c) Dimerization of thiol-specific antioxidant and the essential role of cysteine 47. *Proceedings of the National Academy of Sciences of the United States of America* **91**, 7022-7026.
- Chang, K.-P., Yu, J.-S., Chien, K.-Y., Lee, C.-W., Liang, Y., Liao, C.-T., Yen, T.-C., Lee, L.-Y., Huang, L.-L., Liu, S.-C., Chang, Y.-S. and Chi, L.-M. (2011) Identification of PRDX4 and P4HA2 as metastasis-associated proteins in oral cavity squamous cell carcinoma by comparative tissue proteomics of microdissected specimens using iTRAQ technology. *Journal of proteome Research* **10**, 4935-4947.

- Chauhan, R. and Mande, S. C. (2001) Characterization of the *Mycobacterium tuberculosis* H37Rv alkyl hydroperoxidase AhpC points to the importance of ionic interactions in oligomerisation and activity. *Biochemical Journal* **354**, 209-215.
- Chen, J.-W., Dodia, C., Feinstein, S. I., Jain, M. K. and Fisher, A. B. (2000) 1-Cys Peroxiredoxin, a bifunctional enzyme with glutathione peroxidase and phospholipase A2 activities. *Journal of Biological Chemistry* **275**, 28421-28427.
- Chen, G., Gharib, T. G., Huang, C. C., Thomas, D. G., Shedden, K. A., Taylor, H.M. G., Kardia, S. L. R., Misek, D. E., Giordano, T. J., Iannettoni, M. D., Orringer, M. B., Hannash, S. M. and Beer, D. G. (2002) Proteomic analysis of lung adenocarcinoma: identification of a highly expressed set of proteins in tumours. *Clinical Cancer Research* **8**, 2298-2305
- Chiarugi, P., Fiaschi, T., Taddei, M. L., Talini, D., Giannoni, E., Raugei, G. and Ramponi, G. (2001) Two vicinal cysteines confer a peculiar redox regulation to low molecular weight protein tyrosine phosphatase in response to platelet-derived growth factor receptor stimulation. *Journal of Biological Chemistry* **276**, 33478-33487.
- Choi, J., Choi, S., Choi, J., Cha, M.-K., Kim, I.-H. and Shin, W. (2003) Crystal structure of *Escherichia coli* thiol peroxidase in the oxidized state. *Journal of Biological Chemistry* **49**, 49478-49486.
- Cimini, A., Gentile, R., Angelucci, F., Benedetti, E., Pitari, G., Giordano, A. and Ippoliti, R. (2013) Neuroprotective effects of Prx1 over-expression in an *in vitro* Alzheimer's disease model. *Journal of Cell Biology* **114**, 708-715.
- Clothin, C. and Janin, J. (1975) Principles of protein-protein recognition. *Nature* **256**, 705-708.
- Cox, A. G., Winterbourn, C. C. and Hampton, M. B. (2010) Mitochondrial peroxiredoxin in antioxidant defence and redox signalling. *Biochemical Journal* **425**, 313-325.
- Declercq, J.-P., Evrard, C., Clippe, A., Stricht, D. V., Bernard, A. and Knoop, B. (2001) Crystal structure of Human Peroxiredoxin 5, a novel type of mammalian peroxiredoxin at 1.5 Å resolution. *Journal of Molecular Biology* **311**, 751-759.
- DeLano, W.L. (2002). The PyMOL Molecular Graphics System (San Carlos, CA: Delano Scientific).
- Devenish, S. R. A. and Gerrard, J. A. (2009) The role of quaternary structure in (β/α)₈-barrel proteins: evolutionary happenstance or a higher level of structure-function relationships? *Organic and Biomolecular Chemistry* **7**, 833-839.
- Doll, T. A. P. F., Raman, S. Dey, R. and Burkhard, P. (2013) Nanoscale assemblies and their biomedical applications. *Journal of the Royal Society Interface* **10**, 20120740
- Eismann, T., Huber, N., Shin, T., Kuboki, S., Galloway, E., Wyder, M., Edwards, M. J., Greis, K. D., Shertzer, H. G., Fisher, A. B. and Lentsch, A. B. (2009) Peroxiredoxin-6 protects against mitochondrial dysfunction and liver injury during ischemia-reperfusion in mice.

American Journal of Physiology – Gastrointestinal and Liver Physiology **296**, G266-G274.

- Ellis, H. R. and Poole, L. B. (1997) Roles for the two cysteine residues of AhpC in catalysis of peroxide reduction by alkyl hydroperoxide reductase from *Salmonella typhimurium*. *Biochemistry* **36**, 13349-13356.
- Epp, O., Ladenstein, R. and Wendel, A. (1983) The refined structure of the selenoenzyme glutathione peroxidase at 0.2-nm resolution. *European Journal of Biochemistry* **133**, 51-69.
- Fenton, H. J. H (1894) Oxidation of tartaric acid in presence of iron. *Journal of the Chemical Society, Transactions* **65**, 899-910.
- Flohé, L., Budde, H., Bruns, K., Castro, H., Clos, J., Hormann, B., Kansal-Kalavar, S., Krumme, D., Menge, U., Plank-Schumacher, K., Sztajer, H., Wissing, J., Wylegalla, C. and Hecht, H.-J. (2002) Tryparedoxin Peroxidase of *Leishmania donovani*: Molecular cloning, heterologous expression, specificity and catalytic mechanism. *Archives of Biochemistry and Biophysics* **397**, 324-335.
- Flohé, R. and Maiorino, M. (2013) Glutathione peroxidases. *Biochimica et Biophysica Acta* **1830**, 3289-3303.
- Forman, H. J. and Torres, M. (2001) Redox signalling in macrophages. *Molecular Aspects of Medicine* **22**, 189-216.
- Fridovich, I. (1995) Superoxide radical and superoxide dismutases. *Annual Review of Biochemistry* **64**, 97-112.
- Fujii, J. and Ikeda, Y. (2002) Advances in our understanding of peroxiredoxin, a multifunctional, mammalian redox protein. *Redox Report* **7**, 123-130.
- Gaté, L., Paul, J., Nguyen Ba, G., Tew, K. D. and Tapiero, H. (1999) Oxidative stress induced in pathologies: the role of antioxidants. *Biomedicine and Pharmacotherapy* **53**, 169-180.
- Gough, D. R. and Cotter, T. G. (2011) Hydrogen peroxide a Jekyll and Hyde signalling molecule. *Cell Death and Disease* **2**, e213.
- Gourlay, L. J., Bhella, D., Kelly, S. M., Price, N. C. and Lindsay, J. G. (2003) Structure-function analysis of recombinant substrate protein 22 kDa (SP-22): a mitochondrial 2-Cys peroxiredoxin organised as a decameric toroid. *Journal of Biological Chemistry* **35**, 32631-32637.
- Gretes, M. C. and Karplus, P. A. (2013) Observed octameric assembly of a *Plasmodium yoelii* peroxiredoxin can be explained by the replacement of native “ball-and-socket” interacting residues by an affinity tag. *Protein Science* **10**, 1445-1452.

- Hall, A., Parsonage, D., Poole, L. B. and Karplus, P. A. (2010) Structural evidence that Peroxiredoxin catalytic power is based on transition-State stabilization. *Journal of Molecular Biology* **402**, 194-209.
- Halliwell, B. and Gutteridge, J. M. C. (1984) Oxygen toxicity, oxygen radicals, transition metals and disease. *Biochemical Journal* **219**, 1-14.
- Han, Y.-H., Kim, S.-U., Kwon, T.-H., Lee, D.-S., Ha, H.-L., Park, D.-S., Woo, E.-J., Lee, S.-H., Kim, J.-M., Chae, H.-B., Lee, S. Y., Kim, B. Y., Yoon, D. Y., Rhee, S. G., Fibach, E. and Yu, D.-Y. (2012) Peroxiredoxin II is essential for preventing haemolytic anaemia from oxidative stress through maintaining haemoglobin stability. *Biochemical and Biophysical Research Communications* **426**, 427-432.
- Haridas, V., Ni, J., Meager, A., Su, J., Yu, G.-L., Zhai, Y., Kyaw, H., Akama, K. T., Hu, J., Can Eldik, L. J. and Aggarwal, B. B. (1998) Cutting edge: TRANK, a novel cytokine that activates NF- κ B and c-Jun N-terminal kinase. *Journal of Immunology* **161**, 1-6.
- Harman, D. (1956) Aging: A theory based on free radical and radiation chemistry. *Journal of Gerontology* **11**, 298-300.
- Harris, J. R. (1968) The isolation and purification of a macromolecular protein component from the human erythrocyte ghost. *Biochimica et Biophysica Acta* **1**, 31-42.
- Harris, J. R. (1969) Some negative contrast staining features of a protein from erythrocyte ghosts. *Journal of Molecular Biology* **46**, 329-335.
- Heddle, J. G. (2008) Protein cages, rings and tubes: useful components of future nanodevices? *Nanotechnology, Science and Applications* **1**, 67-78.
- Higueruelo, A. P., Schreyer, A., Bickerton, G. R. G., Pitt, W. R., Groom, C. R. and Blundell, T. L. (2009) Atomic interactions and profile of small molecules disrupting protein-protein interfaces: the TIMBAL database. *Chemical and Biological Drug Design* **74**, 457-467.
- Hirotsu, S., Abe, Y., Okada, K., Nagahara, N., Hori, H., Nishino, T. and Hakoshima, T. (1999) Crystal structure of a multifunctional 2-Cys peroxiredoxin heme-binding protein 23 kDa/proliferation-associated gene product. *Proceedings of the National Academy of Science of the USA* **96**, 12333-12338.
- Hofmann, B., Hecht, H.-J. and Flohé, L. (2002) Peroxiredoxins. *Biological Chemistry* **383**, 347-364.
- Hu, Y. and Coates, A. R. M. (2009) Acute and persistent *Mycobacterium tuberculosis* infections depend on the Thiol Peroxidase TPx. *PLoS ONE* **4**, e5150.
- Hugo, M., Turell, L., Manta, B., Botti, H., Monteiro, G., Netto, L. E. S., Alvarez, B., Radi, R. and Trujillo, M. (2009) Thiol and Sulfenic acid oxidation of AhpE, the 1-Cysteine peroxiredoxin from *Mycobacterium tuberculosis*: kinetics, acidity constants and conformational dynamics. *Biochemistry* **48**, 9416-9426.

- Imlay, J. A. (2003) Pathways of oxidative damage. *Annual Review of Microbiology* **57**, 395-418.
- Inoue, M., Sato, E. F., Nishikawa, M., Park, A.-M., Kira, Y., Imada, I. and Utsumi, K. (2003) Mitochondrial generation of reactive oxygen species and its role in aerobic life. *Current Medicinal Chemistry* **10**, 2495-2505.
- Jaeger, T., Budde, H., Flohé, L., Menge, U., Singh, M., Trujillo, M. and Radi, R. (2004) Multiple thioredoxin-mediated routes to detoxify hydroperoxides in *Mycobacterium tuberculosis*. *Archives of Biochemistry and Biophysics* **423**, 182-191.
- Jaeger, L. and Chworos, A. (2006) The architectonic of programmable RNA and DNA nanostructures. *Current Opinion in Structural Biology* **16**, 531-549.
- Jang, H. H., Lee, K. O., Chi, Y. H., Lee, J. R., Lee, S. S., Moon, J. C., Yun, J. W., Choi, Y. O., Kim, W. Y., Kang, J. S., Cheong, G.-W., Yun, D.-J., Rhee, S. G., Cho, M. J. and Lee, S. Y. (2004) Two enzymes in one: Two yeast peroxiredoxins display oxidative stress-dependent switching from a peroxidase to a molecular chaperone function. *Cell* **117**, 625-635.
- Jang, H. H., Chi, Y. H., Park S. K., Lee, S. S., Lee, J. R., Park, J. H., Moon, J. C., Lee, Y. M., Kim, S. Y., Lee, K. O and Lee, S. Y. (2006) Structural and functional regulation of eukaryotic 2-Cys peroxiredoxins including the plant ones in cellular defence signalling mechanisms against oxidative stress. *Physiologia Plantarum* **126**, 549-559.
- Jeong, W., Cha, M.-K. and Kim, I.-H. (2000) Thioredoxin-dependent hydroperoxidase activity of Bacterioferritin Comigratory Protein (BCP) as a new member of the thiol-specific antioxidant protein (TSA)/alkyl hydroperoxide. *Journal of Biological Chemistry* **275**, 2924-2930.
- Jin, D.-Y., Chae, H. Z., Rhee, S. G. and Jeang, K.-T. (1997) Regulatory role for a novel human thioredoxin peroxidase in NG- κ B activation. *Journal of Biological Chemistry* **49**, 30952-30961.
- Jönsson, T. J., Johnson, L. C. and Lowther, W. T. (2008) protein engineering of the quaternary sulfiredoxin-peroxiredoxin enzyme-substrate complex reveals the molecular basis for cysteine sulfinic acid phosphorylation. *Journal of Biological Chemistry* **284**, 33305-33310.
- Kang, S. W., Baines, I. C. and Rhee, S. G. (1998) Characterization of a mammalian peroxiredoxin that contains a conserved cysteine. *Journal of Biological Chemistry* **273**, 6303-6311.
- Karplus, P. A., Hall, A. (2007) Structural survey of the peroxiredoxins. In: Flohé, L. and Harris, J. R. (Ed) *Peroxiredoxin Systems*. pp. 41–60 Springer; New York.
- Kato, H., Asanoi, M., Nakazawa, T. and Maruyama, K. (1985) Cylinder protein isolated from rat liver mitochondria. *Zoological Science* **2**, 485-490.

- Kern, R., Malki, A., Holmgren, A. and Richarme, G. (2003) Chaperone properties of *Escherichia coli* thioredoxin and thioredoxin reductase. *Biochemical Journal* **371**, 965-972.
- Kim, K., Rhee, S. G. and Stadtman, E. R. (1985) Nonenzymatic cleavage of proteins by reactive oxygen species generated by dithiothreitol and iron. *Journal of Biological Chemistry* **260**, 15394-15397.
- Kim, K., Kim, I. H., Lee, K.-Y., Rhee, S. G. and Stadtman, E. R. (1988) The isolation and purification of a specific "protector" protein which inhibits enzyme inactivation by a Thiol/Fe/O₂ mixed-function oxidation system. *Journal of Biological Chemistry* **263**, 4704-4711.
- Kim, I. H., Kim, K. and Rhee, S. G. (1989) Induction of an antioxidant protein of *Saccharomyces cerevisiae* by O₂, Fe³⁺ or 2-mercaptoethanol. *Proceedings of the National Academy of Sciences of the United States of America* **86**, 6018-6022.
- Kim, E. and Whiteside, G. M. (1995) Use of minimal free energy and self-assembly to form shapes. *Chemical Materials* **7**, 1257-1264.
- Kim, T.-S., Sundaresh, C. S., Feinstein, S. I., Dodia, C., Skach, W. R., Jain, M. K., Nagase, T., Seki, N., Ishikawa, K.-I., Nomura, N. and Fisher, A. B. (1997) Identification of a human cDNA clone for lysosomal type Ca²⁺ independent phospholipase A2 and properties of the expressed protein. *Journal of Biological Chemistry* **272**, 2542-2550.
- Kim, S. H., Fountoulakis, M., Cairns, N. and Lubec, G. (2001) Protein levels of human peroxiredoxin subtypes in brains of patients with Alzheimer's disease and Down syndrome. *Journal of Neural Transmission Supplementa* **61**, 223-235.
- Kim S. J., Woo, J. R., Hwang, Y. S., Jeong, D. G., Shin, D. H., Kim, K. and Ryu, S. E. (2003) The tetrameric structure of *Haemophilus influenza* hybrid Prx5 reveals interactions between electron donor and acceptor proteins. *Journal of Biological Chemistry* **278**, 10790-10798.
- Koo, K. H., Lee, S., Jeong, S. Y., Kim, E. T., Kim, H. J., Kim, K., Song, K. and Chae, H. Z. (2002) Regulation of Thioredoxin Peroxidase activity by C-terminal truncation. *Archives of Biochemistry and Biophysics* **397**, 312-318.
- Krissinel, E. and Henrick, K. (2007) Inference of macromolecular assemblies from crystalline state. *Journal of Molecular Biology* **372**, 774-797.
- Kristensen, P., Rasmussen, D. E. and Kristensen, B. I. (1999) Properties of thiol-specific antioxidant protein or calpromotin in solution. *Biochemical and Biophysical Research Communications* **262**, 127-131.
- Kümin, A., Schäfer, M., Epp, N., Bugnon, P., Born-Berclaz, C., Oxenius, A., Klippel, A., Bloch, W. and Werner, S. (2007) Peroxiredoxin 6 is required for blood vessel integrity in wounded skin. *Journal of Cell Biology* **179**, 747-760.

- Kumsta, C. and Jakob, U. (2009) Redox-regulated chaperones. *Biochemistry* **48**, 4666-4676.
- Li, S., Peterson, N. A., Kim, M-Y., Kim C-Y., Hung, L-W., Yu, M., Lakin, T., Segelke, B. W., Lott, J. S., Baker, E. N. (2005) Crystal structure of AhpE from *Mycobacterium tuberculosis*, a 1-Cys peroxiredoxin. *Journal of Molecular Biology*, **346**, 1035-1046.
- Li, L., Zhang, Y.-G. and Chen, C.-L. (2013) Anti-apoptotic role of peroxiredoxin III in cervical cancer cells. *Federation of European Biochemical Societies Open Bio*, **3**, 51-54.
- Low, F., Hampton, M. B., Peskin, A. V. and Winterbourn, C. C. (2007) Peroxiredoxin 2 functions as a noncatalytic scavenger of low-level hydrogen peroxide in the erythrocyte. *Blood*, **109**, 2611-2617.
- Lu, J. and Holmgren, A. (2008) Selenoproteins. *Journal of Biological Chemistry* **284**, 723-727.
- Martin, J. L. (1995) Thioredoxin – a fold for all reasons. *Structure* **3**, 245-250.
- Matsumura, T., Okamoto, K., Iwahara, S.-I., Hori, H., Takahashi, Y., Nishino, T. and Abe, Y. (2008) Dimer-oligomer interconversion of wild-type and mutant rat 2-Cys peroxiredoxin. *Journal of Biological Chemistry* **283**, 284-293.
- McCord, J. M. and Fridovich, I. (1969) Superoxide dismutase an enzymatic function for erythrocyte (Hemocuprein). *Journal of Biological Chemistry* **244**, 6049-6055.
- Matsui, H., Porrata, P. and Douberly, G. E. Jr. (2001) Protein tubule immobilisation on self-assembled monolayer on Au substrates. *Nanoletters* **1**, 461-464.
- Meissner, U., Schröder, E., Scheffler, D., Martin, A. G. and Harris, J. R. (2007) Formation, TEM study and 3D reconstruction of the human erythrocyte peroxiredoxin-2 dodecahedral higher-order assembly. *Micron* **38**, 29-39.
- Medalsy, I., Dgany, O., Sowwan, M., Cohen, H., Yukashevskaya, A., Wolf, S. G., Wolf, A., Koster, A., Almog, O., Marton, I., Pouny, Y., Altman, A., Shoseyov, O. and Porath, D. (2007) SP1 protein-based nanostructures and arrays. *Nanoletters* **8**, 473-477.
- Mendes, A. C., Baran, E. T., Lisboa, P., Reis, R. L. and Azevedo, H. S. (2012) Microfluidic fabrication of self-assembled peptide-polysaccharide microcapsules as 3D environment for cell culture. *Biomacromolecules* **13**, 4039-4048.
- Miranda, F. F., Iwasaki, K., Akashi, S., Sumitomo, K., Kobayashi, M., Yamashita, I., Tame, J. R. H. and Heddl, J. G. (2009) A self-assemble protein nanotube with high aspect ratio. *Small*, **5**, 2077-2084.
- Moon, J. C., Hah, Y.-S., Kim, W. Y., Jung, B. G., Jang, H. H., Lee, J. R., Kim, S. Y., Lee, Y. M., Jeong, M. G., Kim, C. W., Cho, M. J. and Lee, S. Y. (2005) Oxidative stress-dependent structural and functional switching of a human 2-Cys peroxiredoxin Isotype II that enhances HeLa cell resistance to H₂O₂-induced cell death. *Journal of Biological Chemistry* **280**, 28775-28784.

- Montemartini, M., Kalisz, H. M., Hecht, H.-J., Steinert, P. and Flohé, L. (1999) Activation of active-site cysteine residues in the peroxiredoxin-type trypanothione peroxidase of *Crithidia fasciculata*. *European Journal of Biochemistry* **264**, 516-524.
- Muller F. L., Lustgarten, M. S., Jang, Y., Richardson, A. and Remmen H. V. (2007) Trends in oxidative aging theories. *Free Radical Biology and Medicine* **43**, 477-503.
- Muthuramalingam, M., Seidel, T., Laxa, M., Nunes de Miranda, S. M., Gärtner, F., Ströher, E., Kandlbinder, A. and Dietz, K.-J. (2009) Multiple redox and non-redox interactions define 2-Cys peroxiredoxin as a regulatory hub in the chloroplast. *Molecular Plant* **2**, 1273-1288.
- Nagy, P., Karton, A., Betz, A., Peskin, A. V., Pace, P., O'Reilly, R. J., Hampton, M. B., Radom, L. and Winterbourn, C. C. (2011) Model for the exceptional reactivity of peroxiredoxins 2 and 3 with hydrogen peroxide: a kinetic and computational study. *Journal of Biological Chemistry* **286**, 18048-18055.
- Nakamura, T., Kado, Y., Yamaguchi, T., Matsumura, H., Ishikawa, K. and Inoue, T. (2009) Crystal structure of peroxiredoxin from *Aeropyrum pernix* K1 complexed with its substrate, hydrogen peroxide. *Journal of Biochemistry* **147**, 109-115.
- Neithammer, P., Grabher, C., Look, A. T. and Mitchison, T. J. (2009) A tissue-scale gradient of hydrogen peroxide mediates rapid wound detection in zebrafish. *Nature* **459**, 996-999.
- Nelson, K. J., Parsonage, D., Hall, A., Karplus, P. A. and Poole, L. B. (2008) Cysteine pK_a values for the bacterial peroxiredoxin AhpC. *Biochemistry* **47**, 12860-12868.
- Neumann, C. A., Krause, D. S., Carman, C. V., Das, S., Dubey, D. P., Abraham, J. L., Bronson, R. T., Fujiwara, Y. Y., Orkin, S. H. and van Etten, R. A. (2003) Essential role for the peroxiredoxin PRDX1 in erythrocyte antioxidant defence and tumour suppression. *Letters to Nature* **424**, 561-565.
- Noguera-Mazon, V., Lemoine, J., Walker, O., Rouhier, N., Salvador, A., Jacquot, J.-P., Lancelin, J.-M. and Krimm, I. (2006) Glutathionylation induces the dissociation of 1-Cys D-peroxiredoxin non-covalent homodimer. *Journal of Biological Chemistry* **281**, 31736-31742.
- Nuraje, N., Banerjee, I. A., MacCuspie, R. I., Yu, L. and Matsui, H. (2004) Biological bottom-up assembly of antibody nanotubes and patterned antigen arrays. *Journal of the American Chemical Society Communications* **126**, 8088-8089.
- Papinutto, E., Windle, H. J., Cendron, L., Battistutta, R., Kelleher, D. and Zanotti, G. (2005) Crystal structure of alkyl hydroperoxide-reductase (AhpC) from *Helicobacter pylori*. *Biochimica et Biophysica Acta* **1753**, 240-246.
- Pascual, M. B., Mata-Cabana, A., Florenci, F. J., Lindahl, M. and Cejudo, F. J. (2010) Overoxidation of 2-Cys peroxiredoxin in prokaryotes: cyanobacterial 2-Cys peroxiredoxins sensitive to oxidative stress. *Journal of Biological Chemistry* **285**, 34485-34492.

- Park, J. W., Piszczek, G., Rhee, S. G., Chock, P.B. (2011) Glutathionylation of peroxiredoxin I induces decamers to dimers dissociation with concomitant loss of chaperone activity. *Biochemistry* **50**, 3204-3210.
- Park, J.-G., Yoo, J.-Y., Jeong, S.-J., Choi, J.-H., Lee, M.-R., Lee, M.-N., Lee, J. H., Kim, H. C., Jo, H., Yu, D.-Y., Kang, S. W., Rhee, S. G., Lee, M.-H. and Oh, G. T. (2011b) Peroxiredoxin 2 deficiency exacerbates atherosclerosis in apolipoprotein E-deficient mice: novelty and significance. *Circulation Research* **109**, 739-749.
- Parsonage, D., Youngblood, D. S., Sarma, G. N., Wood, Z. A., Karplus, P. A. and Poole, L. B. (2005) Analysis of the link between enzymatic activity and oligomeric state in AhpC, a bacterial peroxiredoxin. *Biochemistry* **44**, 10583-10592.
- Peskin, A. V., Low, F. M., Paton, L. N., Maghzal, G. J., Hampton, M. B. and Winterbourn, C. C. (2007) The high reactivity of peroxiredoxin 2 with H₂O₂ is not reflected in its reaction with other oxidants and thiol reagents. *Journal of Biological Chemistry* **282**, 11885-11892.
- Peskin, A. V., Dickerhof, N., Poynton, R. A., Paton, L. N., Pace, P. E., Hampton, M. B. and Winterbourn, C. C. (2013) Hyperoxidation of peroxiredoxins 2 and 3: Rate constants for the reactions of the sulfenic acid of the peroxidatic cysteine. *Journal of Biological Chemistry* **268**, 14170-14177.
- Placzek, S. (2013, July) EC 1.11.1.9 – glutathione peroxidase. BRENDA, retrieved 9th November 2013 from <http://www.brenda-enzymes.org>.
- Poole, L. B. (2007) The catalytic mechanism of peroxiredoxins. In: Flohé, L. and Harris, J. R. (Eds) *Peroxiredoxin Systems*. pp. 61-81 Springer; New York.
- Prabhakar, R., Vreven, T., Morokuma, K. and Musaev, D. G. (2005) Elucidation of the mechanism of selenoprotein glutathione peroxidase (GPx)-catalysed hydrogen peroxide reduction by two glutathione molecules: A density functional study. *Biochemistry* **44**, 11864-11871.
- Prosperi, M.-T, Ferbus, D., Karczinski, I. and Goubin, G. (1993) A human cDNA corresponding to a gene overexpressed during cell proliferation encodes a product sharing homology with amoebic and bacterial proteins. *Journal of Biological Chemistry* **268**, 11050-11056.
- Rabilloud, T., Heller, M., Gasnier, F., Sylvie, L., Rey, C., Aebersold, R., Benahmed, M., Louisot, P. and Lunardi, J. (2002) Proteomics analysis of cellular response to oxidative stress: evidence for *in vivo* overoxidation of peroxiredoxins at their active site. *Journal of Biological Chemistry* **277**, 19396-19401.
- Radyuk, S. N., Michalak, K., Klichko, V. I., Benes, J., Rebrin, I., Sohal, R. S. and Orr, W. C. (2009) Peroxiredoxin 5 confers protection against oxidative stress and apoptosis and also promotes longevity in *Drosophila*. *Biochemical Journal* **419**, 437-445.

- Rego, A. C. and Oliveira, C. R. (2003) Mitochondrial dysfunction and reactive oxygen species in excitotoxicity and apoptosis: Implications for the pathogenesis of neurodegenerative diseases. *Neurochemical Research* **28**, 1563-1574.
- Rhee, S. G., Chae, H. Z. and Kim, K. (2005) Peroxiredoxins: A historical overview and speculative preview of novel mechanisms and emerging concepts in cell signalling. *Free Radical Biology and Medicine* **38**, 1543-1552.
- Rothemund, P. W. K. (2006) Folding DNA to create nanoscale shapes and patterns. *Nature* **440**, 297-302.
- Rouhier, N., Gelhaye, E., Gualberto, J. M., Jordy, M.-N., De Fay, E., Hirasawa, M., Duplessis, S., Lemaire, S. D., Frey, P., Martin, F., Manieri, W., Knaff, D. B. and Jacquot, J.-P. (2004) Poplar peroxiredoxin Q. A thioredoxin-linked chloroplast antioxidant functional in pathogen defence. *Plant Physiology* **134**, 1027-1038.
- Roussel, X., Béchade, G., Kritznik, A., Dorselaer, A. V., Sanglier-Clanferani, S., Branlant, G. and Rahuel-Clermont, S. (2008) Evidence for the formation of a covalent thiosulfinate intermediate with peroxiredoxin in the catalytic mechanism of sulfiredoxin. *Journal of Biological Chemistry* **283**, 22371-22382.
- Roussel, X., Kritznik, A., Richard, C., Rahuel-Clermont, S. and Branlant, G. (2009) Catalytic mechanism of sulfiredoxin from *Saccharomyces cerevisiae* passes through an oxidised disulfide sulfiredoxin intermediate that is reduced by thioredoxin. *Journal of Biological Chemistry* **285**, 33048-33055.
- Saccoccia, F., Micco, P. D., Bournis, G., Brunori, M., Koutris, I., Miele, A. E., Morea, V., Sriratana, P., Williams, D. L., Bellelli, A. and Angelucci, F. (2012) Moonlighting by different stressors: crystal structure of the chaperone species of a 2-cys peroxiredoxin. *Structure* **20**, 429 – 439.
- Safaeian, M., Hildesheim, A., Gonzalez, P., Yu, K., Porras, C., Li, Q., Rodriguez, A. C., Sherman, M. E., Schiffman, M., Wacholder, S., Burk, R., Herrero, R., Burdett, L., Chanock, S. J. and Wang, S.S. (2013) Single nucleotide polymorphisms in the PRDX3 and RPS19 and risk of HPV persistence and cervical precancer/cancer. *PLoS One* **7**, e33619.
- Sarma, G. N., Nickel, C., Rahlfs, S., Fischer, M., Becker, K. and Karplus, P. A. (2005) Crystal structure of a novel *Plasmodium falciparum* 1-Cys peroxiredoxin. *Journal of Molecular Biology* **346**, 1021-1034.
- Schröder, E., Willis, A. C. and Ponting, C. P. (1998) Porcine natural-killer-enhancing factor-B: oligomerisation and identification as a calpain substrate *in vitro*. *Biochimica et Biophysica Acta* **1383**, 279-291.
- Schröder, E., Isupov, M. N., Naran, A. and Littlechild, J. A. (1999) Crystallization and preliminary X-ray analysis of human thioredoxin peroxidase-B from red blood cells. *Acta Crystallographica Section D* **55**, 536-5398.

- Schröder, E., Littlechild, J. A., Lebedev, A. A., Errington, N., Vagin, A. A. and Isupov, M. N. (2000) Crystal structure of decameric 2-Cys peroxiredoxin from human erythrocytes at 1.7Å resolution. *Structure* **8**, 605-615.
- Schröder, E., Parther, T., Rücknagel, K. P., Wagner, M. and Andreessen, J. R. (2001) A Selenocysteine-containing peroxiredoxin from the strictly anaerobic organism *Eubacterium acidaminophilum*. *Biological Chemistry* **382**, 979-986.
- Schulte, J. (2011) Peroxiredoxin 4: a multifunctional biomarker worthy of further exploration. *BioMed Central Medicine* **9**, 137-141.
- Seeman, N. C. (2005) From genes to machines: DNA nanomechanical devices. *TRENDS in Biochemical Science* **30**, 119-125.
- Shau, H., Kim, A. T., Hedrick, C. C., Lusi, A. J., Tompkins, C., Finney, R., Leung, D. W. and Paglia, D. E. (1997) Endogenous natural killer enhancing factor-B increases cellular resistance to oxidative stresses. *Free Radical Biology and Medicine* **22**, 497-507.
- Sies, H. (1993) Strategies of antioxidant defence. *European Journal of Biochemistry* **215**, 213-219.
- Simoni, S., Goemaere, J. and Knoop, B. (2007) Silencing of peroxiredoxin 3 and peroxiredoxin 5 reveals the role of mitochondrial peroxiredoxins in the protection of human neuroblastoma SH-SY5Y cells toward MPP⁺. *Neuroscience Letters* **433**, 219-224.
- Stadtman, E. R. (1992) Protein oxidation and aging. *Science* **257**, 1220-1224.
- Stone J. R. and Yang, S. (2006) Hydrogen peroxide: a signaling messenger. *Antioxidants and Redox Signaling* **8**, 243-270.
- Su, D., Wang X., Simard, M. and Wuest, J. D. (1995) Molecular tectonics. *Special Issue: 8th International Symposium on Molecular Recognition and Inclusion* **6**, 171-178.
- Switala, J. and Loewen, P. C. (2002) Diversity of properties among catalases. *Archives of Biochemistry and Biophysics* **401**, 145-154.
- Thorley, A. J. and Tetlye, T. D. (2013) New perspectives in nanomedicine. *Pharmacology and Therapeutics* **140**, 176-185.
- Trujillo, M., Mauri, P., Benazzi, L., Comini, M., De Palma, A., Flohé, L., Radi, R., Stehr, M., Singh, M., Ursini, F. and Jaeger, T. (2006) The Mycobacterial thioredoxin peroxidase can act as a 1-Cys peroxiredoxin. *Journal of Biological Chemistry* **281**, 20555-20566.
- Valenzuela, R. and Deymier, H. (2008) Formation of Copper Nanowires by Electroless deposition using Microtubules as Templates, *Journal of Nanoscience and Nanotechnology* **8**, 3416.

- Veal, E. A., Day, A. M. and Morgan, B. A. (2007) Hydrogen peroxide sensing and signalling. *Molecular Cell Review* **26**, 1-14.
- Verdoucq, L., Vignols, F., Jacquot, J.-P., Chartier, Y. and Meyer, Y. (1999) *In vivo* characterization of a thioredoxin target protein defines a new peroxiredoxin family. *Journal of Biological Chemistry* **274**, 19714-19722.
- Wallace, D. C. (2005) A mitochondrial paradigm of metabolic and degenerative diseases. *Annual Review of Genetics* **39**, 359-407.
- Weichsel, A., Gasdaska, J. R., Powis, G. and Montfort, W. R. (1996) Crystal structures of reduced, oxidized, and mutated human thioredoxins: evidence for a regulatory homodimer. *Structure* **4**, 735-751.
- Wiesner, K. (1962) The reaction mechanism of catalase. *Brèves Communications* **3**, 115-116.
- Woo, H. A., Chae, H. Z., Hwang, S. C., Yang, K.-S., Kang, S. W., Kim, K. and Rhee, S. G. (2003) Reversing the inactivation of peroxiredoxins caused by cysteine sulfinic acid formation. *Science* **300**, 653-656.
- Wood, Z. A., Poole, L. B., Hantgan, R. R. and Karplus, P. A. (2002) Dimers to doughnuts: redox-sensitive oligomerisation of 2-Cys peroxiredoxins. *Biochemistry* **41**, 5493-5504.
- Wood, Z. A., Schröder, E., Harris, J. R. and Poole, L. B. (2003a) Structure, mechanism and regulation of peroxiredoxins. *Trends in Biochemical Sciences* **28**, 32-40.
- Wood, Z. A., Poole, L. B. and Karplus, P. A. (2003b) Peroxiredoxin evolution and the regulation of hydrogen peroxide signalling. *Science* **300**, 650-6.
- Xu, Z., Horwich, A. L. and Sigler, P. B. (1997) Asymmetric GroEL-GroES-(ADP)₇chaperonin complex. *Nature* **388**, 741-750.
- Yang, B., Ran, P., Xu, A., Lam, K. S. L., Berger, T., Mak, T. W., Tse, H.-F., Yue, J. W. S., Song, E., Vanhoutte, P. M., Sweeney, G. and Wang, Y. (2012) Improved functional recovery to I/R injury in hearts from lipocalin-2 deficiency mice: restoration of mitochondrial function and phospholipids remodelling. *American Journal of Translational Research* **4**, 60-71.

Chapter 2 Materials and Methods

2.1 Materials

2.1.1 Chemicals

Unless otherwise stated all chemicals were obtained from Sigma-Aldrich (Auckland, New Zealand), or Invitrogen (Victoria, Australia). Sodium dodecyl sulfate polyacrylamide gel electrophoresis (SDS-PAGE) gels were supplied by Invitrogen, and protein ladders by BioRad. Protein standards for gel filtration calibration were also obtained from BioRad. Chromatography media were obtained as pre-packed columns or loose gel from GE Healthcare Lifesciences (Auckland, New Zealand). Milli-Q H₂O was produced in house using an Advance A10 Water Purification System (Millipore).

2.1.2 Enzymes

Polymerase, polymerase chain reaction (PCR) enzymes and horse radish peroxidase (HRP) were obtained from Invitrogen (Victoria, Australia). Recombinant Tobacco Etch Virus (rTEV) protease plasmid was obtained from in house stocks in the Lott Laboratory (University of Auckland), the pMHT238Δ construct had been produced previously in the laboratory and seen to give high yields of soluble protein (see section 2.3.3.1).

2.1.3 Bacterial strains

All media and equipment for bacterial culture were sterilised by autoclaving prior to use, or were purchased sterile. All bacterial work was carried out under sterile conditions either in a laminar flow hood or with an updraft generated by a flame, and standard aseptic technique was employed (Bykowski and Stevenson, 2008). A number of *E. coli* strains were used throughout this research for plasmid propagation and storage, cloning, and protein expression (Terpe, 2006). Competent cells of each strain were either purchased from Invitrogen or home-made as detailed in section 2.2.1.

XL1-Blue (Stratagene [1998]; genotype – *recA1*, *endA1*, *gyrA96*, *thi-1*, *hsdR17*, *supE44*, *relA1*, *lac* [*F'* *proAB lacI^q ZΔM15 Tn10 (Tet^R)*]) and DH5α (Invitrogen, 2004; genotype – *F'* ϕ 80*lacZΔM15 Δ[lacZYA-argF]U169*, *recA1*, *endA1*, *hsdR17*, (*rk-*, *mk+*), *phoA*, *supE44*, *thi-1*, *gyrA96*, *relA1*, *tonA*) cells were used as cloning and plasmid propagation host to give high miniprep quality and DNA stability.

Rosetta(DE3) (Novagen, 2013; genotype – *F'* *ompT hsdS_B[B⁻ m_B⁻] gal dcm* [DE3] *pRARE* [*Cam^R*]) competent cells were used for *HsPrx3* and *MtAhpE* protein expression, chosen as the *pRARE* codon which supplies tRNAs for the rare codons of *HsPrx3* and *MtAhpE* (appendix 4; Terpe 2006), and the cells contain the gene for T7 RNA polymerase allowing expression from the pET vector used for *HsPrx3* expression. The cells also recognise the *trc* promoter allowing expression from the pProEx vector used for *MtAhpE*.

BL21 (DE3) RIPL codon plus (Stratagene; genotype – *F'* *ompT*, *hsdS(rB⁻ mB⁻)*, *dcm⁺*, *Tet^R*, *galλ*(DE3), *endA*, *Hte* [*argU proL Cam^R*] [*argU ileY leuW Strep/Specr*]) were used for expression of rTEV as they allow expression of rare codons including ArgU, which is important for high levels of protein (Kapust, 2002; Blommel and Fox, 2007).

2.1.4 Plasmids

The *MtAhpE* gene – *Rv2238c* from *M. tuberculosis* genomic DNA – was gratefully received from collaborator Dr Shaun Lott at Auckland University, cloned into pProEx with *NcoI* and *SacI* restriction sites. The *HsPrx3* gene was originally obtained from Dr Mark Hampton in the Christchurch School of Medicine, and subsequently cloned into a pET151/D-TOPO vector (Novagen, 1999) by Pam Zhu in the Gerrard laboratory. pET151 contains the pBR322 origin of replication and the *lac* operator, allowing induction of expression through the addition of isopropyl galactosidase IPTG (section 2.1.6 and 2.3.1). The vector used harbours an N-terminal 6xHis tag and rTEV cleavage site, the *bla* gene encoding beta-lactamase for ampicillin (Amp) resistance, and expression is under the control of the bacteriophage T7 promoter.

The pProEx expression system was used for expression of *MtAhpE*, which is inducible by addition of IPTG. The plasmid harbours an N-terminal 6xHis tag and the *bla* gene for Amp resistance.

2.1.5 Media

All media and containing vessels to be used for bacterial culture were sterilised by autoclaving prior to use. Media were stored at 4°C if not immediately used, for no more than two days. Antibiotics and other additives were added to the required final concentration just prior to use (section 2.1.6).

Lysogeny Broth Medium (LB): LB Broth Base was supplied in ready to use powder from Invitrogen. 20 g was added to 1 L of deionised water, to give a composition of 10 g peptone, 5 g yeast extract, and 5 g NaCl per L (Bertani, 1951).

LB agar: 15 g of agar was dissolved in 1 L of LB medium, sterilised by autoclaving and stored sealed at room temperature. Prior to use the agar was melted by microwaving, and plates poured using appropriate aseptic technique.

Super Optimal Broth (SOB): 20 g bacto-tryptone, 5 g bacto-yeast extract, and 0.5 g NaCl were added to 10 mL of a 250 mM KCl solution. Milli-Q water was added to bring the volume to 1 L, and the pH adjusted to 7.0. 5 mL of sterile 2 M MgCl₂ solution were added just prior to use (Hanahan, 1983).

SOB with catabolite suppression (SOC): SOC medium was prepared by supplementing SOB medium with 1.8% [v/v] glucose.

ZY media: 10 g tryptone and 5 g yeast extract were added to 925 mL of Milli-Q H₂O (Studier, 2005).

2.1.6 Antibiotics and other media additives

Stock solutions of antibiotics were made up in the appropriate solvent and stored at -20°C until use. They were added directly to the medium or agar at a dilution to give the desired working concentration (detailed in table 2.1). Stock IPTG was made up to a concentration of 0.6 M and added to the medium at a 1/1000 dilution to give a working concentration of 0.6 mM.

Table 2.1: Antibiotic concentrations

Antibiotics were dissolved in deionised water with the exception of chloramphenicol which was dissolved in ethanol.

Antibiotic	Stock concentration	Working concentration
Kanamycin (Kan)	50 mg/ mL	25 µg/ Ml
Ampicillin (Amp)	100 mg/ mL	100 µg/ Ml
Chloramphenicol (Cam)	35 mg/ mL	35 µg/ mL
Tetracycline (Tet)	100 mg/ mL	100 µg/ Ml

2.1.7 Oligodeoxyribonucleotides

Table 2.2 presents the oligodeoxyribonucleotides primers that were used during this research for PCR amplification. Differences to the genomic sequence used for site-directed mutagenesis (SDM) are shown in bold and underlined. Primers were designed following the guidelines in the QuikChange® SDM kit (Stratagene, 1998). PrimerX online software (Lapid, 2003) was used to characterise primers and ensure formation of secondary structures or primer dimers would be minimal. Oligodeoxyribonucleotides were synthesised by Invitrogen or Integrated DNA Technologies, Inc. (IDT, Coralville, IA, USA).

2.1.8 Sodium dodecyl sulfate polyacrylamide gel electrophoresis (SDS-PAGE)

SDS-PAGE analysis (Shapiro *et al.*, 1967) was carried out using Novex® Sharp pre-stained protein ladder to provide molecular mass markers on gels, which give 12 bands marking masses from 3.5 to 260 kDa. BioRad pre-stained protein ladder was also routinely used, which give 12 bands marking masses from 2 to 250 kDa.

Table 2.2: Primers used for PCR reactions

The above primers were used throughout this research for SDM and sequencing of the pProEx vector. Sequencing of genes in the pET151 vector was carried out using standard T7 primers.

Primer	Gene Target	Sequence (5' to 3')
T104W Forward	<i>HsPrx3</i>	CGCACTCTTGTCTCAGACTTA <u>TGG</u> AAGCAGATTTCCCGAGAC
T104W Reverse	<i>HsPrx3</i>	GTCTCGGGAAATCTGCT <u>TTCC</u> ATAAGTCTGACAAGAGTGCG
W95A Forward	<i>MtAhpE</i>	CTGTTGTCTCGGACTTC <u>GCG</u> CCACACGGCGCGGTC
W95A Reverse	<i>MtAhpE</i>	GACCGCGCCGTGTGGC <u>GCG</u> AAGTCCGACAACAG
T76A Forward	<i>MtAhpE</i>	GTGGGCCCCGCCACCC <u>GCG</u> CACAAGATCTGGGC
T76A Reverse	<i>MtAhpE</i>	GCCCAGATCTTGTG <u>GCG</u> GGGTGGCGGGCCCAC
E109A Forward	<i>MtAhpE</i>	GCGTCTTCAACG <u>GCG</u> CAGGCCGGGCATC
E109A Reverse	<i>MtAhpE</i>	GATGCCGGCCTGCG <u>GCG</u> TTGAAGACGC
Q83A Forward	<i>MtAhpE</i>	CAAGATCTGGGCGACG <u>GCG</u> GAGCGGATTACGTTTC
Q83A Reverse	<i>MtAhpE</i>	GAAACGTGAATCCGCTC <u>GCG</u> CGTCGCCCAGATCTTG
Sequencing primer	<i>MtAhpE</i>	AACGACCGAAAACCTGTAT
C47S Forward	<i>HsPrx3</i>	CCTTTGGATTTCACCTTTGTG <u>A</u> GCCTACAGAAATTGTTGC
C47S Reverse	<i>HsPrx3</i>	GCAACAATTTCTGTAGGACT <u>T</u> CACAAAGGTGAAATCCAAAGG
S78A Forward	<i>HsPrx3</i>	GTGGATTCCCACCTTT <u>GCC</u> CATCTTGCCTGG
S78A Reverse	<i>HsPrx3</i>	CCAGGCAAGATGGG <u>GCA</u> AAAGTGGAATCCAC

Gels were either obtained commercially from Invitrogen, or home-made in gel casters, composed of a resolving gel to separate proteins by molecular mass, topped with a stacking gel. A resolving gel was made (see table 2.3), then 100 µL of 10% [w/v] ammonium persulfate (APS) and 10 µL tetramethylethylenediamine (TEMED) added to induce polymerisation. This was poured into the gel cast leaving a 1 cm gap at the top

and a layer of isopropanol added to create a smooth surface. Once set, the isopropanol was poured off and the gel rinsed with distilled water. A stacking gel was made (see table 2.3), then 50 μ L of 10% [w/v] APS and 5 μ L TEMED added and poured on top of the resolving gel. A ten or fifteen tooth comb was placed into the top of the gel to create wells. Quantities described were sufficient for one gel. Typically, 5 – 10 gels would be made, and stored wrapped with wet towels at 4°C.

Table 2.3: SDS-PAGE gel recipes

Gels were home-made according to the following recipes.

Solutions	Resolving Gel	Stacking Gel
30% [w/v] Acrylamide	4 mL	0.7 mL
Resolving Buffer (section 2.1.9.4)	2.6 mL	0 mL
Stacking Buffer (section 2.1.9.4)	0 mL	1.25 mL
10% [w/v] SDS	0.1 mL	0.05 mL
Milli-Q H ₂ O	3.2 mL	3 mL
Bromothymol Blue	0 mL	1 Drop

Pre-made gradient gels were also routinely run using a NuPAGE® system from Invitrogen.

2.1.9 Buffers and solutions

2.1.9.1 Buffers and solutions for protein purification

Lysis mix: 100 mg lysozyme, 25 mg *RNase A*, 5 mg *DNase I*, 1 mL 1 M MgCl₂ made up to 5 mL with Milli-Q H₂O.

Lysis buffer: 20 mM 4-(2-hydroxyethyl)-1-piperazineethanesulfonic acid (HEPES), 150 mM NaCl, 10 mM imidazole, 100 μ L lysis mix per 10 mL, complete mini protease inhibitor (Roche Applied Science); pH 8.0.

2.1.9.2 Buffers and solutions for chromatography

Immobilised Metal Affinity Chromatography (IMAC) column stripping buffer: 20 mM NaH_2PO_4 , 0.5 mM NaCl, 50 mM ethylenediaminetetraacetic acid (EDTA); pH 7.4 (GE Healthcare, 2005)

IMAC loading buffer: 20 mM HEPES, 150 mM NaCl, 10 mM imidazole; pH 8.0.

IMAC elution buffer: 20 mM HEPES, 150 mM NaCl, 500 mM – 1 M imidazole; pH 8.0.

Gel filtration running buffer: 20 mM HEPES, 150 mM NaCl, pH 8.0.

Reducing buffer: 20mM HEPES, 50 mM NaCl, 2 mM tris(2-carboxyethyl)phosphine (TCEP) pH 8.0.

Chelation buffer: 20mM HEPES, 50 mM NaCl, 2mM EDTA pH 8.0.

2.1.9.3 Buffers and solutions for circular dichroism

Circular Dichroism (CD) buffer: 5 – 20 mM NaH_2PO_4 ; pH 7.5.

2.1.9.4 Buffers and solutions for SDS-PAGE

Resolving buffer: 375 mM Tris/HCl, 0.1% [w/v] SDS; pH 8.8.

Stacking buffer: 200 mM Tris/HCl, 0.1% [w/v] SDS; pH 6.8.

Sample loading buffer: 4 mL stacking buffer, 4 mL glycerol, 0.8 g SDS, 400 µl β-mercaptoethanol (BME).

Running buffer: 20 mM Tris-HCl, 192 mM glycine, 0.1% [w/v] SDS; pH 6.8.

2-(N-morpholino)ethanesulfonic acid (MES) buffer: (10x stock) 40 mM MES, 100 mM NaAc, 10 mM EDTA, pH 7.0.

Coomassie stain: 0.1% [w/v] Coomassie Brilliant Blue R250, 50% [v/v] methanol, 40% [v/v] Milli-Q H₂O, 10% [v/v] glacial acetic acid.

Coomassie destain: 50% [v/v] Milli-Q H₂O, 40% [v/v] methanol, 10% [v/v] glacial acetic acid.

2.1.9.5 Buffers and solutions for mass spectroscopy

Matrix solution: 30 mg ferulic acid dissolved in 0.5 mL 2-propanol and 0.5 mL 0.5% trifluoroacetic acid (TFA).

2.1.9.6 Buffers and solutions for plasmid extraction

Buffer S1: 50 mM Tris-HCl, 10 mM EDTA, 100 µg/mL RNase A, pH 8.0.

Buffer S2: 200 mM NaOH, 1% SDS.

Buffer S3: 4.2 M guanadinium HCl, 900 mM potassium acetate, pH 4.8.

Wash Buffer: 10 mM Tris-HCl, 80% ethanol, pH 7.5.

Tris-EDTA (TE) Buffer: 10 mM Tris-HCl, 1 mM EDTA, pH 8.0.

2.1.9.7 Buffers and solutions for DNA electrophoresis

Tris-acetate-EDTA (TAE) buffer: 40 mM Tris-acetate, 1 mM EDTA, pH 8.3.

2.1.9.8 Buffers and solutions for rTEV purification

rTEV lysis buffer: 20 mM NaH₂PO₄, 500 mM NaCl, 0.3 mM TCEP, 50 mM imidazole, pH 7.5 (Blommel and Fox, 2007).

rTEV storage buffer: 50 mM Tris-HCl, 0.5 mM EDTA, 1 mM DTT; pH 8.0 (Blommel and Fox, 2007).

rTEV IMAC elution buffer: 20 mM NaH₂PO₄, 500 mM NaCl, 0.3 mM TCEP, 500 mM imidazole, pH 7.5 (Blommel and Fox, 2007).

2.1.9.9 Buffers and solutions for autoinduction

50x 5052: 250 g glycerol, 25 g glucose, 10 g lactose, 730 mL Milli-Q H₂O (Studier, 2005).

20x NPS: 500 mM (NH₄)₂SO₄, 1 M KH₂PO₄, 1 M Na₂HPO₄, pH 6.75 (Studier, 2005).

2.1.9.10 Buffers and solutions for peroxidase activity assay

Assay buffer: 100 mM potassium phosphate, 0.1 mM diethylene triamine pentaacetic acid (DTPA), pH 7.5 made up in ultrapure water (Thermo Fisher Scientific Inc.).

Stock BME: 20 mM in ultrapure water, adjusted to pH 7.5 with 3 M KOH in ultrapure water.

2.2 Molecular biology

2.2.1 Competent cells

2.2.1.1 Making chemically competent cells

A fresh plate was streaked from glycerol stocks (section 2.2.2.1) of chemically competent cells using a sterile pick or flame-sterilised nichrome wire. This was incubated overnight at 37°C, and a single colony used to inoculate 10 mL of LB and incubated overnight at 37°C, with shaking at 160 rpm. The 10 mL culture was added to a 200 mL flask of LB, and incubated with shaking at 160 rpm, 37°C until the optical density (OD) reached ~1. Cells were harvested by centrifugation at 3,500 rpm, 4°C for 15 minutes and resuspended gently in 1/5 the original volume of 0.1 M CaCl₂. Centrifugation was repeated, and the pellet resuspended in 1/25 the original volume of 0.1 M CaCl₂. 100 µL aliquots were dispensed into 1 mL Eppendorf tubes and flash frozen to be stored at -80°C (Inoue *et al.*, 1990).

2.2.1.2 Making electrocompetent cells

200 mL cultures were produced from glycerol stocks of electrocompetent cells as for chemically competent cells (section 2.2.1.1), and incubated similarly until the OD reached ~0.3 (no higher than 0.4). At this point the culture was placed on ice and swirled occasionally to speed cooling. Cells were harvested by centrifugation at 2,500 rpm for 20 minutes at 4°C. The supernatant was decanted and the cells washed by resuspending in 200 mL distilled water. This wash step was repeated twice, the second

time resuspending in 100 mL distilled water. Cells were harvested as before, and the resulting pellet resuspended in 200 mL of 10% glycerol. The suspension was centrifuged at 2,500 rpm for 20 minutes, and the supernatant removed, this time by gentle aspiration as glycerol destabilises the pellet. The pellet was resuspended in 2 mL 10% glycerol, and 50 μ L aliquots dispensed into cryovials, flash frozen and stored at -80°C.

2.2.1.3 Transformation of chemically competent cells

An aliquot of chemically competent cells was taken from -80°C storage and thawed gently on ice. 1 μ L of DNA was added, mixed gently with a pipette tip and the transformation mixture incubated on ice for 30 minutes. Cells were heat shocked in a heating block at 42°C for 45 seconds, then immediately placed on ice for 2 minutes to cool. 1 mL of sterile LB, pre-warmed to 37°C, was added to the cells and the mixture incubated at 37°C with shaking at 250 rpm for 1 hour. Cells were harvested with centrifugation at 4,000 rpm for 10 minutes, most of the media decanted and the pellet resuspended in the remaining media (~50 μ L). This was spread onto a plate containing the appropriate antibiotics and incubated overnight at 37°C.

2.2.1.4 Transformation of electrocompetent cells

A vial of electrocompetent cells was taken from -80°C storage and thawed gently on ice. 1 μ L of DNA was added, mixed gently with a pipette tip and the transformation mixture incubated on ice for 30 minutes. The mixture was transferred to a pre-chilled 1 mm electroporation cuvette, and placed into the electroporator (BioRad Gene Pulser™). A 2.5 kV pulse was applied and 1 mL room temperature sterile LB added immediately. The solution was transferred to an Eppendorf tube and incubated at 37°C with shaking at 250 rpm for 1 hour. Cells were harvested with centrifugation at 4,000 rpm for 10 minutes, most of the media decanted and the pellet resuspended in the remaining media

(~50 μ L). This was spread onto a plate containing the appropriate antibiotics and incubated overnight at 37°C.

2.2.2 Bacterial culture

Agar plates containing the appropriate antibiotics (section 2.1.6) were streaked with the desired strain from a fresh transformation (section 2.2.1.3 and 2.2.1.4) using a sterile pick or flame-sterilised nichrome wire. Plates were incubated overnight at 37°C. Single colonies were picked and used to inoculate 5 mL of LB medium containing appropriate antibiotics. Starter cultures were incubated overnight at 37°C with shaking at 160 rpm, and subsequently used to inoculate larger quantities of media (section 2.3.1).

2.2.2.1 Glycerol stock preparation

Glycerol stocks were prepared for longer term storage of bacterial strains and cells transformed with plasmids of interest. 5 mL cultures were grown as described above, then used to inoculate 250 mL sterile LB. This was incubated at 37°C until the OD₆₀₀ was about 0.6, then centrifuged at 3000 rpm for 15 minutes at 4°C. The pellet was resuspended in 250 mL ice cold, sterile 30% glycerol. Centrifugation was repeated and supernatant discarded, then the pellet resuspended in 20 mL 30% glycerol. The resulting cell suspension was split into 1 mL aliquots in screw-top cryo-vials, flash frozen and stored at -80°C.

2.2.3 Polymerase chain reaction (PCR)

PCR was used to carry out SDM (Flavell *et al.*, 1975) to introduce single amino acid changes to the wildtype protein primary structure. SDM primers were designed as described in section 2.1.7.

HsPrx3 template DNA was routinely methylated to ensure complete digestion by DpnI (Li *et al.*, 1999) and prevent false positives. This was achieved by incubating template DNA with the New England Biolabs (NEB) methyltransferase system (table 2.4) for one hour at 37°C. Primers from Invitrogen and IDT were rehydrated to 100 ng/μL concentration and stored at -20°C. *Pfu*Turbo DNA polymerase was used (Takara). A standard PCR reaction was set up with the reagents as shown in table 2.5 and run in the thermocycler on the programme shown in table 2.6. The DNA polymerase system PrimerSTAR HS with GC buffer from Takara (*via* Norrie Biotech, Auckland, New Zealand) was used for SDM of the *MtAhpE* gene, as it shows high accuracy and amplification rates for high GC templates such as the *M. tuberculosis* genome (Takara, PrimeSTAR HS instruction manual).

Table 2.4: Methylation of template DNA

Plasmids containing the gene to be mutated were incubated with the following reagents at 37°C for one hour. This ensured all parental DNA was degraded, as DpnI recognises methylated DNA.

Reagent	Amount used
10 x NEBuffer™ 2	1.6 μL
NEB DNA methylation enzyme	1 μL
Template plasmid	125 ng
10 x S-Adenosyl methionine	1.6 μL
H ₂ O	To a final volume of 10 μL

Table 2.5: Standard PCR reaction

The reaction mixture suggested in the QuikChange[®] manual was used as a standard protocol to be optimised if initial reactions were unsuccessful.

Reagent	Amount used
2x GC reaction buffer	12.5 µL
Template plasmid	1 ng
Forward primer	125 ng
Reverse primer	125 ng
dNTP mix	1 µL
MillQ H ₂ O	To a final volume of 50 µL
Polymerase enzyme	1 µL added last

Table 2.6: Standard thermocycler programme

The following programme was adapted from the QuikChange[®] manual to suit the gene and polymerase being used: initial denaturation time was increased to optimise strand separation of a high GC content gene; a short annealing time was used to suit the polymerase (following manufacturer's instructions); template concentration was lowered to suit the polymerase.

Segment	Cycles	Temperature	Time
1 – Initial denaturation	1	95°C	5 minutes
2 – Denaturation	16	95°C	10 seconds
Annealing		65°C	5 seconds
Extension		72°C	5 minutes
3 – Final extension	1	72°C	2 minutes

Once the thermocycler programme was complete the reaction mixture was cooled to 4°C on ice or in the machine. Presence of an amplified product was checked by running the mixture on a 1% agarose gel (2.2.4.4). 1 µL DpnI restriction enzyme was added to the mixture, pipetted up and down to distribute the enzyme, and incubated at 37°C for 1 hour. DpnI exclusively digests methylated DNA (Li *et al.*, 1999) and is therefore used to remove the parental (template) plasmid. 1 µL of the digestion mixture was used to transform the appropriate cells (see section 2.2.1).

Control reactions were carried out in parallel with SDM reactions to ensure efficiency of mutagenesis and transformation. The pWhitescript plasmid and control primers (provided in the QuikChange[®] kit) were subjected to identical PCR conditions, and after thermocycling and digestion, XL1-Blue cells were transformed and plated onto LB plates with Amp, IPTG, and 5-bromo-4-chloro-3-indolyl- β -D-galactopyranoside (X-gal). On this medium mutant transformants form blue colonies, unsuccessful mutagenesis results in white colonies, allowing mutagenesis efficiency to be calculated (Stratagene, 1998) using equation 2.1.

$$\text{Mutagenesis efficiency} = (\text{Blue cfu} / \text{Total cfu}) \times 100 \quad \textbf{Equation 2.1}$$

Where cfu is the number of colony forming units. According to the manufacturer's guidelines (Stratagene, 1998), transformation of the pWhitescript plasmid can be expected to result in 50 – 800 colonies, with a mutagenesis efficiency of over 80%.

2.2.4 DNA manipulations

2.2.4.1 Plasmid preparation by alkaline lysis

Plasmid extractions were performed from propagation strains (section 2.1.3). Transfected cells containing the desired plasmid were used to prepare 5 mL cultures (section 2.2.1 and 2.2.2) and a plasmid extraction performed, using a commercial Qiagen kit (Bio-Strategy, Auckland, New Zealand) through alkaline lysis (Birnboim and Doly, 1979) and purification with an affinity column (Qiagen, 2012). Purified plasmids were stored at -20°C to be used in PCR reactions or transformation by electroporation or chemical transformation (section 2.2.1).

1-4 mL of the culture was collected, centrifuged at 12,000 rpm for 1 minute to pellet the bacteria and the supernatant pipetted off. 250 μ L of buffer S1 was added to the pellet

(buffer compositions are described in section 2.1.9.6) and vortexed to resuspend. 250 μ L of buffer S2 was added and mixed gently so as not to shear the genomic DNA and contaminate the plasmid DNA. These buffers provide a suitable, alkaline lysis environment, contain EDTA and RNase to reduce contamination and inhibit nucleases, and SDS to destroy cell membranes. 350 μ L of buffer S3 was added within 5 minutes and mixed by inversion to neutralise the lysate, renature plasmid DNA, and precipitate cell debris. Lysate was clarified by centrifuging at 12,000 rpm for 10 minutes. The supernatant was applied to a QIAprep column inside a microfuge tube, the DNA allowed to bind, and flow through removed by spinning at 12,000 rpm for 1 minute. The column was washed twice with wash buffer by adding 750 μ L and spinning at 12,000 rpm for 1 minute, to elute RNA, protein and other contaminants. The filtrate was discarded and the column placed back into the microfuge tube and spun to remove all traces of wash buffer and salt. 60-80 μ L of TE low salt buffer was applied to the column membrane and allowed to absorb at room temperature for 1 minute, after which it was centrifuged at 12,000 rpm for 1 minute to collect the eluted plasmid in the microfuge tube.

2.2.4.2 DNA purification

Ethanol precipitation was carried out to increase the purity of plasmid preparations and concentrate plasmids where necessary. The salt concentration of the solution was adjusted by adding 1/10 of the volume of the plasmid solution of 3 M sodium acetate, pH 5.2 and mixed well. 2 volumes of cold ethanol were added and the mixture placed on ice for 20 minutes before centrifuging at 12,000 rpm for 15 minutes. The supernatant was decanted carefully as the pellet was not always visible, and the pellet resuspended in 1 mL of 70% ethanol. Pelleting and supernatant removal was repeated and the pellet resuspended in 60 μ L water.

2.2.4.3 Commercially prepared plasmids

Customised sequences were ordered using the SDM services offered by GenScript USA Inc., NJ, USA, or Epoch Life Science, TX, USA. Designed gene sequences were supplied in the vectors described in 2.1.4.

2.2.4.4 DNA gel electrophoresis

DNA gel electrophoresis was routinely carried out to check the purity of DNA preparations, the success of PCR amplification, and the presence of primer dimers. Agarose gels were prepared by dissolving 1% agarose [w/v] in TAE buffer (section 2.1.9.7), pouring into a gel caster, adding 5 μ L Sybr®Safe dye and inserting a 10 well comb. When the gel had set the cassette was placed into an electrophoresis chamber and just covered with TAE buffer. Protein samples were mixed with 1/6 volume of 6x DNA loading dye (purchased from Bio-strategy, Auckland, New Zealand) and 10 μ L volumes were loaded into the wells of the gel. 5 μ L of 1 kilobase plus DNA ladder (Invitrogen) was loaded into lane 1 as a size marker.

2.2.4.5 Determination of DNA concentration

Concentration of DNA solutions was analysed by ultra-violet (UV) absorption at 260 nm on a NanoDrop 2000 spectrophotometer (Thermo Fisher Scientific Inc.), using the automatic function of the machine which uses equation 2.2.

$$\text{Concentration} = (A_{260} / \epsilon_{260}) * l \quad \text{Equation 2.2}$$

Where A_{260} is absorption at 260 nm in AU, ϵ_{260} is the wavelength-dependent extinction coefficient at 260 nm (ng/cm/ μ L), and l is the path length in cm (0.1 cm in the NanoDrop 2000). The average extinction coefficient of double stranded DNA is 50 ng/cm/ μ L (Thermo Fisher Scientific, 2009). The molarity of polymers such as DNA

does not depend on length, therefore the more useful units of mass per volume are employed in this case. Purity of the sample was also determined on the NanoDrop by looking at the 260/280 ratio, taking 1.8 as the value for pure DNA.

2.2.4.6 DNA sequencing

Fidelity of mutagenesis reactions was confirmed by Sanger sequencing (Sanger and Coulson, 1975), carried out through Canterbury Sequencing and Genotyping at the University of Canterbury using an Applied Biosystems 3130xl Genetic Analyzer; through ABI Sequencing and Genotyping Services at Massey University using an Applied Biosystems ABI3730 Genetic Analyser, or through the Auckland Genomics facility on the Applied Biosystems 3130xl Genetic Analyser.

2.3 Recombinant protein production

2.3.1 Protein expression

2.3.1.1 Small scale expression trials

Five 5 mL cultures of the desired transformant bacteria were prepared (section 2.2.2). These were added to 100 mL flasks of LB with appropriate antibiotics, and incubated at 37°C with shaking at 160 rpm to an OD₆₀₀ of ~0.6. Cultures were cooled if required to ensure they were induced at the correct temperature, and IPTG added to a final concentration of 0.6 mM. Flasks were transferred to incubators with shaking at 160 rpm for the appropriate time (see table 2.7). Protein expression levels were assessed by SDS-PAGE analysis of the cell suspension (section 2.4.3).

Table 2.7: Protein expression trials

A range of temperatures and incubation times were used to optimise protein expression. 100 mL cultures were each incubated in the following conditions and protein expression assessed by band intensity on SDS-PAGE.

Induction temperature	Time of incubation
18°C	Overnight
22°C	Overnight
26°C	8 hours
30°C	6 hours
37°C	4 hours

2.3.1.2 Large scale expression

5 mL cultures were grown as before and used to inoculate 1 L flasks of sterile LB media containing the appropriate antibiotics (section 2.1.6). Cultures were grown at 37°C with shaking at 160 rpm until an OD₆₀₀ of ~0.6 was reached (typically 4 hours). IPTG was added to a final concentration of 0.6 mM, and the cultures transferred to the temperature for optimal expression (as indicated by small scale trials; section 2.3.1.1), for the appropriate time with shaking at 160 rpm. Induced cells were harvested by centrifugation at 6,000 rpm for 15 minutes at 4°C.

2.3.1.3 Expression using autoinduction

Autoinduction media provides a number of sugars, and works on the basis that growing bacteria will preferentially metabolise glucose and glycerol before lactose. Once glucose and glycerol have been metabolised, the bacteria switch to metabolising lactose which activates the *lac* operon, and, therefore, expression from the plasmid (Studier, 2005). This means the point of induction is tightly controlled, and “leaky” expression is minimised, which is seen to give higher final cell densities and increased protein expression (Grabski *et al.*, 2005). Autoinduction buffers (section 2.1.9.9) and all

solutions were made and autoclaved in Schott bottles, to be used once after opening. 925 mL ZY media (section 2.1.9.9) were combined with 1 mL 1 M MgSO_4 , 20 mL 50x 5052 and 50 mL 20x NPS (section 2.1.9.9) in a sterile flask. A 5 mL starter culture was grown and added to the media, and cultures incubated at 26°C overnight.

2.3.1.4 Cell lysis for protein extraction

Harvested cells were resuspended in lysis buffer (section 2.1.9.1), pelleted again (10,000 rpm, 15 minutes at 4°C) and the supernatant discarded. The pellet was resuspended in 50 mL of lysis buffer and kept on ice throughout lysis. The suspension was split into two aliquots and two methods of cell lysis were tested for efficiency.

Sonication: Sonication utilises a metal probe which oscillates at ultrasonic frequency, causing localised low pressure and membrane disruption through cavitation. Lysis of small volumes (< 5 mL) was carried out using a Sonicator 3000 (Misonix) equipped with a Microprobe (Misonix), for larger volumes (up to 50 mL) a standard probe was used. The cell suspension was prepared in a 50 mL Falcon tube placed in a beaker of ice slurry to minimise sample heating, and sonicated at 50% amplitude in 1 second pulses with 9 second delays, for a total on time of 5 minutes.

High pressure homogenisation: Homogenisation achieves cell lysis as the sample is pumped through a needle valve at high pressure, causing cell disruption through shear stresses and decompression as the cells return to atmospheric pressure after the valve. Large volumes of cell suspension (> 50 mL) or those that could not tolerate sonication were lysed by passing through a Microfluidics M-110P cell disrupter, run at 18,000 Pa, 4°C. The sample was passed through the system three times to ensure complete lysis. Resulting lysates from both conditions were clarified by centrifugation (10,000 rpm, 15 minutes, at 4°C), the supernatant collected and analysed by SDS-PAGE (section 2.4.3). Prior to further purification, lysates were filtered through a Millipore 0.2 µm syringe filter (EMD Millipore, MA, USA).

2.3.2 Protein purification by chromatography

2.3.2.1 Small scale affinity purification

Batch purification using Talon® affinity resin (Takara *via* Norrie Biotech, Auckland, New Zealand) was used to purify small volumes during lysis buffer screening (section 3.6.3.2). Talon® resin was chosen as the cobalt charged beads give higher affinity and specificity in comparison to nickel resin. Batch purification was also used when proteins did not bind well, as the increased incubation time increased binding.

1 mL Talon® resin slurry was prepared by centrifugation at 600 rpm for 2 minutes, and the storage buffer removed by decanting the supernatant. Resin was equilibrated by resuspending the pelleted resin in buffer, re-pelleting with centrifugation at 600 rpm for 2 minutes, and removing the supernatant. This was repeated twice, then the resin was resuspended in 1 mL lysis buffer. The lysis supernatant (section 2.3.1.1) was added to the resin, and incubated overnight at 4°C on a rocker. The resin and bound protein was collected by centrifugation at 600 rpm for 2 minutes, and the supernatant removed. The resin was washed twice with lysis buffer as before to remove non-specifically bound protein. Protein remaining bound to the resin was eluted with an appropriate buffer (typically, lysis buffer with 500 mM imidazole added). The supernatant from each step for analysis by SDS-PAGE.

2.3.2.2 Immobilised Metal Affinity Chromatography (IMAC) purification

His-tagged proteins were purified from the cell lysate using IMAC using a 5 mL HiTrap™ chelating column. The column was stripped and recharged by washing with the following:

3 column volumes (cv) stripping buffer (section 2.1.9.2)

5 cv Milli-Q H₂O

5 mL 0.1 M NiCl₂

5 cv Milli-Q H₂O

Prior to sample loading the column was equilibrated with three cv IMAC loading buffer. All solutions to be loaded on the column were filtered through a 0.2 µm sterile syringe filter (EMD Millipore, MA, USA). The lysis supernatant (section 2.3.1.2) was loaded onto the column and the column attached to the ÄKTAprime fast protein liquid chromatography system (FPLC). Three cv of lysis buffer (section 2.1.9.2) were passed through to remove unbound proteins, and bound proteins eluted with 10 mM – 500 mM or 1 M imidazole using the gradient function of the machine and the IMAC elution buffer. 1 mL fractions were collected and those that contained high concentrations of eluted protein as assessed by SDS-PAGE analysis of fractions (section 2.4.3) were pooled and concentrated to about 2 mL (section 2.3.4) with an appropriate molecular mass cut off (one third the mass of the protein being purified). This solution was then subjected to further purification and preparative steps as required.

2.3.2.3 Gel filtration chromatography

Gel filtration was used to increase sample purity and to swap buffers as required. Chromatography was carried out on the Superdex 200 16/60 column which was washed with three cv of Milli-Q water then equilibrated with two cv of buffer at a rate of 0.5 mL/min prior to use. Proteins were eluted with the desired buffer run at 0.5 mL/min, 1 mL fractions collected and peaks identified by UV absorbance at 280 nm. Peak fractions were collected and analysed with SDS-PAGE (section 2.4.3).

2.3.3 His-tag removal

2.3.3.1 Tobacco etch virus protease expression and purification

Recombinant tobacco etch virus protease (rTEV) was expressed in *E. coli* from the pMHT238Δ construct obtained from in house stocks at Auckland University (section 2.1.4). The enzyme was produced using a protocol based on the methods developed by Blommel and Fox (2007). The pMHT238Δ construct developed by this group includes mutations to enhance solubility (T17S, I77V and N68D), and minimise autocatalytic inactivation (S219V). It produces rTEV with a non-cleavable N-terminal his-tag, and self-cleaving maltose binding protein domain (MBP). This allows the protease to be removed from samples by IMAC (section 2.3.2.2).

The pMHT238Δ plasmid was transformed into electrocompetent BL21(DE3) Codon Plus expression hosts (section 2.1.3 and 2.2.1.4), streaked onto an LB + Kan plate and incubated at 37°C overnight. A single colony was picked and used to inoculate 10 mL LB + Kan culture, which was grown overnight at 37°C with shaking at 160 rpm. The 10 mL culture was used to inoculate 1 L LB + Kan, which was incubated at 37°C until the OD reached ~0.8 when expression was induced by adding IPTG to a final concentration of 0.5 mM. The culture was incubated at 27°C overnight with shaking at 160 rpm. Cells were harvested by centrifugation (6,000 rpm, 15 minutes at 4°C) and resuspended in rTEV lysis buffer (section 2.1.9.8). Cells were lysed using the cell press (section 2.3.1.2), and the cell debris separated by centrifugation at 10,000 rpm for 15 minutes at 4 °C. The supernatant was loaded onto a 5 mL HiTrapTM column attached to the ÄKTAprime FPLC system (section 2.3.2.2), washed with three column volumes of rTEV lysis buffer, and eluted with rTEV elution buffer (section 2.1.9.8) using the gradient function of the machine. Fractions containing rTEV as judged by SDS-PAGE (section 2.4.3) were then desalted using a GE HiPrepTM 26/10 desalting column and exchanged into rTEV storage buffer (section 2.1.9.8). The solution was incubated at 4°C for one hour to allow MBP-tag cleavage, then loaded onto a GE HiTrapTM Q

Sepharose anion exchange column attached to the ÄKTAprime FPLC system. Protein was eluted with rTEV high salt buffer (section 2.1.9.8) using the gradient function of the machine, collecting 1 mL fractions. Fractions containing rTEV were pooled and diluted with rTEV storage buffer to a final protein concentration of 2 mg/mL as judged by nanodrop analysis (section 2.4.2). 500 µL aliquot were snap frozen and stored at -80°C.

2.3.3.2 rTEV cleavage

MtAhpE was expressed in a pProEx vector, which encodes an N-terminal 6xHis tag, followed by a 15 residue linker peptide which includes the sequence ENLYFQG – the most commonly used recognition sequence for rTEV, which cleaves between Q and G (Dougherty *et al.*, 1989; Carrington and Dougherty, 1989). *HsPrx3* was expressed in a pET151 vector, which encodes a 6xHis tag, followed by a 26 residue linker peptide, including the ENLYFQG cleavage site. Cleavage trials were run to optimise ratios, temperature, and duration of cleavage. The conditions tested are detailed in table 2.8.

Table 2.8: rTEV cleavage trials

A range of temperatures and protease concentrations were trialled to achieve optimal tag removal while avoiding non-specific cleavage. Cleavage was generally seen to be efficient even at the lowest concentration of rTEV. Incubation times and temperatures were selected based on results of trials with individual proteins.

Ratio rTEV:Protein	Incubation temperature	Incubation time
1:20	4°C	Overnight
1:50	4°C	Overnight
1:100	4°C	Overnight
1:20	21°C	6 hours
1:50	21°C	6 hours
1:100	21°C	6 hours
1:20	37°C	1 hour
1:50	37°C	1 hour
1:100	37°C	1 hour

2.3.4 Protein concentration

Protein samples were concentrated to required volumes, using centrifugal concentrators or polyethylene glycol (PEG) dialysis.

Centrifugal concentration: Vivaspin centrifugal concentrators were selected to have a molecular weight cut off (MWCO) of one third the molecular of the protein to be concentrated. Samples were centrifuged at 4,000 rpm at 4°C until the desired volume was reached. Amicon Ultra-0.5 mL centrifugal concentrators (Millipore) were used for small volumes.

Dialysis concentration: Where centrifugal concentration was not able to be used (for example, when proteins were found to adhere to the concentrator membrane), concentration was achieved using dialysis. 10,000 MWCO dialysis tubing was prepared by wetting with Milli-Q water, then boiling twice for ten minutes in a solution of 10 mM sodium bicarbonate, 10 mM EDTA, pH 8.0, 20% [v/v] ethanol. Tubing was then washed and stored in 0.1% [w/v] sodium azide if not used immediately. Protein samples were transferred into the prepared tubing and dialysed against a solution of buffer substituted with 50% [w/v] PEG₈₀₀₀. Samples were exchanged into a PEG-free buffer (section 2.3.5). Repeated buffer exchange was carried out to ensure complete removal of PEG₈₀₀₀.

2.3.5 Buffer exchange

Buffer exchange was carried out to remove glycerol from buffers used for storage, or where purification buffers were not appropriate for further experiments.

Buffer exchange by dialysis: 10,000 MWCO dialysis tubing was prepared as described previously (section 2.3.4). Protein samples were transferred into dialysis tubing, and dialysed against the required buffer. Sample to dialysis solution ratios would typically be 1:2,000. Dialysis was carried out at 4°C with stirring to increase the rate of exchange. Typically, this would be repeated to achieve complete exchange.

Buffer exchange by chromatography: 5 mL HiTrap™ Desalting columns (GE Healthcare) were purchased pre-packed with Sephadex G-25 Superfine cross-linked dextran. These employ the same principles as gel filtration (see appendix 1) to separate molecules with a mass larger than 5 kDa from those with a mass below 1 kDa, thereby separating proteins from buffer salts. The column was connected to the Äktapurifier 10 FPLC system, and equilibrated with 3 column volumes of the required buffer at 2 mL/min. The sample was loaded onto the column at a maximum volume of 1 mL. Protein was eluted at 2 mL/min using the required buffer, 0.5 mL fractions collected and the elution of protein monitored by UV absorbance at 280 nm.

2.4 Protein characterisation

2.4.1 Peptide sequencing

The presence of a protein in purified solutions or chromatography fractions was indicated by the appearance of a band of appropriate size on SDS-PAGE (2.4.3). When a band of the appropriate size was present but the identity of this band was still in question, peptide sequencing was used to confirm the band was the protein of interest.

The protein was extracted from the band on SDS-PAGE using a method adapted from Jin and Manabe, (2005). The band was excised with a razor and washed in distilled water before soaking in destain solution (100 µL ammonium bicarbonate, 50%

acetonitrile). When the gel was completely destained, the slice was washed again with distilled water, transferred to a clean 1.5 mL Eppendorf tube and 20 μ L of 0.1 M NaOH pH 13 added. The gel was crushed and incubated in the NaOH solution for 10 minutes at room temperature. 30 μ L TFA was added and the resulting solution desalted using a ZipTipC₁₈ pipette desalting tip (Millipore) which had previously been equilibrated with 0.1% TFA. The protein was eluted from the ZipTip using 2 μ L of 70% (v/v) acetonitrile and 0.1% TFA and the solution analysed using liquid chromatography tandem mass spectrometry (LC-MS/MS) by Martin Middleditch at the centre for Genomics and Proteomics, University of Auckland; or by Stefan Clerens at AgResearch, Lincoln.

2.4.2 Determination of protein concentration

2.4.2.1 Bradford assay

The Bradford assay (Bradford, 1976) relies on the colour of Coomassie Brilliant Blue G-250 changing from brown to blue. Under acidic conditions the dye is brown, but binding to protein stabilises the anionic form of the molecule, which is blue and shows an absorbance maximum at $\lambda = 595$ nm. Assays were performed in 96-well plates in triplicate, as per the instructions of the BioRad kit. Assay reagent was diluted 1:4 in Milli-Q H₂O, and filtered through a 0.2 μ m syringe filter (EMD Millipore, MA, USA). A bovine serum albumin (BSA) standard was prepared in Milli-Q water. 10 μ L protein solution or standard were pipetted into the wells, to which 200 μ L Bio-Rad protein assay reagent was added and the solutions mixed thoroughly by pipetting. The mixture was incubated for five minutes at room temperature before the absorbance at 595 nm was measured using the Molecular Devices Spectramax M5 equipped with Softmax Pro 5.4.1 software (Biostrategy, Auckland, New Zealand). A standard curve was generated by plotting the absorbance of BSA at four or more concentrations in the linear range (0.2 – 0.9 mg/mL).

2.4.2.2 NanoDrop spectrophotometric analysis

Purified protein solutions were analysed by UV absorption at 280 nm on the NanoDrop 2000. Extinction coefficients of protein samples were calculated from amino acid sequence using the ExPasy online bioinformatics server (Gasteiger *et al.*, 2005), and were used to determine concentration using the calculation in equation 2.3.

$$\text{Concentration} = (A_{280} / \epsilon_{280}) * l \quad \text{Equation 2.3}$$

Where A_{280} is the absorption at 280 nm in AU, ϵ_{280} is the extinction coefficient at 280 nm ($\text{M}^{-1} \text{cm}^{-1}$), and l is the path length in cm (0.1 in the case of the NanoDrop 2000). Protein samples were concentrated to required volumes (section 2.3.4). Comparison of NanoDrop analysis to Bradford analysis showed good agreement, therefore, NanoDrop analysis was routinely used to ascertain protein concentration.

2.4.3 SDS-PAGE analysis

Protein samples were run on sodium dodecyl sulfate polyacrylamide gel electrophoresis (SDS-PAGE) in reducing, denaturing conditions to estimate monomer size (Shapiro *et al.*, 1967) by comparison to the migration pattern of protein standards which were always run on the same gel as the sample to be analysed. The purity of the sample could also be determined by the presence or absence of bands on the gel additional to the major band indicating the protein of interest. Denaturation was carried out by the addition of 5 μL of sample loading buffer (see 2.1.9.4) to 5 μL protein solution and the mixture heat shocked at 96°C for three minutes to activate the SDS. The gel cassette was assembled into the gel dock and 10 μL of the denaturation mixture loaded into the wells. Home-made 12% acrylamide gels (section 2.1.8) were run using running buffer (section 2.1.9.4) for 1 hour at 120 V. 4-12% Bis-Tris gels were loaded into the gel cassette and run in MES buffer (Good *et al.*, 1966; section 2.1.9.4) in an electrophoresis

gel cassette at 200 V for 35 minutes. After electrophoresis, gels were removed, washed three times for five minutes in Milli-Q H₂O, then stained for thirty minutes in Coomassie stain (section 2.1.9.4). Destaining was carried out by soaking for one hour in destain (section 2.1.9.4), and the results examined on a gel dock.

Where cross-linking was required prior to SDS-PAGE analysis, proteins were incubated with 2.3% glutaraldehyde for the time required for the individual experiment as detailed in the results.

2.4.4 Mass Spectrometry

Matrix assisted laser desorption/ionisation time of flight mass spectrometry (MALDI-TOF MS) was used to obtain accurate molecular masses of native and mutant proteins, to confirm the purity and identity of the protein, and rule out any degradation of the sample (Mann *et al.*, 2001). 1 µL of matrix solution (see 2.1.9.5) was applied to discrete spots on a 100-well sample plate (Applied Biosystems Incorporated) and allowed to air dry. Dilutions of 1:20 and 1:50 protein:matrix were made up and 1 µL overlayed onto the matrix spots. Once dried MALDI-TOF spectra were obtained using the Voyager DE PRO Biospectrometry workstation equipped with Voyager 5 and Data Explorer software (Applied Biosystems Incorporated) at Auckland University. Spectra were obtained using the following conditions:

Manual control

Accelerating voltage: 25,000 V

Guide wire voltage: 0.3%

Delay time: 200-300 ns

Grid voltage: 94%

Low mass gate: 3000 Da

2.5 Biophysical techniques

A number of biophysical techniques were used to characterise the proteins studied in this research, and assess the influence of introduced mutations. The theory and applications of the techniques can be found in appendix 1.

2.5.1 Circular dichroism

Circular dichroism (CD) data sets were collected on a Jasco J-815 circular dichroism spectrophotometer. Protein solutions of 0.1 – 0.5 mg/mL were prepared in CD buffer (section 2.1.7.3) or water. A quartz cuvette with a 1 mm path length was used, and the instrument initialised with Milli-Q H₂O and blanked with CD buffer. Data were analysed using the Spectra Analysis v1.5 program (Jasco) to subtract blank traces and the DichroWeb online server (Whitmore and Wallace, 2004) was used to estimate secondary structure using the CDSSTR program (Compton and Johnson, 1986). The program uses a reference set of CD spectra, which was chosen to be representative of the protein being analysed (Sreerama, 2000).

2.5.2 Analytical size-exclusion chromatography (SEC)

2.5.2.1 Data collection

An S200 10/300 analytical column (GE Healthcare) was connected to an Äktapurifier FPLC system (GE Healthcare). This column was packed with Superdex beads, composed of dextran covalently linked to cross-linked agarose. The total volume of the column was 24 mL and the void volume 7.2 mL, as judged by the elution of blue dextran (Andrews, 1965).

Prior to sample injection the SEC column and FPLC were equilibrated with three column volumes of the appropriate buffer (section 2.1.9.2), run at 0.5 mL/min. Bio-Rad gel filtration standard mix was used for calibration, and contains a mixture of lyophilised proteins from 1,350 to 670,000 Da. This was rehydrated in the buffer to be used for analysis, in the quantity recommended by the manufacturer which gave final compositions as detailed in table 2.9. 100 μ L of the mixture was injected onto the column, and eluted at a flow rate of 0.5 mL/min (figure 2.1) with constant monitoring of the refractive index (RI) and UV absorbance at 280 nm. Standards were run twice and the elution volumes used to derive a calibration curve (section 2.5.2.2). Samples to be analysed were injected onto the column, at a volume of 100 μ L and concentration of 1 mg/mL unless otherwise stated. Protein was eluted using the appropriate buffer at a flow rate of 0.3 mL/min, and 0.5 mL fractions collected.

Table 2.9: Protein standard concentrations

Lyophilised protein standard mixture (Bio-Rad) was rehydrated with running buffer to give final protein concentrations as shown.

Component	Molecular Weight (Da)	Working concentration (mg/mL)
Thyroglobulin	670, 000	5
γ -globulin	158, 000	5
Ovalbumin	44, 000	5
Myoglobin	17,000	2.5
Vitamin B ₁₂	1,350	0.5

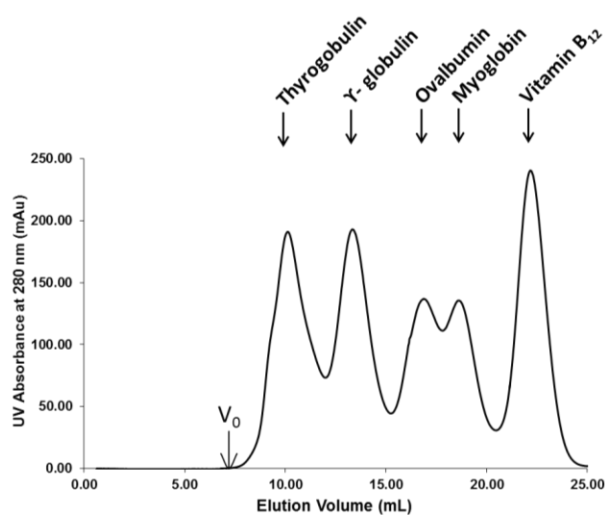


Figure 2.1: Typical elution profile of protein standards

The five protein species in the mixture eluted at different volumes, indicated by peaks in the UV absorbance trace. Standards were run twice.

2.5.2.2 Data analysis

The partition coefficient (K_{av}) was calculated for each of the protein standards (using equation 2.4) and plotted against the $\text{Log}_{10}M_w$ for each (figure 2.2).

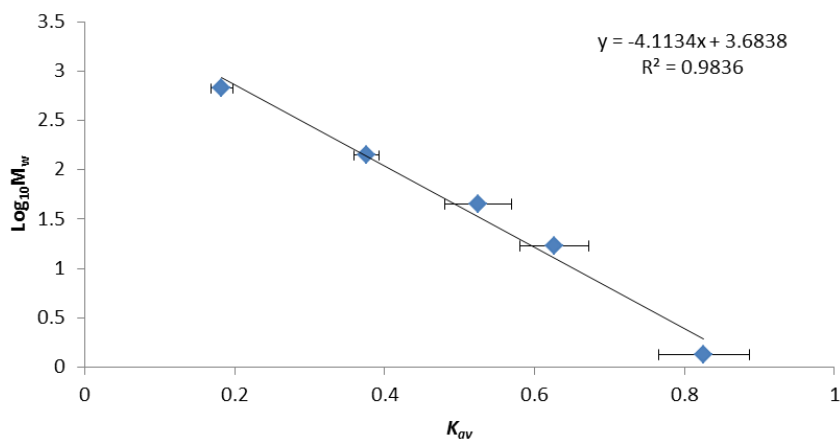


Figure 2.2: A typical size-exclusion chromatography calibration curve

The calculated K_{av} values were used to plot a calibration curve, from which the molecular weight of unknown samples could be calculated.

K_{av} of sample proteins were calculated from the experimental elution profiles using equation 2.4. The $\text{Log}_{10}M_w$ was then acquired from interpolation from the calibration curve (figure 2.2), and the molecular weight calculated using equation 2.5, derived from the slope of the calibration curve.

$$K_{av} = (V_e - V_0) / (V_t - V_0) \quad \text{Equation 2.4}$$

Where V_e is the elution volume of the protein, V_t is the total column volume and V_0 is the void volume (24 and 7.3 mL respectively in the case of the S200 10/300 column).

$$M_w = 10^{((-4.1134 \times K_{av}) + 3.6838)} \quad \text{Equation 2.5}$$

2.5.3 Size-exclusion chromatography with in-line light scattering (SEC/SLS)

A Superdex 200 10/300 column (GE Healthcare) connected to a Viscotek 302-040 Triple Detector GPC/SEC system (ATA Scientific) operated at 28°C was equilibrated with gel filtration buffer (2.1.9.2) by passing through the column at 0.5 mL/min for a minimum of three column volumes. 130 μL samples were injected onto the column and eluted at a flow rate of 0.5 mL/min. Absolute molecular weight, radius of hydration and size distributions were calculated using the refractive index (RI), intrinsic viscosity, and right-angle light scattering (RALS) measurements calibrated against bovine serum albumin (BSA) (66.5 kDa, Sigma), which was run at the beginning and end of each sample sequence. Calibration was carried out using the OmniSEC software as per the manufacturer's instructions (appendix 1).

2.5.4 Electron microscopy

2.5.4.1 Recording of images

Copper grids overlaid with a thin layer of carbon were rendered hydrophilic by glow discharge just prior to use (Aebi and Pollard, 1987). Protein samples were prepared at 0.02 – 0.1 mg/mL, and 5 μ L pipetted onto the grid. Protein was allowed to adsorb for 60 seconds then blotted dry using filter paper (Whatman #1). 5 μ L of stain was immediately added to the grid, and left to stain for 60 seconds before excess stain was removed with filter paper. NanoVan solution (NanoprobesTM) or uranyl acetate were used to negatively stain particles. NanoVan was obtained as a 2% solution in water at pH 8.0; uranyl acetate was made up as a 1% solution, and filtered prior to use through a 0.2 μ m syringe filter (EMD Millipore, MA, USA). Both were stored in the dark at 4°C to be used within 1 year.

Low dose TEM was performed using an FEI Tecnai 12 electron microscope equipped with an LaB₆ filament operated at 120 kV. Images were recorded on Kodak ISO-163 film using ~ 2 μ m underfocus at a nominal magnification of 52,000 x and developed for 10 minutes in D19 (Kodak) diluted 1:1 with deionised water. Digital electron micrographs were also recorded using a CCD camera but these were not used for image processing.

2.4.5.2 Processing of images and generation of 3D models

Electron micrographs were digitised using a Nikon Super Coolscan 9000 scanner at a raster step of 7.8 μ m corresponding to a spacing of 1.5 Å on the specimen. Isolated particles were automatically selected using the boxer module of the EMAN v1.9 image processing suite (Ludtke *et al.*, 1999) and a window size of 200 x 200 pixels. To reduce high-and low-frequency noise components, a 20 Å to 200 Å band-pass filter was applied

to the raw images, which were subsequently normalised. Automatically picked particles were inspected manually and false positives removed. Typically, 100 reference-free class averages were generated in 9 rounds of iterative refinement by using the *refine2d.py* routine in EMAN v1.9.

To initiate 3D reconstructions from conformationally homogeneous subsets of raw images, initial reference models were built using the *startcsym* routine of EMAN v1.9. Typically, 5 initial models were simultaneously refined by 9 iterative rounds of multi-model refinement of EMAN v1.9 with D6 symmetry imposed. The resulting models were separately refined with imposed D6 symmetry using only the selected set of raw images that the process of multi-model refinement had associated with a given reference model. Resolution of the reconstruction was determined by Fourier-shell correlation of two reconstructions obtained from evenly split datasets using the $FSC_{0.5}$ criterion.

2.5.5 Small angle X-ray scattering

2.5.5.1 Data Collection

Small angle X-ray scattering (SAXS) measurements were carried out at the Australian Synchrotron on the SAXS/WAXS beamline. The X-ray energy was 12 kV, corresponding to a wavelength λ of 1.0332 Å, and a Dectris-Pilatus detector used to record scattering patterns (1 M, 170 mm x 170 mm, effective pixel size, 172 x 172 µm). The sample to detector distance was 1600 mm to provide a ' q ' (Fourier spacing) range of 0.0126-0.500 Å⁻¹. Highly pure protein samples in gel filtration buffer were centrifuged and filtered using 0.2 µm Amicon Ultrafree-MC centrifugal filter units (Millipore, Billerica, MA, USA) to remove any aggregates prior to data collection. 50 µL samples were automatically loaded from a multi-well plate into a 1.5 mm glass capillary at 10°C, using dialysis buffer as a blank. Samples were run at concentrations of 0.5 – 2 mg/mL, and data collected at 2 second intervals under continuous flow to

minimise possible damage to the sample from radiation. Where necessary, samples were also run through a gel filtration column prior to SAXS data collection – a Superdex S200 5/125 column (GE Healthcare) was attached to a BioLogic DuoFlow FPLC, and samples passed through the column then routed into the capillary mounted on the beamline. This allowed scattering data collection concurrent with chromatography analysis and removed aggregates which formed rapidly in relation to experiment time. In the case of samples run through the FPLC, frames from the first part of the chromatography run prior to protein elution were used as the blank measurement. Samples run through FPLC were injected at around 10 mg/mL to allow for dilution on the column, estimated to be tenfold.

2.5.5.2 Data analysis

2D scattering plots were averaged and background scattering subtracted using *Scatterbrain* software (Petoukhov *et al.*, 2007), and the AUTOPOROD function of the program used to calculate maximum particle size (D_{\max}), Porod volume, and molecular mass. Data sets were recorded in the form of 30 images, and PRIMUS software (Konarev *et al.*, 2003) used for scattering pattern analyses and to generate Guinier plots. PRIMUS was also used to generate Kratky plots to ensure that proteins that were being analysed were correctly folded, and radius of gyration (R_G) was calculated from the slope of Guinier plots. GNOM (Svergun, 1992) was used to perform indirect Fourier transforms and generate pairwise distance distribution function $P(r)$ to indicate the relative probabilities of distances between scattering centres and D_{\max} . R_G was also calculated from GNOM and compared to that calculated from the Guinier region, to assess the quality of the data. Theoretical scattering patterns and D_{\max} values were generated from atomic coordinates of known structures, and compared with experimental scattering using CRY SOL (Svergun *et al.*, 1995).

2.5.6 Protein crystallisation

2.5.6.1 Crystal trials

Crystallisation trials were routinely carried out at the University of Auckland using the Hamilton Robotics Cartesian Honeybee Nanodispenser, operated by Dr Ivan Ivanovich. Highly pure samples were concentrated (section 2.3.5) to around 10 mg/mL. Initial screens utilised the sitting drop vapour diffusion method, and were set up using six in house screens (appendix 2). Screens were designed to vary parameters typically used to influence crystallisation including precipitant type, pH and buffer additives (Kingston *et al.*, 1994). For each condition 70 μ L of solution from the crystallisation screen was dispensed into the reservoir of a 96-well Intelliplate (Art Robbins Instruments). 400 nL of protein sample was dispensed onto the sample well and 400 nL of reservoir solution mixed with the protein in the well. Plates were sealed with ClearSeal Film (Hampton Research), incubated at 18°C for at least 4 weeks, and examined under a light microscope at regular intervals to monitor crystal growth.

2.5.6.2 Fine-screening

Conditions that produced microcrystals or non-amorphous aggregation were optimised to increase crystal size and quality. Depending on the conditions and type of crystals seen, pH, salt, precipitant and protein concentration were used as variables across a 24-well plate. Fine screens were set up using the hanging drop vapour diffusion method in 24-well VDX crystallisation plates (Hampton Research) 750 μ L reservoir solution pipetted into the wells and 1 μ L of protein sample pipetted onto the centre of a siliconised coverslip. 1 μ L of reservoir solution was added into the protein sample and the coverslip inverted over the reservoir and sealed. Plates were incubated at 18°C for 4 weeks and examined under a light microscope at regular intervals.

2.5.6.3 Freezing of viable crystals

Crystals of an acceptable size and quality were tested for X-ray diffraction patterns using the in house X-ray source (Mardtb Desktop Beamline) or the MX beamlines at the Australian Synchrotron. Crystals were transferred to a cryoprotectant (typically 70% [v/v] Paratone-N [Hampton Research], 30% [v/v] paraffin oil) using a thin fibre loop (Hampton Research) to prevent ice formation and associated mechanical damage during flash freezing (Kriminski *et al.*, 2002). The loop was plunged into liquid nitrogen, and stored in these conditions.

2.6 Peroxidase activity assay

2.6.1 Data collection

The assay used to monitor Prx activity is adapted from the work of Ogusucu *et al.* (2007). 5 mg HRP was dissolved in assay buffer to give solution ~80 μM . The precise concentration was checked by measuring the absorbance at 403 nm using a glass cuvette with a path length of 1 cm ($\epsilon_{403} = 1.02 \times 10^6 \text{ M}^{-1} \text{ cm}^{-1}$; Dolman, 1975). All spectrophotometric measurements were carried out in the Molecular Devices Spectramax M5 equipped with Softmax Pro 5.4.1 software (Biostrategy, Auckland, New Zealand). Serial dilutions of stock H_2O_2 were made in phosphate assay buffer (section 2.1.9.10) to give 1 mL each of 1:10, 1:100, 1:1,000 and 1:10,000 dilutions. The concentration of the stock solution was calculated by measuring the absorbance at 240 nm in a quartz cuvette with a path length of 1 cm ($\epsilon_{240} = 43.6 \text{ M}^{-1} \text{ cm}^{-1}$; Hildebraunt and Roots, 1975).

The Prx to be analysed was concentrated to ~ 30 mg/mL, in a volume of at least 50 μ L (section 2.3.5), and reduced by incubating on ice with 2 mM BME for at least one hour. Buffer exchange was carried out to remove all traces of reductant using Micro Bio-Spin® P-6 gel columns (Bio-Rad). Columns were inverted several times to resuspend the gel, the tips and caps removed, and storage buffer allowed to drain by gravity flow for two minutes. The columns were placed into a 2 mL Eppendorf tube and centrifuged at 1,000 x g for two minutes to remove residual buffer. Equilibration was carried out by resuspending the beads in 500 μ L assay buffer, and centrifuging at 1,000 x g for one minute. This was repeated four times for >99.9% buffer exchange. 50 - 65 μ L of the reduced Prx sample was applied to the centre of the column and incubated at 4°C for two minutes to ensure all low molecular weight particles enter the beads (Peskin, personal communication). Columns were centrifuged at 1,000 x g for two minutes and the flow through collected. Final Prx concentration was checked using the NanoDrop 2000 (2.4.2.2).

Reactions were set up in triplicate in a Greiner 96-well clear bottom plate (Sigma-Aldrich, Auckland, New Zealand). Prx samples were diluted to ~2 mg/mL (~100 μ M) with assay buffer, and each sample was analysed at concentrations of, 1, 2, 3, 4, 6, 8, and 10 μ M. Prx was dispensed using a multichannel manual pipette (Eppendorf), and HRP added with a Repetman® automated dispenser (Gilson Inc., WI, USA). Assay buffer was added as required (table 2.10) and the mixture incubated for ten minutes. Reaction mix compositions are given in table 2.10.

H₂O₂ was added to the wells using the multichannel pipette, and the reactions mixed by pipetting up and down three times. The plate was immediately transferred to the spectrophotometer and the absorbance at 403 nm recorded for ten minutes at intervals of eight seconds. The absorbance of two control reactions were always measured concurrently – 8 μ M HRP alone, and 8 μ M HRP with 3 μ M H₂O₂ with no Prx. As the reduced protein was exchanged into a buffer containing no reductant, the protein could not be recycled and therefore only the first cycle of catalysis was measured.

Table 2.10: Composition of well solutions for activity assay

Required volumes of reagents were calculated depending on stock concentrations (section 2.1.9.10). An example is shown, as calculated for reagents at the following starting concentrations: Prx 100 μM , HRP 80 μM , H_2O_2 160 μM . H_2O_2 was not added until immediately prior to spectrophotometric measurement.

Prx Conc (μM) Vol (μL)		HRP Conc (μM) Vol (μL)		H_2O_2 Conc (μM) Vol (μL)		Assay Buffer Vol (μL)
1	2.5	8	25	3	4.69	217.81
2	5	8	25	3	4.69	215.31
3	7.5	8	25	3	4.69	212.81
4	10	8	25	3	4.69	210.31
6	15	8	25	3	4.69	205.31
8	20	8	25	3	4.69	200.31
10	25	8	25	3	4.69	195.31

2.6.2 Data analysis

Relative activity was calculated by determining the relative amounts of the substrate that are catalysed by HRP and *HsPrx3*. This was achieved by monitoring the change in absorbance at 403 nm, which indicated the degree to which HRP was out competed by *HsPrx3*. The rate was calculated using the absorbance at the time point of 120 seconds, at which point the reaction had finished and absorbance had stabilised. k_{HsPrx3} was calculated using equation 2.6.

$$\left(\frac{F}{1-F}\right) k_{\text{HRP}}[\text{HRP}] = k_{\text{HsPrx3}}[\text{HsPrx3}] \quad \text{Equation 2.6}$$

Where $(F/1-F)$ is the ratio of inhibition of HRP. This is derived from the change in absorbance at 403 nm (ΔA_{403}) compared to that of the HRP reaction with H_2O_2 without a competing peroxidase (figure 2.3; equations 2.7 and 2.8; Winterbourn, 1987). The baseline is given by the recorded absorbance of HRP with no peroxide or *HsPrx3* (i.e. no change in A_{403}).

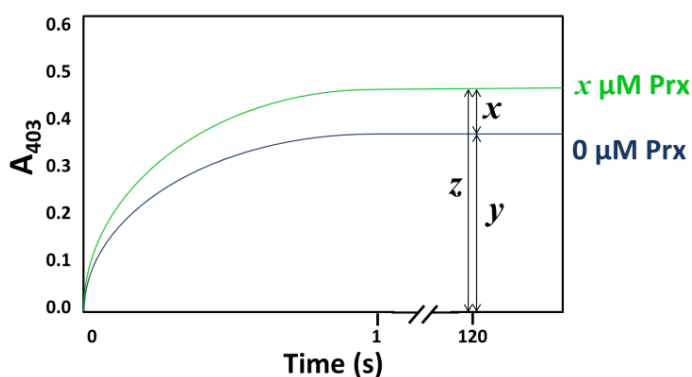


Figure 2.3: Calculation of HRP inhibition

The figure shows a representation of the change in absorbance at 403 nm when *HRP* and *Prx* react with H_2O_2 . The hyperbolic part of the reaction occurs over a very small timescale, and measurements at the arbitrary time point of 120 s were used for calculations. At this point the change in absorbance had stabilised.

$$F = x/z$$

Equation 2.7

$$1-F = y/z$$

Equation 2.8

The value of $\left(\frac{F}{1-F}\right)k_{HRP}[HRP]$ was calculated for each concentration of *HsPrx3* and plotted against the concentration. The slope of the graph yielded the relative activity of *HsPrx3* (k_{HsPrx3}) with the units $\text{M}^{-1}\text{s}^{-1}$.

2.7 References

- Aebi, W. and Pollard, T. D. (1987) A glow discharge unit to render electron microscope grids and other surfaces hydrophilic. *Journal of Electron Microscopy Techniques* **7**, 29-33
- Andrews, P. (1965) The gel-filtration behaviour of proteins related to their molecular weights over a wide range. *Biochemical Journal* **3**, 595-606
- Birnboim, H. C., Doly, J. (1979) A rapid alkaline extraction procedure for screening recombinant plasmid DNA. *Nucleic Acids Research* **7**, 1513–1523.
- Blommel, P. G. and Fox, B. G. (2007) A combined approach to improving large-scale production of tobacco etch virus protease. **55**, 53-68.
- Bykowski, T. and Stevenson, B. (2008) APPENDIX 4D aseptic technique *Current. Protocols in Microbiology* **11**, A.4D.1-A.4D.1
- Carrington, J. C. and Dougherty, W. G. (1988) A viral cleavage site cassette: Identification of amino acid sequences required for tobacco etch virus polyprotein processing. *Proceedings of the National Academy of Science of the United States of America* **85**, 3391-3395.
- Compton, L. A. and Johnson, W. C. Jr. (1986) Analysis of protein circular dichroism spectra for secondary structure using a simple matrix multiplication. *Analytical Biochemistry* **155**, 155-167.
- Dolman, D., Newell G. A., Thurlow, M. D. and Dunford, H. B., (1975) A study of the reaction of horseradish peroxidase with hydrogen peroxide. *Biochemistry* **53**, 495-501.
- Dougherty, W. G., Cary, S. M. and Parks, T. D. (1989) Molecular genetic analysis of a plant virus polyprotein cleavage site: a Model. *Microbiology* **171**, 356-364.
- Flavell, R. A., Sabo, D. L., Bandle, E. F. and Weissmann, C. (1975) Site-directed mutagenesis: effect of an extracistronic mutation on the in vitro propagation of bacteriophage Qbeta RNA. *Proceedings of the National Academy of Science of the United States of America* **72**, 367–371.
- GE Healthcare. (2005) *HiTrap IMAC FF instruction manual*.
- Good, N. E., Winget, G. D., Winter, W., Connolly, T. N., Izawa, S., Singh, R. M. M. (1966) Hydrogen ion buffers for biological research. *Biochemistry* **5**, 467–477.
- Hildebraunt, A. G. and Roots, I. (1975) Reduced nicotinamide adenine dinucleotide phosphate (NADPH)-dependent formation and breakdown of hydrogen peroxide during mixed function oxidation reactions in liver microsomes. *Archives of Biochemistry and Biophysics* **171**, 385-397.
- Inoue, H., Nojima, H. and Okayama, H. (1990) High efficiency transformation of *Escherichia coli* with plasmids. *Gene* **96**, 23-28

- Invitrogen. (2004) *OneShot® max efficiency DH5α® competent cells: manual*
- Jin, Y. and Manabe, T. (2005) Direct targeting of human plasma for matrix-assisted laser desorption/ionization and analysis of plasma proteins by time of flight-mass spectrometry. *Electrophoresis* **36**, 2823-2834.
- Kapust, R. B., Routzahn, K. M. and Waugh, D. S. (2002) Processive degradation of nascent polypeptides, triggered by tandem AGA codons, limits the accumulation of recombinant tobacco etch virus protease in *Escherichia coli* BL21(DE3) *Protein Expression and Purification* **24**, 61–70.
- Kingston, R. L., Baker, H. M. and Baker, E. N. (1994) Search designs for protein crystallization based on orthogonal arrays. *Acta Crystallographica Section D* **50**, 429-440.
- Konarev, P. V., Volkov, V. V., Sokolova, A. V., Koch M. H. J. and Svergun, D. I. (2003) PRIMUS: a Windows PC-based system for small-angle scattering data analysis. *Journal of Applied Crystallography* **36**, 1277-1282.
- Kozin, M. B. and Svergun, D. I. (2001) Automated matching of high- and low-resolution structural models. *Journal of Applied Crystallography* **34**, 33-41
- Kriminski, S., Caylor, C. L., Nonato, M. C., Finkelstein, K. D. and Thorne, R. E. (2002) Flash-cooling and annealing of protein crystals. *Acta Crystallographica Section D* **58**, 459-471.
- Lathe, G. H. and Ruthven, C. R. (1956) The separation of substances and estimation of their relative molecular sizes by the use of columns of starch in water. *Biochemical Journal* **62**, 665-674
- Li, F., Liu, S. L. and Mullins, J. I. (1999) Site-directed mutagenesis using uracil-containing double-stranded DNA templates and DpnI digestion. *Biotechniques* **27**, 734-738.
- Ludtke, S. J., Baldwin, P. R. and Chiu, W. (1999) EMAN: Semi-automated software for high-resolutions single-particle reconstructions. *Journal of Structural Biology* **128**, 82 – 97.
- Malvern. (2010) Typical protein applications for advanced analytical SEC: Viscotek application note.
- Mann, M., Hendrickson, R. C. and Pandey, A. (2001). Analysis of proteins and proteomes by mass spectrometry. *Annual Reviews in Biochemistry* **70**, 437–473.
- Novagen. (1999) *pET system manual*.
- Novagen. (2013) *Rosetta™(DE3)Competent Cells*.
- Petoukhov, M. V., Konarev, P. V., Kikhney A. G. and Svergun, D.I. (2007) ATSAS 2.1 - towards automated and web-supported small-angle scattering data analysis. *Journal of Applied Crystallography* **40**, s223-s228.
- Qiagen. (2012) *QIAGEN® plasmid purification handbook*

- Sanger, F. and Coulson, A. R. (1975) A rapid method for determining sequences in DNA by primed synthesis with DNA polymerase *Journal of Molecular Biology* **94**, 441–448.
- Shapiro, A. L., Viñuela, E., Maizel, J. V. Jr. (1967) Molecular weight estimation of polypeptide chains by electrophoresis in SDS-polyacrylamide gels. *Biochemical and Biophysical Research Communications* **28**, 815–820.
- Sreerama, N. and Woody, R.W. (2000) Estimation of protein secondary structure from CD spectra: Comparison of CONTIN, SELCON and CDSSTR methods with an expanded reference set. *Analytical Biochemistry* **287**, 252–260.
- Stratagene. (1998) *Quikchange site-directed mutagenesis kit: instruction manual*.
- Stratagene. (2005) *BL21-CodonPlus® Competent Cells: instruction manual*
- Studier, F. W. (2005) Protein expression by autoinduction in high density shaking cultures. *Protein Expression and Purification* **41**, 207–234
- Svergun D.I. (1992) Determination of the regularization parameter in indirect-transform methods using perceptual criteria. *Journal of Applied Crystallography* **25**, 495–503.
- Svergun D. I., Barberato C. and Koch M. H. J. (1995) CRY SOL - a program to evaluate X-ray solution scattering of biological macromolecules from atomic coordinates. *Journal of Applied Crystallography* **28**, 768–773.
- Svergun, D. I. (1999) Restoring low resolution structure of biological macromolecules from solution scattering using simulated annealing. *Biophysical Journal* **76**, 2879–2886.
- Svergun, D. I., Petoukhov, M. V. and Koch, M. H. J. (2001) Determination of domain structure of proteins from X-ray solution scattering. *Biophysical Journal* **80**, 2946–2953.
- Terpe, K. (2006) Overview of bacterial expression systems for heterologous protein production: from molecular and biochemical fundamentals to commercial systems. *Applied Microbiology and Biotechnology* **72**, 211–222.
- Thermo Fisher Scientific Inc. (2009) *NanoDrop 2000 UV-vis spectrophotometer c1.0 user manual*.
- Volkov, V. V. and Svergun, D. I. (2003) Uniqueness of *ab initio* shape determination in small-angle scattering. *Journal of Applied Crystallography*. **36**, 860–864.
- Whitmore, L. and Wallace, B. A., (2004) DICHROWEB, an online server for protein secondary structure analyses from circular dichroism spectroscopic data. *Nucleic Acids Research* **1**, 32.
- Winterbourn C. C. (1987) The ability of scavengers to distinguish OH[•] production in the iron-catalyzed Haber-Weiss reaction: comparison of four assays for OH[•] *Free Radical Biology and Medicine*. **3**, 33–39.

Chapter 3 *Mycobacterium tuberculosis* AhpE

3.1 Introduction

The quaternary structure of the 1-Cys Prx *MtAhpE* (section 1.4.2.1) has been described in solution studies (Hugo *et al.*, 2009; Li *et al.*, 2005), and the crystal structure (Li *et al.*, 2005). However, the octameric arrangement in the crystal has been suggested to be an artefact (Jönsson and Lowther in Flohé and Harris, 2007), and the molecular weight in solution had been misinterpreted (Dr S. Lott, University of Auckland, personal communication). A change in oligomeric state in response to redox conditions has been reported (Hugo *et al.*, 2009), but the stoichiometry of the complex had not been confirmed in solution. All studies to date have been carried out on his-tagged constructs of *MtAhpE*, which has been seen to affect the quaternary structure of Prxs (Cao *et al.*, 2011; section 4.3.1.3). The first part of this research focused on elucidating and characterising the oligomer in solution (section 3.4.1). The redox sensitivity was studied to allow comparison with typical 2-Cys Prxs, in order to gain insight into the important features that contribute to the “redox switch” mechanism.

The N-terminal tail has been suggested to be important in *MtAhpE* oligomerisation (Li *et al.*, 2005), therefore modifications to this region of the protein were explored to gain insight into its role in self-assembly (section 3.5). Further modifications to the native protein were studied to increase understanding of the unusually stable A-type interface (section 3.6). Four mutations were introduced to this interface to identify key residues.

As the dimer interface of *MtAhpE* is equivalent to the oligomer-building interface of typical 2-Cys Prxs, a comparative study of the two interfaces was of interest. This also suggested equivalent mutations to the A-type interface of hPrx3 in order to stabilise the toroid (chapter four).

3.2 Design and generation of *MtAhpE* interface mutations

The dimer interface of *MtAhpE* is a unique, highly stable example of the conserved Prx A-type interface (section 1.3.2.2). Comparison with the A-type interface of the typical 2-Cys Prx *BtPrx3* indicates that the interface architecture is conserved in *MtAhpE*, with no gross morphological differences (figure 3.1). The major difference is an additional small helix at the top of the *BtPrx3* interface. The increased stability must therefore be conferred through subtle sequential differences at the interface. The contribution of particular residues and possibility to disrupt the dimer interface was investigated by mutating predicted interacting residues to alanine.

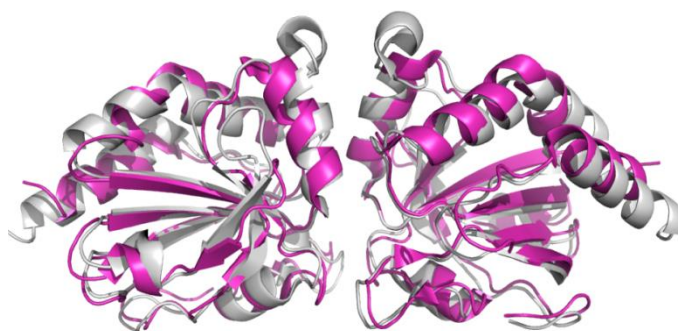


Figure 3.1: The A-type interfaces from *MtAhpE* and a typical Prx overlay well

The A-type interface of *MtAhpE* (magenta) and a typical 2-Cys Prx (*BtPrx3*) are structurally very similar. The lack of gross morphological differences suggests specific interactions contribute to the stability of the *MtAhpE* A-type interface.

3.2.1 Dimer interface analysis

The residues involved in the dimer interface were determined through analysis of the interface carried out using the PDBePISA online bioinformatics tool (Krissinel and Henrick, 2007), which predicts interactions by identifying the residues that become buried when two subunits come together and analysing the proximity and bonding

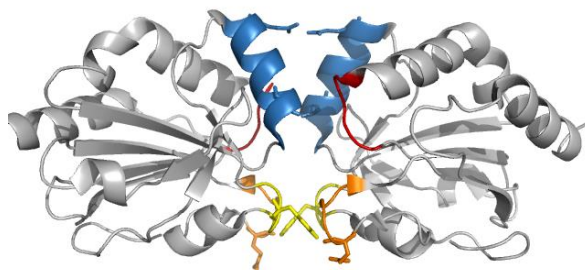
potential of these residues. 21 residues were identified as interfacing residues, comprised of 17 hydrophobic and four hydrophilic residues, of which 12 are more than 50 % buried by monomer association. Four H-bonds were suggested: between glutamine 83 (Q83) and its counterpart on the other apposing monomer; threonine 76 (T76) and its counterpart; and between tryptophan 95 (W95) of chain A and glutamic acid 109 (E109) of chain B (figure 3.2A). The interface is symmetric, with the fourth H-bond occurring between W95 of chain B and E109 of chain A. Pymol analysis (DeLano, 2002) of this dimer interface suggested that three of the predicted bonds were direct bonds, with the H-bond between T76 of each subunit being water-mediated (figure 3.2B; see also section 1.3.2.2).

The buried surface in the dimer interface is 730.8 \AA^2 , which makes a slightly larger interface with more interactions than that of a typical A-type interface – for example, *BtPrx3*, whose A-type interface buries 673.4 \AA^2 and contains three H-bonds. Previous studies attempting to disrupt the A-type interface of typical Prxs with single residue mutations have been successful (Parsonage *et al.*, 2005; Zhu, 2010 unpublished work), but the increased interfacing area and H-bonds of the *MtAhpE* interface suggested that multiple mutations may be necessary.

Only single mutations of residues not involved in the active site were introduced in order to identify the contribution of individual residues to interface stability, and to minimise the chance of affecting protein folding. The four bonding residues were therefore chosen as mutation candidates. Alanine scanning has been used in many studies to identify important “hotspots” in protein interfaces and to successfully disrupt interactions (the production of monomeric insulin is one example [Chen *et al.*, 2000]). Mutation to alanine is effectively a side chain deletion, as the H-bonding potential, charge, and steric properties of the residue are removed. Single residue alanine substitutions were therefore introduced to the A-type interface of *MtAhpE* at the positions of the four bonding residues.

A: Interfacing residues

PRO 65	PRO 65
LEU 66	LEU 66
ALA 67	ALA 67
PHE 68	PHE 68
THR 69	THR 69
SER 70	SER 70
VAL 71	VAL 71
GLY 72	GLY 72
PRO 73	PRO 73
PRO 74	PRO 74
PRO 75	PRO 75
THR 76	THR 76
HIS 77	HIS 77
LYS 78	LYS 78
ILE 79	ILE 79
TRP 80	TRP 80
ALA 81	ALA 81
THR 82	THR 82
GLN 83	GLN 83
SER 84	SER 84
GLY 85	GLY 85
PHE 86	PHE 86
THR 87	THR 87
PHE 88	PHE 88
PRO 89	PRO 89
LEU 90	LEU 90
LEU 91	LEU 91
SER 92	SER 92
ASP 93	ASP 93
PHE 94	PHE 94
TRP 95	TRP 95
PRO 96	PRO 96
HIS 97	HIS 97
GLY 98	GLY 98
ALA 99	ALA 99
VAL 100	VAL 100
SER 101	SER 101
GLN 102	GLN 102
ALA 103	ALA 103
TYR 104	TYR 104
GLY 105	GLY 105
VAL 106	VAL 106
PHE 107	PHE 107
ASN 108	ASN 108
GLU 109	GLU 109
GLN 110	GLN 110
ALA 111	ALA 111
GLY 112	GLY 112
ILE 113	ILE 113
ALA 114	ALA 114
ASN 115	ASN 115
ARG 116	ARG 116

B: Cartoon representation of dimer interface**Figure 3.2: Interactions at the *MtAhpE* interfaces**

A: PISA interface analysis suggested the presence of 3 H-bonds, which stabilise the interface. H-bonds are shown as black lines. **B:** located in the interface helix (helix $\alpha 4$ – see section 1.2.3.1). Bonding residues are shown with stick representation. In A and B region I is shown in red, region II is blue, region III is yellow, region IV is orange (section 1.2.4.2).

3.3 Purification of wildtype *MtAhpE*

3.3.1 Expression in an *E. coli* host

MtAhpE has been successfully expressed and purified as a soluble protein by several groups (Li *et al.*, 2005; Hugo *et al.*, 2009; Reyes *et al.*, 2011). The protocol put forward by Li *et al.* was used as an initial purification method and optimised. *E. coli* expression strains were transformed with the plasmid containing the Rv2238c gene encoding *MtAhpE* with an N-terminal his-tag and linker peptide (appendix 3). BL21 Rosetta (DE3) cells were used for protein expression as this strain contains a co-plasmid which complements the CCC rare proline codon (Looman *et al.*, 1987). Bacteria were cultured as described in section 2.2.2 and lysed using the cell press to avoid the heating caused by sonication (section 2.2.3). Expression trials indicated that optimum expression was achieved when induced cells were cultured at 20°C overnight (figure 3.3). These conditions were used for large scale expression. When cells were cultured above this temperature two dominant bands were seen when lysates were analysed by SDS-PAGE; a band at the expected size for the 19.9 kDa his-tagged *MtAhpE* construct, and a faster migrating band. This suggested a smaller species, thought to be a degradation product, as the protein was seen to be unstable even at room temperature (21°C). Trials indicated that at 20 and 18°C degradation was less prominent, and when large scale expression and chromatography steps were carried out in quick succession this species was eliminated (section 3.3.2). It is likely that the N-terminal tail and his-tag were degraded as this band could be removed by IMAC purification. A similar band was seen in one mutagen sample (section 3.6.3), which was confirmed by peptide sequencing to be a degradation product. It seemed likely that this was due to N-terminal degradation, making it likely that the low molecular weight band in wildtype samples was a similar product.

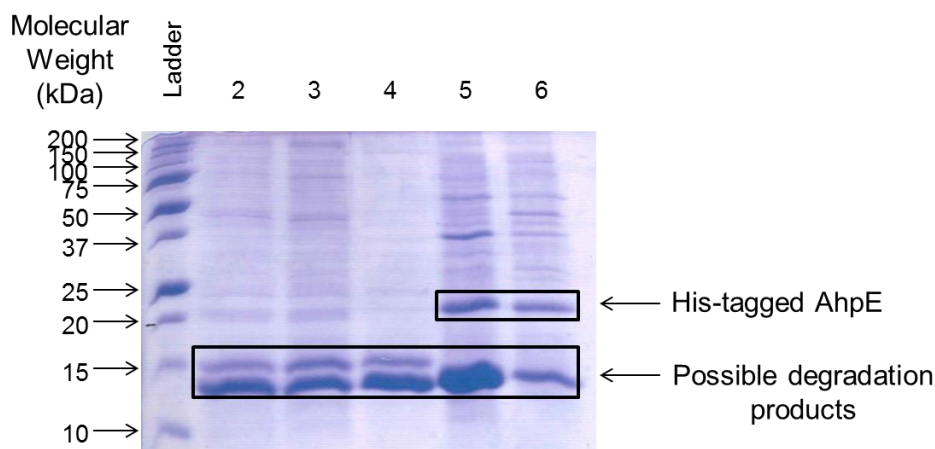


Figure 3.3: Expression trials indicated 20°C was the optimal growth temperature for expression of *MtAhpE*

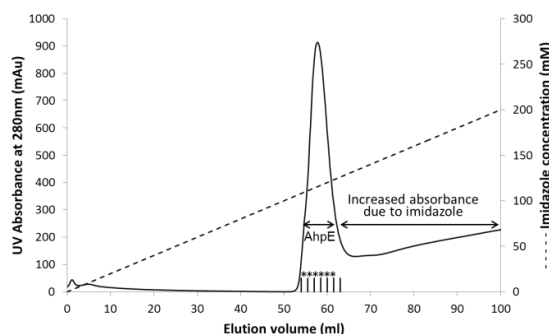
SDS-PAGE analysis of whole cell lysate of cultures incubated at: lane 2: 37°C for 4 hours; lane 3: 30°C for 6 hours; lane 4: 26°C for 8 hours; lane 5: 20°C overnight; lane 6: 18°C overnight after IPTG induction. The double band migrating at a distance below the 15 kDa marker indicates degradation. At 20 or 18°C full length *MtAhpE* was present and able to be purified. The box indicating *MtAhpE* shows the position that his-tagged *MtAhpE* migrated to on all subsequent gels.

3.3.2 IMAC purification

Filtered lysate was loaded manually onto a 5 mL HiTrap™ chelating column which had been charged and equilibrated as described in 2.2.4. The column was then washed with loading buffer (section 2.1.7) and protein eluted with buffers containing a gradient of 10 – 500 mM of imidazole. Wildtype *MtAhpE* bound successfully to the nickel resin, with very little protein being seen in the flowthrough or wash fractions. Desired protein eluted consistently as a single peak at an imidazole concentration of approximately 120 mM (figure 3.4A). 0.5 mL fractions were collected across the course of the elution and analysed by SDS-PAGE (figure 3.4B). A typical yield of 10 mg protein per 1 L culture was achieved after IMAC purification.

The monomeric unit of wildtype *MtAhpE* including the his-tag and linker residues has a molecular weight of 19.9 kDa (calculated using the ExPasy online bioinformatics tool; Gasteiger *et al.*, 2005; appendix 3). A major band that migrated equivalent to the 20 kDa marker of the protein ladder on SDS-PAGE analysis was observed in samples taken from fractions representing the single peak of the elution phase of IMAC (figure 3.4A) and assumed to be *MtAhpE*. Fractions that contained high concentrations of *MtAhpE* (lanes 5-10 of figure 3.4B) were pooled and concentrated (section 2.3.4).

A: IMAC elution profile



B: SDS-PAGE gel

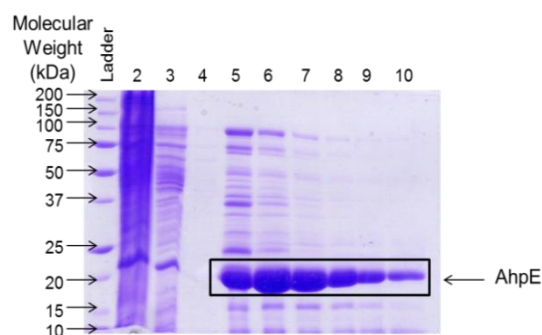


Figure 3.4: IMAC purification of wildtype *MtAhpE*

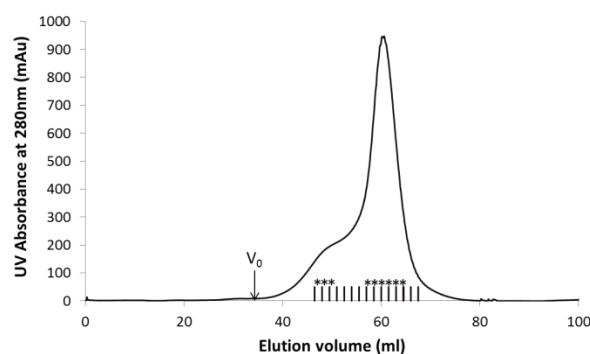
A: A representative chromatogram obtained from IMAC purification of *MtAhpE*. Typical loading volumes contained 20 mg his-tagged protein. **B:** A representative reducing SDS-PAGE gel of cell lysate and IMAC fractions of wildtype *MtAhpE*. *MtAhpE* was identified as the 20 kDa band indicated. The following preparations from the course of purification were loaded: lane 2: crude cell extract; 3: soluble fraction after lysis and centrifugation; lane 4: IMAC flowthrough; 5-10: fractions across the main peak, as indicated with stars on the chromatogram.

3.3.3 Gel filtration chromatography

Considerable impurities remained after IMAC purification. Therefore further purification using size exclusion chromatography (section 2.3.2.3) and elution with gel filtration buffer (section 2.1.8.2) was always performed. This also exchanged the sample into a buffer which was compatible with further experiments and for storage (section

2.1.8.2). Typically, a single major peak at an elution volume of about 90 mL was seen, with a shoulder indicating a higher weight species at around 75 mL (figure 3.5A). Fractions of both the major peak and the shoulder peak ran as a single band at around 20 kDa on SDS-PAGE (figure 3.5B). The gels revealed good levels of purity with very little contaminating protein, consistent with both peaks being *MtAhpE* and suggesting an equilibrium of oligomers in solution. Fractions were collected from regions of the peaks indicated to contain over 0.5 mg/mL total protein concentration (section 2.4.2), and the purity checked by SDS-PAGE. These fractions were pooled and concentrated as described above (section 3.3.2). MS analysis of the purified protein (section 2.4.4) gave a molecular weight of 19.83 kDa, confirming the protein to be his-tagged *MtAhpE*. From a typical run, the yield of pure *MtAhpE* was 60% of the protein loaded.

A: Gel filtration elution profile



B: SDS-PAGE of peak fractions

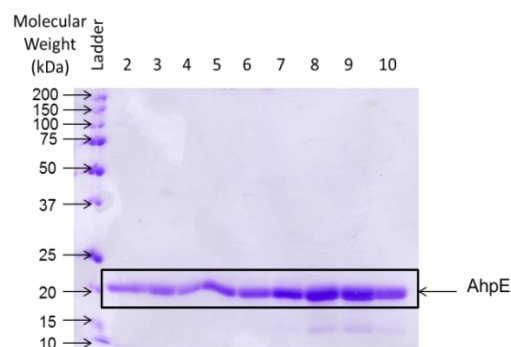


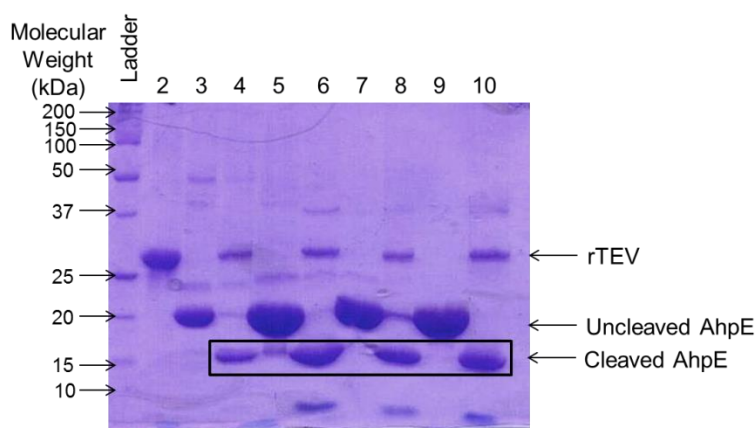
Figure 3.5: Gel filtration resulted in homogeneous samples of *MtAhpE*

A: A representative chromatogram obtained from gel filtration purification of *MtAhpE*. 1 mL volumes of IMAC preparations were loaded, typically containing 10 mg of protein. **B:** A representative reducing SDS-PAGE gel showing gel filtration purification of wildtype *MtAhpE*; lanes 2-4: selected fractions across the small peak seen at 75 mL; lanes 5-10: selected fractions across the major peak eluting at 90 mL, as indicated on the chromatogram. Occasionally small amounts of degradation products were seen (as in lanes 8-10). If these persisted after a second gel filtration step the sample was discarded.

3.3.4 His-tag removal by rTEV protease

For experiments with native protein the fusion tag first had to be removed, which was achieved using recombinant tobacco etch virus protease (rTEV). This left just two residues of the peptide linker (see appendix 3). After trialing several conditions (figure 3.6), cleavage was carried out by incubating *MtAhpE* with rTEV at a ratio of 1:20 *MtAhpE* rTEV at 4°C overnight – this was chosen to maximise cleavage as the *MtAhpE* was unstable at room temperature (Lott, personal communication; section 3.3.1), while rTEV is effective at a range of temperatures and incubation times (see section 2.3.4.2; figure 3.6). Following his-tag removal the cleaved product was purified through IMAC to remove tags, rTEV and uncleaved protein.

A: rTEV cleavage in various conditions



B: Final sample purity

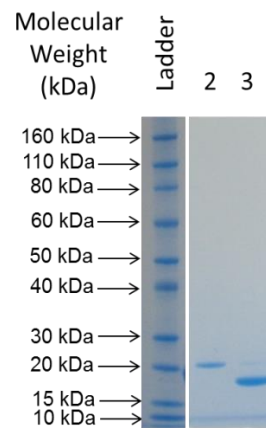


Figure 3.6: rTEV cleavage of *MtAhpE* was successful in number of conditions

A: A range of conditions were tested to optimise rTEV cleavage. The gel shows a representative group of conditions: Lane 2: rTEV alone; lanes 2,5,7 and 9: *MtAhpE* before cleavage; lanes 4, 6, 8 and 10: incubation mix after 6 hours at 21°C (1:20 *MtAhpE* : rTEV), 1 hour at 37°C (1:20 *MtAhpE* : rTEV), 6 hours at 4°C (1:20 *MtAhpE* : rTEV), overnight at 4°C (1:20 *MtAhpE* : rTEV) respectively. **B:** SDS-PAGE gel of purified *MtAhpE* protein at 1 mg/mL, as used in further experiments. Lane 2 shows his-tagged protein; lane 3 shows cleaved protein.

3.4 Characterisation of wildtype *MtAhpE*

3.4.1 Quaternary structure

3.4.1.1 PAGE analysis

Native-PAGE was used to investigate how physically homogeneous the sample was, and indicate the size and proportions of oligomers in solution. This technique separates species on their charge and hydrodynamic radius as well as the molecular mass, and has the advantage over SDS-PAGE that samples are not denatured and native assemblies are maintained (Walker, 2002). Initial analysis was carried out using non-denaturing native-PAGE electrophoresis (section 2.4.3.1) which appeared to show the presence of some oligomers (data not shown), but did not give a clear molecular weight distribution. The inconclusive results meant it was decided not to further pursue native-PAGE analysis.

Secondly, the effect of redox conditions on the oligomeric state of the protein was analysed. Despite only containing one cysteine residue, it has been suggested that *MtAhpE* monomers are able to form disulfide bonds (Hugo *et al.*, 2009). To test this possibility, samples of *MtAhpE* were incubated in either non-reducing, reducing or hyperoxidising conditions (2 mM TCEP or 10 mM H₂O₂ were added to the buffer for reducing and hyperoxidising conditions respectively) to determine if higher molecular weight covalent species were formed. It was predicted that the protein would be mostly oxidised in non-reducing conditions due to atmospheric oxygen, and could form a disulfide bond. Following incubation samples were subjected to both reducing and non-reducing SDS-PAGE.

After incubation in reducing conditions, wildtype *MtAhpE* migrated as a single major band at a distance equivalent to the 20 kDa marker on a non-reducing SDS-PAGE gel (figure 3.7A). When incubated in non-reducing conditions prior to electrophoresis a second, higher weight band was seen. This band represented a ~50 kDa species, slightly

higher than that expected for a dimer, with a number of higher weight bands indicating the presence of larger oligomers. The band intensities suggested that around 50% of the monomers present did not form disulfide bonds. Although MS analysis of gel slices was not possible at the time of experiment, this would be useful to confirm the oxidation state of the protein.

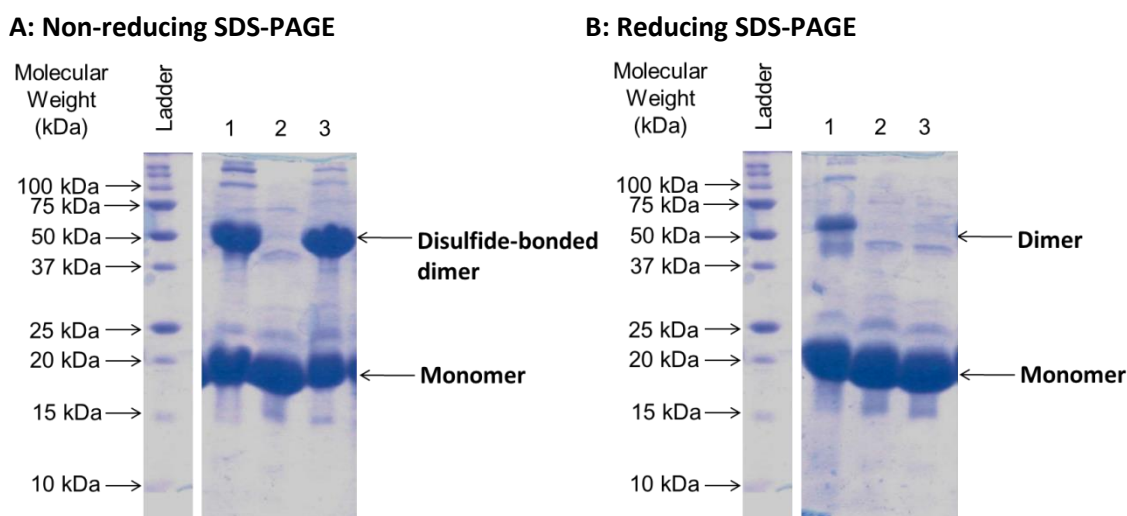


Figure 3.7: SDS-PAGE analysis of (1) hyperoxidised, (2) reduced and (3) non-reduced *MtAhpE* showed the presence of dimers

A: Non-reducing SDS-PAGE revealed the existence of SDS-resistant dimers in the case of hyperoxidised and non-reduced *MtAhpE*, although only about 50 % of the total protein existed in this state. Reduced protein was unable to form stable dimers. **B:** Reducing SDS-PAGE confirmed that the dimers seen in the non-reduced sample were due to disulfide bond formation. A significant amount of hyperoxidised *MtAhpE* still migrated as a dimer.

Hyperoxidised *MtAhpE* also showed dimers, along with a number of larger oligomers. When in the sulfenic or sulfonic acid state, disulfide bonds are not able to form (Wood *et al.*, 2003a), so these SDS-resistant complexes are likely due to the formation of strong hydrophobic interactions or non-disulfide cross-links. These bands were seen irrespective of whether or not the sample was heated after addition of SDS, indicating that they are not due to amide cross-linking. It is possible that these complexes were

formed through oxidative cross-linking of tyrosine residues. This has been seen to occur in the case of some proteins when incubated with a peracid and metal ions (for example, Gill *et al.*, 1997). It is possible that nickel ions remaining after IMAC purification could allow this tyrosine cross-link to form.

When run on reducing SDS-PAGE, the dimer was only seen in hyperoxidising conditions, confirming that the dimer of the non-reduced sample was disulfide bonded (figure 3.7B). Bands indicating higher weight species of the hyperoxidised sample also persisted in these conditions. This confirms that the interactions are strong non-covalent bonds. The reduction in intensity suggests that although hyperoxidation is only reversible *in vivo* by sulfiredoxin (section 1.2.5.1; Woo *et al.*, 2003; Biteau *et al.*, 2003), chemical reductants used *in vitro* may be able to reduce this state. Hyperoxidation is not thought to be a feature of 1-Cys Prxs (Wood *et al.*, 2003b; Koo *et al.*, 2002). The observation that a band of equal intensity representing the monomer was seen in hyperoxidised samples suggests that it may not be a response that occurs readily in MtAhpE, and therefore may not be physiologically relevant.

3.4.1.2 Protein-protein cross-linking experiments

Cross-linking experiments have been used to assess the oligomeric state of other Prxs (for example, Gourlay *et al.*, 2003) and were therefore trialled as an analytical step for identifying the oligomeric state of MtAhpE in solution (section 2.1.6). The presence of lysine residues in the regions involved in dimerisation and oligomerisation (Li *et al.*, 2005) mean that associated monomers in solution will be chemically linked after incubation with glutaraldehyde. Cross-linking was carried out in non-reducing conditions (section 2.4.3.3), and samples were analysed by SDS-PAGE (figure 3.8). Glutaraldehyde is a commonly used protein cross-linking reagent, and although non-specific will fix lysine residues within just 4.8 Å under the conditions of this experiment (alkaline HEPES buffer; Wine *et al.*, 2007). Cross-linking was carried out at a range of

protein concentrations to indicate whether the oligomeric state of *MtAhpE* is concentration dependent.

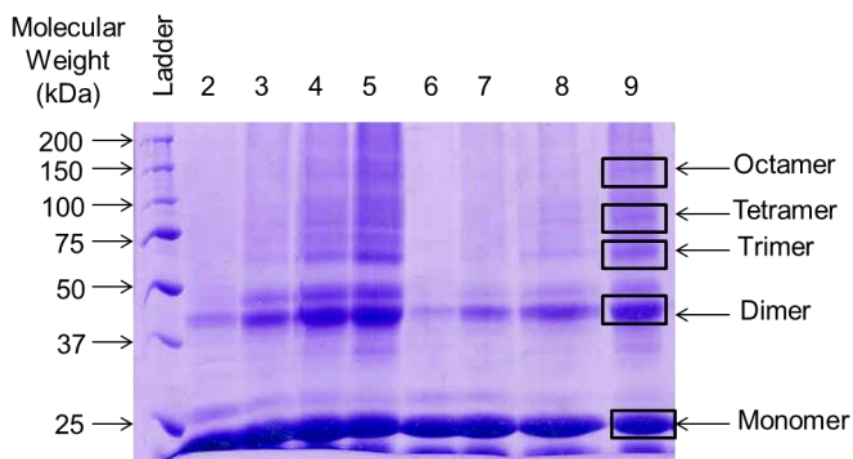


Figure 3.8: SDS-PAGE analysis of cross-linked wildtype *MtAhpE* suggests the presence of oligomers in solution

A representative SDS-PAGE gel showing migration of samples previously cross-linked with glutaraldehyde. Lanes 2-5: Protein concentration of 10 mg/mL cross-linked for 5 minutes, 15 minutes, 1 hour, 3 hours; Lanes 6-9 Protein concentration of 5 mg/mL cross-linked for 5 minutes, 15 minutes, 1 hour, 3 hours.

Cross-linked *MtAhpE* migrated primarily as two bands, corresponding to 20kDa and 40kDa, suggesting the presence of a monomeric and a dimeric species. Higher weight bands were also seen, indicating the presence of larger oligomers including trimers and tetramers. At higher protein concentrations the increased staining and smearing indicates non-specific cross-linking is occurring. Whilst cross-linking is useful for indicating a trend, a more specific cross-linking agent would be necessary to draw firm conclusions about monomer interactions with this technique.

3.4.1.3 Analytical size-exclusion chromatography

Solution studies were carried out to further probe the oligomeric state and build a clearer picture of *MtAhpE* self-assembly. Samples of purified *MtAhpE* were loaded onto the column at a concentration of 1 mg/mL. In non-reducing conditions, wildtype *MtAhpE* ran as two main peaks with near baseline separation (figure 3.9A). The protein eluted as a small peak corresponding to a 32 kDa species, and a larger peak corresponding to a 274 kDa species (calculated as described in section 2.5.3). The smaller species is consistent with a dimer, but the larger species does not fit with the expected weight of an octamer (135 kDa), instead in line with two associated octamers. A small early eluting peak was also seen; however, the propensity of *MtAhpE* to aggregate and the position of this peak close to the void volume suggest that it was due to aggregation.

In reducing conditions the elution profile of *MtAhpE* was dramatically changed (figure 3.9B). The protein eluted as one main peak, at a volume equivalent to the dimer seen in non-reducing conditions. Calculations suggested a species of 29 kDa. No oligomer peak was seen in these conditions, although the dimer peak did display a shoulder on the leading edge. This shoulder was not well resolved, but had an elution volume which corresponded to a 76 kDa species, indicative of a tetramer. These results confirm that *MtAhpE* is a unique example of a 1-Cys Prx which forms redox sensitive oligomers. The redox switch is similar to that seen in typical examples of 2-Cys Prxs; however, the switch is reversed with oligomers forming in oxidising rather than reducing conditions, which is seen for typical Prxs (Wood *et al.*, 2003a; section 1.2.4).

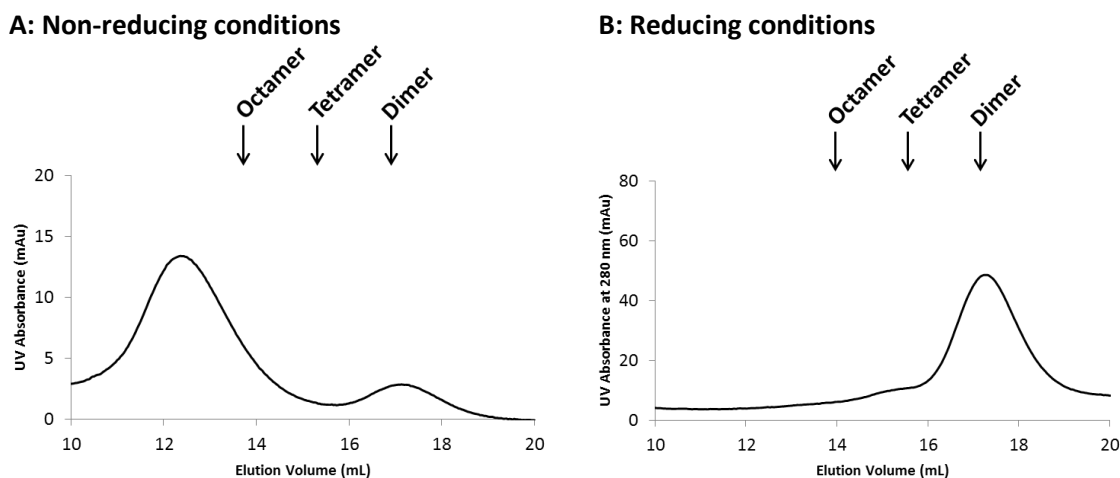


Figure 3.9: Analytical SEC indicated the redox sensitivity of wildtype *MtAhpE*

A: In non-reducing conditions *MtAhpE* consistently eluted as a small peak indicating a dimeric species, and a large main peak. These corresponded to molecular masses of 32 and 274 kDa respectively. **B:** In reducing conditions *MtAhpE* eluted as a single peak corresponding to a 27 kDa species, with a shoulder possibly indicating the presence of a tetramer. Traces are shown from 10 mL for clarity as peaks earlier than this volume represented aggregates.

3.4.1.4 Small angle X-ray scattering

SAXS experiments were carried out at the Australian Synchrotron (section 2.3.5.8), and were used to provide information relating to the protein in free solution, removing potential matrix interactions which can occur during chromatography, and to improve the accuracy of molecular weight calculations. As *MtAhpE* was prone to aggregation, data were collected from samples as they eluted from a size exclusion chromatography column, which was routed directly through the capillary (section 2.3.5.8). Samples were injected at 10 mg/mL, allowing for dilution on the column of about tenfold (section 2.3.5.8) for sample analysis at ~1mg/mL. SAXS was not carried out in reducing conditions as the tendency for aggregation made data acquisition not possible.

In non-reducing conditions, SAXS data appeared to contradict SEC results somewhat. Molecular weight calculations (Konarev *et al.*, 2003; section 2.5.5.2) gave a value of 31 kDa, consistent with a dimer. The R_G calculated from the Guinier region and GNOM

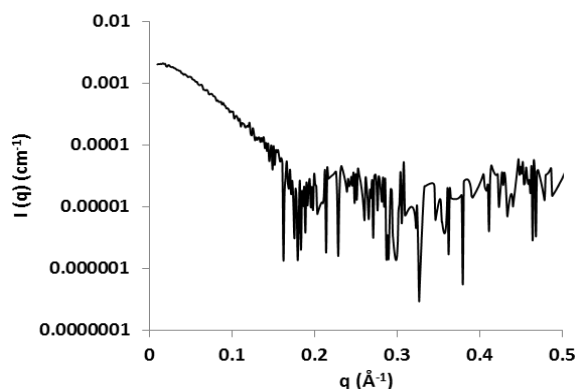
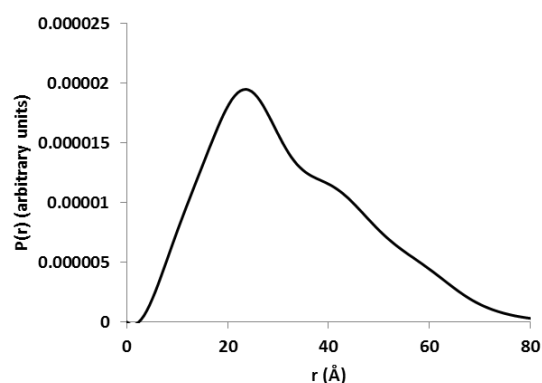
plot agree well at 27.3 and 27.5 nm respectively. Although this value is larger than the theoretical R_G calculated from the crystal structure, 60 residues of the dimer were not able to be modelled (Li *et al.*, 2005), which could account for this difference. D_{\max} was calculated to be 80 nm, in line with the expected size of a dimer (82.7 nm; table 3.1). The scattering profile (figure 3.10A) showed a smooth curve with no oscillations, indicative of a spherical particle (Mertens and Svergun, 2010). The pairwise distance distribution function ($P(r)$) plot showed a bell shaped curve (figure 3.10B), again suggesting a spherical particle (Svergun and Koch, 2003). The curve is negatively skewed, with an indication of a second maximum. This suggests an elongated, dumbbell shaped particle, consistent with the A-type dimer.

Scattering profiles were compared to theoretical profiles generated from crystal structures of a dimeric and octameric species (generated from the PDB file, accession number 1XXU, Li *et al.*, 2005). Experimental data showed good agreement with the theoretical scattering for a dimer (figure 3.11A), but significant misalignment with that for an octameric toroid (figure 3.11B), suggesting that an octameric arrangement was not present in the samples of *MtAhpE* analysed.

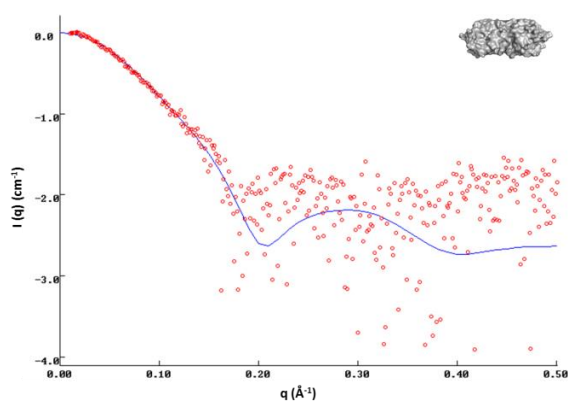
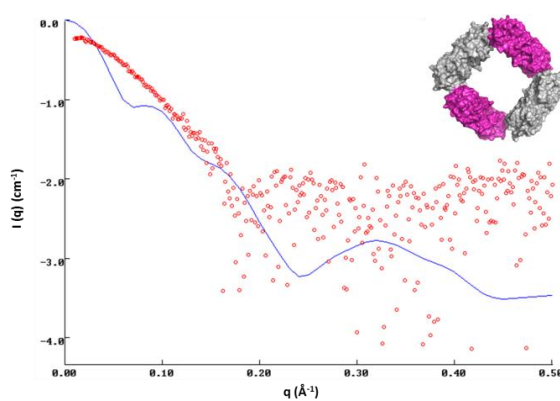
Table 3.1: Particle dimensions suggest that *MtAhpE* exists primarily as a dimer

Comparison of the experimentally derived values are in line with that expected for a dimeric species.

	D_{\max} (Å)	R_G from Guinier (Å)	R_G from GNOM (Å)	MW (kDa)
Untagged <i>MtAhpE</i> non-reduced	80	27.3	27.5	31
Theoretical dimer	~ 83	Theoretical R_G : 23		34
Theoretical tetramer	~ 90	Theoretical R_G : 27		68
Theoretical octamer	~ 130	Theoretical R_G : 42		135

A: Scattering profile**B: $P(r)$ plot****Figure 3.10: X-ray scattering data of *MtAhpE* in non-reducing conditions suggest a spherical particle**

A: The scattering profile showed a smooth curve, indicative of a spherical, globular particle. **B:** The $P(r)$ plot shows one maximum, typical of a spherical particle.

A: Fitted to theoretical dimer scattering**B: Fitted to theoretical octamer scattering****Figure 3.11: Comparison to theoretical scattering patterns suggested a dimeric species**

A: Overlaying the experimental scattering of non-reduced *MtAhpE* samples with that predicted from the crystal structure of a dimeric species gave a good fit, with a χ^2 value of 0.47. **B:** When overlaid with theoretical scattering produced from an octameric species, the traces were clearly misaligned, with a χ^2 value of 1.7, suggesting that this arrangement was not present in experimental samples.

3.4.1.5 Transmission electron microscopy

Electron microscopy has been successful in visualising the toroidal structures of other Prxs (for example, Harris *et al.*, 2001), and also revealed higher order structures including intricate cages and concatenated rings (Meissner *et al.*, 2007; Cao *et al.*, 2005; section 1.2.5.3). This technique was used to examine the morphology of the *MtAhpE* assemblies. Initial TEM imaging of negatively stained wildtype *MtAhpE* showed the presence of ring structures (figure 3.12). A 1-Cys Prx from *Plasmodium yoelii* (*PyTrx-Px1*) was suggested to form octameric oligomers (Qiu *et al.*, 2012); however, the formation of these toroidal oligomers was recently shown to be an artefact which arises due to the N-terminal modifications of the *PyTrx-Px1* protein (Gretes and Karplus, 2013). This study therefore presents the first 1-Cys Prx to be seen to form the rings characteristic of the Prx family in solution. Measurement from the micrographs using ImageJ software showed the rings to be around 7 nm in diameter; significantly smaller than the 15 nm toroid of a typical Prx, and smaller than the 10 nm diameter ring that is suggested from the crystal structure of *MtAhpE* (Li *et al.*, 2005). Grid interactions or stain artefacts could cause this apparent compression of the ring.

An interesting feature of the micrographs was the presence of higher order structures. A number of micrographs revealed spherical objects which appeared to be clusters of rings (figure 3.12). The clusters were heterogeneous, ranging from 6 to 22 nm in diameter, which provides some explanation for the inconsistency of SEC results. The presence of clusters across a number of TEM grids indicates that they are not artefacts, which is supported by very similar observations by other groups (Jang *et al.*, 2004). The tendency for aggregation and heterogeneity of *MtAhpE* samples prevented further investigation of these assemblies and image processing; however, later studies revealed the presence of similar assemblies in samples of mutated *HsPrx3* (described in chapter 5).

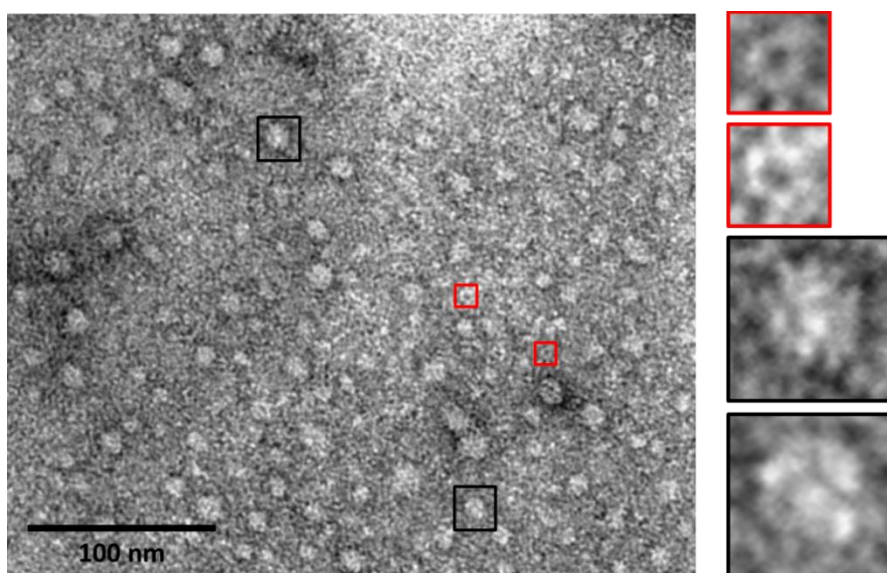


Figure 3.12: A typical TEM micrograph show toroidal oligomers and HMW clusters of *MtAhpE*

TEM revealed the presence of toroids (highlighted with red boxes and enlarged), along with apparent clusters of protein (highlighted with black boxes and enlarged).

3.5 The effect of N-terminal modifications

Crystal packing data of *MtAhpE* suggests that the N-terminal tail may be involved in the interactions that stabilise the oligomer building interface (section 1.4.2.3; figure 3.13; Li *et al.*, 2005). Modifications to this tail were predicted to influence the self-assembly of the dimers, and so were investigated to gain insight into the mechanism behind *MtAhpE* oligomer formation. Leaving the additional residues that form the his-tag and linker attached was studied, which added an additional 21 residues to the tail of the protein.

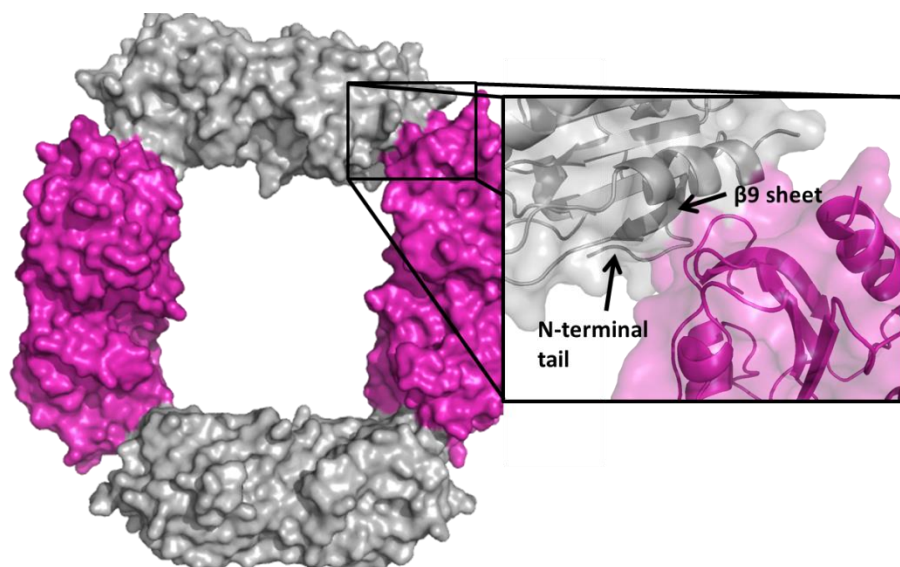


Figure 3.13: The octamer building interface is composed of loop interactions

The crystal structure indicates that the putative B-type interface of *MtAhpE* is small, burying 470 Å² per monomer, and made of interactions between loop regions. The N-terminal tail is suggested to contribute to the interface, and makes significant bonds to the β9 sheet.

3.5.1 Analytical size-exclusion chromatography

In reducing conditions his-tagged *MtAhpE* eluted as a single peak (figure 3.14A), calculated to represent a species of 74 kDa, in line with the tetrameric species seen in the untagged sample. An early eluting shoulder was observed, with an elution volume that was calculated to represent a 156 kDa species. This agrees well with the 159 kDa expected for an octameric species. In non-reducing conditions, the elution profile of the his-tagged protein was unchanged from that seen in reducing conditions (figure 3.14B). These results suggest that the presence of the his-tag has a considerable impact on *MtAhpE* self-assembly. The formation of higher order structures was prevented, with a tetrameric assembly favoured. The presence of an octameric species agrees with previously published results, which were obtained from tagged samples (Li *et al.*, 2005).

The absence of this arrangement in untagged samples may suggest that it is in fact an artefact of the affinity tag.

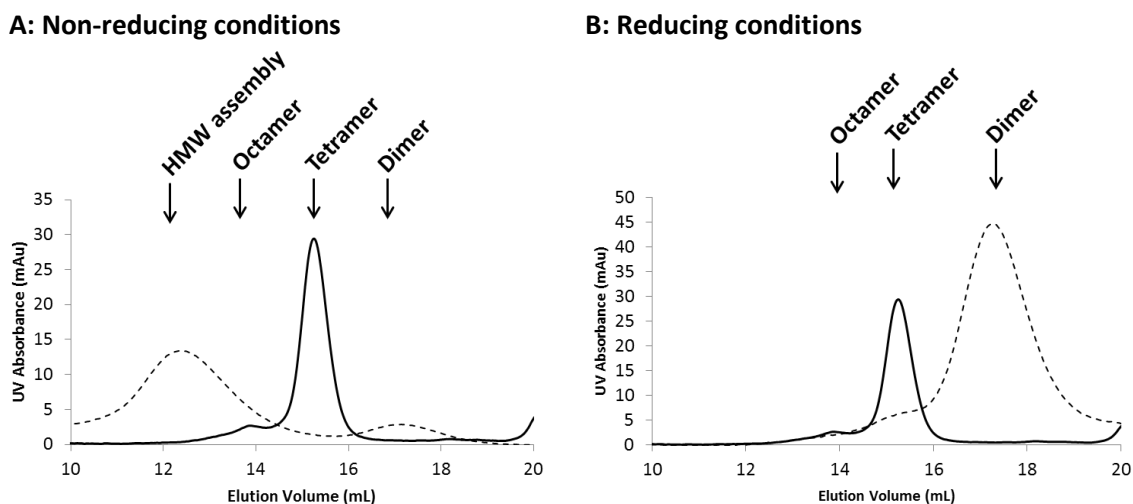


Figure 3.14: His-tagged *MtAhpE* is insensitive to redox conditions

A: The elution profile of his-tagged *MtAhpE* in non-reducing conditions showed a single peak, which corresponded to a 74 kDa species. A small shoulder was seen, at a volume suggesting a 156 kDa species. **B:** The elution profile was unchanged upon the addition of reducing agent. The elution profiles of untagged *MtAhpE* in equivalent conditions is shown as a dashed line for comparison (data as in figure 3.10). Elution profiles are shown from 10 – 20 mL for clarity, as earlier eluting species were aggregates.

3.5.2 Small angle X-ray scattering

In non-reducing conditions, the molecular weight calculated from scattering data was 37 kDa (see table 3.2). R_G calculated from both the Guinier region and GNOM program (Svergun *et al.*, 1992) agreed well, giving values of 27.6 and 28 Å respectively. A total of 109 residues are missing in the crystal structure of the his-tagged dimer, which could explain the increased R_G compared to theoretical values. D_{\max} was calculated to be 82.5

Å. All calculations were consistent with a dimer, with the presence of higher weight structures not apparent. In reducing conditions the his-tagged construct gave very similar results to those recorded in non-reducing conditions (table 3.2).

Table 3.2: Particle dimensions suggest that his-tagged *MtAhpE* exists primarily as a dimer

Comparison of the experimentally derived dimensions agree very well with that expected for a dimeric species.

	D_{\max} (Å)	R_G from Guinier (Å)	R_G from GNOM (Å)	MW (kDa)
Tagged <i>MtAhpE</i>				
Reduced	84	26	27	36
Non-reduced	82.5	27.6	28	37
Tagged dimer	~ 83	Theoretical R_G : 23		40
Tagged tetramer	~ 90	Theoretical R_G : 27		80
Tagged octamer	~130	Theoretical R_G : 42		159

Overlaying the experimental scattering from his-tagged *MtAhpE* with theoretical scattering generated from the A-type dimer in the crystal structure (Li *et al.*, 2005) showed a fairly poor fit (Figure 3.15A). As the N-terminal tail is thought to be involved in the *MtAhpE* B-type interface, it was considered that the modification may have stabilised this interaction and a B-type dimer might be forming. The experimental scattering was therefore also overlaid with that predicted from the crystal structure of two monomers associated about the B-type interface (figure 3.15B). This showed a slightly better fit than to the A-type dimer, but still did not overlay well. The N-terminal linker and his-tag are not modelled in the crystal structure, which could account for the poor overlay with experimental scattering.

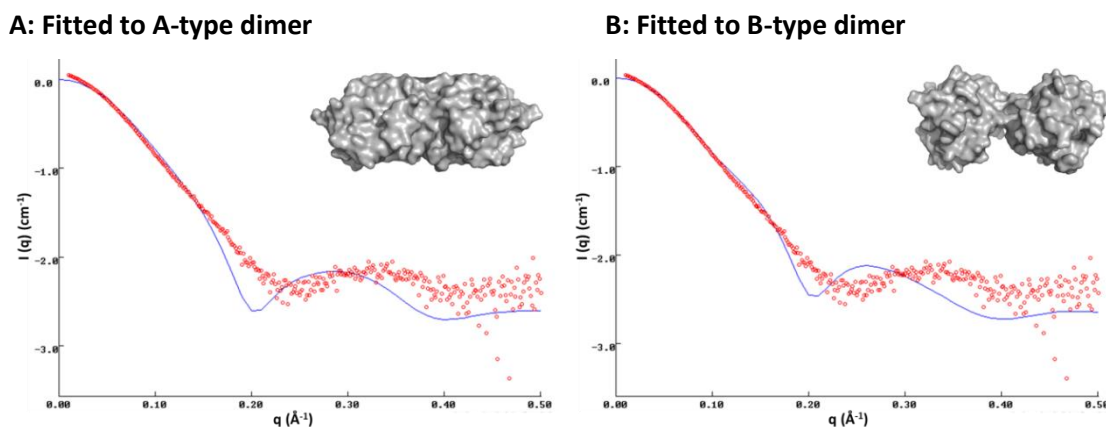


Figure 3.15: Comparison to theoretical scattering suggests the presence of a B-type dimer in non-reducing conditions

A: When overlaid to theoretical scattering generated from the crystal structure of an A-type dimer, the scattering profile of his-tagged *MtAhpE* did not align well, with a χ^2 value of 2.7. **B:** When overlaid with theoretical scattering generated from the putative *MtAhpE* B-type dimer in the crystal structure, the fit of the scattering profile was improved, with a χ^2 value of 1.6.

Taken together, these data are consistent with his-tagged *MtAhpE* existing as a dimer, which is unable to associate into higher order structures. Further studies would be useful to investigate the nature of this interface. Intrinsic fluorescence or fluorescence resonance energy transfer (FRET) experiments could be used to probe the associating regions (Huebsch and Mooney, 2007). It is unclear why the SAXS and SEC results suggest different oligomeric states for both the tagged and untagged sample. *MtAhpE* was found to be very unstable, and so it is possible that during transport to the synchrotron degradation occurred and affected the protein's behaviour. Similarly, exposure to ionising radiation can affect a protein's quaternary structure (for example, that of some protein kinases; Ahn *et al.*, 2002), and although X-ray doses were kept low this may have affected the structure of *MtAhpE*.

3.6 Generation of interface mutations

Mutagenesis of the wildtype gene was carried out using SDM. The double stranded, circular plasmid template was mutated using a commercial Quikchange™ kit from Stratagene (section 2.2.3).

3.6.1 Mutagenesis

3.6.1.1 Quikchange™ primer design

Primers were designed to substitute residues T76, Q83, W95 and E109 with alanine. Codon changes were designed to be as conservative as possible. The *Rv2238c* gene insert on the pProEx Hta vector (see appendix 3) was used as the template for primer design.

3.6.1.2 PCR generation of mutants

PCR reactions were carried out as detailed in section 2.2.2, the presence of amplified plasmid confirmed by gel electrophoresis and success of mutagenesis checked with sequencing (section 4.3.3). Initial reactions using the basic PCR protocol described in section 2.2.2 were found to be unsuccessful with the *Rv2238c* gene, and so a number of potential solutions were explored in an attempt to optimise the mutagenesis protocol, including annealing and extension temperature and time, polymerase choice and the concentration of magnesium ions. *M. tuberculosis* genes are known to be difficult to mutate, due in part to their high GC content (Cole *et al.*, 1998) which can lead to inadequate separation of the double stranded template, potential mispriming (Frey *et al.*, 2008), or secondary structure formation in the template or primers. The addition of chemical denaturants or adjuvants such as dimethyl sulfoxide (DMSO) or glycerol can

improve strand separation and specificity of the reaction (Varadaraj and Skinner, 1994; Winship *et al.*, 1989) and so were tested (table 3.3). Positive and negative controls were routinely run to ensure the fidelity of the enzymes and reagents, and confirm contamination was not occurring. Single-primer and mega-primer methods (section 2.2.3; Edelheit, 2009; Ke and Madison, 1997) were also utilised to try to achieve successful SDM.

Table 3.3: A number of factors were varied in attempts to optimise SDM

The steps of the PCR reaction that could fail and lead to unsuccessful mutagenesis are summarised below, along with the approaches taken to optimise the reaction.

Possible problem	Trialled solution	Reference
Incomplete strand separation	<ul style="list-style-type: none"> • Trialled a range of annealing temperatures from 45 – 70 °C • 5% DMSO was added to the reaction mixture 	<ul style="list-style-type: none"> • Mamedov <i>et al.</i>, 2008 • Sahdev <i>et al.</i>, 2007
Formation of secondary structures in primers	<ul style="list-style-type: none"> • Primers were re-checked for secondary structure propensity • 5% DMSO was added to the reaction mixture 	<ul style="list-style-type: none"> • Li <i>et al.</i>, 2010 • Sahdev <i>et al.</i>, 2007;
Formation of secondary structures in template	<ul style="list-style-type: none"> • Checked for their presence by agarose gel • 5% DMSO was added to the reaction mix • 5% glycerol was added to the reaction mix 	<ul style="list-style-type: none"> • Sahdev <i>et al.</i>, 2007 • Varadaraj and Skinner, 1994
Parental DNA persisting in transformation mix	<ul style="list-style-type: none"> • Varied DpnI digest time and temperature • Methylated parental DNA prior to PCR 	<ul style="list-style-type: none"> • Stratagene Quikchange™ manual • Betz, personal communication
Non-specific priming	<ul style="list-style-type: none"> • Trialled a range of MgCl₂ concentrations from 0.75 – 2 mM • Used a “hot-start” polymerase • Trialled a range of annealing temperatures • Used touchdown PCR • 5% glycerol/DMSO was added to the reaction mix 	<ul style="list-style-type: none"> • Roux, 2003 • Roux, 2003 • Li <i>et al.</i>, 2010 • Don <i>et al.</i>, 1991 • Pomp and Medrano, 1991

The Q83A mutation was successfully generated upon the addition of 5% DMSO into the reaction mixture. Presence of the alanine codon at position 83 was confirmed by gene sequencing, carried out by the Auckland Genomics facility. The other three mutations were not successful and so the mutated genes for these constructs were instead synthesised and purchased from GenScript.

3.6.2 Expression and purification of non-native proteins

Expression and purification was carried out as for wildtype protein (section 3.3). The T76A, W95A and E109A muteins bound successfully to the nickel resin, with very little protein being seen in the flowthrough or wash fractions, and a clear peak eluting from the IMAC column (figure 3.16). Although the trace often showed additional peaks suggesting the presence of contaminating proteins, the desired proteins were easily identifiable as discrete major peaks. The imidazole concentration at which they eluted varied, with T76A, W95A, and E109A eluting consistently at imidazole concentrations of approximately 200 mM, 500 mM and 1 M respectively. 0.5 mL fractions were collected across the course of the elution, and peak fractions analysed by SDS-PAGE (figure 3.17). Typical yields are shown in table 3.4. Following expression and lysis, no Q83A protein could be purified by IMAC, and analysis of the extraction steps revealed that the protein was insoluble. This is further discussed in section 3.6.

A major band that migrated at a distance equivalent to just lower than the 20 kDa marker of the protein ladder on SDS-PAGE analysis was seen in samples taken from fractions representing the single peak seen in the elution phase of IMAC (figures 3.16 and 3.17). MS of the purified samples confirmed the molecular weight to be correct; in the case of the E109A mutein shown here, MS analysis gave a monomer weight of 19.78 kDa compared with a theoretical weight of 19.87 kDa (section 2.4.4). Fractions that contained high concentrations of *MtAhpE* were pooled and concentrated.

Mutants were subjected to gel filtration, as for wildtype *MtAhpE* (section 2.2.4.1 and 3.3.3), and typically eluted with a similar profile to wildtype (figure 3.18). Fractions were collected across both peaks, and both ran as major bands at around 20 kDa on SDS-PAGE (figure 3.19).

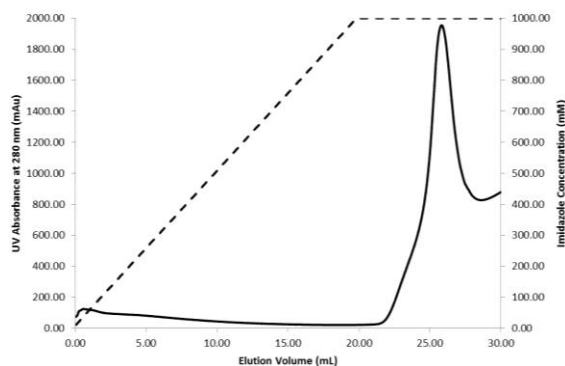
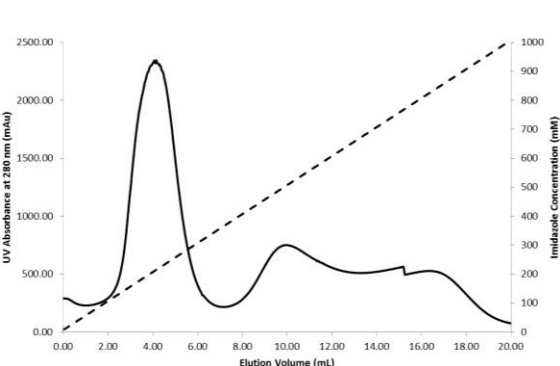
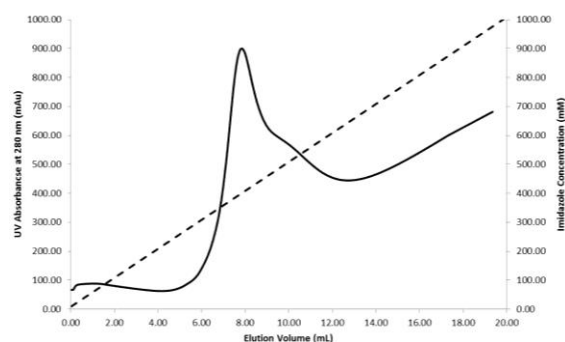
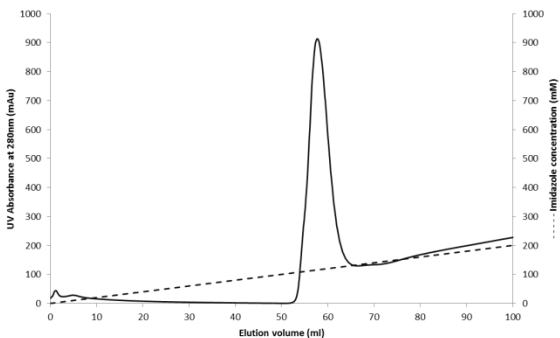
A: E109A**B: T76A****C: W95A****D: Wildtype**

Figure 3.16: Representative chromatograms obtained from IMAC purification

A: E109A; B: T76A and C: W95A mutant constructs of *MtAhpE*. The chromatogram obtained for wildtype *MtAhpE* is shown in **D** for comparison. Typical loading volumes would contain about 20 mg protein. The dashed line represents the 10 mM – 1 M imidazole gradient used to elute the protein.

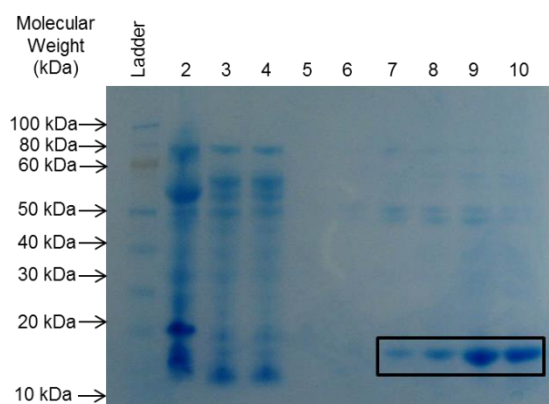


Figure 3.17: Representative SDS-PAGE gel of cell lysis and IMAC purification

Gel obtained from steps of E109A purification shows typical results. Lane 2: whole cell lysate; lane 3: soluble fraction; lane 4: insoluble fraction; lane 5: IMAC flowthrough; lanes 6-9: fractions across the peak seen in figure 3.16A. The mutein was identified as the band of approximately 18 kDa indicated by the black box. SDS-PAGE gels for the other mutated protein purifications can be found in appendix 3.

Both the major peak and the smaller shoulder peak of gel filtration purification ran as a single band at around 20 kDa on SDS-PAGE. The gels revealed good levels of purity with very little contaminating protein, and were consistent with both the major and shoulder peaks being due to UV absorbance of *MtAhpE* muteins. Fractions were collected and pooled as for wildtype, resulting in sufficiently pure preparations (figure 3.20).

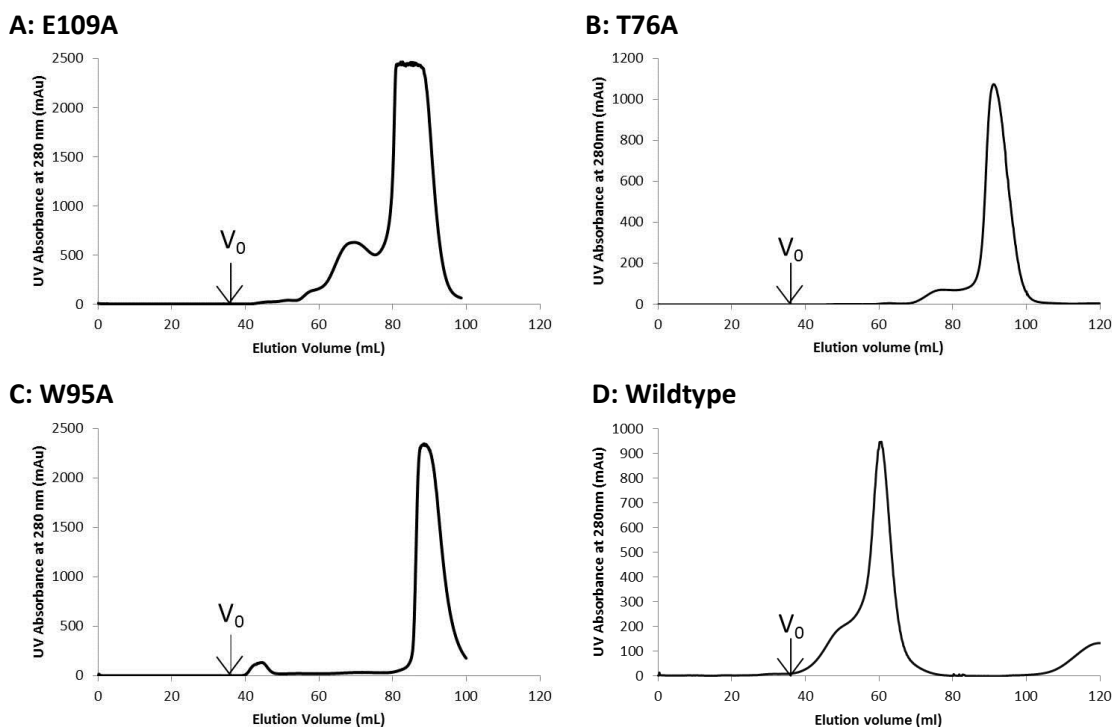


Figure 3.18: Representative chromatograms obtained from gel filtration purification of *MtAhpE* mutants

A: E109A; **B:** T76A; and **C:** W95A. The gel filtration elution profile of wildtype *MtAhpE* is shown in **D** for comparison. All mutants showed similar elution profiles with one major peak, and a shoulder peak in the case of the E109A and T76A constructs. SDS-PAGE analysis of the main and shoulder peaks confirmed them to represent *MtAhpE* mutants (figure 3.16; appendix 3).

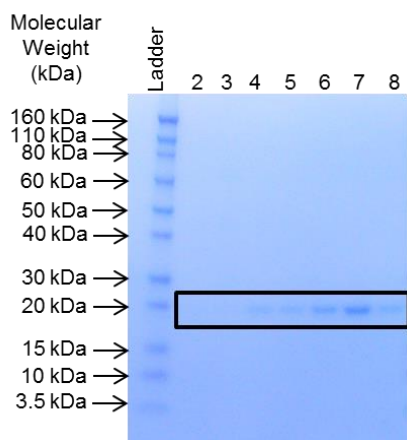


Figure 3.19: Representative reducing SDS-PAGE gels of gel filtration purification

Gel obtained from steps of E109A purification shows typical results. Lanes 2-4: fractions across the shoulder peak; lanes 5-8: fractions across the later eluting major peak seen in figure 3.15A. The mutant was identified as the band of approximately 19 kDa indicated by black box. SDS-PAGE gels for the other mutated protein purifications can be found in appendix 3.

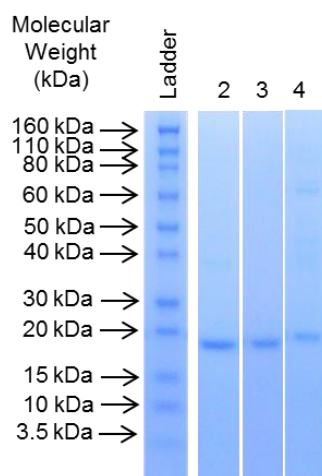


Figure 3.20: Two steps of chromatography resulted in highly pure mutein samples

SDS-PAGE analysis of mutein samples loaded at 1 mg/mL. Lane 1: E109A; lane 2: T76A and lane 4: W95A muteins.

Table 3.4: *MtAhpE* and muteins expressed at low levels

Although expression and purification of the wildtype protein and muteins was achieved to a high level of purity, the total amount of protein was low.

Construct	Pellet weight (g)	Mass of protein after IMAC (mg)	Mass of protein after gel filtration (mg; final yield)	Mass of protein per gram cells (mg)
Wildtype <i>MtAhpE</i>	3.9	9.6	6.6	1.7
E109A	4	9.8	3	0.75
T76A	3.6	6.2	1.7	0.47
W95A	3.6	8.3	2.6	0.72

3.6.3 Expression of the Q83A mutein

3.6.3.1 Q83A mutein was expressed following IPTG induction

Introduction of interface mutations often leads to insolubility of the corresponding protein, due to changes in tertiary structure, or more commonly, exposure of a large hydrophobic area which would normally be buried in the interface. This results in association of mutated proteins, forming insoluble aggregates (for example, attempts to disrupt the dimerization of the HIV-1 integrase enzyme resulted in insoluble protein for most of the mutations tried; Serrao *et al.*, 2012). No protein was able to be purified from the gene containing the Q83A mutation in the conditions used for wildtype purification. Transformation into BL21 Rosetta (DE3) competent cells (section 2.2.1.4) was successful, with antibiotic resistance confirming the uptake of the pProEx vector containing the mutated gene. Bacteria grew well in the conditions described in section 2.2.2, and addition of IPTG led to expression of the mutein, as determined by SDS-PAGE analysis of lysed samples which had been grown in standard conditions (figure 3.23A). The major band on the gel migrated at a distance equivalent to the 15 kDa marker (figure 3.21A), suggesting a monomer significantly smaller than the 19.9 kDa expected for the his-tagged construct. Samples of the whole cell lysate were taken at time points after IPTG induction and analysed by SDS-PAGE (figure 3.23B). The increase in the intensity of the band following induction indicated that it is expressed in response to IPTG so is likely the Q83A mutein.

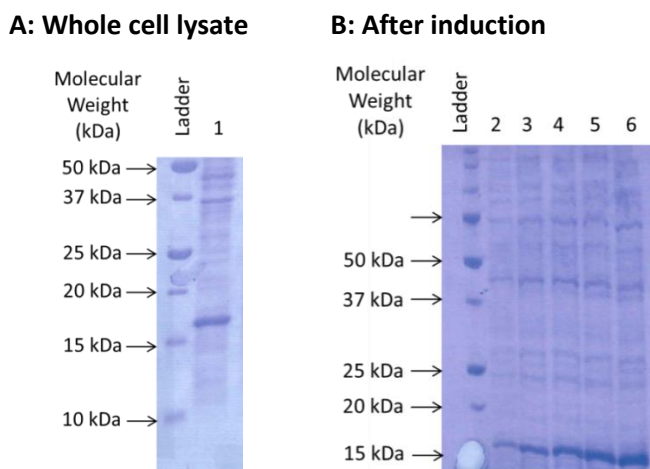


Figure 3.21: SDS-PAGE analysis suggested successful expression of the Q83A mutein

A: Analysis of the whole cell lysate grown at 20 °C overnight post induction revealed a major band around 16 kDa. **B:** SDS-PAGE analysis of whole cell lysate from cells 1 hour (lane 2), 2 hours (lane 3), 4 hours (lane 4), 6 hours (lane 5) and 12 hours (lane 6) after induction with 0.6 mM IPTG showed an increase in intensity of the band at 16 kDa.

3.6.3.2 Solubility screening of the Q83A mutein

Following expression and lysis, no protein could be purified by IMAC. Analysis of the extraction steps revealed that the protein had all remained in the insoluble fraction after cell lysis, which was confirmed by SDS-PAGE (figure 3.22). The Q83 interaction appears to stabilise the dimer by connecting the top of the alpha helices at the interface (figure 3.2B). This interaction is unique to *MtAhpE* and so could be important in creating the stable A-type interface. The insolubility of the construct appears to confirm the importance of this interaction, and possibly suggests that mutation has successfully disrupted the dimer interface. Disruption of this interface would lead to the exposure of a large hydrophobic area, which could result in aggregation and insolubility. The Q to A mutation would also increase the hydrophobicity of the region, further increasing the chance of aggregation.

In order to overcome the purification problems, solubility screens were carried out. Altering the growth media, induction time and temperature down to 10°C, and autoinduction (section 2.3.1.3) were not successful. The composition of the lysis buffer was then tested as summarised in tables 3.4 and 3.5.

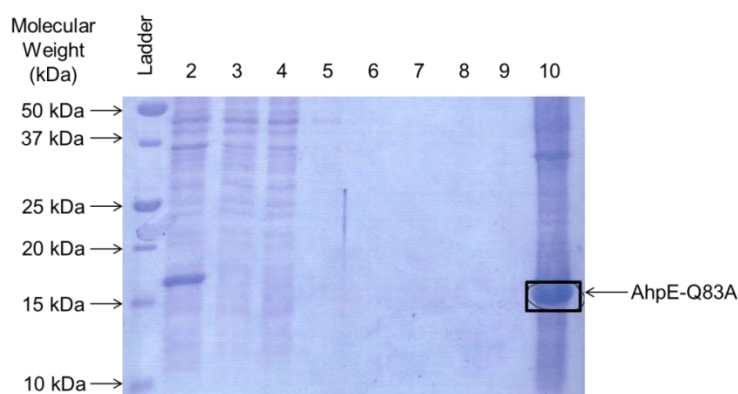


Figure 3.22: Q83A expression resulted in insoluble protein

A typical SDS-PAGE gel of Q83A expression trials. For small scale trials, IMAC purification was carried out using the batch method (section 2.3.2.1). Overexpression of Q83A was achieved, as indicated by the strong band in the whole cell lysate, but no mutein was seen in any fractions other than the insoluble fraction. Lane 2: whole cell lysate; lane 3: soluble fraction; lane 4: first IMAC flowthrough; lane 5: second IMAC flowthrough; lane 6: first IMAC wash; lane 7: second IMAC wash; lane 8: first IMAC elution; lane 9: second IMAC elution; lane 10: insoluble fraction.

Table 3.5: A number of variations to the lysis buffer were considered to optimise solubility

The alterations to buffer composition that were trialled are described below. The alterations have been seen to be successful for solubilising other proteins, often those that are highly insoluble such as membrane proteins.

Alteration to buffer composition	Rationale	Reference
Increased ionic strength	Salts shield electrostatic effects, and can prevent aggregation caused by exposure of acidic residues	Elcock and McCammon, 1998
Decreased ionic strength	Lower salt concentration is known to decrease the hydrophobic effect thus preventing the exclusion of water molecules from hydrophobic surfaces	Zhou, 2005
Nature of the ionic strength	Different ions can affect the solubility of a protein through their interaction with the protein	Hofmeister, 1888 Zhou, 2005
Inclusion of detergents	Non-ionic amphipathic detergents counteract the hydrophobic effect. Commonly used for membrane protein solubilisation with denaturation	Rosenow <i>et al.</i> , 2002
Inclusion of glycerol	Glycerol coats the surface of protein molecules, stabilising hydrophobic areas. It may also alter the volume of the protein which can aid solubility.	Vagenende, 2009 Farnum and Zukoski, 1999
Increased or decreased pH	Although mutation does not alter the pI of the protein, solvent-exposed residues may change. Altering the charges present on the protein surface through pH changes may increase solubility	Perry, 2009
Inclusion of reductant	The presence of cysteine residues in the sequence may lead to disulfide bond formation and aggregation	
Addition of L-amino acids	L-glutamic acid and L-arginine may mask surface charges or coat hydrophobic regions and are often used in crystallography to increase solubility	Golovanov <i>et al.</i> , 2004

Table 3.6: Lysis buffer compositions

The lysis buffers detailed below were trialled for small scale protein extraction.

Salt concentration screen
20 mM HEPES, 10 mM Imidazole, 50 mM NaCl , pH 8.0
20 mM HEPES, 10 mM Imidazole, 150 mM NaCl , pH 8.0
20 mM HEPES, 10 mM Imidazole, 250 mM NaCl , pH 8.0
20 mM HEPES, 10 mM Imidazole, 500 mM NaCl , pH 8.0
Detergent screen
20 mM HEPES , 10 mM Imidazole, 150 mM NaCl, pH 8.0
0.2% Tween , 10 mM Imidazole, 150 mM NaCl, pH 8.0
0.2% Triton-X , 10 mM Imidazole, 150 mM NaCl, pH 8.0
Stabiliser screen
20 mM HEPES, 10 mM Imidazole, 150 mM NaCl, 5% Glycerol , pH 8.0
20 mM HEPES, 10 mM Imidazole, 150 mM NaCl, 10% Glycerol , pH 8.0
20 mM HEPES, 10 mM Imidazole, 150 mM NaCl, 25% Glycerol , pH 8.0
20 mM HEPES, 10 mM Imidazole, 150 mM NaCl, 50% Glycerol , pH 8.0
pH screen
20 mM HEPES, 10 mM Imidazole, 150 mM NaCl, pH 2.0
20 mM HEPES, 10 mM Imidazole, 150 mM NaCl, pH 5.0
20 mM HEPES, 10 mM Imidazole, 150 mM NaCl, pH 7.0
20 mM HEPES, 10 mM Imidazole, 150mM NaCl, pH 9.0
Reductant screen
20 mM HEPES, 10 mM Imidazole, 150 mM NaCl, 2 mM DTT pH 8.0
20 mM HEPES, 10 mM Imidazole, 150 mM NaCl, 2 mM BME , pH 8.0

Cells were cultured as for wildtype protein expression, and lysed in the appropriate buffer. Soluble protein was produced from only one buffer condition – 20 mM HEPES, 10 mM imidazole, 150 mM NaCl, 50% glycerol. The apparent low molecular weight of the muterin suggested degradation, and correct folding was checked through examination

of the CD spectrum and subsequent tertiary structure analysis (section 2.5.1), which indicated that the construct was correctly folded (table 3.6, figure 3.23).

Table 3.7: CD analysis indicated that the Q83A mutein was correctly folded

CD spectra were analysed using the Dichroweb online server (Whitmore and Wallace, 2004), which revealed both the wildtype and Q83A constructs of *MtAhpE* contained equivalent helix, strand and loop structures.

Construct	Helices	Beta sheets	Turns	Disordered loops	Total
Wildtype <i>MtAhpE</i>	6.3%	38.7%	22%	33%	100%
Q83A	5.7%	39.3%	22%	33%	100%

Although the mutein appeared correctly folded, MS analysis gave an absolute weight of 16.87 (compared to an expected 19.9 for his-tagged mutein) confirming that degradation was occurring (appendix 5). Complete peptide sequencing could not be achieved, and so this could not be confirmed. Inclusion of protease inhibitors or EDTA into the lysis buffer did not prevent this degradation, suggesting it may not be due to contaminating proteases. Due to the difficulty in preventing degradation and incompatibility of the lysis buffer for additional analysis, further characterisation of the mutein was not carried out.

3.7 Characterisation of muteins

3.7.1 Analytical size-exclusion chromatography

Although initial purification of *MtAhpE* muteins indicated successful expression, and soluble protein was purified, the propensity of the constructs to aggregate and their instability at room temperature made obtaining sufficient amounts of protein for experimentation difficult. His-tag cleavage with rTEV protease required a third step of chromatography, with the associated loss of protein meaning that the final amount of mutein was minimal. Therefore only tagged muteins were able to be analysed.

When analysed by analytical SEC, all three muteins appeared to behave in an identical manner. The elution profile showed a single peak, at an elution volume that corresponded to a species of 31 kDa (figure 3.23). This was consistent with muteins degrading to a 15 kDa species (as was seen in some conditions for wildtype protein, and Q83A mutein; sections 3.3.1 and 3.6.3), leading to formation of dimers with a lower weight than expected. MS analysis was carried out on the T76A and E109A muteins (MS of the W95A mutein was unsuccessful), and gave molecular weight values of 19.69 and 19.87 kDa respectively, indicating no degradation. It is likely, therefore, that muteins were in fast equilibrium between a dimer and a monomer, compared to the time of experiment. The peaks seen on the elution profile were broad, supporting this. This shift to a later elution volume indicates that the introduction of alanine substitutions at the dimer interface has successfully destabilised one of the interfaces, likely the A-type interface. The monomer-dimer equilibrium suggests that the A-type interface is still able to form, though more weakly, and therefore easily dissociates. A second possibility is that the dimers are forming about the B-type interface, which is a weaker interface, and therefore exist in this equilibrium. Further studies would be useful to confirm the nature of the mutein dimers, intrinsic fluorescence or FRET could reveal the interface that is forming.

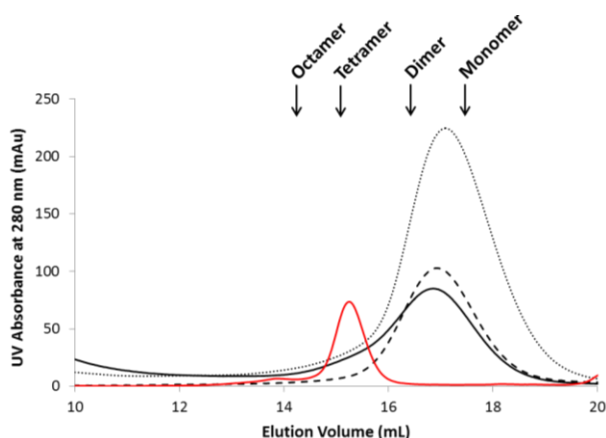


Figure 3.23: Analytical SEC suggested *MtAhpE* muteins exist as a mixture of species

All three of the muteins eluted as a single broad peak. The peak appeared to correspond to a mixture of dimeric and monomeric species, with no larger assemblies seen. The trace is shown from 10 – 25 mL for clarity. Prior to 10 mL any peaks seen are due to aggregation. Muteins are shown as: E109A black line; T76A dashed line; W95A dotted line. Tagged wildtype *MtAhpE* is shown in red for comparison.

3.7.2 SDS-PAGE analysis

As insufficient amounts of the muteins were produced to be able to carry out further solution studies, SDS-PAGE analysis was used to assess the quaternary structure of the samples as small volumes of protein could be used. Wildtype *MtAhpE* was seen to change its oligomeric state in response to a change in redox conditions (section 3.4.1.2), with oxidation inducing oligomerisation. This suggested that intermolecular disulfide bonds may be forming and stabilising the oligomeric species, which was supported by SDS-PAGE analysis (section 3.4.1.1). This response was investigated in the case of the muteins by subjecting them to hyperoxidising or reducing conditions through incubation for one hour with 10 mM H_2O_2 or 2 mM TCEP respectively. Non-reduced samples were also analysed with the assumption that these would be oxidised due to atmospheric oxygen. In the hyperoxidising buffer the cysteine residues would be oxidised to the sulfinic or sulfonic acid form. The pre-treated samples were then analysed by non-reducing SDS-PAGE (section 2.4.3.2) to test for disulfide bonded assemblies. The

samples were further analysed by subjecting them to reducing SDS-PAGE to confirm that any assemblies seen were due to intermolecular disulfide bonds.

Non-reducing SDS-PAGE

Hyperoxidised and non-reduced wildtype *MtAhpE* was able to form SDS resistant dimers due to strong non-covalent interactions or non-disulfide cross-links (section 3.4.1.1), and disulfide bonds respectively (section 3.4.1.1). Non-reduced muteins were also able to form a disulfide bonded dimer, but to a lesser degree than the wildtype. The presence of dimeric species was indicated in E109A and T76A hyperoxidised mutein samples (figure 3.24; W95A was unable to be analysed in hyperoxidising conditions due to its tendency to aggregate). Again, the intensity of this band was significantly reduced compared to that of the wildtype sample. The decrease in dimeric species suggests that in all cases studied, the interface was weakened by mutation. Visual examination of the gel image suggests the dimer band of the W95A mutein to be the most intense, and that of E109A to be the least. This implies an order of the degree of interface disruption: E109A > T76A > W95A. This could be confirmed by carrying out analytical ultracentrifugation (AUC) to test the equilibrium constants of the muteins.

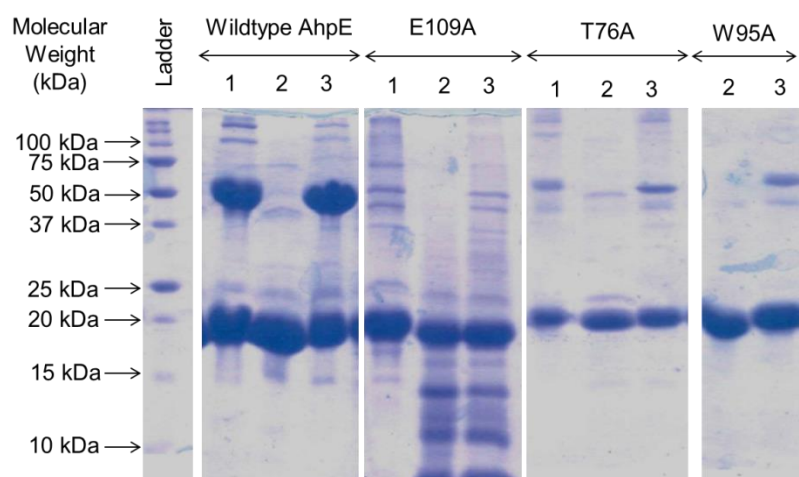


Figure 3.24: Non-reducing SDS-PAGE revealed the ability of muteins to form dimers

Constructs were (1) hyperoxidised, (2) reduced or (3) untreated prior to reducing SDS-PAGE analysis. All muteins formed dimers after incubation in non-reducing or hyperoxidising conditions, although to a lesser degree than wildtype, with the monomer being the predominant species for all three. The E109A mutein appeared to be an unstable construct, with laddering and lower weight bands suggesting significant degradation. Interestingly, this did not occur when the protein was hyperoxidised. Wildtype results as discussed in section 3.4.1.1 are shown for comparison.

Reducing SDS-PAGE

Samples were also run on reducing SDS-PAGE to differentiate between non-covalent, and disulfide bonded dimers. In contrast to wildtype (discussed in section 3.4.1.1), none of the muteins appeared to form significant non-disulfide interactions. In all cases the predominant band seen was that relating to a monomeric species. Some faint bands were seen in the case of the T76A and W95A mutein, but did not represent a considerable amount of the total population. This further supports that the mutations disrupt the A-type interface, preventing stabilisation due to hyperoxidation which was seen in wildtype samples.

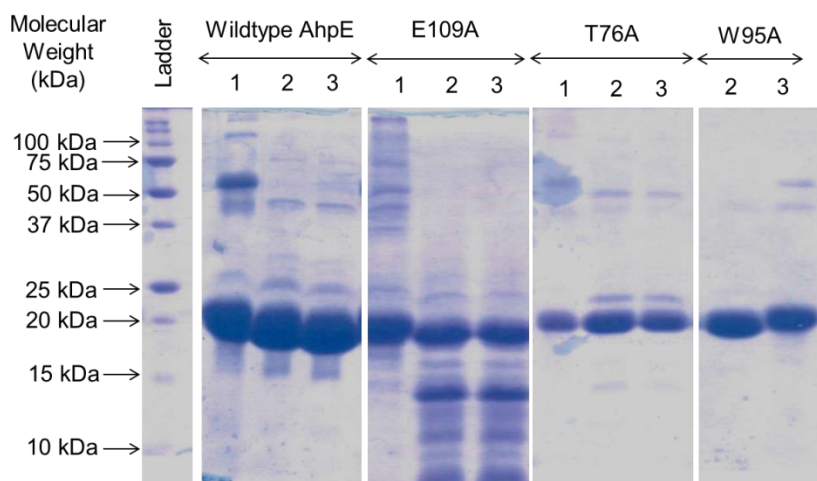


Figure 3.25: Reducing SDS-PAGE revealed that the oligomers seen previously were mostly due to disulfide bond formation

Constructs were (1) hyperoxidised, (2) reduced or (3) untreated prior to reducing SDS-PAGE analysis. All mutants showed a significant reduction in the formation of dimers, with the monomer being the predominant species on SDS-PAGE. Wildtype results as discussed in section 3.4.1.1 are shown for comparison.

3.8 Discussion

Enzymes involved in *M. tuberculosis* antioxidant defence have been seen to be upregulated during the pathogen's dormant phase (Murphy and Brown, 2007; Voskuil *et al.*, 2004). This dormancy is responsible for the latency of tuberculosis, during which the bacteria are resistant to antimicrobial agents (Wayne, 1994), and so is an important target for prevention of disease progression. Although the role of *MtAhpE* is poorly studied, its regulated expression in response to stress conditions has been reported (Murphy and Brown, 2007), and has led to the suggestion of *MtAhpE* as a possible drug target, worthy of further investigation (Hugo *et al.*, 2009). An octameric oligomer is rare among members of the Prx family, and the mechanisms behind its formation were therefore of interest from both a biomedical and nanotechnological stand point (section

1.6). The data presented here provide some insight into the oligomeric properties of *MtAhpE*, and the factors that affect oligomerisation.

3.8.1 Quaternary structure of untagged *MtAhpE*

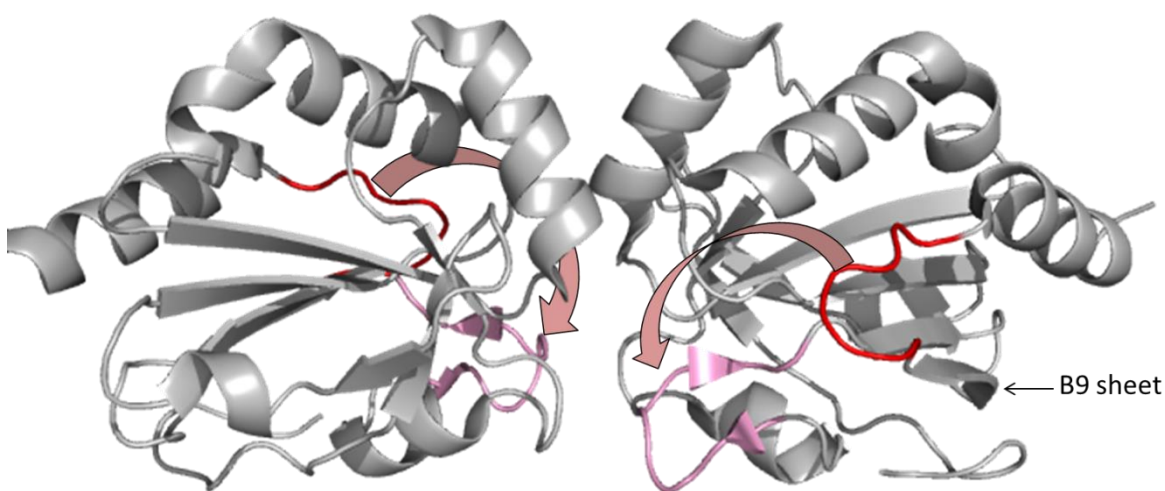
The results of this study confirm that untagged *MtAhpE* forms large redox-sensitive assemblies, which dissociate to dimers in the presence of a reducing agent. Disulfide-bonded dimers were seen to occur, a feature that has not been observed in any other of the 1-Cys Prxs. The disulfide bond likely forms across the A-type interface, and is therefore unlikely to be directly responsible for stabilising the oligomer-building B-type interface. Its formation may instead induce conformational changes that facilitate the formation of the B-type interface. Reduction has been reported to cause the movement of the $\beta 9$ - $\alpha 5$ external loop toward the $\alpha 4$ - $\beta 8$ loop and the A-type interface (Li *et al.*, 2005, figure 3.26), thereby causing a shift in the $\beta 9$ -sheet. This sheet is equivalent to the $\beta 7$ sheet that forms the B-type interface of typical 2-Cys Prxs (Wood *et al.*, 2002), and is thought to be involved in the putative B-type interface of *MtAhpE* (Li *et al.*, 2005). The shift in reducing conditions could therefore lead to disruption of the interface, with the opposite movement during oxidation putting the $\beta 9$ sheet into a favourable position to allow oligomerisation.

A small amount of tetrameric species was seen in reducing conditions, which has not been reported by other groups. The existence of tetrameric assemblies of an equivalent Prx (Prx5 from *Haemophilus influenzae*, which forms analogous A-type, redox insensitive dimers; Kim *et al.*, 2003), supports the data presented here. Tetramers of *MtAhpE* may be a physiologically relevant arrangement. In the crystal structure, octameric oligomers were seen to associate laterally and form long tubes (Li *et al.*, 2005), similar to the HMW species seen in other Prxs (section 1.2.5.3).

Table 3.8: Oligomeric states of Prxs change with redox state

MtAhpE shows unusual oligomeric properties, with the dimer being predominant in reducing conditions, and the oligomer favoured in oxidising conditions. Oligomerisation appeared more complex than that of 2-Cys Prxs, with a number of high weight structures forming in non-reducing conditions.

Protein	Oxidised	Reduced	Hyperoxidised
Untagged <i>MtAhpE</i>	HMW, Dimer	Dimer, Tetramer	Unknown
Tagged <i>MtAhpE</i>	Tetramer, Octamer	Tetramer, Octamer	Dimer (Hugo <i>et al.</i> , 2009)
Typical 2-Cys Prx	Dimer	Decamer	Decamer

**Figure 3.26: Loop movements may lead to B-type interface formation**

The authors (Li *et al.*, 2005) suggest that in the reduced form, an external loop (residues 133 – 139, coloured red) moves 4 Å towards the α 4- β 8 loop (residues 107 – 115, coloured pink) as indicated by the arrows. This would cause a movement of the β 9 sheet, which is equivalent to the β 7 sheet that forms the B-type interface of typical 2-Cys Prxs.

Hyperoxidation led to the formation of SDS resistant dimers, likely due to persistent hydrophobic interactions. Hyperoxidation has been seen to result in highly stable

interactions between monomers in typical 2-Cys Prxs (Pace *et al.*, 2013), and the data presented here suggest that *MtAhpE* is capable of forming equivalent interactions. Hyperoxidation is thought to lead to the unwinding of helix $\alpha 2$ and the C_P loop of Prxs, due to the increased volume and hydrophilicity of the sulfinic/sulfonic acid group (Saccoccia *et al.*, 2012). In *MtAhpE* this loop is in close proximity with the $\beta 9$ - $\alpha 5$ and $\alpha 4$ - $\beta 8$ loops, therefore, movement of the C_P loop in response to hyperoxidation may cause similar movements to that seen upon reduction (i.e. a shift in the $\beta 9$ -sheet, discussed above, figure 3.22). This could prevent oligomerisation of hyperoxidised dimers of *MtAhpE*, which has been reported (Hugo *et al.*, 2009). It is likely that the SDS-resistant dimers are forming about the A-type interface, analogous to typical 2-Cys Prxs (Low *et al.*, 2008), but further study using FRET or intrinsic fluorescence would be useful to confirm this.

The formation of the hyperoxidised and reduced toroids seen in typical 2-Cys Prxs is thought to occur through different mechanisms (Muthuramalingam *et al.*, 2009). The nature of the A-type interface stabilisation in hyperoxidised 2-Cys Prxs is not known (Pace *et al.*, 2013), and the observation of the 1-Cys *MtAhpE* behaving in a similar manner may provide some insight. There is some debate as to whether the conformational changes that lead to toroid formation occur while the subunits are free dimers, or while they are assembled into toroids (König *et al.*, 2013; Muthuramalingam *et al.*, 2009; Pace *et al.*, 2013). It seems unlikely that the mechanism for hyperoxidised toroid formation involves the dissociation of the reduced toroid, as this would require formation of the disulfide bond which would protect the cysteine from further attack by oxidising agents (section 1.2.4.4). It can be theorised that hyperoxidation occurs without dissociation, and the results of this chapter supports this theory. The *MtAhpE* A-type interface is maintained in all conditions; disassembly is therefore not a requirement for the transition from the reduced to hyperoxidised state. The conservation of this interface across the Prx family could mean that these results are relevant to the typical 2-Cys Prxs (figure 3.27). It has also been suggested that the influences that lead to oligomerisation (Wood *et al.*, 2003a, section 1.2.4.4) are intrinsically different in reducing and

hyperoxidising conditions, although the same interface is stabilised (Saccocia *et al.*, 2012). This chapter supports this theory, as although *MtAhpE* forms strong dimers in reducing or hyperoxidising conditions, differences are seen in the stability of the dimer, indicating a different mechanism of stabilisation. Further analysis by AUC would be useful to probe the differences in stability.

A: Propensity to hyperoxidation may be determined by dimer conformation.

B: Hyperoxidation may occur once assembled into toroids.

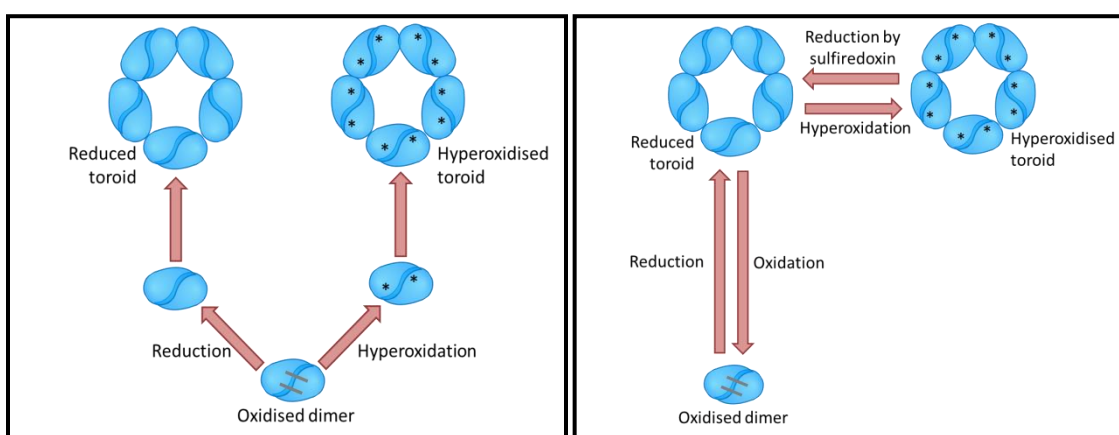


Figure 3.27: Possible mechanisms for reduced and hyperoxidised toroid formation of typical 2-Cys Prxs

A: It has been suggested that conformational changes within the dimer determine its propensity to hyperoxidation, and therefore toroid formation forms from either reduced or hyperoxidised dimers (König *et al.*, 2013). **B:** A second mechanism has been proposed which suggests that reduced dimers associate to toroids, which can then be hyperoxidised to a more stable toroid whilst assembled (Pace *et al.*, 2013). It is proposed here that the A-type interface may not need to dissociate for hyperoxidation to occur.

Electron microscopy revealed the presence of oligomeric rings. Along with the published X-ray structure of the his-tagged protein, this provides evidence for the existence of a typical oligomeric toroid being accessible to *MtAhpE*. However, as solution studies were limited and lack of a homogeneous sample made TEM image processing not possible, the precise nature of these toroids remains unclear, and the octameric arrangement in dilute solution remains unconfirmed.

3.8.2 Quaternary structure of his-tagged *MtAhpE*

When the his-tag was present, the sample was more stable and homogeneous (section 3.3). It also had a significant effect on the quaternary structure. The differences between the reduced and oxidised state were not clear, but the primary arrangement seen in solution appeared to be a tetramer (figure 3.14). Although not previously reported in the case of *MtAhpE*, a tetrameric arrangement has been seen to occur in other 1-Cys Prxs (Kim *et al.*, 2003). Crystallisation drives the formation of crystal packing contacts, which can be artefacts, but are usually representative of biologically relevant protein-protein interactions (Janin and Rodier, 1995). However, non-physiological associations can occur (Carugo and Argos, 1997), and it may be that the crystal packing favoured the octamer, which represented only one of many species in solution (figure 3.14). The octamer was not detected in any conditions in the untagged sample. The N-terminal region is suggested to be involved in the octamer-building, B-type interface of *MtAhpE* (Li *et al.*, 2005). It is apparent that the N-terminal his-tag affects quaternary structure, possibly through altering the conformation of this region. It may be that the tag causes the N-terminal tail to adopt a more ordered secondary structure, or the 25 residues of the his-tag and linker may force movement of this region, leading to the formation of the tetrameric and octameric species. While it is obvious that *MtAhpE* is capable of forming a number of arrangements, it is concluded that the octamer seen in the crystal structure is likely to be an artefact of the his-tag, and may not be the primary arrangement of native *MtAhpE*. The his-tag also appears to be responsible for the lack of high molecular weight structures seen in some solution studies (Hugo *et al.*, 2009). It is clear that detailed study of the untagged protein are necessary to complete our understanding of the oligomeric properties of *MtAhpE*.

Further investigation into the role of the N-terminal tail in oligomerisation may also be beneficial. In future the quaternary structure of a N-terminal truncation mutein could be analysed in solution and through X-ray crystallography, to ascertain whether the N-terminal tail does contribute to the interface, and the arrangement it adopts. This would

also highlight the influence that the his-tag has on the structure of this region. Further investigation through adding N-terminal extensions, including residues to introduce rigidity (such as proline) could provide more insight.

3.8.3 HMW forms of *MtAhpE*

The solution data presented here revealed the presence of HMW species in solution, although molecular weights for such species were not able to be ascertained. Although the SEC data presented in section 3.4.1.2 show a typical trace, results were not easily reproducible. Additional peaks were sometimes present, and the elution volume of the major peak varied, suggesting different species were present. This is consistent with the association of toroids in transient assemblies that formed on the time scale of the SEC experiment. Oxidation resulted in the formation of higher weight forms, which until now had not been reported in the case of 1-Cys Prxs. The data presented here suggest that *MtAhpE* may be capable of forming a number of higher molecular weight structures, which may have contributed to the paucity of information in the literature regarding the nature of *MtAhpE* quaternary structure, as aggregation occurred quickly, and samples were not homogeneous. TEM suggested the presence of very high weight “clusters” of protein, which are possibly represented by the void volume peaks that appeared on SEC (section 3.4.1.2). These are similar to those reported by other groups, formed by hyperoxidised 2-Cys Prxs (Jang *et al.*, 2004), which suggests they are not artefacts or random aggregates. A switch from peroxidase to chaperone activity through changing the oxidation state of C_P has been reported for 1-Cys Prxs (Kim *et al.*, 2011). Although the quaternary structure was not investigated, the change in activity strongly suggests that HMW structures may be forming. No structures of 1-Cys Prx HMW species have been reported, and although more work is needed to confirm the precise nature, this thesis therefore presents the first suggestion of such a structure. The presence of these species may indicate potential chaperone activity of *MtAhpE*, which could be tested using a holdase activity as described in Jang *et al.* (2004). The

appearance of these structures when oxidised rather than hyperoxidised (as seen for 2-Cys Prxs) could be because the highly oxidising environment that *M. tuberculosis* exists in requires high levels of chaperone activity. Therefore the oxidative stress threshold at which *MtAhpE* HMW species formation occurs is lower than that seen for typical 2-Cys Prxs, and oxidation rather than hyperoxidation is sufficient to induce this aggregation.

3.8.4 Quaternary structure of *MtAhpE* muteins

Substitution of three of the bonding residues at the A-type interface disrupted the association. Given the stability of the A-type interface of *MtAhpE*, it was somewhat surprising that single mutations appeared to have a significant impact on the formation of this interface. This could suggest that individual interactions contribute considerably to the bonding energy, rather than interface formation being driven mostly through the hydrophobic effect. It could also be that individual residue mutations have indirect effects and lead to the loss of more than one interaction. Further structural studies such as crystallography would clarify this. The concept of interface hotspots is well known, and the mutation of single residues resulting in prevention of interactions has been observed (Bogan and Thorn, 1998). The results of the mutations introduced here suggest that the binding energy of *MtAhpE* dimers is maintained by a small number of specific interactions. Isothermal titration calorimetry and AUC could be used to probe this theory, and also provide information regarding the concomitant changes in stability upon the introduction of the mutations. This could be useful to assess the relative impact of each mutation, that was suggested by SDS-PAGE analysis to be E109A > T76A > W95A. The A-type interface is thought to be linked to catalytic activity (Sarma *et al.*, 2005), and it is possible that disruption of this interface could decrease *MtAhpE* activity. The muteins generated in this study could provide useful constructs to test this hypothesis, and identification of interface hotspots could reveal avenues to design small molecule interface disruptors with the potential to influence protein activity. However,

the inherent instability of the protein and its mutants meant that further study took a lower priority than work on *HsPrx3* (chapters four to six).

3.8.5 Summary and outlook

This study reveals that the behaviour of *MtAhpE* is considerably more complex than previously thought, and although some new information was obtained, further study is very much needed to understand the quaternary structure. The protein is capable of forming a number of different oligomers, and its propensity to aggregation made the analysis of these challenging. The discrepancies in the literature and variation of results seen in this study between techniques, and even repeated experiments, suggest that oligomerisation of *MtAhpE* is highly dynamic and tightly controlled by a number of factors. Slight differences in factors such as temperature during, or prior to sample analysis could account for the variations seen in behaviour between samples run in different locations.

The A-type interface is thought to be the more ancestral mode of Prx association, as it is more widespread than the B-type interface (Sarma *et al.*, 2005). It is proposed that 2-Cys Prxs evolved from ancient bacterial Prxs, whose function was exclusively as protective antioxidant enzymes, to become regulators of peroxide signalling in higher organisms (Wood *et al.*, 2003b). The ability of *MtAhpE* to form oligomers and HMW structures, unique among the 1-Cys Prxs, and its sensitivity to hyperoxidation despite the lack of motifs thought to be required, could be suggestive that *MtAhpE* represents an evolutionary intermediate. This could explain the apparent ease with which the A-type interface was disrupted, as an evolutionary shift could have occurred to favour a B-type dimer, with the A-type interface therefore becoming less stable. Study of this protein could therefore be of high significance to all members of the widespread Prx family.

While the study of wildtype *MtAhpE* has provided some insight into the protein's behaviour, and potentially informed some of the mechanisms involved in typical Prx assembly, a detailed characterisation was unable to be carried out. A robust, reproducible method for producing high yields of the protein is necessary, and techniques for characterisation need to be optimised. This was not possible during the course of this research. Controlling the self-assembly of Prx subunits was a major goal of this research (section 1.6). Although the unusual potential octamer made *MtAhpE* an attractive system to study in parallel with the typical *HsPrx3*, the difficulties described meant that at this time it was not considered a useful candidate for the design of structures with altered or controllable assembly.

3.9 References

- Ahn, J.-Y., Li, X., Davis, H.L. and Canman, C. E. (2002) Phosphorylation of threonine 68 promotes oligomerisation and autophosphorylation of the Chk2 protein kinase via the forkhead-associate domain. *Journal of Biological Chemistry* **277**, 19389-19395.
- Biteau, B., Labarre, J. and Toledano, M. B. (2003) ATP-dependent reduction of cysteine-sulfinic acid by *Saccharomyces cerevisiae* sulfiredoxin. *Nature* **425**, 980-984.
- Bogan, A. A. and Thorn, K. S. (1998) Anatomy of hot spots in protein interfaces. *Journal of Molecular Biology* **280**, 1-9.
- Carugo, O. and Argos, P. (1997) Protein-protein crystal packing contacts. *Protein Science* **6**, 2261-2263.
- Cao, Z., Roszak, A. W., Gourlay, L. J., Lindsay, J. G. and Isaacs, N. W. (2005) Bovine mitochondrial Peroxiredoxin III forms a two-ring catenane. *Structure* **13**, 1661-1664.
- Cao, Z., Tavender, T. J., Roszak, A. W., Cogdell, R. J. and Bulleid, N. J. (2011) Crystal structure of reduced and of oxidized peroxiredoxin IV enzyme reveals a stable oxidized decamer and a non-disulfide-bonded intermediate in the catalytic cycle. *Journal of Biological Chemistry* **286**, 42257-42266.
- Chen, J.-W., Dodia, C., Feinstein, S. I., Jain, M. K. and Fisher, A. B. (2000) 1-Cys Peroxiredoxin, a bifunctional enzyme with glutathione peroxidase and phospholipase A2 activities. *Journal of Biological Chemistry* **275**, 28421-28427.
- Cole, S.T., Brosch, R., Parkhill, J., Garnier, T., Churcher, C., Harris, D., Gordon, S. V., Eiglhmeier, K., Gas, S., Barry C. E. 3rd., Tekaiia, F., Badcock, K., Basham, D., Brown, D., Chillingworth, T., Connor, R., Davies, R., Devlin, K., Feltwell, T., Gentles, S., HamLin, N., Holroyd, S., Hornsby, T., Jagels, K., Krogh, A., McLean, J., Moule, S., Murphy, L., Oliver, K., Osborne, J., Quail M. A., Rajandream, M.A., Rofers, J., Rutter, S., Seeger, K., Skelton, J., Squares, R., Squares, S., Sulston, J. E., Taylor, K., Whitehead, S., Barrel, B. G., (1998) Deciphering the biology of *Mycobacterium tuberculosis* from the complete genome sequence. *Nature*, **393**, 537-544.
- DeLano, W.L. (2002) The PyMOL Molecular Graphics System (San Carlos, CA: Delano Scientific).
- Don R, Cox P, Wainwright B, Baker K, Mattick J (1991) 'Touchdown' PCR to circumvent spurious priming during gene amplification. *Nucleic Acids Research* **19**, 4008
- Edelheit, O., Hanukoglu, A. and Hanukoglu, I. (2009) Simple and efficient site-directed mutagenesis two single-primer reactions in parallel to generate mutants for protein structure-function studies. *BioMed Central Biotechnology* **9**, 61.
- Farnum, M. and Zukoski, C. (1999) Effect of interactions and solubility of bovine pancreatic trypsin inhibitor. *Biophysical Journal* **76**, 2716-2726.

- Frey, U.H., H.S. Bachmann, J. Peters, and W. Siffert. (2008) PCR-amplification of GC-rich regions: 'slowdown PCR'. *Nature Protocols* **3**, 1312-1317.
- Gasteiger, E., Hoogland, C., Gattiker, A., Duvaud, S., Wilkins, M.R., Appel, R. D. and Bairoch, A. (2005) Protein Identification and Analysis Tools on the ExPASy Server. In John M. Walker (Ed): *The Proteomics Protocols Handbook* (pp. 571-607) New York, NY: Humana Press.
- Gill, G., Richter-Rusli, A. A., Ghosh, M., Burrows, C. J., and Rokita, S. E. (1997) Nickel-dependent oxidative cross-linking of a protein. *Chemical Research in Toxicology* **10**, 302-309.
- Gretes, M. C. and Karplus, P. A. (2013) Observed octameric assembly of a *Plasmodium yoelii* peroxiredoxin can be explained by the replacement of native "ball-and-socket" interacting residues by an affinity tag. *Protein Science* **10**, 1445-1452.
- Golovanov, A. P., Haulbergue, G. M., Wilson, S. A. and Lian, L.-Y. (2004) A simple method for improving protein solubility and long-term stability. *Journal of the American Chemical Society* **126**, 8933-8939.
- Gourlay, L. J., Bhella, D., Kelly, S. M., Price, N. C. and Lindsay, J. G. (2003) Structure-function analysis of recombinant substrate protein 22 kDa (SP-22): a mitochondrial 2-Cys peroxiredoxin organised as a decameric toroid. *Journal of Biological Chemistry* **35**, 32631-32637.
- Harris, J. R., Schröder, E., Isupov, M. N., Scheffler, D., Kristensen, P., Littlechild, J. A., Vagin, A. A., Meissner, U. (2001) Comparison of the decameric structure of peroxiredoxin-II by transmission electron microscopy and X-ray crystallography. *Biochimica et Biophysica Acta* **1547**, 221-234.
- Huebsch, N. D. and Mooney, D. J. (2007) Fluorescence Resonance Energy Transfer: a tool for probing molecular cell-biomaterial interactions in three dimensions. *Biomaterials* **28**, 2424-2437.
- Hugo, M., Turrell, L., Manta, B., Botti, H., Monteiro, G., Netto, L. E., Alvarez, B., Radi, R. and Trujillo, M. (2009) Thiol and sulfenic acid oxidation of *MtAhpE*, the one-cysteine peroxiredoxin from *Mycobacterium tuberculosis*: kinetics, acidity constants and conformational dynamics. *Biochemistry* **48**, 9416-9426.
- Jang, H. H., Lee, K. O., Chi, Y. H., Lee, J. R., Lee, S. S., Moon, J. C., Yun, J. W., Choi, Y. O., Kim, W. Y., Kang, J. S., Cheong, G.-W., Yun, D.-J., Rhee, S. G., Cho, M. J. and Lee, S. Y. (2004) Two enzymes in one: Two yeast peroxiredoxins display oxidative stress-dependent switching from a peroxidase to a molecular chaperone function. *Cell* **117**, 625-635.
- Janin, J. and Rodier, F. (1995) Protein-protein interaction at crystal contacts. *Proteins* **23**, 580-587.

- Jönsson T. J. and Lowther W. T. (2007) The peroxiredoxin repair proteins. In Flohé, L. and Harris, J. R. (Eds.) *Peroxiredoxin systems* (pp. 41 – 60). New York, NY: Springer Science and Business Media Inc.
- Ke, S.-H. and Madison, E. L. (1997) Rapid and efficient site-directed mutagenesis by single-tube ‘megaprimer’ PCR method. *Nucleic Acids Research* **25**, 3371-3372.
- Kim S. J., Woo, J. R., Hwang, Y. S., Jeong, D. G., Shin, D. H., Kim, K. and Ryu, S. E. (2003) The tetrameric structure of *Haemophilus influenza* hybrid Prx5 reveals interactions between electron donor and acceptor proteins. *Journal of Biological Chemistry* **278**, 10790-10798.
- Kim, S. Y., Paeng, S. K., Nawkar, G. M., Maibam, P., Lee, E. S., Kim, K. S., Lee, D. H., Park, D. J., Kang, S. B., Kim, M. R., Lee, J. H., Kim, Y. H., Kim, W. Y. and Kang, C. H. (2011) The 1-Cys peroxiredoxin, a regulator of seed dormancy, functions as a molecular chaperone under oxidative stress conditions. *Plant Science* **181**, 119-124.
- Koo, K. H., Lee, S., Jeong, S. Y., Kim, E. T., Kim, H. J., Kim, K., Song, K. and Chae, H. Z. (2002) Regulation of Thioredoxin Peroxidase activity by C-terminal truncation. *Archives of Biochemistry and Biophysics* **397**, 312-318.
- Konarev, P. V., Volkov, V. V., Sokolova, A. V., Koch M. H. J. and Svergun, D. I. (2003) PRIMUS: a Windows PC-based system for small-angle scattering data analysis. *Journal of Applied Crystallography* **36**, 1277-1282.
- König, J., Lotte, K., Plessow, R., Brockinke, A., Baier, M. and Dietz, K.-J. (2013) Reaction mechanism of plant 2-Cys peroxiredoxin: role of the C-terminus and the quaternary structure. *Journal of Biological Chemistry* **278**, 24409-24420.
- Krissinel, E. and Henrick, K. (2007) Inference of macromolecular assemblies from crystalline state. *Journal of Molecular Biology* **372**, 774-797.
- Kunz, W. and Ninham, H. B. W. (1988) ‘Zur Lehre von der Wirkung der Salze’ (about the science of the effect of salts): Franz Hofmeister’s historical papers. *Current Opinion in Colloid and Interface Science* **9**, 19-37.
- Li, S., Peterson, N. A., Kim, M. Y., Kim, C. Y., Hung, L. W., Yu, M., Legin, T., Segelke, B. W., Lott, J. S. and Baker, E. N. (2005) Crystal Structure of MtAhpE from *Mycobacterium tuberculosis*, a 1-Cys peroxiredoxin. *Journal of Molecular Biology* **346**, 1035-1046.
- Li, Y. (2010) Commonly used tag combinations for tandem affinity purification. *Biotechnology and Applied Biochemistry* **55**, 73-83.
- Looman, A. C., Bodlaender, J., Cornstock, L. J., Eaton, D. Jhurani, P., de Boer, H. A. and van Knippenberg, P. H. (1987) Influence of the codon following the AUG initiation codon on expression of a modified *lacZ* gene in *Escherichia coli*. *The EMBO Journal* **8**, 2489-2492.

- Low, F., Hampton, M. B., Peskin, A. V. and Winterbourn, C. C. (2007) Peroxiredoxin 2 functions as a noncatalytic scavenger of low-level hydrogen peroxide in the erythrocyte. *Blood*, **109**, 2611-2617.
- Mamedov, T. G., Pienaar, E., Whitney, S. E., TerMaat, J. R., Carvill, G., Goliath, R., Subramanian, A. and Viljoen, H. J. (2008) A fundamental study of the PCR amplification of GC-rich DNA templates. *Computational Biology and Chemistry* **32**, 452-457.
- Meissner, U., Schröder, E., Scheffler, D., Martin, A. G. and Harris, J. R. (2007) Formation, TEM study and 3D reconstruction of the human erythrocyte peroxiredoxin-2 dodecahedral higher-order assembly. *Micron* **38**, 29-39.
- Mertens, H. D. and Svergun, D. I. (2010) Structural characterization of proteins and complexes using small-angle X-ray solution scattering. *Journal of Structural Biology* **172**, 128-141.
- Moon, J. C., Hah, Y.-S., Kim, W. Y., Jung, B. G., Jang, H. H., Lee, J. R., Kim, S. Y., Lee, Y. M., Jeong, M. G., Kim, C. W., Cho, M. J. and Lee, S. Y. (2005) Oxidative stress-dependent structural and functional switching of a human 2-Cys peroxiredoxin Isotype II that enhances HeLa cell resistance to H₂O₂-induced cell death. *Journal of Biological Chemistry* **280**, 28775-28784.
- Murphy, D. J. and Brown, J. R. (2007) Identification of gene targets against dormant phase *Mycobacterium tuberculosis* infections. *BioMed Central Infectious Diseases* **7**, 84.
- Muthuramalingam, M., Seidel, T., Laxa, M., Nunes de Miranda, S. M., Gärtner, F., Ströher, E., Kandlbinder, A. and Dietz, K.-J. (2009) Multiple redox and non-redox interactions define 2-Cys peroxiredoxin as a regulatory hub in the chloroplast. *Molecular Plant* **2**, 1273-1288.
- Parks, T. D., Leuther, K. K., Howard, E. D., Johnston, S. A., and Dougherty, W. G., (1994) Release of proteins and peptides from fusion proteins using a recombinant plant virus protease. *Analytical Biochemistry*, **216**, 413-417.
- Parsonage, D., Youngblood, D. S., Sarma, G. N., Wood, Z. A., Karplus, P. A. and Poole, L. B. (2005) Analysis of the link between enzymatic activity and oligomeric state in AhpC, a bacterial peroxiredoxin. *Biochemistry* **44**, 10583-10592.
- Pace, P. E., Peskin, A. V., Han, M. H., Hampton, M. B. and Winterbourn, C. C. (2013) Hyperoxidized peroxiredoxin 2 interacts with the protein disulfide-isomerase ERp46. *Biochemical Journal* **453**, 475-485.
- Pomp, D. and Medrano, J. F. (1991) Organic solvents as facilitators of polymerase chain reaction. *Biotechniques* **10**, 58-59.
- Rosenow, M. A., Magee, C. L., Williams, J. C. and Allen, J. P. (2002) The influence of detergents on the solubility of membrane proteins. *Acta Crystallographica Section D* **58**, 2076-2081.
- Qiu, W., Dong, A., Pizarro, J. C., Botchkarev, A., Min, J., Wernimont, A. K., Hills, T., Hui, R. and Art, J. D. (2012) Crystal structures from the Plasmodium peroxiredoxins: new

- insights into oligomerization and product binding. *BioMed Central Structural Biology* **12**, 2.
- Reyes, A. M., Hugo, M., Trostchansky, A., Capece, L., Radi, R. and Trujillo, M. (2011) Oxidising substrate specificity of *Mycobacterium tuberculosis* alkyl hydroperoxide reductase E: kinetics and mechanism of oxidation and overoxidation. *Free Radical Biology and Medicine* **51**, 464-473.
- Roux, K. H. (2003) Optimizing and troubleshooting in PCR. *Cold Spring Harbour Protocols* **4**, pdb.ip66.
- Saccoccia, F., Micco, P. D., Bournis, G., Brunori, M., Koutris, I., Miele, A. E., Morea, V., Sriratana, P., Williams, D. L., Bellelli, A. and Angelucci, F. (2012) Moonlighting by different stressors: crystal structure of the chaperone species of a 2-cys peroxiredoxin. *Structure* **20**, 429 – 439.
- Sahdev, S., Saini, S., Tiwari, P., Saxena, S. and Saini, K. S. (2007) Amplification of GC-rich genes by following a combination strategy of primer design, enhancers and modified PCR cycle conditions. *Molecular and Cellular Probes* **21**, 303-307.
- Sarma, G. N., Nickel, C., Rahlfs, S., Fischer, M., Becker, K. and Karplus, P. A. (2005) Crystal structure of a novel *Plasmodium falciparum* 1-Cys peroxiredoxin. *Journal of Molecular Biology* **346**, 1021-1034.
- Serrao, E., Thys, W., Demeulemeester, J., Al-Mawsawi, L. Q., Christ, F. Debyser, Z. and Neamati, N. (2012) A symmetric region of the HIV-1 integrase dimerization interface is essential for viral replication. *PLoS one* **7**, e45177.
- Svergun D.I. (1992) Determination of the regularization parameter in indirect-transform methods using perceptual criteria. *Journal of Applied Crystallography* **25**, 495-503.
- Svergun, D. I. and Koch, M. H. J. (2003) Small-angle scattering studies of biological macromolecules in solution. *Reports on Progress in Physics* **66**, 1735-1782.
- Thompson, J. D., Higgins, D. G., and Gibson, T. J., (1994) CLUSTAL W: Improving the sensitivity of progressive multiply sequence alignment through sequence weighting, position-specific gap penalties and weight matrix choice. *Nucleic acids research*, **22**, 4673-4680.
- Vaganende, V., Yap, M. G. S. and Trout, B. L. (2009) Mechanism of protein stabilization and prevention of protein aggregation by glycerol. *Biochemistry* **48**, 11084-11096.
- Varadaraj, K. and Skinner, D. M. (1994) Denaturants or cosolvents improve the specificity of PCR amplification of a G + C-rich DNA using genetically engineered DNA polymerases. *Gene* **140**, 1-5.
- Voskuil, M. I., Visconti, K. C. and Schoolnik, G. K. (2004) *Mycobacterium tuberculosis* gene expression during adaptation to stationary phase and low-oxygen dormancy. *Tuberculosis* **84**, 218-227.

- Walker, J. M. (2002) Nondenaturing polyacrylamide gel electrophoresis of proteins. In Walker J. M. (Ed.) *The Protein Protocols Handbook Second Edition* (pp. 57-60). Humana Press Inc., Totowa, NJ.
- Wayne, L. G. (1994) Dormancy of *Mycobacterium tuberculosis* and latency of disease. *European Journal of Clinical Microbiology and Infectious Disease* **13**, 908-914.
- Weichsel, A., Gasdaska, J. R., Powis, G. and Montfort, W. R. (1996) Crystal structures of reduced, oxidised and mutated human thioredoxins: evidence for a regulatory homodimer. *Structure* **15**, 735-751.
- Whitmore, L. and Wallace, B. A., (2004) DICHROWEB, an online server for protein secondary structure analyses from circular dichroism spectroscopic data. *Nucleic Acids Research* **1**, 32.
- Wine, Y., Cohen-Hadar, N., Freeman, A. and Frolow, F (2007) Elucidation of the mechanism and end products of glutaraldehyde crosslinking reaction by X-ray structure analysis. *Biotechnology and Bioengineering* **98**, 711-718.
- Winship, P. R. (1989) An improved method for directly sequencing PCR amplified material using dimethyl sulphoxide. *Nucleic Acids Research* **17**, 1266-1271.
- Woo, H. A., Kang, S. W., Kim, H. K., Yang, K.-S., Chae, H. Z. and Rhee, S. G. (2003) Reversible oxidation of the active site cysteine of peroxiredoxins to cysteine sulfinic acid. *The Journal of Biological Chemistry* **278**, 47361-47364.
- Wood, Z. A., Poole, L. B., Hantgan, R. R. and Karplus, P. A. (2002) Dimers to doughnuts: redox-sensitive oligomerisation of 2-Cys peroxiredoxins. *Biochemistry* **41**, 5493-5504.
- Wood, Z. A., Poole, L. B. and Karplus, P. A. (2003a) Peroxiredoxin evolution and the regulation of hydrogen peroxide signalling. *Science* **300**, 650-6.
- Wood, Z. A., Schröder, E., Harris, J. R. and Poole, L. B. (2003b) Structure, mechanism and regulation of peroxiredoxins. *Trends in Biochemical Sciences* **28**, 32-40.

Chapter 4 Human Prx3

4.1 Introduction

This chapter describes the detailed characterisation of *HsPrx3* using a number of biophysical techniques. After expression and purification, the influence of environmental factors on oligomeric state was assessed. The factors studied were redox conditions, the presence of an N-terminal his-tag, solution pH and protein concentration. SEC/SLS was used to indicate the size and relative proportion of protein species in solution, and SAXS data were collected to more accurately determine the weight of species present when the samples were monodisperse. TEM gave finer morphological detail and enabled close examination of the structures formed by *HsPrx3*.

The X-ray crystal structure of *HsPrx3* has not yet been solved, and so the crystal structure of the bovine homologue, *BtPrx3*, which shares 93% sequence homology with *HsPrx3* (Cao *et al.*, 2005), has been used as a structural reference. The pH of the mitochondrial matrix is ~7.8 (Porcelli *et al.*, 2005), and with early trials showing *HsPrx3* to be stable and soluble at pH 8.0 all buffers were kept at this pH throughout this work (except when the effect of altered pH on quaternary structure was investigated).

4.2 Purification of wildtype *HsPrx3*

4.2.1 Expression in an *E. coli* host

The *HsPrx3* gene contains a number of rare codons (see appendix 4), therefore BL21 Rosetta (DE3) competent cells (Invitrogen) were used for protein expression (section 2.1.3). Bacteria were cultured as described in section 2.2.2. Various induction times and temperatures were trialled (as in section 3.3.1), with high levels of expression achieved using standard expression protocols (section 2.3.1.2) and overnight culturing at 21°C following induction. Cells were lysed using a cell press (section 2.3.1), which was found in early expression trials to be up to ten times as efficient as sonication, based on soluble protein yield (table 4.1; figure 4.1). The supernatant was collected for IMAC purification, which typically resulted in a final yield of 80 – 100 mg/L.

Table 4.1: Cell press extraction provided a more efficient lysis technique

Comparisons of the weight of protein extracted from 1L cell cultures grown in identical conditions differed drastically depending on lysis technique. Sonication was seen to be inefficient with low yields compared to that of cells lysed with the cell press, and so was not used for cell lysis during protein production.

Lysis method	Pellet weight (g)	Weight of protein after IMAC (mg)	Weight of protein after gel filtration (mg; final yield)	Weight of protein per gram cells (mg)
Sonication	4.3	40	9	2.1
Cell press	5.6	120	80	14.3

4.2.2 Purification by chromatography

Filtered lysate was loaded manually onto a 5 mL HiTrap™ IMAC chelating column which had been charged and equilibrated as described in section 2.3.3.1. The column was then washed with loading buffer (section 2.1.8.2) and protein eluted with elution buffers containing a gradient of 10 – 500 mM of imidazole. Wildtype *HsPrx3* bound successfully to the nickel resin, with very little in the flowthrough or wash fractions. *HsPrx3* eluted consistently as a single peak at an imidazole concentration of approximately 250 mM (figure 4.2A).

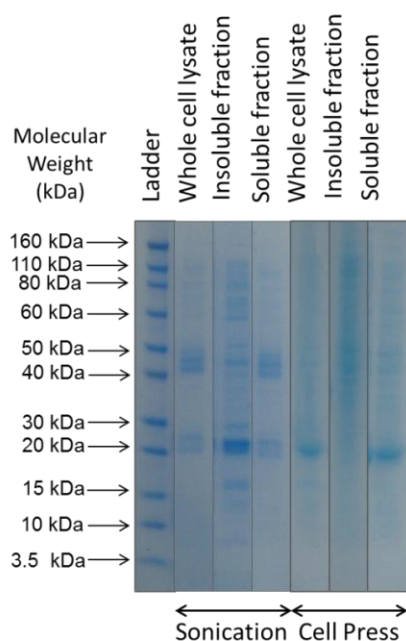
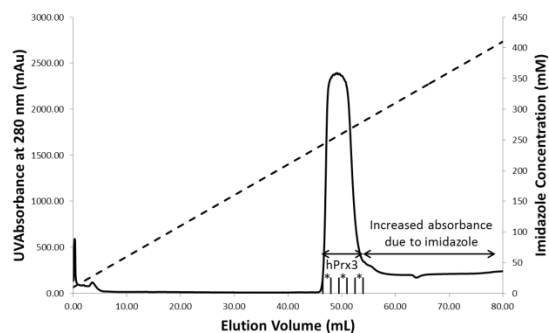
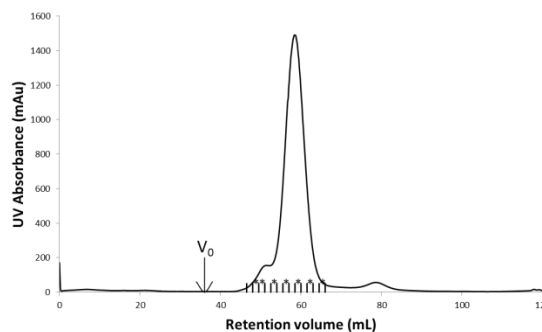


Figure 4.1: Sonication resulted in incomplete lysis

Very little *HsPrx3* was seen in the insoluble fraction when cells were lysed using the cell press. After sonication, a large amount of protein remained in the insoluble fraction, suggesting that complete lysis has not occurred, resulting in a significant decrease in the amount of protein in the soluble fraction.

A: IMAC elution**B: Gel filtration elution****Figure 4.2: Representative purification chromatograms**

A: IMAC purification of *HsPrx3* resulted in a single peak. The dashed line represents the 10 mM – 500 mM imidazole gradient used to elute the protein. **B:** Typical chromatogram from gel filtration purification of *HsPrx3*. A major peak was seen around 60 mL, with a small shoulder indicating the presence of a higher molecular weight species. Stars indicate fractions analysed by SDS-PAGE (figure 4.3).

A major band that migrated at 25 kDa was seen on SDS-PAGE analysis of fractions across the single peak recorded in the elution phase of IMAC (figures 4.2A and 4.3A). Further analysis by peptide sequencing (section 2.3.5) confirmed this band to be *HsPrx3* (appendix 5). Copurification of other *E. coli* proteins is common with IMAC (reviewed in Block *et al.*, 2009, and *HsPrx3* has been seen to interact with a large number of *E. coli* proteins (A. Betz, University of Otago, personal communication). Fractions that contained high levels of *HsPrx3* (for example, lanes 4 and 5 of figure 4.3A) were therefore pooled and concentrated, and subjected to gel filtration. Protein was eluted using gel filtration buffer (section 2.1.8.2), and a single peak was typically observed at a retention volume of about 60 mL, with a small shoulder around 50 mL (figure 4.2B). Fractions collected across both peaks showed a single major band at 25 kDa on SDS-PAGE (figure 4.3A).

Fractions were collected from regions of the peaks indicated to contain over 0.5 mg/mL total protein concentration, using visual estimation by comparison to a band of pure protein at known concentration. The purity and specific concentration of *HsPrx3* protein

was checked by SDS-PAGE. Fractions deemed to contain sufficient amounts of pure *HsPrx3* (for example, lanes 11-14 figure 4.3A) were pooled and concentrated. The pooled sample was purified to homogeneity as judged by SDS-PAGE. When analysed at the concentration typically used for experiments (1 mg/mL), the absence of additional bands indicated that the amount of contaminating proteins was below 10 ng (the detection limit of colloidal Coomassie blue; Weiss *et al.*, 2009), which was deemed acceptable (figure 4.3B). From a typical purification, the approximate yield was 60 % that of the protein loaded onto the gel filtration column.

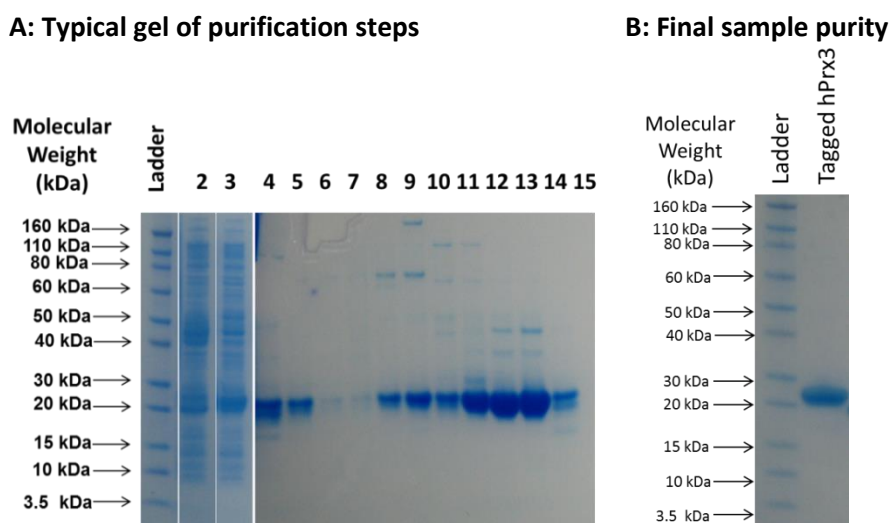


Figure 4.3: SDS-PAGE gel of *HsPrx3* purification

A: A representative reducing SDS-PAGE gel of chromatography steps of *HsPrx3* purification. *HsPrx3* was identified as the 25 kDa band. Lanes 2 and 3: soluble and insoluble fractions after lysis and centrifugation; 4-7: fractions across the main peak of the IMAC chromatogram (figure 4.2A); 8-9: fractions across the shoulder peak of the gel filtration chromatogram (figure 4.2B); 10-15: fractions across the main peak of gel filtration. **B:** An SDS-PAGE gel of purified, his-tagged *HsPrx3* at 1 mg/mL.

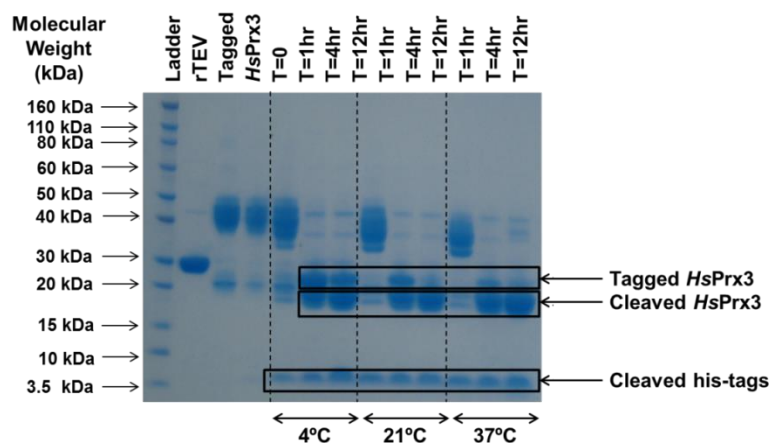
4.2.3 His-tag removal by rTEV protease

Consistent with reports from previous research (M. B. Hampton, University of Otago, personal communication), complete his-tag cleavage of tagged *HsPrx3* was challenging, with multiple steps of cleavage and purification required. This could be due to the toroidal nature of Prxs, which perhaps accommodates the additional residues of the his-tag and linker peptide in the centre of the ring, hindering access to the cleavage site. A number of cleavage conditions were trialled in an attempt to overcome this problem (see figure 4.4). The most successful conditions were seen to be overnight incubation with rTEV at 4°C, with the addition of <1 mM TCEP. rTEV protease is a member of the 3C cysteine proteases, which achieve proteolysis through nucleophilic attack of the substrate by the active site cysteine (reviewed in Malcolm, 1995). This residue must therefore be reduced to carry out the reaction, necessitating the addition of TCEP in the reaction buffer.

All cleavage trials were carried out at a ratio of 1:100 rTEV:*HsPrx3*, as this was seen to be equally efficient as a ratio of 1:20. Control reactions of *HsPrx3* alone were subjected to the same incubation times and temperatures to ensure that any decrease in molecular weight was due to his-tag cleavage rather than non-specific degradation. It was noticed that when left at 4°C overnight (and to a greater extent after incubation at 37°C) SDS resistant dimers appeared in the sample (indicated by a band migrating at a distance equivalent to the 50 kDa marker – figure 4.4). This has been reported by other groups, and has been opined to be due to strong non-covalent linkage between monomers (C. C. Winterbourn, personal communication). It has also been seen in mutants prone to hyperoxidation, due to the formation of persistent hydrophobic interactions (König *et al.*, 2013). The appearance of these bands in samples that were subjected to high temperatures suggests that the protein may be becoming denatured and forming strong hydrophobic interactions as suggested by König *et al.* All samples were therefore flash frozen after purification in aliquots of 200 µL, thawed immediately prior to using and

kept at 4°C during experiments where possible. Comparison of SEC/SLS traces of *HsPrx3* from freshly prepared samples and those that had been flash frozen and thawed prior to analysis showed no differences (data not shown), indicating that freezing does not affect the protein.

A: Cleavage trials



B: Final sample purity

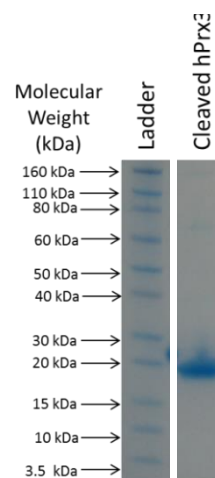


Figure 4.4: SDS-PAGE of his-tag cleavage trials

A: A range of conditions were tested to optimise rTEV cleavage. The gel shows a representative group of conditions. **B:** Successful cleavage was found to require a 1:100 rTEV:protein ratio, with 21°C providing sufficient cleavage.

4.3 Characterisation of wildtype *HsPrx3*

4.3.1 Quaternary structure of *HsPrx3*

The first part of this research aimed to build on existing literature (Wood *et al.*, 2003, sections 1.2.5 and 1.2.5.1), elucidate the quaternary organisation of *HsPrx3*, and firmly characterise the factors that influence this. A number of techniques were used to analyse

HsPrx3 and obtain a detailed picture of the solution structure of the protein. Unless otherwise stated all data sets were collected at a protein concentration of 1 mg/mL. The native monomer of *HsPrx3* has a molecular weight of 21.4 kDa (molecular weight calculated using the ExPasy online bioinformatics tool; Gasteiger *et al.*, 2005) (see appendix 4). Recombinant expression in *E. coli* using a pET151 vector resulted in the production of *HsPrx3* with an N-terminal affinity tag and a 26 residue linker peptide, with a weight of 25.2 kDa (see section 4.2.3). This leaves six additional residues even when the tag is cleaved, thus the predicted monomer weight is 22 kDa. Prxs generally exist as obligate dimers (Wood *et al.*, 2003), therefore the smallest unit in solution was expected to be the 44 kDa dimer.

While *BtPrx3* provides a useful structural reference for *HsPrx3*, there has been some debate as to the precise nature of the bovine toroidal oligomer structure. Some results suggest that the protein exists as a decamer (Gourlay *et al.*, 2003), while others suggest that it is dodecameric (Cao *et al.*, 2005). The crystal structure of *BtPrx3* shows an unusual concatenated arrangement of dodecameric toroids which may only be representative of a subpopulation of the species in solution (Cao *et al.*, 2005; Karplus and Hall in Flohé and Harris, 2007). Therefore it was important to establish if *HsPrx3* dimers would associate in dodecameric or, analogous to all other human 2-cys Prxs, decameric toroids (Schröder *et al.*, 2000; Cao *et al.*, 2011), before further characterisation could be carried out.

Size Exclusion Chromatography/Static Light Scattering

HsPrx3 samples were initially analysed using SEC/SLS (section 2.5.6) to identify the size and distribution of species present in solution. Analysis of the quaternary structure of *HsPrx3* in reducing buffer (section 2.1.8.2) indicated that *HsPrx3* existed predominantly as one species (figure 4.5), represented by a large peak in the RI trace at around 12 mL. This peak was calculated (section 2.3.5.6) to represent a 249 kDa species, suggesting a dodecameric oligomer. The molecular weight was consistent

across the peak indicating a stable, monodisperse sample, with weight calculations not affected by the presence of other species.

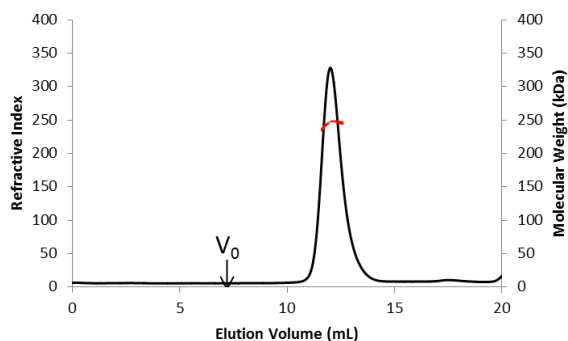


Figure 4.5: SEC/SLS of *HsPrx3* in reducing conditions

The RI trace of *HsPrx3* showed a homogeneous solution, consisting of a large oligomeric species of around 250 kDa. Molecular weight as calculated from RI and light scattering by calibration to a BSA standard is indicated by the red line across the peak.

Small angle X-ray scattering

Data were collected from samples injected directly into a single, suspended capillary as this approach achieves the most constant possible background (H. D. T. Mertens, Australian Synchrotron, personal communication; information provided at www.synchrotron.com.au), and also allows analysis of samples at precisely known concentrations.

In the reducing conditions, SAXS data supported SEC/SLS results. The average molecular weight of the solution was found to be 255 kDa (see table 4.2). The theoretical weight for a decameric oligomer is 214 kDa, and that of a dodecamer is 257 kDa, therefore SAXS calculations were consistent with *HsPrx3* forming a dodecamer in solution. R_G calculated from both the Guinier region and GNOM program (Svergun *et al.*, 1992) agree well, indicating good sample quality and no aggregation. Although

these values and D_{\max} calculated from the Porod volume are slightly larger than the theoretical values for a dodecameric oligomer (calculated from the crystal structure of *BtPrx3* [Cao *et al.*, 2005] using CRY SOL [Svergun *et al.*, 1995; section 2.5.5.2]), this is likely due to 32 N-terminal residues that are not modelled in the crystal structure.

Table 4.2: Molecular weights from SAXS studies of *HsPrx3*

Experimental data were compared with theoretical values for a dimeric, decameric and dodecameric structure. Values for each concentration were calculated from three scattering images and averaged. Theoretical dimensions were generated using GNOM and the specified crystal structures, and molecular weight using the weight of *HsPrx3*. Experimental data agreed well with expected values calculated for a dodecameric species. The consistency in weight calculated across the range of concentrations tested indicated particle size of *HsPrx3* is not concentration dependent in these conditions, as confirmed by superposition of scaled scattering curves (figure 4.6A).

		D_{\max} (Å)	R_G from Guinier (Å)	R_G from GNOM (Å)	Volume (Å ³)	MW (kDa)
<i>HsPrx3</i>	0.5 mg/mL	170	59	59	417000	254
	1 mg/mL	178	59	59	417000	255
	2 mg/mL	175	60	58	415000	256
<i>BtPrx3</i> dimer	PDB ID: 1ZYE	~ 60	Theoretical R_G : 20		49800	43
<i>BtPrx3</i> decamer	PDB ID: 1QMV	~ 135	Theoretical R_G : 47		393000	214
<i>BtPrx3</i> dodecamer	PDB ID: 1ZYE	~ 155	Theoretical R_G : 55		441000	257

The scattering profile (figure 4.6A) showed an oscillating curve, indicative of a multi-domain protein with a number of different inter- and intra-subunit distances (Mertens and Svergun, 2010). The $P(r)$ plot showed an asymmetric curve (figure 4.6B). The presence of two maxima on this plot suggested well separated subunits, with the first peak representing intrasubunit distances (Svergun and Koch, 2003) and the second relating to intersubunit distances. Together, these data support that the dodecamer formed by *HsPrx3* is a toroidal oligomer as seen for many other Prxs. Scattering profiles of reduced *HsPrx3* were compared to theoretical profiles generated from crystal structures of a decameric (PDB accession number 1QMV, Schröder *et al.*, 2000) and dodecameric (PDB accession number 1ZYE, Cao *et al.*, 2005) Prx toroid. Reduced

HsPrx3 showed very good agreement with the theoretical scattering for a dodecameric toroid (figure 4.7A), but significant misalignment with that for a decameric toroid (figure 4.7B), suggesting that a decameric arrangement is not present in samples of *HsPrx3*.

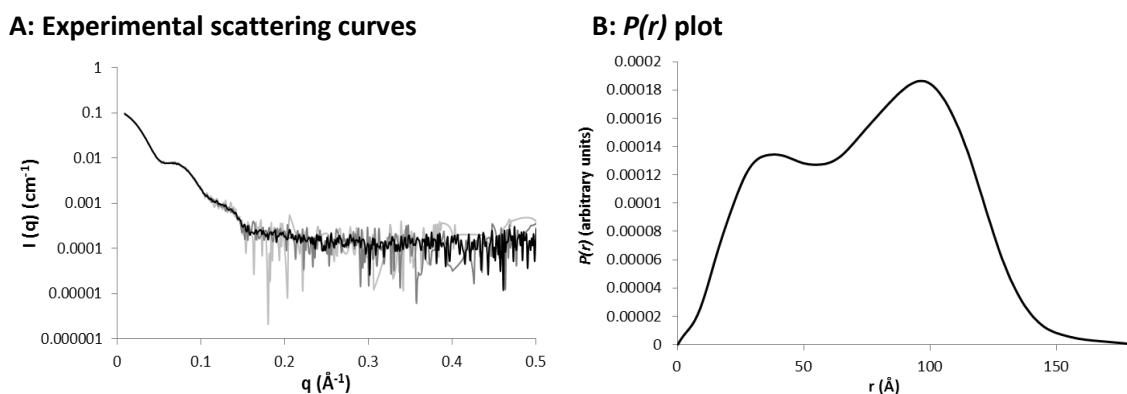


Figure 4.6: X-ray scattering data suggested a toroidal particle

A: Scaled scattering curves of 0.5 mg/mL (light grey), 1 mg/mL (dark grey) and 2 mg/mL (black line) align well when overlaid, suggesting that within this range the oligomeric state is not sensitive to concentration. The multiple shoulders suggest a toroidal species. **B:** In reducing conditions the presence of two maxima on the $P(r)$ plot indicate a multidomain particle (Mertens and Svergun, 2010).

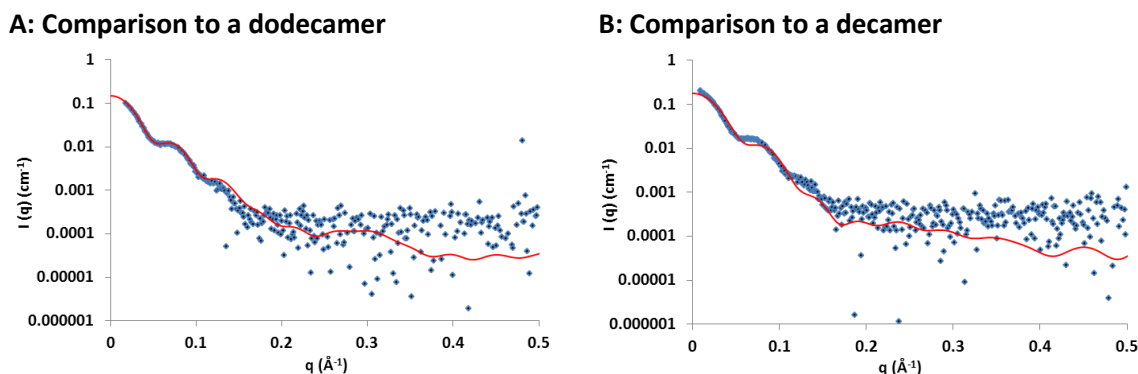


Figure 4.7: Experimental scattering data and theoretical scattering profiles

A: When fitted to theoretical scattering profiles (indicated with the red line) for a dodecameric Prx (PDB ID: 1QMV; Schröder *et al.*, 2000), experimental scattering (blue diamonds) showed good agreement (χ^2 value 0.59). **B:** Comparison to that of a decameric Prx (PDB ID: 1ZYE; Cao *et al.*, 2005) showed significant misalignment (χ^2 value 1.51) suggesting that this is not a likely arrangement of *HsPrx3*.

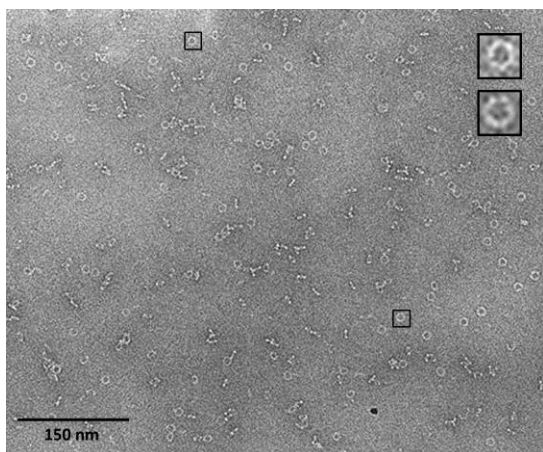
4.3.1.1 The 3D structure of the *HsPrx3* toroid

Reduced *HsPrx3* was examined by TEM to unequivocally confirm the nature of the toroid. Initial trials to determine optimum sample concentration and conditions for TEM were carried out by recording images from samples prepared on copper mesh grids, overlaid with carbon coated Formvar®. These gave noisy images, with a high degree of background variation, and so for further studies copper mesh grids overlaid with continuous carbon were used. Samples were negatively stained with NanoVan solution (NanoprobesTM) as this was found to give a more even stain than initial trials with uranyl acetate stain, potentially due to the smaller grain size of vanadate. NanoVan also offered the advantage of a near physiological pH (8.0), compared to that of acetate (pH 4.0), which can be prone to artefacts (Hainfeld *et al.*, 1994). Samples were adsorbed onto the grids from solution at a concentration of 0.01 mg/mL, using a method based on that of Radjainia *et al.*, (2010).

From initial inspection of electron micrographs, the presence of toroids in the negatively stained sample was immediately obvious (figure 4.8). The images were recorded on Kodak film, and these showed particles assuming random orientations, which allowed visualisation of this structure from a number of angles. In a number of individual particles, a hexagonal shape was easily discernible (see insets, figure 4.8A), supporting the dodecameric toroid. The fidelity of TEM images is often questioned, due to the possibility of interactions with the grid affecting the protein structure, or potentially selecting for a certain conformation and misrepresenting the populations present in the sample. In order to minimise these possibilities, and confirm that the grid does not influence *HsPrx3* structure in TEM samples, images were also acquired using Quantifoil® “holey” grids prepared identically to the continuous carbon grids. As the protein in aqueous solution is deposited onto the grid it forms a film across the holes. The aqueous film spanning the holes is subsequently replaced by the stain, leaving the protein samples suspended in a thin film of stain (Harris, 2008). Micrographs of specimens prepared on holey grids showed toroids of the same dimensions to those seen

on continuous carbon grids (figure 4.8B). This confirmed that the support film on the grid was not affecting the sample.

A: Continuous carbon grid



B: Holey grid

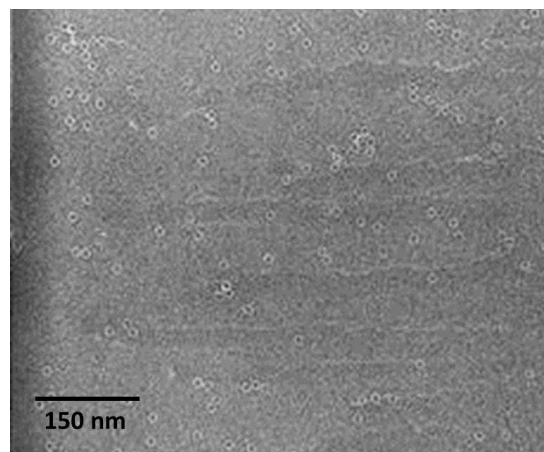


Figure 4.8: Electron micrographs of *HsPrx3* revealed hexagonal toroids

A: Negatively stained *HsPrx3* samples at 0.05 mg/mL showed the presence of toroids, with both top and side views visible. Hexagonal features were clearly discernible in the case of some particles (indicated by black boxes; inset shows enlarged views of these particles). **B:** Images of *HsPrx3* stained across holes of Quantifoil® holey grids. The prevalence of these structures in these preparations indicates that grid interactions or selection for certain conformations is not occurring on continuous carbon grids.

7130 Particles of *HsPrx3* were automatically selected from 12 micrographs, then aligned and averaged using reference-free class averaging of the EMAN v1.9 image processing suite (Ludtke *et al.*, 1999). 100 reference-free class averages were generated by 9 rounds of iterative refinement (section 2.3.5.7.2; figure 4.9A). In these class averages, the hexagonal features seen in the micrographs were greatly enhanced, with individual dimers distinguishable in many cases. Class averages from micrographs recorded of samples on holey grids confirmed the hexameric arrangement.

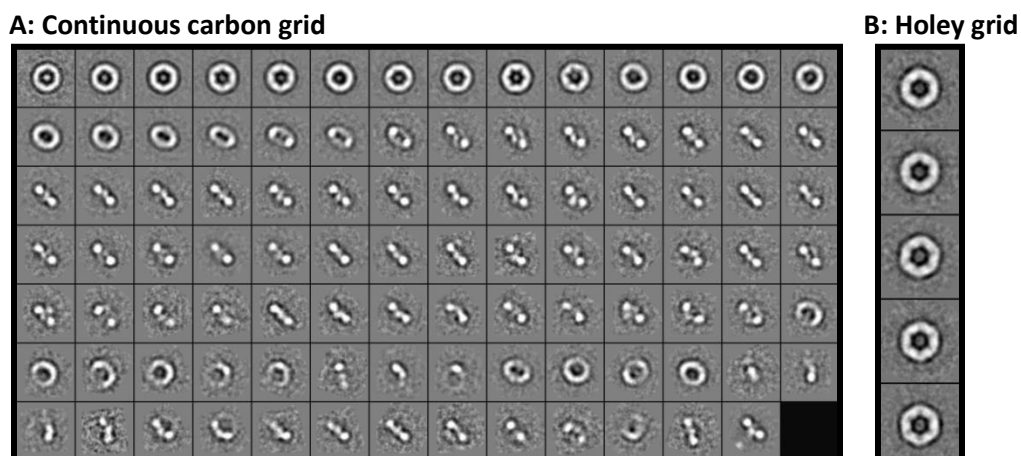


Figure 4.9: Class averages confirm the hexameric oligomer

A: 100 class averages were generated from 7130 particles, showing clear *en face* profiles as well as side views of rings. Six-fold symmetry is clear in a number of images. **B:** A selection of class averages produced from images recorded from holey grids is shown, revealing clear six-fold symmetry and an absence of particles with alternative symmetries, indicating that grid interactions had not influenced *HsPrx3* assembly or selected for the hexameric structures.

Initial 3D models were built from raw images using the *startcsym* routine of EMAN v1.9 with C6 symmetry (section 2.3.5.7.2; Ludtke *et al.*, 1999). These models were generated using a selected set of raw images, and were simultaneously refined by twelve iterative rounds of multi-model refinement in EMAN with imposed D6 symmetry. The resulting models were separately refined with imposed D6 symmetry using only the selected set of raw images that the process of multi-model refinement had associated with a given reference model. This resulted in a reconstruction which agrees well with X-ray crystal structure of *BtPrx3* (figure 4.10; Cao *et al.*, 2005), which was docked into the 3D reconstruction using UCSF Chimera (Pettersen *et al.*, 2004). The resolution of the reconstruction was estimated to be 26 Å based on the FSC_{0.5} criterion, and shows density additional to that observed for the dodecameric Prx crystal structure, well placed to account for the 32 missing C-terminal residues from the crystal structure of the bovine analogue (Cao *et al.*, 2005). Measurement of the models using Chimera suggested the toroids have an external diameter of 16 nm and an internal diameter of 7

nm, which is consistent with the crystal structure of the dodecameric *BtPrx3* (Cao *et al.*, 2005).

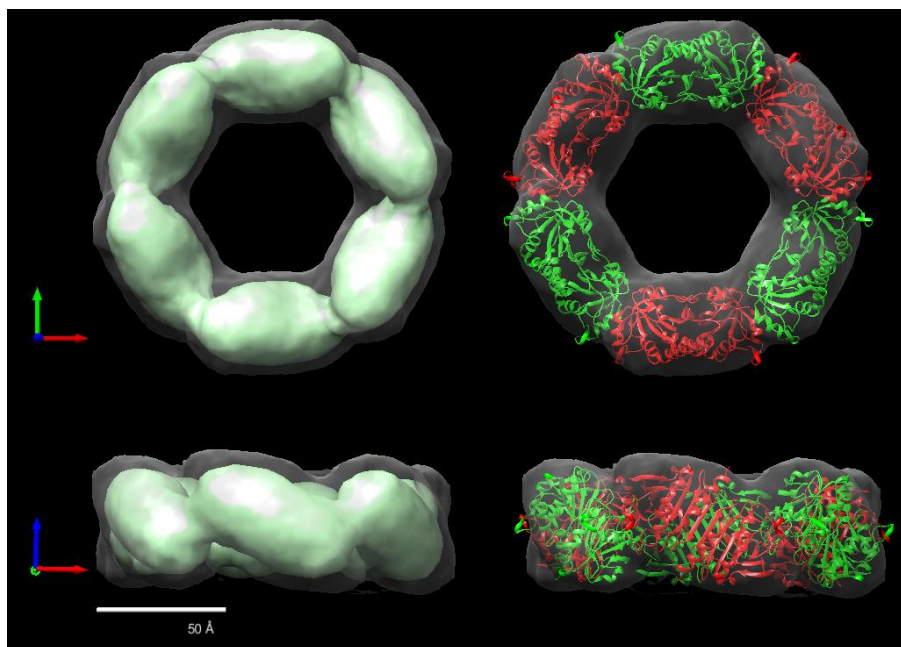


Figure 4.10: 3D reconstructions from *HsPrx3* TEM data show a dodecameric toroid

A 26 Å 3D reconstruction was generated by single-particle analysis with imposed D6 symmetry and contoured with a threshold of 5.5 (green) and 2 (transparent grey) sigma (left column). The model is consistent with the crystal structure of a dodecameric Prx (PDB ID: 1ZYE; Cao *et al.*, 2005), as evidenced by a good fit upon docking with the crystal structure (which gave a density cross-correlation coefficient of 0.94; right column). Scale bar is 50 Å.

The results described above confirm that the oligomer formed by *HsPrx3* is in a dodecameric arrangement, resolving a discrepancy in the previous literature (Gourlay *et al.*, 2003; Cao *et al.*, 2005). TEM micrographs showed uniform toroidal particles; however, close inspection did reveal the presence of irregular toroids, some appearing slightly distorted, or with varying diameters. Exact quantification or measurement of these particles is difficult due to the potential for flattening of particles caused by

staining, therefore cryo-electron microscopy (cryo-EM) was carried out to provide insight into the possibility of toroids with differing dimension, without the influence of grid interactions and any stain-induced. Preliminary 3D models were generated from micrographs of frozen hydrated samples following the procedures described in 4.3.1.1. Grid preparation, recording of TEM images and initial processing of cryo-EM samples was carried out by Dr Mazdak Radjainia at the University of Auckland. The refinement resulted in two models with notably different conformations. Although these represent very coarse models, differences appearing to be a movement of the subunits and an increased inner diameter can be seen (figure 4.11). This would support the suggestion that *HsPrx3* toroids may vary in their dimensions, which has been previously proposed (Harris, 1971; Hall *et al.*, 2011), but until now no experimental evidence was available. Work is ongoing to confirm this initial finding.



Figure 4.11: Cryo-EM supported the hypothesis of open and closed toroids

The presence of toroids with different dimensions was suggested by cryo-EM 3D model reconstruction. Refinement resulted in two models. One was comparable with the reconstruction produced from negative stain EM (left), whilst the other (middle) appeared to represent an expanded toroid with an increased inner diameter. Exact measurements are difficult at this stage but these early models are a promising start to confirming the presence of distinct toroidal conformations. Docking the models (right) clearly shows the difference in toroid internal diameter.

4.3.1.2 Influence of redox state on quaternary structure

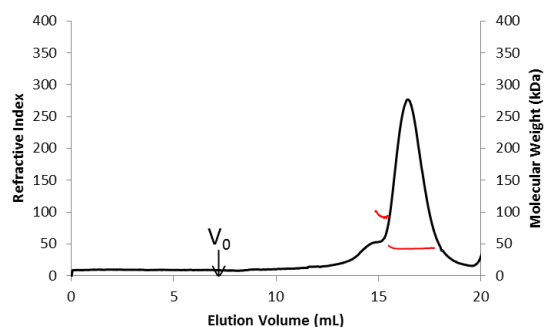
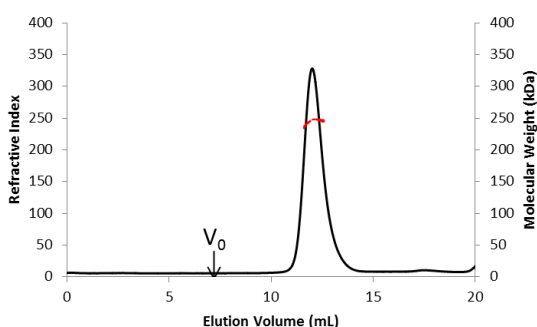
Redox conditions are the most well-reported environmental factor to affect Prx assembly (reviewed in Barranco-Medina *et al.*, 2009). The presence of an intermolecular disulfide bond destabilises the oligomer interface (see section 1.2.5.3), therefore the formation or reduction of this bond influences the propensity of assembly. Being a typical 2-Cys Prx, *HsPrx3* has been assumed to exist in an equilibrium which shifts to favour a dimeric species in oxidising conditions, and the larger oligomer in reducing conditions (Cox *et al.*, 2010).

Size Exclusion Chromatography/Static Light Scattering

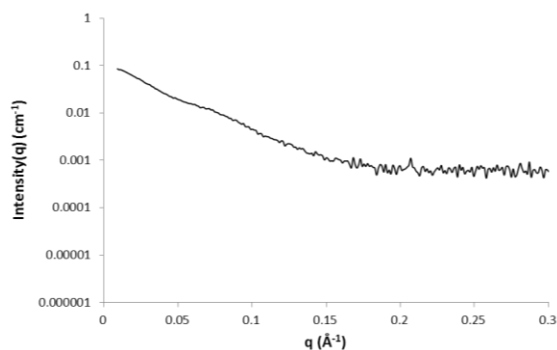
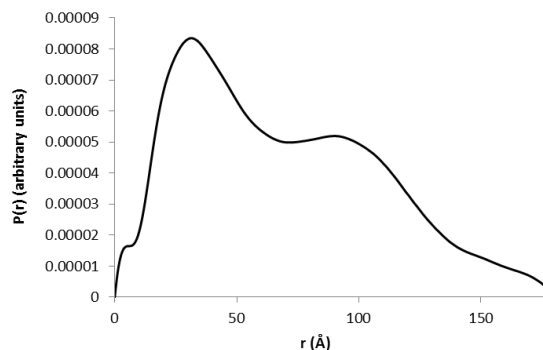
SEC/SLS data were collected under non-reducing conditions (figure 4.12A). In these conditions the elution profile of *HsPrx3* was significantly shifted compared to that previously collected in reducing conditions (figure 4.12B; section 4.3.1.1), with one major peak indicating that *HsPrx3* exists almost completely as a single, small species. This peak was calculated to represent a 42 kDa particle, consistent with the predicted dimer. A small shoulder was seen, suggesting that there may be some larger particles present, with calculations resulting in a weight of around 100 kDa. This suggests a tetramer, which has not previously been reported for *HsPrx3*.

Small Angle X-ray Scattering

In non-reducing conditions, the SAXS data were significantly different to the reduced sample, consistent with the change seen in SEC/SLS results. The scattering profile showed a smoother curve, suggesting a more elongated particle (figure 4.13). The slower rate of decrease of scattering intensity seen at low q values suggests a smaller average R_G . (Svergun and Koch, 2003; appendix one). Molecular weight calculations were not conclusive, with particle size showing a concentration dependence which was not seen in reducing conditions (table 4.3).

A: Non-reducing conditions**B: Reducing conditions****Figure 4.12: Redox conditions significantly affect the oligomeric state of *HsPrx3***

A: *HsPrx3* in non-reducing conditions elutes primarily as a single species, with a molecular weight consistent with a dimer. The peak shows a slight shoulder indicating the presence of a small amount of larger species ~100 kDa. **B:** Under reducing conditions *HsPrx3* exists as a large assembly, calculated to be 249 kDa. A slight deviation from the baseline is seen around 17 mL, possibly suggesting very small amounts of free dimer may remain in solution. Red lines show molecular weights across the peaks.

A: Scattering curve**B: $P(r)$ plot****Figure 4.13: X-ray scattering profiles indicate different structures in response to redox changes**

The scattering profile of non-reduced *HsPrx3* at 1 mg/mL shows a gradual fall in scattering intensity, suggesting an average smaller particle than the reduced sample. **B:** The shifted $P(r)$ plot to favour lower r values indicates that small species dominate, although the second maximum reveals larger assemblies are still present.

Table 4.3: The oligomeric state of non-reduced *HsPrx3* is sensitive to concentration

Calculated weights suggest that non-reduced *HsPrx3* exists in equilibrium between the dodecameric and dimeric species, favouring the dimer. The proportion of species is concentration dependent.

		D_{max} (Å)	R_G from Guinier (Å)	R_G from GNOM (Å)	Volume (Å ³)	MW (kDa)
Reduced <i>HsPrx3</i>	0.5 mg/mL	170	59	59	417000	254
	1 mg/mL	178	59	59	417000	255
	2 mg/mL	175	60	58	415000	256
Non-reduced <i>HsPrx3</i>	0.5 mg/mL	165	54	51	146000	89
	1 mg/mL	179	56	56	179000	108
	2 mg/mL	176	57	57	210000	127
Dimer	PDB ID: 1ZYE	~ 60	Theoretical R_G : 20		49800	43
Decamer	PDB ID: 1QMV	~ 135	Theoretical R_G : 47		393000	214
Dodecamer	PDB ID: 1ZYE	~ 155	Theoretical R_G : 55		441000	257

This is in line with previous groups findings on other members of the Prx family, suggesting the non-reduced state to be heterogeneous and concentration dependent (Wood *et al.*, 2002). The dimeric species seen in SEC/SLS was not able to be distinguished, with scattering data at the lowest concentration (0.5 mg/mL) yielding a molecular weight of 89 kDa. The $P(r)$ plot showed two maxima at the same positions as the reduced sample, but skewed toward lower r values (figure 4.13B). This indicates that some oligomers were present, but made up a smaller proportion of the population. As SAXS data yield a solution average (Mertens and Svergun, 2010), this value is likely due to the presence of multiple species in solution, thus agreeing with the SEC/SLS data (figure 4.12A).

The SAXS data confirm that *HsPrx3* quaternary structure changes dramatically in response to redox conditions. Together with SEC/SLS these results show that *HsPrx3* exists in a dynamic equilibrium between a dodecamer, a tetramer, and a dimer; particular conditions favouring one state without eliminating the others. Consistent with

the literature on other Prxs (reviewed in Wood *et al.*, 2003; Barranco-Medini *et al.*, 2009; Schröder *et al.*, 2000), the oligomer was favoured in reducing conditions, and the equilibrium shifted to favour the dimeric species when reducing agents are present. The appearance of a 100 kDa species suggesting the presence of a tetramer has not previously been seen in the case of *HsPrx3*. This could give insight into the assembly mechanism of the dodecamer, possibly indicating a modular mechanism whereby dimers firstly assemble into tetramers, which then associate further to form the toroid. Very recently the presence of a tetramer was noted in mutated constructs of an *A. thaliana* 2-Cys Prx (PrxA; König *et al.*, 2013). Two mutants were reported to form this intermediate, which was explained to occur through an increased predisposition to hyperoxidation. The tetramer of non-reduced *HsPrx3* preparations may therefore represent associated hyperoxidation-sensitive dimers, which are not seen once the protein is reduced.

4.3.1.3 Influence of the N-terminal his-tag on quaternary structure

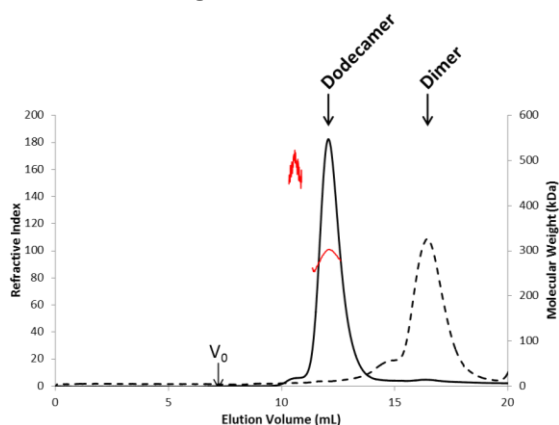
The use of a his-tag for purification is often considered to have no effect on protein structure (Chant *et al.*, 2005), due to its small size and lack of charge (Li *et al.*, 2010; the pK_a of histidine is 6.0 [Dawson *et al.*, 1969], which means that at physiological pH it is mostly deprotonated and uncharged). However, it has been shown that the use of a his-tag can in some cases influence protein structure or activity (Carson *et al.*, 2007). In the case of Prxs it can have a dramatic effect on their quaternary structure, seemingly stabilising the toroidal oligomer (Cao *et al.*, 2007; chapter three). Care must be taken when comparing previous data, such as the apparent conflicting results regarding the link between ionic strength and Prx assembly – one group investigating this relationship in *Helicobacter pylori* AhpC found that high ionic strength stabilised the decamer (Papinutto *et al.*, 2005), while another group found it encouraged dissociation of the *M. tuberculosis* homologue. (Chauhan and Mande, 2001). It is possible that slight differences in sequence may cause this discrepancy, but it should be noted that one

group (Papinutto *et al.*, 2005) studied the native form of the protein, while Chauhan and Mande used a his-tagged variant.

Size Exclusion Chromatography/Static Light Scattering

When his-tag cleavage was not carried out, non-reduced *HsPrx3* existed almost exclusively as a dodecameric species (figure 4.14A). As well as the strong shift toward the dodecameric species, a small shoulder is seen indicating a HMW species (figure 4.14A). This peak was calculated to represent a ~470 kDa particle. This does not agree with theoretical weights for more than one associated dodecamer. Calculations yield an average of the species eluting at that point, and the varying weight across this peak indicates that a mixture of species is present in rapid equilibrium, therefore, the number of single dodecamers is fluctuating.

A: Non-reducing conditions



B: Reducing conditions

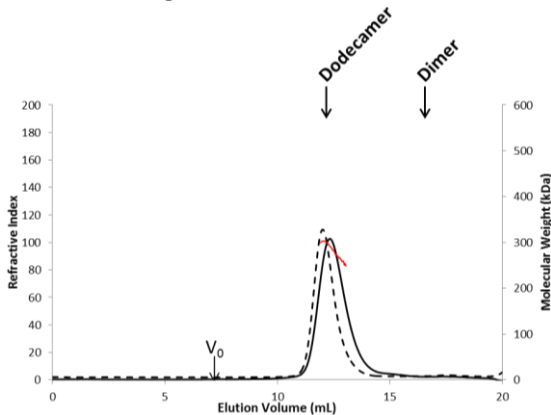


Figure 4.14: An N-terminal his-tag stabilises the dodecameric oligomer of *HsPrx3*

A: In non-reducing conditions, his-tagged *HsPrx3* exists almost completely as a 291 kDa species, consistent with a tagged dodecamer (302 kDa). A small peak indicative of a ~470 kDa species is present. **B:** In reducing conditions the HMW species is not present, with the protein existing as a dodecamer. Although calculated to represent equivalent sized species, the elution volume of the dodecamer peaks are shifted slightly. This could be due to the compaction of the toroid in reducing conditions (further discussed in section 4.4).

In reducing conditions, the peak representing the HMW is not seen, and the RI trace is similar to that of reduced, untagged *HsPrx3* in these conditions. Although the single peak seen in the reduced sample, and the main peak of the non-reduced sample were both calculated to represent a dodecameric species, the elution volume was slightly shifted. This could be due to the compaction of the toroid in reducing conditions (further discussed in section 4.4); a theory which is supported by comparing the calculated R_h , which suggested particle diameters of 10 nm and 13 nm for the reduced and non-reducing samples respectively. Although this does not agree well with the expected diameter of a dodecamer (15 nm), this presented an interesting possibility which would benefit from further examination.

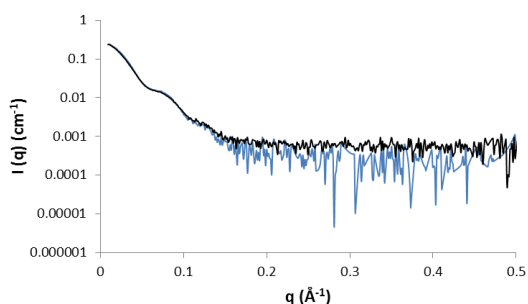
Small Angle X-ray Scattering

Under both reducing and non-reducing conditions, scattering profiles of tagged *HsPrx3* exhibited very similar traces (figure 4.15A), consistent with the toroid seen in untagged samples, indicated by the oscillating scattering profile (Mertens and Svergun, 2010). In non-reducing conditions, molecular weight was ~330 kDa, consistent with the dominant species being the dodecameric oligomer. This did not appear to be concentration dependent within the range tested, as indicated by molecular weight calculations and superposition of scaled scattering curves (table 4.4; figure 4.15B). Although the presence of the ~470 kDa species observed in the SEC/SLS experiments was not seen in the SAXS data, the molecular weight calculations were slightly higher than that expected for a tagged dodecamer (302 kDa) consistent with the presence of small amounts of larger species. To address this issue, SAXS data were also collected from his-tagged samples run through an in-line FPLC column, to separate any larger species (section 2.3.5.7). Calculations carried out on scattering data collected at the apex of the gel filtration peak gave a molecular weight of 297 kDa, confirming that the previous calculations were indeed influenced by the presence of larger assemblies. These assemblies were not seen as discrete species through analysis of scattering data, which

is to be expected as SEC/SLS indicated that at 1 mg/mL these species represented less than 1% of the total population (section 4.3.1.5).

In line with SEC/SLS data, when tagged *HsPrx3* was analysed in reducing conditions the amount of HMW species decreased, indicated by the lower average molecular weight (table 4.4). Together these results demonstrate that the presence of an N-terminal his-tag strongly influences the quaternary structure of *HsPrx3*, in line with the results of Cao *et al.*, (2007). As the scattering profile and molecular weight are consistent with the dominant species being the dodecameric toroid, this suggests that the his-tag stabilises a native arrangement, rather than causing random aggregation. Although there is a clear stabilising effect on the dodecamer, the redox state of C_P still contributes to the assembly of HMW species, highlighting the importance of this residue in *HsPrx3* quaternary structure.

A: Altered redox conditions



B: Altered protein concentration

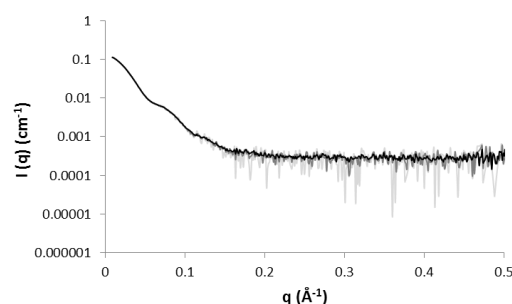


Figure 4.15: Scattering data for his-tagged *HsPrx3* appears unchanged by redox conditions

A: In non-reducing conditions (black line) the scattering profile suggests a multi-domain particle. In reducing conditions (blue line) the scattering profile is largely unchanged, indicating that the toroidal structure is the predominant species in both conditions. **B:** Overlaid scaled scattering curves generated from data collected at (light grey line) 0.5 mg/mL, (dark grey line) 1 mg/mL, and (black line) 2 mg/mL showed that the oligomeric state was not concentration dependent within this range.

Table 4.4: Molecular weights and dimensions from SAXS show tagged *HsPrx3* is a constitutive dodecamer

In reducing conditions molecular weight calculations of *HsPrx3* suggest a dodecameric species which is not concentration dependent. In non-reducing conditions tagged *HsPrx3* shows a shift in weight. Comparison with SEC/SLS results suggest this is due to the presence of small amounts of larger species.

		D_{\max} (Å)	R_G from Guinier (Å)	R_G from GNOM (Å)	Volume (Å ³)	MW (kDa)
Reduced	0.5 mg/mL	179	57	57	485000	301
His₆-<i>HsPrx3</i>	1 mg/mL	192	57	56	502000	311
	2 mg/mL	181	56	56	487000	302
Non-reduced	0.5 mg/mL	202	59	60	552000	321
His₆-<i>HsPrx3</i>	1 mg/mL	206	60	60	526000	323
	2 mg/mL	203	59	60	534000	326
Tagged dimer	PDB ID: 1ZYE	60	Theoretical R_G : 20		49800	50
Tagged decamer	PDB ID: 1QMV	136	Theoretical R_G : 47		393000	252
Tagged dodecamer	PDB ID: 1ZYE	154	Theoretical R_G : 55		441000	302

It was considered that the stabilisation of the dodecamer may be due to the his-tags binding to metal ions after IMAC purification. To further investigate the nature of this stabilisation, his-tagged samples were analysed after chelation of metal ions by dialysis into running buffer with the addition of 2 mM EDTA (section 2.1.8.2). Subsequently, the buffer was exchanged for standard running buffer to remove EDTA. In these conditions his-tagged *HsPrx3* existed almost completely as a dimeric species (figure 4.16A). When this sample was subjected to reducing conditions, the shift to favour the dodecameric species was not seen, indicating that the construct is not sensitive to redox conditions (figure 4.16B). A small peak around the elution volume of the untagged tetramer was seen, however the molecular weight calculations for this peak were noisy and inconclusive. When untagged *HsPrx3* is transferred to an EDTA containing buffer, normal behaviour is seen (data not shown).

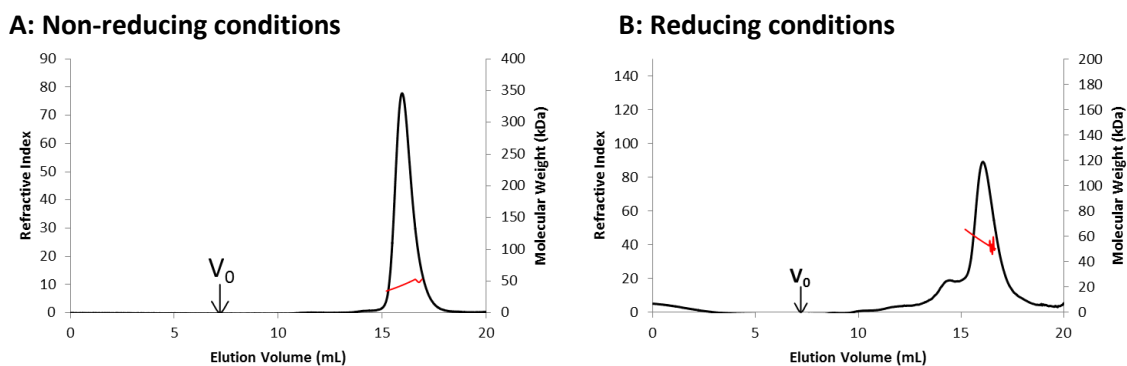


Figure 4.16: EDTA caused the dissociation of his-tagged toroids

A: His-tagged *HsPrx3* ran as a dimeric species when analysed in standard running buffer, after chelation of metal ions. Molecular weight calculations suggested a 52 kDa species, consistent with a dimer. **B:** After chelation of metal ions, the his-tagged construct was insensitive to redox conditions, remaining dimeric in reducing conditions.

As histidine residues are thought to associate to nickel ions in a 1:6 ratio (Valenti *et al.*, 2006), therefore, one nickel ion per hexa-histidine tag, it was considered that addition of equimolar Ni_2Cl to previously chelated his-tagged *HsPrx3* could switch the protein to a dodecameric state. However, direct addition of nickel into the sample caused localised aggregation, and the use of dialysis made it difficult to control the total ion concentration *HsPrx3* was exposed to. Initial results using dialysis showed a shift toward HMW species, but these were very heterogeneous and prone to aggregation. Although further optimisation would be required to find conditions in which assembly of the dodecamer can be activated without the formation of larger assemblies, these results are a promising start towards controllable, triggered assembly of *HsPrx3* subunits. The possibility of controlling *HsPrx3* subunit assembly is further explored in chapters five and six.

4.3.1.4 Influence of solution pH on quaternary structure

HsPrx3 is a mitochondrial enzyme – an environment in which many processes, including membrane transport and ATP synthesis, are suggested to be controlled by changes in matrix pH (Akhmedov *et al.*, 2010; Palmieri., 2004). Given this environment, and its involvement in cellular processes such as apoptosis which involve pH changes (Chang *et al.*, 2004), the effects of solution pH on *HsPrx3* assembly were investigated. The mitochondrial matrix is estimated to be pH 7.8 (Porcelli *et al.*, 2005). During apoptosis the matrix is acidified to around 7.3 (Lagadic-Gossman *et al.*, 2004; Takahashi *et al.*, 2004). Therefore, solutions with pH levels around these values were investigated to study changes in oligomeric structure that may be physiologically relevant. Extreme pH changes were found to lead to interesting, possibly non-native arrangements, and are described in chapter six.

When the untagged sample was dialysed into a neutral pH buffer (pH 7.0), the quaternary structure of *HsPrx3* assembly was markedly changed. In non-reducing conditions a major peak indicating a dodecameric species was seen (figure 4.17A). A small peak suggesting the presence of some tetrameric species was observed, although no dimeric species were present. The broad nature of this peak, and calculations resulting in a weight of 277 kDa, suggested that some larger assemblies of dodecamers were present, but were rapidly forming and dissociating and therefore not resolved. At pH 7.5 the size of the tetramer peak increased, accounting for a significant portion of the population (figure 4.17B). The dodecamer still predominates, with no indication of HMW species seen in the RI trace.

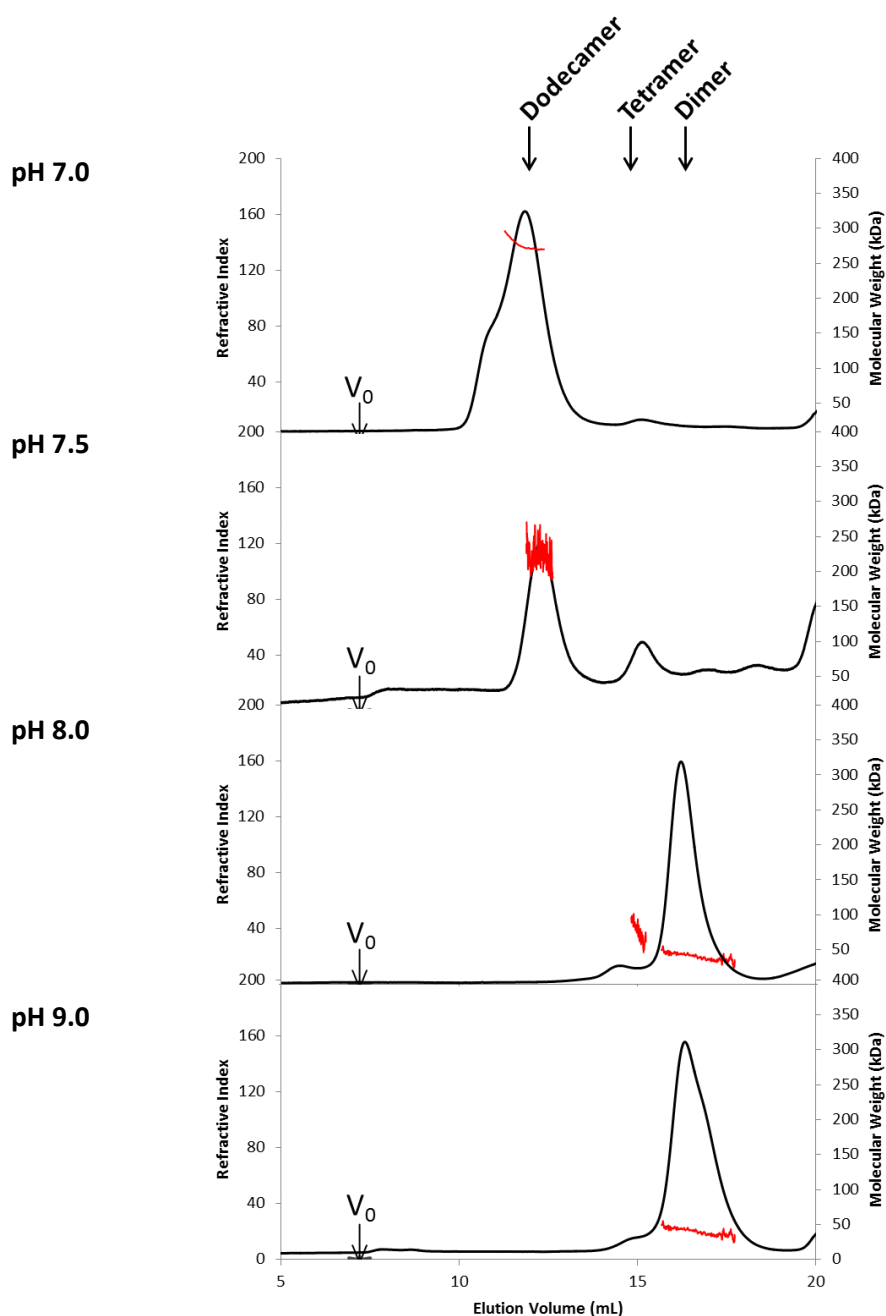


Figure 4.17: pH changes significantly affect *HsPrx3* oligomerisation

Traces recorded at **A:** pH 7.0; **B:** pH 7.5; **C:** pH 8.0; **D:** pH 9.0. In non-reducing conditions, high pH (9.0) favours dissociation of the dodecamer, whereas low pH (7.0) stabilises the dodecamer, with no redox sensitivity seen at either pH. Red lines show molecular weights across the peaks.

At higher pH (pH 9.0) in non-reducing conditions, one major peak was observed, representing a 45 kDa species, with no indication of the presence of dodecameric species (figure 4.17D). The peak showed some differences to the dimer peak seen at pH 8.0 – specifically, a broadening to shift the peak toward later elution volumes, possibly due to dissociation of the dimers occurring. Some 1-Cys Prxs have been seen to be stable in alkaline conditions (Wen *et al.*, 2007), however this has not been tested in the case of dimeric Prxs; these results suggest that high pH may disrupt the usually stable B-type dimer interface. A small peak representing a ~100 kDa species was also seen, although this was less prominent than that at pH 8.0. Further analysis at smaller pH intervals would be useful to investigate the point at which the equilibrium shifts.

4.3.1.5 Influence of protein concentration on quaternary structure

In the case of Prxs, it has been seen that in oxidising conditions oligomer formation is sensitive to concentration, with this factor being able to override the redox response and force self-assembly to occur (Wood *et al.*, 2002), and may have influenced some of the conformations seen in crystal structures. For example, mutated Prxs generated by Parsonage *et al.*, (2005) were seen to form decameric arrangements in the crystal structure, but remained dimeric up to concentrations of 480 μ M in solution. Similarly, the octamer of *MtAhpE* seen in the crystal structure has been opined to be an artefact of high concentration (Karplus and Hall, in Flohé and Harris., 2007). The influence of this factor was therefore determined in the case of the solution state of *HsPrx3*, through examining the effect of varying protein concentration on the dimer-dodecamer equilibrium of *HsPrx3* in non-reducing conditions. Following the observation that *HsPrx3* dodecamers may be able to associate further to HMW species (section 4.3.1.3) the stabilised, his-tagged dodecamers were also investigated at high concentrations.

Size Exclusion Chromatography/Static Light Scattering

SEC/SLS was used to investigate the effect of concentration on *HsPrx3* assembly, as other solution techniques cannot be used at high concentrations. SAXS data was collected at a range of concentrations from 0.5 – 2 mg/mL, beyond these concentrations data collection was not possible due to protein burning onto the capillary. Within this range the oligomeric state of both tagged and untagged *HsPrx3* did not appear to be sensitive to concentration in reducing conditions. Untagged *HsPrx3* showed some change in oligomeric state within this range when conditions were non-reducing (section 4.3.1.2; table 4.3). Therefore, this was the first state to be studied at higher concentrations. SEC/SLS experiments were carried out using protein concentrations of up to 5 mg/mL. At increasing protein concentrations the relative size of the peak representing the tetramer increased, and at 5 mg/mL a small peak corresponding to the dodecamer was seen (figure 4.18A).

To investigate the possibility to drive the formation of HMW species in high protein concentrations, SEC/SLS was carried out using samples of his-tagged *HsPrx3* at concentrations up to 5 mg/mL. At increased concentrations the size of the peak pertaining to these HMW structures did increase (figure 4.18B), as did the calculated molecular weight. At 5 mg/mL calculations suggested a 726 kDa species (compared to 470 kDa calculated from 1 mg/mL (section 4.3.1.3; figure 4.14A), indicating that at this concentration larger associations of dodecamers were forming. The molecular weight across the peak was noisy, likely due to the low signal, meaning that although molecular weight calculations can be taken as an indication, firm conclusions of oligomer size cannot be drawn.

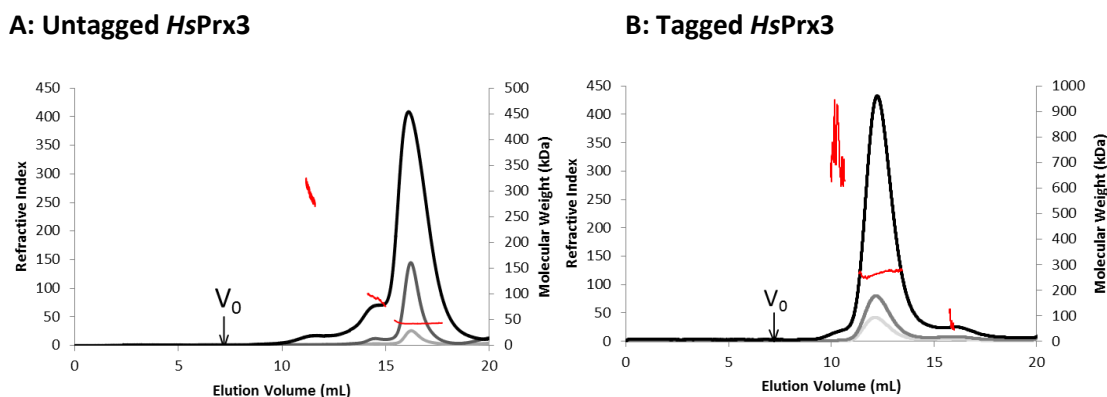


Figure 4.18: Oligomeric state of non-reduced *HsPrx3* shows concentration dependence

A: Untagged *HsPrx3* exists mainly as a dimer at 1 mg/mL (light grey). At increasing protein concentrations (2 mg/mL – dark grey), the appearance of a ~100 kDa species is seen. At the highest concentration studied (5 mg/mL – black) a small amount of dodecameric oligomer is seen. **B:** His-tagged *HsPrx3* exists primarily as a dodecamer, with small amounts of HMW species seen as the concentration increases. Molecular weight across the peak (red line) is not constant, suggesting these species are rapidly forming and dissociating.

Table 4.5: Relative proportions of oligomeric species in non-reducing conditions at various concentrations

Numbers indicate percentage of total population, as judged by RI peak areas. Untagged *HsPrx3* favours the dimer in non-reducing conditions, with the dodecamer seen as a discrete species at high concentration (5 mg/mL). Tagged protein exists primarily as a dodecamer, the appearance of a HMW species not seen in untagged samples is noted above 1 mg/mL. Samples were run in triplicate, errors indicate the variation.

Sample	Concentration	HMW species	Dodecamer	Dimer
His-tagged	0.5 mg/mL		89 ±1	11 ±1
	1 mg/mL	1 ±1	92 ±2	7 ±3
	5 mg/mL	1 ±1	96 ±1	3 ±2
Untagged	0.5 mg/mL		4 ±2	96 ±2
	1 mg/mL		10±3	90±3
	5 mg/mL	3±1	9±1	88±2

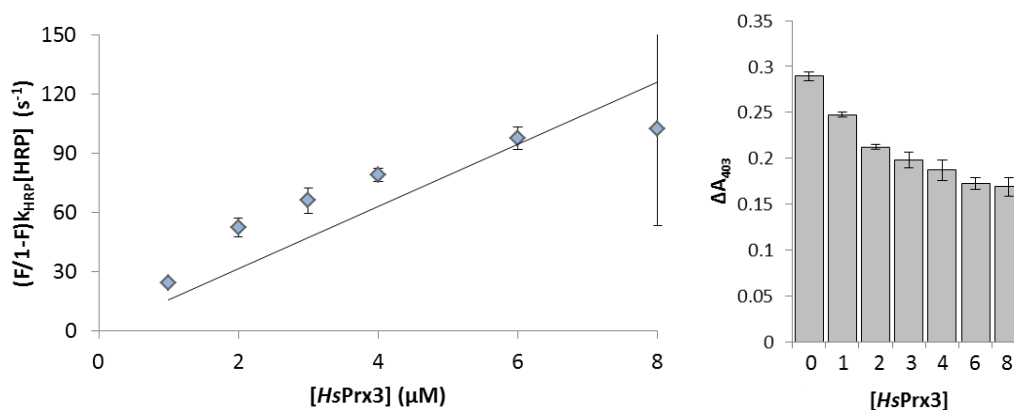
4.3.2 Peroxidase activity of *HsPrx3*

The relative activity of *HsPrx3* and variants was determined through a competitive assay using a method developed by Dr Alexander Peskin (University of Otago, Christchurch), based on that of Ogusucu *et al.* (2007). The protocol was optimised in house for *HsPrx3* analysis by N. Amy Yewdall (Yewdall, 2013, unpublished data). The assay relies on the peroxidase activity of horse radish peroxidase (HRP), which breaks down H_2O_2 at a rate of $1.78 \times 10^7 \text{ M}^{-1} \text{ s}^{-1}$ (Dolman *et al.*, 1975) – a comparable rate to that of the Prxs, which are generally in the order of $10^7 \text{ M}^{-1} \text{ s}^{-1}$ (Poole, in Flohé *et al.*, 2007). HRP contains a haem cofactor in the active site, which absorbs at 403 nm. Catalysis leads to the production of Compound I due to oxidation of haem, with a concomitant decrease in absorbance at 403 nm (Dunford, 1999). This decrease is inhibited by the addition of Prx, as it competes with HRP to react with H_2O_2 . The inhibition of the decrease in absorbance at 403 nm can be used to calculate the apparent second-order rate constant of the Prx (section 2.6.1; Ogusucu *et al.*, 2007). Prx rate constants determined from this assay have been seen to agree with those obtained from pseudo-first order approach (Nelson *et al.*, 2008). Therefore, the values can be considered an accurate representation of the protein's activity. Although a direct rate is not measured, the assay can be used to give valuable information about the relative activities of *HsPrx3* variants. As the assay was carried out at concentrations of $\sim 0.2 \text{ mg/mL}$, the activity cannot be directly related to the quaternary structure, as structural analysis was not carried out at this concentration. However, the relative activity can be compared to the observed shift in oligomeric equilibrium, giving an indication of how an increased propensity for assembly or disassembly affects protein activity.

The activity of pure samples of *HsPrx3* was assayed, with and without the his-tag. The untagged protein was found to react with H_2O_2 at a rate of $1.6 \times 10^7 \text{ M}^{-1} \text{ s}^{-1}$. This is in line with other groups' results, who suggest *HsPrx3* reacts with a rate of $2 \times 10^7 \text{ M}^{-1} \text{ s}^{-1}$.

When the his-tag was attached the relative activity was significantly reduced, reacting at a rate of $4.6 \times 10^6 \text{ M}^{-1} \text{ s}^{-1}$. This is just over a two-fold decrease in activity – in line with results obtained for *BtPrx3*, which suggested a three-fold decrease in activity when the his-tag was attached (Cao *et al.*, 2007).

A: Untagged *HsPrx3*



B: Tagged *HsPrx3*

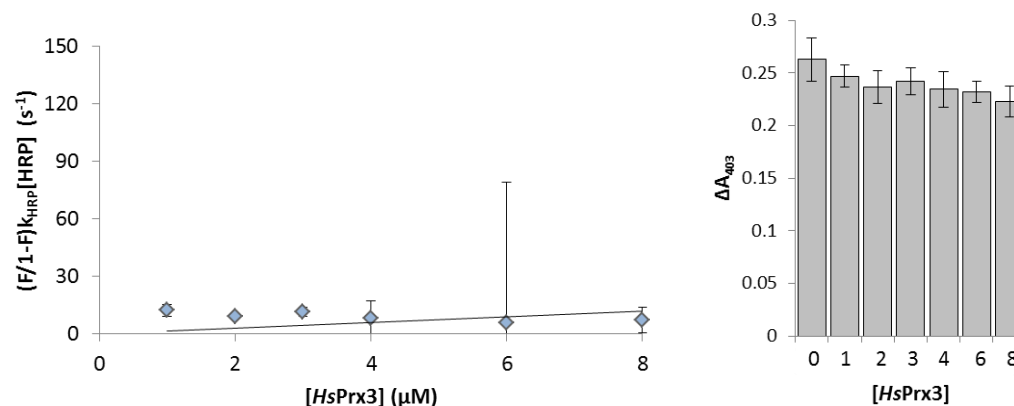


Figure 4.19: Tagged *HsPrx3* showed lower activity than the untagged construct

A: The untagged construct reacted with a relative activity of $1.6 \times 10^7 \text{ M}^{-1} \text{ s}^{-1}$. **B:** The tagged construct reacted at $4.6 \times 10^6 \text{ M}^{-1} \text{ s}^{-1}$. Bar graphs show the formation of Compound I in the presence of the specified *HsPrx3* concentrations.

4.3.3 Crystallisation

Solving the crystal structure would enable comparison of the arrangement of the subunits within the toroid, establishing whether the his-tags are simply coordinating to the metal ions, or inducing a conformational change which may encourage dimer-dimer interactions to occur. To investigate the nature of the stabilising effect of the his-tag, reduced, cleaved *HsPrx3* and non-reduced his-tagged protein were subjected to crystallisation trials.

Previous groups had been unsuccessful in their efforts to crystallise the wildtype Bovine Prx3, obtaining only microcrystals (Cao *et al.*, 2005). Similarly, crystallisation screening of *HsPrx3* did not provide crystals suitable for diffraction. Promising results were achieved in the initial screen, with crystalline precipitation seen and crystals forming in three conditions (figure 4.20). Where crystals were seen, the morphology was exclusively clusters of needles, and appeared to favour PEG based conditions, growing in around 7 days (table 4.6). Fine screens were set out around all conditions in which crystals were seen for both tagged and untagged *HsPrx3* (section 2.5.6.1). The needle-like crystals seen in the initial screens were not reproducible in the hanging drop vapour diffusion method (section 2.5.6.2); and so crystallisation efforts are ongoing.

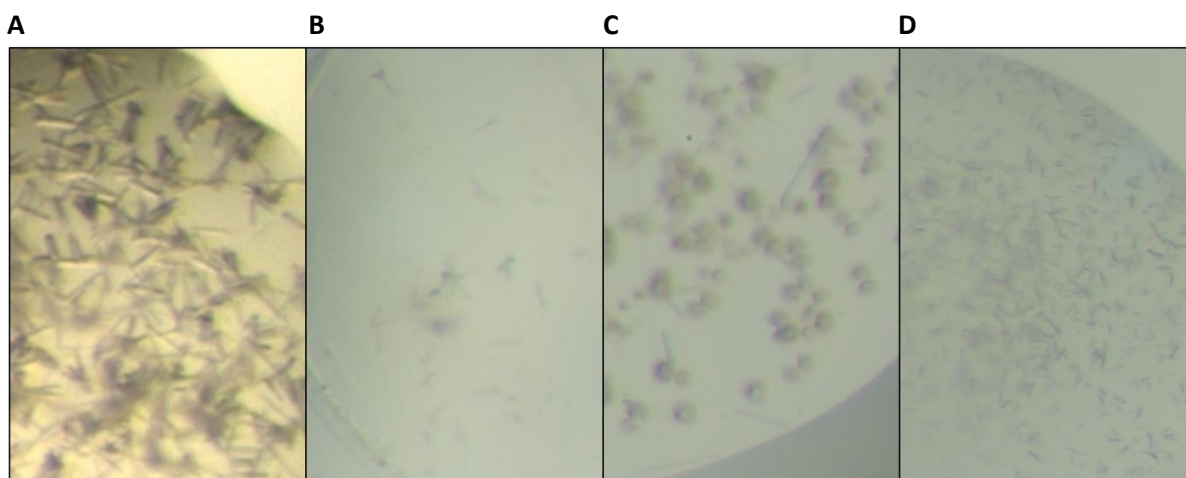


Figure 4.20: Needle-like crystals of *HsPrx3* were seen in initial screens

A: Clusters of needles were seen in his-tagged *HsPrx3* screens. **B, C, D:** Untagged *HsPrx3* yielded small needles, spherulites and clusters of needles. Details of crystallisation conditions are given in table 4.6 below.

Table 4.6: Positive crystallisation conditions

His-tagged and untagged *HsPrx3* formed needle-like crystals in PEG-based and alcohol screens. The alcohol mix used in the Morpheus screen was composed of: 0.2 M 1,6-hexanediol, 0.2 M 1-butanol, 0.2 M (RS)-1,2-propanediol, 0.2 M 2-propanol, 0.2 M 1,4-butanediol, 0.2 M 1,3-propanediol. Samples are lettered corresponding to figure 4.13.

Sample	Conditions	Observations
A (His-tagged <i>HsPrx3</i>)	20% w/v PEG 1500, 0.15 M KSCN, 0.1 M Tris, pH 7.5	Needles
B (Untagged <i>HsPrx3</i>)	20% 2 methyl 2,4 pentanediol, 0.1 M AMP/HCL, pH 9.7	Small clusters of needles
C (Untagged <i>HsPrx3</i>)	10% w/v PEG 4000, 20% v/v glycerol, 0.02 M alcohol mix, 0.1 M MES/imidazole, pH 6.5	Spherulites and small needles
D (Untagged <i>HsPrx3</i>)	10 % w/v PEG 8000, 20% v/v ethylene glycol, 0.02 M alcohol mix, 0.1 M bicine/Trizma base pH 8.5	Fine separate needles

4.4 Discussion

Within the 2-cys Prxs, the structural differences between a decameric and dodecameric Prx are often surprisingly minor (figure 4.21), suggesting that the size of the oligomer is finely tuned and governed by subtle sequence modifications. The information presented here reveals the factors controlling the oligomeric state of *HsPrx3*, providing a firm base to unravel the mechanisms that control self-assembly, and potentially design higher order structures.

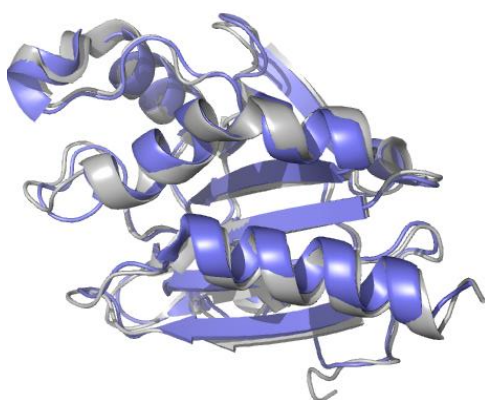


Figure 4.21: Structural comparison of a decameric and dodecameric Prx

The tertiary structure of a Prx that forms a decamer (grey; human erythrocytic thioredoxin peroxidase B [Schröder *et al.*, 2000], PDB ID: 1QMV) overlays well with that of one which forms a dodecamer (blue; bovine mitochondrial Prx3 [Cao *et al.*, 2005], PDB ID: 1ZYE). Structural variations are minor despite low sequence identity (65%), with some small differences being seen in loop regions that would be expected from intrinsic flexibility, and so provide few clues as to the factors determining oligomer size.

4.4.1 *HsPrx3* quaternary structure

The results of this study unequivocally demonstrate that the toroid of *HsPrx3* is a dodecamer. This is an unusual arrangement; only two other Prxs have been seen to adopt this conformation (Guimarães *et al.*, 2005; Cao *et al.*, 2005), both of which contain cysteine mutations. The functional implications of the differing multimeric states of Prxs are unclear. It has been suggested that large assemblies of toroids act as molecular chaperones, which may mean the size of the oligomer may be tuned to accommodate various substrates. This hypothesis is somewhat supported by the observation that the only other eukaryotic Prx seen to assume a dodecameric arrangement is also mitochondrial (Cao *et al.*, 2005). Control of the multimeric state of Prxs has been suggested to rely on minor shifts at the B-type interface (Gretes and Karplus, 2013). An interesting experiment to test this hypothesis would be to introduce mutations at the B-type interface and assess the multimeric state of new muteins.

The Prx toroid has been seen to be the dominant species when the subunits are reduced, but also when the protein is hyperoxidised (Schröder *et al.*, 2000; reviewed in Wood *et al.*, 2003). These states have been reported to be toroids with different conformations (Muthuramalingam *et al.*, 2009), with the reduced and hyperoxidised subunits forming tight and loose toroids respectively (Hall *et al.*, 2011). Despite these suggestions, there remains little insight into the existence of these conformations, with no structural data available relating to the possible variations in the toroids. During the course of this thesis, a report was published in which a mutation was introduced to the sequence of a decameric plant 2-Cys Prx (substitution of C_P with aspartic acid) to mimic the hyperoxidised state (König *et al.*, 2013), and stabilise the toroid. The solution studies detailed by the authors provided hint toward the existence of the two toroid conformations suggested by Muthuramalingam. This could explain the varying dimensions and presence of distorted toroids noted in *HsPrx3* samples (section 4.3.1.1).

The models produced in this work represent the first direct evidence to support their existence, and suggest that this conformational flexibility may be present in all Prxs, whether decameric or dodecameric. Although these are preliminary models and pronounced features are not discernible, they are a promising start to unravelling the conformational changes involved, and ongoing work is being carried out to further characterise these species. The concept that these two conformations correspond to reduced and hyperoxidised protein also suggests that hyperoxidation of protein may be occurring during the experiment. Although H_2O_2 was not present in experimental solutions, hyperoxidation has been seen to occur during purification by other groups, even when reductant was present, and could therefore be occurring in this case (Low, *et al.*, 2007). Further work is needed to clarify this; one approach could be the use of antibodies to identify the hyperoxidised form and enable further characterisation.

4.4.2 His-tag stabilisation occurs through the coordination of metal ions

His-tags have been seen to influence oligomerisation of some proteins, with the exact mechanism remaining unknown (Carson *et al.*, 2007; Chant *et al.*, 2005; Cao *et al.*, 2005). The loss of toroid stabilisation upon the addition of EDTA in the case of *HsPrx3* revealed that the effect was brought about through the association of the his-tags with metal ions. This provides a useful approach to controlling the quaternary structure of *HsPrx3*. Purified protein, once stripped of metal ions, will remain dimeric regardless of redox state. Reintroduction of these metal ions triggers the assembly of the dodecameric species, which are stable, also regardless of redox conditions. The presence of metal ions can be controlled through their addition or removal of chelating agents, thereby effectively switching the quaternary structure.

The his-tag appears to stabilise the native dodecamer, however, the nature of this stabilisation is not known. It is plausible that the his-tags coordinate to metal ions within

the lumen of the toroid. However, it is clear that the presence of the tag has a larger influence on *HsPrx3* tertiary structure, as the dimers are unable to assemble once the metal ions are removed. This is in line with the observations of the effect of the his-tag on *MtAhpE* (chapter three). Comparison of tagged and untagged crystal structures would provide insight into this, and ongoing research in the Gerrard laboratory will seek to gain further information on the nature of this interaction. These results highlight an important consideration for structural research as the his-tag is generally not thought to influence protein structure. However, in the case of the Prxs it has a significant impact on the quaternary structure. Care should also be taken when comparing published studies, as conflicting results regarding oligomerisation may be due to the presence or absence of the his-tag (one example is detailed in section 4.3.1.3).

4.4.3 *HsPrx3* dodecamer assembly is controlled by a number of factors

This work presents a thorough picture of *HsPrx3* oligomerisation and the factors that influence the process, summarised in figure 4.22. An interesting observation was the appearance in many conditions of what appeared to be a tetrameric assembly intermediate. Although this has not been previously recorded for Prxs from higher species, a ~100 kDa assembly has been seen in cross-linking experiments (Gourlay *et al.*, 2003). A step-wise mechanism for oligomer formation is hereby proposed, whereby dimers first associate into tetramers, which further associate to result in the dodecameric toroid.

Results indicate that this self-assembly is primarily controlled by redox conditions, confirming the relationship between catalysis and the oligomeric state of *HsPrx3*. However, other factors can override this regulation, suggesting that the control of *HsPrx3* quaternary structure may be more complicated than currently thought, and formation of oligomeric structures may have discrete functions beyond the typical Prx peroxidase activity.

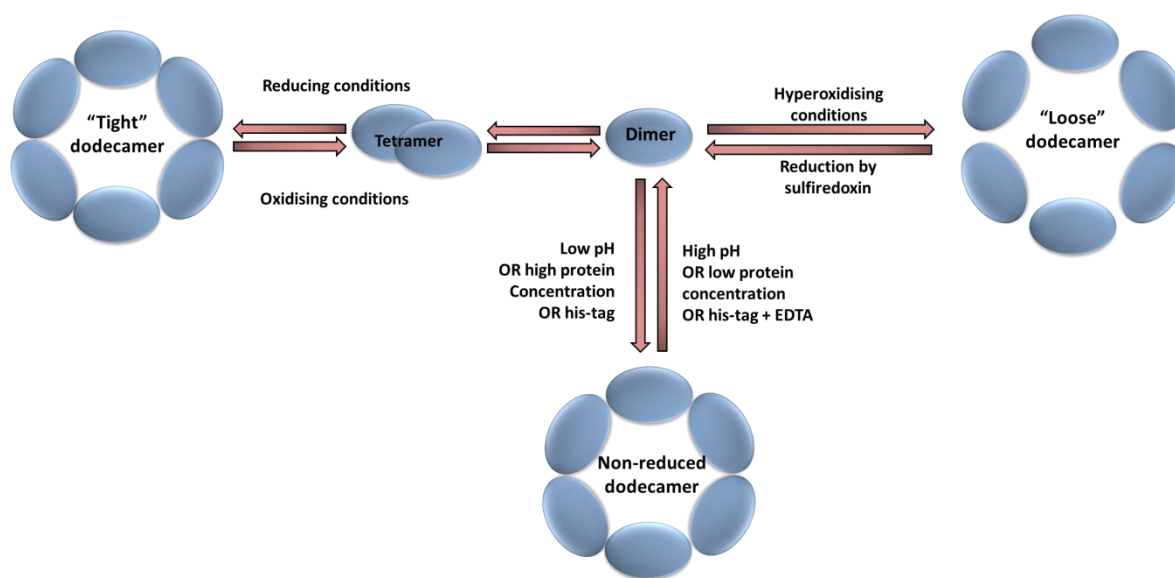


Figure 4.22: Formation of the Prx toroid is dependent on a number of factors and may involve an oligomerisation intermediate

This work found the dimer to be the predominant species in oxidising conditions, high pH, and when protein concentration was low. The presence of a tetrameric species is indicative of an oligomerisation intermediate, and it suggested here that the dodecamer assembly occurs via this intermediate. The observation of toroids with differing dimensions appears to support the suggestion that a "loose" toroid may form in certain conditions, which require further investigation. The nature of the toroid formed in response to high pH or his-tag presence is unknown. As the protein is not reduced it is possible that this conformation is different to the reduced dodecamer.

A switch in structure in response to a change in pH could indicate that the protein function is altered by local changes within the cell, and often indicates that the protein acts a sensor, or is involved in signalling pathways. For example, thylakoid lumen acidification occurs in response to light, and leads to oligomerisation of the chloroplast protease Deg1 (Kley *et al.*, 2011). This provides a mechanism of detecting potentially damaging conditions, and initiates the role of Deg1 in repairing damage caused by ROS during photosynthesis (Kapris-Pardes *et al.*, 2007). Changes in cellular pH are also an important factor in apoptosis, with mitochondrial matrix acidification associated with the early stages (Takahashi *et al.*, 2004). Unsurprisingly, the activities of many proteins involved in apoptotic pathways show pH dependence. For example, oligomerisation of the BclXL protein is driven by acidic pH – a response which is speculated to act as a

switch to activate the anti-apoptotic functions of the enzyme (Bhat *et al.*, 2012). Collapse of the mitochondrial membrane potential is another key part of apoptosis, implicating proteins involved in ion transport across the membrane in apoptosis or its prevention (Marzo *et al.*, 1998; Peng *et al.*, 2009).

The resemblance to the oligomeric behaviour of other apoptotic proteins, combined with its localisation in the mitochondria, could highlight an important physiological role of *HsPrx3* in early apoptotic signalling cascades. This has been previously suggested (Cox *et al.*, 2008; Nonn *et al.*, 2003), and the results of this study could provide clues to the mechanism behind this involvement. Acidification of the mitochondrial matrix that occurs during apoptosis is within the range investigated in this work (Takahashi *et al.*, 2004; section 4.3.1.4), and so would induce *HsPrx3* self-assembly. Oligomerisation of *HsPrx3* has been linked with membrane adhesion (Cha *et al.*, 2000), a process which has been seen in some Prxs to stimulate membrane channels and alter ion transport. This could suggest a role for *HsPrx3* in pH sensing, and the subsequent activation of ion channels in response to early apoptotic events.

Increases in local concentration can be caused *in vivo* through compartmentalisation of proteins, or binding events. For example, in the case of certain HIV structural proteins, self-assembly has been speculated to occur in response to an increase in local concentration due to RNA binding (Campbell and Vogt, 1995). In the case of *HsPrx3*, typical cellular concentrations are ~2.5 mg/mL (Cox *et al.*, 2009). As concentration did not have a significant effect up to 5 mg/mL, it is unlikely that this effect is relevant *in vivo*, with factors such as redox state playing a much larger role in controlling *HsPrx3* oligomerisation.

The appearance of HMW species formed through further association of dodecamers was seen in some conditions, most notably when his-tagged protein was studied at high concentrations. HMW species have been recorded in samples of other Prxs (Moon *et al.*, 2005; Jang *et al.*, 2004; Saccoccia *et al.*, 2012) with a concomitant switch in activity

suggested. Although it had been seen to stabilise the dodecamer in a homologous Prx, the his-tag had not previously been seen to encourage HMW species formation (Cao *et al.*, 2007). The appearance of these species of *HsPrx3* could indicate the protein has functions beyond peroxidase activity, which are activated through changes in oligomeric state. As well as providing insight into the complex physiological role that Prxs play, deeper understanding of these HMW species and the factors that govern their formation could enable the design of mutations or engineered structures with increased propensity to form higher order structures. The mechanisms behind formation of these structures and their possibly relevance *in vivo* are further examined in chapter five and six.

4.5 References

- Akhmedov, D., Braun, M., Matak, C., Park, K. S., Pozzan, T., Schoonjans, K., Rorsman, P., Wollheim, C. B. and, Wiederkehr, A. (2010) Mitochondrial matrix pH controls oxidative phosphorylation and metabolism-secretion coupling in INS-1E clonal beta cells. *Journal of the Federation of American Societies for Experimental Biology* **24**, 4613–4626.
- Barranco-Medina, S., Lázaro, J.-J. and Dietz, K.-J. (2009) The oligomeric conformation of peroxiredoxins links redox state to function. *Federation of European Biochemical Societies Letters* **583**, 1809-1816.
- Bhat, V., Kurouski, D., Olenick, M. B., McDonald, C. B., Mikles, D. C., Deegan, B. J., Seldeen, K. L., Lednev, I. K. and Farooq, A. (2012) Acidic pH promotes oligomerisation and membrane insertion of the BclXL apoptotic repressor. *Archives of Biochemistry and Biophysics* **528**, 32-44.
- Block, H., Maertens, B., Spriestersbach, A., Brinker, N., Kubicek, J., Fabis R., Labahn, J. and Schäfer, F. (2009) Immobilized-Metal Affinity Chromatography (IMAC): a review. *Methods in Enzymology* **436**, 439-473.
- Campbell, S. and Vogt, V. M. Self-assembly in vitro of purified CA-NC proteins from Rous sarcoma virus and human immunodeficiency virus type 1. *Journal of Virology* **69**, 6487-6497.
- Cao, Z., Roszak, A. W., Gourlay, L. J., Lindsay, J. G. and Isaacs, N. W. (2005) Bovine mitochondrial Peroxiredoxin III forms a two-ring catenane. *Structure* **13**, 1661-1664.
- Cao, Z., Bhella, D. and Lindsay, J. G. (2007) Reconstitution of the mitochondrial PrxIII antioxidant defence pathway: General properties and factors affecting PrxIII activity and oligomeric state. *Journal of Molecular Biology* **372**, 1022-1033.
- Cao, Z., Tavender, T. J., Roszak, A. W., Cogdell, R. J. and Bulleid, N. J. (2011) Crystal structure of reduced and of oxidized peroxiredoxin IV enzyme reveals a stable oxidized decamer and a non-disulfide-bonded intermediate in the catalytic cycle. *Journal of Biological Chemistry* **286**, 42257-42266.
- Carson, M., Johnson, D. H., McDonald, H., Brouillett, C. and DeLucas, L. J. (2007) His-tag impact on structure. *Acta Crystallographica Section D* **63**, 295-301.
- Cha, M.-K., Yun, C.-H. and Kim, I.-H. (2000) Interaction of human thiol-specific antioxidant protein 1 with erythrocyte plasma membrane. *Biochemistry* **39**, 6944-6950.
- Chang, T.-S., Cho, C.-S., Park, S., Yu, S., Kang, S. W. and Rhee, S. G. (2004) Peroxiredoxin III, a mitochondrion-specific peroxidase, regulates apoptotic signalling by mitochondria. *Journal of Biological Chemistry* **279**, 41975-41984.
- Chant, A., Kraemer-Pecore, C. M., Watkin, R. and Kneale, G. G. (2005) Attachment of a histidine tag to the minimal zinc finger protein of the *Aspergillus nidulans* gene

regulatory protein AreA cause a conformational change at the DNA-binding site. *Protein Expression and Purification* **39**, 152-159.

Chauhan, R. and Mande, S. C. (2001) Characterization of the *Mycobacterium tuberculosis* H37Rv alkyl hydroperoxidase AhpC points to the importance of ionic interactions in oligomerisation and activity. *Biochemical Journal* **354**, 209-215.

Cox, A. G., Pullar, J. M., Hughes, G., Ledgerwood, E. C. and Hampton, M. B. (2008) *Free Radical Biology and Medicine* **44**, 1001-1009.

Cox, A. G., Peskin, A. V., Pation, L. N., Winterbourn, C. C. and Hampton, M. B. (2009) Redox potential and peroxide reactivity of human peroxiredoxin 3. *Biochemistry* **48**, 6495-6501.

Cox, A. G., Winterbourn, C. C. and Hampton, M. B. (2010) Mitochondrial peroxiredoxin in antioxidant defence and redox signalling. *Biochemical Journal* **425**, 313-325.

Dawson, R. M. C., Elliott, D. C., Elliott, W. H. and Jones, K. M. (1969) In: Data for Biochemical Research. pp. 103-114 Oxford University Press; Bocatón, Florida.

Dunford, H. B. (1999) Heme Peroxidases. Wiley-VCH Press; New York

Gasteiger, E., Hoogland, C., Gattiker, A., Duvaud, S., Wilkins, M.R., Appel, R. D. and Bairoch, A. (2005) Protein Identification and Analysis Tools on the ExPASy Server. In John M. Walker (Ed): *The Proteomics Protocols Handbook* (pp. 571-607) New York, NY: Humana Press.

Gourlay, L. J., Bhella, D., Kelly, S. M., Price, N. C. and Lindsay, J. G. (2003) Structure-function analysis of recombinant substrate protein 22 kDa (SP-22): a mitochondrial 2-Cys peroxiredoxin organised as a decameric toroid. *Journal of Biological Chemistry* **35**, 32631-32637.

Grete, M. C. and Karplus, P. A. (2013) Observed octameric assembly of a *Plasmodium yoelii* peroxiredoxin can be explained by the replacement of native "ball-and-socket" interacting residues by an affinity tag. *Protein Science* **10**, 1445-1452.

Guimarães, B. G., Souchon, H., Honoré N., Saint-Joanis, B., Brosch, R., Shepard, W., Cole, S. T. and Alzari, P. M. (2005). Structure and Mechanism of the alkyl hydroperoxidase AhpC, a key element of the *Mycobacterium tuberculosis* defense system against oxidative stress. *Journal of Biological Chemistry* **280**, 25735-25742.

Hall, A., Nelson, K., Poole, L. B. and Karplus, P. A. (2010) Structure-based insights into the catalytic power and conformational dexterity of peroxiredoxins. *Antioxidant and Redox Signaling* **15**, 795-815.

Hainfeld, J. F., Safer, D., Wall, J. S., Simon, M., Lin, B. and Powell, R. D. (1994) Methylamine vanadate (NanoVan) negative stain. In: Bailey, G. W. and Garratt-Reed, A. J. (Eds) Proceedings of the Fifty-Second Annual Meeting, Microscopy Society of America. pp. 132-133 San Francisco Press; San Francisco, CA.

Harris, J. R. (1971) The proteins released from intact erythrocyte 'ghosts' at low ionic strength. *Proceedings of the Biochemical Society* **122**, 38P-40P.

Harris, J. R. (2008) Negative staining across holes: application to fibril and tubular structures. *Micron* **39**, 168-176.

Jang, H. H., Lee, K. O., Chi, Y. H., Lee, J. R., Lee, S. S., Moon, J. C., Yun, J. W., Choi, Y. O., Kim, W. Y., Kang, J. S., Cheong, G.-W., Yun, D.-J., Rhee, S. G., Cho, M. J. and Lee, S. Y. (2004) Two enzymes in one: Two yeast peroxiredoxins display oxidative stress-dependent switching from a peroxidase to a molecular chaperone function. *Cell* **117**, 625-635.

Kapri-Pardes, E., Naveh, L. and Adam, Z. (2007) The thylakoid lumen protease Deg1 is involved in the repair of photosystem II from photoinhibition in *Arabidopsis*. *The Plant Cell* **19**, 10390-1047.

Karplus, P. A., Hall, A. (2007) Structural survey of the peroxiredoxins. In: Flohé, L. and Harris, J. R. (Ed) *Peroxiredoxin Systems*. pp. 41–60 Springer; New York.

Kley, J., Schmidt, B., Boyanov, B., Stolt-Bergner, P. C., Kirk, R., Ehrmann, M., Knopf, R. R., Naveh, L., Adam, Z. and Clausen, T. (2011) Structural adaptation of the plant protease Deg1 to repair photosystem II during light exposure. *Nature Structural and Molecular Biology: Brief Communications* **18**, 728-731.

König, J., Lotte, K., Plessow, R., Brockinke, A., Baier, M. and Dietz, K.-J. (2013) Reaction mechanism of plant 2-Cys peroxiredoxin: role of the C-terminus and the quaternary structure. *Journal of Biological Chemistry* **278**, 24409-24420.

Lagadic-Gossman, D., Huc, L. and Lecureur, V. (2004) Alterations of intracellular pH homeostasis in apoptosis: origins and roles. *Cell Death and Differentiation* **11**, 953-961.

Li, Y. (2010) Commonly used tag combinations for tandem affinity purification. *Biotechnology and Applied Biochemistry* **55**, 73-83.

Low, F., Hampton, M. B., Peskin, A. V. and Winterbourn, C. C. (2007) Peroxiredoxin 2 functions as a noncatalytic scavenger of low-level hydrogen peroxide in the erythrocyte. *Blood*, **109**, 2611-2617.

Ludtke, S. J., Baldwin, P. R. and Chiu, W. (1999) EMAN: Semi-automated software for high-resolutions single-particle reconstructions. *Journal of Structural Biology* **128**, 82-97.

Marzo, B. I., Brenner, C., Zamzami, N., Susin, S. A., Beutner, G., Brdiczka, D., Rémy, R., Xie, Z.-H., Reed, J. C. and Kroemer G. (1998) The permeability transition pore complex: a target for apoptosis regulation by caspases and Bcl-2-related proteins. *Journal of Experimental Medicine* **187**, 1261-1271.

Malcolm, B. A. (1995) The picornaviral 3C proteinases: Cysteine nucleophiles in serine proteinase folds. *Protein Science* **4**, 1439-1445.

- Mertens, H. D. and Svergun, D. I. (2010) Structural characterization of proteins and complexes using small-angle X-ray solution scattering. *Journal of Structural Biology* **172**, 128-141.
- Moon, J. C., Hah, Y.-S., Kim, W. Y., Jung, B. G., Jang, H. H., Lee, J. R., Kim, S. Y., Lee, Y. M., Jeong, M. G., Kim, C. W., Cho, M. J. and Lee, S. Y. (2005) Oxidative stress-dependent structural and functional switching of a human 2-Cys peroxiredoxin Isotype II that enhances HeLa cell resistance to H₂O₂-induced cell death. *Journal of Biological Chemistry* **280**, 28775-28784.
- Muthuramalingam, M., Seidel, T., Laxa, M., Nunes de Miranda, S. M., Gärtner, F., Ströher, E., Kandlbinder, A. and Dietz, K.-J. (2009) Multiple redox and non-redox interactions define 2-Cys peroxiredoxin as a regulatory hub in the chloroplast. *Molecular Plant* **2**, 1273-1288.
- Nonn, L., Berggre, M. and Powis, G. (2003) Increased expression of mitochondrial peroxiredoxin -3 (thioredoxin peroxidase-2) protects cancer cells against hypoxia and drug-induced hydrogen peroxide -dependent apoptosis. *Molecular Cancer Research* **1**, 682-689.
- Ogusucu, R., Rettori, D., Munhoz, D. C., Nettor, L. E. S. and Augusto, O. (2007) Reactions of yeast thioredoxin peroxidases I and II with hydrogen peroxide and peroxyxynitrite: rate constants by competitive kinetics. *Free Radical Biology and Medicine* **42**, 326-334.
- Palmieri, F. (2004) The mitochondrial transporter family (SLC25): physiological and pathological implications. *European Journal of Physiology* **447**, 689-709.
- Papinutto, E., Windle, H. J., Cendron, L., Battistutta, R., Kelleher, D. and Zanotti, G. (2005) Crystal structure of alkyl hydroperoxide-reductase (AhpC) from *Helicobacter pylori*. *Biochimica et Biophysica Acta* **1753**, 240-246.
- Parsonage, D., Youngblood, D. S., Sarma, G. N., Wood, Z. A., Karplus, P. A. and Poole, L. B. (2005) Analysis of the link between enzymatic activity and oligomeric state in AhpC, a bacterial peroxiredoxin. *Biochemistry* **44**, 10583-10592.
- Peng, J., Ding, J., Tan, C., Baggenstoss, B., Zhang, Z., Lapolla, S. M. and Lin, J. (2009) Oligomerization of membrane-bound Bcl-2 is involved in its pore formation induced by tBid. *Apoptosis* **14**, 1145-1153.
- Pettersen, E. F., Goddard, T. D., Huang, C. C., Couch, G. S., Greenblatt, D. M., Meng, E. C. and Ferrin, T. E. (2004) UCSF Chimera: a visualization system for exploratory research and analysis. *Journal of Computational Chemistry* **25**, 1605-1612.
- Petoukhov, M. V., Konarev, P. V., Kikhney A. G. and Svergun, D.I. (2007) ATSAS 2.1 - towards automated and web-supported small-angle scattering data analysis. *Journal of Applied Crystallography* **40**, s223-s228.
- Poole, L. B. (2007) The catalytic mechanism of peroxiredoxins. In: Flohé, L. and Harris, J. R. (Eds) *Peroxiredoxin Systems*. pp. 61-81 Springer; New York.

- Porcelli, A. M., Ghelli, A., Zanna, C., Pinton, P., Rizzuto, R and Rugolo, M. (2005) pH difference across the outer mitochondrial membrane measured with a green fluorescent protein mutant. *Biochemical and Biophysical Research Communications* **326**, 799-804.
- Radjainia, M., Huang, B., Bai, B., Schmitz, M., Yang, S. H., Harris, P. W. R., Griffin, M. D. W., Brimble, M. A., Wang, Y. and Mitra, A. K. (2012) A highly conserved tryptophan in the N-terminal variable domain regulates disulfide bond formation and oligomeric assembly of adiponectin. *The Federation of European Biochemical Societies Journal* **279**, 2495-2507.
- Saccoccia, F., Micco, P. D., Bournis, G., Brunori, M., Koutris, I., Miele, A. E., Morea, V., Sriratana, P., Williams, D. L., Bellelli, A. and Angelucci, F. (2012) Moonlighting by different stressors: crystal structure of the chaperone species of a 2-cys peroxiredoxin. *Structure* **20**, 429 – 439.
- Schröder, E., Littlechild, J. A., Lebedev, A. A., Errington, N., Vagin, A. A. and Isupov, M. N. (2000) Crystal structure of decameric 2-Cys peroxiredoxin from human erythrocytes at 1.7Å resolution. *Structure* **8**, 605-615.
- Svergun D.I. (1992) Determination of the regularization parameter in indirect-transform methods using perceptual criteria. *Journal of Applied Crystallography* **25**, 495-503.
- Takahashi, A., Masuda, A., Sun, M., Centonze, V. E. and Herman, B. (2004) Oxidative stress-induced apoptosis is associated with alterations in mitochondrial caspase activity and Bcl-2-dependent alteration in mitochondrial pH (pH_m) *Brain Research Bulletin* **62**, 497-504.
- Valenti, L. E., de Pauli, C. P. and Giacomelli, C. E. (2006) The binding of Ni(II) ions to hexahistidine as a model system of the interaction between nickel and His-tagged proteins. *Journal of Inorganic Biochemistry* **100**, 192-200.
- Wood, Z. A., Poole, L. B., Hantgan, R. R. and Karplus, P. A. (2002) Dimers to doughnuts: redox-sensitive oligomerisation of 2-Cys peroxiredoxins. *Biochemistry* **41**, 5493-5504.
- Wood, Z. A., Schröder, E., Harris, J. R. and Poole, L. B. (2003) Structure, mechanism and regulation of peroxiredoxins. *Trends in Biochemical Sciences* **28**, 32-40.
- Wen, L., Huang, H.-M., Juang, R.-H., Lin, C.-T., (2007) Biochemical characterization of 1-Cys peroxiredoxin from *Antrodia camphorate*. *Applied Microbiology and Biotechnology* **73**, 1314-1322.

Chapter 5 Influencing *HsPrx3* quaternary structure

5.1 Introduction

The dynamic quaternary structure of the Prx family is well documented, but the mechanisms are poorly understood (Wood *et al.*, 2002). Constructs that favour one or another structure have been generated (Parsonage *et al.*, 2005; König *et al.*, 2013), but locked structures are yet to be reported.

An improved understanding of the factors involved is required in order to control the structural switching of *HsPrx3*; this chapter therefore explores the introduction of mutations, with the aim to influence self-assembly. Following investigations into the effect of environmental conditions on *HsPrx3* quaternary structure (chapter four), mutations were introduced to the interface and active site regions of the protein, to mimic the structural changes thought to occur in response to environmental changes. This could lead to a greater level of control over the oligomerisation of *HsPrx3*, potentially highlighting nanotechnology applications.

Toroid formation is linked to protein activity (Parsonage *et al.*, 2005), but the exact causality is unclear. The non-native structures were assayed to ascertain the impact on altered quaternary structure on protein activity, and therefore gain preliminary insight into this link.

5.2 Design and generation of *HsPrx3* modifications

The conservation of the A-type interface (see section 1.2.5.2), along with its involvement in the redox switch, and therefore Prx function, led to this interface being

chosen as the first target for site-directed mutagenesis. Most of the binding energy of protein-protein interfaces is due to a small number of amino acids known as hotspots (reviewed in Moreira *et al.*, 2007). A targeted mutagenesis approach allowed the investigation of potential hotspots at the *HsPrx3* interface, and subsequent assessment of the structure of the muteins generated. The approaches used when designing modifications to the interface followed the considerations detailed in chapter three (section 3.2). Previous studies attempting to alter the stability of the A-type interface of a different Prx with single residue mutations have been successful (Parsonage *et al.*, 2005), therefore the substitution of single native residues for alanine residues at potential H-bonding sites of the A-type interface was carried out in order to disrupt interactions. The loss of side chains removed any possibility for H-bonds, or electrostatic interactions forming.

A second target of mutagenesis was the active site of *HsPrx3*. The architecture of this site along with the C_P loop region has been seen to change in response to redox state (Wood *et al.*, 2003), and was suggested to be involved in the control of Prx oligomeric state (section 1.2.3.2 – 1.2.5). Transition of the C_P loop into the LU conformation is associated with the dissociation of the dodecamer to dimers, whilst the reduced form is stabilised by the FF loop (section 1.2.5.2). Preventing this loop from refolding, or increasing its mobility, was therefore explored as another avenue for designing oligomer-disrupting mutations.

5.2.1 A-type interface analysis

A detailed analysis of the A-type interface identified residues in this protein-protein interaction that could be targeted for mutagenesis. Potential bonding residues were determined through analysis of the *BtPrx3* interface, carried out using the PDBePISA online bioinformatics tool (Krissinel and Henrick, 2007). This predicts interactions by identifying the residues that become buried when two subunits come together, and

analysing the proximity and bonding potential of these residues. Sequence alignment to *HsPrx3* indicated that 98% of the residues at the interfaces are conserved (figure 5.1A). Therefore, the *BtPrx3* interface was an appropriate model for informing site-directed mutagenesis of *HsPrx3*.

The A-type interface is mainly stabilised through hydrophobic interactions which comprise a dense core (figure 5.1B). 26 residues were identified as contributing to the stability, comprised of 11 hydrophobic, 10 neutral and five hydrophilic residues (Monera, *et al.*, 1995). 13 of the contributing residues are more than 50% buried by monomer association. These residues are located within the typical interfacial regions of 2-Cys Prxs suggested by previous studies (Wood *et al.*, 2002; figure 5.2A). Three H-bonds were identified between serine 75 (S75) and aspartic acid 74 (D74) residues of opposing monomers, and between serine 78 (S78) and its counterpart on the other subunit (figure 5.2B). The interface is symmetric, with a second D74-S75 H-bond, and buries 673.4 \AA^2 per monomer. Pymol (DeLano, 2002) analysis of this oligomer interface suggested that the S78-S78 predicted bond is a direct bond, with the H-bond between D74 and S75 of each subunit being water-mediated.

BtPrx3: ↓ ↓ ↓
 APAVTQHAPYFKGTAVVNGEFKDLSLDDFKGKYLVLFFYP LDFTEVCPTETVAFSDKANEFHDVN

HsPrx3:
 APAVTQHAPYFKGTAVVSGEFKEISLDDFKGKYLVLFFYP LDFTEVCPTETIAFSDKASEFHDVN

BtPrx3: ↓
 CEVVAVSVDSHFSHLAWINTPRKNGGLGHMNIALLSDLTKQISR DYGVLL EGSGLALRGLFIDVN

HsPrx3:
 CEVVAVSVDSHFSHLAWINTPRKNGGLGHMNIALLSDLTKQISR DYGVLL EGPGLALRGLFIDVN

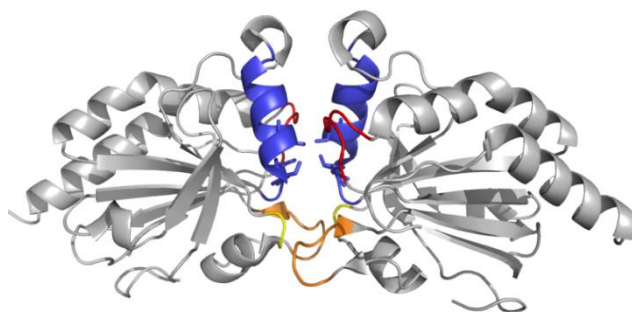
BtPrx3: ↓ ↓ ↓ ↓ ↓ ↓ ↓ ↓
 GVIKHL SVNDLPVGRSVEETLRLVKAFQYVETHGEVCPANWTPDSPTIKPSPAASKKEYFQKVN

HsPrx3:
 GVIKHL SVNDLPVGRSVEETLRLVKAFQFVEAHGEVSPANWTPESPTIKPHPTASREYFEKVN

A: Sequence alignment shows 93% sequence identity (*BtPrx3* is shown as the top line of text, *HsPrx3* the bottom). Differences are shown in red letters and highlighted with arrows. Interface regions are almost completely conserved. **B:** Cartoon representation of the BtPrx3 A-type interface. Side chains of the major contributors to the hydrophobicity of the A-type interface are shown. Labels are shown for the right hand monomer only for clarity. PDB ID: 1ZYE (Cao *et al.*, 2005).

A: Interfacing residues

PHE 38		PHE 38
TYR 39		TYR 39
PRO 40		PRO 40
LEU 41		LEU 41
ASP 42		ASP 42
PHE 43		PHE 43
THR 44		THR 44
PHE 45		PHE 45
VAL 46		VAL 46
CYS 47		CYS 47
PRO 48		PRO 48
<hr/>		
VAL 71		VAL 71
SER 72		SER 72
VAL 73		VAL 73
ASP 74		ASP 74
SER 75		SER 75
HIS 76		HIS 76
PHE 77		PHE 77
SER 78		SER 78
HIS 79		HIS 79
LEU 80		LEU 80
ALA 81		ALA 81
TRP 82		TRP 82
ILE 83		ILE 83
ASN 84		ASN 84
THR 85		THR 85
PRO 86		PRO 86
ARG 87		ARG 87
LYS 88		LYS 88
ASN 89		ASN 89
GLY 90		GLY 90
GLY 91		GLY 91
LEU 92		LEU 92
GLY 93		GLY 93
HIS 94		HIS 94
MET 95		MET 95
ASN 96		ASN 96
ILE 97		ILE 97
ALA 98		ALA 98
LEU 99		LEU 99
LEU 100		LEU 100
SER 101		SER 101
ASP 102		ASP 102
LEU 103		LEU 103
THR 104		THR 104
LYS 105		LYS 105
GLN 106		GLN 106
ILE 107		ILE 107
SER 108		SER 108
ARG 109		ARG 109
ASP 110		ASP 110
TYR 111		TYR 111
GLY 112		GLY 112
VAL 113		VAL 113
LEU 114		LEU 114
LEU 115		LEU 115
GLU 116		GLU 116
GLY 117		GLY 117
PRO 118		PRO 118
GLY 119		GLY 119
LEU 120		LEU 120
ALA 121		ALA 121
LEU 122		LEU 122
ARG 123		ARG 123

B: Cartoon representation of dimer interface**Figure 5.2: Interface regions of *BtPrx3***

A: PISA interface analysis suggested the presence of 3 H-bonds, which stabilise the interface. H-bonds are shown as black lines. **B:** Stabilising H-bonds occur between residues located in the interface helix (helix $\alpha 4$ – see section 1.2.3.1). Bonding residues are shown with stick representation. In A and B, region I is shown in red, region II is blue, region III is yellow, and region IV is orange. PDB ID: 1ZYE (Cao *et al.*, 2005).

The A-type interface of the *MtAhpE* is a unique, redox insensitive A-type interface (Li *et al.*, 2005; section 3.2.1). It was hypothesised that particular stabilising interactions of this interface could be introduced at the *HsPrx3* A-type interface to increase stability of the dodecamer. Inspection of the sequence alignments (figure 5.3A) and overlaying the structures revealed some key differences. The *MtAhpE* A-type interface shows additional interactions between the loop regions at the outer and inner areas of this interface (figure 5.3B), contributed to by a high proportion of aromatic residues (section 3.3.1). A notable difference is W95 of *MtAhpE*, which aligns with a threonine residue in the *HsPrx3* interface (T104). W95 of each monomer forms an H-bond with E109 of the opposing subunit at the *MtAhpE* A-type interface, accounting for two unique interactions. In both *MtAhpE* and *BtPrx3* all four and six (respectively) oligomer building interfaces identified within the crystal structure by PDBePISA showed minimal variations in residues involved or area, indicating a good level of confidence in the predicted interactions.

5.2.2 Selection of mutations to alter assembly

Five mutations were designed with the aim of altering the propensity of toroid formation or dissociation. Two of these were located at the A-type interface of *HsPrx3* and three were located in the active site pocket. A summary of the mutations that were introduced to the *HsPrx3* sequence is shown in table 5.1.

5.2.2.1 Interface mutations

Residue S78 is located at the core of the interface (figure 5.3), and forms a direct H-bond to the other monomer (as opposed to the water mediated bond of the D74-S75 interaction). These suggest an important role in the interface. This interaction is

conserved in the stable *MtAhpE* A-type interface, further supporting its importance. An equivalent mutation of *StAhpC*, T77V, was shown by Parsonage *et al.* (2005) to affect the toroid stability. Preliminary studies in the Gerrard laboratory indicated that the S78A mutation also significantly influenced toroid assembly (Zhu, 2010, unpublished data; Littlejohn, Master's thesis 2013), therefore this mutation was studied. Whilst W95 of *MtAhpE* aligns with T104 of *HsPrx3*, E109 is conserved. This suggests that the mutation of residue 104 of *HsPrx3* to tryptophan may allow equivalent H-bonds to form. Therefore, a T104W mutation was studied.

A: Sequence alignment

***HsPrx3*:**
 LSLDDFKG-KYLVLFYPLIDFTEVCPTETIVAFSDKANEFHVDNCEVVAVSVDSHFSLAWNTPRKNGGLG
***MtAhpE*:**
 VTLRGYRGAKNVLLVFPLAFTGICQGEIDQLRDHLPEFENDDSAALAIISVGPPPTHKIWAT---QSG--

***HsPrx3*:**
 HMNIALLLSDLTQK--ISRDYGVLLEGSGIALRGLFIIDPNGVIK
***MtAhpE*:**
 -FTFPLLLSDFWPHGAVSQAYGVFNEQAGIANRGTFVVDMSGIIR

B: Cartoon representation

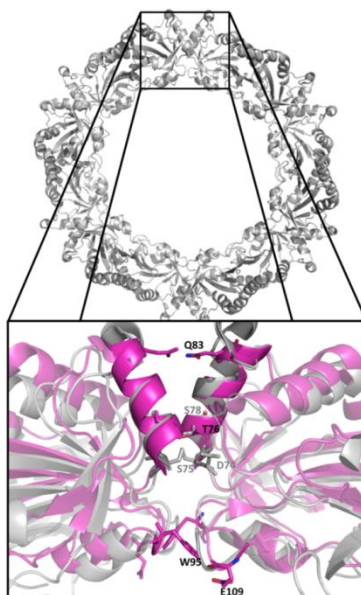


Figure 5.3: Bonding residues of the *BtPrx3* and *MtAhpE* A-type interfaces show some differences

A: Sequence alignment shows significant differences in the interface regions (coloured as in figure 5.2). **B:** The interfaces overlay well. The *MtAhpE* interface shows additional interactions, namely the Q83-Q83 and the W95-E109 interaction. *BtPrx3* chains and labels are shown in grey, *MtAhpE* chains and labels are shown in magenta and black respectively. Labels are shown for the right hand monomers only for clarity. The S78-S78 interaction of *BtPrx3* is conserved, corresponding with a T76-T76 H-bond in *MtAhpE*. E109 of *MtAhpE* aligns with E116 of *BtPrx3*, however W95 is not conserved.

Table 5.1: Summary of rationale behind mutational design

Interface mutations were designed based on bonding potential in the area, active site mutations were designed to mimic the conformational changes that occur naturally during assembly or disassembly.

Mutation	Intended outcome	Rationale
Interface Mutations		
S78A	Stabilise the A-type interface	Altered packing at the interface as seen by Parsonage <i>et al.</i> , could lead to increased stability.
T104W	Stabilise the A-type interface	Introduce the potential for a novel H-bond, mimicking the <i>MtAhpE</i> A-type interface.
Active Site Mutations		
C47S	Prevent dodecamer dissociation; encourage HMW species	Prevent disulfide bond formation and interface destabilisation; mimic the protonated form of C _P .
P48A	Prevent dodecamer dissociation	Reduce the propensity of the C _P loop to unfold
R123G	Promote dodecamer dissociation	Remove the possibility of the C _P thiolate-R123 ionic bond, encouraging loop unfolding.

5.2.2.2 Active site mutations

A serine substitution was introduced at the peroxidatic cysteine, C47. Serine lacks a thiol group and cannot form the disulfide bond. This mutation was predicted to prevent dissociation, as without disulfide bond formation the loop will not be trapped in the LU conformation (section 1.2.4.4), and the A-type interface will not be destabilised. Furthermore, protonation of C_P caused by acidification has been seen to encourage the formation of HMW structures (Saccoccia *et al.*, 2012). Serine will not be deprotonated in the active site, therefore this mutation was predicted to mimic the protonated form, with associated unwinding of helix $\alpha 2$ leading to toroid association (section 1.2.5.4). Decreasing the propensity of the C_P loop to unfold was also predicted to stabilise the dodecamer. A conserved proline (P48 in *HsPrx3*) has been highlighted as important to

the ability of this region to unwind (Saccoccia *et al.*, 2012). The $\alpha 2$ helix of *MtAhpE* does not unwind as extensively upon oxidation (section 1.4.2.4), and sequence comparisons showed that this proline is not conserved in *MtAhpE*, strengthening the hypothesis that it contributes to interface dissociation. P48 of *HsPrx3* was therefore mutated to alanine. The gene encoding the P48A mutation was designed and obtained by Jacob Littlejohn in the Gerrard Laboratory.

The deprotonated form of C_P is stabilised by a conserved arginine – R123 in the case of *HsPrx3* (section 1.2.3.2). Upon oxidation, C_P moves away from R123 to form the disulfide bond with C_R , allowing the C_P loop to unfold (section 1.2.4.3; Wood *et al.*, 2003; figure 1.7). It follows therefore, that without the stabilising interaction between C_P and R123, the LU conformation may be stabilised, mimicking the oxidised state. Early studies have shown this conserved arginine residue to be important for catalytic activity (König *et al.*, 2003), and during the course of this thesis results were published confirming its importance in the activity of *HsPrx3* with H_2O_2 (Nagy *et al.*, 2011). R123 was therefore chosen as a target for mutation.

A double mutation combining the active site and interface mutations C47S and S78A was also designed (C47SS78A). The results obtained for the single muteins informed its design, and so this is further discussed in section 5.4.1.

5.3 Preparation of mutated *HsPrx3* constructs

5.3.1 Expression of non-native proteins in an *E. coli* host

E. coli expression strains were transformed with the pET151/D-TOPO® plasmid containing the modified *HsPrx3* gene and cultured as described in section 2.2.2.

Expression trials indicated that optimum expression was achieved using identical conditions to wildtype *HsPrx3* (see section 4.2.1). BL21 High yields of soluble protein were obtained, typically 60-70 mg of protein per 1 L culture after purification (section 5.3.2; table 5.2). The C47S mutein was an exception, with a tendency to aggregate throughout the purification resulting in low yields.

Table 5.2: Good expressions of the *HsPrx3* muteins were seen in conditions optimised in chapter three

Sufficient quantities of pure protein were easily obtained, with yields often higher than those obtained from wildtype purification in identical conditions (detailed in section 4.2.1).

Construct	Pellet weight (g)	Weight of protein after IMAC (mg)	Weight of protein after gel filtration (mg; final yield)	Weight of protein per gram cells (mg)
WT	5.6	120	80	14.3
S78A	4	122	64	16
T104W	4.4	140	80	18
P48A	5.2	150	90	17
R123G	4.8	100	56	9.6
C47S	4.9	41	22	4.5
C47SS78A	4.9	100	42	8.6

5.3.2 Purification by chromatography

The molecular weight and pI of the mutated *HsPrx3* constructs were similar to that of the wildtype (see appendix four). Muteins did show some differences in their elution volumes from IMAC and gel filtration chromatography (figures 5.4 and 5.5). However, these did not affect purification, therefore standard protocols optimised for wildtype *HsPrx3* continued to be used for mutein purification (section 4.2). Muteins bound successfully to the nickel resin, with very little being seen in the flowthrough or wash fractions (figure 5.6A). S78A, T104W, C47S, P48A, and R123G constructs consistently

eluted as single peaks at imidazole concentrations of around 390 mM, 475 mM, 500 mM, 270 mM, and 500 mM respectively (figure 5.4).

Gel filtration chromatography was carried out as for wildtype (section 4.2.2). Muteins typically eluted with a clear major peak, seen at retention volumes of about 60 mL, 77 mL, 47 mL and 90 mL for S78A, T104W, P48A and R123G constructs respectively (figure 5.5). Fractions were collected across peaks, and a single major band was seen on SDS-PAGE (figure 5.6C). Muteins often ran below the 20 kDa marker (for example, figure 5.6D). MS analysis of purified S78A mutein confirmed the molecular weight of 25.2 kDa, indicating that degradation had not occurred but that muteins had slightly different electrophoretic mobility to wildtype. The difference to the wildtype elution profile (figure 5.5F) suggested that the oligomeric state may have been altered. In some cases, peaks near to the void volume (36.3 mL; seen in S78A, P48A and C47S elution profiles) indicated that aggregation was occurring. SDS-PAGE analysis of these peaks confirmed them to represent assemblies of *HsPrx3* muteins, rather than contamination (figure 5.6D; appendix six).

His-tag removal was carried out using the conditions seen to be optimal during trials with wildtype *HsPrx3* (section 4.2.4). Cleavage was successful in these conditions, as judged by SDS-PAGE analysis (figure 5.7). In some cases (notably, cleaved T104W and tagged C47S; appendix six), SDS resistant dimers and higher order structures were noted. In the case of tagged P48A a double band was seen at the size of a dimer, with no dissociation to monomers being seen after incubation with reducing SDS buffer (figure 5.7). Although this resolved to monomers after tag cleavage in the case of P48A, the higher weight band persisted after cleavage in the case of T104W and C47S. This has been seen by other groups (discussed in section 4.2.3). As with those observed in *MtAhpE* samples (section 3.4.1.1), incubation with SDS at room temperature instead of heating did not reduce their appearance, indicating they were not due to amide cross-linking. Further analysis by MS would be useful to unequivocally confirm the identity of these bands.

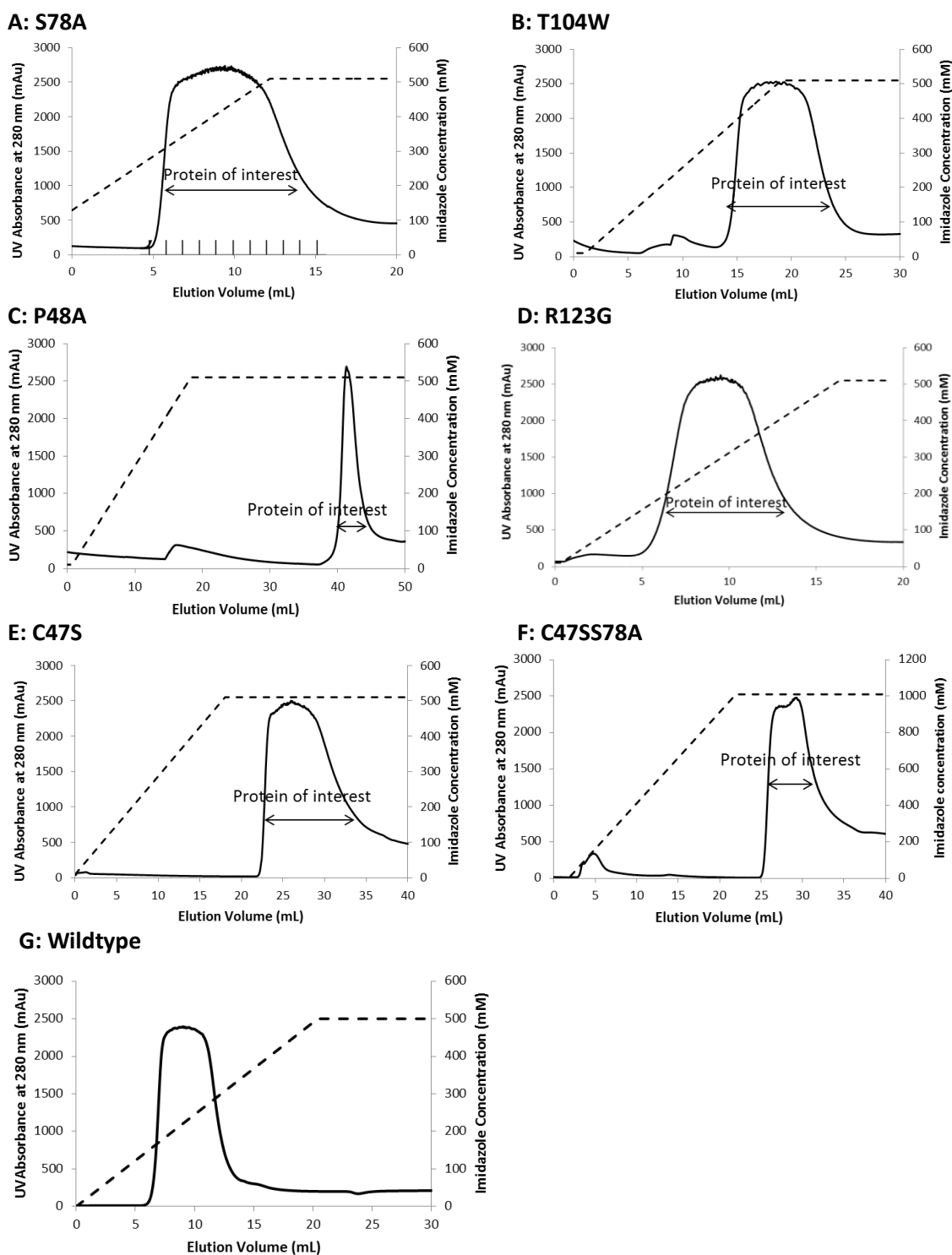


Figure 5.4: Mutated proteins elute at different imidazole concentrations to wildtype *HsPrx3*

Elution profiles of (A) S78A (marked fractions relate to figure 5.6), (B) T104W, (C) P48A, (D) R123G, (E) C47S and (F) C47SS78A variants of *HsPrx3* elute at different imidazole concentrations than wildtype *HsPrx3* (F, for comparison).

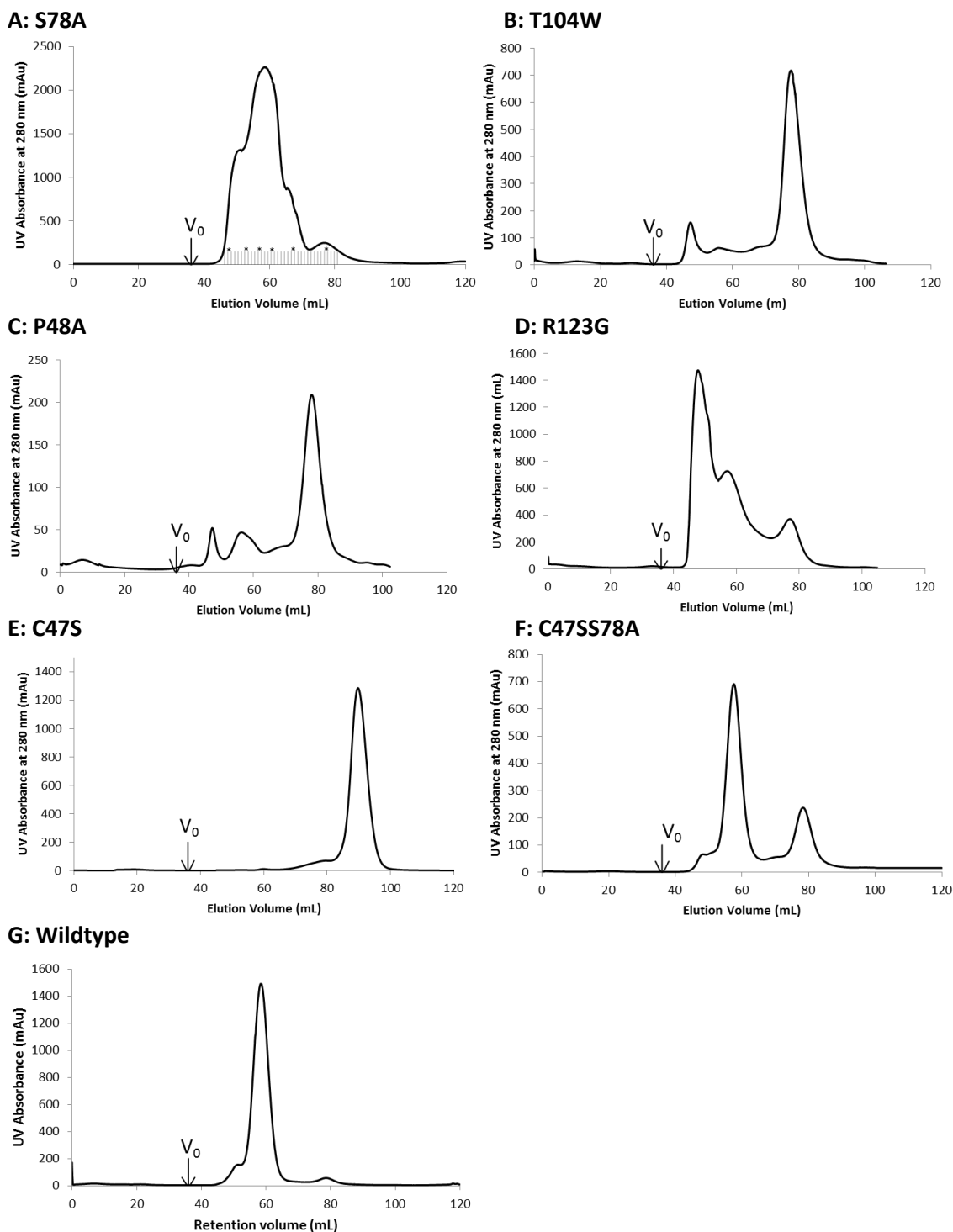


Figure 5.5: Gel filtration profiles of mutated *HsPrx3* proteins differed from wildtype

Whereas wildtype *HsPrx3* eluted consistently as a single major peak around 60 mL from an S200 16/60 gel filtration column (GE Healthcare), mutated constructs (A) S78A (marked fractions relate to figure 5.6), (B) T104W, (C) C47S, (D) P48A, (E) R123G, (F) C47SS78A showed peaks at different elution volumes compared to wildtype (G, for comparison).

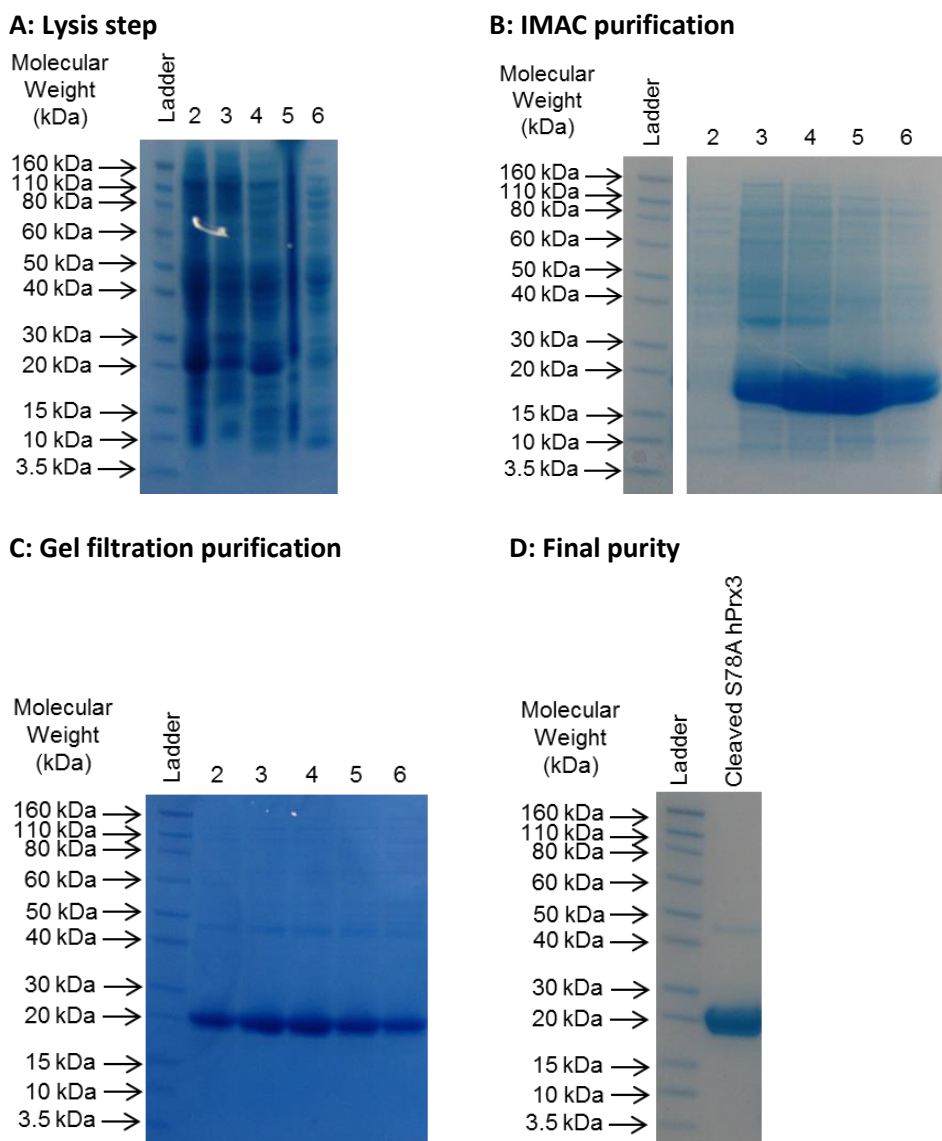


Figure 5.6: Representative muterin purification gels exemplified by S78A

A: Lysis steps shows: lane 2: whole cell lysate; lane 3: insoluble fraction; lane 4: soluble fraction; lane 5: IMAC flowthrough; lane 6: IMAC wash fraction. **B:** Fractions across the wide single peak of IMAC elution (figure 5.4A). **C:** Selected fractions across the gel filtration peaks (figure 5.5A): lane 2: shoulder peak; lanes 3 and 4: main peak; lane 5: late shoulder peak; lane 6: late eluting minor peak. **D:** Gel showing acceptable purity of a final sample to be used for experimental data collection. SDS-PAGE gels for the other mutated protein purifications can be found in appendix six.

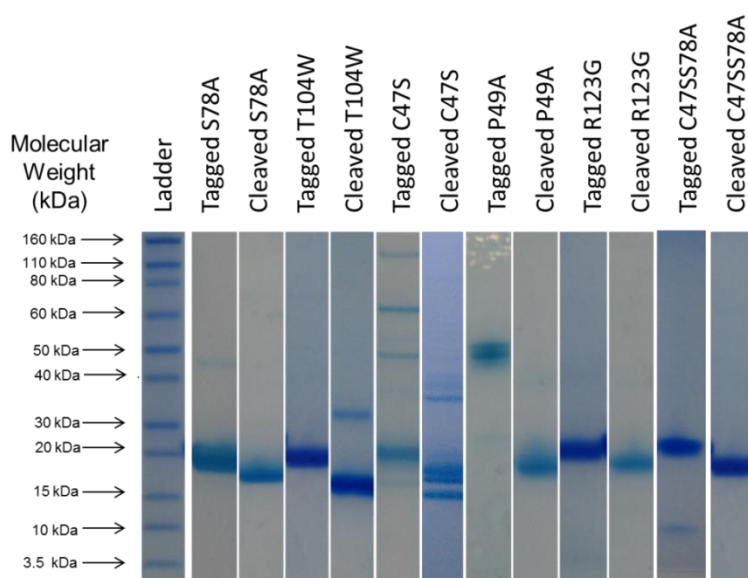


Figure 5.7: All muteins were successfully prepared to high levels of purity

5µg of final samples after purification were loaded at 1 mg/mL for SDS-PAGE analysis.

All samples analysed were from homogeneous preparations, as judged by SDS-PAGE with Coomassie blue staining (figure 5.7). The possibility of contaminating proteins contributing to elution peaks or weight calculations during biophysical analysis is low.

5.4 Characterisation of single residue mutations of *HsPrx3*

Data collected for *HsPrx3* muteins without his-tags is presented, as the tag had been seen to affect wildtype oligomeric state (section 4.3.1.3). This gave a clear picture of the influence of the mutation on *HsPrx3* structure. Samples were also characterised with his-tags, although for most this did not provide useful information as it was not possible to differentiate the influence of the his-tag and of the mutation. Where his-tagged characterisation was considered meaningful the results are discussed. All SEC/SLS and SAXS data for his-tagged muteins can be found in appendix seven. Additional SAXS

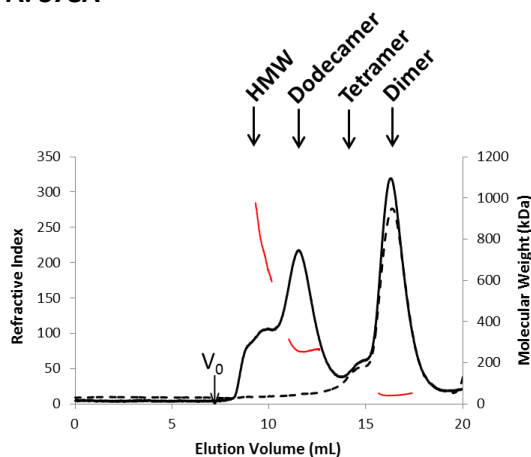
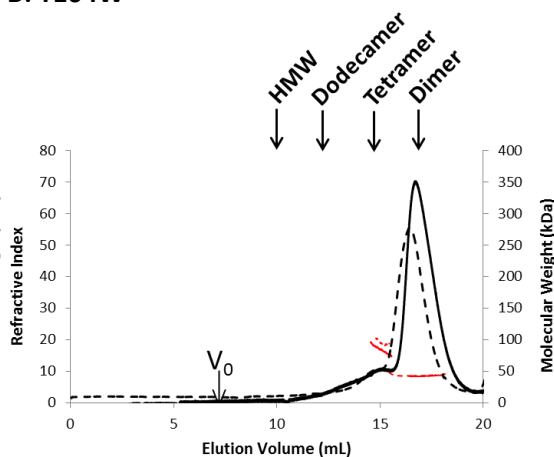
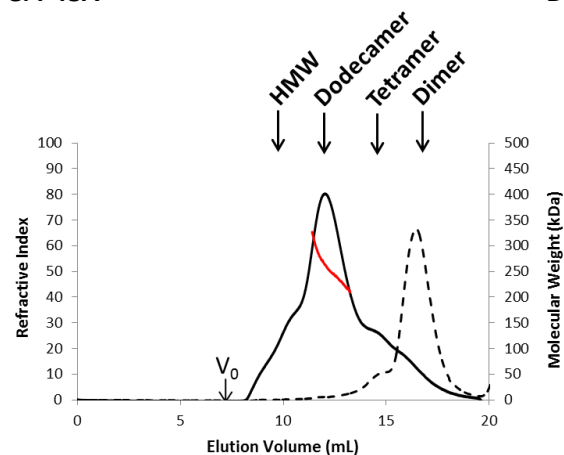
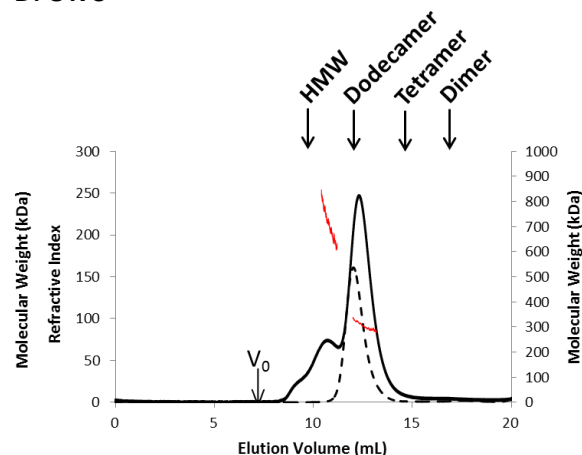
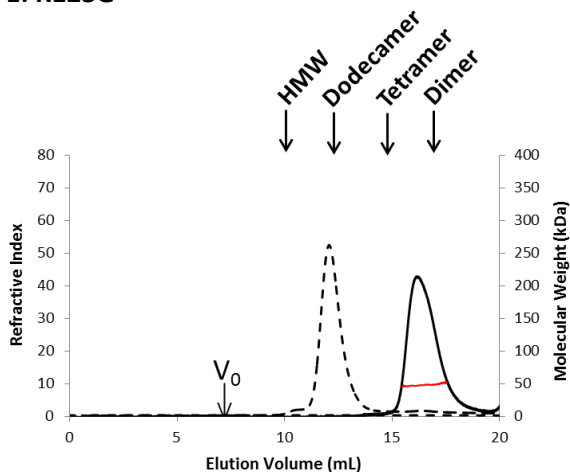
data is also recorded in appendix 7 (as detailed in section 5.4.1.2). The C47S mutein was an exception as untagged samples were difficult to prepare and aggregated in the time required to run experiments. Therefore, only the tagged mutein, which was more stable, was characterised.

5.4.1 Quaternary structure of *HsPrx3* muteins

5.4.1.1 Size Exclusion Chromatography/Static Light Scattering (SEC/SLS)

Non-reducing conditions

Wildtype *HsPrx3* had been seen to exist as a dimer when the sample was not reduced (section 4.3.1.2). In identical conditions, it was apparent that single residue substitutions, in most cases, significantly altered the assembly properties of *HsPrx3*. The S78A mutein existed in a heterogeneous state, with four species including the dimer and dodecamer observed (figure 5.8A). The RI trace indicated large amounts of HMW species were also present, calculated to be a 748 kDa species; possibly three associated dodecamers. However, the molecular weight dropped across the peak, making accurate calculations difficult. As the peaks do not show baseline separation it is difficult to discern if the decreasing molecular weight across the peak is due to species in equilibrium, or discrete species with overlapping elution peaks. Although a considerable amount of dimer remained in solution, the dodecamer represented a significant proportion of the species present. This is in contrast to the wildtype protein in comparable conditions, in which no dodecamers were observed (section 4.3.1.2, figure 4.10A). Increasing the protein concentration up to 5 mg/mL did not change the species distribution (data not shown).

A: S78A**B: T104W****C: P48A****D: C47S****E: R123G****Figure 5.8: In non-reducing conditions, muteins showed altered quaternary structures**

A: S78A mutein existed as a mixture of dimeric and dodecameric species, with HMW aggregates. **B:** T104W behaved similarly to wildtype, mostly existing as a dimer with a small amount of tetramer observed. **C:** The P48A mutation was mostly dodecameric, with some tetramer present. **D:** C47S mutein existed primarily as a dodecamer, with two peaks representing larger species. **E:** R123G existed as a stable dimer. Wildtype *HsPrx3* in non-reducing conditions is shown with the dashed lines. Molecular weight across the peaks is shown with the red lines.

Untagged T104W mutein behaved similarly to wildtype *HsPrx3*, with the 42 kDa dimer being the predominant species in non-reducing conditions (figure 5.8B). Similar to wildtype samples, a tetrameric species was seen. However, the decreasing molecular weight across the peak suggested that the mutein tetramer was less stable than that of wildtype *HsPrx3*, and rapidly dissociates. This indicated a reduced propensity of the dimers to oligomerise, possibly suggesting a weakened interface. Interestingly, When T104 was mutated, the his-tag did not stabilise the dodecamer (appendix seven). In non-reducing conditions the his-tagged mutein exists as a 49 kDa species, unlike the his-tagged wildtype which remained dodecameric in identical conditions (section 4.3.1.3). These results suggest that the mutation introduces a change in tertiary structure which prevents his-tag stabilisation.

In non-reducing conditions, no dimer peak was seen in the RI trace of the P48A mutein. Although one 266 kDa species appeared to predominate, this peak was broadened by shoulders at both the leading and trailing edges (figure 5.8C). The continuous drop in molecular weight across the peak and long leading edge indicates the presence of HMW assemblies in fast equilibrium.

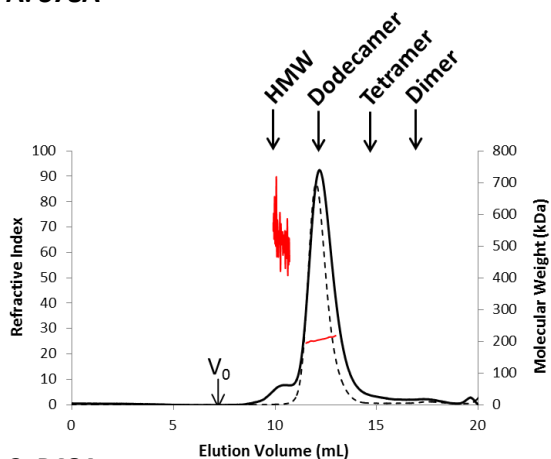
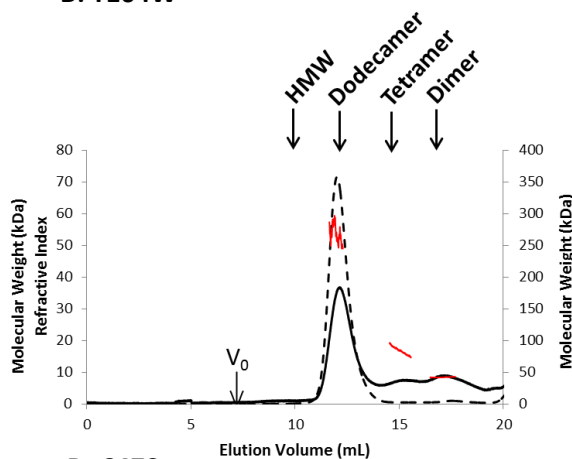
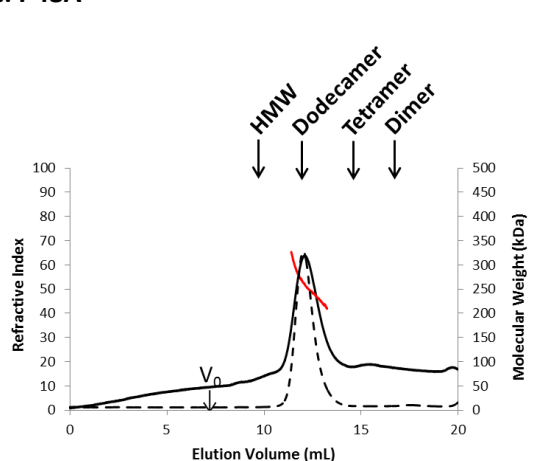
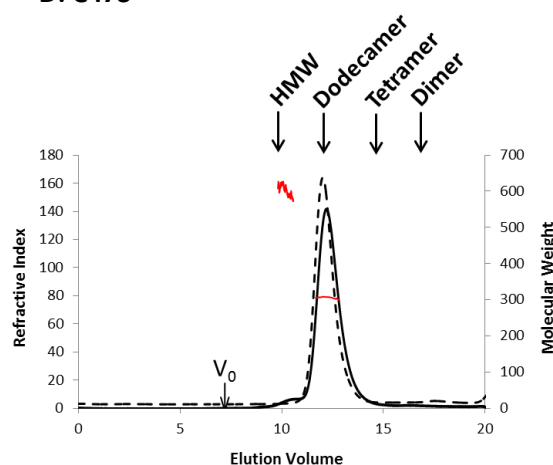
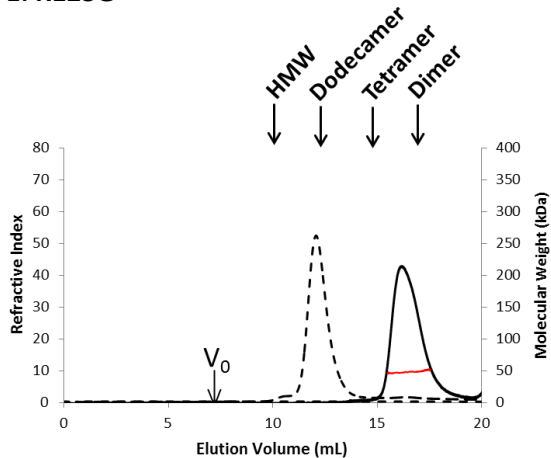
In non-reducing conditions the tagged C47S mutein eluted as a major peak representing a 319 kDa assembly, with no deviation from the baseline at later elution volumes (figure 5.8D). The molecular weight is slightly higher than that of a tagged dodecamer (302 kDa), and the upward trend in molecular weight at the beginning of the peak indicates that the HMW assemblies present affected calculations. These assemblies appeared to comprise at least one discrete population, calculated to have a weight of 800 kDa. A leading edge shoulder was seen, indicating a second population of high weight species, however calculations gave inconclusive results for this species. The low elution volume and trailing nature of the peak suggested that this shoulder may represent heterogeneous aggregates rather than a discrete assembly.

The R123G mutein eluted as a single peak in non-reducing conditions, with molecular weight calculations revealing this to correspond to a 42 kDa dimeric species (figure 5.8E). The constant molecular weight across the peak indicated that the dimer was stable, and the tetrameric species seen in wildtype preparations (section 4.3.1.2) was not observed.

Reducing conditions

In reducing conditions, wildtype protein existed as a dodecamer, with very small amounts of smaller species seen (section 4.3.1.2). Overall, muteins appeared more homogeneous in reducing conditions. The primary species seen was the dodecamer (with the exception of the R123G mutein), and in all cases where HMW species had been seen in non-reducing conditions, their presence was significantly lessened or eliminated in reducing conditions. This supports early work (Zhu 2010, unpublished work) who observed that HMW species of the S78A mutein dissociated upon addition of a reducing agent.

When reduced, the S78A mutein existed almost completely as a dodecamer (figure 5.9A). The presence of HMW species was significantly diminished, and the calculated weight for this species was 521 kDa, in line with two associated dodecamers. However, the molecular weight across the peak is noisy due to low signal, so firm conclusions cannot be drawn. Interestingly, a slight shift is seen in elution volume of the dodecamer between reduced and non-reduced samples (12.0 and 11.5 mL respectively), although calibration to light scattering produces equivalent molecular weights for the peaks. Elution volume is affected by particle size and shape, and so this shift could indicate that the dodecamer of the non-reduced sample is comprised of oxidised dimers which, despite stabilisation of this conformation by the mutation, adopt a more open ring (in line with the theory proposed in section 4.4 regarding the dimensions of an oxidised toroid).

A: S78A**B: T104W****C: P48A****D: C47S****E: R123G****Figure 5.9: In reducing conditions mutants showed a variety of oligomeric states**

A: S78A mutant existed primarily as a dodecamer, with a small amount of HMW species seen. **B:** The T104W mutation appeared to destabilise the dodecamer, as dimeric and tetrameric species were seen in reducing conditions. **C:** P48A mutant existed as a dodecamer, however the protein was unstable in these conditions. **D:** The HMW species of the C47S construct were less apparent in reducing conditions, indicating a dodecameric arrangement to be the favoured species. **E:** No large species were seen in R123G preparations, with the dimer being the only assembly present.

The equilibrium of the T104W mutein was shifted to favour the dodecamer, with calculations indicating a weight of 265 kDa species (figure 5.9b). Later peaks indicated that small amounts of tetrameric and dimeric species remained in solution, which was not seen in reducing wildtype preparations, possibly indicating a weakened A-type interface. The his-tagged construct eluted as one major peak in reducing conditions, with a calculated weight of 315 kDa, consistent with a dodecamer (appendix seven). No smaller species were seen in the tagged sample, and the peak showed a leading edge which could indicate the presence of HMW species.

The P48A mutein showed a smaller amount of HMW species in reducing conditions (figure 5.9C), and the trailing edge of the peak lessened. This suggested that sample was more homogeneous, with the dodecamer being the predominant species. This is similar to the profile of the S78A mutein, where the addition of a reducing agent led to the dissociation of HMW species. The RI profile of the C47S mutein was also similar to that of S78A, showing a reduction in high weight species (figure 5.9D). Instead, reduced mutein exists as an almost homogeneous population, with a single peak corresponding to the dodecamer. As with non-reducing conditions no dimer peak is seen, suggesting that all dimers are assembled into dodecameric arrangements.

R123G was the only mutein that did not oligomerise in reducing conditions. Instead, SEC/SLS gave identical results to in non-reducing conditions, with mutein continuing to elute as a single peak. Molecular weight calculations corresponded to a dimer, with weight consistent across the peak, indicating that no larger species are present (figure 5.9E). This is dramatically different to the redox switching of the wildtype (section 4.3.1.2) and indicates that mutation of R123 removes the redox sensitivity of *HsPrx3*. As reduction no longer induced self-assembly, the potential of other factors to drive association of the R123G mutein was therefore investigated. The presence of an N-terminal his-tag, and increased protein concentration (sections 4.3.1.3; 4.3.1.5) had been seen to encourage dodecamer assembly of wildtype *HsPrx3*, regardless of redox state. These conditions were examined in the case of the R123G mutein. Neither addition of

the his-tag, nor increased protein concentration showed any evidence of a dodecameric species, with R123G remaining as free dimers in solution as indicated by SEC/SLS analysis (appendix seven).

5.4.1.2 Small Angle X-ray Scattering (SAXS)

SAXS data for muteins were compared to theoretical values for wildtype *HsPrx3* oligomeric states, calculated using CRY SOL (section 2.5.5.2; Svergun *et al.*, 1995). R_G calculated using the GNOM program (Svergun, 1992) is presented. This is considered to be more accurate than Guinier region calculations as it uses the entire scattering range for the calculation (Semenyuk and Svergun, 1991). Concentration dependence was only seen in the case of untagged T104W and S78A and concluded to not be significant (discussed below), therefore only data collected from samples injected at 1 mg/mL are presented for ease of comparison. All calculated values including errors can be found in appendix seven. As calculations represent a solution average, and in many cases the muteins existed as heterogeneous solutions, the tendency toward a particular species was assessed by the deviation from the theoretical masses for a homogeneous sample of dodecameric or dimeric species.

Non-reducing conditions

The S78A sample was calculated to have an average mass of 364 kDa (table 5.3), indicating that HMW species make up a significant percentage of the total population, in line with SEC/SLS results. The presence of these species appeared to increase with concentration, however, the non-reduced sample was inclined to aggregate, and the disagreement of R_G calculations from the Guinier region and GNOM at higher concentrations suggested this was occurring (appendix seven). The nonlinear dependence of $\log(I(q))$ vs. q^2 over the range in which the Guinier approximation is valid supported this (appendix 7, figure A7.2A). It was therefore not concluded to be a valid concentration dependence.

Table 5.3: SAXS data supported SEC/SLS results

Species distributions in non-reducing conditions were assessed by the deviation from the theoretical values for homogeneous samples. S78A, P48A and C47S all showed average weights indicative of the presence of HMW species, whereas T104W and R123G existed as small species.

Sample	D_{\max} (Å)	R_G from GNOM (Å)	Volume (Å ³)	MW (kDa)	Number of dimers
S78A	223	83	70000	364	17
T104W	118	30	95000	60	4
P48A	221	66	613000	346	16
C47S	204	60	607000	369	17
R123G	87	25	74100	46	2
Wildtype Dimer	~60	Theoretical R_G : 20	49800	42	2
Wildtype Decamer	~130	Theoretical R_G : 48	392000	214	10
Wildtype Dodecamer	~180	Theoretical R_G : 59	417000	257	12

SAXS data collected for the T104W sample gave an average weight that was between that of a theoretical dimer and a tetramer, very similar to that seen for non-reduced wildtype (section 4.3.1.2.). This agrees with SEC/SLS results that indicated the dimer was the predominant species, with a small amount of tetramer present. The weight calculations were slightly concentration dependent, however, aggregation began to occur at 2 mg/mL (as judged similarly to that for S78A described above, appendix seven, figure A7.2), therefore weight calculations cannot be considered accurate at this concentration.

SAXS analysis of the P48A mutant was somewhat inconclusive as the presence of multiple species did not allow characterisation of individual populations. However, the average weight of particles solution showed a shift towards higher weights than wildtype samples, suggesting that the mutation promoted the formation of HMW species (table 5.3). In non-reducing conditions an average weight of 346 kDa was recorded, which showed no concentration dependence. R_G calculated from the Guinier

region and GNOM are not in agreement, indicating that the sample was aggregated (appendix seven). Data collected from samples run through the in line FPLC column did not improve the accuracy of results, with calculations yielding values from 283 to 880 kDa, confirming that aggregation was occurring even as the protein elutes from the column. This is in line with the broad RI peak and SEC/SLS analysis, indicating the presence of a number of species in rapid transition. The tagged C47S mutein produced a fairly stable population of species, as judged by SAXS data. The average molecular weight of 369 kDa calculated at 1 mg/mL, which indicates the presence of HMW species. However, the increase compared to a homogeneous dodecameric sample is not dramatic (~60 kDa), suggesting that the dodecamer remains the dominant species, in line with chromatographic analysis. The standard error across the sample was low, suggesting that the species distribution is stable (appendix seven).

The R123G mutein was found to be fairly unstable, and was prone to aggregation and rapid degradation, even when kept at 4°C, and was particularly problematic with synchrotron samples. This was indicated by the appearance of a second band migrating at a distance indicating a species 5 kDa smaller than the original sample on SDS-PAGE. Similar degradation had been seen to occur in wildtype samples, and has been observed by other groups (Winterbourn, personal communication). Peptide sequencing of this lower band in the case of wildtype *HsPrx3*, confirmed it to represent a truncated version of the protein, where the N-terminal residues were not seen, consistent with degradation (appendix five). Care was taken during purification to ensure that experimental samples showed no degradation (figure 5.7) and the timescale of experiments was kept to a minimum. However, the tendency to aggregate made data collection challenging and so only samples run through the in-line FPLC column were used for SAXS analysis. In non-reducing conditions, SAXS data confirmed the SEC/SLS data. The molecular weight of the untagged mutein at the apex of the peak eluting from the column indicated a species of 46 kDa, consistent with the theoretical weight of a dimer (table 5.3). However, the nonlinear Guinier plot (appendix seven, figure A7.2) indicated significant aggregation, and so results cannot be interpreted with confidence.

Reducing conditions

As the SEC/SLS data had revealed, the HMW species were redox sensitive, which was confirmed by SAXS. The average weight of three muteins that had shown a propensity to form assemblies larger than the dodecamer (S78A, P48A and C47S) decreased in reducing conditions (table 5.4). The S78A mutein had an average weight of 310 kDa when analysed at 1 mg/mL. This is considerably lower than the non-reduced sample, but reveals that HMW species are still contributing to the population.

Table 5.4: SAXS analysis indicated that the HMW species are redox sensitive

The S78A, P48A and C47S muteins in reducing conditions showed a decrease in average mass, consistent with a loss of HMW species. T104W showed an increased weight, indicating a shift to favour the oligomer, while R123G did not change significantly.

Sample	D_{\max} (Å)	R_G from GNOM (Å)	Volume (Å ³)	MW (kDa)	Number of dimers
S78A	194	62	513000	310	15
T104W	178	54	206000	127	6
P48A	211	62	506000	302	14
C47S	187	57	532000	331	15
R123G	100	29	97500	51	2
Wildtype Dimer	~60	Theoretical R_G : 20	49800	42	2
Wildtype Decamer	~130	Theoretical R_G : 48	392000	214	10
Wildtype Dodecamer	~190	Theoretical R_G : 57	502000	302	12

In reducing conditions the average weight of T104W was increased compared to non-reducing conditions, indicating that the equilibrium was shifted toward to the dodecamer (table 5.4). A slight concentration dependence was seen in reducing conditions, with average molecular weight increasing to 215 kDa at 2 mg/mL (appendix seven), though again some aggregation is occurring at this concentration. The values obtained are lower than that expected for a dodecamer, and it is unlikely that the small amount of dimeric species present when the protein is at 1 mg/mL (as judged by

SEC/SLS, figure 5.9B) would influence the average weight so significantly. This result hinted toward the presence of some decameric species, and is further investigated in section 5.4.1.3.

The P48A mutein showed a decrease in average weight, revealing that the sample was more homogeneous and the predominant species was the dodecamer. Some influence from HMW species was seen as the weight was increased compared to that expected for a homogeneous population of dodecameric species (table 5.4).

5.4.1.3 Transmission Electron Microscopy (TEM)

Prxs have been reported to form a number of high weight structures. TEM was utilised to gather further data relating to the assemblies accessible to *HsPrx3*. Muteins that were seen to form HMW species were therefore considered for TEM analysis. The P48A and C47S muteins were found to be unstable in solution, and preliminary attempts to characterise the constructs by TEM showed amorphous aggregation. Therefore, further characterisation was not carried out on these proteins.

The S78A mutein

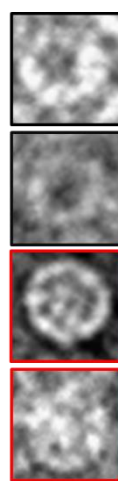
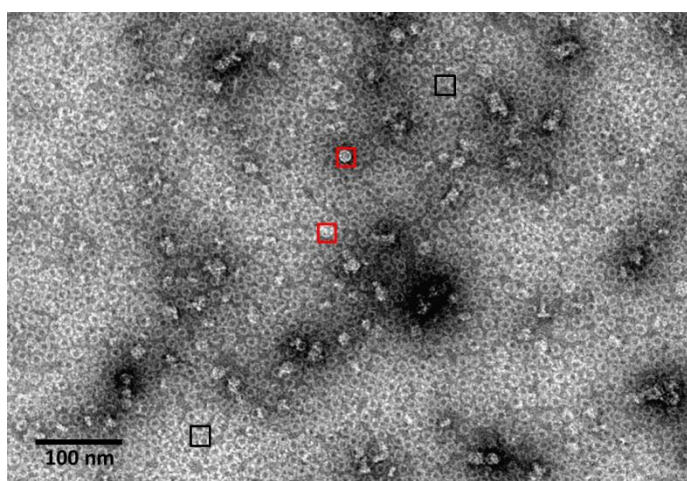
Examination of the S78A micrographs revealed the presence of dodecameric toroids. A striking feature of the micrographs was the appearance of clusters of toroids, which had not been seen in wildtype samples (figure 5.10A). The recurrence of these clusters over a number of grids of different samples and dilutions, consistency of the images and similarity to other groups' results (Jang *et al.*, 2004; Meissner *et al.*, 2007) suggested that these structures were not artefacts, nor random aggregation. Comparison to particles seen in raw images as published by Meissner *et al.* (2007) showed a strong resemblance (figure 5.10B). The published particles were used to generate a 3D reconstruction which resulted in a dodecahedral cage (section 1.2.5.3, Meissner *et al.*, 2007). Similar structures have also been observed for other Prxs when hyperoxidising

conditions are imposed (Jang *et al.*, 2004), although detailed structural characterisation was not carried out. Higher resolution TEM studies of S78A samples could provide a link between the cage-like structures and hyperoxidised state, and would be useful future work.

The T104W mutein

Although SEC/SLS indicated the presence of a dodecamer in reducing conditions, this was not seen by SAXS. Although the smaller species that were seen by SEC/SLS would influence the average mass, the oligomer was seen to be the predominant species (figure 5.9B). It was therefore surprising that at the highest concentration studied (2 mg/mL), the average weight was 215 kDa, closer to the weight of a decamer. The T104W mutation was designed based on the A-type interface of *MtAhpE* (section 3.3.1). This is a stable, redox-insensitive interface found in an octamer forming Prx. It was therefore hypothesised that the mutation may have induced some changes to the geometry of the interface, possibly altering the oligomer composition.

A: S78A micrograph



B: Particles from Meissner *et al.*, 2007

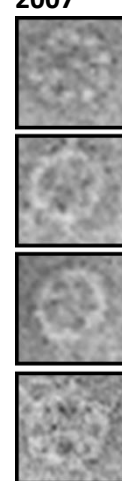


Figure 5.10: Untagged S78A forms dodecameric rings and clusters

A: The toroids (black squares, top two enlargements) appeared similar to wildtype dodecamers. Clusters were observed (red squares, bottom enlargements), which had not been seen in wildtype samples. **B:** Enlarged particles from the raw micrographs published by Meissner *et al.*, (2007) show striking similarity to the clusters of S78A.

The prevailing structure in the T104W micrographs was the dodecameric oligomer, with many of the particles showing clear hexameric arrangements of dimers. However, a number of toroids had a smaller diameter and an apparent five-fold symmetry (figure 5.11). Analysis using ImageJ software suggested these particles to have a diameter of ~13 nm. This is smaller than the expected diameter for a dodecameric toroid (15 nm, Cao *et al.*, 2005), and be more in line with that expected for a decamer (13 nm, Schröder *et al.*, 2000). A change in toroid dimensions could prevent the coordination of his-tags in the centre of the dodecamer (section 4.3.1.3), explaining the inability of the his-tag to stabilise the mutein. However, this only accounts for a small percentage of the particles, which indicates the his-tag is also causing subtle tertiary structure changes. It could also account for the weight of the untagged sample by SAXS, which was more in line with a decamer. Side views of stacked toroids were also seen, though these were not present in solution and so were concluded to be promoted by the conditions or increased protein concentration of TEM grid preparation, their absence in wildtype preparations (section 4.3.1) suggests that the T104W mutation is influencing their formation. The structure of toroid stacks and possible mechanisms of formation are discussed in chapter six.

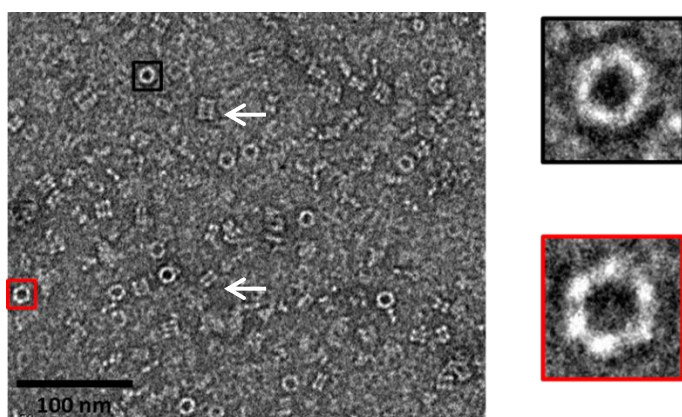


Figure 5.11: Electron micrograph of T104W revealed a heterogeneous population of toroidal species

Raw images of T104W in reducing conditions revealed a number of toroidal oligomers with 6 dimeric subunits clearly discernible (red box and enlargement). Some particles showed five-fold symmetry (black box and enlargement), and a number of stacks of toroids were observed, indicated by white arrows.

5.4.2 A combination of mutations generated a stable species

Although the C47S, S78A and P48A muteins showed a propensity to form HMW structures, these constructs were unstable and prone to aggregation. Aggregation of other Prxs with active site mutations has been seen by other groups (Angelucci *et al.*, 2013). Although this suggested that the aim of the mutation to influence self-assembly has been successful, the instability meant the constructs were not useful for further experiments. One of the goals of this study was to produce stable, locked structures of HsPrx3, which were of interest from a bionanotechnological stand point (section 1.5). The C47S mutation removed the redox sensitivity which meant that precise control of the redox state was not necessary to maintain a single conformation. It was considered that the C47S mutein may aggregate due to random association of oligomeric intermediates such as tetramers, about the R-type interface (section 1.2.5.4). The S78A mutation was seen to discourage dissociation of the dodecamer into dimers, and was therefore introduced to the C47S construct (section 2.2.3), with the aim to produce a more stable species. Design of mutagenic primers for this reaction and mutagenesis reactions were carried out by Dr. Céline Valéry at the University of Canterbury. It was predicted that the loss of the R123-C47 ionic bond would result in $\alpha 2$ helix unwinding. When this occurs within the subunits of the interface mutation stabilised toroid, it was predicted that an increase in stable, HMW structures would be seen.

5.4.2.1 Size Exclusion Chromatography/Static Light Scattering

In non-reducing conditions, untagged C47SS78S existed as an almost homogeneous population, with a major peak eluting at 11.9 mL, corresponding to a species of 257 kDa (figure 5.12A). One earlier eluting peak was seen, with calculations suggesting a species of 600 kDa, which appears to correspond to a species composed of 28 subunits. It is likely that this represents two associated toroids. In reducing conditions the elution

profile was unchanged (figure 5.12B), which was unsurprising as C_P is responsible for the redox sensitivity of *HsPrx3*. No aggregation was seen and the molecular weight across the HMW species peak was constant, indicating that this assembly is stable. In non-reducing conditions the molecular weight shows an upward trend, indicating that high weight species not detectable by the RI may be present. The sensitivity of the quaternary structure to redox state is surprising given the lack of C_P . Covalent intermolecular bonds are thought to be possible through C_R - C_R disulfide bonds after random association of monomers (Chae *et al.*, 1994; Ellis and Poole, 2007), and could be responsible for the inconsistent weight seen in the non-reduced double mutein.

A: Non-reducing conditions

B: Reducing conditions

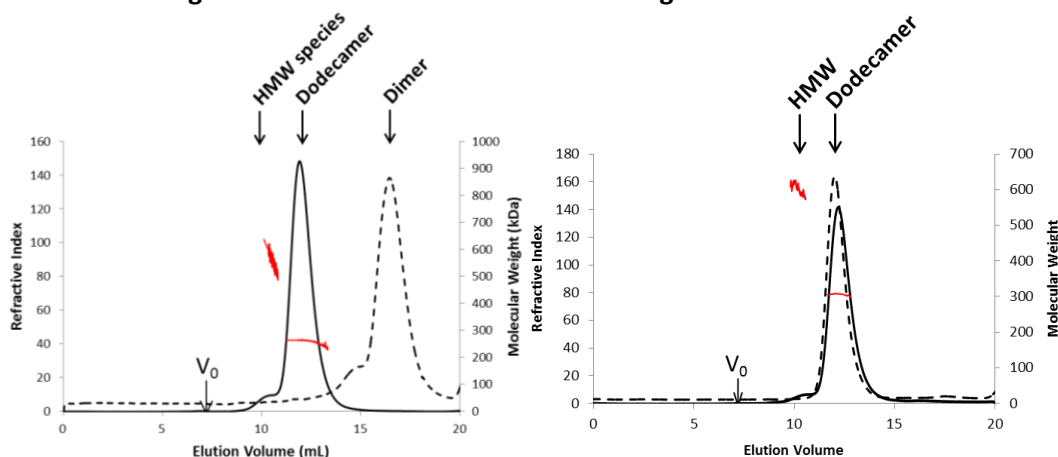


Figure 5.12: The C47SS78A mutein prevents dodecamer dissociation

A: In non-reducing conditions the elution profile of the mutein suggests the weight of the major species in solution is 257 kDa, which agrees well with a dodecamer. A shoulder peak is seen which suggests a double dodecameric species. This is markedly different to the non-reduced wildtype sample, which exists as single dimers (shown as a dashed line for comparison). **B:** In reducing conditions the mutein elution profile appears largely unchanged, although the shoulder peak represents a slightly smaller proportion of the population. Molecular weight across the peak is shown as a red line.

5.4.2.2 Small Angle X-ray Scattering

In both reducing and non-reducing conditions SAXS data agreed with SEC/SLS data. The average molecular weight was ~80 kDa higher than that expected for a dodecameric species (table 5.5), indicating that larger species were also present. The consistent impact on the average weight suggests that this HMW species is stable. Very little variability or errors were seen between images taken within a sample (table 5.5 and appendix seven) – this is in contrast to the single S78A or C47S muteins which showed variations of up to 60 kDa between images recorded from a single sample. This suggests the double mutation increased the stability and uniformity of assemblies compared to single muteins. The average weight was not concentration dependent within the range tested, as indicated by calculations and superposition of scaled scattering curves (data not shown). No indication of aggregation was seen in any condition.

Table 5.5: The C47SS78A mutation stabilises the dodecamer

Molecular weight calculations obtained from SAXS analysis suggest that the dodecamer is the predominant species, as the average weight is fairly close to that of a dodecamer. It is skewed, however, indicating the presence of higher weight complexes.

	D_{\max} (Å)	R_G from GNOM (Å)	Volum e (Å ³)	MW (kDa)	Number of dimers
C47SS78A non-reduced	206	59	56200 0	344	14
C47SS78A reduced	201	58	53700 0	331	14
Wildtype dodecamer	178	59	41700 0	257	12

The data presented indicate that mutation of C_P prevents dodecamer dissociation, presumably as the conformational changes associated with oxidation will not occur

(section 1.2.4.4). However, a number of factors other than oxidation have been seen to encourage changes in oligomeric state without a change in redox conditions (section 4.3.1.4; Wood *et al.*, 2003). Therefore, a number of other conditions were trialled in order to assess the degree of toroid stabilisation. The presence or absence of the his-tag, redox conditions, and protein concentration were investigated. None of these factors affected the assembly properties of the mutein, with the SEC/SLS elution profile unchanged in each case (figure 5.13). This indicates that the mutations have resulted in a strikingly consistent distribution of species.

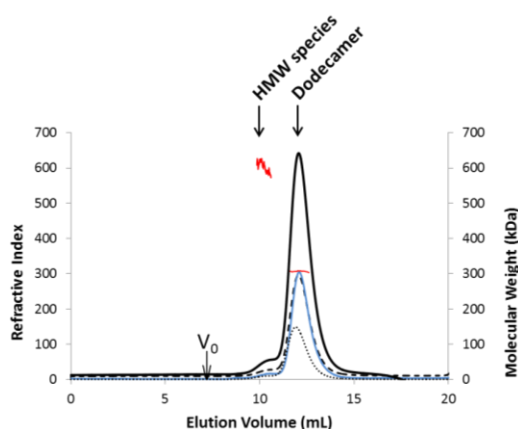


Figure 5.13: The C47SS78A mutein shows no environmental sensitivity

Untagged mutein at 1 mg/mL (dotted line), 5 mg/mL (solid line), reduced (blue line) or tagged (dashed line) elutes at a volume that was calculated to represent a ~300 kDa species, with a shoulder suggesting a larger ~600 kDa species is present. The dimer seen in the wild type sample never appears to be present in the mutant samples.

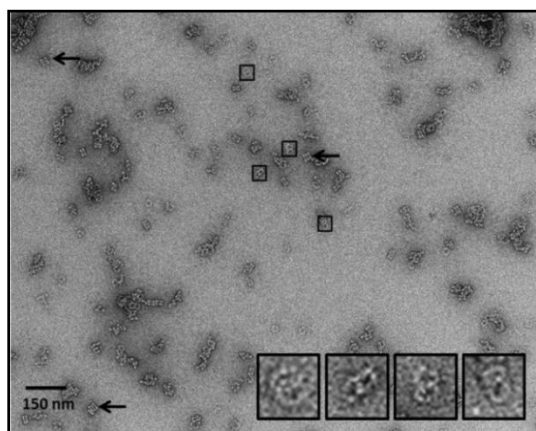
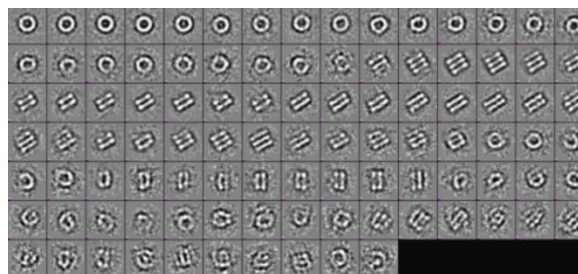
5.4.2.3 Transmission Electron Microscopy

The mutation was predicted to promote stacking of toroids, as the unwinding of helix α_2 contributes to the formation of the stacking interface (section 1.2.5.4). A small peak representing HMW species was seen in the RI trace of the C47SS78A, and so TEM was carried out to characterise the nature of these structures. As his-tagged mutein showed no significant difference in its behaviour in solution to that of untagged mutein (see also

appendix seven), this was used for TEM analysis due to the increased ease of production.

Initial examination of raw images obtained under non-reducing conditions showed few side views of single toroids, with a large number of other morphologies present (figure 5.14A). A proportion of these particles were comprised of stacks of rings. Single particle averaging (SPA) of 3001 negatively stained particles was used to generate 100 class averages (as for wildtype, section 4.3.1). This revealed that stacks of up to three toroids represented a significant percentage of the population (figure 5.14B). Although stacks of up to six toroids were seen in micrographs, their absence in class averages suggested that they do not comprise a significant percentage of the population. Projection averages representing top views do not show clear six-fold symmetry, which suggests these are top views of stacked toroids, supporting the absence of single toroids. This is in contrast to solution data which indicated that the dodecamer was the predominant species, with HMW assemblies accounting for only a small proportion of the total population. It is therefore likely that EM grid preparation or conditions favour the HMW form.

A striking feature of the mutein micrographs was the presence of morphological variants that had not been seen in other samples. Most notably, a percentage of the toroids were seen to interlock (figure 5.14A). Furthermore, projection averages that match this conformation can be seen in classification, validating their presence in the sample (figure 5.14B). Concatenation of Prxs has been reported previously (Cao *et al.*, 2005), and the agreement with this crystal structure supports that these structures in the micrographs are valid, and promoted by the double mutation. Further processing would be useful to confirm these structures, and is ongoing.

A: C47SS78A electron micrograph**B: C47SS78A class averages****Figure 5.14: EM analysis of the C47SS78A mutein revealed stacks and interlocked toroids**

A: A typical micrograph of mutein samples shows the presence of stacks of toroids (indicated by black arrows), and interlocked toroids (highlighted with black boxes and enlarged). **B:** 100 class averages generated from SPA show the presence of stacks and interlocking toroids. The lack of clear six-fold symmetry of the top views suggests they result from stacks of two or more toroids.

5.4.3 Peroxidase activity of *HsPrx3* muteins

Data from other Prxs indicated that altering the quaternary structure can lead to differences in the rate of reaction with H_2O_2 , compared to wildtype (Parsonage *et al.*, 2005). Although the focus of this chapter was to control the self-assembly of *HsPrx3* with a view to designing new tectons (section 1.5), preliminary activity assays were also carried out to assess the effect of altering quaternary structure on protein activity. The calculated values are shown in table 5.6. The C47S and C47SS78A muteins were not assayed as catalysis relies on the C47 residue (section 1.1.2.4).

S78A showed a marked increase in activity, with the rate constant almost 2.5-fold higher than that of the wildtype protein (section 4.3.2; figure 5.15A). The mutation is in

line with a similar mutation of *StAhpC* which has been seen to stabilise the decamer, and also showed increased activity compared to the wildtype *StAhpC* (Parsonage *et al.*, 2005). Both T104W and P48A mutations caused a decrease in activity, by around an order of magnitude compared to wildtype (figure 5.15B and 5.15C). The P48A mutein favours the dodecameric state, indicating that while dodecamer stabilisation may increase activity, maintenance of the active site architecture is vital for correct protein function. Although the T104W mutein did not show dramatic differences to wildtype in its quaternary structure, the decrease in activity indicates that correct interface formation is essential for optimal reaction rates.

Table 5.6: Muteins showed altered activity rates

The S78A mutein reacted with H_2O_2 at a faster rate than wildtype *HsPrx3*. All other mutations caused a decrease in reactivity, with R123G activity not able to be measured.

Mutein	Relative activity
Wildtype <i>HsPrx3</i>	$1.1 \times 10^7 \text{ M}^{-1} \text{ s}^{-1}$
S78A	$2.7 \times 10^7 \text{ M}^{-1} \text{ s}^{-1}$
T104W	$0.45 \times 10^7 \text{ M}^{-1} \text{ s}^{-1}$
P48A	$0.4 \times 10^7 \text{ M}^{-1} \text{ s}^{-1}$
R123G	Not calculated

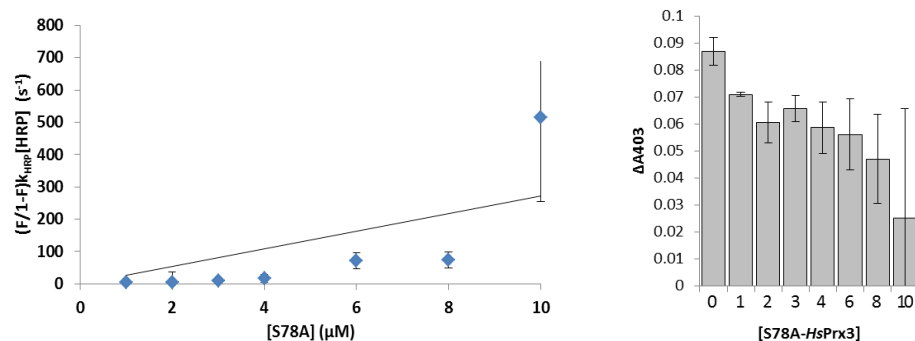
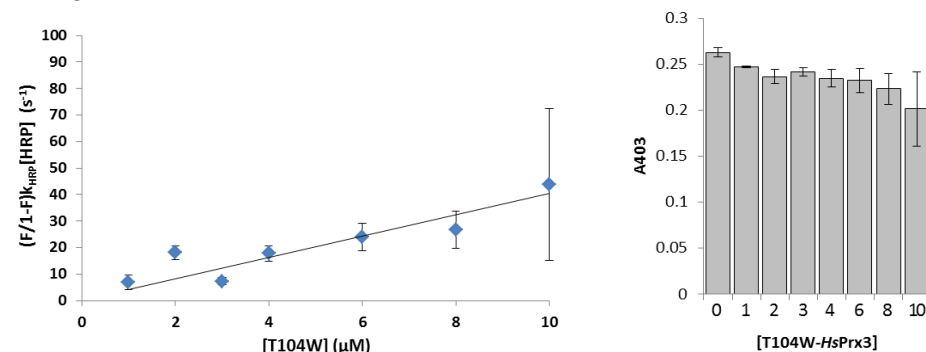
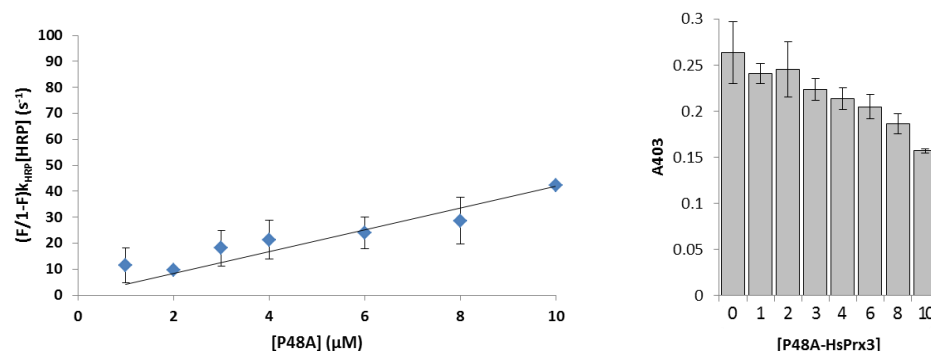
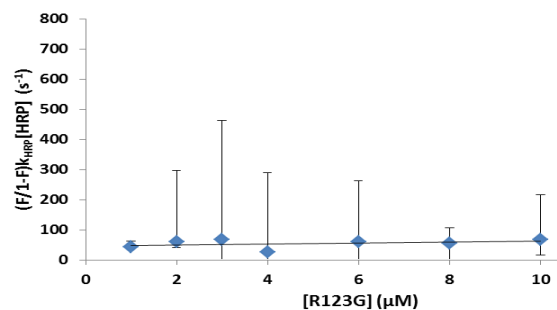
A: S78A**B: T104W****C: P48A****D: R123G**

Figure 5.15: Activity data suggests all mutants affect protein function

The S78A mutant showed increased activity compared to the wildtype. All other mutations impeded the reaction with H₂O₂, with the rate of the R123G mutant unable to be measured. Error bars indicate standard error. Bar graphs show the formation of Compound I in the presence of the specified protein concentrations. This is not shown in the case of R123G as the change in absorbance at 403 nm was often negative.

The rate constant for R123G was not able to be calculated. The raw data did not show any trend, reflected in the activity plot (figure 5.15D). There appeared to be no decrease in the production of Compound I (as indicated by the horizontal trend line), suggesting HRP is reacting significantly faster than the mutein and making analysis by this assay not possible. The recorded data were close to the baseline (section 2.6.1), and in some cases below the baseline, yielding negative values. This distorts the deviation within the data, resulting in the large errors that were observed (figure 5.15D). Early studies had shown this conserved arginine residue to be important for catalytic activity (König *et al.*, 2003), and during the course of this thesis results were published confirming its importance in the specific activity of C_P with H₂O₂ in the case of *HsPrx3* (Nagy *et al.*, 2011). A reduction in activity by five orders of magnitude has previously been seen for this mutein compared to wildtype *HsPrx3* when measured by stop-flow (Nagy *et al.*, 2011), supporting the results presented here. High errors are seen in some cases at the highest concentrations, possibly due to the amplified effect of small pipetting errors as the volumes were small. This is an effect that has been seen previously for this assay (Yewdall, 2013, unpublished data).

5.5 Discussion

The introduction of mutations to the *HsPrx3* monomer gave insight into the mechanism behind self-assembly, and the role of the active site in this assembly. Table 5.7 summarises the effects of the mutations of the protein's structure and function.

Table 5.7: Summary of mutein quaternary structures and activities

The structure in reducing and non-reducing conditions is described, as well as the activity relative to wildtype *HsPrx3*.

Mutation	Quaternary Structure		Relative activity
	Reducing Conditions	Non-reducing Conditions	
S78A	Dodecamer + Dimer	HMW + Dodecamer + Dimer	Increased
T104W	Dodecamer + Tetramer	Dimer + Tetramer	Decreased
C47S	Dodecamer	HMW + Dodecamer	N/A
P48A	Heterogeneous	Mostly Dodecamer	Decreased
R123G	Dimer	Dimer	Inactive

5.5.1 A-type interface stabilisation may rely on hydrophobic forces

The increased stability of the A-type interface seen in S78A mutein samples is consistent with the stabilisation was seen by Parsonage *et al.*, (2005) upon mutation of the equivalent residue in *StAhpC*. The authors do not observe large structural changes at the interface despite a significant change in toroid stability, attributing this to the burial of an extra methyl group of valine compared to the native threonine. In the case of *HsPrx3*, the energy associated with burial of the more hydrophobic of alanine compared to that of the native, polar serine (Monera *et al.*, 1995), and consequent changes in packing at the interface must be more favourable than that of the formation of an H-bond. Hydrophobic packing at the interface may have a larger influence than specific interactions, therefore mutations that increase the hydrophobicity of this area and allow closer packing could be a successful approach to locking the interface. The T77V mutein of *StAhpC* (Parsonage *et al.*, 2005) was seen to have increased mobility of the C_P loop region (Nirudodhi *et al.*, 2011). By analogy it was hypothesised that the S78A mutein has a similar increase in loop mobility, possibly through prevention of the dissociation usually caused by C_P loop unfolding forcing the loop to adopt a different

conformation. Hyperoxidation has been suggested to drive the formation of HMW species (Moon *et al.*, 2005; Jang *et al.*, 2004), though unwinding of helix $\alpha 2$ (Saccoccia *et al.*, 2012). Increased mobility of the C_P loop in the case of the S78A mutein could therefore mimic the hyperoxidised state, resulting in toroid association. Although preliminary studies using protocols employed to hyperoxidise other Prxs were trialled with *HsPrx3* (Cox *et al.*, 2010), no HMW species were seen by TEM and a comparison with the S78A HMW species could not be made (further discussed in section 6.4).

The increased activity of this mutein compared to wildtype suggests that the stabilisation of the dodecamer promotes the reaction with H₂O₂, which has been seen in similar muteins of other Prxs (Parsonage *et al.*, 2005). However, when dissociation is completely prevented with the his-tag, activity is dramatically reduced (section 4.3.2). This reveals that simply stabilising the dodecamer does not increase activity, but that the ability to switch oligomeric states is required. This has been hypothesised to be a compromise, as a stabilised toroid may be more active, be also more susceptible to inactivation hyperoxidation (section 1.2.4.5; Wood *et al.*, 2003b). The HMW structures of the S78A mutein support this.

5.5.2 Toroid formation relies on the folded C_P loop

Encouraging the folded active site through introducing rigidity to the C_P loop prevented toroid dissociation, as demonstrated by the P48A mutein. The mobility of this loop is therefore clearly responsible for the dodecamer to dimer transition. This is supported by the R123G mutein which is predicted to have a more mobile C_P loop (section 5.2.2.2), and is unable to oligomerise. In native Prxs, the conserved P48 closes off one side of the active site, and is thought to prevent unwanted reactions (Poole in Banerjee *et al.*, 2008). When mutated to alanine, the reactive thiolate would be exposed and could be protonated by water molecules in the solvent. This could explain the reduced activity of

the mutein, as some spurious reactions could occur before the protein can react with H_2O_2 , and without reductant in the buffer recycling is not possible (section 1.2.2.3). These results provide some support for the theory of the role of this residue (Wood *et al.*, 2002), and although the mutein was unstable and therefore not a good candidate for further use to develop controlled structures, it provides some insight into approaches to lock to the dodecamer through altering C_P loop mobility.

5.5.3 Interface mutations may alter toroid geometry

Although it did not have an obvious effect on the dimer-dodecamer equilibrium, the T104W mutation may have affected the diameter of the toroid. The *MtAhpE* A-type interface which inspired the mutation exists as part of an octameric oligomer, and could adopt a different angle to that in a dodecameric arrangement. Introduction of the T104W could lead to stabilisation of the loop regions at the interface, and a shift in interface angle to mimic that seen in *MtAhpE* (see figure 5.3). This shift could result in a different toroid diameter to wildtype, and possibly the formation of decamers. The structure and sequence of the interface regions are highly conserved across the Prxs, with only small sequential discrepancies seen between those that form different multimers. This study indicates that the multimeric state may be able to be controlled by subtle differences in interface structure. This is an exciting possibility and further study of the mutein would be beneficial, particularly processing of the EM data. The introduction of mutations to the B-type interface would also be worthwhile, as the geometry of this interface has been suggested to be key in determining the multimeric state (Gretes and Karplus, 2013).

5.5.4 HMW formation relies on the unwinding of the $\alpha 2$ helix

Although the C47S mutation has been considered to mimic the reduced form of the enzyme (König *et al.*, 2013), it is more accurately representative of the protonated form, as the reduced form still exists as a thiolate ion stabilised by the active site arginine. The protonated form of C_P would prevail at pH levels below the pK_a of cysteine, and in these conditions an increased propensity to form HMW structures has been seen in the case of some Prxs (Saccoccia *et al.*, 2012; Angelucci *et al.*, 2013). These are when the wildtype enzyme is reduced, therefore protonation has been suggested to lead to unwinding of helix $\alpha 2$ and concomitant HMW formation. It can be concluded that in the case of *HsPrx3* mutation of C_P to serine increases helix unwinding and stabilisation of the toroid and HMW structures, in the same way that protonation does.

The lack of R123 could be expected to result in destabilisation of the thiolate form of C_P, and, therefore, protonation of C_P (Wood *et al.*, 2003). However, the R123G mutein showed a different quaternary structure to the C47S mutein. The dimeric nature of the R123G mutein could mean that this residue has roles beyond maintaining the active site structure. R123 has been suggested to interact with a second conserved arginine residue (R146 in *HsPrx3*; Hall *et al.*, 2010). The sequentially distal nature of these residues implies that R123 has significant roles in maintaining a global tertiary structure conducive to dimer self-assembly, supported by the oligomeric behaviour of the mutein. Comparison with Prxs from the Prx5, TPx or bacterioferritin comigratory protein (BCP) family (which are a-typical 2-Cys and 1-Cys Prxs) lends further credence to this theory. The more C-terminal arginine is not present in these proteins, and they do not form assemblies beyond the dimer (Declercq *et al.*, 2001; D'Ambrosio *et al.*, 2009; reviewed in Wood *et al.*, 2003).

The results presented here show that the dimer-dodecamer inter-conversion is a tightly regulated phenomenon, requiring the correct global structure of the dimer, a correctly

folded active site and appropriate C_P loop mobility. Three approaches to prevent dodecamer dissociation and encourage HMW structures are presented: (1) Imitate protonation of C_P; (2) Decrease C_P loop mobility; and (3) Imitate hyperoxidation of C_P. Interestingly, the morphology of the HMW assemblies seen in samples of S78A and C47S muteins were dramatically different. It has been suggested that protonation and hyperoxidation of C_P lead to helix unwinding through different mechanisms (Saccoccia *et al.*, 2012). It is proposed that S78A mutein represents a hyperoxidised state, and C47S a protonated state, therefore the results presented here support the theory of two discrete mechanisms. This also highlights that Prxs may be able to form a number of different structures depending of the mechanism of helix unwinding, and presents an exciting approach to driving the formation of different structures from one tecton.

It would be useful to test this hypothesis and elucidate the different mechanisms of helix unwinding through studying other mutations that cause similar conformational changes. The hyperoxidised state could be mimicked through mutation of C_P to a residue with an increased volume and hydrophilicity, such as aspartic acid. Increasing the propensity of $\alpha 2$ helix unwinding without introducing mutations that alter the active site residues could help to separate the influence of unwinding, and loss of active site architecture on self-assembly. Introducing a helix-disrupting residue such as glycine would be one approach, however, this can have a large impact on tertiary structure and may result in incorrect folding. The role of R123 could be further by mutating residue R146 residue to probe the importance of this interaction. NMR analysis of the S78A mutein could indicate whether increased loop mobility is in fact a feature of the stabilised dodecamer, and if so, similar interface mutations could be designed to further test this theory. Introduction of multiple mutations at the interface may increase the stability further. In all cases, crystal structures would be valuable to confirm hypothesised structural changes of muteins.

5.5.5 Muteins give insight into HMW structure formation

The appearance of concatenated toroids demonstrated the conformational flexibility that is present in the Prxs, with individual constructs able to form a number of different HMW structures. The agreement with a previously published crystal structure leads to the conclusion that this represents a valid assembly. Interestingly, in both cases where concatenation has been seen, the proteins contained a mutation of a cysteine residue (the resolving cysteine, C_R, in the work of Cao *et al.*, [2005]; C_P in this work). The disulfide-bonded dimer of native Prxs forms as the C-terminal arm of one monomer reaches across the other, forming a domain swapped dimer (Barranco-Medina, 2009). An assembly intermediate has recently been seen, suggesting that the dimers may in fact associate while they are still disulfide-bonded (Cao *et al.*, 2011). Without the ability to form a disulfide bond, the mutein dimers may have slightly different dimensions, which could allow concatenation as they begin to associate into the toroid.

5.5.6 Summary and outlook

Despite the well-known concept that protein structure is linked to function, in many cases the precise relationship remains unknown (for example, Devenish and Gerrard, 2009). Prxs are a striking example of the complex nature of this relationship; although there is a correlation between the oxidation state of C_P and quaternary structure, the exact causality is unclear. Furthermore, in a family which shows such high conservation, a surprising number of individuals exist which appear to contradict any conclusions which are drawn. For example, in some cases dimers can form about a redox-insensitive A-type interface (Li *et al.*, 2005, Mizohata *et al.*, to be published, [PDB ID: 2CX4] and Ebihara *et al.*, to be published [PDB ID: 2YWN]). The factors that control Prx quaternary structure remain unclear, as are the physiological implications of

the varying dimensions of toroids. This work reveals that single residues have significant contributions to the structure and function of Prxs, and provides some important structural insights into the subtleties that govern the formation, and potentially size, of Prx toroids. The dramatic effect that single residue mutations can induce reveal that Prx self-assembly is finely tuned, and under tight control within the cell.

This study revealed that in the case of *HsPrx3*, mutation of single residues that contribute to active site architecture can dramatically alter the oligomeric properties. It is concluded that the controlled folding and unfolding of the C_P loop is the force behind dimer assembly and disassembly, and the unwinding of the $\alpha 2$ helix drives HMW formation. The activities of the muteins compared to his-tagged wildtype revealed that the mobility of the C_P loop and helix $\alpha 2$ were more important for the high reactivity of *HsPrx3* than influencing the dimer-dodecamer equilibrium. Increasing the mobility of the C_P loop without disrupting the active site could be a means to promote peroxidase activity. This could provide a useful avenue to study Prxs in a biomedical realm, though was not addressed in this work which focussed instead on controlling the self-assembly properties of the protein.

Through the rational design of mutations, and the work presented in chapter four, a set of non-native structures have been generated which successfully lock the toroid (his-tagged *HsPrx3*), disrupt the toroid (R123G), and potentially alter toroid dimensions (T104W). The C47S and P48A muteins highlighted prospective avenues toward engineering HMW structures, which were explored through the generation of the C47SS78A double mutein. Various HMW organisations were seen to be accessible to *HsPrx3*, and it is proposed that a number of discrete mechanisms exist for high weight assembly, which may be driven by different factors. This supports the early theory by Jang *et al.* (2004) who suggested that toroid association may occur through either an H₂O₂-dependent, or an H₂O₂-independent mechanism, which could be explained by Saccoccia's theory (Saccoccia *et al.* 2012) that protonation and hyperoxidation cause

assembly through different routes. The different high weight arrangements of the S78A and C47SS78A muteins support this theory, and highlight the possibility that, through minor alterations to primary structure, *HsPrx3* molecules can be driven to form different supramolecular structures.

This chapter presents a promising start to controlling the dimer-dodecamer switch of *HsPrx3*, and HMW structures. Further in depth analysis of the larger structures could reveal more details regarding the interactions and factors that contribute to their stabilisation, which would allow further modification of subunits and a greater level of control. From this, a set of novel subunits could be designed, that assemble into a variety of structures in response to environmental triggers.

5.6 References

- Angelucci, F., Saccoccia, F., Ardini, M., Boumis, G., Brunori L., Di Leandro, R., Ippoliti, R., Miele, A.E., Natoli, G., Scotti, S. and Bellelli, A. (2013) Switching between the alternative structures and functions of a 2-Cys peroxiredoxin by site-directed mutagenesis. *Journal of Molecular Biology* **425**, 4556-4568.
- Barranco-Medina, S., Lázaro, J.-J. and Dietz, K.-J. (2009) The oligomeric conformation of peroxiredoxins links redox state to function. *Federation of European Biochemical Societies Letters* **583**, 1809-1816.
- Cao, Z., Roszak, A. W., Gourlay, L. J., Lindsay, J. G. and Isaacs, N. W. (2005) Bovine mitochondrial Peroxiredoxin III forms a two-ring catenane. *Structure* **13**, 1661-1664.
- Cao, Z., Bhella, D. and Lindsay, J. G. (2007) Reconstitution of the mitochondrial PrxIII antioxidant defence pathway: General properties and factors affecting PrxIII activity and oligomeric state. *Journal of Molecular Biology* **372**, 1022-1033.
- Cao, Z., Tavender, T. J., Roszak, A. W., Cogdell, R. J. and Bulleid, N. J. (2011) Crystal structure of reduced and of oxidized peroxiredoxin IV enzyme reveals a stable oxidized decamer and a non-disulfide-bonded intermediate in the catalytic cycle. *Journal of Biological Chemistry* **286**, 42257-42266.
- Chae, H. Z., Uhm, T. B. and Rhee, S. G. (1994) Dimerization of thiol-specific antioxidant and the essential role of cysteine 47. *Proceedings of the National Academy of Sciences of the United States of America* **91**, 7022-7026.
- Cox, A. G., Winterbourn, C. C. and Hampton, M. B. (2010) Mitochondrial peroxiredoxin in antioxidant defence and redox signalling. *Biochemical Journal* **425**, 313-325.
- D'Ambrosio, K., Limauro, D., Pedone, E., Galdi, I., Pedone, C., Bartolucci, S. and de Simone, G. (2009) Insights into the catalytic mechanism of the Bcp family: functional and structural analysis of Bcp1 from *Sulfolobus solfataricus*. *Proteins: Structure, Function, Bioinformatics* **76**, 995-1006.
- Declercq, J.-P., Evrard, C., Clippe, A., Stricht, D. V., Bernard, A. and Knoops, B. (2001) Crystal structure of Human Peroxiredoxin 5, a novel type of mammalian peroxiredoxin at 1.5Å resolution. *Journal of Molecular Biology* **311**, 751-759.
- DeLano, W.L. (2002). The PyMOL Molecular Graphics System (San Carlos, CA: DeLano Scientific).
- Devenish, S. R. A. and Gerrard, J. A. (2009) The role of quaternary structure in (β/α)₈-barrel proteins: evolutionary happenstance or a higher level of structure-function relationships? *Organic and Biomolecular Chemistry* **7**, 833-839.

- Ellis, H. R. and Poole, L. B. (1997) Roles for the two cysteine residues of AhpC in catalysis of peroxide reduction by alkyl hydroperoxide reductase from *Salmonella typhimurium*. *Biochemistry* **36**, 13349-13356.
- Gourlay, L. J., Bhella, D., Kelly, S. M., Price, N. C. and Lindsay, J. G. (2003) Structure-function analysis of recombinant substrate protein 22 kDa (SP-22): a mitochondrial 2-Cys peroxiredoxin organised as a decameric toroid. *Journal of Biological Chemistry* **35**, 32631-32637.
- Gretes, M. C. and Karplus, P. A. (2013) Observed octameric assembly of a *Plasmodium yoelii* peroxiredoxin can be explained by the replacement of native “ball-and-socket” interacting residues by an affinity tag. *Protein Science* **10**, 1445-1452.
- Hall, A., Parsonage, D., Poole, L. B. and Karplus, P. A. (2010) Structural evidence that Peroxiredoxin catalytic power is based on transition-State stabilization. *Journal of Molecular Biology* **402**, 194-209.
- Haynes, A. C., Qian, J., Reisz, J. A., Furdui, C. M., Lowther, W. T. (2013) Molecular basis for the resistance of human mitochondrial 2-Cys peroxiredoxin 3 to hyperoxidation. *Journal of Biological Chemistry* **288**, 29714-29723.
- Hedde, J. G. (2008) Protein cages, rings and tubes: useful components of future nanodevices? *Nanotechnology, Science and Applications* **1**, 67-78.
- Jang, H. H., Lee, K. O., Chi, Y. H., Lee, J. R., Lee, S. S., Moon, J. C., Yun, J. W., Choi, Y. O., Kim, W. Y., Kang, J. S., Cheong, G.-W., Yun, D.-J., Rhee, S. G., Cho, M. J. and Lee, S. Y. (2004) Two enzymes in one: Two yeast peroxiredoxins display oxidative stress-dependent switching from a peroxidase to a molecular chaperone function. *Cell* **117**, 625-635.
- König, J., Lotte, K., Plessow, R., Brockinke, A., Baier, M. and Dietz, K.-J. (2013) Reaction mechanism of plant 2-Cys peroxiredoxin: role of the C-terminus and the quaternary structure. *Journal of Biological Chemistry* **278**, 24409-24420.
- Krissinel, E. and Henrick, K. (2007) Inference of macromolecular assemblies from crystalline state. *Journal of Molecular Biology* **372**, 774-797.
- Li, S., Peterson, N. A., Kim, M.-Y., Kim C.-Y., Hung, L.-W., Yu, M., Lakin, T., Segelke, B. W., Lott, J. S., Baker, E. N. (2005) Crystal structure of AhpE from *Mycobacterium tuberculosis*, a 1-Cys peroxiredoxin. *Journal of Molecular Biology*, **346**, 1035-1046.
- Ludtke, S. J., Baldwin, P. R. and Chiu, W. (1999) EMAN: Semi-automated software for high-resolutions single-particle reconstructions. *Journal of Structural Biology* **128**, 82-97.
- Meissner, U., Schröder, E., Scheffler, D., Martin, A. G. and Harris, J. R. (2007) Formation, TEM study and 3D reconstruction of the human erythrocyte peroxiredoxin-2 dodecahedral higher-order assembly. *Micron* **38**, 29-39.

- Moon, J. C., Hah, Y.-S., Kim, W. Y., Jung, B. G., Jang, H. H., Lee, J. R., Kim, S. Y., Lee, Y. M., Jeong, M. G., Kim, C. W., Cho, M. J. and Lee, S. Y. (2005) Oxidative stress-dependent structural and functional switching of a human 2-Cys peroxiredoxin Isotype II that enhances HeLa cell resistance to H₂O₂-induced cell death. *Journal of Biological Chemistry* **280**, 28775-28784.
- Monera, O. D., Sereda, T. J., Zhou, N. E., Kay, C. M. and Hodges, R. S. (1995) Relationship of sidechain hydrophobicity and α -helical propensity on the stability of the single-stranded amphipathic α -helix. *Journal of Peptide Science* **1**, 319-329.
- Moreira, I. S., Fernandes, A. and Ramos, M. J. (2007) Hot spots – a review of the protein-protein interface determinant amino acid residues. *Proteins: Structure, Function, Bioinformatics* **68**, 803-812.
- Nagy, P., Karton, A., Betz, A., Peskin, A. V., Pace, P., O'Reilly, R. J., Hampton, M. B., Radom, L. and Winterbourn, C. C. (2011) Model for the exceptional reactivity of peroxiredoxins 2 and 3 with hydrogen peroxide: a kinetic and computational study. *Journal of Biological Chemistry* **286**, 18048-18055.
- Nirudodhi, S., Parsonage, D., Karplus, P. A., Poole, L. B. and Maier, C. S. (2011) Conformational studies of the robust 2-Cys peroxiredoxin *Salmonella typhimurium* AhpC by solution phase hydrogen/deuterium (H/D) exchange monitored by electrospray ionization weight spectrometry. *International Journal of Weight Spectrometry* **302**, 93-100.
- Parsonage, D., Youngblood, D. S., Sarma, G. N., Wood, Z. A., Karplus, P. A. and Poole, L. B. (2005) Analysis of the link between enzymatic activity and oligomeric state in AhpC, a bacterial peroxiredoxin. *Biochemistry* **44**, 10583-10592.
- Poole, L. B. and Fridovich, I. (2008) ROS-dependent enzymes. In: Banarjee, R. (Ed) Redox Biochemistry. pp. 50-68 John Wiley and Sons, Inc.; Hoboken, New Jersey.
- Saccoccia, F., Micco, P. D., Bournis, G., Brunori, M., Koutris, I., Miele, A. E., Morea, V., Sriratana, P., Williams, D. L., Bellelli, A. and Angelucci, F. (2012) Moonlighting by different stressors: crystal structure of the chaperone species of a 2-cys peroxiredoxin. *Structure* **20**, 429 – 439.
- Schröder, E., Littlechild, J. A., Lebedev, A. A., Errington, N., Vagin, A. A. and Isupov, M. N. (2000) Crystal structure of decameric 2-Cys peroxiredoxin from human erythrocytes at 1.7Å resolution. *Structure* **8**, 605-615.
- Semenyuk, A. A. and Svergun, D. I. (1991) GNOM – a program package for small-angle scattering data processing. *Journal of Applied Crystallography* **24**, 537–540.
- Svergun D.I. (1992) Determination of the regularization parameter in indirect-transform methods using perceptual criteria. *Journal of Applied Crystallography* **25**, 495-503.

- Svergun D. I., Barberato, C. and Koch M. H. J. (1995) CRY SOL - a program to evaluate X-ray solution scattering of biological macromolecules from atomic coordinates. *Journal of Applied Crystallography* **28**, 768-773.
- Wood, Z. A., Poole, L. B., Hantgan, R. R. and Karplus, P. A. (2002) Dimers to doughnuts: redox-sensitive oligomerisation of 2-Cys peroxiredoxins. *Biochemistry* **41**, 5493-5504.
- Wood, Z. A., Schröder, E., Harris, J. R. and Poole, L. B. (2003) Structure, mechanism and regulation of peroxiredoxins. *Trends in Biochemical Sciences* **28**, 32-40.

Chapter 6 Engineering HMW structures of *HsPrx3*

6.1 Introduction

In this chapter, a careful analysis of the literature is presented; focussing on published structures of HMW forms of Prxs (section 6.2.1). This provided some suggestions of the factors which control the formation of these assemblies. Previous work detailed in chapter four gave insight into the mechanisms behind *HsPrx3* assembly, and chapter five highlighted the potential to control the quaternary structure through subtle changes to the primary structure. Preliminary analysis of *HsPrx3* had indicated that the toroids may be able to associate into HMW assemblies when the his-tag is attached. As Prxs are able to form a wide range of HMW assemblies (section 1.2.5.3), the 3D structure of the HMW form of his-tagged *HsPrx3* was analysed. Building on these results, the possibility to drive native *HsPrx3* toroids to assemble into large structures by altering environmental conditions was investigated. A clear understanding of the conditions that regulate the formation and size of these structures is lacking, and the results presented here provide some insight. Electron microscopy was used to analyse the interactions involved, and provides the first high resolution information on these assemblies.

6.2 Toroid stacking occurs in response to a number of factors

6.2.1 Analysis of the literature

A number of groups have reported the presence of stacks of toroids in Prx preparations, with organisations ranging from small assemblies of two or three toroids, to nanotubes

of various lengths (Kato, 1985; Cao *et al.*, 2007; Gourlay *et al.*, 2003). The antiapoptotic roles of Prx, and their upregulation and aggregation in response to cellular stress imply biomedical implications (Jang *et al.*, 2004). Published HMW structures have been obtained using mutated or modified Prx constructs, or samples spiked with metal ions (discussed in section 1.2.5.3). This leads to the question of whether these assemblies are physiologically relevant, or even possible *in vivo*, or if they are *in vitro* artefacts.

The work of Harris (1969) suggests *in vivo* significance, as similar stacks were observed in native Prx2 from erythrocyte extracts. In this case, protein was extracted from the membrane fraction of erythrocyte preparations. Prx2 is known to associate with membranes when hyperoxidised (Cha *et al.*, 2000), and immunostaining has revealed that Prx2 appears to assemble into long filaments in cells that are exposed to oxidative stress (Phalen *et al.*, 2006). It is therefore possible that the authors had preferentially selected for the hyperoxidised form of the protein, which were prone to assembling into HMW structures.

Although previous studies do not present a clear trend between conditions and the resultant structures formed, some common factors can be identified when the permutations in the purification protocol are considered. Table 6.1 details the HMW structures currently published, and the conditions in which they were observed. A notable feature is the presence of a his-tag in many of the structures. This has been seen to promote the formation of HMW structures and may suggest that these are not native arrangements of the proteins (section 4.3.1.3).

Table 6.1: Published structures of HMW are obtained from modified constructs

Comparison of preparative methods which have resulted in Prx HMW formation provides insight into the mechanism behind toroid stacking. A notable feature of the publications which report HMW forms of Prxs is the presence of a his-tag.

Reference	Recorded structure	Method of visualisation	Notable conditions of preparation
Harris, 1969	Small stacks	TEM	Membrane extraction
Kato, 1985	Long tubes	TEM	Addition of magnesium ions
Jang <i>et al.</i> , 2004	Clusters	TEM	Overoxidation or heat shock
Cao <i>et al.</i> , 2005	Interlocked rings	Crsytal structure	His-tagged with C _R mutation
Cao <i>et al.</i> , 2007	Interlocked rings	TEM	His-tagged with C _R mutation
Saccoccia <i>et al.</i> , 2012	Double toroid	Crystal structure	His-tagged, low pH (4.2)
Angelucci <i>et al.</i> , 2013	Stacks	TEM	His-tagged with C _P mutation
Gourlay <i>et al.</i> , 2003	Small stacks; Longer tubes	TEM TEM	His-tagged protein His-tagged with C _R mutation

6.2.2 The R-type interface

The recent crystal structure containing two stacked toroids of *SmPrx1* gave some insight into the interactions involved in the R-type interface (Saccoccia *et al.*, 2012; discussed in section 1.2.5.4). This crystal structure provides some explanation for earlier observations of Prx HMW assemblies. When hyperoxidised, the increased volume of C_P-SO₂H or C_P-SO₃H may favour the movement of C_P out of the active site pocket, similar to what is seen to occur at low pH (Saccoccia *et al.*, 2012), and allowing the R-type interface interactions to occur. This is supported by the crystal structure of a hyperoxidised Prx, where unwinding of helix α_2 is observed (section 1.2.4.3; Jönsson *et al.*, 2008), and could also provide an explanation for the stacks seen by Harris (1969).

Mutation of C_P is likely to cause similar rearrangements as hyperoxidation. In both cases the integrity of the active site is no longer maintained (section 5.2.2.2), which

could explain the increase in the size of the tubes recorded by when this residue is mutated (Gourlay *et al.*, 2003). Recent crystal structures and solution data of *SmPrx1* (Angelucci *et al.*, 2013) confirm that mutation of C_P leads to unfolding of the $\alpha 2$ helix, which encourages R-type interface formation.

Many Trx fold proteins contain a conserved proline residue, but in the case of Prxs it is replaced by an arginine (R123 in the case of *HsPrx3*). When the proline of a Trx protein is mutated to an arginine to mimic the Prx structure, the Trx proteins are able to coordinate an Fe₂S₂ cluster (Su *et al.*, 2007). This led to the theory that the proline exists to prevent metal binding at the thiolate-based active site. The absence of this residue in the similar active site of Prxs strongly suggests that they may accommodate metal ions in their active sites, supported by some crystal structures (Wood *et al.*, 2002; Choi *et al.*, 1998). This possible binding of metal ions would likely alter the interactions that maintain the correct architecture, leading to movement of C_P and concomitant rearrangements to allow the R-type interface formation. This could explain the formation of Prx tubes in the presence of magnesium as seen by Kato *et al.*, as well as the dissociation of the tubes upon addition of chelating agents (Kato *et al.*, 1985).

To conclude, the literature indicates that the primary factor influencing the stacking of untagged Prx toroids is the movement of C_P out of the active site, either through loss of stabilising interactions, or disruption by bulky groups or metal ions. This provides a testable hypothesis, and an approach to drive the formation of Prx stacks in a controlled manner.

6.2.3 His-tagged *HsPrx3* forms stacks of toroids

Preliminary studies of his-tagged *HsPrx3* indicated that the protein forms a stable dodecamer, with small amounts of HMW species observed, appearing to be ~470 kDa (section 4.3.1.3). TEM was used to elucidate structural differences between native and his-samples. Comparison of fields of views revealed striking structural differences that appear to be introduced by the his-tag (figure 6.1A). Some side views of single his-tagged toroids were seen; however, the majority of the particles showed higher quaternary states. Stacks of up to four toroids were apparent in his-tagged samples, which were not seen in untagged samples. 6850 His-tagged particles were automatically selected and subjected to SPA. Reference-free image classification in EMAN was used to group the raw projections into 100 classes (figure 6.1B; Ludtke *et al.*, 1999; section 2.4.5.2).

The class averages obtained confirmed that stacks of up to four toroids represent a significant percentage of the population. Particle averaging gave a clear picture of the stacks, with contacts occurring at discrete points, resulting in large gaps between the toroids. Side views of single toroids were notably absent from class averages, indicating that they represent a very small percentage of the total population. Large assemblies appear more abundant in the TEM images than in solution. Although automatic particle picking was supervised, it is possible that stacked toroids are more readily selected by the routine than single side views. Quantification of the number of stacked species observed by TEM could also be complicated by the possibility that different species may vary in their propensity to attach to the carbon substrate. Mindful of this caveat, an approximation of the populations present for wildtype protein, with and without the tag was determined through manual examination. Three electron micrographs of untagged *HsPrx3* and tagged *HsPrx3* were selected for manual particle picking (figure 6.2), which demonstrated that the population is markedly shifted towards stacks by the presence of a his-tag.

Under reducing conditions, the only observed species of untagged *HsPrx3* were single toroids, comprising 100% of the particles that were manually counted. In tagged samples, under both non-reducing and reducing conditions, the proportion of single toroids was determined to be less than 1% of the population, while double toroids accounted for the majority (>90%). The proportion of stacks with three or more toroids was <10%.

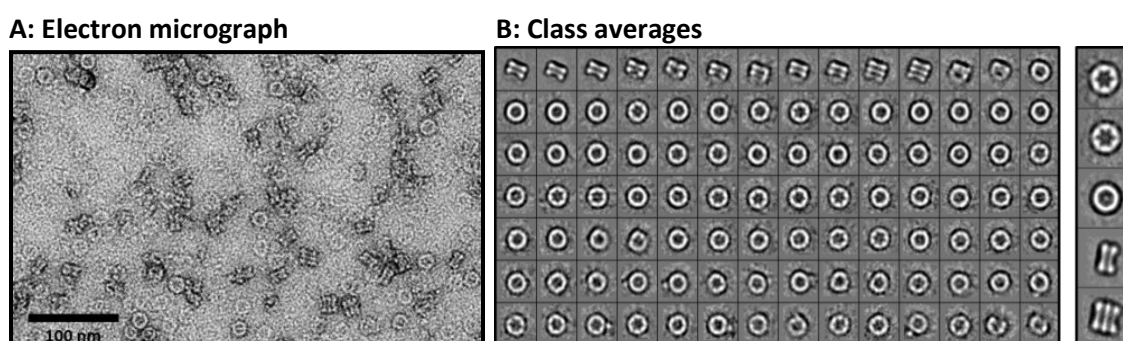


Figure 6.1: His-tagged *HsPrx3* forms stacks of toroids

A: Electron micrographs revealed the presence of stacks of up to four toroids. No stacks or single toroids were seen in micrographs of *HsPrx3* in identical (non-reducing) conditions (data not shown) **B:** Single particle analysis yielded class averages that showed clear representations of the stacked toroids. Stacks of up to three represented a considerable proportion of the his-tagged *HsPrx3* sample. The right hand panel shows an enlargement of selected projection averages.

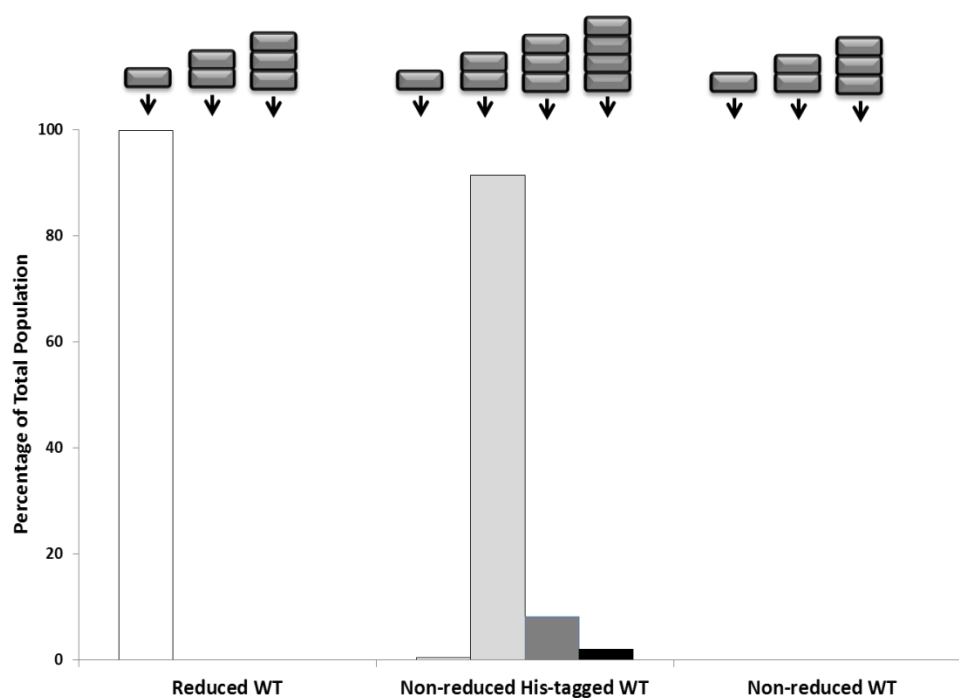


Figure 6.2: Histogram representing the relative proportions of structures in wildtype constructs

Percentages were calculated from manually counting particles across three micrographs. A single micrograph typically contained ~500 particles. The distributions show that wildtype *HsPrx3* exists almost completely as single toroids, whereas the his-tagged protein favours a double toroid structure. Non-reduced wildtype showed no oligomeric structures.

6.3.2 3D TEM reconstruction of the double toroid stacks

A 3D reconstruction was produced in collaboration with Dr. Mazdak Radjainia at the University of Auckland (as for the single toroid, section 4.3.1), and gave modest resolution (21 Å) structural information (section 2.5.4.2). Although precise atomic arrangements were not discernable, the reconstruction has sufficient detail for atomic structures to be docked, to yield pseudo-atomic resolution models. Two toroids were clear, with the density envelope indicating contact between them (figure 6.3A). Overlaying the reconstruction with the crystal structure of *BtPrx3* (Cao *et al.*, 2005;

figure B) showed significant additional density on the inner face of the toroids, which was not apparent in the 3D reconstruction of the untagged toroid (section 4.3.1). It is plausible that the additional densities correspond to the N-terminal region and his-tag, which are not resolved in the crystal structure (Cao *et al.*, 2005). This suggests that the N-terminal region and his-tag could adopt an ordered conformation in the stacked toroids and stabilise the dodecamer through coordination of metal ions in the lumen of the toroid (section 4.3.1.3). In general, the EM density map and the crystal structure of the *BtPrx3* toroid agree well, with top views showing matching protrusions in the toroid (figure 6.3B). However, some areas of misalignment are seen, hinting at conformational changes within the stacked *HsPrx3* toroids. Notably, the $\alpha 2$ and $\alpha 6$ helices of the *BtPrx3* structure appear to project into the gap between the toroids of the *HsPrx3* reconstruction. The dimers have adopted a different arrangement in the stack, forming a less acute angle to each other (figure 6.3B). This is consistent with the change in angle of the B-type interface seen in the crystal structure of the stacked toroids of *SmPrx1* (section 1.2.5.4; Saccoccia *et al.*, 2012).

The two stacked decamers that were solved in the crystal structure of the *SmPrx1* HMW species (Saccoccia *et al.*, 2012) are rotated by 18° around the five-fold symmetry axis – a rotation caused by conformational changes of secondary structure elements, which allow the necessary interactions for stacking to occur. A similar pitch appears to be present in the 3D structure of his-tagged *HsPrx3*, as judged by the lack of symmetry between toroids (figure 6.3A). The reconstruction of stacked *HsPrx3* also shows a similar height to that of the *SmPrx1* stack – around 8 nm at the farthest points, indicating that the toroids assemble in a similar manner.

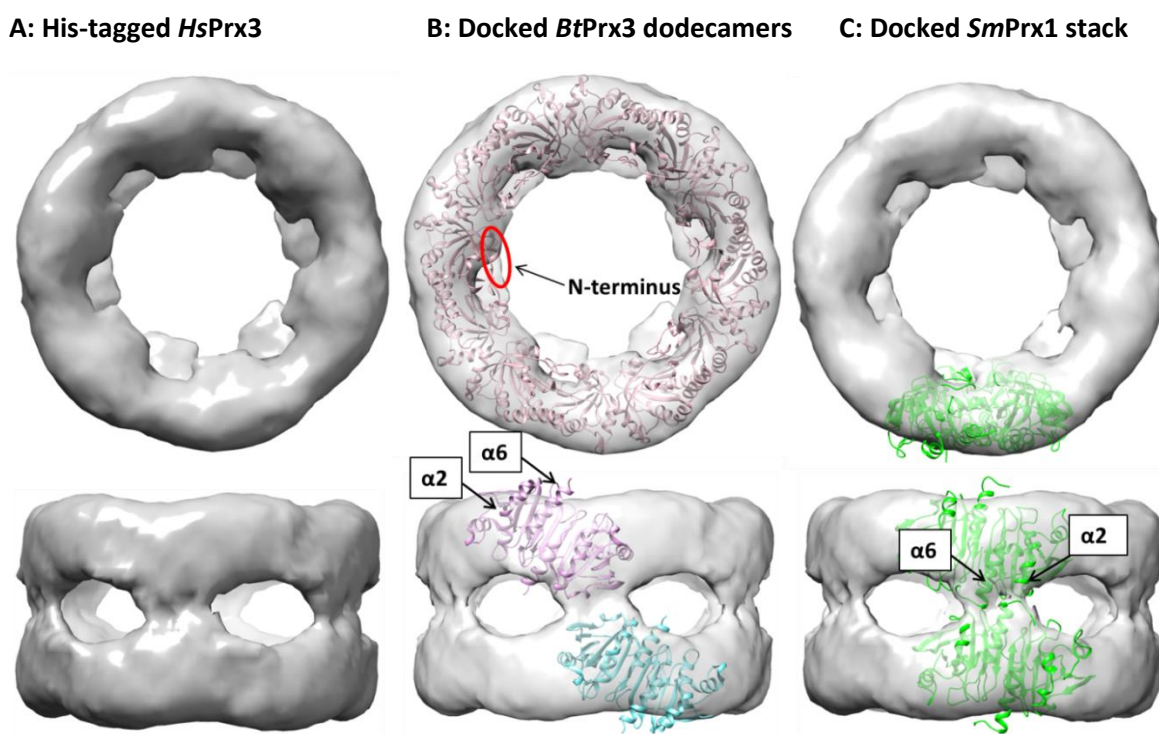


Figure 6.3: The 3D reconstruction of *HsPrx3* stacks suggests a conserved mechanism

A: 3D reconstruction of two stacked *HsPrx3* toroids shows that contact between the dodecamers appears to result in rotation of the toroids relative to each other. The gaps seen in side-on views are likely caused by contributions to the interface being made only by one monomer of each dimer. **B:** The crystal structures of two *BtPrx3* toroids (PDB accession number: 1ZYE) were individually docked into the reconstruction (the pink toroid was docked to the top of the stack, cyan to the bottom). The top view shows good agreement, the position of the N-terminus is circled for one monomer, which agrees with the additional density seen in the reconstruction. The side view shows misalignment (only one dimer from each toroid is shown for clarity), with helices of the crystal structure projecting above and below the toroids of the reconstruction. **C:** The crystal structure of stacked decameric *SmPrx1* (PDB accession number: 3ZVJ) was docked into the 3D reconstruction. The top view showed misalignment due to the difference in toroid diameter, therefore only two dimers are shown. The shifted $\alpha 6$ and $\alpha 2$ helices that contribute to the interface (indicated) align well with the regions of contact between the toroids of the reconstruction.

To identify gross conformational changes, and ascertain whether the mode of stacking that is seen in *SmPrx1* is present in the *HsPrx3* HMW species, the *SmPrx1* HMW (Saccoccia *et al.*, 2012) crystal structure was docked into the EM reconstruction. The entire double toroid was docked as one object, then all chains except two dimers are

hidden for clarity (figure 6.3C). Although a perfect fit could not be expected because of the decameric nature of the toroid of *SmPrx1*, the regions of contact between the toroids in the two proteins align very well. The shifted $\alpha 6$ and $\alpha 2$ helices of *SmPrx1* correspond to the electron density between the toroids of the *HsPrx3* reconstruction, indicating that *SmPrx1* and *HsPrx3* toroids can assemble via a conserved mechanism, despite the difference in multimeric states of toroids.

Three of the four residues proposed to be involved in the interface are conserved in *HsPrx3* (E20, K22 and H164; Saccoccia *et al.*, 2012), implying that these interactions are specifically required to optimise the electrostatic stabilisation of the stacked toroids. The interaction of these residues at the $\alpha 6$ and $\alpha 2$ helices of alternate monomers is consistent with the large gap that can be seen between toroids in the class averages and 3D model, suggesting that *HsPrx3* toroids are able to form equivalent interactions to those seen in *SmPrx1*. It therefore appears plausible that the conformational changes of secondary structure elements that were observed in *SmPrx1* may be conserved in *HsPrx3*, involving the unwinding of helix $\alpha 2$.

6.4 Generating nanotubes of controllable length

The antiparallel association of dimers results in a symmetric toroid, with equivalent top and bottom faces. It is therefore unclear why the conditions discussed above appeared to encourage the R-type formation, though they resulted in small, fairly uniform stack sizes. It is possible that small stacks are the most energetically favourable conformation, and could be that the his-tags coordinate to the metal ions within the lumen of the stacks, in a manner that favours an assembly of two toroids. The mechanism of his-tag coordination to nickel ions is not completely understood, but there are several possible arrangements (Valenti *et al.*, 2006). It may be that the most favourable coordination of his-tags to nickel ions corresponds to two toroids. Further investigation would be useful

to unravel the nature of this interaction, which is clearly an important factor in Prx assembly, but until now disregarded.

A number of approaches were trialled in order to generate large assemblies of *HsPrx3*. Metal ions have been reported encourage the formation of large assemblies of toroids (Kato *et al.*, 1985); however, the addition of metal salts (including MgCl_2 , NiCl_2 , and CdCl_2) to untagged *HsPrx3* samples were inconclusive. Aggregation occurred easily, and when the concentration of metal salts was sufficiently low to avoid aggregation, no larger structures were seen by TEM (data not shown). Hyperoxidation has also been suggested to cause HMW formation (Moon *et al.*, 2005). This was attempted with *HsPrx3* using protocols that have been successful for other Prxs (Pace *et al.*, 2013). However, TEM analysis again revealed that HMW structures were not present. Despite containing the motifs that confer hyperoxidation sensitivity (section 1.2.5), *HsPrx3* is somewhat resistant to hyperoxidation *in vitro* (Haynes *et al.*, 2013), so it is possible that hyperoxidation was not actually achieved in this work. Further studies of this state of *HsPrx3* using MS or antibodies to identify whether hyperoxidation has been successful could be valuable.

6.4.1 Acid pH leads to toroid association

Given the *in vitro* resistance of *HsPrx3*, mimicking the effects of hyperoxidation by altering environmental conditions was considered. Disruption of the C47-R123 ionic bond through mutation encouraged the R-type interface to form (section 5.4.1); therefore, disrupting this interaction through altered pH was trialled. The pK_a of C_P in Prxs is around 6.0 (Nelson *et al.*, 2008; Ogusucu *et al.*, 2007). Lowering the pH below this was hypothesised to disrupt the active site architecture, and low pH has been suggested to mimic the effects of hyperoxidation (Saccoccia *et al.*, 2012). This was investigated in the case of *HsPrx3*.

TEM was utilised to investigate HMW structures. Altering solution pH within a physiologically relevant range was seen to affect the oligomeric state of *HsPrx3* (section 4.3.1.4). As the focus of this study was to drive the formation of novel structures, pH levels outside of these ranges were explored. Protein samples were dialysed into a buffer at the appropriate pH (standard running buffer [section 2.1.9.2] was adjusted with HCl). Previous studies of the effect of solution pH had indicated greater formation of HMW species at pH 7.0 (section 4.3.1.4), and TEM analysis revealed that these structures were laterally associated toroids that appeared to form chains (figure 6.4B). Side views of single toroids were observed, consistent with SEC/SLS which indicated that the primary species in these conditions was the dodecamer (section 4.3.1.4). This was reproducible, indicating that the association was not random, supporting previous reports (Meissner *et al.*, 2007). Electrostatic interactions such as those predicted to stabilise the R-type interface (described above) are sensitive to solution pH, relying on the charge of side groups. As lysine residues are charged at physiological pH (pK_a is ~ 10), increasing the protonation and, therefore, charge of the histidine at the interface was hypothesised to encourage stacking. Following this rationale, lowering the pH below the pK_a of histidine to 6.0 was examined (in its environment in the Prx monomer the histidine is thought to have a slightly higher pK_a than its usual value ~ 6 [Saccoccia *et al.*, 2012]). This led to a dramatic change in the structures observed by TEM (figure 6.4C). Large stacks of >10 toroids were observed, indicating that formation of the R-type interface was more favourable at this pH. These stacks were very heterogeneous and irregular, with varying lengths, and clear breaks being seen.

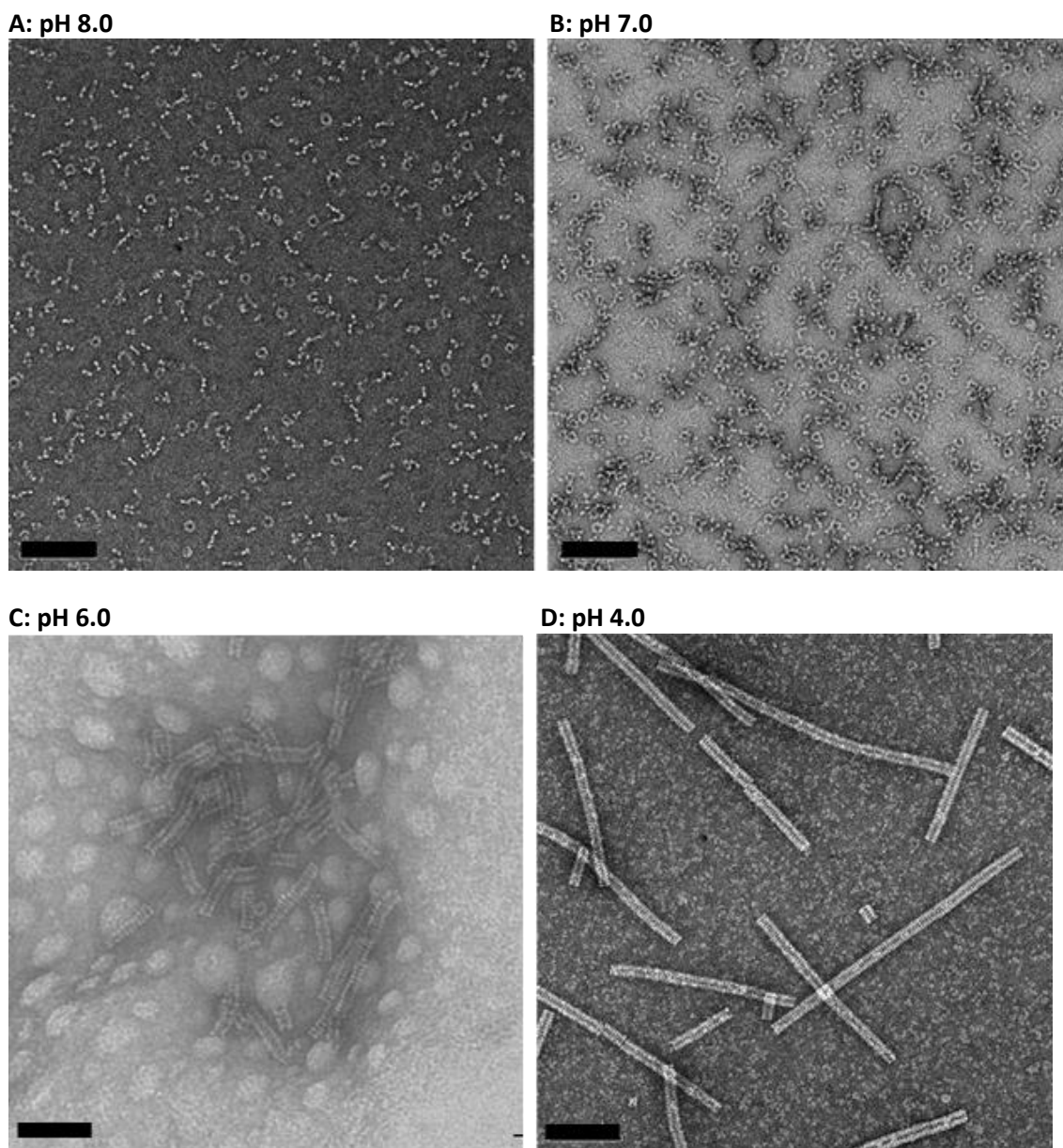


Figure 6.4: Toroid association occurs in response to pH

A: Untagged wildtype *HsPrx3* at 0.05 mg/mL exists as single toroids indicated by dumb-bell shapes. **B:** At pH 7.0 toroids appear to associate side by side, with a number of chain-like arrangements seen. **C:** At pH 6.0 large, irregular stacks are seen. **D:** At 0.1 mg/mL at pH 4.0 strikingly ordered nanotubes are seen. Scale bars indicate 100 nm.

It has been suggested that the R-type interface is stabilised by H-bonds as well as electrostatic interactions between the key residues mentioned above (Saccoccia *et al.*, 2012). It was therefore hypothesised that lowering the pH below the pK_a of all residues thought to be involved may further stabilise the toroid stacks. Glutamic acid has the lowest pK_a of 4.2; therefore a pH of 4.0 was examined. TEM revealed the presence of strikingly ordered nanotubes composed of stacked toroids, up to 400 nm in length (figure 6.4D). Lowering the pH has been suggested to encourage the movement of the α_6 helix to enable the R-type interface interactions to occur in the case of a decameric Prx (section 1.2.5.4). These results indicate that the mechanism is conserved in the dodecameric *HsPrx3*. It appears that length and uniformity do not increase with lowered pH, as samples at pH 5.5, 5.0 and 4.5 behaved identically to pH 6.0. Rather, pH 4.0 appears to be the critical point at which toroid stacking is favoured. Dialysis of the acidified sample to a higher pH caused the tubes to dissociate into toroids (data not shown).

6.4.2 Controlling nanotube length

Very recently, a crystal structure of the C_P mutein of the decameric *SmPrx1* was published (Angelucci *et al.*, 2013). Although this crystallised as a single dodecamer it was seen to aggregate easily in solution. The authors increased the solubility by including ammonium sulfate ($[(NH_4)_2SO_4]$) in their buffers. Despite the C_P mutation, the active sites remain in the fully folded conformation. This may be due to a sulfate ion binding in the active site and making polar contacts with the serine (mutated C_P) and conserved arginine of the catalytic triad. It was hypothesised that sulfate ions may stabilise the active site of *HsPrx3* in a similar way and therefore restrict tube length.

Protein samples were dialysed into a buffer containing 100 mM, 200 mM or 400 mM $(\text{NH}_4)_2\text{SO}_4$ at pH 4.0. Electron micrographs revealed that ammonium sulfate did cause a decrease in nanotube length, in a concentration dependent manner (figure 6.5). Simply changing the ionic strength by altering the NaCl concentration of the buffer had no effect on nanotube length. Similarly, adding sulfate ions to the sample at pH 8.0 had no effect on morphology. This strongly suggests that sulfate ions specifically inhibit tube formation; potentially by binding to the unfolded active site, encouraging transition to a folded conformation and therefore preventing the toroids associating. Even at the highest sulfate concentration, nanotube formation was not completely inhibited, as was seen for the *SmPrx1* HMW species. This may be due to the C_P to S mutation of *SmPrx1* – the increased electronegativity of the oxygen in the side chain (compared to sulfur of cysteine) could increase the strength of polar interactions with the sulfate ion. In the case of *HsPrx3* weaker binding could lead to a higher instance of unfolded active sites, and therefore stacking would be facilitated. As this effect is not seen with other ions, a useful future study would be to examine the effect of nanotube formation in a pH 4.0 phosphate buffer as the phosphate anion has similar properties to that of sulfate. Preliminary studies in the Gerrard laboratory (Littlejohn, Master's thesis) indicate that the dodecameric state of *HsPrx3* is indeed stabilised when the protein is in a phosphate buffer. This suggests that the phosphate anion may be binding in the active site, preventing the transition to the locally unfolded state and, therefore, toroid dissociation upon oxidation.

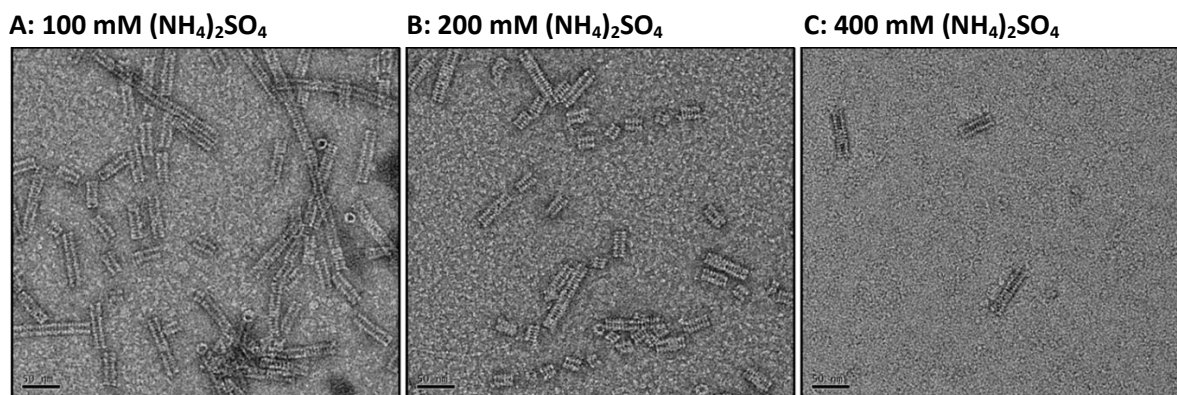


Figure 6.5: The presence of sulfate ions influences nanotube length

Samples of untagged *HsPrx3* at pH 4.0 dialysed into: **A:** 100 mM sulfate, **B:** 200 mM sulfate and **C:** 400 mM sulfate decreased in length in response to the increasing sulfate ion concentration.

6.4.3 3D cryo-electron microscopy structure of the nanotubes

Cryo-electron microscopy (cryo-EM) was used to examine the nanotubes in native conditions, and to provide higher resolution data. For cryo-EM, the sample was applied to Quantifoil® holey grids and rapidly frozen in liquid ethane using a FEI Vitrobot™ Mark IV. The sample is therefore maintained in a thin film of the vitrified sample buffer, in a frozen hydrated state, allowing examination without the potential for interactions with the support film or artefacts of negative staining, and giving a close-to-native representation of protein structure in solution. Initial examination of micrographs revealed the presence of ordered nanotubes with an average length ~ 300 nm (± 100 nm; figure 6.6). Negatively-stained samples sometime showed defects in the tubes, seen as bends or apparent misalignment of toroids. These were not seen in cryo-EM and so were concluded to be an artefact of adhesion to the grid or heavy metal stain. Cryo-EM specimen preparation and freezing was carried out by Dr. Mazdak Radjainia at the University of Auckland.

Generation of a 3D reconstruction was carried out by Dr. Hariprasad Venugopal at the University of Auckland. Manually picked tubes were subjected to real space helical reconstruction using Bsoft (Heymann and Belnap, 2007). This resulted in a reconstruction with a resolution estimated to be 10 – 15 Å and significantly improved the resolvable structural details compared to negative stain reconstructions (figure 6.7A). This resolution is close to resolving secondary features. Inspection of the reconstruction indicated precise, discrete areas of contact between the toroids. The cryo-EM reconstruction of the nanotubes of untagged *HsPrx3* revealed a striking difference compared to the 3D reconstruction of the his-tagged stacked toroids. This is characterised by a lack of rotation between the toroids that make up the untagged protein nanotubes (figure 6.7). This finding suggests that the stacking mode is different between the stacks promoted by his-tags compared to tubes triggered by low pH.

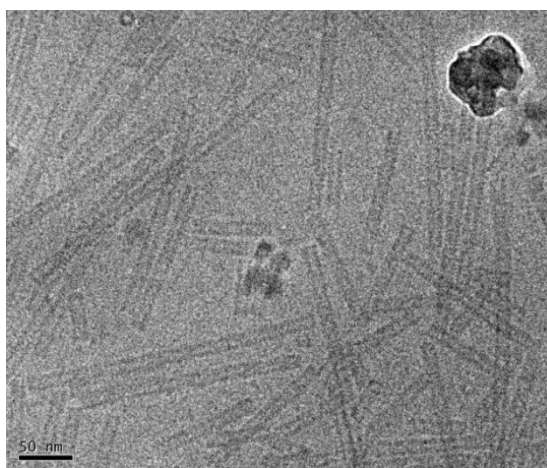


Figure 6.6: Cryo-EM revealed straight nanotubes exist in solution

Strikingly ordered stacks of *HsPrx3* toroids were seen by cryo-EM, forming tubes up to 400 nm.

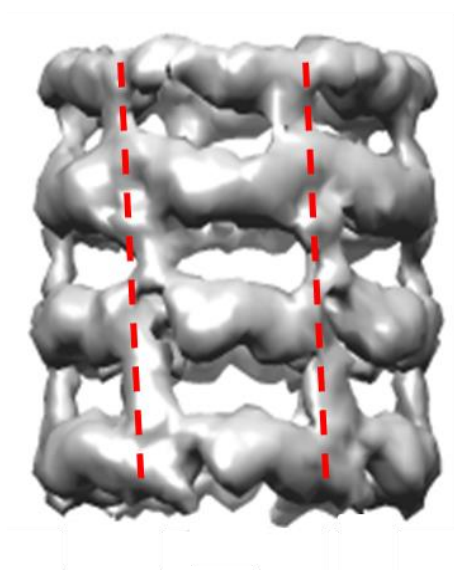
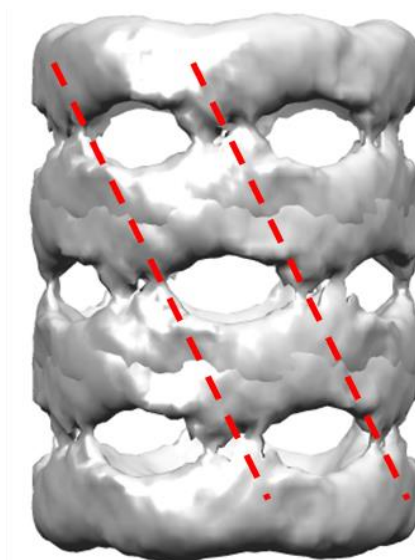
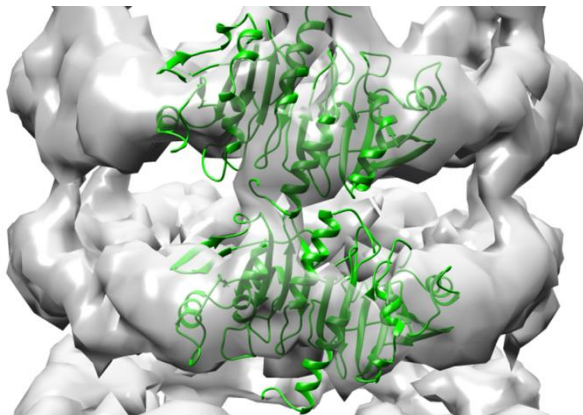
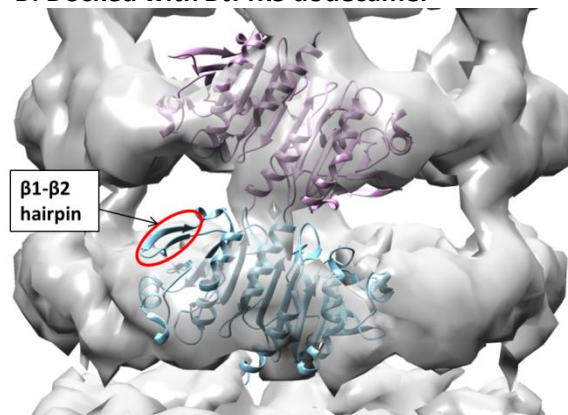
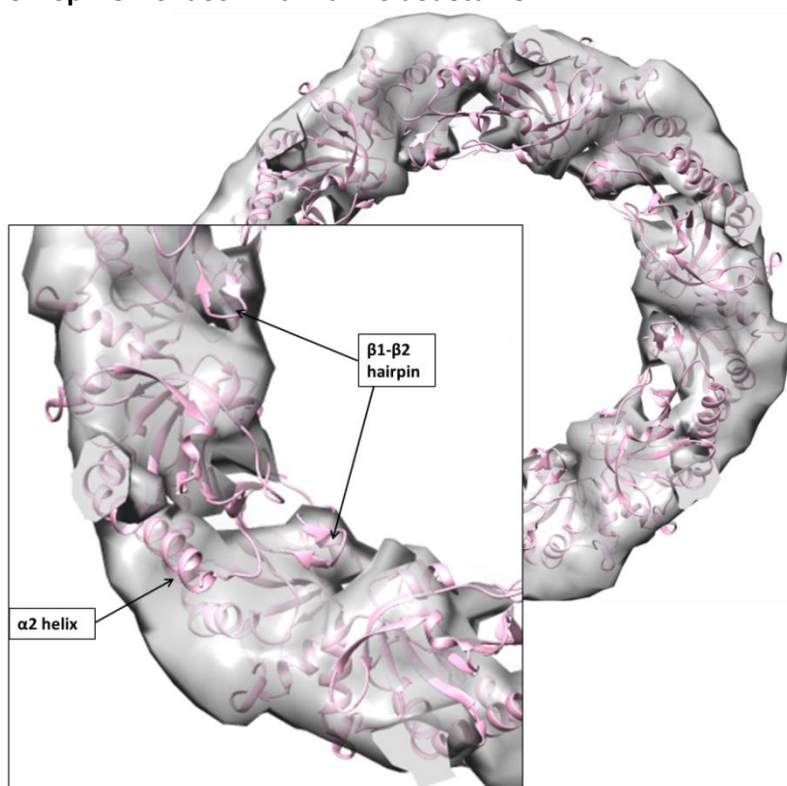
A: Untagged *HsPrx3* stack**B: His-tagged *HsPrx3* stack**

Figure 6.7: 3D reconstructions indicate differences in assembly mechanisms between tagged and untagged *HsPrx3* toroids

A: 3D reconstruction generated from cryo-EM data of untagged *HsPrx3* molecules shows that the points of contact between toroids align laterally along the nanotube, resulting in symmetry between the toroids. **B:** The lack of symmetry between his-tagged toroids is due to a rotation, meaning points of contact do not align. The structure of four stacked toroids was generated by overlaying three of the 3D reconstructions of double toroids discussed in section 6.3.1.

The crystal structures of the *BtPrx3* dodecamer and the *SmPrx1* double decamer were docked into the cryo-EM 3D reconstruction to provide some insight into the mechanism behind nanotube formation. Both structures were docked as in section 6.3.1. When the *SmPrx1* HMW structure was docked, the fit was surprisingly poor (figure 6.8A). The interdigitated helices of the *SmPrx1* R-type interface did not align with the regions of contact between the *HsPrx3* toroids. This is consistent with the theory that the *HsPrx3* nanotubes are composed of toroids that do not stack with a rotation relative to each other. This is supported by docking two separate *BtPrx3* toroids – the structures dock well into the reconstruction, and inspection of the alignment reveals they are stacked without rotation (figure 6.8A).

Docking of the *BtPrx3* tertiary structure gave some insight into the tertiary structure changes associated with nanotube formation. In some areas it is possible to see very good alignment, with density corresponding to individual helices apparent. In the reconstruction (figure 6.8B), it is possible to see the kink in helix $\alpha 2$ in the EM map, for example, with conformational changes suggested by the regions that are misaligned. Particularly, the $\alpha 2$ helix and $\beta 1$ - $\beta 2$ hairpin regions of the crystal structure project beyond the density seen in the reconstruction, which is in agreement with the suggestion of Saccoccia *et al.* (2012), who highlighted this region to be important in forming the R-type interface. The generation of the reconstruction from cryo-EM data means that any staining artefacts are eliminated. Therefore, speculations can be made in good confidence that the differential alignment to the crystal structure is due to conformational changes that facilitate toroid stacking. From this reconstruction it can be proposed that the unwinding of the C_P loop due to low pH results in movement of the $\alpha 2$ helix through a slipping of the B-type interface that reorients the dimers. The $\alpha 2$ and $\alpha 6$ helices contact those of the dimer above in a “tip to tip” fashion rather than the interdigitation seen in *SmPrx1* (Saccoccia *et al.*, 2012). The $\beta 1$ - $\beta 2$ hairpin is shifted through the movement of the dimers; however, due to the lack of rotation in the untagged structure it seems unlikely that this will make the contacts with the monomer above as seen in *SmPrx1* (described in 1.2.5.4; Saccoccia *et al.*, 2012).

A: Docked with *SmPrx1* HMW structure**B: Docked with *BtPrx3* dodecamer****C: Top view of dock with *BtPrx3* dodecamer****Figure 6.8: Docking the 3D reconstruction with crystal structures gave insight into the assembly mechanism**

A: The *SmPrx1* HMW structure (Saccoccia *et al.*, 2012) aligned poorly, most notable, the interdigitated arrangement of the $\alpha 2$ and $\alpha 6$ helices of the crystal structure did not fit well with the EM density map. **B:** Docking two *BtPrx3* toroids suggested that the toroids may stack directly on top of each other, without the rotation seen in the *SmPrx1* HMW species. Misalignment of the $\beta 1$ - $\beta 2$ hairpin suggests rearrangements occur in this region to facilitate stacking. **C:** Top views of the docking with the *BtPrx3* toroid show a good dock, with clues to conformational changes. Notably, the $\alpha 2$ helices and $\beta 1$ - $\beta 2$ hairpins of the monomers in the crystal structure project outside of the density seen by EM.

6.5 Discussion

The data presented in this chapter and chapter five reveal that a number of discrete HMW structures are accessible to *HsPrx3*, and controllable through the introduction of affinity tags, mutations, or alterations to environmental conditions. Protein tubes and cages have potential uses in bionanotechnology (section 1.5), therefore an increased understanding and greater level of control over their formation was sought. The recent publication of the double toroid produced by sample acidification (Saccoccia *et al.*, 2012) provided valuable insight to approach driving *HsPrx3* to form HMW structures. Larger stacks, and finally long nanotubes were successfully generated, for which two mechanisms of formation are presented: his-tag mediated assembly, and stacking in response to acidification. The clear differences of the *HsPrx3* untagged nanotube structure to the tagged stacked toroids of *SmPrx1* lead to the proposal that these assembly mechanisms involve different routes, and possibly different interactions.

6.5.1 His-tag mediated assembly

The EM structure presented here agrees well with the suggestion of Saccoccia *et al.* that assembly involves contact between the $\alpha 2$ and $\alpha 6$ helices of dimers, even when his-tagged *HsPrx3* is studied at pH 8.0. In the case of *HsPrx3*, acidification of his-tagged samples eliminated HMW species, presumed to be due to electrostatic repulsion of the protonated histidine residues. The major species of acidified, tagged *SmPrx1* in solution is in fact the dimer, with small amounts of HMW structures present (Saccoccia *et al.*, 2012). It may be that *SmPrx1* exists in equilibrium, with opposing forces of protonated his-tag repulsion and the formation of pH-induced R-type interface interactions

resulting in a heterogeneous sample, with the HMW species promoted by crystallisation.

6.5.2 Low pH induced assembly

Acidification resulted in a significant increase in stack size, with high resolution structures revealing a different assembly mechanism to that of his-tag stacking. Toroids align directly above each other, and although the rotation seen in the crystal structure of Saccoccia *et al.* is not seen, equivalent regions appear to be involved in interface formation. Alignment with the *BtPrx3* toroid indicated that the *HsPrx3* dimers have shifted to form the nanotubes, possibly involving a slip at the B-type interface. This is consistent with the conformational changes proposed to be induced by low pH by Saccoccia *et al.* The agreement of the tertiary structure changes of acidified *SmPrx1* with the *HsPrx3* nanotubes, but gross morphology of *SmPrx1* being more similar to the *HsPrx3* his-tagged stacks, may suggest that the local conformational changes are induced by low pH, but rotated stacking of the *SmPrx1* toroids is in fact driven by the his-tag or crystal packing.

Angelucci *et al.* (2013) suggest that C_P loop unwinding is not sufficient to cause toroid stacking, and the results presented here lend some credence to that hypothesis. At pH 6.0 the peroxidatic cysteine is protonated, the stabilising C47-R123 bond therefore disrupted, and (according to the structural data presented by Saccoccia *et al.*, 2012), the C_P loop and helix $\alpha 2$ would unwind and the active site architecture would be lost. In the case of *HsPrx3* this is sufficient for stacking, but results in nanotubes of modest length. Only when the pH is lowered to 4.0 are the stable, ordered nanotubes seen, indicating that other factors are involved. This level of acidification could be expected to affect many parts of the tertiary structure so it may be that further conformational changes

promote the R-type interface, or it could be through the encouragement of polar interactions in this region (as hypothesised in section 6.4.1). Crystal structures of the tagged, untagged and untagged acidified protein could provide some support to these suggestions.

6.5.3 Control of the length of the nanotubes

Although the samples were not completely uniform, the addition of varying concentrations of ammonium sulfate allowed some control over nanotube length. The crystal structure of the *SmPrx1* C_P mutein provides some explanation for this effect. The authors attribute the single decamer conformation of this mutein to a requirement for further conformational change than the unfolding of the $\alpha 2$ helix. Together with the C47SS78A mutein data presented in chapter five (section 5.4.1), and the stacking of *HsPrx3* at pH 6.0, this suggests that the conformational changes associated with mutation are sufficient for HMW formation. In solution the *SmPrx1* C_P mutein is prone to aggregation unless ammonium sulfate as included in the buffer (Angelucci *et al.*, 2013). In the crystal structure of *SmPrx1*-C48S, SO_4^{2-} ions are present in the active site, holding the helix in a folded conformation. Together with the reduction in nanotube length seen when *HsPrx3* is acidified in the presence of sulfate ions, this indicates that SO_4^{2-} ions that impede toroid stacking. It is proposed, therefore, that $\alpha 2$ helix unwinding is primarily responsible and sufficient for HMW formation.

Coordination of the his-tags to metal ions in solution may cause aggregation of the tags, rather than assembly being driven by the formation of protein-protein interfaces. It is hypothesised that the stacks seen in the first part of this chapter, and in many cases in the literature, are an artefact of the his-tag. This is a significant result, as the presence of a his-tag is generally not considered when Prx quaternary structures are studied (for example, Cao *et al.*, 2005; Saccoccia *et al.*, 2012); this study highlights that it can

stabilise particular conformations (section 4.3.1.3), and even lead to the formation of non-native structures (section 6.3.1).

6.5.4 Conclusion

This work confirms that the R-type interface plays the dominant role in higher order assemblies of *HsPrx3*, and provides important structural information relating to the process of self-assembly. The presence of a his-tag has been seen in this study and by other groups (Cao *et al.*, 2007) to stabilise oligomeric forms of Prxs and therefore influence their natural self-assembly, but until now has received no attention when analysing HMW structures. This study indicates that some of the structures seen in preparations of recombinant Prxs may in fact be artefacts of the affinity tag, and therefore analysis of untagged proteins is essential. Whilst the double toroid crystal structure of *SmPrx1* revealed some important pH-induced conformational changes, it is becoming clear that the his-tag has a major role in toroid association, and may even affect oligomerisation indirectly by causing subtle conformational changes (discussed in section 5.1.4.2). It is therefore unclear whether the stacking of *SmPrx1* is driven by the pH-induced movements, or if the his-tag contributes to this assembly, which has been seen to be the case in the oligomerisation of other Prxs (Gretes and Karplus, 2013).

Angelucci *et al.* (2013) postulated that formation of stacks at low pH is relevant to the pathology of *schistosomiasis*, where low pH is encountered in the life cycle. Other Prxs shown to do this include Prx2 (formerly known as calpromotin), that has been seen to shift to a higher molecular weight species at pH 5.0 (Kristensen *et al.*, 1999) as well as the *HsPrx3* results that we present here. It is therefore proposed that *HsPrx3*, and potentially all Prxs that form toroidal oligomers, may be able to form HMW structures driven by acidification-mediated assembly. A systematic survey of Prxs from different organisms would be interesting to unravel the extent to which the pHs encountered in

the natural biological environment influence the tendency of these proteins to assemble into higher order forms.

The presence of HMW structures *in vivo* remains uncertain. It has been indicated that tubular structures can form in response to cellular stress (Phalen *et al.*, 2006), and these have been visualised with immunostaining. However, this technique is indirect, and it is clear that a detailed analysis of the HMW forms of Prx, their mechanism of formation, and direct analysis of their appearance *in vivo* is needed. A useful future study would be electron tomography investigations of these HMW species, which has been successful in studying large complexes such as the ribosome (Ortiz *et al.*, 2006).

6.6 References

- Angelucci, F., Saccoccia, F., Ardini, M., Boumis, G., Brunori L., Di Leandro, R., Ippoliti, R., Miele, A.E., Natoli, G., Scotti, S. and Bellelli, A. (2013) Switching between the alternative structures and functions of a 2-Cys peroxiredoxin by site-directed mutagenesis. *Journal of Molecular Biology* **425**, 4556-4568.
- Cao, Z., Roszak, A. W., Gourlay, L. J., Lindsay, J. G. and Isaacs, N. W. (2005) Bovine mitochondrial Peroxiredoxin III forms a two-ring catenane. *Structure* **13**, 1661-1664.
- Cao, Z., Bhella, D. and Lindsay, J. G. (2007) Reconstitution of the mitochondrial PrxIII antioxidant defence pathway: General properties and factors affecting PrxIII activity and oligomeric state. *Journal of Molecular Biology* **372**, 1022-1033.
- Cha, M.-K., Yun, C.-H. and Kim, I.-H. (2000) Interaction of human thiol-specific antioxidant protein 1 with erythrocyte plasma membrane. *Biochemistry* **39**, 6944-6950.
- Choi, H.-J., Kang, S. W., Yang, C.-H., Rhee, S. G. Ryu, S. E. (1998) Crystal structure of a novel human peroxiredoxin enzyme at 2.0 Å resolution. *Nature Structural Biology* **5**, 400-406.
- Kato, H., Asanoi, M., Nakazawa, T. and Maruyama, K. (1985) Cylinder protein isolated from rat liver mitochondria. *Zoological Science* **2**, 485-490.
- Gourlay, L. J., Bhella, D., Kelly, S. M., Price, N. C. and Lindsay, J. G. (2003) Structure-function analysis of recombinant substrate protein 22 kDa (SP-22): a mitochondrial 2-Cys peroxiredoxin organised as a decameric toroid. *Journal of Biological Chemistry* **35**, 32631-32637.
- Gretes, M. C. and Karplus, P. A. (2013) Observed octameric assembly of a *Plasmodium yoelii* peroxiredoxin can be explained by the replacement of native “ball-and-socket” interacting residues by an affinity tag. *Protein Science* **10**, 1445-1452.
- Harris, J. R. (1969) Some negative contrast staining features of a protein from erythrocyte ghosts. *Journal of Molecular Biology* **46**, 329-335.
- Heymann, J. B. and Belnap, D. M. (2007) Bsoft: Image processing and molecular modelling for electron microscopy. *Journal of Structural Biology* **157**(1), 3 - 18.
- Jang, H. H., Lee, K. O., Chi, Y. H., Lee, J. R., Lee, S. S., Moon, J. C., Yun, J. W., Choi, Y. O., Kim, W. Y., Kang, J. S., Cheong, G.-W., Yun, D.-J., Rhee, S. G., Cho, M. J. and Lee, S. Y. (2004) Two enzymes in one: Two yeast peroxiredoxins display oxidative stress-dependent switching from a peroxidase to a molecular chaperone function. *Cell* **117**, 625-635.
- Jönsson, T. J., Johnson, L. C. and Lowther, W. T. (2008) protein engineering of the quaternary sulfiredoxin-peroxiredoxin enzyme-substrate complex reveals the molecular basis for

cysteine sulfinic acid phosphorylation. *Journal of Biological Chemistry* **284**, 33305-33310.

Kristensen, P., Rasmussen, D. E. and Kristensen, B. I. (1999) Properties of thiol-specific anti-oxidant protein or calpromotin in solution. *Biochemical and Biophysical Research Communications* **262**, 127-131.

Meissner, U., Schröder, E., Scheffler, D., Martin, A. G. and Harris, J. R. (2007) Formation, TEM study and 3D reconstruction of the human erythrocyte peroxiredoxin-2 dodecahedral higher-order assembly. *Micron* **38**, 29-39.

Nelson, K. J., Parsonage, D., Hall, A., Karplus, P. A. and Poole, L. B. (2008) Cysteine pK_a values for the bacterial peroxiredoxin AhpC. *Biochemistry* **47**, 12860-12868.

Ogusucu, R., Rettori, D., Munhoz, D. C., Nettor, L. E. S. and Augusto, O. (2007) Reactions of yeast thioredoxin peroxidases I and II with hydrogen peroxide and peroxynitrite: rate constants by competitive kinetics. *Free Radical Biology and Medicine* **42**, 326-334.

Ortiz, J. O., Förster, F., Kürner, J., Linaroudis, A. A. and Baumeister, W. (2006) Mapping 70S ribosomes in intact cells by cryoelectron tomography and pattern recognition. *Journal of Structural Biology* **156**, 334-341.

Pace, P. E., Peskin, A. V., Han, M.-H., Hampton, M. B. and Winterbourn, C. C. (2013) Hyperoxidized peroxiredoxin 2 interacts with the protein disulfide-isomerase ERp46. *Biochemical Journal* **453**, 475-485.

Phalen, T. J., Weirather, K., Deming, P. D., Anathy, V., Howe, A. K., van der Vliet, A., Jönsson, T. J., Poole, L. B. and Heintz, N. H. (2006) Oxidation state governs structural transitions in peroxiredoxin II that correlate with cell cycle arrest and recovery. *Journal of Chemical Biology* **175**, 779-789.

Saccoccia, F., Micco, P. D., Bournis, G., Brunori, M., Koutris, I., Miele, A. E., Morea, V., Sriratana, P., Williams, D. L., Bellelli, A. and Angelucci, F. (2012) Moonlighting by different stressors: crystal structure of the chaperone species of a 2-cys peroxiredoxin. *Structure* **20**, 429 – 439.

Su, D., Berndt, C., Fomenko, D. E., Holmgren, A. and Gladyshev, V. N. (2007) A conserved *cis*-proline precludes metal binding by the active site thiolates in members of the thioredoxin family of proteins. *Biochemistry* **46**, 6903-6910.

Valenti, L. E., de Pauli, C. and Giacomelli, C. E. (2006) The binding of Ni(II) ions to hexahistidine as a model system of the interaction between nickel and his-tagged proteins. *Journal of Inorganic Biochemistry* **100**, 192-200.

Wood, Z. A., Poole, L. B., Hantgan, R. R. and Karplus, P. A. (2002) Dimers to doughnuts: redox-sensitive oligomerisation of 2-Cys peroxiredoxins. *Biochemistry* **41**, 5493-5504.

Chapter 7 Summary and conclusions

7.1 Introduction

The aim of this thesis, as outlined in section 1.6, was to characterise the two peroxiredoxin systems, *MtAhpE* and *HsPrx3*. In particular, clarification of the proteins' quaternary structures and response to environmental conditions was a goal. Secondly, the potential for the proteins to form HMW structures was investigated, with a view to control their formation.

These Prxs were chosen as a model self-assembling protein system, due to the variety of quaternary structures seen across the Prx family, and the potential for triggered self-assembly. Modifications were designed to influence protein quaternary structure with two goals:

1. Mimic structural changes thought to occur during the normal cycle of the protein, and gain insight into the interactions involved;
2. Drive the formation of non-native structures which may have applications in nanotechnology.

Solution characterisation was carried out using chromatography, complemented by light and X-ray scattering experiments. The activity of mutated proteins was tested using a kinetic assay, and TEM was used for further structural characterisation. Cryo-EM and 3D reconstruction were employed to obtain detailed information of the HMW structures.

7.2 Quaternary structure of the proteins studied

7.2.1 *MtAhpE*

Despite its key role in the *M. tuberculosis* antioxidant system (Hugo *et al.*, 2009), limited information is available. The instability and propensity to aggregate which was seen *in vivo* in this study (chapter three) suggest that the lack of published information may in part be due to difficulties in characterisation and manipulation. *MtAhpE* had previously been crystallised as an octamer (Li *et al.*, 2005), though the reported observation of this arrangement in solution was a misinterpretation (Dr J. S. Lott, personal communication), and has been suggested to be an artefact of crystallisation (Karplus and Hall, in Flohé and Harris, 2007). This study revealed that untagged *MtAhpE* forms dimers which associate to aggregates in non-reducing conditions; although the precise nature of these aggregates was not able to be determined. The presence of the octamer could only be inferred when the his-tag was attached, and a tetramer was found to be the dominant species under these conditions (section 3.5). A tetrameric arrangement of *MtAhpE* is readily recognised in the crystal unit cell (PDB ID: 1XXU, Li *et al.*, 2005). Notably, a recent paper was published that refuted the octameric arrangement of a Prx from a *P. yoelii*, revealing that it was in fact an artefact caused through the presence of an N-terminal affinity tag (Gretes and Karplus, 2012). Although the N-terminal his-tag of *MtAhpE* does not replace native residues as it does in *P. yoelii*, it is possible that it causes a rearrangement of this region, leading to the formation of non-native assemblies. It is therefore proposed that the tetramer and octamer of *MtAhpE* are artefacts of the his-tag. Furthermore, the tetramer is the predominant species in solution, with the octamer comprising only a very small population, suggesting that the conditions of crystallisation selected for this species.

In typical Prxs, the A-type interface is stabilised when the protein is reduced or hyperoxidised, leading to the formation of toroids (Wood *et al.*, 2003; Ogasawara *et al.*,

2012). However, it has been suggested that different mechanisms drive the formation of the interface in either reducing or hyperoxidising conditions (Muthuramalingam *et al.*, 2009). The dimer of *MtAhpE* forms about an A-type interface (Li *et al.*, 2005) and was present in all conditions, but showed increased stability in hyperoxidising conditions (section 3.4.1.1). This supports the theory that formation of the interface is driven by different mechanisms in different conditions.

Preliminary characterisation of mutations of the A-type interface (section 3.7.2) indicated destabilisation of the *MtAhpE* dimer was achieved, resulting in dissociation of the his-tagged tetramer to a dimer-monomer mixture. Disruption through single-residue mutation suggests that the interface is highly specific and relies on essential “hotspots”. Knowledge of these interactions could open up an avenue for small molecule interface disruptors, to influence assembly and potentially activity.

7.2.2 *HsPrx3* forms a dodecamer in response to reduction and neutral pH

The involvement of *HsPrx3* in cellular processes such as apoptosis, and its potential role in preventing carcinogenesis has meant much research has been devoted to unravelling the controlled expression and *in vivo* roles and interactions of the protein (for example, Wang *et al.*, 2013; Whitaker *et al.*, 2013; Li *et al.*, 2013). Little attention has been focussed on the quaternary structure or supramolecular assemblies, with the size of the toroid ambiguous until now. The generation of a 3D structure of the native *HsPrx3* toroid unequivocally demonstrated that the protein existed as a dodecameric arrangement. This corrected a previous assumption that the protein adopted a decameric arrangement, which was generally accepted in the field (C. C. Winterbourn, University of Otago, personal communication). Introduction of a single residue interface mutation did not alter the oligomeric state, suggesting that the *HsPrx3* interface may be stabilised

primarily by hydrophobic packing rather than specific interactions as was seen for the *MtAhpE* interface.

As discussed in chapter four, the dimer-dodecamer equilibrium of *HsPrx3* was seen to be controlled primarily by redox state, with pH and protein concentration having some influence (section 4.4). The anti-apoptotic roles of *HsPrx3* (Li *et al.*, 2013) and pH-induced oligomerisation observed in this study, led to the hypothesis that the shift in quaternary structure may serve a protective mechanism in the cellular context. A shift toward neutral pH occurs in the mitochondria during early apoptosis (Takahashi *et al.*, 2004), and leads to the stabilisation of non-reduced *HsPrx3* toroids and possibly higher order assemblies (section 4.3.1.4 and 6.4.1). The toroids of other Prxs have been seen to associate with the membrane (Cha *et al.*, 2000), and through this adhesion, stimulate ion channels (Low *et al.*, 2007). *HsPrx3* could act as a signal for early apoptosis, and prevent unwanted apoptosis through a similar membrane association..

7.2.3 *HsPrx3* active site architecture is key in toroid formation

Chapter five describes the design and generation of a set of modified *HsPrx3* molecules with altered self-assembly properties. It was discovered that the dodecamer could be eliminated through mutating residue R123, presumably by increasing C_P loop mobility and possibly causing further disruptions to the tertiary structure (section 5.4.1). Mutation of C_P would be expected to cause a similar increase in loop mobility, but resulted in a stabilised dodecamer and some stacking of toroids. This was concluded to be due to more extensive unwinding of the C_P loop and helix $\alpha 2$, allowing the R-type interface to form (section 1.2.5.4). The propensity of helix $\alpha 2$ to unwind has been suggested to be increased by the presence of a proline residue (P48; Saccoccia *et al.*, 2012). This was confirmed by mutation of this residue, which resulted in stabilisation of the toroid, likely due to the prevention of the C_P loop transitioning into the LU

conformation. Interface mutations have a less dramatic effect on the dimer-dodecamer equilibrium (section 5.4.1), indicating that the primary factor in maintaining appropriate self-assembly properties is the correct active site structure. However, the S78A interface mutation did encourage the formation of HMW structures, highlighting the potential to increase $\alpha 2$ helix and C_P loop unwinding indirectly.

Mimicking the structural changes that occur in physiological conditions has been achieved for a number of states as summarised in table 7.1.

Table 7.1: Muteins mimicked different states of *HsPrx3*

Through altering the conformation of the C_P loop and $\alpha 2$ helix, the mutations that were introduced to the *HsPrx3* sequence gave insight into the conformational changes that occur during the catalytic cycle. This also provided means to controlling the quaternary structure.

Construct	Possible structural changes	Mimicked state
R123G	Unfolding of C _P loop	Oxidised C _P
S78A	Unwinding of helix $\alpha 2$	Hyperoxidised C _P
P48A	Prevention of helix $\alpha 2$ and C _P loop unwinding	Reduced C _P
C47S	Increased helix $\alpha 2$ and C _P loop unwinding	Protonated C _P

The instability and propensity for aggregation of many of these constructs meant that further experiments were not carried out as they did not present a useful means to control the quaternary structure of *HsPrx3*. However, they do provide valuable information as to the factors which influence the dimer-dodecamer equilibrium, and, therefore, a starting point to design modifications which provide a greater level of control. This was explored through the combination of the C47S and S78A mutations, and resulted in the production of a highly stable toroid, with an increased propensity to form HMW structures of fairly uniform size.

7.2.4 HMW species of *HsPrx3*

Protonation and hyperoxidation have been suggested to lead to $\alpha 2$ helix unwinding and HMW structure formation, possibly through intrinsically different stereochemical effects (Angelucci *et al.*, 2013). The different morphologies seen in the C47SS78A and S78A muteins support this hypothesis, and indicate that a number of HMW assemblies may be accessible to all toroid-forming Prxs under different conditions. The appearance of stacked toroids in the C47SS78A sample revealed that *HsPrx3* contains elements that contribute to the R-type interface, leading to the proposal that this may be conserved across the Prx family.

Further investigation of the R-type interface through lowered pH revealed that long, ordered nanotubes could be generated at pH 4.0. The formation of small stacks at low pH had been hypothesised to be relevant to the physiology of *Schistosoma mansoni* (Saccoccia *et al.*, 2012); however, the data presented in this thesis suggest this pH sensitivity may be present in all Prxs. The acidified sample of *SmPrx1* was seen to only form small assemblies of two toroids, despite the symmetrical nature of the toroids. The data presented relating to wildtype *HsPrx3* indicated that the favoured arrangement of his-tagged protein was an assembly of two toroids. It is therefore proposed that the small stack of *SmPrx1* seen in the crystal structure is in fact driven by his-tag association. This theory was supported by the examining the stacking modes of his-tagged *HsPrx3* and untagged acidified *HsPrx3* through high resolution EM, which revealed significant differences.

7.4 Summary and future work

This thesis presents some valuable insight into the self-assembly of *HsPrx3*, which represents a typical member of the 2-Cys Prx family. Approaches to control this self-assembly were developed, along with protocols to produce highly ordered HMW assemblies. These are summarised in figure 7.1. Characterising the quaternary structures in solution presented some challenges as the species were often in dynamic equilibrium. This highlighted the existence of possible oligomeric intermediates which had not been previously reported, and confirmed the necessity to use multiple complementary techniques to analyse the species present.

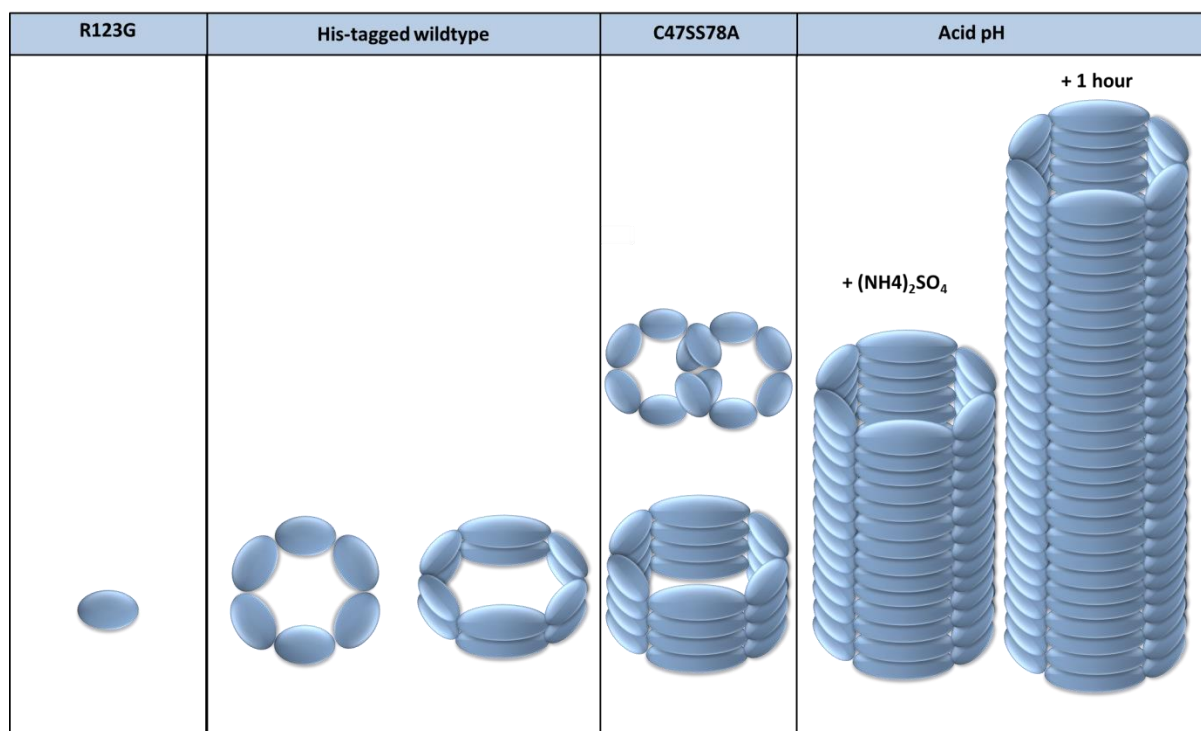


Figure 7.1: Modifications of *HsPrx3* produced a variety of supramolecular structures

Disruption of the toroid to single dimers was achieved with the R123G mutein. Dissociation could be prevented with the his-tag, which also led to toroid stacking. Larger stacks and interlocked toroids were generated by introducing the C47SS78A mutations. Low pH caused toroids to stack to long nanotubes; some control of length was possible through the addition of ammonium sulfate. Nanotubes grew fairly slowly, therefore regulating growth time could also be a means to control length.

Future work should focus on high resolution structural analyses of the various conformations, to unravel more details of the precise quaternary structure. Crystal structures of each of the muteins and the tagged and untagged wildtype would confirm the loop movements that have been suggested to occur. Although diffracting crystals were not produced in the course of this thesis, small crystals were seen in trials and indicated conditions for fine screening. The lack of published crystal structures of *HsPrx3* or muteins hint at intrinsic flexibility of the protein, and so further optimisation is necessary. The generation of more mutated constructs could also be beneficial. Table 7.2 contains suggestions for mutations of *HsPrx3* and *MtAhpE* which could provide complementary structural variants to test the hypotheses presented here.

A C47D mutation of *HsPrx3* would mimic the hyperoxidised state as the aspartic acid side chain is similar to the cysteine sulfinic acid (as was investigated in the case of *SmPrx1*, Angelucci *et al.*, 2013). This could provide support to the theory that hyperoxidation leads to different structures than protonation. Further protocol optimisation could allow the examination of the hyperoxidised state, and provide support for the suggested different HMW forms. The R123G mutation was hypothesised to lead to increased C_P loop movements, which are often associated with HMW formation (Saccoccia *et al.*, 2012). However, the R123G mutein was dimeric, hypothesised to be due to A-type interface destabilisation. It was considered that stabilising the A-type interface of this mutein with a second mutation could lead to an increase in the HMW structures, as the C_P loop will remain unwound within the locked toroid. Hence, the S78AR123G double mutein is proposed as this work has shown the S78A mutation to increase the stability of the A-type interface. This would give direct insight into the role of C_P loop mobility in the formation of HMW structures. To further probe the possibility to role of C_P loop mobility, the introduction of a glycine residue at the beginning of this loop (T49G) is suggested.

Table 7.2: Suggestions for future mutational studies

New mutations to represent the hyperoxidised, oxidised and reduced states could provide more insight into the *HsPrx3* quaternary structure.

Construct	Intended structural changes
<i>HsPrx3</i> -C47D	Force movement of C _P out of the active site
<i>HsPrx3</i> -S78AR123G	Further increase C _P loop mobility
<i>HsPrx3</i> -T49G	Increase unfolding of C _P loop
<i>MtAhpE</i> -Q47P	Encourage helix $\alpha 2$ unwinding
<i>HsPrx3</i> -S78C	Introduce a redox switch to the interface

The conserved active site proline (P48 in *HsPrx3*) is thought to encourage the unwinding of helix $\alpha 2$ (Saccoccia *et al.*, 2012). This residue is conserved throughout the Prx family, but is not present in *MtAhpE*. Introducing this proline with a Q47P mutation could give insight into the role of this residue in the structural transitions.

This thesis presents new information regarding the stacked toroids and nanotubes that *HsPrx3* can form. The S78A mutein also hinted at the possibility to generate protein cages, similar to the icosahedra published by previous groups (Meissner *et al.*, 2007; section 1.2.5.4). This mutein would benefit from further TEM studies, to provide clues to the nature of the clusters observed and the interactions involved. Other groups (Meissner *et al.*, 2007) reported cages of toroids in the presence of PEG, therefore investigations using other precipitants could be worthwhile. These structures have potential in nanotechnology, and their functionalization would be an important next stage of research. Possible applications could be the use of protein nanotubes to grow metal nanowires (Valenzuela and Deymier, 2008), or providing a microenvironment within a protein cage to contain a reaction (Allen *et al.*, 2002). The controlled assembly and disassembly of Prx subunits could also have biomedical applications. Peptides are attractive molecules for drug and vaccine development, but are often limited by their very short half-life *in vivo*. One strategy to overcome this is the conjugation of the peptides to molecules which are not broken down or cleared by the body (Pollaro and

Heinis, 2010). Carbon nanotubes have attracted attention for their potential as drug delivery vehicles (for example, Klumpp, 2006; Bianco *et al.*, 2006), and naturally occurring proteins such as *HsPrx3* could be useful alternatives for this role, as the risk of nanotoxicity could be lower. The dynamic nature of toroid assembly also means that a number of different preparations could be produced with different peptides, and simply mixing the samples would produce toroids containing multiple potential therapeutics.

The future applications for controlled, supramolecular protein assemblies are broad. The nanotubes and putative cages of *HsPrx3* offer a wide range of benefits to the carbon or polymers which are typically used. Proteins have the potential to be reversible, and functionalisable; provide a variety of architectures and produce flawless assemblies. Proteins are attracting attention as materials for nanotechnology, but a firm understanding and ability to precisely control their self-assembly must first be achieved. This work presents significant progress toward this goal in the case of *HsPrx3*, and proposes the consideration of the Prx family as versatile tectons for nanotechnology. The potential to encourage the formation of different HMW structures from a single molecule is presented, and the ability to control the assembly through simple changes to the primary structure or environmental conditions is demonstrated. Additional work is needed to validate the Prxs as candidates for nanotechnology, but this study identifies *HsPrx3* as versatile and manipulable tecton, worthy of further attention.

7.5 References

- Allen, M., Willits, D., Mosolf, J., Young, M. and Douglas, T. (2002) Protein cage constrained synthesis of ferromagnetic iron oxide nanoparticles. *Advanced Materials* **14**, 1562-1565.
- Angelucci, F., Saccoccia, F., Ardini, M., Boumis, G., Brunori L., Di Leandro, R., Ippoliti, R., Miele, A.E., Natoli, G., Scotti, S. and Bellelli, A. (2013) Switching between the alternative structures and functions of a 2-Cys peroxiredoxin by site-directed mutagenesis. *Journal of Molecular Biology* **425**, 4556-4568.
- Bianco, A., Kostarelos, K. and Prato, M. (2005) Applications of carbon nanotubes in drug delivery. *Current Opinion in Chemical Biology* **9**, 674-679.
- Cha, M.-K., Yun, C.-H. and Kim, I.-H. (2000) Interaction of human thiol-specific antioxidant protein 1 with erythrocyte plasma membrane. *Biochemistry* **39**, 6944-6950.
- Gretes, M. C. and Karplus, P. A. (2013) Observed octameric assembly of a *Plasmodium yoelii* peroxiredoxin can be explained by the replacement of native “ball-and-socket” interacting residues by an affinity tag. *Protein Science* **10**, 1445-1452.
- Hugo, M., Turrell, L., Manta, B., Botti, H., Monteiro, G., Netto, L. E., Alvarez, B., Radi, R. and Trujillo, M. (2009) Thiol and sulfenic acid oxidation of MtAhpe, the one-cysteine peroxiredoxin from *Mycobacterium tuberculosis*: kinetics, acidity constants and conformational dynamics. *Biochemistry* **48**, 9416-9426.
- Karplus, P. A., Hall, A. (2007) Structural survey of the peroxiredoxins. In: Flohé, L. and Harris, J. R. (Ed) Peroxiredoxin Systems. pp. 41–60 Springer; New York.
- Klumpp, C. (2006) Functionalized carbon nanotubes as emerging nanovectors for the delivery of therapeutics. *Biochimica et Biophysica Acta* **1758**, 404-412
- Li, S., Peterson, N. A., Kim, M. Y., Kim, C. Y., Hung, L. W., Yu, M., Legin, T., Segelke, B. W., Lott, J. S. and Baker, E. N. (2005) Crystal Structure of MtAhpE from *Mycobacterium tuberculosis*, a 1-Cys peroxiredoxin. *Journal of Molecular Biology* **346**, 1035-1046.
- Li, L., Zhang, Y.-G. and Chen, C.-L. (2013) Anti-apoptotic role of peroxiredoxin III in cervical cancer cells. *Federation of European Biochemical Societies Open Bio*, **3**, 51-54.
- Low, F., Hampton, M. B., Peskin, A. V. and Winterbourne, C. C. (2007) Peroxiredoxin 2 functions as a noncatalytic scavenger of low-level hydrogen peroxide in the erythrocyte. *Blood*, **109**, 2611-2617.
- Meissner, U., Schröder, E., Scheffler, D., Martin, A. G. and Harris, J. R. (2007) Formation, TEM study and 3D reconstruction of the human erythrocyte peroxiredoxin-2 dodecahedral higher-order assembly. *Micron* **38**, 29-39.
- Muthuramalingam, M., Seidel, T., Laxa, M., Nunes de Miranda, S. M., Gärtner, F., Ströher, E., Kandlbinder, A. and Dietz, K.-J. (2009) Multiple redox and non-redox interactions define

2-Cys peroxiredoxin as a regulatory hub in the chloroplast. *Molecular Plant* **2**, 1273-1288.

- Ogasawara, Y., Ohminato T., Nakamura, Y. and Ishii, K. (2012) Structural and functional analysis of native Peroxiredoxin 2 in human red blood cells. *The International Journal of Biochemistry and Cell Biology*, **44**, 1072-1077.
- Pollaro, L. and Heinis, C. (2010) Strategies to prolong the plasma residence time of peptide drugs. *Medicinal Chemical Communications* **1**, 319-324.
- Saccoccia, F., Micco, P. D., Bournis, G., Brunori, M., Koutris, I., Miele, A. E., Morea, V., Sriratana, P., Williams, D. L., Bellelli, A. and Angelucci, F. (2012) Moonlighting by different stressors: crystal structure of the chaperone species of a 2-cys peroxiredoxin. *Structure* **20**, 429 – 439.
- Takahashi, A., Masuda, A., Sun, M., Centonze, V. E. and Herman, B. (2004) Oxidative stress-induced apoptosis is associated with alterations in mitochondrial caspase activity and Bcl-2-dependent alterations in mitochondrial pH (pH_m). *Brain Research Bulletin* **62**, 497-504/
- Valenzuela, R. and Deymier, H. (2008) Formation of Copper Nanowires by Electroless deposition using microtubules as templates, *Journal of Nanoscience and Nanotechnology* **8**, 3416.
- Wang, X. Y., Wang, H. J. and Li, X. Q. (2013) Peroxiredoxin II protein expression is associated with platinum resistance in epithelial ovarian cancer. *Tumour Biology* **34**, 2275-2281.
- Whitaker, H. C., Patel, D., Howat, W. J., Warren, A. Y., Kay, J. D., Sangan, T., Marioni, J. C., Mitchell, J., Aldridge, S., Luxton, H. J., Massie, C., Lynch, A. G., Neal, D. E., (2013) Peroxiredoxin-3 is overexpressed in prostate cancer and promotes cancer cell survival by protecting cells from oxidative stress. *British Journal of Cancer* **109**, 983-993.
- Wood, Z. A., Poole, L. B. and Karplus, P. A. (2003b) Peroxiredoxin evolution and the regulation of hydrogen peroxide signalling. *Science* **300**, 650-6.

Appendix 1 Biophysical techniques

A1.1 Circular Dichroism

UV circular dichroism (CD) is an excellent technique for fast and simple analysis of the secondary structure of proteins. In this study it was used to assess the correct folding of recombinant proteins and muteins.

Polarisation of light through an appropriate filter results in the electric field oscillating in a wave that is the resultant of two vectors (figure A1.1). This oscillation traces out a circle which can be either clockwise (right-handed) or anticlockwise (left-handed). Optically active chiral molecules will interact with polarised light, absorbing left-hand and right-handed circularly polarised light to different degrees and resulting in circular dichroism. Optically active molecules also have different refractive indices for the two forms of light, which results in the rotation of the light, in a wavelength dependent manner. The differential absorption in conjunction with rotation leads to elliptically polarised light (figure A1.1C; Tinoco and Canter, 1970).

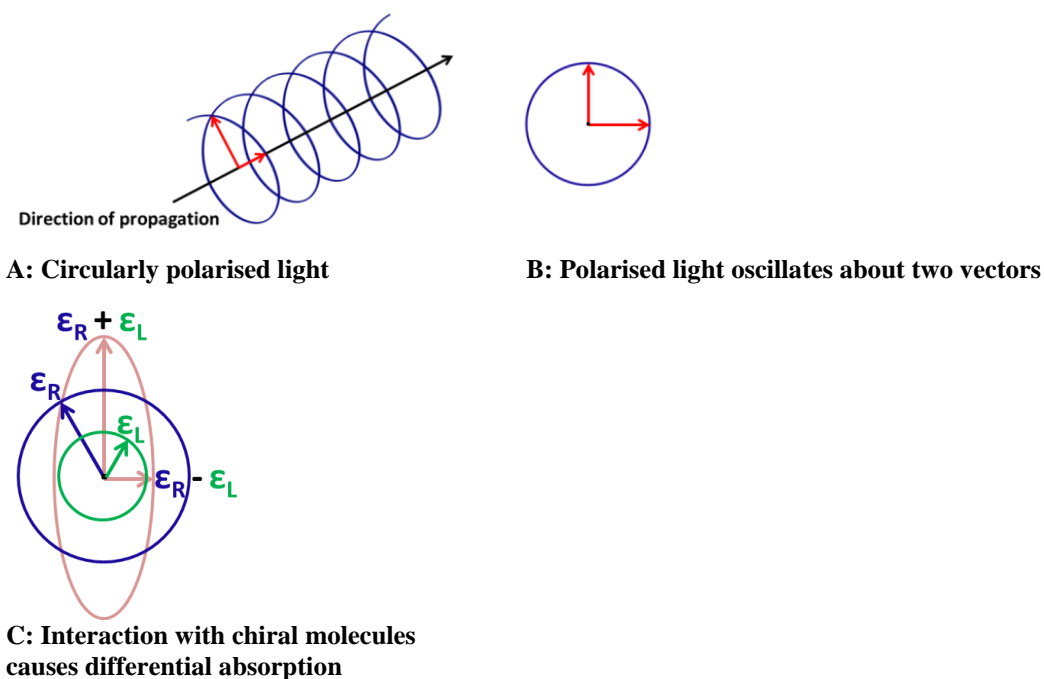


Figure A1.1: UV-CD relies on the optical properties of proteins: **A:** By passing through a prism or suitable filter, light can be circularly polarised, rotating about the direction of propagation. Right-hand polarisation is shown **B:** When viewed from the point of the source, the oscillation can be viewed as the result of two equal length vectors. **C:** Upon interacting with an asymmetric molecule, the differential absorption of left- and right-hand polarised right leads to the resultant vectors tracing out an ellipse.

The major optically active groups in proteins are the amide bonds of the backbone, and aromatic side chains (Greenfield, 1996). When these chromophore groups are arranged in ordered arrays (such as α helices or β sheets), the excitation of one molecule by light is translated through the neighbouring molecules, resulting in a characteristic CD spectra (figure A1.2). Predominantly α -helical proteins have absorption minima at 222 nm and 208 nm and a maximum at 193 nm (Holzwarth and Doty, 1965). Proteins with well-defined β -sheet arrangements have a negative maximum at 218 nm and a maximum at 195 nm (Greenfield and Fasman, 1969), while disordered proteins have a minimum near 195 nm (Venyaminov *et al.*, 1993; figure A1.2). Raw data is converted to mean residue ellipticity using equation A1.1, which produces a value that is normalised per residue and therefore allows comparison between different proteins (Greenfield, 2006).

$$\text{Mean residue ellipticity} = \frac{\theta * \text{mean residue weight}}{\text{path length} * [\text{protein}]}$$

Equation A1.1

Where θ is the optical rotation reported in millidegrees, the path length is in mm and the protein concentration is in mg/mL. The resultant mean residue ellipticity is therefore reported in $\text{deg.cm}^2 \text{dmol}^{-1}$.

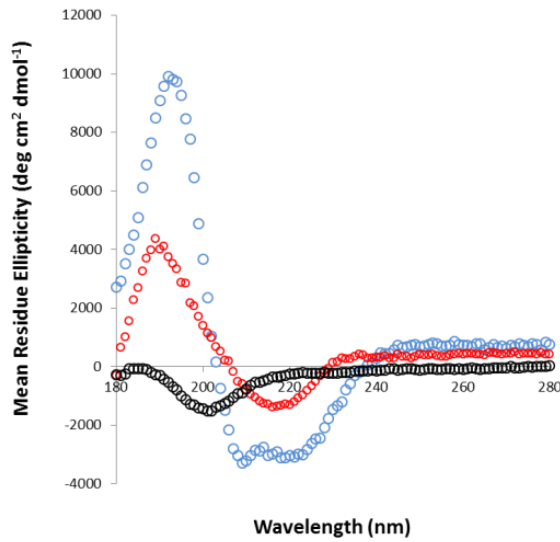


Figure A1.2: Typical CD spectra of secondary structure elements: Spectra were plotted using data obtained from the Protein Circular Dichroism Databank (Whitmore *et al.*, 2011). A predominantly α -helical spectrum is shown in blue (as exemplified by Sensory rhodopsin 2, CD0000117000); β -sheet spectrum in red (as exemplified by OmpG, CD0000118000) and a random coil spectrum in black (Ferredoxin, CD0000032000).

The analysis of protein CD spectra is based on the principle that the CD spectrum (C_λ) can be expressed as a combination of the individual secondary structure components (equation A1.2).

$$C_\lambda = \sum f_k B_{k\lambda}$$

Equation A1.2

Where f_k is the fraction of the secondary structure k . The component secondary structure spectra, $B_{k\lambda}$, are determined through comparison with a set of reference proteins. The fractions of the secondary structure elements of the reference proteins are calculated from the corresponding crystal structure (Sreerama *et al.*, 2000). In the case of this study, the

relative percentages of the secondary structure elements were calculated automatically using the CDSSTR program (Compton and Johnson, 1986) through the online server Dichroweb (Whitmore and Wallace, 2004).

A1.2 Size-exclusion chromatography

Size-exclusion chromatography (SEC) is a commonly used technique to analyse the size of protein particles, and, therefore, the oligomeric species present in solution. The technique works to separate a mixture by distributing the individual components between a stationary phase (the partially permeable gel matrix within the column), and a mobile phase (the eluent), which carries the mixture through the column. Originally made from starch (Lathe and Ruthen, 1955), the matrix is typically composed of dextran – the analytical S200 10/300 columns used in this study were prepacked with Superdex beads, composed of dextran covalently linked to cross-linked agarose, which gives a stable and high resolution matrix (reviewed in Einstein, 2006). The matrix size is selected to provide pores of comparable size to the analyte – in this case, the average bead size was 13 μm which allowed separation of particles from 10 – 600 kDa (GE Healthcare, 2002). Small particles diffuse into the beads of the matrix, and are slowed in their passage through the column, whilst large particles cannot enter the beads and pass through the column quickly with the mobile phase. The volume at which a particle elutes is a function of its penetration of the matrix; represented by the distribution coefficient (K_d), the ratio of the concentrations of the particle in the stationary and mobile phases (equation A1.3; Stellwagen, 2009). Elution of proteins is typically determined by UV absorbance. The Äktapurifier used in this work contains a triple wavelength detector at the end of the column, which was used to monitor the UV absorbance at 280 nm as the elution was run.

$$K_d = \frac{[\text{analyte}]_s}{[\text{analyte}]_m}$$

Equation A1.3

Where $[\text{analyte}]_s$ is the concentration of the analyte in the stationary phase, and $[\text{analyte}]_m$ is that in the mobile phase. In practice, K_d is difficult to measure and so K_{av} is routinely used, as $K_d:K_{av}$ is constant for a given matrix. K_{av} is easily determined experimentally using equation A1.4 (Squire, 1985).

$$K_{av} = \frac{(V_e - V_0)}{(V_t - V_0)} \quad \text{Equation A1.4}$$

Where V_e is the volume at which the analyte elutes, V_t is the total volume of the volume of the column and V_0 is the void volume. K_{av} is related to the log of the molecular weight (Squire, 1985), and therefore mass can be calculated by interpolation from a calibration curve generated from protein standards of known masses.

A1.3 Size-exclusion chromatography with in line light scattering

Although analytical SEC is a commonly used and highly informative technique for globular proteins, some factors such as the hydration of the protein and shape of the particle can lead to non-typical movement through the column. This can yield inaccurate molecular weight calculations, as K_{av} is related to the radius of gyration (Andrews, 1965). SEC also assumes that the protein to be analysed is of similar shape and behaviour to the standards. The toroid of Prx oligomers may give unexpected results, as the presence of a large central cavity leads to a larger radius than would be expected for the mass. Although still not well understood, it is becoming accepted that the movement of a protein through the matrix may be more reliant on the Stoke's (hydrodynamic) radius than the weight, and this may be a more appropriate parameter to evaluate by SEC (Winzor, 2003). Given the variations between individual proteins, there is no standard relationship between the hydrodynamic radius and molecular weight of a protein (Cabr  et al., 1989). Therefore, these parameters were directly examined using SEC with in-line static light scattering and viscometry (SEC/SLS) where available, which allowed calculation of molecule dimensions independent of elution volume.

A1.3.1 Instrument set up and recording of parameters

The Viscotek 302-040 Triple Detector GPC/SEC system (ATA Scientific) used in this study uses a 24 mL S200 10/300 analytical SEC column as a fractionation step, combined with a triple detector method to calculate molecular weight, radius of hydration (R_H), and concentration of species. As the eluent leaves the column, the refractive index (RI), UV absorbance at 280 nm (UV_{280}), differential pressure (DP; a measure of intrinsic viscometry) and light scattering at 90° is measured. The refractive index was used to calculate molecular weight as it is considered to give more precise values (Oliva *et al.*, 2001).

As the sample elutes from the column it enters a light scattering cell. A laser beam is focussed on the end of this cell, and a detector measures light that is scattered at 90° to the incident light. The solvent will scatter light to some degree, and the increase in scattering intensity is directly proportional to the molecular weight and sample concentration. Scattering at 90° is used as this provides optimum signal-to-noise performance (Viscotek Instrument Manual). The sample then passes through a dual cell, deflection RI detector. Light is passed through the dual cell and into a prism which splits the beam into two component beams (figure A1.3). These are detected by two photodiode detectors, which generate electric currents proportional to the light that hits them. The currents are subtracted and the amplified difference forms the RI output. When the cells contain the same solution no deflection is seen. This would be expected for the chromatographic baseline, and equilibration of the column is carried out until the RI output is stable (section 2.5.3). At this point the detector is reset by aligning the mirror so that the output is zero.

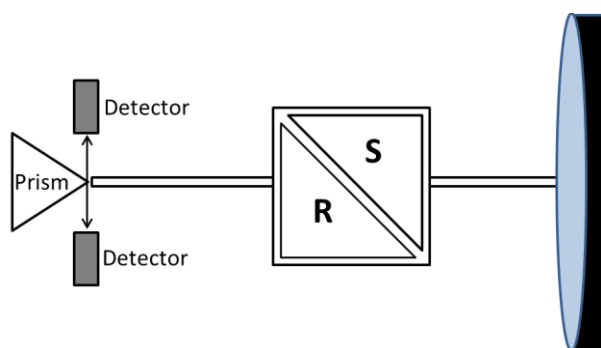


Figure A1.3: Simplified diagram of the refractometer: The beam reflected from the concave mirror passes through the dual cell containing the sample (s) and reference (r) solution, and the difference between split beams detected by photodiode detectors. The currents generated pass to an amplifier (not shown) and produce an output in millivolts (mV).

The RI peak area is exactly proportional to the amount of protein and the dn/dc value, and can therefore be used to calculate the concentration of a species as indicated by a peak on the chromatogram:

$$RI = k_{ri} \frac{dn}{dc} c \quad (\text{Takagi, 1990}) \quad \text{Equation A1.5}$$

k_{ri} is an instrument calibration constant (calculated by running known standards), c is the relative concentration, and dn/dc is constant at 0.186 mL/g for proteins independent of amino acid content (Wen *et al.*, 1996). dn/dc is defined as the specific refractive index increment and represents the change in refractive index for a given increment of concentration (Huglin, 1972). Assuming that all of the sample that is injected elutes from the column, then the sum of all data points across the chromatogram can be taken, and the relative concentration of each species determined. Details of the calculations involved and instrument set-up can be found in the Viscotek Instrument Manual (Malvern, version 2.0). Finally, the viscosity of the sample is measured through a four capillary system. When pure solvent is flowing, the differential pressure (DP) is zero. As sample elutes, the pressure in three of the capillaries increases, while a delay column before the fourth capillary ensures this remains filled with pure solvent. The DP is now no longer zero, and the intrinsic viscosity of the sample can be calculated (Pamies *et al.*, 2008). The DP is

reported in Pascals (Pa), and as it is nearly proportional to the intrinsic viscosity, provides the viscometer “chromatogram”.

A1.3.2 Determination of molecular weight

The triple detector method can be used to calculate molecular weight using the light scattering viscometer signals, after calibration to a standard (BSA). Although the use of a triple detector system in theory eliminates the requirement for calibration, the refractometer is in fact designed to be a detector and not an absolute refractometer and therefore the instrument calibration constant (equation A1.5) must be found by calibration to a known standard. This value will remain constant until the buffer is changed, and so one standard is necessary at the beginning of any sample run. A BSA standard was also routinely run after any experimental samples, to ensure that the calibration was still valid.

The calibration and determination of the calibration constant was carried out automatically by the OmniSEC software provided with the instrument (Viscotek Instrument Manual, Malvern, version 2.0). The calibration was carried out and verified through analysing the BSA chromatogram as an unknown sample (OmniSEC Technical Note MRK1664-01, Malvern 2011). Molecular weights of samples were automatically calculated from the RI, light scattering signal and DP of the chromatogram using the OmniSEC software, which employs the following equations:

$$\frac{K.c}{R_{\theta}} = \frac{1}{Mw.P(\theta)} \quad \text{Equation A1.6}$$

Where K is an optical constant (derivation can be found in Viscotek Instrument Manual; Malvern, version 2.0); $P(\theta)$ is the particle scattering function (the angular dependence of light scattering intensity; Kratochvil 1987). The R_H can then be derived using equation 1.6. These calculations are carried out automatically using the OmniSEC software.

$$R_H = \left[\frac{3}{4\pi} \left(\frac{[\eta]M_w}{0.025} \right) \right]^{1/3}$$

Equation A1.7

A1.4 Small-angle X-ray scattering

Chromatography carries with it the potential of matrix interactions, shear stress and elution of particulate matter that is shed from the beads, all of which can influence the quality and accuracy of the data obtained. Small angle X-ray scattering (SAXS) was routinely carried out to give information about the oligomeric state of the protein in free solution, without the influence of a matrix. SAXS can provide highly accurate molecular mass calculations, as well as providing structural information (Feigin and Svergun, 1987). Although the resolution is lower than the popular structure-determination techniques of X-ray crystallography and nuclear magnetic resonance (NMR), SAXS is a useful complementary technique, and examines the proteins in the experimental buffer, eliminating the potential influence of unusual additives used for crystallisation, or artefacts due to crystal packing. Recent advances in the field have led to the development of high-throughput data collection and analysis, along with improvements in *ab initio* modelling. Analysis of intrinsic flexibility and quaternary structure of proteins have made SAXS a powerful and increasingly popular tool in modern molecular biology (Mertens and Svergun, 2010). An advantage of SAXS is the minimal sample preparation compared to other techniques, and quantity of information that can be derived even from the raw data. However, the data are solution averaged and extracting data from polydisperse systems is challenging (Jacques and Trewhella, 2010).

The scattering of X-rays from a solution of biomolecules depends on the difference in electron density between the solvent and the solute (in this case, the protein molecules). The scattered X-rays interfere either constructively or destructively, and an interference pattern is detected by the detector. The SAXS/WAXS beamline of the Australian Synchrotron uses a 1M Pilatus detector, which is a hybrid pixel detector, and allows

single photon per pixel resolution and 30 frames per second resolution (details of the detector can be found in Broenniman *et al.*, 2005). The interference pattern can be used to determine the distance between the incident and scattered wave, and therefore calculate the magnitude of the scattering vector q (figure A1.4; equation A1.8; Mertens and Svergun, 2007). The units of q are the inverse of the units of the wavelength used, typically \AA^{-1} or nm^{-1} .

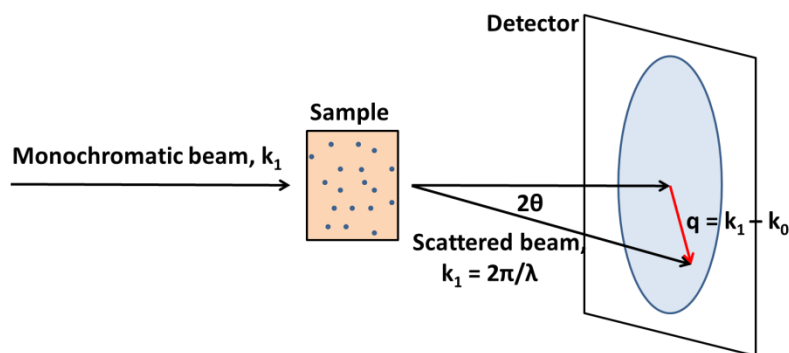


Figure A1.4: Standard set-up of a SAXS experiment. Collimated and focussed X-rays from a synchrotron source were passed through the sample and the interference pattern used to calculate the distance between scattering centres, and from this gain information relating to particle size and shape.

$$q = \frac{4\pi \sin(\theta)}{\lambda} \quad \text{Equation A1.8}$$

2θ is the angle between the incident wave and the scattered intensity. Aqueous solutions of proteins give rise to isotropic scattering intensity as the molecules will be randomly orientated (Mertens and Svergun, 2010). The scattering intensity (I) is recorded as a function of q . For data analysis, 2 dimensional (2D) interference patterns were averaged and the buffer scatter subtracted using the automated software SCATTERBRAIN (Petoukhov *et al.*, 2007). After subtraction, the corrected intensity ($I(q)$) is proportional to the averaged scattering of the particles in solution (Mertens and Svergun, 2007), and is presented as radially averaged 1 dimensional (1D) curves for data analysis (figure A1.5).

$$(I(q))_{\Omega} = (A(q)A^*(q))_{\Omega} \quad \text{Equation A1.9}$$

Where the scattering amplitude ($A(q)$) is a Fourier transformation of the excess scattering length density, and the intensity is average over all orientations (Ω).

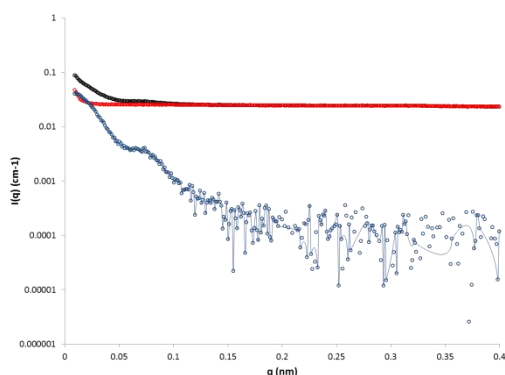


Figure A1.5: Typical X-ray scattering pattern: Exemplified by wildtype *HsPrx3*. Buffer alone is shown in red, *HsPrx3* in black, and the subtraction is blue, representing the contribution of the protein alone.

The 1D scattering curve can be used to obtain information about particle size and shape, and computational methods also allow the determination of modest resolution 3D models. Interpretation of the scattering data can be carried out by model-independent methods such as Guinier and Porod volume analysis; or model-dependent methods such as the pairwise distribution analysis (Konarev et al. 2003; Mertens & Svergun 2010).

A1.4.1 Guinier analysis

At low q values the scattering intensity is dependent only on the radius of gyration R_G , which relies on the average squared distances of each scattering centre from the particle centre. At low q values, scattering can be described by the Guinier approximation (equation A1.9; Glatter & Kratky 1982).

$$I(q) = I(0) e^{-\frac{(qR_G)^2}{3}}$$

Equation A1.10

Plotting $\log I(q)$ against q^2 will give the Guinier plot, from which R_G and $I(0)$ can be extracted (Guinier & Fournet, 1955). R_G is determined by the slope of the graph, which can be automatically determined using software such as *AutoRg* (Petoukhov et al. 2012; Petoukhov et al. 2007). For globular proteins the Guinier approximation is typically valid over a q -range of $qR_G < 1.3$, and the linearity of the plot within this range gives an indication of the quality of the sample, with a non-linear dependence indicating aggregation (figure A1.6). When this is seen the Guinier approximation is not able to be used to determine R_G (Glatter & Kratky 1982).

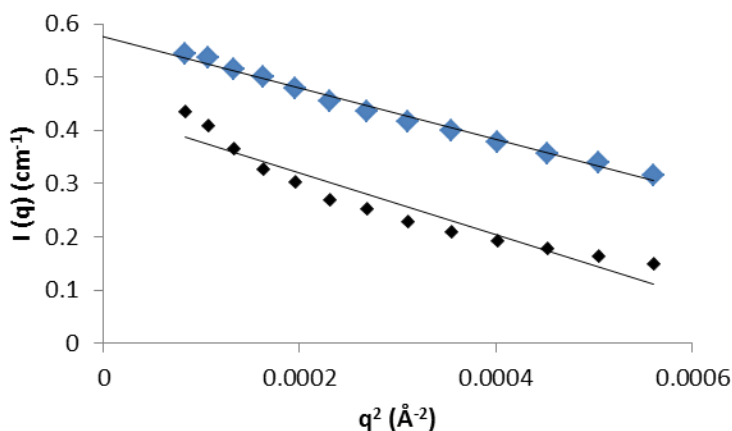


Figure A1.6: Guinier plots for an aggregated and non-aggregated sample: A good quality sample yields a linear plot within the Guinier region (as exemplified by the C47SS78A mutein, chapter five, blue diamonds). An aggregated sample (the S78A mutein, chapter five, black diamonds) shows a non-linear trend, with a significant upward trend at the lowest q values. Primus was used to generate Guinier plots (Konarev *et al.*, 2003).

$I(0)$ can be found by extrapolation, and is the square of the number of electrons in the solution (equivalent to the value of $I(0, 0, 0)$ in X-ray crystallography). $I(0)$ is independent of particle shape and can be used for molecular weight determination (equation A1.10).

$$I(0)/c = \frac{N_A M}{\mu^2} (1 - \rho_0 \phi)^2 \quad \text{Equation A1.11}$$

Where N_A is Avogadro's number, μ is the ratio of the molecular weight to the number of electrons (take as 1.87 for proteins, Putnam *et al.*, 2007), ρ_0 is the average electron

density of the solvent, and ϕ is the ratio of the particle volume to its number of electrons (Vachette and Svergun, 2000; Koch *et al.*, 2003).

A1.4.2 Porod analysis

Where low q values give information relating to the R_G and molecular weight, high q values information regarding molecular shape can be derived. The intensity of the scattering decreases by Porod's law for folded macromolecules (Porod, 1951; equation A1.11).

$$I(q) \propto q^{-d_f}$$

Equation A1.12

Where d_f is the fractal degrees of freedom. For example, scattering from flat ellipsoids had a $d_f = 2$ in the high q -range, whereas scattering from needle-like ellipsoids has a $d_f = 1$ in the high q -range. The Porod volume of the molecule in nm^3 is typically twice the molecular mass in kDa for globular proteins, and can be derived from the Porod invariant (Q ; Porod, 1982; full details and derivations can be found in Putnam *et al.*, 2007). These calculations require accurate data across the entire q -range and can therefore yield errors, however, they provide a useful confirmation of parameters calculated from the Guinier region. The AUTOPOROD function of *Scatterbrain* software was used to automatically calculate the molecular weight, particle volume and D_{max} from the Porod volume.

A1.4.3 Pairwise distribution function

Pairwise distance distribution function ($P(r)$) plots represent a histogram of the distances between scattering atoms in a particle. The $P(r)$ function is calculated by an indirect Fourier transformation (details of the calculations can be found in Mertens and Svergun, 2010). The GNOM program (Semenyuk and Svergun, 1991) constructs trial $P(r)$

functions that are Fourier transformed, then back projects them to assess the fit with the experimental scattering. The program then uses a regularising multiplier to balance the smoothness of the trial functions with the goodness of fit to the data. The plot provides an easily interpreted depiction of information relating to particle shape. For example globular particles yield bell-shaped curves, with a maximum at $\sim D_{\max}/2$. Particles with multiple domains yield profiles with multiple shoulders corresponding to intra and inter-subunit distances (Mertens and Svergun, 2010; figure A1.7).

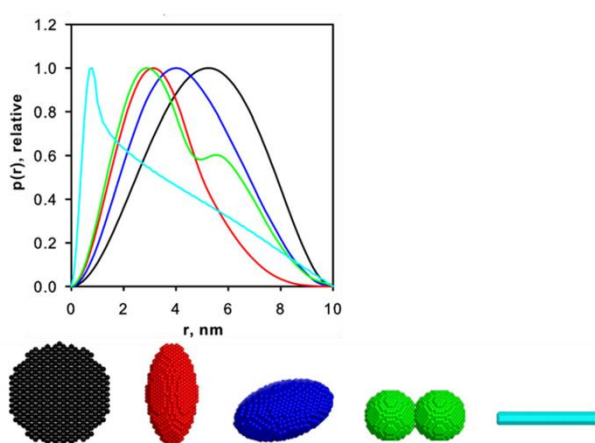


Figure A1.7: Typical $P(r)$ plots from particles of different shapes: Spherical particles yield a bell shaped curve with a maximum at $D_{\max}/2$. Elongated particles show a negatively skewed profile, and multi-domain particles show multiple maxima. Figure adapted from Mertens and Svergun, 2010.

The $P(r)$ function is zero at $r = 0$ and at $r = D_{\max}$, and for processing of data calculations are constrained to zero at these values. As the $P(r)$ plot takes into account the whole range of the data, it is often considered a better estimation of the R_G and $I(0)$ than the Guinier approximation as it is not limited to a small region (Putnam *et al.*, 2007). Presence of aggregates within a sample can therefore also be identified by comparing R_G and $I(0)$ values calculated from $P(r)$ plots and those generated from the Guinier plots.

A1.5 Transmission Electron Microscopy

The resolution of a light microscope is mainly limited by the wavelength of the light used (Abbe, 1873; equation A1.12).

$$r = \frac{0.61\lambda}{\mu \sin \alpha}$$

Equation A1.13

Where r is the resolution limit, μ is the refractive index of the material between the object and objective lens, and α is the angle above which the light is stopped by the aperture (figure A1.8).

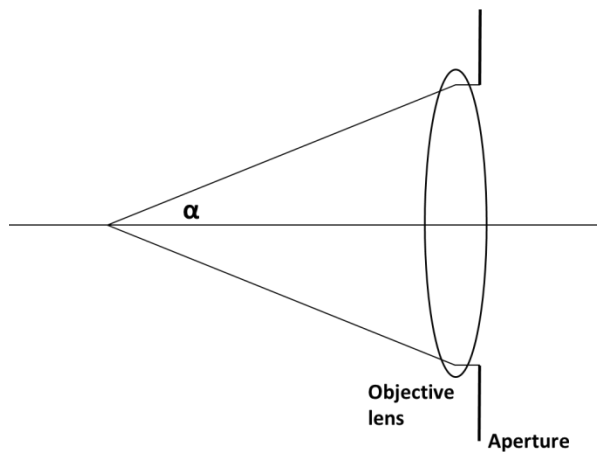


Figure A1.8: The definition of the angle α

Both light and electron microscopes produce an image from the transmission of illuminating radiation through the sample, either light or electron waves. The TEM therefore relies on the wave-particle duality of electrons proposed by de Broglie, and as the wavelength of electrons in a TEM operated at 200 kV is 0.025 Å (full calculation can be found in Zou *et al.*, 2011), this technique provides superior resolution. Furthermore, the increased scattering of electrons compared to X-rays mean that they can be used to obtain more structural detail about small structures than X-ray scattering techniques

(Henderson, 1995). In practice, the resolution limit of TEM is limited to $\sim 1\text{\AA}$ due to spherical and chromatographic aberrations of the lenses. In the case of proteins the best resolution achieved to date is 1.9 \AA (for lens-specific aquaporin-0; Gonen *et al.*, 2005).

In the TEM a beam of electrons is produced by a thermionic or field emission electron gun, and accelerated by high voltage (100-300 kV). The beam can be focused by magnetic condenser lenses onto the sample (figure A1.9), in the same way that light can be focused by glass lenses. The transmitted beam is focussed onto either photographic film or a charge-coupled device (CCD) camera by the objective and projection lenses, and the electron density, phase and periodicity of the transmitted electrons are used to produce an image. This image is a 2D projection of information in 3 dimensions, therefore the TEM acts like a projector to superimpose information from all regions of the specimen which the electron beam passed through.

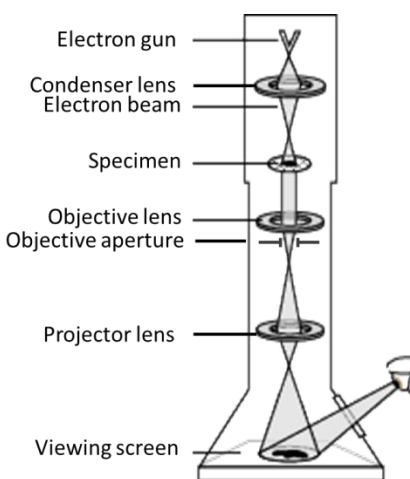


Figure A1.9: Simplified schematic of the TEM: High energy electrons pass through the condenser lens and are scattered by the sample. The objective lens does the first step of image focusing and, together with the objective aperture, screens out electrons according to their scattering angle. The projector lens then focuses and projects electrons onto the imaging surface. Figure taken from nobelprize.org, accessed 18th December 2013.

A1.5.1 The contrast transfer function

A projection image of an object produced from TEM is the result of amplitude and phase contrast. In bright-field EM (the most commonly used mode) the transmitted beam is imaged, and the amplitude contrast is produced by the loss of electrons within the coherent electron beam (Kleinschmidt, 2010) by high angle scattering (falling outside of the lens aperture), and inelastic scattering (figure A1.10). The level of contrast depends on the atomic number of the species that the electron beam interacts with. Therefore, the scattering by biological molecules shows little difference to that by the aqueous surroundings, and the contribution of amplitude contrast is small (~10% when no contrasting agent is used, Toyoshima and Unwin, 1988). This can be improved to some degree by using lower accelerating voltages or a smaller objective aperture, which screens out highly deflected electrons.

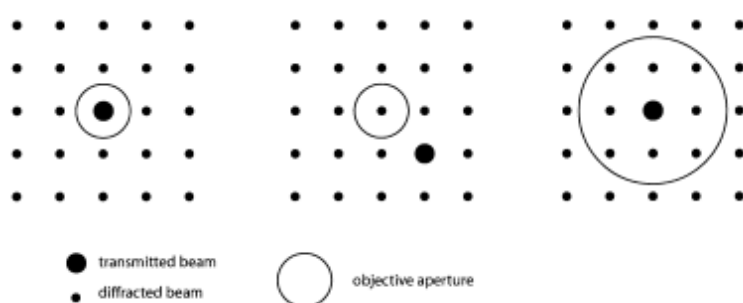


Figure A1.10: **A:** Bright field EM images the transmitted beam. **B:** In dark field EM the aperture is positioned to use one of the diffracted beams. In both bright and dark field microscopy image contrast is produced by the change in amplitude of the respective beam. **C:** High resolution EM (HREM) uses a large objective aperture and focuses more than one beam on the back focal plane. This produces an image as the result of the phase difference of the transmitted and diffracted beams – the phase contrast image. Highly deflected electrons contain the most high resolution information, however contrast is lost. A balance between resolution and contrast must be found. Taken from Bendersky and Gayle, (2001).

Phase contrast arises from the differences in phase of elastically scattered and unscattered electrons, and the interference of these electrons. Spherical aberrations of the objective lens contribute to the phase shifts, and their contribution can be compensated by adjusting the defocus. This changes the path length of scattered electrons more than unscattered electrons, and can therefore increase the contrast. Most modern microscopes correct aberration to bring all the scattered electrons to a common focus (Hawkes, 2009), so that the reachable resolution can become equal to the information limit. Image formation in the EM is therefore a function of the lens aberration, aperture and defocus, termed the contrast transfer function (CTF).

The CTF relates the Fourier transform of the image to that of the object being examined, which takes into account the aberrations of the lens (equation 1.13). These imperfections result in an oscillating CTF (figure A1.11). Phase reversals mean that the CTF is equal to zero at several points in the spatial frequency spectrum, which produces the series of black rings seen in the optical diffraction pattern, known as Thon rings (Amos *et al.*, 1982). The first zero crossing is usually taken to impose a resolution limit if no correction due to the CTF is applied (Wade, 1992).

$$-\sin\chi(\alpha)$$

$$\text{Where, } -\sin\chi(\alpha) = (2\pi/\lambda)(-\frac{1}{4}C_s\alpha^4 + \frac{1}{2}\Delta f^2) \quad \textbf{Equation 1.14}$$

λ is the electron wavelength

α is the angle of scattering in the microscope expressed in terms of the frequency of the scattered wave (resolution)

C_s -the coefficient of spherical aberration

Δf is the defocus value

From (Ruprecht and Nield, 2001)

The reversals and points of information loss seen in the CTF produces artefacts, and an unreliable representation. CTF correction must be carried out to produce a reliable image

past the resolution limit of the first zero crossing. Multiplying the image transform with the reverse of the CTF corrects for the reversals. Changing the defocus shifts the spatial frequency at which the CTF crosses zero, so to compensate for the loss of information at these points, images are taken at a number of defocus values.

A1.5.2 Cryo-electron microscopy

Maintaining the hydrated state is essential to minimise artefacts that may occur when proteins are removed from the aqueous environment of the cell. Cryo-electron microscopy (cryo-EM) was developed at the EMBL (Dubochet *et al.*, 1981; Dubochet *et al.*, 1988) and has the advantage that samples are frozen so as to maintain this state, enabling examination in conditions very close to the native environment. The sample is prepared on holey grids, meaning that the potential for grid interactions is removed, and blotted to leave a thin protein solution film. The grid is frozen rapidly (usually with liquid ethane or propane), resulting in the specimen embedded in a vitrified layer of buffer. The thickness of the vitrified layer is important, as the formation of ice crystals or thick ice can distort structures, and lead to difficulties in imaging the sample due to the reduction in electron transmission.

Once frozen, the sample is handled in liquid nitrogen (at around -170 °C) to prevent the formation of crystalline ice which can destroy structures.

A1.5.2 Single particle analysis

In order to reduce radiation damage to the sample, low dose techniques are used in the EM. However, this produces noisy images with a low signal-to-noise ratio, which must be overcome by multiple averaging. This also allows the generation of 3D representations of a protein by determining relative orientations of projections, without the requirement of crystallisation, which can be difficult.

To produce a 3D image CTF correction must occur, and images with different defocus values must be used (as described previously). For negatively stained particle analysis, the spatial frequencies beyond the first zero crossing are typically filtered out, as the resolution available within the region before the crossing is usually satisfactory.

Particles are picked using a box size typically twice the width of the particle to reduce artefacts whilst avoiding overlap with nearby particles. This step is usually carried out semi-automatically using software such as EMAN (Ludtke *et al.*, 1999). The noise observed in images can be reduced by “binning”, whereby neighbouring pixels are combined, and their grey values averaged to produce a larger pixel. Very high and low spatial frequencies are due to stain non-uniformity and systematic noise respectively. These are removed by applying a band-pass filter with the inverse of the object length as the low-frequency cut-off, and the first zero crossing of the CTF as the high-frequency cut-off.

A1.5.3 Multi-reference refinement and classification

Noise and random information in images can be removed with averaging, as the information from particles of a homogeneous sample is constant. In a typical sample, the data set will be composed of particles in different orientations, and therefore, more than one 2D structure is seen. If identical 2D structures are aligned and averaged, the result is a number of projection structures which represent different orientations of the particles. These can be used for initial 3D reconstructions, which are less likely to suffer from noise. As it is difficult to group and align noisy images without having the class averages, an iterative process is required (Schatz *et al.*, 1995). A number of class averages is decided to represent the structural heterogeneity within the sample, and these averages are iteratively refined until movement of images between classes and variations of the class averages minimise. Starting references are typically built by randomly averaging images, to reduce bias.

A1.5.4 3D structure determination

If projection images representing a number of particle orientations are available, and their relative orientations are known, then the 2D images can be combined to reconstruct a 3D structure. Several software suites are available to carry out this process, including EMAN (Ludtke *et al.*, 1999), SPIDER and BSoft (Heymann and Belnap, 2007). If the specimen shows random orientation on the grid, angular reconstruction or projection matching can be used to determine the relative orientations of particles (Frank *et al.*, 1996; van Heel, 1987).

Angular reconstruction

Angular reconstruction utilises a common lines approach. This is based on the theory that 2D projections of the same 3D structures will have a common 1D projection in real space (the “common line”). This is analogous to the common line at which Fourier transforms of 2D projections intersect. Common lines are usually determined for the class averages, as the signal-to-noise ratio is better than the raw images.

Projection matching

Projection matching requires a pre-existing model, which provides projections with known orientations. Projections from the data set are then compared with these known orientations, and the angle that matches best is assigned. In multi-reference refinement, several starting models are used and simultaneously refined as recorded projections are matched with the models. This allows the sorting of a heterogeneous data set in homogeneous groups.

Once the orientations of class averages have been assigned, a 2D model can be built, either in real space or Fourier space (Frank, 2005; Ruprecht *et al.*, 2001). The projections can be back-projected along their assigned Euler angle in real space, or the Fourier transforms of 2D projections can be aligned to a 3D Fourier transform of the object in reciprocal space. The inverse transformation will then yield the 3D structure.

In the case of this study, EMAN was primarily used for image processing and 3D reconstruction. This program uses a hybrid approach to build 3D reconstructions which uses projection matching and a common lines approach. The 3D model is built using the common lines approach using class averages of known orientation rather than raw images, then the model is refined using projection matching. Once the model is built, reliability can be assessed by comparison to raw images and projection averages. The resolution of the model can be assessed by examining the Fourier shell correlation (FSC) between two reconstructions that were built using half of the data set. Normalised cross-correlation coefficients between the two reconstructions are plotted against spatial frequencies, and the resolution is taken as that where the FSC value is 0.5.

The 3D structures produced from EM are of modest resolution compared to that achieved from X-ray crystallography. Typical resolution of EM single-particle reconstructions are $\sim 8 - 40 \text{ \AA}$. Although this can be sufficient in many cases, pseudo-atomic interpretation of the reconstructions can be carried out by docking known atomic coordinates. This was carried out in the case of *HsPrx3* reconstructions, detailed in chapter six.

A1.5.5 References

- Abbe, E. (1873) Beiträge zur Theorie des Mikroskops und der mikroskopischen Wahrnehmung. *Archiv für Mikroskopische Anatomie*. **9**, 413-468.
- Bendersky, L. A. and Gayle, F. W. (2001) Electron diffraction using electron microscopy. *Journal of Research of the National Institute of Standards and Technology* **106**, 997-1012.
- Broennimann, C., Eikenberry, E. F., Henrich, B., Horisberger, R., Huelsen, G., Pohl, E., Schmitt, B., Schulze-Bries, C., Suzuki, M., Tomizaki, T., Toyokawa, H., and Wagner, A. (2006) The PILATUS 1M detector. *Journal of Synchrotron Radiation*. **13**, 120-130.
- Dubochet, J. and McDowell, A. W. (1981) Vitrification of pure water for electron microscopy. *Journal of Microscopy* **124**, RP3-RP4.
- Dubochet, J., Adrian, M., Chang, J-J., Homo, J-C., LePault, J., McDowell, A. W. and Schultz, P. (1988) Cryo-electron microscopy of vitrified specimens. *Quarterly Review of Biophysics* **21**, 129-228.
- Frank, J., Radermacher, M., Penczek, P., Zhu, J., Li, Y., Ladjadj, M. and Leith, A. (1996) SPIDER and WEB: processing and visualization of images in 3D electron microscopy and related fields, *Journal of Structural Biology* **116**, 190-199.
- Frank, J. (2005) Three-dimensional electron microscopy of macromolecular assemblies: visualization of biological molecules in their native state. 2nd ed., Oxford University Press, New York ; Oxford
- Gonen, T., et al., (2005) Lipid-protein interactions in double-layered two-dimensional AQP0 crystals. *Nature* **438**, 633-8.
- Greenfield, N. and Fasman, G. D. (1969) Computed circular dichroism spectra for the evaluation of protein conformation. *Biochemistry* **8**, 4108-4116.
- Hawkes, P. W. (2009) Aberration correction past and present. *Philosophical Transactions of the Royal Society* **367** 3637-3664.
- Henderson, R. (1995) The potential and limitations of neutrons, electrons and X-rays for atomic resolution microscopy of unstained biological molecules. *Quarterly Review of Biophysics* **28**, 171-93.
- Heymann, J. B. and Belnap, D. M. (2007) Bsoft: Image processing and molecular modelling for electron microscopy. *Journal of Structural Biology* **157**(1), 3 - 18.
- Holzwarth, G. and Doty, P. (1965) The Ultraviolet Circular Dichroism of Polypeptides. *Journal of the American Chemical Society* **87**, 218-228.
- Huglin, M. B. (1972) in M.B. Huglin, (Ed) Light Scattering from Polymer Solutions, Academic Press, Ch. 6.

- Kleinschmidt, A. K. (2010) Bright Field and Dark Field Electron Microscopy of Biomacromolecules Mounted on Thin Support Films. *Berichte de Bunsengesellschaft für physikalische Chemie* **74**, 1190-1196.
- Kratochvíl, P. (1987) in Kratochvíl, P. (Ed). Polymer Characterization. Classical Light Scattering from Polymer Solutions. Elsevier; Amsterdam pp. 334
- Ludtke, S. J., Baldwin, P. R. and Chiu, W. (1999) EMAN: Semi-automated software for high-resolutions single-particle reconstructions. *Journal of Structural Biology* **128**, 82 – 97.
- Oliva, A., Llabrés, M., Fariña, J. B., (2001) Comparative study of protein molecular weights by size-exclusion chromatography and laser-light scattering. *Journal of Pharmaceutical and Biomedical Analysis* **25**, 833-841.
- Pamies, R., Cifre, J. G. H., Martínez, M. C. L., de la Torre, J. G. (2008) Determination of intrinsic viscosities of macromolecules and nanoparticles. Comparison of single-point and dilution procedures. *Colloid Polymer Science* **286**, 1223-1231.
- Rose, H. H. (2008) Optics of high-performance electron microscopes. *Science and Technology of Advanced Materials* **9**, 1-30.
- Ruprecht, J. and Nield, J. (2001) Determining the structure of biological macromolecules by transmission electron microscopy, single particle analysis and 3D reconstruction. *Progress in biophysics and molecular biology* **75**, 121-164.
- Schatz, M., Orlova, E. V., Dube, P., Jager, J. and van Heel, M. (1995) Structure of *Lumbricus terrestris* hemoglobin at 30Å resolution determined using angular reconstitution, *Journal of Structural Biology* **114**, 28-40.
- Takagi, T. (1980) Application of low-angle laser light scattering detection in the field of biochemistry : Review of recent progress. *Journal of Chromatography A* **506**, 409-416.
- Tinoco, I. Jr .and Cantor, C. R. (1970) in Glick, D. (Ed) Methods of Biochemical Analysis, Volume 18, John Wiley and Sons; New York.
- Toyoshima, C. and Unwin, N. (1988) Contrast transfer for frozen-hydrated specimens: determination from pairs of defocused images. *Ultramicroscopy* **25**, 279-91.
- Venyaminov, S., Baikalov, I. A., Shen, Z. M., Wu, C. S. and Yang, J. T. (1993) Circular dichroic analysis of denatured proteins: inclusion of denatured proteins in the reference set. *Analytical Biochemistry* **214**, 17–24.
- Wade, R.H. (1992) A brief look at imaging and contrast transfer. *Ultramicroscopy* **46**, 145-156.
- Whitmore, L., Woollett, B., Miles, A. J., Klose, D. P., Janes, R. W. and Wallace, B.A., (2011) PCDDb: the protein circular dichroism data bank, a repository for circular dichroism spectral and metadata. *Nucleic Acids Research* **39**, D480-D486.

Zou, X., Hovmöller, S. and Oleynikov, P. (2011) in Zou, X. (Ed) Electron crystallography: Electron microscopy and electron diffraction. Oxford University Press Inc., New York.

Appendix 2 In house crystallisation screens

Robot Screen I

	1	2	3	4	5	6	7	8	9	10	11	12
A	50% (w/v) PEG 400, 0.2 M Li ₂ SO ₄ , 0.1 M acetate pH 5.1	20% (w/v) PEG 3350, 0.2 M ammonium chloride pH 6.3	40% (v/v) MPD, 5% (w/v) PEG 8000, 0.1 M cacodylate pH 7.0	30% MPD, 0.02 M CaCl ₂ , 0.1 M NaOAc pH 4.6	20% ethanol, 0.1 M Tris pH 8.5	30% (w/v) PEG 8000, 0.2 M Li ₂ SO ₄ , 0.1 M acetate pH 4.5	16% (w/v) PEG 8000, 0.04 M KH ₂ PO ₄ , 20% glycerol	1.0 M (NH ₄) ₂ HPO ₄ , 0.1 M acetate pH 4.5	20% Jeffamine M-600, 0.1 M HEPES pH 6.5	0.2 M sodium chloride, 20% PEG 3350	0.2 M magnesium nitrate, 20% PEG 3350	0.2 M ammonium acetate, 20% PEG 3350
B	20% (w/v) PEG 3000, 0.1 M citrate pH 5.5	20% (w/v) PEG 3350, 0.2 M potassium formate pH 7.3	40% ethanol, 5% (w/v) PEG 1000, 0.1 M phosphate-citrate pH 5.2	20% (w/v) PEG 8000, 0.2 M NaCl, 0.1 M phosphate-citrate pH 4.2	25% (v/v) 1,2-propanediol, 0.1 M Na/K phosphate, 10% (v/v) glycerol pH 6.8	70% (v/v) MPD, 0.2 M MgCl ₂ , 0.1 M HEPES pH 7.5	1.0 M sodium citrate, 0.1 M cacodylate pH 6.5	1.6 M MgSO ₄ , 0.1 M MES pH 6.5	50% (v/v) ethylene glycol, 0.2 M MgCl ₂ , 0.1 M Tris pH 8.5	0.2 M calcium chloride, 20% PEG 3350	0.2 M sodium nitrate, 20% PEG 3350	0.2 M lithium sulfate, 20% PEG 3350
C	20% (w/v) PEG 3350, 0.2 M diammonium hydrogen citrate pH 5.0	50% MPD, 0.2 M (NH ₄) ₂ HPO ₄ , 0.1 M Tris pH 8.5	8% (w/v) PEG 4000, 0.1 M NaOAc pH 4.6	20% (w/v) PEG 6000, 1.0 M LiCl, 0.1 M citric acid pH 4.0	10% (w/v) PEG 20,000, 2% dioxane, 0.1 M bicine pH 9.0	20% (w/v) PEG 8000, 0.1 M Tris pH 8.5	2.0 M (NH ₄) ₂ SO ₄ , 0.2 M NaCl, 0.1 M cacodylate pH 6.5	10% (w/v) PEG 6000, 0.1 M bicine pH 9.0	10% MPD, 0.1 M bicine pH 9.0	0.2 M potassium chloride, 20% PEG 3350	0.2 M sodium formate, 20% PEG 3350	0.2 M magnesium sulfate, 20% PEG 3350
D	30% (v/v) MPD, 0.02 M CaCl ₂ , 0.1 M NaOAc pH 4.6	20% (w/v) PEG 3350, 0.2 M potassium nitrate pH 6.9	10% (w/v) PEG 8000, 0.2 M MgCl ₂ , 0.1 M Tris pH 7.0	20% (w/v) PEG 3350, 0.2 M ammonium nitrate pH 6.3	2.0 M (NH ₄) ₂ SO ₄ , 0.1 M acetate pH 4.6	40% (v/v) PEG 400, 0.2 M Li ₂ SO ₄ , 0.1 M Tris pH 8.4	10% 2-propanol, 0.2 M NaCl, 0.1 M HEPES pH 7.5	14.4% (w/v) PEG 8000, 0.16 M Ca(OAc) ₂ , 0.08 M cacodylate pH 6.5, 20% glycerol	0.2 M sodium fluoride, 20% PEG 3350	0.2 M sodium iodide, 20% PEG 3350	0.2 M magnesium acetate, 20% PEG 3350	0.2 M sodium sulfate, 20% PEG 3350
E	20% (w/v) PEG 3350, 0.2 M magnesium formate pH 5.9	0.8 M (NH ₄) ₂ SO ₄ , 0.1 M citric acid pH 4.0	20% (w/v) PEG 6000, 0.1 M citric acid pH 5.0	10% (w/v) PEG 6000, 0.1 M HEPES pH 7.0	10% (w/v) PEG 1000, 10% (w/v) PEG 8000	40% (v/v) MPD, 0.1 M Tris pH 8.0	1.26 M (NH ₄) ₂ SO ₄ , 0.2 M Li ₂ SO ₄ , 0.1 M Tris pH 8.5	10% (w/v) PEG 8000, 0.1 M imidazole pH 8.0	0.2 M potassium fluoride, 20% PEG 3350	0.2 M potassium iodide, 20% PEG 3350	0.2 M zinc acetate, 20% PEG 3350	0.2 M potassium sulfate, 20% PEG 3350

F	20% (w/v) PEG 1000, 0.2 M Li ₂ SO ₄ , phosphate-citrate pH 4.2	20% (w/v) PEG 3350, 0.2 M sodium thiocyanate pH 6.9	50% (v/v) PEG 200, 0.2 M MgCl ₂ , 0.1 M cacodylate pH 6.6	0.8 M NaH ₂ PO ₄ /0.8 M KH ₂ PO ₄ , 0.1 M HEPES pH 7.5	24% (w/v) PEG 1500, 20% glycerol	25.5% (w/v) PEG 4000, 0.17 M (NH ₄) ₂ SO ₄ , 15% glycerol	40% (v/v) MPD, 0.1 M CAPS pH 10.1	30% Jeffamine M-600, 0.05 M CsCl, 0.1 M MES pH 6.5	0.2 M ammonium fluoride, 20% PEG 3350	0.2 M ammonium iodide, 20% PEG 3350	0.2 M sodium acetate, 20% PEG 3350	0.2 M ammonium sulfate, 20% PEG 3350
G	20% (w/v) PEG 8000, 0.1 M CHES pH 9.5	20% (w/v) PEG 6000, 0.1 M bicine pH 9.0	1.6 M sodium citrate pH 6.5	40% (v/v) PEG 300, 0.1 M phosphate-citrate pH 5.2	30% (v/v) PEG 400, 0.2 M MgCl ₂ , 0.1 M HEPES pH 7.5	40% (v/v) PEG 300, 0.2 M Ca(OAc) ₂ , 0.1 M cacodylate pH 7.0	20% (w/v) PEG 3000, 0.2 M Zn(OAc) ₂ , 0.1 M imidazole pH 8.0	3.2 M (NH ₄) ₂ SO ₄ , 0.1 M citric acid pH 5.0	0.2 M lithium chloride, 20% PEG 3350	0.2 M potassium thiocyanate, 20% PEG 3350	0.2 M calcium acetate, 20% PEG 3350	0.2 M di-sodium tartrate, 20% PEG 3350
H	20% (w/v) PEG 3350, 0.2 M ammonium formate pH 6.6	10% (w/v) PEG 8000, 8% ethylene glycol, 0.1 M HEPES pH 7.5	20% (w/v) PEG 3350, 0.2 M tripotassium citrate monohydrate pH 8.3	10% (w/v) PEG 3000, 0.2 M Zn(OAc) ₂ , 0.1 M acetate pH 4.5	50% (v/v) PEG 200, 0.2 M NaCl, 0.1 M Na/K phosphate pH 7.2	14% 2-propanol, 0.14 M CaCl ₂ , 0.07 M acetate pH 4.6, 30% glycerol	10% 2-propanol, 0.2 M Zn(OAc) ₂ , 0.1 M cacodylate pH 6.5	20% MPD, 0.1 M Tris pH 8.0	0.2 M magnesium chloride, 20% PEG 3350	0.2 M lithium nitrate, 20% PEG 3350	0.2 M potassium acetate, 20% PEG 3350	0.2 M potassium sodium tartrate, 20% PEG 3350

Robot Screen II

	1	2	3	4	5	6	7	8	9	10	11	12
A	0.2 M di-ammonium tartrate, 20% PEG 3350	0.2 M tri-sodium citrate, 20% PEG 3350	0.2 M tri-sodium citrate dihydrate, 0.1 M sodium cacodylate pH 6.5, 30% (v/v) iso-propanol	0.1 M HEPES-Na pH 7.5, 1.5 M lithium sulfate monohydrate	0.2 M calcium chloride dihydrate, 0.1 M sodium acetate trihydrate pH 4.6, 20% (v/v) isopropanol	4.0 M sodium formate	30% (w/v) PEG 1500	25% (v/v) ethylene glycol	0.1 M cadmium chloride dihydrate, 0.1 M sodium acetate trihydrate pH 4.6, 30% (v/v) PEG 400	0.1 M sodium dihydrogen phosphate mono, 0.1 M mono-potassium dihydrogen phosphate, 0.1 M MES pH 6.5, 2.0 M sodium chloride	0.1 M sodium chloride, 0.1 M HEPES pH 7.5, 1.6 M ammonium sulfate	1.5 M ammonium sulfate, 0.1 M Tris pH 8.5, 12% (v/v) glycerol anhydrous
B	0.2 M sodium dihydrogen phosphate, 20% PEG 3350	0.02 M calcium chloride dihydrate, 0.1 M sodium acetate trihydrate pH 4.6, 30% (v/v) 2-methyl-2,4-pentanediol	0.2 M ammonium acetate, 0.1 M tri-sodium citrate dihydrate pH 5.6, 30% (w/v) PEG 4000	0.2 M lithium sulfate monohydrate, 0.1 M Tris HCl pH 8.5, 30% PEG 4000	0.2 M ammonium acetate, 0.1 M tri-sodium citrate dihydrate pH 5.6, 30% (v/v) 2-methyl-2,4-pentanediol	0.1 M sodium acetate trihydrate pH 4.6, 2.0 M sodium formate	0.2 M magnesium formate	35% (v/v) dioxane	0.2 M ammonium sulfate, 0.1 M sodium acetate trihydrate pH 4.6, 30% (w/v) PEGME 2000	0.1 M MES pH 6.5, 12% (w/v) PEG 20,000	0.1 M HEPES pH 7.5, 2.0 M ammonium formate	0.01 M nickel (II) chloride hexahydrate, 0.1 M Tris pH 8.5, 20% (w/v) PEGME 2000
C	0.2 M di-sodium hydrogen phosphate, 20% PEG 3350	0.4 M potassium sodium tartrate tetrahydrate	0.2 M ammonium acetate, 0.1 M sodium acetate trihydrate pH 4.6, 30% (w/v) PEG 4000	0.2 M magnesium acetate tetrahydrate, 0.1 M sodium cacodylate pH 6.5, 20% PEG 8000	0.2 M tri-sodium citrate dihydrate, 0.1 M HEPES-Na pH 7.5, 20% (v/v) isopropanol	0.1 M Tris HCl pH 8.5, 8% (w/v) PEG 8000	0.2 M zinc acetate dihydrate, 0.1 M sodium cacodylate pH 6.5, 18% (w/v) PEG 8000	2.0 M ammonium sulfate, 5% (v/v) iso-propanol	0.2 M potassium sodium tartrate tetrahydrate, 0.1 M tri-sodium citrate dihydrate pH 5.6, 2.0 M ammonium sulfate	1.6 M ammonium sulfate, 0.1 M MES pH 6.5, 10% (v/v) dioxane	0.05 M cadmium sulfate hydrate, 0.1 M HEPES pH 7.5, 1.0 M sodium acetate trihydrate	0.1 M sodium chloride, 0.1 M bicine pH 9.0, 20% (w/v) PEGME 550

D	0.2 M potassium dihydrogen phosphate, 20% PEG 3350	0.4 M mono-ammonium dihydrogen phosphate	0.1 M tri-sodium citrate dihydrate pH 5.6, 1.0 M mono-ammonium dihydrogen phosphate	0.2 M ammonium acetate, 0.1 M Tris HCl, pH 8.5, 30% (v/v) isopropanol	0.2 M sodium acetate trihydrate, 0.1 M sodium cacodylate pH 6.5, 30% (w/v) PEG 8000	0.1 M HEPES-Na pH 7.5, 1.4 M tri-sodium citrate dihydrate	0.2 M calcium acetate hydrate, 0.1 M sodium cacodylate pH 6.5, 18% (w/v) PEG 8000	1.0 M imidazole pH 7.0	0.5 M ammonium sulfate, 0.1 M tri-sodium citrate dihydrate pH 5.6, 1.0 M lithium sulfate monohydrate	0.01 M cobaltous chloride hexahydrate, 0.1 M MES pH 6.5, 1.8 M ammonium sulfate	0.1 M HEPES pH 7.5, 4.3 M sodium chloride	0.1 M bicine pH 9.0, 2.0 M magnesium chloride hexahydrate
E	0.2 M di-potassium hydrogen phosphate, 20% PEG 3350	0.1 M Tris HCl pH 8.5, 2.0 M ammonium sulfate	0.2 M magnesium chloride hexahydrate, 0.1 M HEPES-Na pH 7.5, 30% (v/v) isopropanol	0.2 M ammonium sulfate, 0.1 M sodium acetate trihydrate pH 4.6, 25% (w/v) PEG 4000	0.1 M HEPES-Na pH 7.5, 0.8 M potassium sodium tartrate tetrahydrate	0.1 M HEPES-Na pH 7.5, 2% (v/v) PEG 400, 2.0 M ammonium sulfate	0.1 M Tris HCl pH 8.5, 2.0 M mono-ammonium dihydrogen phosphate	1.5 M sodium chloride, 10% (v/v) ethanol	0.5 M sodium chloride, 0.1 M tri-sodium citrate dihydrate pH 5.6, 2% (v/v) ethylene imine polymer	0.2 M ammonium sulfate, 0.1 M MES pH 6.5, 30% (w/v) PEGME 5000	0.1 M HEPES pH 7.5, 20% (w/v) PEG 10,000	3.2 M ammonium sulfate pH 5.0
F	0.2 M ammonium dihydrogen phosphate, 20% PEG 3350	0.2 M tri-sodium citrate dihydrate, 0.1 M HEPES-Na pH 7.5, 30% (v/v) 2-methyl-2,4-pentanediol	0.2 M tri-sodium citrate dihydrate, 0.1 M Tris HCl pH 8.5, 30% (v/v) PEG 400	0.2 M magnesium acetate tetrahydrate, 0.1 M sodium cacodylate pH 6.5, 30% (v/v) 2-methyl-2,4-pentanediol	0.2 M ammonium sulfate, 30% (w/v) PEG 8000	0.1 M tri-sodium citrate dihydrate pH 5.6, 20% (v/v) isopropanol, 20% (w/v) PEG 4000	1.0 M lithium sulfate monohydrate, 2% (w/v) PEG 8000	0.1 M sodium acetate trihydrate pH 4.6, 2.0 M sodium chloride	0.1 M tri-sodium citrate dihydrate pH 5.6, 35% (v/v) tert-butanol	0.01 M zinc sulfate heptahydrate, 0.1 M MES pH 6.5, 25% (v/v) PEGME 550	0.2 M magnesium chloride hexahydrate, 0.1 M Tris pH 8.5, 3.4 M 1,6 hexanediol	3.2 M ammonium sulfate pH 6.0
G	0.2 M di-ammonium hydrogen phosphate, 20% PEG 3350	0.2 M magnesium chloride hexahydrate, 0.1 M Tris HCl pH 8.5, 30% (w/v) PEG 4000	0.2 M calcium chloride dihydrate, 0.1 M HEPES-Na pH 7.5, 28% (v/v) PEG 400	0.2 M sodium acetate trihydrate, 0.1 M Tris HCl pH 8.5, 30% (w/v) PEG 4000	0.2 M ammonium sulfate, 30% (w/v) PEG 4000	0.1 M HEPES-Na pH 7.5, 10% (v/v) isopropanol, 20% (w/v) PEG 4000	0.5 M lithium sulfate monohydrate, 15% (w/v) PEG 8000	0.2 M sodium chloride, 0.1 M sodium acetate trihydrate pH 4.6, 30% (v/v) MPD	0.01 M ferric chloride hexahydrate, 0.1 M tri-sodium citrate dihydrate pH 5.6, 10% (v/v) Jeffamine M-600	0.5 M ammonium sulfate, 0.1 M HEPES pH 7.5, 30% (v/v) MPD	0.1 M Tris pH 8.5, 25% (v/v) tert-butanol	3.2 M ammonium sulfate pH 7.0

H	0.2 M tri-lithium citrate, 20% PEG 3350	0.1 M sodium cacodylate pH 6.5, 1.4 M sodium acetate trihydrate	0.2 M ammonium sulfate, 0.1 M sodium cacodylate pH 6.5, 30% (w/v) PEG 8000	0.2 M magnesium chloride hexahydrate, 0.1 M HEPES-Na pH 7.5, 30% (v/v) PEG 400	2.0 M ammonium sulfate	0.05 M mono-potassium dihydrogen phosphate, 20% (w/v) PEG 8000	0.01 M hexadecyltrimethylammonium bromide, 0.5 M sodium chloride, 0.01 M magnesium chloride hexahydrate	0.01 M cobaltous chloride hexahydrate, 0.1 M sodium acetate trihydrate pH 4.6, 1.0 M 1,6 hexanediol	0.1 M tri-sodium citrate dihydrate pH 5.6, 2.5 M 1,6 hexanediol	0.1 M HEPES pH 7.5, 10% (w/v) PEG 6000, 5% (v/v) MPD	0.01 M nickel (II) chloride hexahydrate, 0.1 M Tris pH 8.5, 1.0 M lithium sulfate monohydrate	3.2 M ammonium sulfate pH 8.0
----------	---	---	--	--	------------------------	--	---	---	---	--	---	-------------------------------

Robot Screen III

	1	2	3	4	5	6	7	8	9	10	11	12
A	7% (w/v) PEG 6000, 0.2 M citric acid pH 4.9	7% (w/v) PEG 6000, 0.2 M succinic acid/KOH pH 5.5	7% (w/v) PEG 6000, 0.2 M cacodylic acid/KOH pH 6.1	7% (w/v) PEG 6000, 0.2 M PIPES/KOH pH 6.7	7% (w/v) PEG 6000, 0.2 M MOPS/KOH pH 7.3	7% (w/v) PEG 6000, 0.2 M EPPS/KOH pH 7.9	7% (w/v) PEG 6000, 0.2 M bis-tris propane/HCl pH 8.5	7% (w/v) PEG 6000, 0.2 M AMPSO/KOH pH 9.1	15% PEG 600, 0.2 M imidazole malate pH 5.5	12.5% PEG 10,000, 0.2 M imidazole malate pH 8.5	1.6 M NaH ₂ PO ₄ /K ₂ HPO ₄ pH 7.0	3.2 M ammonium sulfate pH 9.0
B	14% (w/v) PEG 6000, 0.2 M acetic acid pH 4.9	14% (w/v) PEG 6000, 0.2 M malic acid/KOH pH 5.5	14% (w/v) PEG 6000, 0.2 M MES/KOH pH 6.1	14% (w/v) PEG 6000, 0.2 M bis-tris propane/HCl pH 6.7	14% (w/v) PEG 6000, 0.2 M HEPES/KOH pH 7.3	14% (w/v) PEG 6000, 0.2 M Tris/HCl pH 7.9	14% (w/v) PEG 6000, 0.2 M TAPS/KOH pH 8.5	14% (w/v) PEG 6000, 0.2 M boric acid/KOH pH 9.1	10% PEG 4000, 0.2 M imidazole malate pH 7.0	1.0 M ammonium sulfate, 0.15 M sodium citrate pH 5.5	1.2 M tri-sodium citrate, 10 mM sodium borate pH 8.5	2.4 M ammonium sulfate pH 5.0
C	21% (w/v) PEG 6000, 0.2 M citric acid pH 4.9	21% (w/v) PEG 6000, 0.2 M succinic acid/KOH pH 5.5	21% (w/v) PEG 6000, 0.2 M cacodylic acid/KOH pH 6.1	21% (w/v) PEG 6000, 0.2 M PIPES/KOH pH 6.7	21% (w/v) PEG 6000, 0.2 M MOPS/KOH pH 7.3	21% (w/v) PEG 6000, 0.2 M EPPS/KOH pH 7.9	21% (w/v) PEG 6000, 0.2 M bis-tris propane/HCl pH 8.5	21% (w/v) PEG 6000, 0.2 M AMPSO/KOH pH 9.1	7.5% PEG 10,000, 0.2 M imidazole malate pH 8.5	1.32 M NaH ₂ PO ₄ /K ₂ HPO ₄ pH 7.0	42% PEG 600, 0.2 M imidazole malate pH 5.5	2.4 M ammonium sulfate pH 6.0
D	28% (w/v) PEG 6000, 0.2 M acetic acid pH 4.9	28% (w/v) PEG 6000, 0.2 M malic acid/KOH pH 5.5	28% (w/v) PEG 6000, 0.2 M MES/KOH pH 6.1	28% (w/v) PEG 6000, 0.2 M bis-tris propane/HCl pH 6.7	28% (w/v) PEG 6000, 0.2 M HEPES/KOH pH 7.3	28% (w/v) PEG 6000, 0.2 M Tris/HCl pH 7.9	28% (w/v) PEG 6000, 0.2 M TAPS/KOH pH 8.5	28% (w/v) PEG 6000, 0.2 M boric acid/KOH pH 9.1	0.75 M ammonium sulfate, 0.15 M sodium citrate pH 5.5	1.0 M tri-sodium citrate, 10 mM sodium borate pH 8.5	25% PEG 4000, 0.2 M imidazole malate pH 7.0	2.4 M ammonium sulfate pH 7.0
E	7% (w/v) MPEG 5000, 0.2 M acetic acid pH 4.9	7% (w/v) MPEG 5000, 0.2 M malic acid/KOH pH 5.5	7% (w/v) MPEG 5000, 0.2 M MES/KOH pH 6.1	7% (w/v) MPEG 5000, 0.2 M bis-tris propane/HCl pH 6.7	7% (w/v) MPEG 5000, 0.2 M HEPES/KOH pH 7.3	7% (w/v) MPEG 5000, 0.2 M Tris/HCl pH 7.9	7% (w/v) MPEG 5000, 0.2 M TAPS/KOH pH 8.5	7% (w/v) MPEG 5000, 0.2 M boric acid/KOH pH 9.1	0.8 M NaH ₂ PO ₄ /K ₂ HPO ₄ pH 7.0	33% PEG 600, 0.2 M imidazole malate pH 5.5	22.5% PEG 10,000, 0.2 M imidazole malate pH 8.5	2.4 M ammonium sulfate pH 8.0

F	14% (w/v) MPEG 5000, 0.2 M citric acid pH 4.9	14% (w/v) MPEG 5000, 0.2 M succinic acid/KOH pH 5.5	14% (w/v) MPEG 5000, 0.2 M cacodylic acid/KOH pH 6.1	14% (w/v) MPEG 5000, 0.2 M PIPES/KOH pH 6.7	14% (w/v) MPEG 5000, 0.2 M MOPS/KOH pH 7.3	14% (w/v) MPEG 5000, 0.2 M EPPS/KOH pH 7.9	14% (w/v) MPEG 5000, 0.2 M bis-tris propane/HCl pH 8.5	14% (w/v) MPEG 5000, 0.2 M AMPSO/KOH pH 9.1	0.75 M tri- sodium citrate, 10 mM sodium borate pH 8.5	20% PEG 4000, 0.2 M imidazole malate pH 7.0	2.0 M ammonium sulfate, 0.15 M sodium citrate pH 5.5	2.4 M ammonium sulfate pH 9.0
G	21% (w/v) MPEG 5000, 0.2 M acetic acid pH 4.9	21% (w/v) MPEG 5000, 0.2 M malic acid/KOH pH 5.5	21% (w/v) MPEG 5000, 0.2 M MES/KOH pH 6.1	21% (w/v) MPEG 5000, 0.2 M bis-tris propane/HCl pH 6.7	21% (w/v) MPEG 5000, 0.2 M HEPES/KOH pH 7.3	21% (w/v) MPEG 5000, 0.2 M Tris/HCl pH 7.9	21% (w/v) MPEG 5000, 0.2 M TAPS/KOH pH 8.5	21% (w/v) MPEG 5000, 0.2 M boric acid/KOH pH 9.1	24% PEG 600, 0.2 M imidazole malate pH 5.5	17.5% PEG 10,000, 0.2 M imidazole malate pH 8.5	2.0 M NaH ₂ PO ₄ / K ₂ HPO ₄ pH 7.0	1.6 M ammonium sulfate pH 5.0
H	28% (w/v) MPEG 5000, 0.2 M citric acid pH 4.9	28% (w/v) MPEG 5000, 0.2 M succinic acid/KOH pH 5.5	28% (w/v) MPEG 5000, 0.2 M cacodylic acid/KOH pH 6.1	28% (w/v) MPEG 5000, 0.2 M PIPES/KOH pH 6.7	28% (w/v) MPEG 5000, 0.2 M MOPS/KOH pH 7.3	28% (w/v) MPEG 5000, 0.2 M EPPS/KOH pH 7.9	28% (w/v) MPEG 5000, 0.2 M bis-tris propane/HCl pH 8.5	28% (w/v) MPEG 5000, 0.2 M AMPSO/KOH pH 9.1	15% PEG 4000, 0.2 M imidazole malate pH 7.0	1.5 M ammonium sulfate, 0.15 M sodium citrate pH 5.5	1.5 M tri- sodium citrate, 10 mM sodium borate pH 8.5	1.6 M ammonium sulfate pH 6.0

Robot Screen IV

	1	2	3	4	5	6	7	8	9	10	11	12
A	0.2 M cadmium chloride, 40% (v/v) MPD	0.2 M ammonium chloride, 40% (v/v) MPD	0.2 M sodium nitrate, 40% (v/v) MPD	0.2 M magnesium acetate tetrahydrate, 40% (v/v) MPD	0.2 M cesium chloride, 40% (v/v) MPD	0.2 M sodium bromide, 40% (v/v) MPD	0.1 M citric acid pH 4.0, 10% (v/v) MPD	0.1 M MES pH 6.0, 20% (v/v) MPD	0.1 M Tris pH 8.0, 40% (v/v) MPD	0.1 M tri-sodium citrate dihydrate, 0.1 M HEPES sodium salt pH 7.5, 10% (w/v) MPD	0.1 M imidazole HCl pH 8.0, 20% (w/v) MPD	0.1 M imidazole-HCl pH 8.0, 30% (w/v) MPD, 10% (w/v) PEG 4000
B	0.2 M potassium fluoride, 40% (v/v) MPD	0.2 M sodium iodide, 40% (v/v) MPD	0.2 M potassium nitrate, 40% (v/v) MPD	0.2 M sodium malonate, 40% (v/v) MPD	0.2 M ferric chloride, 40% (v/v) MPD	0.2 M di-potassium hydrogen phosphate, 40% (v/v) MPD	0.1 M sodium acetate anhydrous pH 5.0, 10% (v/v) MPD	0.1 M HEPES pH 7.0, 20% (v/v) MPD	0.1 M bicine pH 9.0, 40% (v/v) MPD	0.05 M magnesium chloride heptahydrate, 0.1 M Tris-HCl pH 8.5, 12% (w/v) MPD	0.2 M sodium chloride, 20% (w/v) MPD, 4% (w/v) glycerol	30% (w/v) MPD, 20% (w/v) ethanol
C	0.2 M ammonium fluoride, 40% (v/v) MPD	0.2 M potassium iodide, 40% (v/v) MPD	0.2 M ammonium nitrate, 40% (v/v) MPD	0.2 M sodium acetate trihydrate, 40% (v/v) MPD	0.2 M ammonium sulfate, 40% (v/v) MPD	0.2 M ammonium dihydrogen phosphate, 40% (v/v) MPD	0.1 M MES pH 6.0, 10% (v/v) MPD	0.1 M Tris pH 8.0, 20% (v/v) MPD	0.1 M citric acid pH 4.0, 65% (v/v) MPD	0.02 M calcium chloride dihydrate, 0.1 M sodium acetate pH 4.6, 15% (w/v) MPD	0.02 M calcium chloride dihydrate, 0.1 M sodium acetate pH 4.6, 30% (w/v) MPD	35% (w/v) MPD
D	0.2 M lithium chloride anhydrous, 40% (v/v) MPD	0.2 M ammonium iodide, 40% (v/v) MPD	0.2 M zinc sulfate heptahydrate, 40% (v/v) MPD	0.2 M calcium acetate hydrate, 40% (v/v) MPD	0.2 M di-sodium tartrate dihydrate, 40% (v/v) MPD	0.2 M di-ammonium hydrogen phosphate, 40% (v/v) MPD	0.1 M HEPES pH 7.0, 10% (v/v) MPD	0.1 M bicine pH 9.0, 20% (v/v) MPD	0.1 M sodium acetate anhydrous pH 5.0, 65% (v/v) MPD	0.1 M imidazole-HCl pH 8.0, 15% (w/v) MPD, 5% (w/v) PEG 4000	0.2 M ammonium acetate, 0.1 M sodium citrate pH 5.6, 30% (w/v) MPD	0.1 M imidazole HCl pH 8.0, 35% (w/v) MPD
E	0.2 M magnesium chloride hexahydrate,	0.2 M sodium thiocyanate, 40% (v/v)	0.2 M sodium formate, 40% (v/v) MPD	0.2 M potassium acetate, 40%	0.2 M potassium sodium tartrate tetrahydrate,	0.2 M tri-lithium citrate tetrahydrate,	0.1 M Tris pH 8.0, 10% (v/v) MPD	0.1 M citric acid, 40% (v/v) MPD	0.1 M MES pH 6.0, 65% (v/v) MPD	0.2 M ammonium acetate, 0.1 M sodium citrate	0.2 M magnesium acetate tetrahydrate,	0.1 M Tris-HCl pH 8.5, 40% (w/v)

	40% (v/v) MPD	MPD		(v/v) MPD	40% (v/v) MPD	40% (v/v) MPD				pH 5.6, 15% (w/v) MPD	0.1 M MES sodium salt pH 6.5, 30% (w/v) MPD	MPD
F	0.2 M sodium chloride, 40% (v/v) MPD	0.2 M potassium thiocyanate, 40% (v/v) MPD	0.2 M potassium formate, 40% (v/v) MPD	0.2 M ammonium acetate, 40% (v/v) MPD	0.2 M di-ammonium tartrate, 40% (v/v) MPD	0.2 M tri-sodium citrate dihydrate, 40% (v/v) MPD	0.1 M bicine pH 9.0, 10% (v/v) MPD	0.1 M sodium acetate anhydrous pH 5.0, 40% (v/v) MPD	0.1 M HEPES pH 7.0, 65% (v/v) MPD	0.2 M magnesium acetate, 0.1 M MES sodium salt pH 6.5, 15% (w/v) MPD	0.5 M ammonium sulfate, 0.1 M HEPES sodium salt pH 7.5, 30% (w/v) MPD	0.1 M HEPES sodium salt pH 7.5, 47% (w/v) MPD
G	0.2 M calcium chloride dihydrate, 40% (v/v) MPD	0.2 M lithium nitrate, 40% (v/v) MPD	0.2 M ammonium formate, 40% (v/v) MPD	0.2 M lithium sulfate monohydrate, 40% (v/v) MPD	0.2 M sodium dihydrogen phosphate monohydrate, 40% (v/v) MPD	0.2 M tri-potassium citrate monohydrate, 40% (v/v) MPD	0.1 M citric acid pH 4.0, 20% (v/v) MPD	0.1 M MES pH 6.0, 40% (v/v) MPD	0.1 M Tris pH 8.0, 65% (v/v) MPD	0.2 M tri-sodium citrate dihydrate, 0.1 M HEPES sodium salt pH 7.5, 15% (w/v) MPD	0.2 M tri-sodium citrate dihydrate, 0.1 M HEPES sodium salt pH 7.5, 30% (w/v) MPD	47% (w/v) MPD, 2% (w/v) tert-butanol
H	0.2 M potassium chloride, 40% (v/v) MPD	0.2 M magnesium nitrate hexahydrate, 40% (v/v) MPD	0.2 M lithium acetate dihydrate, 40% (v/v) MPD	0.2 M magnesium sulfate heptahydrate, 40% (v/v) MPD	0.2 M potassium bromide, 40% (v/v) MPD	0.2 M di-ammonium hydrogen citrate, 40% (v/v) MPD	0.1 M sodium acetate anhydrous pH 5.0, 20% (v/v) MPD	0.1 M HEPES pH 7.0, 40% (v/v) MPD	0.1 M bicine pH 9.0, 65% (v/v) MPD	0.1 M tri-sodium citrate dihydrate, 0.1 M HEPES sodium salt pH 7.5, 20% (w/v) MPD	0.1 M HEPES sodium salt pH 7.5, 30% (w/v) MPD, 5% (w/v) PEG 4000	50% (w/v) MPD

Robot Screen V

	1	2	3	4	5	6	7	8	9	10	11	12
A	2 M Am ₂ SO ₄ , 2% PEG 400 (pH 5.5)	2 M NaKPO ₄ , 2% PEG400 (pH 6.5)	2 M Li ₂ SO ₄ , 8% MPD (pH 6.5)	1 M AmCitrate, 15% isopropanol (pH 8.5)	10% PEG 1500, 30% isopropanol, 0.2 M Li ₂ SO ₄ (pH 5.5)	20% PEG 3350, 25% PEG 400, 0.1 M MgCl ₂ (pH 8.5)	25% PEG 3350, 4% isopropanol, 0.1 M CaCl ₂ (pH 7.5)	2.5 M NaCl, 12% PEG 1500, 1.5% MPD (pH 5.5)	0.3 M Na acetate, 25% PEG 2000 MME	0.2 M MgCl ₂ , 15% PEG 4000	0.2 M KSCN, 10% PEG 8000, 10% PEG 1000	1.6 M ammonium sulfate pH 7.0
B	2 M Am ₂ SO ₄ , 10% glycerol, 0.1 M MgSO ₄ (pH 6.5)	2.5 M NaKPO ₄ , 20% Glycerol (pH 7.5)	2 M Li ₂ SO ₄ , 2% PEG 400 (pH 8.5)	2 M NaFormate, 2.5% PEG 3350, 15% isopropanol (pH 8.5)	15% PEG 8000, 40% isopropanol (pH 6.5)	30% PEG 1500, 3% MPD, 0.2 M MgSO ₄ (pH 5.5)	20% PEG 8000, 10% PEG 400, 0.5 M NaCl (pH 5.5)	3 M NaCl, 20% PEG 3350, 0.1 M MgCl ₂ (pH 6.5)	0.2 M Li ₂ SO ₄ , 25% PEG 2000 MME	0.2 M KBr, 15% PEG 4000	0.8 M Na formate, 10% PEG 8000, 10% PEG 1000	1.6 M ammonium sulfate pH 8.0
C	2 M Am ₂ SO ₄ , 1% MPD (pH 7.5)	1 M NaKPO ₄ , 8% MPD (pH 8.5)	1 M Li ₂ SO ₄ , 15% MPD, 0.1 M MgSO ₄ (pH 4.5)	25% PEG 1500, 30% MPD (pH 4.5)	15% PEG 3350, 20 % isopropanol, 0.2 M AmCitrate (pH 7.5)	30% PEG 1500, 10% isopropanol, 0.1 M CaCl ₂ (pH 6.5)	20% PEG 8000, 3% MPD (pH 6.5)	3 M NaFormate, 4% PEG 8000 (pH 6.5)	0.2 M MgCl ₂ , 25% PEG 2000 MME	0.2 M KSCN, 15% PEG 4000	0.3 M Na acetate, 8% PEG 20,000, 8% PEG 550 MME	1.6 M ammonium sulfate pH 9.0
D	2 M Am ₂ SO ₄ , 5% PEG 400, 0.1 M MgSO ₄ (pH 8.5)	2 M AmCitrate, 1% MPD (pH 4.5)	0.75 M AmCitrate, 25% MPD (pH 5.5)	15% PEG 8000, 30% MPD, 0.1 M CaCl ₂ (pH 5.5)	30% PEG 3350, 30% isopropanol (pH 8.5)	30% PEG 1500, 20% PEG 400 (pH 7.5)	20% PEG 8000, 10% isopropanol, 0.2 M Am ₂ SO ₄ (pH 7.5)	1 M NaKPO ₄ , 0.5% PEG 4000 (pH 7.5)	0.2 M KBr, 25% PEG 2000 MME	0.8 M Na formate, 15% PEG 4000	0.2 M Li ₂ SO ₄ , 8% PEG 20,000, 8% PEG 550 MME	0.8 M ammonium sulfate pH 5.0
E	4 M NaCl, 2% PEG 400, 0.1 M MgCl ₂ (pH 5.5)	2 M AmCitrate, 5% isopropanol (pH 6.5)	1.5 M Am ₂ SO ₄ , 12% isopropanol (pH 6.5)	10% PEG 3350, 30% MPD, 0.2 M Am ₂ SO ₄ (pH 6.5)	20% PEG 8000, 40% PEG 400 (pH 4.5)	30% PEG 1500, 8% MPD (pH 8.5)	20% PEG 8000, 20% PEG 400, 0.1 M MgCl ₂ (pH 8.5)	1.4 M NaKPO ₄ , 10% PEG 3350 (pH 7.5)	0.2 M KSCN, 25% PEG 2000 MME	0.3 M Na acetate, 10% PEG 8000, 10% PEG 1000	0.2 M MgCl ₂ , 8% PEG 20,000, 8% PEG 550 MME	0.8 M ammonium sulfate pH 6.0
F	3 M NaCl, 5% MPD, 0.1 M CaCl ₂ (pH	2 M AmCitrate, 5% PEG 400	1.3 M NaCl, 30% isopropanol,	4% PEG 1500, 30%	5% PEG 3350, 40% PEG 400 (pH	25% PEG 3350, 15% isopropanol,	3 M NaFormate, 25% PEG	0.8 M AmCitrate, 2% PEG	0.8 M Na formate, 25% PEG 2000	0.2 M Li ₂ SO ₄ , 10% PEG 8000, 10%	0.2 M KBr, 8% PEG 20,000, 8%	0.8 M ammonium sulfate pH

	6.5)	(pH 7.5)	0.1 M CaCl ₂ (pH 6.5)	MPD (pH 7.5)	5.5)	0.2 M AmCitrate (pH 4.5)	3350, 0.1 M CaCl ₂ (pH 4.5)	8000 (pH 8.5)	MME	PEG 1000	PEG 550 MME	7.0
G	4 M NaCl, 5% isopropanol (pH 7.5)	2 M Li ₂ SO ₄ , 5% isopropanol, 0.1 M MgSO ₄ (pH 4.5)	4 M NaCl, 10% PEG 400 (pH 7.5)	8% PEG 8000, 30% MPD, 0.5 M NaCl (pH 8.5)	15% PEG 1000, 40% PEG 400, 0.15 M NaKPO ₄ (pH 6.5)	25% PEG 3350, 5% PEG 400 (pH 5.5)	0.75 M Am ₂ SO ₄ , 7.5% PEG 3350, 5% isopropanol (pH 4.5)	2 M NaCl, 5% PEG 4000 (pH 8.5)	0.3 M Na acetate, 15% PEG 4000	0.2 M MgCl ₂ , 10% PEG 8000, 10% PEG 1000	0.2 M KSCN, 8% PEG 20,000, 8% PEG 550 MME	0.8 M ammonium sulfate pH 8.0
H	2.5 M NaKPO ₄ , 5% isopropanol (pH 5.5)	2 M Li ₂ SO ₄ , 5% PEG 400, 0.1 M MgSO ₄ (pH 5.5)	0.8 M NaKPO ₄ , 20% PEG 400 (pH 7.5)	4% PEG 3350, 30% isopropanol, 0.1 M CaCl ₂ (pH 4.5)	8% PEG 8000, 40% PEG 400 (pH 7.5)	25% PEG 3350, 15% MPD, 0.2 M Li ₂ SO ₄ (pH 6.5)	1 M AmCitrate, 1% PEG 4000 (pH 5.5)	0.5 M AmCitrate, 15% PEG 8000 (pH 8.5)	0.2 M Li ₂ SO ₄ , 15% PEG 4000	0.2 M KBr, 10% PEG 8000, 10% PEG 1000	0.8 M Na formate, 8% PEG 20,000, 8% PEG 550 MME	0.8 M ammonium sulfate pH 9.0

Appendix 3 *MtAhpE* information

pProEx Hta vector map

Map and sequence of the pProEx Hta vector are shown below. When used for expression the gene of interest (Rv2338c, detailed below) was cloned in using *NcoI* and *SacI* restriction sites in the multiple cloning region. The point of insertion is indicated by a red star in the vector sequence.

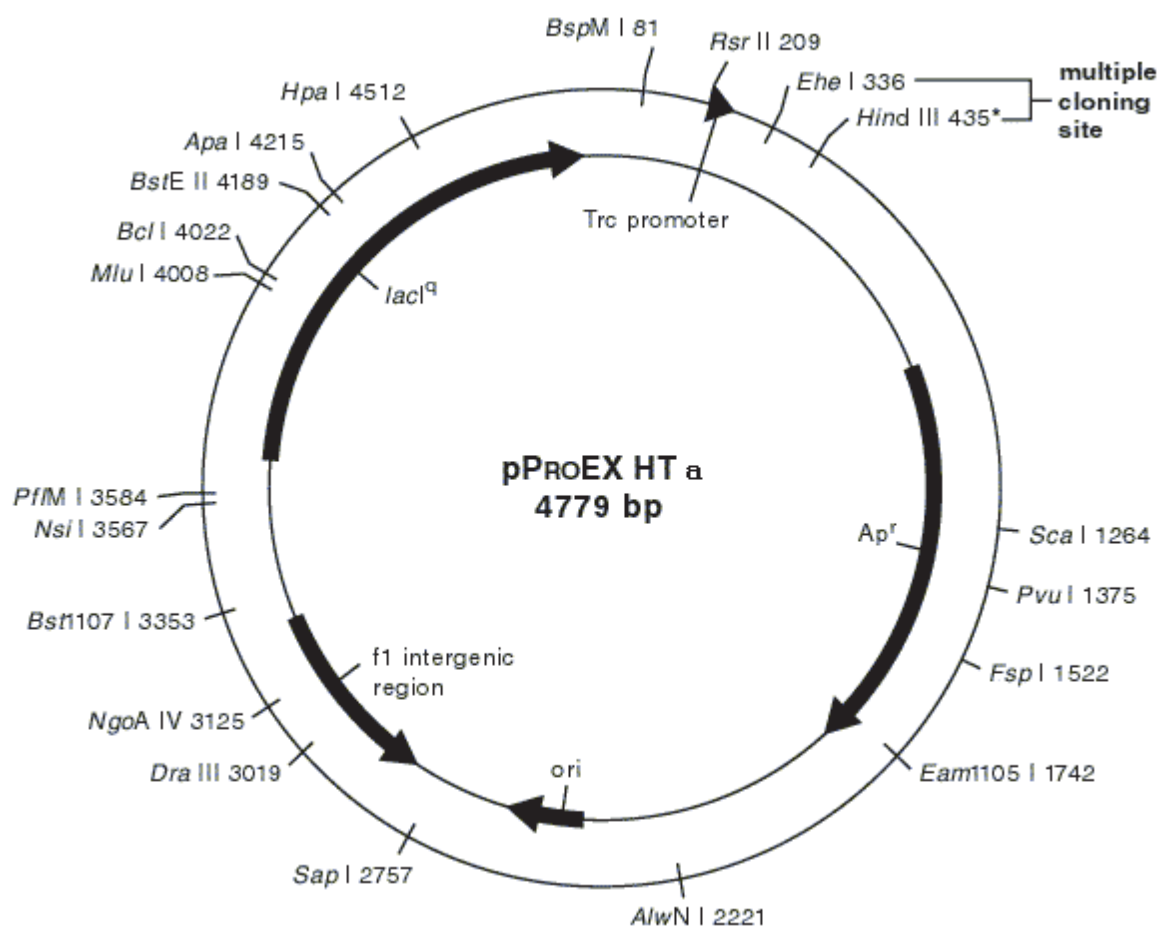


Figure A3.1: pProEX HTa vector map (Invitrogen): This vector was used for routine expression of *MtAhpE* protein.

Vector sequence

GTTTGACAGCTTATCATCGACTGCACGGTGCACCAATGCTTCTGGCGTCAGGCAGCCATCGGAAGCTG
 TGGTATGGCTGTGCAGGTCGTAAATCACTGCATAATTCGTGTCGCTCAAGGCGCACTCCC GTTCTGGAT
 AATGTTTTTTGCGCCGACATCATAACGGTTCTGGCAAATATTCTGAAATGAGCTGTTGACAATTAATCAT
 CCGGTCCGTATAATCTGTGGAATTGTGAGCGGATAACAATTTACACAGGAAACAGACCATGTCGTACT
 ACCATCACCATCACCATCACGATTACGATATCCCAACGACCGAAAAACCTGTATTTTCAGGGCGCC*ATG
 GATCCGGAATTCAAAGGCCTACGTGACGAGCTCAACTAGTGCGGCCGCTTTCGAATCTAGAGCCTGC
 AGTCTCGAGGCATGCGGTACCAAGCTTGGCTGTTTTGGCGGATGAGAGAAGATTTTCAGCCTGATACA
 GATTAAATCAGAACGCAGAAGCGGTCTGATAAAACAGAATTTGCCTGGCGGCAGTAGCGCGGTGGTCC
 CACCTGACCCCATGCCGAACCTAGAAGTAAAACGCCGTAGCGCCGATGGTAGTGTGGGGTCTCCCCA
 TGCGAGAGTAGGGAACCTGCCAGGCATCAAATAAAACGAAAGGCTCAGTCGAAAGACTGGGCCTTTCGT
 TTTATCTGTTGTTTGTGCGGTGAACGCTCTCCTGAGTAGGACAAATCCGCCGGGAGCGGATTTGAACGTT
 GCGAAGCAACGGCCCGGAGGGTGGCGGGCAGGACGCCCGCCATAAACTGCCAGGCATCAAATTAAG
 CAGAAGGCCATCCTGACGGATGGCCTTTTTGCGTTTTCTACAAACTCTTTTTGTTATTTTTCTAAATACAT
 TCAAATATGTATCCGCTCATGAGACAAATAACCCTGATAAATGCTTCAATAATATTGAAAAAGGAAGAGTA
 TGAGTATTCAACATTTCCGTGTCGCCCTTATTCCCTTTTTTTCGCGCATTTTGCCTTCCTGTTTTTGTCTCAC
 CCAGAAACGCTGGTGAAAGTAAAGATGCTGAAGATCAGTTGGGTGCACGAGTGGGTACATCGAACT
 GGATCTCAACAGCGGTAAGATCCTTGAGAGTTTTCGCCCCGAAGAACGTTTTCCAATGATGAGCACTTT
 TAAAGTTCTGCTATGTGGCGCGGTATTATCCCGTGTGACGCCGGGCAAGAGCAACTCGGTGCGCCGA
 TACACTATTCTCAGAATGACTTGTTGAGTACTCACCAGTCACAGAAAAGCATCTTACGGATGGCATGA
 CAGTAAGAGAATTATGCAGTGCTGCCATAACCATGAGTGATAACACTGCGGCCAACTTACTTCTGACAA
 CGATCGGAGGACCGAAGGAGCTAACCCTTTTTTGCACAACATGGGGGATCATGTAACCTGCCTTGAT
 CGTTGGGAACCGGAGCTGAATGAAGCCATACCAAACGACGAGCGTGACACCACGATGCCTACAGCAAT
 GGCAACAACGTTGCGCAAACTATTAACCTGGCGAACTACTTACTCTAGCTTCCCGGCAACAATTAAGA
 CTGGATGGAGGCGGATAAAGTTGCAGGACCACTTCTGCGCTCGGCCCTTCCGGCTGGCTGGTTTATTG
 CTGATAAATCTGGAGCCGGTGAGCGTGCGGTCTCGCGGTATCATTGCAGCACTGGGGCCAGATGGTAA
 GCCCTCCCGTATCGTAGTTATCTACACGACGGGGAGTCAGGCAACTATGGATGAACGAAATAGACAGA
 TCGCTGAGATAGGTGCCTCACTGATTAAGCATTGGTAACTGTCAGACCAAGTTTACTCATATATACTTTA
 GATTGATTTAAACTTCATTTTTAATTTAAAGGATCTAGGTGAAGATCCTTTTTGATAATCTCATGACCA
 AAATCCCTTAACGTGAGTTTTCGTTCCACTGAGCGTCAGACCCCGTAGAAAAGATCAAAGGATCTTCTT
 GAGATCCTTTTTTCTGCGCGTAATCTGCTGCTTGCAAACAAAAAACACCGCTACCAGCGGTGGTTT
 GTTTGCCGGATCAAGAGCTACCAACTCTTTTTCCGAAGGTAACCTGGCTTCAGCAGAGCGCAGATACCAA
 ATACTGTCCTTCTAGTGAGCCGTAGTTAGGCCACCACTTCAAGAACTCTGTAGCACCGCCTACATACC
 TCGCTCTGCTAATCCTGTTACCAAGTGGCTGCTGCCAGTGCGGATAAGTCGTGTCTTACCGGGTTGGAC
 TCAAGACGATAGTTACCGGATAAGGCGCAGCGGTGCGGCTGAACGGGGGGTTCGTGCACACAGCCCA
 GCTTGAGCGAACGACCTACACCGAACTGAGATACCTACAGCGTGAGCTATGAGAAAGCGCCACGCTT
 CCCGAAGGGAGAAAGGCGGACAGGTATCCGTAAGCGGCAGGGTCGGAACAGGAGAGCGCACGAGG
 GAGCTTCCAGGGGGAAACGCCTGGTATCTTTATAGTCCTGTGCGGGTTTCGCCACCTCTGACTTGAGCG
 TCGATTTTTGTGATGCTCGTCAGGGGGGCGGAGCCTATGGAAAAACGCCAGCAACGCGGCCCTTTTTAC
 GGTTCTGCGCCTTTTGCTGGCCTTTTGCTCACATGTTCTTTCTGCGTTATCCCCTGATTCTGTGGATAA
 CCGTATTACCGCCTTTGAGTGAGCTGATACCGCTCGCCGAGCCGAACGACCGAGCGCAGCGAGTCA
 GTGAGCGAGGAAGCGGAAGAGCGCCTGATGCGGTATTTTCTCCTTACGCATCTGTGCGGTATTTACA
 CCGCATAATTTTGTTAAATTCGCGTTAAATTTTTGTTAAATCAGCTCATTTTTTAACCAATAGGCCGAAA
 TCGGCAAAATCCCTTATAAATCAAAGAATAGACCGAGATAGGGTTGAGTGTGTTCCAGTTTGAACA
 AGAGTCCACTATTAAGAACGTGGACTCCAACGTCAAAGGGCGAAAAACCGTCTATCAGGGCGATGGC
 CCACTACGTGAACCATCACCTAATCAAGTTTTTGGGGTCGAGGTGCCGTAAAGCACTAAATCGGAAC
 CCTAAAGGGAGCCCCCGATTAGAGCTTGACGGGGAAGCCGGCGAACGTGGCGAGAAAGGAAGGGA
 AGAAAGCGAAAGGAGCGGGCGCTAGGGCGCTGGCAAGTGATAGCGGTACGCTGCGCGTAACCAACA
 CACCCGCCGCGCTTAATGCGCCGCTACAGGGCGCGTCCCATTCGCCATTACGGCTGCTATGGTGCCT
 CTCAGTACAATCTGCTCTGATGCCGCATAGTTAAGCCAGTATACACTCCGCTATCGCTACGTGACTGGG
 TCATGGCTGCGCCCCGACACCCGCCAACACCCGCTGACGCGCCCTGACGGGCTTGTCTGCTCCCGGC
 ATCCGCTTACAGACAAGCTGTGACCGTCTCCGGGAGCTGCATGTGTCAGAGGTTTTACCGTCATCAC

CGAAACGCGCGAGGCAGCAGATCAATTCGCGCGCGAAGGCGAAGCGGCATGCATTTACGTTGACACC
 ATCGAATGGTGCAAAACCTTTTCGCGGTATGGCATGATAGCGCCGGAAGAGAGTCAATTCAGGGTGGT
 GAATGTGAAACAGTAACGTTATACGATGTGCGAGAGTATGCCGGTGTCTCTTATCAGACCGTTTCCCG
 CGTGGTGAAACAGGCCAGCCACGTTTCTGCGAAAACGCGGGAAAAAGTGGAAGCGGCGATGGCGGAG
 CTGAATTACATTCCCAACCGCGTGGCACAACAACCTGGCGGGCAAACAGTCGTTGCTGATTGGCGTTGC
 CACCTCCAGTCTGGCCCTGCACGCGCCGTGCGAAATTGTCGCGGCGATTAAATCTCGCGCCGATCAAC
 TGGGTGCCAGCGTGGTGGTGTGATGGTAGAACGAAGCGGCGTGAAGCCTGTAAAGCGGCGGTGCA
 CAATCTTCTCGCGCAACGCGTCAGTGGGCTGATCATTAACTATCCGCTGGATGACCAGGATGCCATTG
 CTGTGGAAGCTGCCTGCACTAATGTTCCGGCGTTATTTCTTGATGTCTCTGACCAGACACCCATCAACA
 GTATTATTTTCTCCCATGAAGACGGTACGCGACTGGGCGTGGAGCATCTGGTCGCATTGGGTACCAG
 CAAATCGCGCTGTTAGCGGGCCCATTAAGTTCTGTCTCGGCGCGTCTGCGTCTGGCTGGCTGGCATAA
 ATATCTCACTCGCAATCAAATTCAGCCGATAGCGGAACGGGAAGGCGACTGGAGTGCCATGTCCGGTT
 TTCAACAAACCATGCAAATGCTGAATGAGGGCATCGTTCCCACTGCGATGCTGGTTGCCAACGATCAGA
 TGGCGCTGGGCGCAATGCGCGCCATTACCGAGTCCGGGCTGCGCGTTGGTGC GGATATCTCGGTAGT
 GGGATACGACGATACCGAAGACAGCTCATGTTATATCCCGCCGTTAACCAACCATCAAACAGGATTTTCG
 CCTGCTGGGGCAAACAGCGTGGACCGCTTGCTGCAACTCTCTCAGGGCCAGGCGGTGAAGGGCAAT
 CAGCTGTTGCCCGTCTCACTGGTGAAAAGAAAAACCACCCTGGCACCCAATACGCAAACCGCCTCTCC
 CCGCGCGTTGGCCGATTCAATTAATGCAGCTGGCACGACAGGTTTCCCGACTGGAAAGCGGGCAGTGA
 GCGCAACGCAATTAATGTGAGTTAGCGCGAATTGATCTG

Rv2338c nucleotide sequence

The 462 bp sequence of the gene encoding the *M. tuberculosis* protein AhpE as cloned into the pProEx vector is shown below. Underlined bases indicate flanking nucleotides that were cloned out of the genome along with the gene of interest. The sequence was cloned into pProEx using NcoI and SacI restriction enzymes.

ATGGTGAACGTCGGAGCCACCGCCCCTGACTTCACGTTGCGCGACCAGAATCAGCAGCTTGTCACCCT
 GCGCGGCTACCGGGGTGCAAAGAACGTGCTGTTGGTGTCTTTCCGTTGGCGTTCACGGGCATCTGCC
 AGGGCGAGCTGGACCAATTGCGTGATCACCTGCCCAGTTTGAGAACGACGACAGCGCCGCGCTAGC
 GATTTCCGGTGGGCCCCGCCACCCACTCACAAGATCTGGGCGACGCAGAGCGGATTCACGTTTCCGCTGT
 TGTCGGACTTCTGGCCACACGGCGCGGTCACTCAGGCCTACGGCGTCTTCAACGAGCAGGCCGGCAT
 CGCTAACCGGGGCACCTTTGTGGTCGATCGGTCAAGGATCATTCGGTTCGCCGAGATGAAGCAGCCG
 GGTGAAGTTCGCGATCAGCGGTGTGGACCGACGCTCTGGCGGCGCTTACGGCCTAAGGTTTTGGGT
 GCTTGGCCGCAAGGCGTGTAGCCTGCGGCGGTTCATGGGCGCGTAGCTCAGCGGTA

MtAhpE amino acid sequence

Underlining indicates the his-tag and linker residues conferred by the pProEx vector, TEV cleavage site is indicated by a red star.

MSYYHHHHHDYDIPTTENLYFQ*GAMVNVGATAPDFTLRDQNQQQLVTLRGYRGAKNVLLVFFPLAFTGIC
 QGELDQLRDHLPEFENDDSAALAIISVGPPPTHKIWATQSGFTFPLLSDFWPHGAVSQAYGVFNEQAGIANR
 GTFVVD RSGIIRFAEMKQPGEV RDQRLWTDALAALTA

Important parameters for *MtAhpE*

Extinction coefficients and molecular masses were used for calculation of protein concentration (section 2.3.5.2), identification of *MtAhpE* and monitoring the efficiency of rTEV cleavage (section 2.3.5.3).

Construct	Molecular Mass (kDa)	Number of residues	Theoretical pI	Extinction Coefficient ($M^{-1} cm^{-1}$)
Native <i>MtAhpE</i>	16.8	153	5.24	Oxidised: 1.16 Reduced: 1.16
Cleaved <i>MtAhpE</i>	16.9	155	5.24	Oxidised: 1.15 Reduced: 1.15
His-tagged <i>MtAhpE</i>	19.9	178	5.62	Oxidised: 1.28 Reduced: 1.28
Cleaved E109A	16.9	155	5.5	Oxidised: 1.15 Reduced: 1.15
His-tagged E109A	19.8	178	5.77	Oxidised: 1.28 Reduced: 1.28
Cleaved W95A	16.8	155	5.24	Oxidised: 0.83 Reduced: 0.83
His-tagged W95A	19.8	178	5.62	Oxidised: 1.01 Reduced: 1.01
Cleaved T76A	16.9	155	5.24	Oxidised: 1.15 Reduced: 1.15
His-tagged T76A	19.9	178	5.62	Oxidised: 1.28 Reduced: 1.28
Cleaved Q83A	16.9	155	5.24	Oxidised: 1.15 Reduced: 1.15
His-tagged Q83A	19.8	178	5.63	Oxidised: 1.28 Reduced: 1.28

Location of rare codons in the *MtAhpE* nucleotide sequence

Rare leucine codons are highlighted in green, and proline in orange. BL21 Rosetta (DE3) cells complement all rare codons.

```

atg gtg aac gtc gga gcc acc gcc cct gac ttc acg ttg cgc gac
cag aat cag cag ctt gtc acc ctg cgc ggc tac cgg ggt gca aag
aac gtg ctg ttg gtg ttc ttt ccg ttg gcg ttc acg ggc atc tgc
cag ggc gag ctg gac cag ttg cgt gat cac ctg CCC gag ttt gag
aac gac gac agc gcc gcg CTA gcg att tcg gtg ggc ccg cca
CCC act cac aag atc tgg gcg acg cag agc gga ttc acg ttt ccg
ctg ttg tcg gac ttc tgg cca cac ggc gcg gtc agt cag gcc tac
ggc gtc ttc aac gag cag gcc ggc atc gct aac cgg ggc acc ttt
gtg gtc gat cgg tca ggg atc att cgg ttc gcc gag atg aag cag
ccg ggt gaa gtt cgc gat cag cgg ctg tgg acc gac gct ctg gcg
gcg ctt acg gcc taa

```

Mutein purifications

W95A

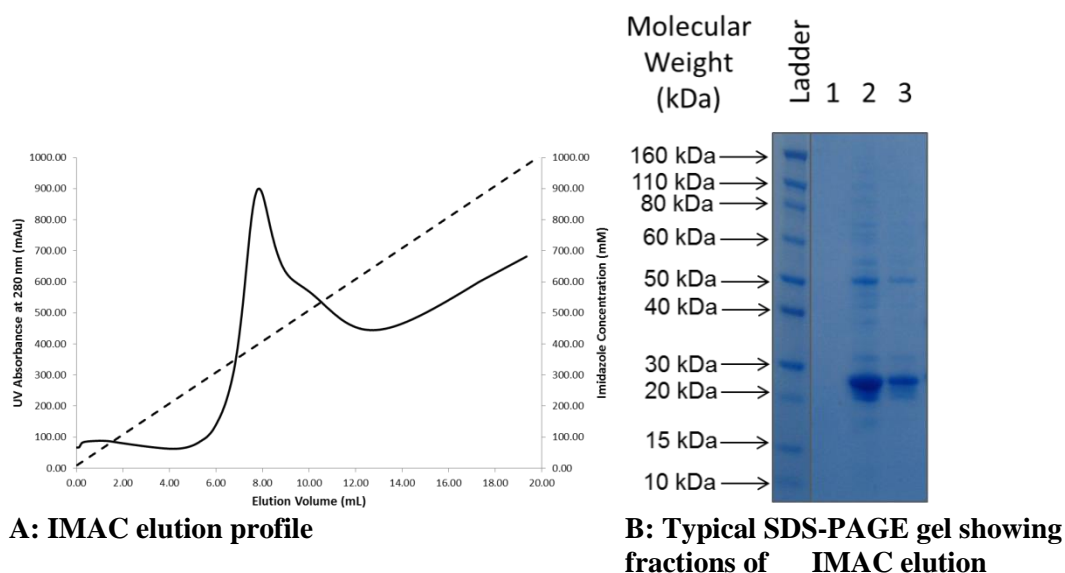


Figure A3.2: **A:** Typical elution profile of IMAC purification of W95A mutein. Protein eluted as a single peak around 500 mM imidazole concentration. **B:** Gel showing IMAC fractions. Lanes 2-4 show selected fractions across the peak from the elution profile (A). SDS-resistant dimers were sometimes seen in small amounts (the faint band at 50 kDa). These were seen in the case of *HsPrx3* as well, and appear to be a feature of Prxs as they have been reported by other groups (discussed in chapter five).

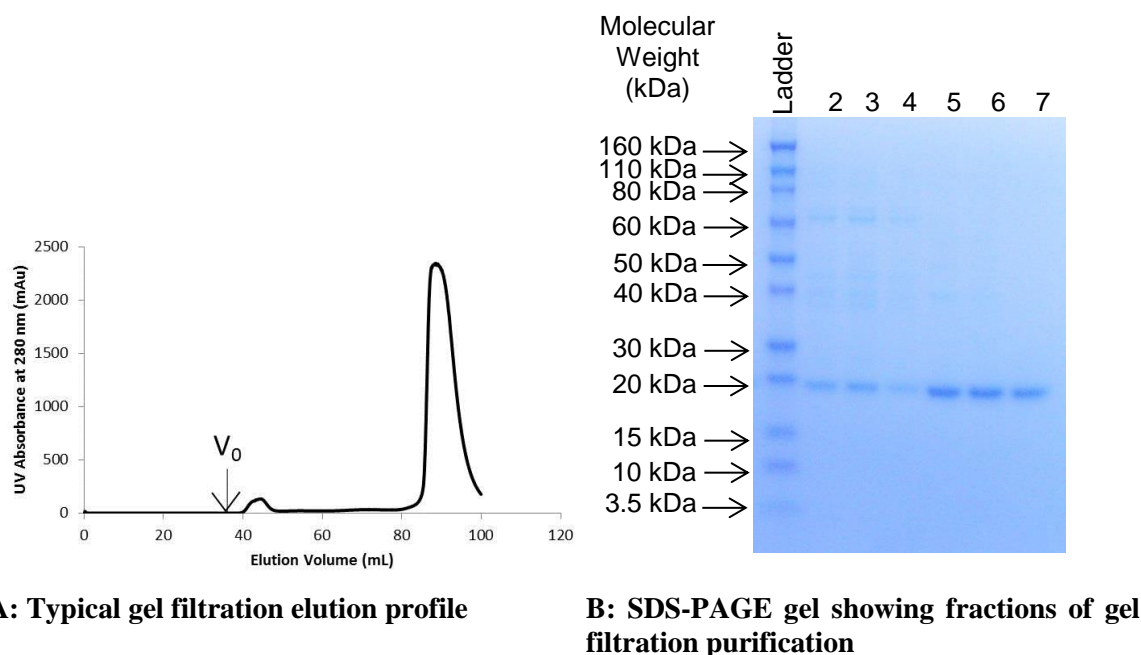


Figure A3.3: Typical gel filtration purification of W95A mutein: **A:** Gel filtration elution profile showed that the mutein eluted at around 90 mL, as a single peak. A small peak was seen near the void volume. **B:** Selected fractions across (lanes 2-4) the small early eluting peak; and (lanes 5-7) the main peak at 90 mL.

T76A

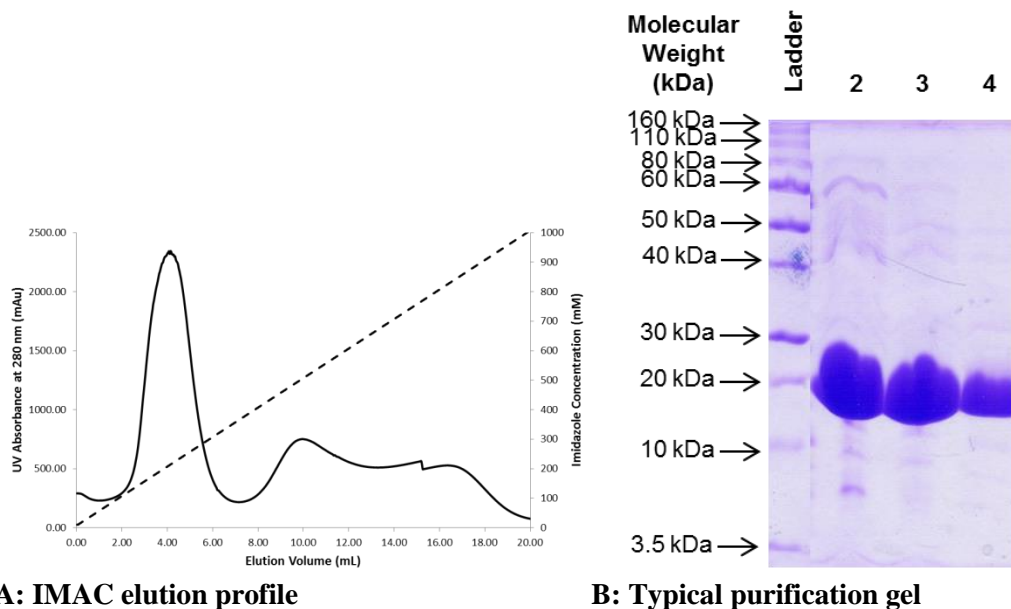


Figure A3.4: A: Typical elution profile of IMAC purification of T76A mutein. Protein eluted as a single peak around 250 mM imidazole concentration. **B:** Gel showing IMAC fractions. Lanes 2-4 show selected fractions across the main peak from the elution profile (A).

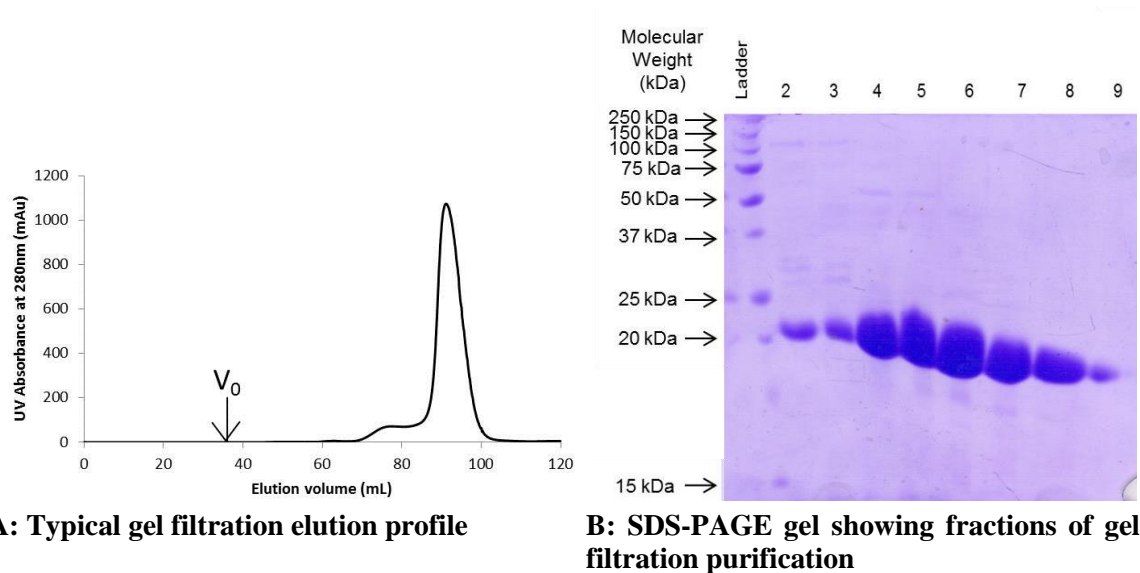
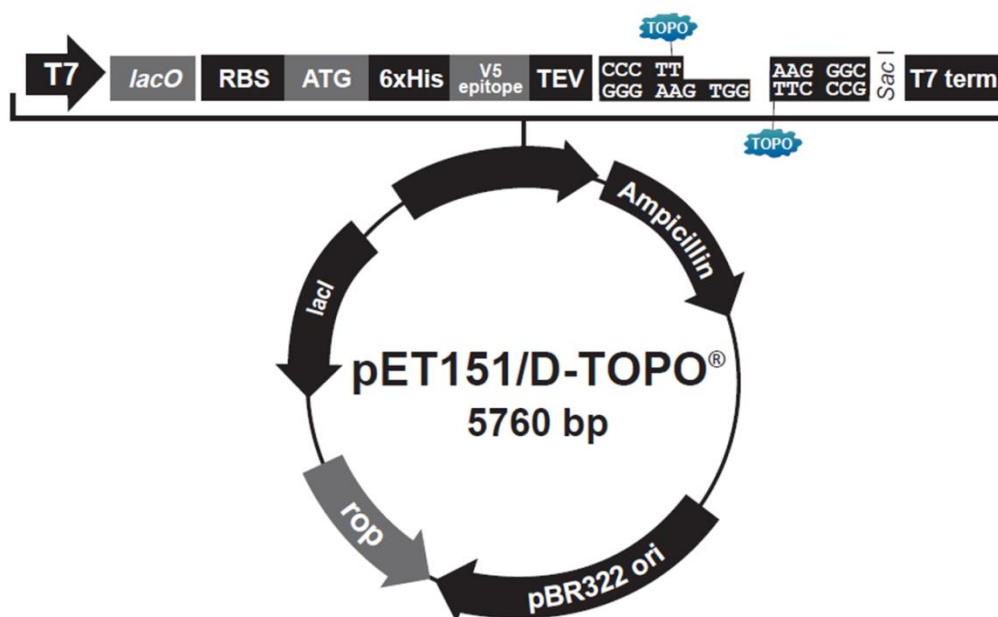


Figure A3.5: Typical gel filtration purification of T76A mutein: **A:** Gel filtration elution profile showed that the mutein eluted at around 90 mL, as a single peak with a small shoulder. **B:** Selected fractions across (lanes 2-3) the early eluting shoulder peak; and (lanes 4-9) the main peak at 90 mL.

Appendix 4 *HsPrx3* information

pET151/D-TOPO vector map

Map and sequence of the pET151 vector are shown below (Invitrogen). When used for expression the gene of interest (NM_006793, detailed below) was cloned in without the mitochondrial leader sequence.



Vector sequenc

```
CAAGGAGATGGCGCCCAACAGTCCCCCGGCCACGGGGCCTGCCACCATACCCACGCCGAAACAAGC
GCTCATGAGCCCGAAGTGGCGAGCCCGATCTTCCCATCGGTGATGTGCGCGATATAGGCGCCAGCA
ACCGCACCTGTGGCGCCGGTGTATGCCGGCCACGATGCGTCCGGCGTAGAGGATCGAGATCTCGATCC
CGCGAAAATTAATACGACTCACTATAGGGGAATTGTGAGCGGATAACAATTCCCCTCTAGAAATAATTTTG
TTAACTTTAAGAAGGAGATATACATATGCATCATCACCATCACCATGGTAAGCCTATCCCTAACCCCTCT
CCTCGGTCTCGATTCTACGGAACCTGTATTTTCAGGGAATTGATCCCTTCACCAAGGGCGAGCTCAG
ATCCGGCTGCTAACAAAGCCCGAAAGGAAGCTGAGTTGGCTGCTGCCACCGCTGAGCAATAACTAGCA
TAACCCCTTGGGGCCTCTAAACGGGTCTTGAGGGGTTTTTGTGCTGAAAGGAGGAACTATATCCGGATAT
CCCGCAAGAGGCCCGGCAGTACCGGCATAACCAAGCCTATGCCTACAGCATCCAGGGTGACGGTGCC
GAGGATGACGATGAGCGCATTGTTAGATTTTCATACACGGTGCCTGACTGCGTTAGCAATTTAACTGTGA
TAACTACCGCATTAAAGCTAGCTTATCGATGATAAGCTGTCAAACATGAGAATTAATTCTGAAGACGA
```


AAGGGCCTCGTGATACGCCTATTTTTATAGGTTAATGTCATGATAATAATGGTTTCTTAGACGTCAGGTG
GCACTTTTCGGGGAAATGTGCGCGGAACCCCTATTTGTTTATTTTTCTAAATACATTCAAATATGTATCC
GCTCATGAGACAATAACCCTGATAAATGCTTCAATAATATTGAAAAAGGAAGAGTATGAGTATTCAACAT
TTCCGTGTGCGCCCTTATTCCTTTTTTTCGCGCATTTTGCCTTCCTGTTTTTGCTCACCCAGAAACGCTGG
TGAAAGTAAAGATGCTGAAGATCAGTTGGGTGCACGAGTGGGTACATCGAACTGGATCTCAACAGC
GGTAAGATCCTTGAGAGTTTTCGCCCCGAAGAACGTTTTCCAATGATGAGCACTTTTAAAGTTCTGCTAT
GTGGCGCGGTATTATCCCGTGTGACGCCGGGAAGAGCAACTCGGTGCGCCGATACACTATTCTCAG
AATGACTTGGTTGAGTACTACCCAGTCACAGAAAAGCATCTTACGGATGGCATGACAGTAAGAGAATTA
TGCAGTGCTGCCATAACCATGAGTGATAAACTGCGGCCAACTTACTTCTGACAACGATCGGAGGACC
GAAGGAGCTAACCGCTTTTTTGACAACATGGGGGATCATGTAAGTGCCTTGATCGTTGGGAACCGG
AGCTGAATGAAGCCATACCAAACGACGAGCGTGACACCACGATGCCTGCAGCAATGGCAACAACGTTG
CGCAAACTATTAAGTGGCGAACTACTTACTCTAGCTTCCCGGCAACAATTAATAGACTGGATGGAGGCG
GATAAAGTTGCAGGACCATTCTGCGCTCGGCCCTCCGGCTGGCTGGTTTATTGCTGATAAATCTGGA
GCCGGTGAGCGTGGGTCTCGCGGTATCATTGCAGCACTGGGGCCAGATGGTAAGCCCTCCCGTATCG
TAGTTATCTACACGACGGGGAGTCAGGCAACTATGGATGAACGAAATAGACAGATCGCTGAGATAGGT
GCCTCACTGATTAAGCATTGGTAAGTGTGACACCAAGTTTACTCATATATACTTTAGATTGATTTAAACT
TCATTTTTAATTTAAAGGATCTAGGTGAAGATCCTTTTTGATAATCTCATGACCAAAATCCCTTAACGTG
AGTTTTCGTTCCACTGAGCGTCAGACCCCGTAGAAAAGATCAAAGGATCTTCTTGAGATCCTTTTTTCT
GCGCGTAATCTGCTGCTTGCAAACAAAAAACACCGCTACCAGCGGTGGTTTGGTTTCCGGGATCAAG
AGCTACCAACTCTTTTTCCGAAGGTAAGTGGCTTCAGCAGAGCGCAGATACCAATACTGTCTTCTAG
TGAGCCGTAGTTAGGCCACCACTTCAAGAACTCTGTAGCACCGCCTACATACCTCGCTCTGCTAATCC
TGTTACCAGTGGCTGCTGCCAGTGGCGATAAGTCGTGTCTTACCGGGTTGGACTCAAGACGATAGTTA
CCGGATAAGGCGCAGCGGTGCGGGCTGAACGGGGGGTTCGTGCACACAGCCCAGCTTGGAGCGAACG
ACCTACACCGAACTGAGATACCTACAGCGTGAGCTATGAGAAAGCGCCACGCTTCCCGAAGGGAGAAA
GGCGGACAGGTATCCGGTAAGCGGCAGGGTCGGAACAGGAGCGCACGAGGGAGCTTCCAGGGGG
AAACGCCTGGTATCTTTATAGTCCTGTGCGGGTTTCGCCACCTCTGACTTGAGCGTCGATTTTTGTGATG
CTCGTCAGGGGGGCGGAGCCTATGGAACAAACGCCAGCAACGCGGCCCTTTTACGGTTCCCTGGCCTTTT
GCTGGCCTTTTGTCTACATGTTCTTTCCTGCGTTATCCCTGATTCTGTGGATAACCGTATTACCGCCTT
TGAGTGAGCTGATACCGCTCGCCGACGCCGAACGACCGAGCGCAGCGAGTCAGTGAGCGAGGAAGC
GGAAGAGCGCCTGATGCGGTATTTCTCCTTACGCATCTGTGCGGTATTTACACCGCATATATGGTGC
ACTCTCAGTACAATCTGCTCTGATGCCGCATAGTTAAGCCAGTATACTCCGCTATCGCTACGTGACT
GGGTCATGGCTGCGCCCCGACACCCGCCAACACCCGCTGACGCGCCCTGACGGGCTTGTCTGCTCCC
GGCATCCGCTTACAGACAAGCTGTGACCGTCTCCGGGAGCTGCATGTGTCAGAGGTTTTACCGTCAT
CACCGAAACGCGCAGGCGAGCTGCGGTAAAGCTCATCAGCGTGGTCTGTAAGCGATTACAGATGTC
TGCCTGTTTATCCGCTCCAGCTCGTTGAGTTTCTCCAGAAGCGTTAATGTCTGGCTTCTGATAAAGCG
GGCCATGTTAAGGGCGGTTTTTCTGTTTGGTCACTGATGCCTCCGTGTAAGGGGGATTTCTGTTTAT
GGGGGTAATGATACCGATGAAACGAGAGAGGATGCTCACGATACGGGTACTGATGATGAACATGCCC
GGTTACTGGAACGTTGTGAGGGTAAACAACGCGGTATGGATGCGGCGGGACCAGAGAAAAATCACT
CAGGGTCAATGCCAGCGCTTCGTTAATACAGATGTAGGTGTTCCACAGGGTAGCCAGCAGCATCCTGC
GATGCAGATCCGGAACATAATGGTGCAGGGCGCTGACTTCCGCGTTTCCAGACTTTACGAAACACGGA
AACCGAAGACCATTTCATGTTGTTGCTCAGGTGCGAGACGTTTTGCAGCAGCAGTCGTTACGTTTCGCT
CGCGTATCGGTGATTCTTCTGCTAACCAGTAAGGCAACCCCGCCAGCCTAGCCGGGTCTCAACGAC
AGGAGCACGATCATGCGCACCCGTGGCCAGGACCAACGCTGCCCGAGATGCGCCGCGTGGCGCTG
CTGGAGATGGCGGACGCGATGGATATGTTCTGCCAAGGGTTGGTTTGGCGATTACAGTTCTCCGCAA
GAATTGATTGGCTCCAATTCTTGAGTGGTGAATCCGTTAGCGAGGTGCCGCCGGCTTCCATTACGGT
CGAGGTGGCCCGGCTCCATGCACCGCGACGCAACGCGGGGAGGCAGACAAGGTATAGGGCGGCGCC
TACAATCCATGCCAACCCGTTCCATGTGCTCGCCGAGGCGGCATAAATCGCCGTGACGATCAGCGGTC
CAGTGATCGAAGTTAGGCTGGTAAGAGCCGCGAGCGATCCTTGAAGCTGTCCCTGATGGTCGTCATCT
ACCTGCCTGGACAGCATGGCCTGCAACGCGGGCATCCCGATGCCGCCGGAAGCGAGAAGAATCATAA
TGGGGAAGGCCATCCAGCCTCGCGTCGCGAACGCCAGCAAGACGTAGCCAGCGCGCTCGGCCGCCA
TGCCGGCGATAATGGCCTGCTTCTCGCCGAAACGTTTGGTGGCGGGACCAGTGACGAAGGCTTGAGC
GAGGGCGTGCAAGATTCCGAATACCGCAAGCGACAGGCCGATCATCGTCGCGCTCCAGCGAAAGCGG
TCCTCGCCGAAAATGACCCAGAGCGCTGCCGGCACCTGTCTACGAGTTGCATGATAAAGAAGACAGT

CATAAGTGC GGCGACGATAGTCATGCCCGCGCCACCGGAAGGAGCTGACTGGGTTGAAGGCTCTC
AAGGGCATCGGTGAGATCCCGGTGCCTAATGAGTGAGCTAACTTACATTAATTGCGTTGCGCTCACT
GCCCCGCTTTCCAGTCGGGAAACCTGTCGTGCCAGCTGCATTAATGAATCGGCCAACGCGCGGGGAGA
GGCGGTTTTCGTATTGGGCGCCAGGGTGGTTTTCTTTTACCAGTGAGACGGGCAACAGCTGATTGC
CCTTCACCGCCTGGCCCTGAGAGAGTTGCAGCAAGCGGTCCACGCTGGTTTGCCCCAGCAGGCGAAA
ATCCTGTTTGATGGTGGTTAACGGCGGGATATAACATGAGCTGTCTTCGGTATCGTCGTATCCCACTAC
CGAGATATCCGCACCAACGCGCAGCCCGGACTCGGTAATGGCGCGCATTGCGCCCAGCGCCATCTGA
TCGTTGGCAACCAGCATCGCAGTGGGAACGATGCCCTCATTGAGCATTTCATGTTTGTGAAAACCG
GACATGGCACTCCAGTCGCCTTCCCGTTCCGCTATCGGCTGAATTTGATTGCGAGTGAGATATTTATGC
CAGCCAGCCAGACGCGAGACGCGCCGAGACAGAACTTAATGGGCCCGCTAACAGCGCGATTGCTGGT
GACCCAATGCGACCAGATGCTCCACGCCAGTCGCGTACCGTCTTCATGGGAGAAAATAATACTGTTG
ATGGGTGTCTGGTCAGAGACATCAAGAAATAACGCCGGAACATTAGTGACAGGCAGCTTCCACAGCAAT
GGCATCCTGGTCATCCAGCGGATAGTTAATGATCAGCCCACTGACGCGTTGCGCGAGAAGATTGTGCA
CCGCCGCTTTACAGGCTTCGACGCCGCTTCGTTCTACCATCGACACCACCGCTGGCACCCAGTTGA
TCGGCGCGAGATTTAATCGCCGCGACAAATTTGCGACGGCGCGTGCAGGGCCAGACTGGAGGTGGCAA
CGCCAATCAGCAACGACTGTTTGCCCGCCAGTTGTTGTGCCACGCGGTTGGGAATGTAATTCAGCTCC
GCCATCGCCGCTTCCACTTTTTCCCGCGTTTTTCGAGAAACGTGGCTGGCCTGGTTCACCACGCGGGA
AACGGTCTGATAAGAGACACCGGCATACTCTGCGACATCGTATAACGTTACTGGTTTTACATTACCCAC
CCTGAATTGACTCTCTTCCGGGCGCTATCATGCCATACCGCGAAAGGTTTTGCGCCATTGATGGTGTC
CGGGATCTCGACGCTCTCCCTTATGCGACTCCTGCATTAGGAAGCAGCCAGTAGTAGGTTGAGGCCG
TTGAGCACCGCCGCGCAAGGAATGGTGCATG

NM_006793 nucleotide sequence

The 771 bp nucleotide sequence encoding the *HsPrx3* protein is shown below, as cloned into the pET151 vector without the mitochondrial leader sequence.

ATGGCGGCTGCTGTAGGACGGTTGCTCCGAGCGTCGGTTGCCCGACATGTGAGTGCCATTCCTTGGG
GCATTTCTGCCACTGCAGCCCTCAGGCCTGCTGCATGTGGAAGAACGAGCTTGACAAATTTATTGTGTT
CTGTTTCCAGTCAAGCAAAATTATTCAGCACCAGTTCCTCATGCCATGCACCTGCTGTCACCCAGCATG
CACCTATTTTAAGGGTACAGCCGTTGTCAATGGAGAGTTCAAAGACCTAAGCCTTGATGACTTTAAGG
GGAAATATTTGGTGCTTTTCTTCTATCCTTTGGATTTACCTTTGTGTGTCTACAGAAATTTGTGCTTTT
AGTGACAAAGCTAACGAATTTACGACGTGAACTGTGAAGTTGTCGCAGTCTCAGTGGAATCCCACTTT
AGCCATCTTGCTGGATAAATACACCAAGAAAGAATGGTGGTTTGGGCCACATGAACATCGCACTCTTG
TCAGACTTAACAAAGCAGATTTCCCGAGACTACGGTGTGCTGTTAGAAGGTTCTGGTCTTGCACTAAGA
GGTCTCTTCATAATTGACCCCAATGGAGTCATCAAGCATTTGAGCGTCAACGATCTCCAGTGCGCCGA
AGCGTGGAAGAAACCCTCCGCTTGGTGAAGGCGTTCCAGTATGTAGAAACACATGGAGAAGTCTGCCC
AGCGAACTGGACACCGGATTCTCCTACGATCAAGCCAAGTCCAGCTGCTTCAAAGAGTACTTTCAGAA
GGTAAATCAGTAG

***HsPrx3* amino acid sequence**

Underlining indicates the his-tag and linker residues conferred by the pET151 vector; rTEV cleavage site is indicated by a red star.

MHHHHHHGKPIPNPLLGLDSTENLYFQ*GIDPFTAPAVTQHAPYFKGTAVVNGEFKDLSLDDFKGKYLVLFF
YPLDFTFVCPTEIVAFSDKANEFHDVNCEVVAVSVDSHFSLAWINTPRKNGGLGHMNIALLSDLTKQISRDY
GVLLEGSGLALRGLFIIDPNGVIKHLVNDLPVGRSVEETLRLVKAFQYVETHGEVCPANWTPDSPTIKPSPA
ASKEYFQKVN

Important parameters for *HsPrx3*

Extinction coefficients and molecular masses were used for calculation of protein concentration (section 2.3.5.2), identification of *HsPrx3* and efficiency of cleavage (section 2.3.5.3).

Construct	Molecular Mass (kDa)	Number of residues	Theoretical pI	Extinction Coefficient (M⁻¹ cm⁻¹)
Native <i>HsPrx3</i>	21.41	194	5.77	Oxidised: 0.94 Reduced: 0.93
Cleaved <i>HsPrx3</i>	22.04	200	5.59	Oxidised: 0.91 Reduced: 0.91
His-tagged <i>HsPrx3</i>	25.19	227	5.97	Oxidised: 0.86 Reduced: 0.85

Location of rare codons in the *HsPrx3* nucleotide sequence

Rare arginine codons are highlighted in red, leucine in green, isoleucine in blue and proline in orange. BL21 Rosetta (DE3) cells complement all rare codons except the CGA arginine codon, which was not found to be a problem for expression.

gca cct gct gtc acc cag cat gca CCC tat ttt aag ggt aca gcc
 gtt gtc aat gga gag ttc aaa gac CTA agc ctt gat gac ttt aag
 ggg aaa tat ttg gtg ctt ttc ttc tat cct ttg gat ttc acc ttt
 gtg tgt cct aca gaa att gtt gct ttt agt gac aaa gct aac gaa
 ttt cac gac gtg aac tgt gaa gtt gtc gca gtc tca gtg gat tcc
 cac ttt agc cat ctt gcc tgg ATA aat aca cca AGG aag aat ggt
 ggt ttg ggc cac atg aac atc gca ctc ttg tca gac tta act aag
 cag att tcc CGA gac tac ggt gtg ctg tta gaa ggt tct ggt ctt
 gcs CTA AGA ggt ctc ttc ATA att gac CCC aat gga gtc atc aag
 cat ttg agc gtc aac gat ctc cca gtg ggc CGA agc gtg gaa gaa
 acc ctc cgc ttg gtg aag gcg ttc cag tat gta gaa aca cat gga
 gaa gtc tgc cca gcg aac tgg aca ccg gat tct cct acg atc aag
 cca agt cca gct gct tcc aaa gag tac ttt cag aag gta aat
 cag tag

Important parameters for *HsPrx3* muteins

Only minor differences were seen in theoretical pI, therefore purification and characterisation protocols used for wildtype *HsPrx3* were suitable.

Construct	Molecular Mass (kDa)	Number of residues	Theoretical pI	Extinction Coefficient (M ⁻¹ cm ⁻¹)
Cleaved P49A	22.02	200	5.59	Oxidised: 0.91 Reduced: 0.91
His-tagged P49A	25.17	227	5.97	Oxidised: 0.86 Reduced: 0.85
Cleaved R123G	21.96	200	5.42	Oxidised: 0.91 Reduced: 0.91
His-tagged R123G	25.11	227	5.85	Oxidised: 0.86 Reduced: 0.85
Cleaved S78A	22.03	200	5.59	Oxidised: 0.91 Reduced: 0.91
His-tagged S78A	25.18	227	5.97	Oxidised: 0.86 Reduced: 0.85
Cleaved T104W	22.07	200	5.59	Oxidised: 1.16 Reduced: 1.15
His-tagged T104W	25.28	227	5.97	Oxidised: 1.07 Reduced: 1.07
Cleaved C47S	22.03	200	5.59	Oxidised: 0.91 Reduced: 0.91
His-tagged C47S	25.18	227	5.97	Oxidised: 0.86 Reduced: 0.85
Cleaved C47SS78A	22.01	200	5.59	Oxidised: 0.81 Reduced: 0.91
His-tagged C47SS78A	25.16	227	5.97	Oxidised: 0.86 Reduced: 0.85

Appendix 5 Peptide sequencing results

Peptide sequencing of *MtAhpE* gel bands was carried out at Auckland University Proteomics Facility using MS/MS following tryptic digest by Kristen Boxen. Peptide sequencing of *HsPrx3* gel bands was carried out at Lincoln University by Stefan Clerens.

Peptide sequencing of the Q83A *MtAhpE* mutain

1. [gi115609375](#) Mass: 16867 Score: 48 Matches: 1(1) Sequences: 1(1)
 peroxiredoxin AhpE [Mycobacterium tuberculosis H37Rv]
☐ Check to include this hit in error tolerant search

Query	Observed	Mr(expt)	Mr(calc)	Delta	Miss	Score	Expect	Rank	Unique
<input checked="" type="checkbox"/> 8	607.8462	1213.6779	1213.6415	0.0364	0	48	0.00025	1	U

Proteins matching the same set of peptides:

[gi161680453](#) Mass: 17578 Score: 48 Matches: 1(1) Sequences: 1(1)
 Chain A, Crystal Structure Of Ahpe From Mycobacterium Tuberculosis, A 1-Cys
[gi1289570359](#) Mass: 7401 Score: 48 Matches: 1(1) Sequences: 1(1)
 peroxiredoxin ahpE [Mycobacterium tuberculosis T17]

Peptide matches not assigned to protein hits: (no details means no match)

Query	Observed	Mr(expt)	Mr(calc)	Delta	Miss	Score	Expect	Rank	Unique
<input checked="" type="checkbox"/> 3	428.7762	855.5378	855.4814	0.0565	0	14	0.61	1	
<input checked="" type="checkbox"/> 2	421.7648	841.5150	841.4844	0.0307	0	6	4.6	1	
<input checked="" type="checkbox"/> 18	737.7239	2210.1499	2210.1379	0.0120	0	5	1.9	1	
<input checked="" type="checkbox"/> 10	423.2028	1266.5865	1266.6608	-0.0743	0	1	7.7	1	
<input checked="" type="checkbox"/> 15	985.9679	1969.9213	1969.9687	-0.0474	0	1	3	1	
<input checked="" type="checkbox"/> 6	523.3068	1044.5991	1044.5200	0.0791	0	0	12	1	
<input checked="" type="checkbox"/> 5	523.2559	1044.4972	1044.5386	-0.0414	0	0	16	1	
<input checked="" type="checkbox"/> 1	608.0220	607.0148							
<input checked="" type="checkbox"/> 4	435.7803	869.5460							
<input checked="" type="checkbox"/> 7	523.9000	1045.7854							
<input checked="" type="checkbox"/> 9	608.0660	1214.1174							
<input checked="" type="checkbox"/> 11	737.7239	1473.4333							
<input checked="" type="checkbox"/> 12	523.9000	1568.6782							
<input checked="" type="checkbox"/> 13	837.2103	1672.4060							
<input checked="" type="checkbox"/> 14	608.0660	1821.1761							
<input checked="" type="checkbox"/> 16	986.2058	1970.3970							
<input checked="" type="checkbox"/> 17	523.9000	2091.5709							
<input checked="" type="checkbox"/> 19	738.0628	2211.1667							
<input checked="" type="checkbox"/> 20	761.7475	2282.2206							
<input checked="" type="checkbox"/> 21	837.2103	2508.6091							
<input checked="" type="checkbox"/> 22	523.9000	2614.4636							
<input checked="" type="checkbox"/> 23	837.1974	4180.9506							

Peptide sequencing of *HsPrx3* wildtype SDS-PAGE bands

Cmpd.	No. of Cmpds.	m/z meas.	Δ m/z [ppm]	z	Rt [min]	Score	P	Range	Sequence	Modification
9	1	511.2400	-57.27	2	7.9	62.4	0	74-83	K.GTAVVNGEFK.D	
88	1	476.7600	52.99	2	11.5	44.9	0	84-91	K.DLSLDDFK.G	
41	2	569.3200	47.51	2	10.1	46.5	1	84-93	K.DLSLDDFKGK.Y	
31	1	716.7600	-72.15	2	9.4	30.3	0	119-130	K.ANEFHQVNCVV.A	Carbamidomethyl: 9
56	2	801.8400	-30.53	2	10.6	29.4	0	119-132	K.ANEFHQVNCVVAV.S	Carbamidomethyl: 9
96	1	679.6700	-16.99	3	11.8	65.9	0	131-148	V.AVSVDSHFSLAWINTPR.K	

Cmpd.	No. of Cmpds.	m/z meas.	Δ m/z [ppm]	z	Rt [min]	Score	P	Range	Sequence	Modification
91	1	655.9700	-49.55	3	11.6	56.0	0	132-148	A.VSVDSHFSLAWINTPR.K	
85	2	622.9500	-47.68	3	11.4	52.5	0	133-148	V.SVDSHFSLAWINTPR.K	
166	1	585.3300	27.86	3	14.2	69.3	0	150-166	K.NGGLGHMNIALLSDLTK.Q	
120	1	487.3500	102.50	2	12.6	49.9	0	158-166	N.IALLSDLTK.Q	
134	1	649.6800	-20.70	3	13.1	41.5	1	167-184	K.QISRQYGVLLGGSLALR.G	
170	6	731.8700	-39.14	2	14.3	121.0	0	171-184	R.DYGVLLGGSLALR.G	
176	14	643.3200	-92.27	2	14.9	79.0	0	185-196	R.GLFIIDPNGVIK.H	
33	19	603.7700	-104.52	2	9.7	69.4	0	197-207	K.HLSVNDLPVGR.S	
57	1	535.3700	123.94	2	10.6	61.1	0	198-207	H.LSVNDLPVGR.S	
4	8	417.2100	-28.28	2	7.0	43.4	0	208-214	R.SVEETLR.L	
14	2	497.7400	9.90	2	8.3	59.3	0	218-225	K.AFQYVETH.G	
12	1	526.2500	7.97	2	8.1	38.5	0	218-226	K.AFQYVETHG.E	
30	1	640.2600	-64.52	2	9.4	52.0	0	218-228	K.AFQYVETHGEV.C	

Appendix 6 *HsPrx3* mutein purification traces and gels

T104W purification

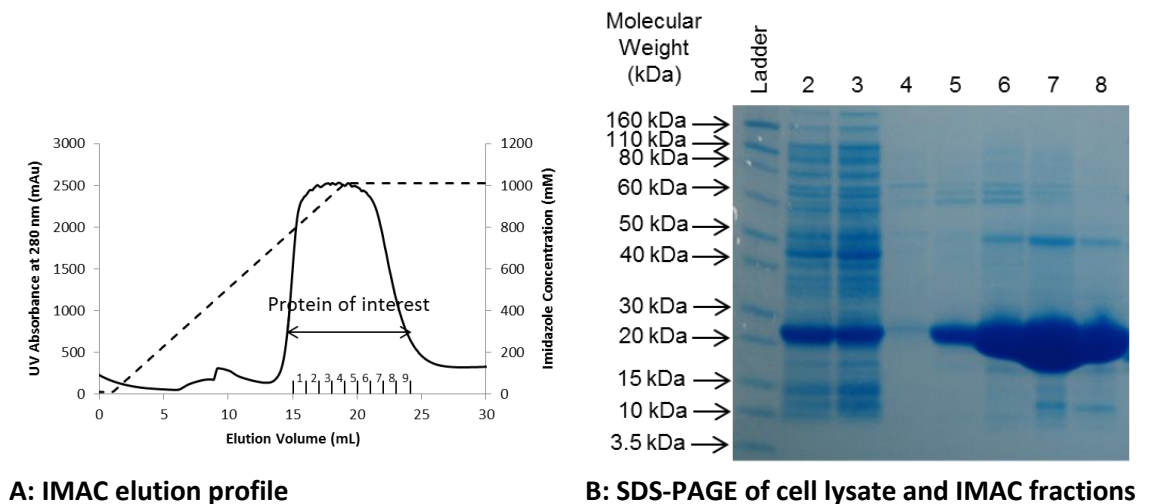


Figure A6.1: **A:** Typical IMAC elution profile of T104W mutein. **B:** SDS-PAGE gel showing: lane 2: whole cell lysate; lane 3: soluble fraction; lane 4: IMAC flow through; lane 5-8: selected fractions across the peak as indicated by stars on the chromatogram.

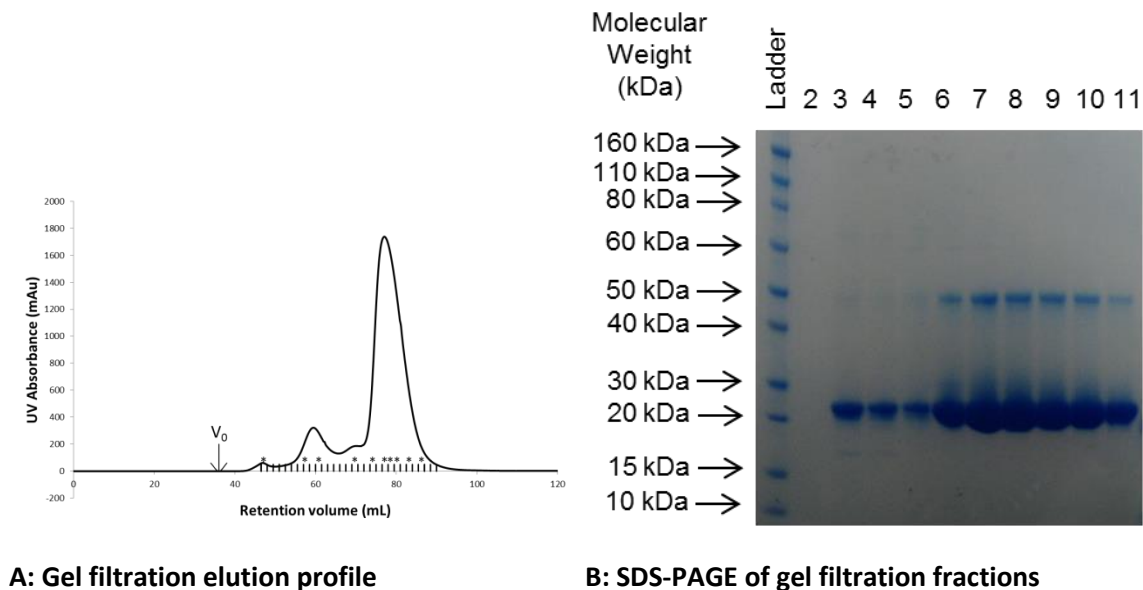


Figure A6.2: **A:** Typical gel filtration elution profile of T104W mutein showed a single main peak around 80 mL, and early eluting small peaks. **B:** SDS-PAGE gel showing: Lane 2: fraction from the peak near the void volume; lanes 3-5: selected fractions across the small peaks; lanes 6-11: selected fractions across the main peak; as indicated by stars on the chromatogram. SDS-resistant dimers were often seen during purification, these are discussed in the text (chapter five).

P48A purification

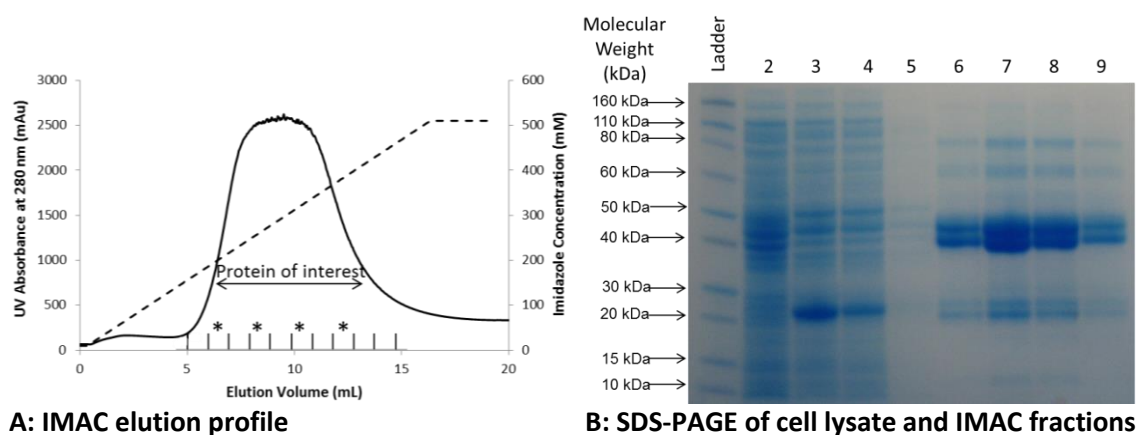


Figure A6.3: **A:** Typical IMAC elution profile of P48A mutein. **B:** SDS-PAGE gel showing: lane 2: whole cell lysate; lane 3: soluble fraction; lane 4: insoluble fraction; lane 5: IMAC flow through; lanes 6-9: selected fractions across the peak as indicated by stars on the chromatogram.

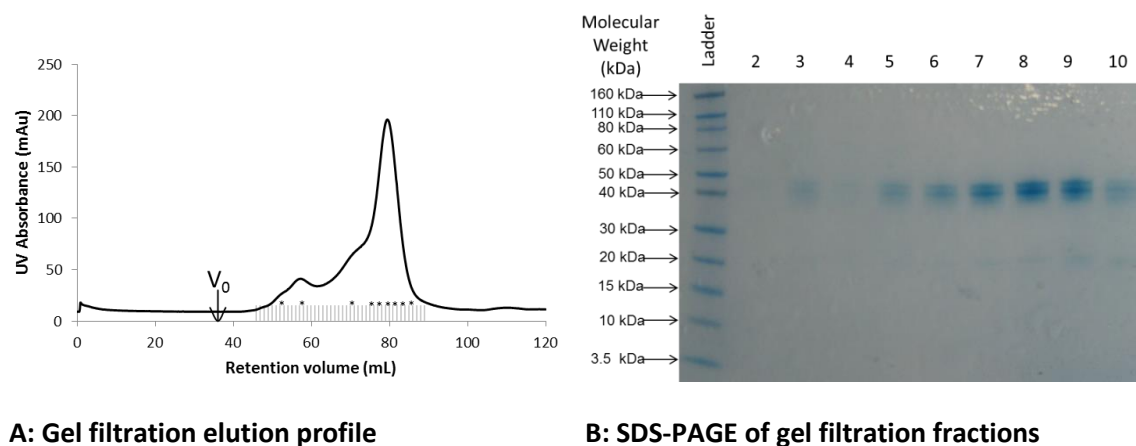


Figure A6.4: **A:** Typical gel filtration elution profile of the P48A mutein showed a single main peak around 80 mL, with a leading edge and early eluting small peaks. **B:** SDS-PAGE gel showing: Lanes 2-4: selected fractions across the small peaks; lanes 6-10: selected fractions across the main peak; as indicated by stars on the chromatogram.

R123G Purification

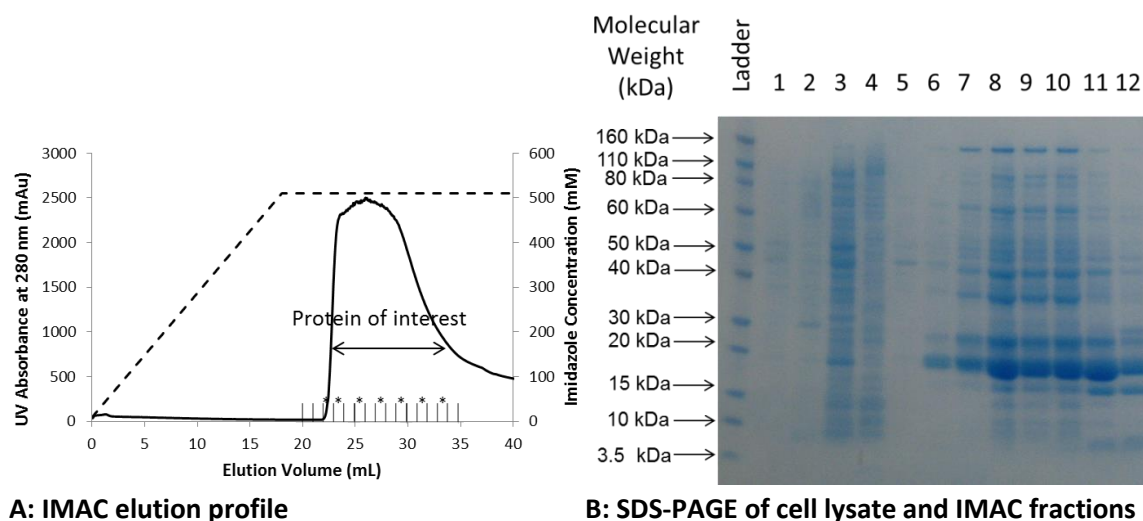


Figure A6.5: **A:** Typical IMAC elution profile of R123G mutein. **B:** SDS-PAGE gel showing: lane 2: whole cell lysate; lane 3: soluble fraction; lane 4: insoluble fraction; lane 5: IMAC flow through; lanes 6-12: selected fractions across the peak as indicated by stars on the chromatogram.

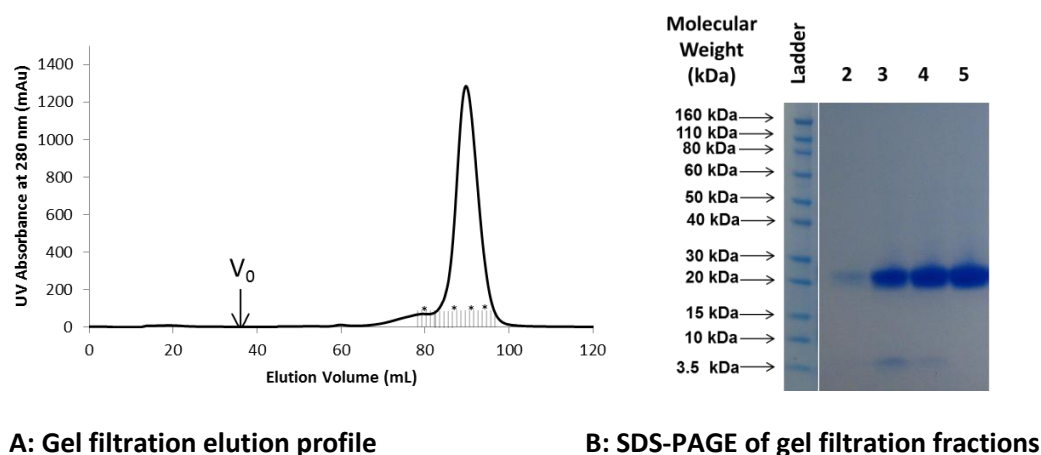


Figure A6.6: **A:** Typical gel filtration elution profile of the R123G mutein showed a single main peak around 90 mL, with a small leading edge. **B:** SDS-PAGE gel showing: Lanes 2-5: selected fractions across the small peak and main peak; as indicated by stars on the chromatogram.

C47S Purification

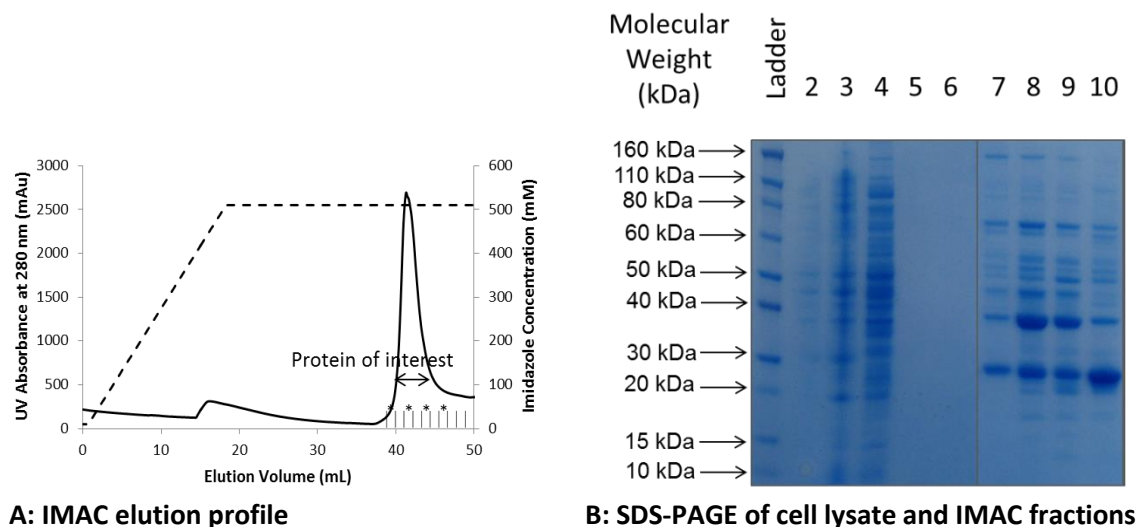
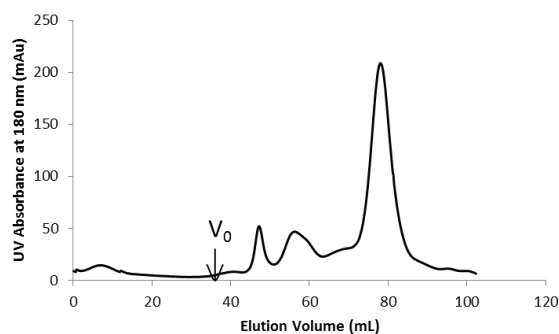


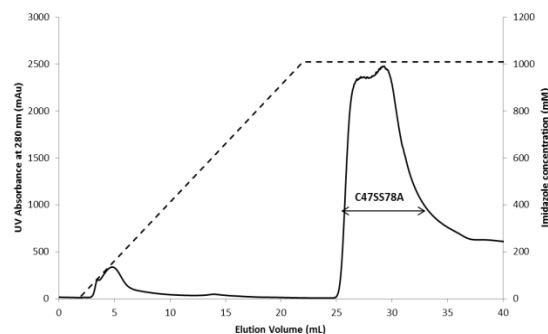
Figure A6.7: **A:** Typical IMAC elution profile of C47S mutein. Protein eluted as a late peak only after considerable washing with high imidazole buffer **B:** SDS-PAGE gel showing: lane 2: whole cell lysate; lane 3: soluble fraction; lane 4: insoluble fraction; lane 5: IMAC flow through; lane 6: IMAC wash; lanes 7-10: selected fractions across the peak as indicated by stars on the chromatogram.



A: Gel filtration elution profile

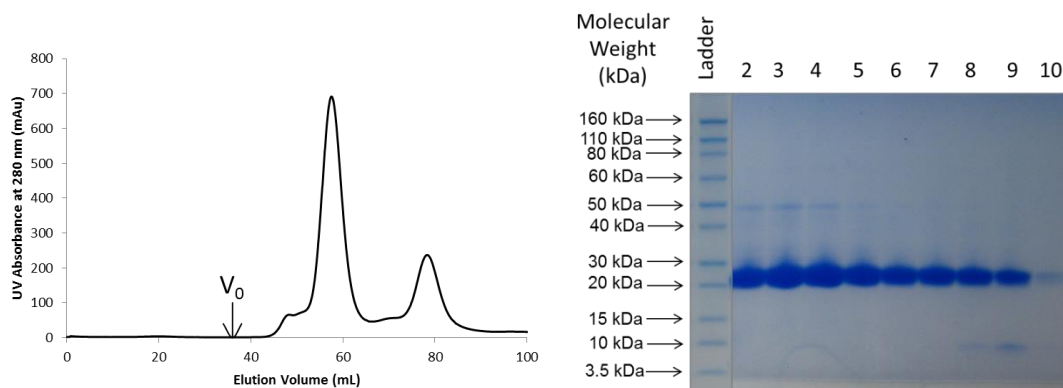
FigureA6.8: **A:** Typical gel filtration elution profile of the C47S mutein showed a single main peak around 80mL, with a number of early eluting peaks suggesting aggregation.

C47SS78A Purification



A: IMAC elution profile

Figure A6.9: A: Typical IMAC elution profile of C47SS78A mutein.



A: Gel filtration elution profile

B: SDS-PAGE of gel filtration fractions

FigureA6.10: A: Typical gel filtration elution profile of the C47SS78A mutein showed a main peak around 60 mL, with a small shoulder. A second peak was seen around 80 mL **B:** SDS-PAGE gel showing: Lanes 2-7: selected fractions across the small peak and main peak; lanes 8-10: selected fractions across the late eluting smaller peak, as indicated by stars on the chromatogram.

Appendix 7 *HsPrx3* mutein SAXS values

Table A7.1: S78A

Sample	Concentration mg/mL	D _{max} (Å)	Standard Error	R _g from Guinier (Å)	Standard Error	R _g from GNOM (Å)	Standard Error	Volume (Å ³)	Standard Error	MW (kDa)	Standard Error
S78A untagged	0.5	195	4	65	1	62	1	519000	21000	314	11
Reduced	1	194	4	63	0	62	0	513000	11000	310	5
	2	191	8	63	0	62	1	511000	18000	307	9
S78A untagged	0.5	249	5	74	0	80	1	601000	14000	336	6
non-reduced	1	223	2	75	0	83	0	700000	12000	364	3
	2	262	1	76	0	85	0	1390000	46000	678	19
S78A tagged	0.5	193	6	60	1	60	1	385000	193000	363	10
reduced	1	197	8	61	0	60	0	586000	17000	361	11
	2	188	9	60	1	59	1	578000	26000	355	14
S78A tagged	0.5	193	0	64	1	62	0	652000	4000	400	3
non-reduced	1	218	8	64	1	66	1	742000	35000	442	17
	2	208	5	64	1	63	1	658000	13000	397	4
Wildtype dodecamer		~180		Theoretical R _g : 59				417000		257	
Wildtype Dimer		~60		Theoretical R _g : 20				49800		42	

Table A7.2: T104W

Sample	Concentration mg/mL	D _{max} (Å)	Standard Error	R _g from Guinier (Å)	Standard Error	R _g from GNOM (Å)	Standard Error	Volume (Å ³)	Standard Error	MW (kDa)	Standard Error
T104W untagged reduced	0.5	169	3	51	1	54	1	224000	29000	137	19
	1	178	5	53	1	54	0	206000	11000	127	7
	2	172	10	57	1	56	0	297000	36000	215	23
T104W untagged non-reduced	0.5	112	4	36	1	34	1	91000	1600	57	1
	1	118	4	37	1	35	0	95000	700	60	0
	2	125	1	37	1	31	1	102000	2100	64	1
T104W tagged reduced	0.5 mg/mL	184	13	56	1	56	0	421000	7200	261	2
	1 mg/mL	158	4	55	0	55	0	425000	3000	264	1
	2 mg/mL	184	6	56	0	55	0	420000	4000	261	3
T104W tagged non-reduced	0.5 mg/mL	98	0	27	0	28	0	90700	3600	55	2
	1 mg/mL	96	1	28	0	29	0	94500	2600	58	1
	2 mg/mL	99	2	29	1	39	0	96600	2200	60	1
Wildtype dodecamer		~180		Theoretical R _g : 59				417000		257	
Wildtype Dimer		~60		Theoretical R _g : 20				49800		42	

Table A7.3: P49A

Non-reduced tagged P49A mutein was not able to be analysed due to the tendency to aggregate.

Sample	Concentration mg/mL	D _{max} (Å)	Standard Error	R _g from Guinier (Å)	Standard Error	R _g from GNOM (Å)	Standard Error	Volume (Å ³)	Standard Error	MW (kDa)	Standard Error
P49A untagged	0.5	210	11	63	1	63	1	563000	16400	325	6
Reduced	1	211	5	63	0	62	0	506000	5900	302	2
	2	219	7	63	0	63	0	554000	13000	326	8
P49A untagged	0.5	218	11	68	1	67	2	673000	45000	378	23
non-reduced	1	221	6	67	0	66	1	613000	18000	346	8
	2	203	1	71	0	65	0	632000	4100	371	2
P49A tagged	0.5	204	6	60	1	60	0	615000	5500	375	4
Reduced	1	197	3	60	1	59	0	577000	7400	353	5
	2	206	0	59	0	60	0	582000	4300	357	2
Wildtype Dodecamer		~180		Theoretical R _g : 59				417000		257	
Wildtype Dimer		~60		Theoretical R _g : 20				49800		42	

Table A7.4: C47S

Untagge C47S mutein was not able to be analysed due to the tendency to aggregate.

Sample	Concentration mg/mL	D _{max} (Å)	Standard Error	R _g from Guinier (Å)	Standard Error	R _g from GNOM (Å)	Standard Error	Volume (Å ³)	Standard Error	MW (kDa)	Standard Error
C47S tagged	0.5	190	10	58	0	57	1	543000	11000	336	6
reduced	1	187	11	57	0	57	1	532000	5000	331	3
C47S tagged	0.5	196	7	60	1	59	1	600000	4700	367	3
non-reduced	1	204	4	60	1	60	0	607000	5800	369	1
Wildtype dodecamer		~180		Theoretical R _g : 59				417000		257	
Wildtype Dimer		~60		Theoretical R _g : 20				49800		42	

Table A7.5: C47SS78A

Sample	Conc. mg/mL	D _{max} (Å)	Standard Error	R _g from Guinier (Å)	Standard Error	R _g from GNOM (Å)	Standard Error	Volume (Å ³)	Standard Error	MW (kDa)	Standard Error
C47SS78A untagged	0.5	170	2	59	0	57	0	532000	3100	331	2
Reduced	1	201	5	58	0	58	0	537000	5500	331	2
	2	196	3	59	0	58	0	529000	5300	327	3
C47SS78A untagged	0.5	199	5	59	0	59	0	555000	7600	341	3
non-reduced	1	206	0	59	0	59	0	562000	590	344	0
		207	1	59	0	59	0	575000	8600	350	5
C47SS78A tagged	0.5	163	2	57	0	56	0	463000	2300	286	1
Reduced	1	185	6	56	0	56	0	465000	1100	287	0
	2	171	1	55	0	55	0	455000	320	281	0
C47SS78A tagged	0.5	158	1	57	0	56	0	461000	460	286	0
non-reduced	1	198	2	57	0	57	0	474000	950	294	1
	2	196	2	58	0	57	0	480000	4400	299	3
Wildtype Dodecamer		~180		Theoretical R _g : 59				417000		257	
Wildtype Dimer		~60		Theoretical R _g : 20				49800		42	

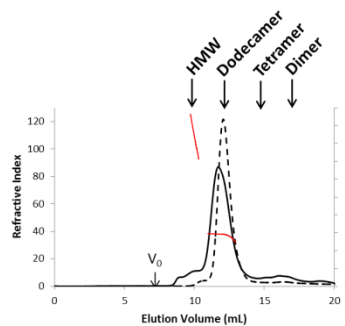
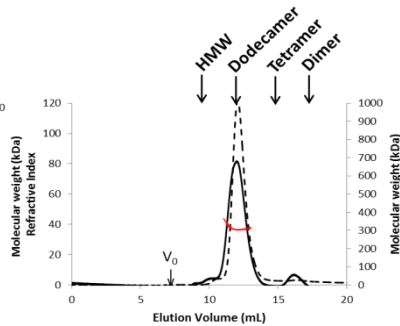
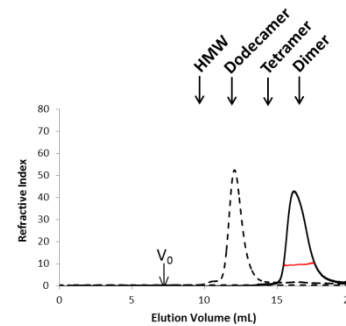
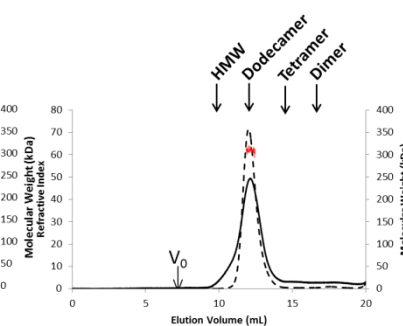
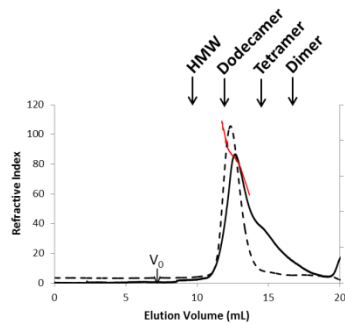
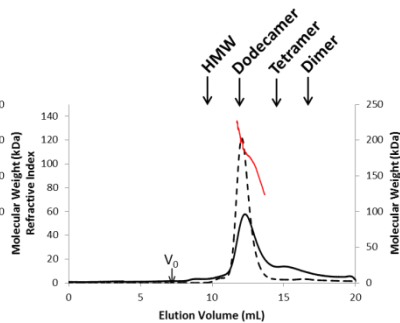
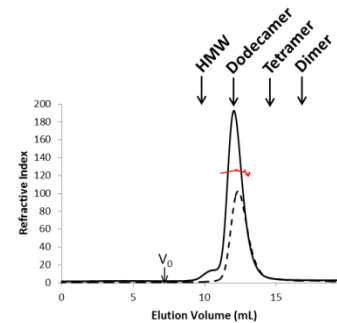
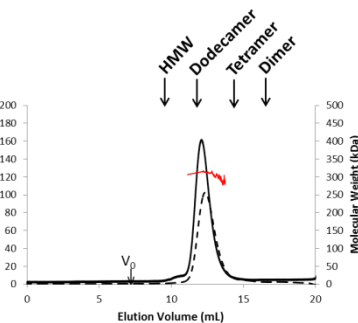
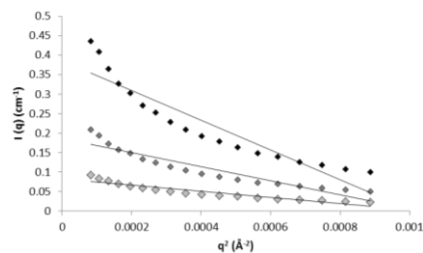
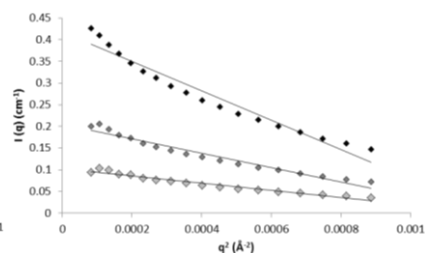
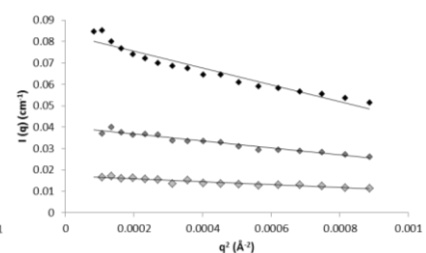
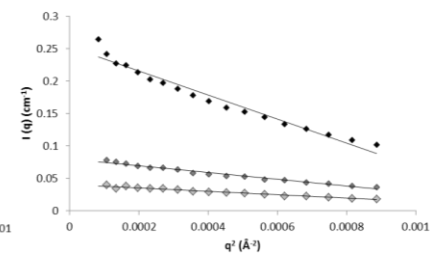
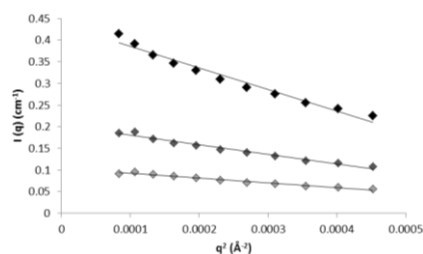
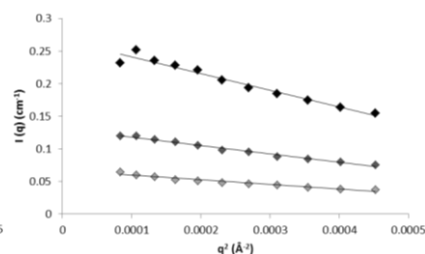
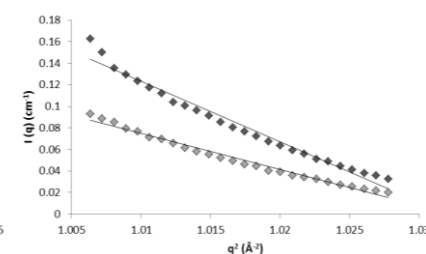
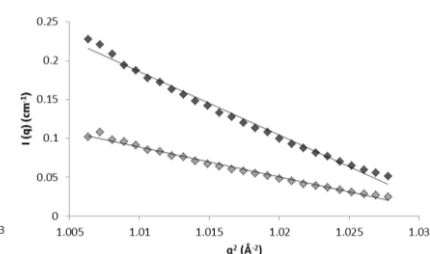
**A: S78A tagged
non-reduced****B: S78A tagged
reduced****C: T104W tagged
non-reduced****D: T104W tagged
reduced****E: P49A tagged
non-reduced****F: P49A tagged
reduced****G: C47SS78A tagged
non-reduced****H: C47SS78A tagged
reduced**

Figure A7.1: SEC/SLS data for tagged muteins: Analysis of tagged muteins generally showed a tendency toward the dodecameric state. This is in line with results for tagged wildtype and so gave no additional insight into the influence of the mutations. The exception was T104W which switched between the dimer and dodecamer even when the tag was attached (discussed in text). Tagged wildtype in identical conditions is shown with the dashed lines, molecular weight across the peaks with red lines.

**A: S78A untagged
non-reduced****B: S78A untagged
reduced****C: T104W untagged
non-reduced****D: T104W untagged
reduced****E: P49A untagged
non-reduced****F: P49A untagged
reduced****G: C47S tagged
non-reduced****H: C47S tagged
reduced**

Continued onto next page

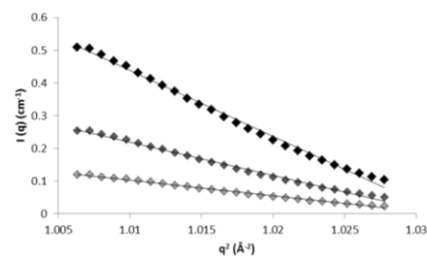
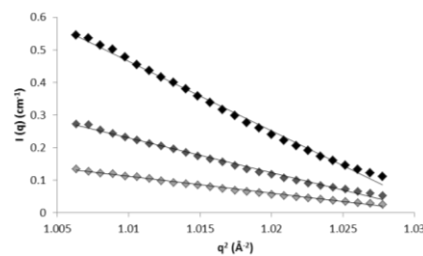
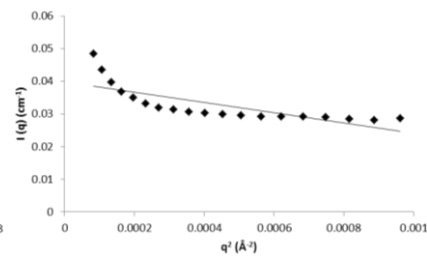
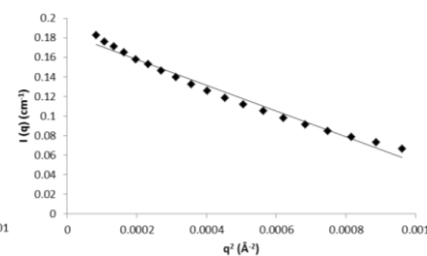
I: C47SS78A untagged non-reduced**J: C47SS78A untagged reduced****K: R123G untagged non-reduced****L: R123G untagged reduced**

Figure A7.2: Guinier region plots of muteins: A number of muteins showed a nonlinear Guinier plot, indicative of aggregation. This was more common in non-reduced samples. R123G was particularly aggregated, as discussed in the text, and only one sample was able to be run through the in line FPLC. All other samples were injected directly into the capillary and analysed at 2 mg/mL (black diamonds); 1 mg/mL (dark grey diamonds); 0.5 mg/mL (light grey diamonds). Cleaved C47S was unable to be produced and the tagged construct was not able to be concentrated to higher than 1 mg/mL.

